Manual of diagnostic ultrasound

vol. 2

During the last decades , use of ultrasonography became increasingly common in medical practice and hospitals around the world, and a large number of scientific publications reported the benefit and even the superiority of ultrasonography over commonly used X-ray techniques, resulting in significant changes in diagnostic imaging procedures.

With increasing use of ultrasonography in medical settings, the need for education and training became essential. WHO took up this challenge and in 1995 published its first training manual in ultrasonography. Soon, however, rapid developments and improvements in equipment and indications for the extension of medical ultrasonography into therapy indicated the need for a totally new ultrasonography manual.

The manual (consisting of two volumes) has been written by an international group of experts of the World Federation for Ultrasound in Medicine and Biology (WFUMB), well-known for their publications regarding the clinical use of ultrasound and with substantial experience in the teaching of ultrasonography in both developed and developing countries. The contributors (more than fifty for the two volumes) belong to five different continents, to guarantee that manual content represents all clinical, cultural and epidemiological contexts

This new publication, which covers modern diagnostic and therapeutic ultrasonography extensively, will certainly benefit and inspire medical professionals in improving 'health for all' in both developed and emerging countries.

ISBN 978 92 4 154854 0

Vol. 2

Manual of diagnostic ultrasound

Manual of diagnostic ultrasound

volume 2

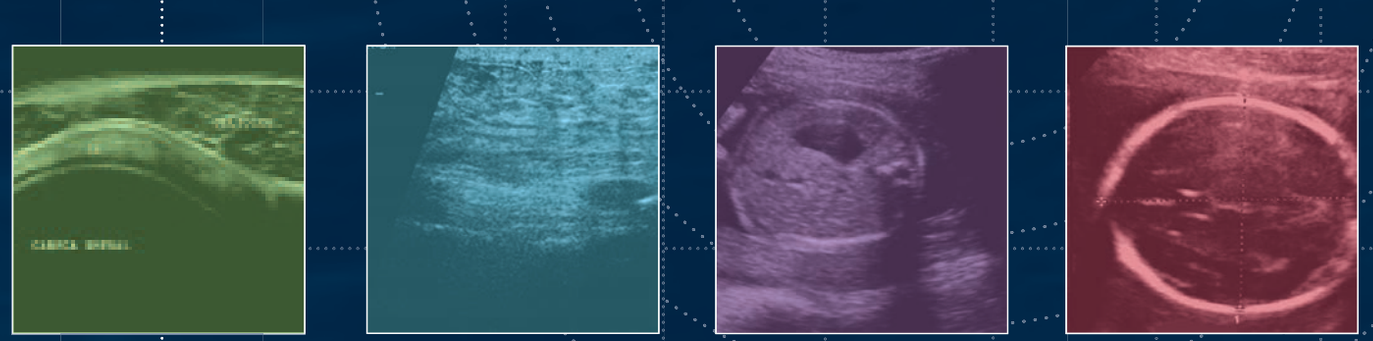

Second edition

WHO

World Health Organization

Manual of diagnostic ultrasound

volume 2

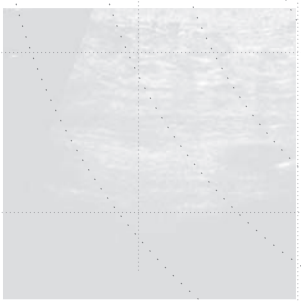
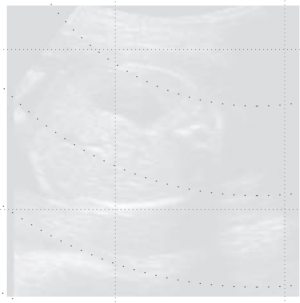
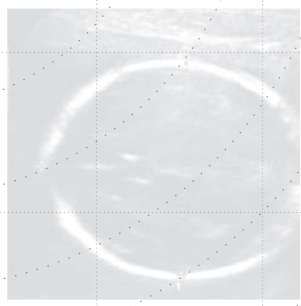

Second edition

World Health Organization

WHO Library Cataloguing-in-Publication Data

Manual of diagnostic ultrasound. Vol. 2 – 2nd ed. / edited by Elisabetta Buscarini, Harald Lutz and Paoletta Mirk.

1.Diagnostic imaging. 2.Ultrasonography. 3.Pediatrics - instrumentation. 4.Handbooks. I.Buscarini, Elisabetta. II.Lutz, Harald. III.Mirk, P. IV.World Health Organization. V.World Federation for Ultrasound in Medicine and Biology.

ISBN 978 92 4 154854 0 (NLM classification: WN 208)

Production editor: Melanie Lauckner
Design & layout: Sophie Guetaneh Aguettant and Cristina Ortiz

Printed in Slovenia

Contents

Acknowledgements

The Editors **Elisabetta Buscarini, Harald Lutz** and **Paoletta Mirk** wish to thank all members of the Board of the World Federation for Ultrasound in Medicine and Biology for their support and encouragement during preparation of this manual.
The Editors also express their gratitude to and appreciation of those listed below, who supported preparation of the manuscript by contributing as co-authors and by providing illustrations and competent advice.

Domenico Arduini: Department of Obstetrics and Gynecology, University of Roma Tor Vergata, Rome, Italy
Stan Barnett: Discipline of Biomedical Science, Faculty of Medicine, University of Sydney, Sydney, Australia
Ibtissem Bellagha: Department of Paediatric Radiology, Tunis Children's Hospital, Tunis, Tunisia
Paolo Belli: Department of Radiological Sciences, Catholic University of the Sacred Heart, Rome, Italy
Leonardo Caforio: Department of Obstetrics and Gynecology, Catholic University of the Sacred Heart, Rome, Italy
Lucia Casarella: Department of Obstetrics and Gynecology, Catholic University of the Sacred Heart, Rome, Italy
Anna Franca Cavaliere: Department of Obstetrics and Gynecology, Catholic University of the Sacred Heart, Rome, Italy
Giovanni Cerri: School of Medicine, University of Sao Paulo, Sao Paulo, Brazil
Maria Cristina Chammas: School of Medicine, University of Sao Paulo, Sao Paulo, Brazil
Ferid Ben Chehida: Department of Radiology, Ibn Zohr Center, Tunis, Tunisia
Melania Costantini: Department of Radiological Sciences, Catholic University of the Sacred Heart, Rome, Italy
Alain Couture: Department of Paediatric Radiology, Arnaud de Villeneuve Hospital, Montpellier, France
Vincenzo D'Addario: Department of Obstetrics, Gynecology and Neonatology, University of Bari, Bari, Italy
Marco De Santis: Department of Obstetrics and Gynecology, Catholic University of the Sacred Heart, Rome, Italy
Josef Deuerling: Department of Internal Medicine, Klinikum Bayreuth, Bayreuth, Germany

Alessandra Di Giovanni: Department of Obstetrics and Gynecology, University of Roma Tor Vergata, Rome, Italy
Alessia Di Legge: Department of Obstetrics and Gynecology, Catholic University of the Sacred Heart, Rome, Italy
Wiem Douira Khomsi: Department of Paediatric Radiology, Tunis Children's Hospital, Tunis El Manar University, Tunis, Tunisia
Caterina Exacoustos: Department of Obstetrics and Gynecology, University of Roma Tor Vergata, Rome, Italy
Hassen A Gharbi: Department of Radiology, Ibn Zohr Center, Tunis, Tunisia
Azza Hammou: National Center for Radio Protection, Tunis, Tunisia
Hela Louati: Department of Paediatric Radiology, Tunis Children's Hospital, Tunis, Tunisia
Lucia Masini: Department of Obstetrics and Gynecology, Catholic University of the Sacred Heart, Rome, Italy
Maria Elena Pietrolucci: Department of Obstetrics and Gynecology, University of Roma Tor Vergata, Rome, Italy
Maurizio Romani: Department of Radiological Sciences, Catholic University of the Sacred Heart, Rome, Italy
Paolo Rosati: Department of Obstetrics and Gynecology, Catholic University of the Sacred Heart, Rome, Italy
Cristina Rossi: Department of Obstetrics, Gynecology and Neonatology, University of Bari, Bari, Italy
Renato A. Sernik: Musculoskeletal Dept. Clinical Radiology, University of Sao Paulo, Sao Paulo, Brazil
Stefania Speca: Department of Radiological Sciences, Catholic University of the Sacred Heart, Rome, Italy
Antonia Carla Testa: Department of Obstetrics and Gynecology, Catholic University of the Sacred Heart, Rome, Italy
Claudia Tomei: Department of Obstetrics and Gynecology, Catholic University of the Sacred Heart, Rome, Italy
Corinne Veyrac: Department of Paediatric Radiology, Arnaud de Villeneuve Hospital, Montpellier, France
Daniela Visconti: Department of Obstetrics and Gynecology, Catholic University of the Sacred Heart, Rome, Italy
Maria Paola Zannella: Department of Obstetrics and Gynecology, Catholic University of the Sacred Heart, Rome, Italy

Chapter 1

Safety of diagnostic ultrasound

1

Safety of diagnostic ultrasound

Ultrasound and the World Health Organization

The World Health Organization (WHO) recognizes ultrasound as an important medical diagnostic imaging technology. Manuals on ultrasound have been published by WHO since 2001, with the purpose of guiding health professionals on the safe and effective use of ultrasound. Among the diagnostic imaging technologies, ultrasound is the safer and least expensive, and technological advances are making it more user friendly and portable. Ultrasound has many uses, both diagnostic and therapeutic. For the purposes of this manual, only diagnostic ultrasound will be considered and further analysed.

Basic physics of ultrasonographic imaging was released in 2005; since then, WHO has addressed the physics, safe use and different applications of ultrasound as an important diagnostic imaging tool. Since it is a nonionizing radiation technology, along with nuclear magnetic resonance imaging, the risks inherent to its use are lower than those presented by other diagnostic imaging technologies using ionizing radiation, such as the radiological technologies (X-rays and computed tomography scanners).

To disseminate policies, programmes and strategies, WHO holds the official collaboration of international nongovernmental organizations. Out of 183 such organizations, at least four deal with topics related to ultrasound:

- ISR: the International Society of Radiology
- ISRRT: the International Society of Radiographers and Radiological Technologists
- IFMBE: the International Federation for Medical and Biological Engineering
- WFUMB: the World Federation for Ultrasound in Medicine and Biology.

It is WFUMB that has authored and edited volumes 1 and 2 of this *Manual of Diagnostic Ultrasound*.

WHO has three collaborating centres working on studies to demonstrate the clinical effectiveness, economic impact and affordability of ultrasound technologies. Today, these studies are being conducted by the following WHO collaborating centres: the National Center for Fetal Medicine, Trondheim University Hospital (Norway), Jefferson Ultrasound Research and Education Institute (USA) and the National Center for Health Technology Excellence (Mexico).

The Diagnostic Imaging and Medical devices unit of the Department of Essential Medicines and Health products of WHO's Health Systems and Innovation cluster, along with WHO's Public Health and Enviroment cluster, are working on the Basic Safety Standards and the Basic Referral Guidelines, which will support and recommend the use of ultrasound for specific diseases and diagnostics.

The WFUMB has been working with WHO for 10 years in the publishing and editing of ultrasound manuals, from the first version to the present one, to increase the safe use of ultrasound for the different pathologies that will be demonstrated in volumes 1 and 2 of this publication.

WHO is now working with the International Commission of Non-Ionizing Radiation to review the safe use of ultrasound for diagnostic and therapeutic applications.

Safety of ultrasound

The use of diagnostic ultrasound is generally accepted as safe, in the absence of plausible, confirmed evidence of adverse outcome in humans. Nevertheless, with rapid technological advances, the possibility of ultrasound-induced adverse effects occurring in the future cannot be ruled out. While there may be no concern with regard to most applications, prudent use is justified. Obstetric applications are of particular concern, as rapidly dividing and differentiating embryonic and fetal tissues are sensitive to physical damage, and perturbation of cell differentiation might have significant biological consequences. Technological advances have resulted in improved diagnostic acuity but have been accompanied by substantially increased levels of acoustic output, and the possible health effects of equivalent levels of exposure have not been studied in humans.

Modern ultrasound equipment combines a range of frequencies in complex scan modes to increase diagnostic accuracy. Misdiagnosis is, however, a real risk to patients, and the clinical benefit of procedures such as Doppler flow embryosonography should be established. Unregulated use of freely available equipment by unaccredited or inadequately trained people increases the risk for misdiagnosis and harm. So-called entertainment or social scanning is frowned upon by professional ultrasound societies and is the subject of a project of the Safety Committee of the World Federation for Ultrasound in Medicine and Biology.

In obstetrics scanning, the amount of ultrasound-induced heating of the fetus correlates with gestational age and increasing mineralization of bone. Because of its particularly high acoustic absorption characteristics, bone is rapidly heated when placed in the path of an ultrasound beam. Significant increases in temperature have been consistently recorded when pulsed Doppler ultrasound beams encounter bone in either transcranial or fetal exposures. The greatest heating is usually associated with the use of pulsed spectral Doppler ultrasound applications, in which a stationary beam of relatively high intensity is directed at a single tissue target. As a result, tissue near bone can be heated by around 5 °C. A responsible, cautious approach

is justified, particularly in the use of Doppler ultrasound in pregnancy; however, there is no risk for adverse heating effects from simple B-mode ultrasound scanning procedures when tissues are insonated for fractions of a second each time a beam passes. Diagnostic ultrasound causes a modest temperature increase in soft embryonic tissue and is unlikely to be a major concern, thermally, during the first trimester.

The World Federation for Ultrasound in Medicine and Biology concluded that the effects of elevated temperatures can be minimized by keeping the time during which the beam passes through any area of tissue as short as possible.

The nonthermal biological effect that has been most thoroughly examined is acoustic inertial cavitation, which involves collapse of bubbles in liquid in a sound field and the sudden release of energy, which can be sufficiently intense to disrupt molecular bonds.

While it is comforting that there is no conclusive evidence of serious adverse health effects caused by antenatal exposure to ultrasound, the scientific database has obvious limitations and inadequacies. The available epidemiological data refer to exposure to ultrasound at levels considerably lower than those from modern ultrasonographic equipment. There are no data on perinatal applications of spectral or colour flow Doppler or of other modern ultrasound procedures, such as harmonic imaging techniques and use of echocontrast agents.

It is important that users of ultrasound for clinical purposes:

- monitor the thermal and mechanical indices and keep them as low as consistent with clinical needs;
- document output display indices as a part of the permanent record of an examination;
- verify the accuracy of the displayed mechanical index, particularly when new hardware or software is introduced;
- examine the adequacy of the mechanical index as a guide to the likelihood of rupture of contrast microbubbles.

It is suggested that manufacturers set the default (switch-on) mechanical index to less than 0.4, except for high mechanical index modes, and that they provide an unambiguous on-screen display of centre frequency (acoustic working frequency). For scientific purposes, it would be helpful if the value of the peak negative acoustic pressure were made available, to allow studies of alternative means of assessing clinical biological responses under particular circumstances.

Conclusion

Ultrasound is a core technology for diagnostics and remains one of the safest. Clinical effectiveness is enhanced when used properly. The following chapters provide information on the best use and applications of diagnostic ultrasound. A responsible, cautious approach to ultrasound is required to maintain safety, particularly in the use of Doppler ultrasound in pregnancy. The output displays on modern ultrasonographic equipment allow users to take greater responsibility in risk–benefit assessments. With new ultrasound applications, continued safety and effectiveness can be assured only if it is used according to recognized guidelines at the lowest exposure necessary to provide essential diagnostic information.

Chapter 2

Obstetrics

2

Obstetrics

First trimester

The first trimester is the gestational period between conception and 13 weeks + 6 days of gestational age. An **embryo** is the product of conception until 10 weeks + 0 days of gestational age; a **fetus** is the product of conception from 10 weeks + 1 day until delivery.

Indications

The indications for ultrasound during the first trimester are:

- vaginal bleeding or pelvic pain;
- a discrepant uterine size for gestational age;
- estimation of gestational age;
- support for an invasive diagnostic procedure (e.g. sampling the chorionic villus);
- prediction of the risk for recurrence of fetal anomalies;
- screening for fetal anomalies and aneuploidies (in selected, high-risk pregnancies);
- routine assessment (screening) of low-risk pregnancies.

The purposes of ultrasound during the first trimester are:

- to visualize the gestational sac inside the uterus and evaluate the number and implant site of sacs;
- to visualize the embryo or fetus, evaluate their number and visualize their cardiac activity;
- to estimate gestational age, by measuring the mean sac diameter or crown–rump length or the biparietal diameter of the head;
- to evaluate the morphology of the uterus and adnexa;
- to provide an early diagnosis of fetal anomalies (in selected cases);
- to screen for aneuploidy (in selected cases).

With these evaluations, it is possible to diagnose during the first trimester:

- a normal (intrauterine) or ectopic (intra- or extrauterine) implant;
- embryo or fetus life or early pregnancy failure (miscarriage, abortion);

- the number of embryos or fetuses (single or multiple pregnancy);
- chorionicity and amnionicity in multiple pregnancies;
- correct gestational age;
- anomalies of the uterus (e.g. malformations, myomas) and adnexa (e.g. cysts, neoplasms);
- morphological fetal abnormalities;
- aneuploidy, by measuring nuchal translucency between 11 and 14 weeks of gestation.

Preparation

For **transabdominal ultrasound**, the woman should have a full bladder. To fill her bladder, the woman should drink 1 l (four glasses) of water 0.5–1 h before the procedure. If the woman cannot drink and transabdominal ultrasound must be used, the bladder can be filled with saline solution through a Foley catheter. For **transvaginal ultrasound**, the woman should have an empty bladder: she must void her bladder immediately before the procedure.

Examination technique

The first trimester scan can be made either transvaginally or transabdominally. If a transabdominal scan does not provide all the necessary information, it should be complemented by a transvaginal scan, and vice versa.

Position and scanning technique

For transabdominal ultrasound, the woman should lie on the examination bed on her back, with extended or flexed legs. After ultrasonographic gel has been applied to the woman's skin, the ultrasonographic probe should be used to examine the pelvis and lower part of the abdomen in horizontal (transverse), vertical (sagittal) and oblique scanning planes (Fig. 2.1a).

For transvaginal ultrasound, the woman must be lying on the examination bed on her back in the gynaecological position, with flexed hips and knees on supports. A clean transvaginal probe placed in an aseptic probe cover (condom) filled with ultrasonographic gel is inserted into the anterior fornix of the vagina. The pelvis should be examined in all planes by smoothly moving and rotating the probe inside the vagina (Fig. 2.1b).

Technical characteristics of ultrasound probes

For transabdominal ultrasound, the probe frequency should be at least 3.5 MHz; for transvaginal ultrasound, the probe frequency should be at least 5.0 MHz.

Fig. 2.1. (a) Transabdominal ultrasound, convex probe. (b) Transvaginal ultrasound, convex probe. P, pelvic bone; B, bladder (full in (a); empty in (b)); U, uterus; star, gestational sac; R, rectum

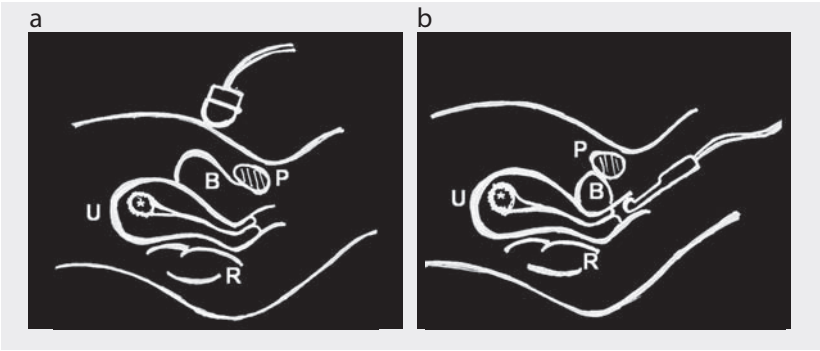

End-points of first-trimester scans

- Establish the presence of a gestational sac inside the uterus.
- Visualize the embryo or fetus.
- Evaluate the number of embryos or fetuses.
- Establish the presence or absence of embryonic or fetal cardiac activity, only with B-mode or M-mode technique up to 10 weeks + 0 days; later, pulse or colour Doppler can be used.
- Estimate gestational age by one of two means.

The mean gestational sac diameter can be measured from 5–6 to 11 weeks but is advisable only if the embryo cannot be assessed. The gestational sac can be visualized from 6 menstrual weeks by transabdominal ultrasound and from 5 weeks by transvaginal ultrasound. It is suggested that the mean sac diameter be measured from the average internal diameter of the gestational sac, calculated by adding the three orthogonal dimensions of the chorionic cavity (anteroposterior, longitudinal and transverse) and dividing by 3, with the calipers inner-to-inner on the sac wall, excluding the surrounding echogenic rim of tissue (Fig. 2.2).

The gestational age, *a*, can be calculated from the mean sac diameter, *d*, with the formula:

$$a = d + 30$$

where *a* is measured in days and *d* in millimetres.

Embryo or fetus size can be measured from the **crown–rump length** or **biparietal diameter**. Crown–rump length can be measured by transvaginal ultrasound when the embryo reaches 2–5 mm (5–6 weeks' menstrual age) and by transabdominal ultrasound at 5–10 mm (6–7 weeks). The conventional crown–rump length

Fig. 2.2. Measurement of diameter of mean gestational sac at 7 weeks' gestational age, using transvaginal ultrasound. (a) Longitudinal and anteroposterior sac diameter. (b) Transverse sac diameter. The yolk sac (arrow) and a subserosal fibroid (F) are also visible

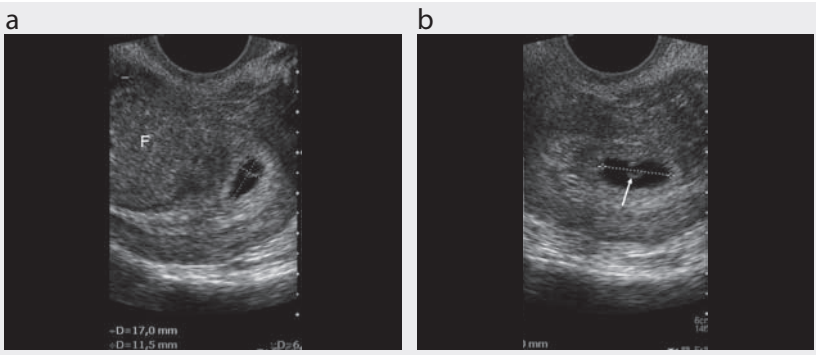

measurement is the maximal straight-line length of the embryo or fetus, obtained along its longitudinal axis; the embryo or fetus must be neither too flexed (curved) nor too extended. The accuracy of crown–rump length for dating pregnancy is ± 3–4 days between 7 and 11 weeks (Fig. 2.3).

Fig. 2.3. Measurement of crown–rump length (calipers) with transvaginal ultrasound, at 8 weeks' gestational age

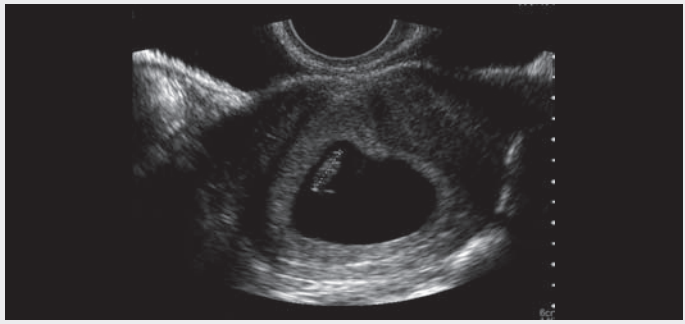

Because normal embryonic growth is almost linear at 1 mm/day, gestational age, *a*, can be estimated with an accuracy of ± 3 days between 43 and 67 days, from the formula:

$$a = l + 42$$

where *a* is measured in days and crown–rump length, *l*, in millimetres.

Towards the end of the first trimester, rapid fetal development and flexion and extension positional changes limit the accuracy of crown–rump length determination, and measurement of the biparietal diameter of the head becomes the preferred biometric for calculating gestational age. The accuracy of measurement of biparietal diameter between 12 and 16 weeks' gestational age is ± 3–4 days. The diameter must be measured in a transverse section of the fetal head at the level of the thalami, the positioning of the calipers depending on the reference curve used (Fig. 2.4).

- Evaluate the morphology of the uterus and adnexa.
- Evaluate chorionicity and amnionicity in twin pregnancies.

Fig. 2.4. Measurement of biparietal diameter, transverse section of fetal head. (a) Transvaginal ultrasound, 11 weeks; the calipers are positioned outer-to-outer on the skull. (b) Transabdominal ultrasound, 13 weeks; the calipers are positioned outer-to-inner on the skull

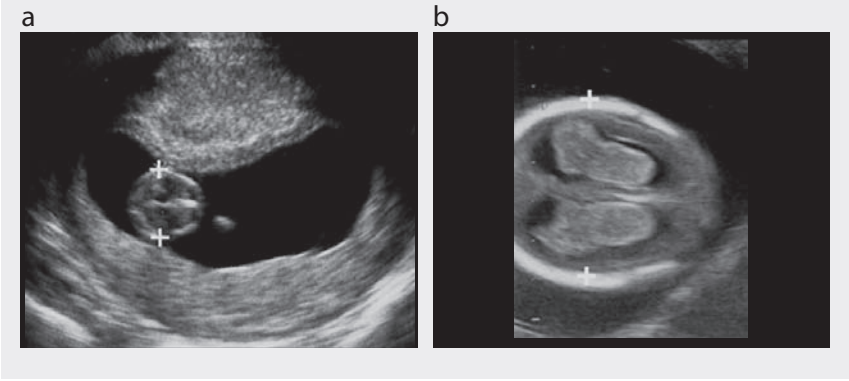

Normal findings

The first sonographic finding to suggest early pregnancy is visualization of the gestational sac. With transabdominal ultrasound, it is possible to visualize the gestational sac at as early as 5 weeks' gestational age; with transvaginal ultrasound, the gestational sac is visible when the mean sac diameter is 2–3 mm, at a gestational age of slightly more than 4 weeks (Fig. 2.5). The sac appears as a small, round fluid collection completely surrounded by an echo-rich rim of tissue, located in a lateral position in the uterine fundus. As the sac implants into the decidualized endometrium, it is possible to visualize the so-called double decidual sac or inter-decidual sign as a second echo-rich ring around the sac, caused by the decidual reaction to sac implantation.

Table 2.1 lists the visible landmarks that can be used for pregnancy dating.

The **yolk sac** is the first anatomical structure to be identified within the gestational sac. With transvaginal ultrasound, it can be seen as early as 5 weeks' gestational

Fig. 2.5. (a) Transverse transvaginal scan of early pregnancy (6 weeks): the round gestational sac (arrow) containing the yolk sac is implanted eccentrically inside the uterine cavity. (b) Three-dimensional reconstruction of the uterine cavity containing the gestational sac (arrow)

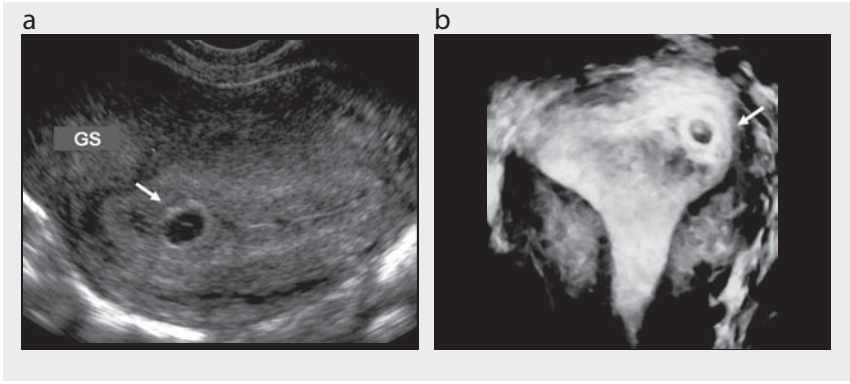

Table 2.1. Guidelines for dating a pregnancy during the first trimester by transvaginal ultrasound

Stage of development	Gestational age (weeks)
Gestational sac (no yolk sac, embryo or heartbeat)	5.0
Gestational sac and yolk sac (no embryo or heartbeat)	5.5
Gestational sac and yolk sac (living embryo too small to be measured, crown–rump length < 5 mm)	6.0
Embryo or fetus ≥ 5 mm in length	Based on crown–rump length[a]

[a] See Table 2.2

age (mean sac diameter, 5 mm), while with transabdominal ultrasound, the yolk sac should be evident by 7 weeks (mean sac diameter, 20 mm). The yolk sac diameter increases steadily between 5 and 10 weeks' gestational age, to a maximum diameter of 5–7 mm, which corresponds to a crown–rump length of 30–45 mm. The yolk sac is spherical, with a well-defined echogenic periphery and a sonolucent centre and is located in the chorionic cavity, outside the amniotic membrane.

Often, the **vitelline duct** is visible. It corresponds to the omphalomesenteric duct, which connects the embryo and the yolk sac; the vitelline vessels can be detected with colour Doppler. By the end of the first trimester, the yolk sac is no longer seen (Fig. 2.6).

Fetal membranes and amniotic cavity: At 6 weeks' gestational age, the amniotic membrane is formed, closely applied to the embryo, but it is not usually identified until 7 weeks because it is very thin. With transvaginal ultrasound, the thin amniotic membrane becomes apparent, surrounding the embryo at 6–7 weeks, with a crown–rump length of 7 mm. The amniotic sac appears as a circular structure inside the coelomic cavity. The diameter of the amniotic sac increases linearly with

Fig. 2.6. (a) Yolk sac (arrow) and easily visible vitelline duct. (b) Yolk sac (arrow) inside the coelomic cavity; the embryo and the amniotic membrane are also visible

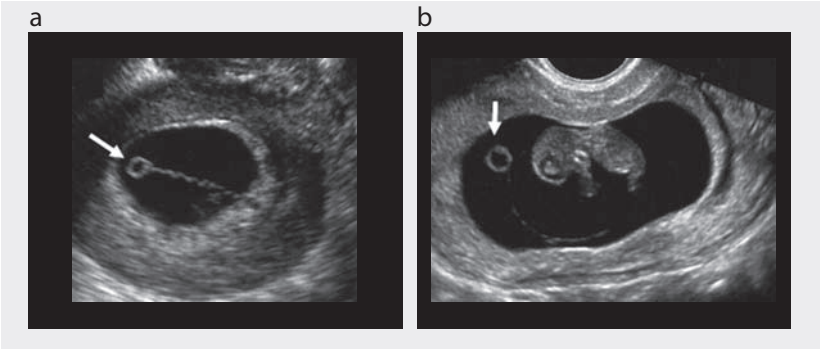

crown–rump length. Because the amniotic cavity enlarges more rapidly than the chorionic cavity, the latter is obliterated as the amniotic membrane reaches the chorion. Apposition begins in the middle of the first trimester but is often incomplete until 12–16 weeks' gestational age (Fig. 2.7).

Fig. 2.7. (a, b) Transvaginal ultrasound, showing the thin amniotic membrane (arrow) dividing the amniotic from the coelomic cavity

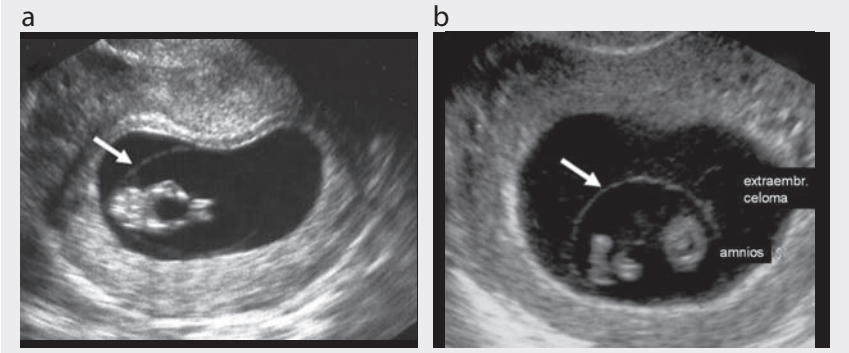

Placenta and umbilical cord: Placental development begins during the 8th week of gestational age. The echo-rich ring surrounding the sac becomes asymmetric, with focal peripheral thickening of the most deeply embedded portion of the sac. At 8 weeks' gestational age, the vitelline and allantoic ducts are visible as a thick structure connecting the embryo to the gestational sac wall. Once the amniotic membrane has developed, the vitelline duct separates from the forming umbilical cord, which then elongates, and its vessels start coiling inside the Wharton jelly (Fig. 2.8).

Embryo and fetus: At 5 weeks' gestational age, the embryonic disc is visible using transvaginal ultrasound as a subtle area of focal thickening (1–2 mm in length)

Fig. 2.8. Umbilical cord and placenta on transvaginal ultrasound. (a) 11 weeks; (b) 9 weeks

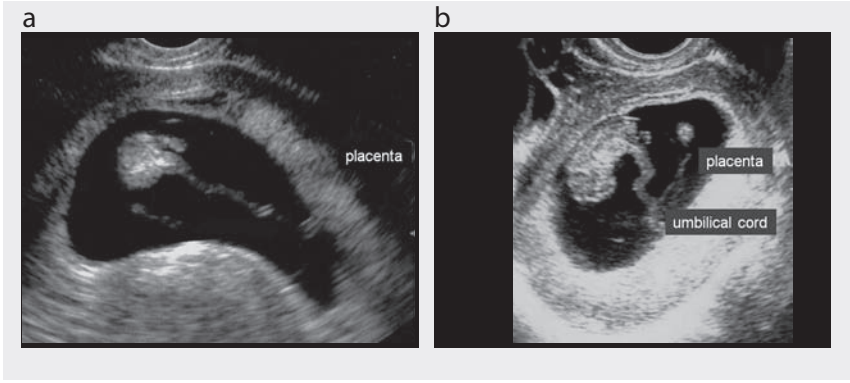

along the periphery of the yolk sac, when the mean diameter of the gestational sac is 5–12 mm. Sonographic observations throughout the embryonic period reveal dramatic changes in anatomical structures between 6 and 10 weeks, with the crown–rump length increasing by 1 mm/day. At 6 weeks, due to the ventral folding of its cranial and caudal ends, the shape of the embryo changes from a flat disc into a C-shaped structure. The rapidly developing brain becomes prominent, and the head size is almost half the total length of the embryo, while the caudal end elongates and curves, generating a tail. At this stage, the amniotic sac develops, and the embryo and the yolk sac diverge progressively. Limb buds appear at 7–8 weeks and evolve, protruding ventrally by 9 weeks. The trunk elongates and straightens, and the midgut herniates into the umbilical cord. At 10 weeks (crown–rump length, 30–35 mm), the embryo has visible hands and feet, and the tail has disappeared. Table 2.2 shows the relations between crown–rump length and gestational age.

The midgut herniation turns into the abdominal cavity at 11–12 weeks' gestational age. Fetal movements can be detected from 7 weeks and increase in complexity at 9 weeks; flexion and extension of the body and limbs are clearly visible by 10–12 weeks. At 10 weeks (72 days from the last menstrual period; 56 days' conceptional age), embryogenesis is almost complete, and the embryo becomes a fetus (Fig. 2.9).

Cardiac activity: Cardiac contractions begin at 5 weeks + 2 days (37 days from the last menstrual period) when the embryonic length is 1.6 mm. The heartbeat can be detected routinely with transvaginal ultrasound at 6 weeks (embryonic length, 4–5 mm; mean sac diameter, 13–18 mm). With transabdominal ultrasound, cardiac activity is evident by 7 weeks (crown–rump length, 8–10 mm; mean sac diameter, 25 mm). Up to 10 weeks' gestational age, cardiac rates can be visualized in B-mode and recorded in M-mode; for safety reasons, pulse or colour Doppler should not be used.

Before 6 weeks, the cardiac rate is relatively slow (100–115 beats per min), although rates of 82 at 5 weeks and 96 beats per min at 6 weeks have been reported. Thereafter, it increases linearly, and by 8 weeks is 144–170 beats per min; after 9 weeks,

Table 2.2. Relations between crown–rump length and gestational age

Crown–rump length (mm)	Mean predicted gestational age (weeks)	Crown–rump length (mm)	Mean predicted gestational age (weeks)
2	5.7	29	9.7–9.9
3	5.9	30	9.9–10.0
4	6.1	31	10.0–10.1
5	6.2–6.3	32	10.1–10.2
6	6.4–6.5	33	10.2–10.3
7	6.6–6.7	34	10.3–10.4
8	6.7–6.9	35	10.4–10.5
9	6.9–7.0	36	10.5–10.6
10	7.1–7.2	37	10.6–10.7
11	7.2–7.4	38	10.7–10.8
12	7.4–7.5	39	10.8–10.9
13	7.5–7.7	40	10.9–11.0
14	7.7–7.9	41	11.0–11.1
15	7.9–8.0	42	11.1–11.2
16	8.0–8.2	43	11.2–11.3
17	8.1–8.3	44	11.2–11.4
18	8.3–8.5	45	11.3–11.4
19	8.4–8.6	46	11.4–11.5
20	8.6–8.7	47	11.5–11.6
21	8.7–8.9	48	11.6–11.7
22	8.9–9.0	49	11.7–11.8
23	9.0–9.1	50	11.7–11.9
24	9.1–9.3	51	11.8–11.9
25	9.2–9.4	52	11.9–12.0
26	9.4–9.5	53	12.0–12.1
27	9.5–9.6	54	12.0–12.2
28	9.6–9.7	55	12.1–12.3

Fig. 2.9. Midgut herniation (arrows) at 12 weeks. (a) Transverse transvaginal ultrasound of fetal abdomen. (b) Longitudinal transvaginal ultrasound of the fetus

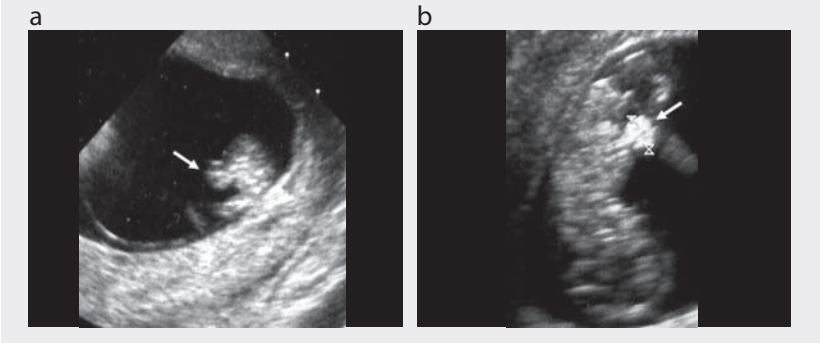

the rate plateaus at 137–150 beats per min. The cardiac rate is stable in early gestation but shows progressively more variation with gestational age.

Embryonic anatomy: With continued technological improvements, imaging of the embryo has progressed beyond identifying cardiac activity and measuring crown–rump length. By 10 weeks' gestational age, the fetal cranium, brain, neck, trunk, heart, bladder, stomach and extremities can be visualized, and gross anomalies can be detected or excluded in the late first trimester (after 12 weeks), mainly with transvaginal ultrasound. Ossification of the skull is reliably seen after 11 weeks, and examination of the four chambers of the heart is possible after 10 weeks (Fig. 2.10).

Fig. 2.10. Anatomical study by transvaginal ultrasound in the first trimester. (a) Inside the fetal head, cerebellum (right) and midline. (b) From the left: cerebellum, fourth ventricle, third ventricle and lateral ventricles. (c) Open fetal hand with fingers

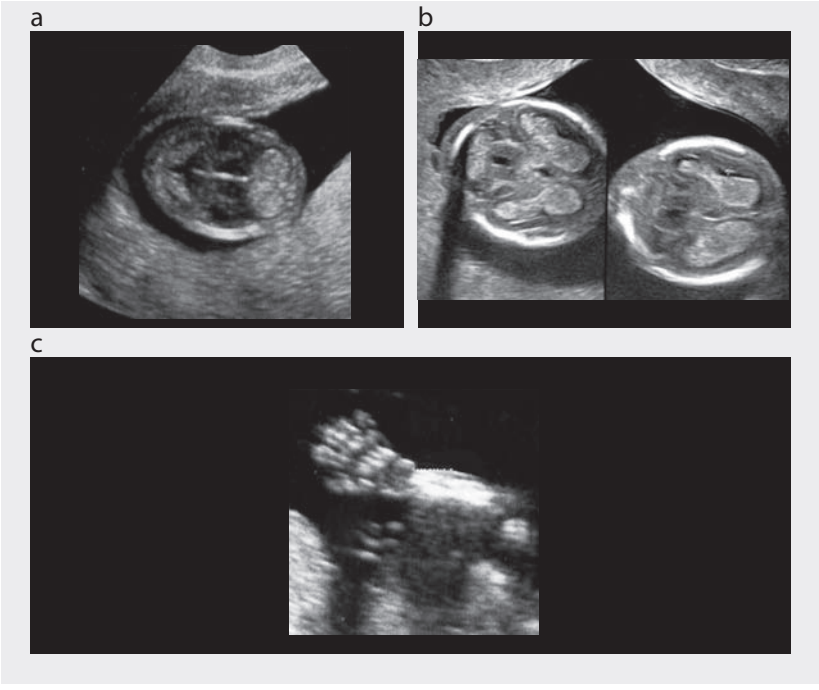

Twin pregnancies, determination of zygosity and chorionicity: Multiple pregnancies can result either from the ovulation and subsequent fertilization of more than one oocyte (to produce polyzygotic or nonidentical twins) or from the splitting of one embryonic mass to form two or more genetically identical fetuses (monozygotic twins). In all polyzygotic multiple pregnancies, each zygote develops its own amnion, chorion and placenta (polychorionic). In monozygotic pregnancies, the twins can share the same placenta (monochorionic), amniotic sac (monoamniotic) or even fetal organs (conjoined). When embryonic splitting occurs, the third day after

fertilization, there is vascular communication of the circulation in the two placentas (monochorionic). Zygosity can be determined only by DNA analysis, but chorionicity can be determined by ultrasound on the basis of the number of placentas, the characteristics of the membrane between the two amniotic sacs and fetal sex.

With transvaginal ultrasound, a multichorionic twin pregnancy, in which each fetus has a different amniotic sac and yolk sac can be easily recognized at 7–9 weeks' gestational age. The chorionic membrane is thick and echo-rich up to 10–11 weeks, and the two yolk sacs are always divided by a membrane. Sonographic examination of the base of the inter-twin membrane allows reliable differentiation of dichorionic and monochorionic pregnancies: in dichorionic twins, the inter-twin membrane is composed of a central layer of chorionic tissue between two layers of amnion; in monochorionic twins, there is no chorionic layer. In dichorionic twins, there is a thick septum between the two gestational sacs, which, at the base of the membrane, appears as a triangular tissue projection called the lambda sign, which is not present in monochorionic twins. The lambda sign is readily visible in the late first trimester but becomes progressively more difficult to identify with advancing gestation (Fig. 2.11).

Fig. 2.11. (a) Twin pregnancy at 9 weeks; transvaginal ultrasound. Thick septum between the two sacs. (b) Triplet pregnancy, of which one is monochorionic with a thin interamniotic septum (arrow). (c) Transabdominal ultrasound: dichorionic twins with thick septum (arrow). (d) Transabdominal ultrasound: quadruplets

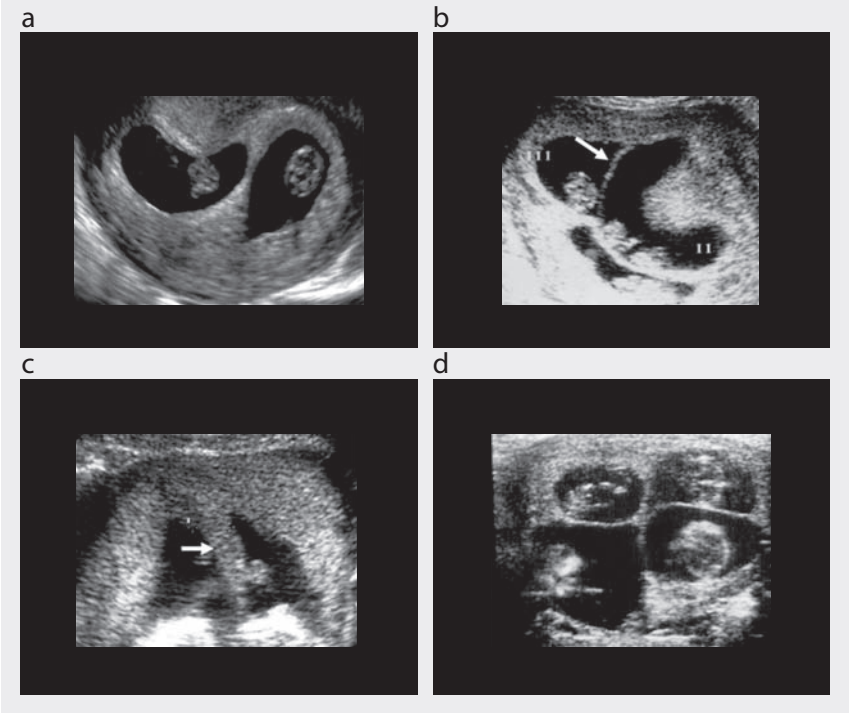

First-trimester screening for aneuploidy

In 1995, it was established that about 75% of fetuses with aneuploidy have greater nuchal translucency thickness, and 65–70% have no nasal bone between 11 and 13 weeks + 6 days of gestational age (crown–rump length, 45–84 mm). Fetal nuchal translucency normally increases with gestation and crown–rump length. The technical reasons for selecting 13 weeks + 6 days as the upper limit for measuring fetal nuchal translucency are that the incidence of abnormal fluid accumulation in fetuses with abnormal karyotypes is maximal before 14 weeks and the success rate of nuchal translucency measurements is 98–100% at 11–14 weeks, falling to 90% after 14 weeks because of the more frequent vertical position of the fetus. The normal upper limit for nuchal translucency changes with gestational age and crown–rump length and never exceeds 2.5 mm (Fig. 2.12).

Fig. 2.12. Nuchal translucency measurement (calipers) by transvaginal ultrasound. (a) Normal nuchal translucency. (b) Increased nuchal translucency with fetal hydrops. (c) Nasal bone (arrow) demonstrated by transvaginal sonography

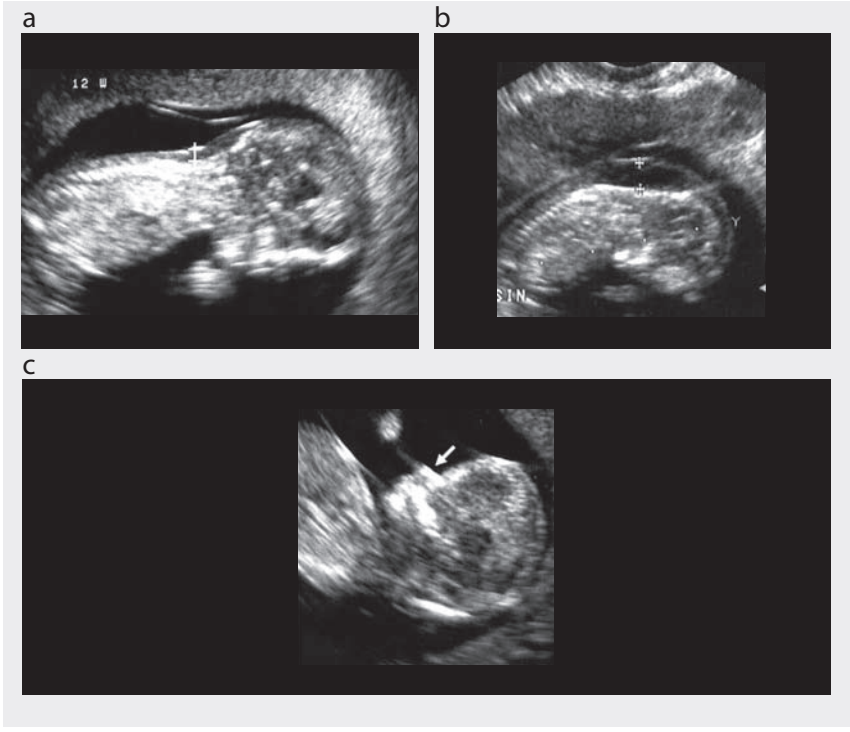

For computerized calculation of risk, abnormal nuchal translucency is expressed as the deviation from the expected normal median for a given crown–rump length.

The ultrasound machine should have high resolution, a video-loop function and calipers that provide measurements to one decimal point. Transabdominal

ultrasound is successful in about 95% of cases. Appropriate training of sonographers and adherence to a standard technique for measuring nuchal translucency are essential prerequisites for good clinical practice and for the success of a screening programme. To measure nuchal translucency:

- A mid-sagittal section of the fetus should be obtained, and nuchal translucency should be measured with the fetus in the neutral position and horizontal on the screen.
- Only the fetal head and upper thorax should be included in the image.
- The magnification should be as great as possible, such that a slight movement of the calipers causes only a 0.1-mm change in the measurement.
- The maximum thickness of the subcutaneous translucency between the skin and the soft tissue overlying the cervical spine should be measured.
- The calipers should be placed on the lines that define the thickness of the nuchal translucency.
- More than one measurement should be taken during the scan, and the maximum should be recorded.

The fetal nasal bone can be visualized at 11–14 weeks. Several studies have shown a strong association between an absent nasal bone in the late first trimester and trisomy 21, as well as other chromosomal abnormalities. The fetal profile can be examined in more than 95% of cases at 11–14 weeks (Fig. 2.12). In chromosomally normal fetuses, the nasal bone is absent in less than 1% of Caucasians and Asians and in about 10% of Afro-Caribbeans. It is absent in 65–70% of cases of trisomy 21, more than 50% cases of trisomy 18 and 30% of cases of trisomy 13. For examination of the nasal bone:

- The image should be magnified so that only the fetal head and upper thorax are included.
- A mid-sagittal view of the fetal profile should be obtained with the ultrasound transducer held in parallel to the direction of the nose.
- The image of the nose should contain three distinct lines: the top line represents the skin, the thicker, more echogenic line represents the nasal bone, and the third line, in continuity with the skin but higher, represents the tip of the nose (Fig. 2.12).

Pathological findings

Because of the complexity of first-trimester development, complications are frequent. Spontaneous miscarriage occurs in approximately 15% of clinically diagnosed pregnancies, but the loss rate is estimated to be two to three times higher in very early, often unrecognized pregnancies. Vaginal bleeding or spotting occurs in 25% of first-trimester pregnancies. Often, the bleeding is mild and self-limited, and

ultrasound usually shows normal findings. In cases of severe pain, uterine contractions, heavy bleeding or a dilated cervix, however, the pregnancy will probably fail, and ultrasound shows abnormal findings.

Intrauterine blood

In many cases of threatened abortion in the first trimester, but also in asymptomatic women, intrauterine blood collections are found on ultrasound examination. In early pregnancy, the genesis of such collections is usually normal implantation; later, it is often due to venous bleeding associated with separation of the placental margin or marginal sinus, with blood collection between the chorion and the endometrium. The finding of an intrauterine fluid collection near the gestational sac is due to subchorionic haemorrhage. The echogenicity of the blood depends on its age and the amount of clotting: recent haemorrhages are echo-poor or isoechoic, depending on the location (Fig. 2.13).

Fig. 2.13. Examples of large subchorionic haemorrhage (arrows) surrounding the gestational sac (dotted arrows). (a), (b) Recent echo-free haemorrhage. (c) Partially organized subchorionic haematoma

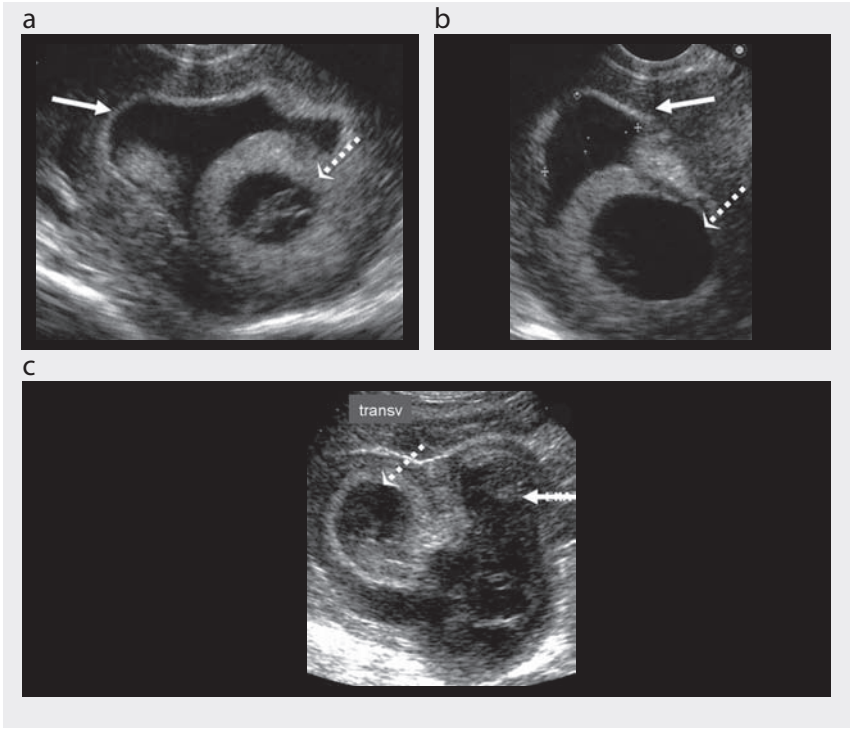

The pregnancy outcome in cases of visible intrauterine haematoma depends on the location and the size of the haematoma. The prognosis of a retroplacental

haematoma or a progressively larger haematoma is poor, but the evidence is equivocal. Despite vaginal bleeding, most women with intrauterine haematoma have successful pregnancy outcomes.

Abortion

Spontaneous abortion is defined as termination of a pregnancy before 20 completed weeks' gestational age. Sixty-five per cent of spontaneous abortions occur during the first 16 weeks of pregnancy. Recurrent abortion is defined as three or more consecutive spontaneous abortions; its occurrence is 0.4–0.8% of all pregnancies.

In cases of threatened abortion (vaginal bleeding with a long, closed cervix), ultrasound examination gives information about the evolution of the pregnancy. The term 'missed abortion' is not clear, and the term 'embryonic demise' should be used when a non-living embryo is found, whereas the term 'blighted ovum' should be used when a gestational sac with no visible embryo is found. Other entities that can present with symptoms suggesting threatened abortion are ectopic pregnancy and gestational trophoblastic disease. The ultrasonographic findings in women with threatened abortion are crucial both for diagnosis and therapy. Sometimes, for a more precise diagnosis, it is necessary to integrate the ultrasound images with the quantity of serum human chorionic gonadotropin (hCG).

The term 'incomplete abortion' is used when partial expulsion of products occurs. The ultrasound scan reveals retained products of conception, endometrial blood and trophoblastic tissue, with no normal gestational sac. In cases of 'complete abortion', with complete expulsion of the products of conception, the ultrasound scan shows an empty uterus with a normal or slightly thickened endometrium. For practical reasons, the ultrasound findings in diagnoses of abortion are divided into those that reveal an absent intrauterine sac, a sac with no embryo visible and a sac containing an embryo.

Absent intrauterine sac: On ultrasound examination, if the uterus appears normal or if the endometrial echoes appear thickened without a visible gestational sac, the differential diagnosis may be early spontaneous abortion, very early intrauterine pregnancy or ectopic pregnancy. The woman's history and the quantity of hCG can often clarify the sonographic findings. With transvaginal ultrasound, the gestational sac is usually visible at 4 weeks' gestational age, when the mean sac diameter is 2–3 mm and the hCG level 800–2600 IU/l; with both transvaginal and transabdominal ultrasound, a sac should be detected when its mean diameter is 5 mm, corresponding to 5 weeks' gestational age. If the hCG concentration is less than 1000 IU/l, it is difficult to identify the gestational sac. In these cases, it is advisable to repeat the hCG measurement and ultrasound after at least 48–72 h. If the hCG level is more than 2500 IU/l and no gestational sac is visible inside the uterus, the probability of an ectopic pregnancy is high.

Intrauterine sac without an embryo or yolk sac: In this situation, there are three possible diagnoses: a normal early intrauterine pregnancy, an abnormal intrauterine pregnancy or a pseudogestational sac in an ectopic pregnancy. In theory, an

Fig. 2.14. Transvaginal ultrasound in cases of spontaneous abortion. (a) Intrauterine sac containing a yolk sac and a small embryo (> 5 mm) without a heartbeat. (b) Non-living embryo (crown–rump length, 20 mm). (c) Bright yolk sac (arrow), often seen in abortion. (d) Twin abortion at 10 weeks' gestational age: transverse scan demonstrates an empty gestational sac (right) and a gestational sac containing a small embryo (< 5 mm; left) near the inter-twin membrane

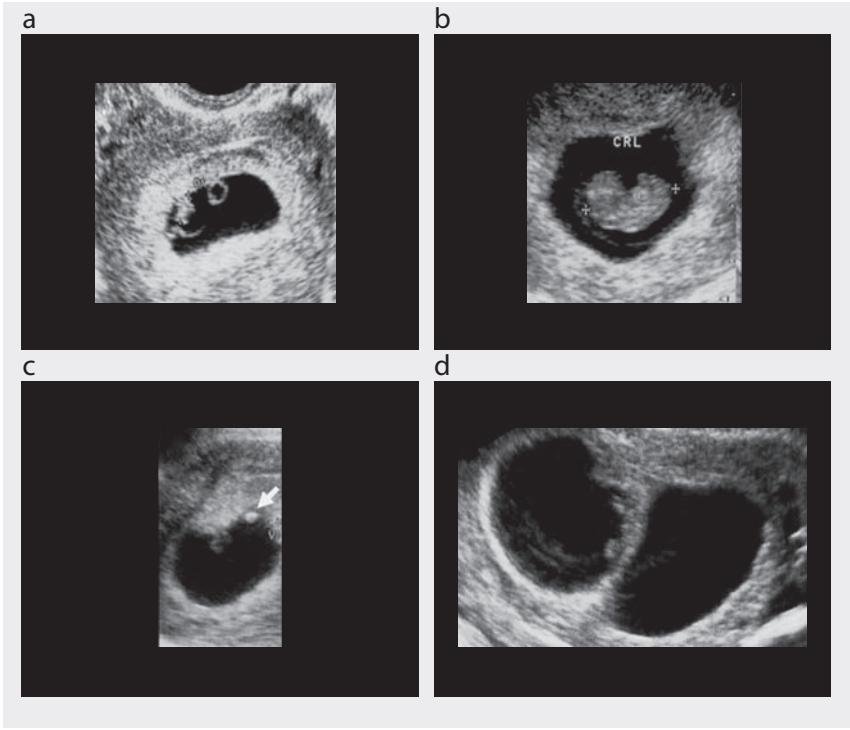

intrauterine sac can be distinguished from a pseudogestational sac, as the former is located within the decidua and the latter is within the uterine cavity. In practice, this distinction is often difficult, and a follow-up ultrasound should be made to verify the subsequent appearance of the yolk sac or the embryo. Size criteria can be used to differentiate a normal from an abnormal intrauterine sac. With transabdominal ultrasound, discriminatory size criteria suggestive of an abortion include: failure to detect a double decidual sac with a mean gestational sac diameter of ≥ 10 mm; failure to detect a yolk sac with a mean gestational sac diameter of ≥ 20 mm; and failure to detect an embryo and its cardiac activity with a mean gestational sac diameter of ≥ 25 mm. With transvaginal ultrasound, the discriminatory size criteria are: failure to detect a yolk sac with a mean gestational sac diameter of ≥ 8 mm; and failure to detect an embryo and its cardiac activity with a mean gestational sac diameter of ≥ 20 mm. The normal gestational sac grows at 1.13 mm/day, whereas an abnormal sac is estimated to grow at only 0.70 mm/day. If the ultrasound findings are controversial, the examination is difficult or the sonographer is inexperienced, caution is

warranted, and follow-up ultrasound should be done after an appropriate interval to obviate the risk of terminating a normal intrauterine pregnancy.

Intrauterine sac containing an embryo: When an embryo is visible with transabdominal ultrasound but cardiac activity is absent, the prognosis is poor. Nevertheless, cardiac activity is not detectable in very small embryos; the discriminatory embryonic size for detecting cardiac motion by transabdominal ultrasound is 10 mm. With transvaginal ultrasound, the discriminatory crown–rump length for visualizing cardiac motion is 5 mm. If the embryonic length is less than the discriminatory size, women should be managed expectantly, and follow-up ultrasound should be done when the expected crown–rump length exceeds the discriminatory value. When the crown–rump length exceeds the discriminatory length and cardiac activity is absent, a nonviable gestation is diagnosed (missed abortion or embryonic demise). Observation of the heartbeat inside the embryo is helpful for evaluating its relation to the yolk sac. At 6–7 weeks' gestational age, the embryo and the yolk sac

Fig. 2.15. Transabdominal ultrasound in cases of spontaneous abortion. (a) Empty gestational sac at 7 weeks + 3 days, with a leiomyoma of the posterior uterine wall (arrow). (b, c) Spontaneous expulsion of gestational sac and placenta (visible as a complex mass) in transverse (b) and longitudinal (c) scans of the uterine cervix. (d) Embryonic demise at 16 weeks' menstrual age, 8 weeks' gestational age: a large gestational sac, filling the uterine cavity completely, shown in transverse (top) and longitudinal (bottom) scans of the uterus

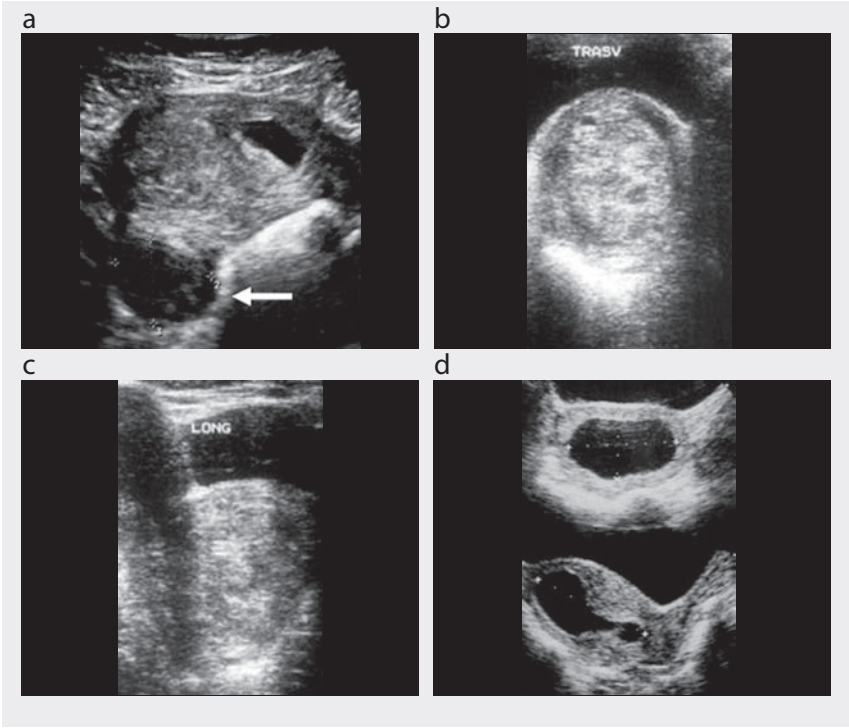

are contiguous; they diverge after 7 weeks. Cardiac activity should be recorded at the highest transducer frequency available in real-time or M-mode; for safety reasons, Doppler should be avoided before 10 weeks' gestational age. The normal cardiac rate should be > 100 beats per min up to 6 weeks + 2 days and > 120 beats per min later (Fig. 2.14, Fig. 2.15).

Ectopic pregnancy

An ectopic pregnancy is defined as a pregnancy that occurs outside the uterine cavity. The incidence of ectopic pregnancy is increasing (2% of all first-trimester pregnancies today) with the steady increase in risk factors (pelvic inflammatory disease and assisted reproductive techniques) and better diagnosis. Ectopic pregnancy can occur in 10% of all cases of medically assisted conception. It is still associated with high morbidity and mortality (6% of all pregnancy-related deaths). Most ectopic pregnancies are implanted in the Fallopian tube (95–97%), although implantation can occur in the ovary (1–3%), abdomen (< 1%), uterine cervix or cornua (interstitial) (< 1%) (Fig. 2.16).

Recently, ectopic pregnancies implanted on the scar of a previous Caesarean section have been described. Heterotopic pregnancies (simultaneous occurrence of two or more implantation sites) can also occur, commonly manifested as concomitant intrauterine and ectopic pregnancies, mainly in women who have undergone assisted reproduction. Diagnosis of this form of ectopic pregnancy is difficult and often delayed. Early detection of ectopic pregnancy can lead to successful medical management and prevention of maternal morbidity and mortality. Diagnosis has been based on clinical examination and physical symptoms of tubal rupture, while it is now possible to diagnose an early ectopic pregnancy before rupture, from serial measurements of hCG associated with serial ultrasonography. With transvaginal ultrasound, it is possible to visualize a gestational sac measuring 2 mm with an hCG level of 1000 IU/l.

Fig. 2.16. Intrauterine ectopic pregnancies. (a) Transvaginal ultrasound of a cervical pregnancy at 8 weeks' gestational age (arrow). (b) Same case seen by transabdominal ultrasound: living embryo present inside the sac (arrow). (c) Longitudinal section by transabdominal ultrasound of an interstitial ectopic pregnancy in the right uterine cornua (arrow) at 8 weeks: no visible embryo (embryonic demise). (d) Same case on transverse transabdominal ultrasound

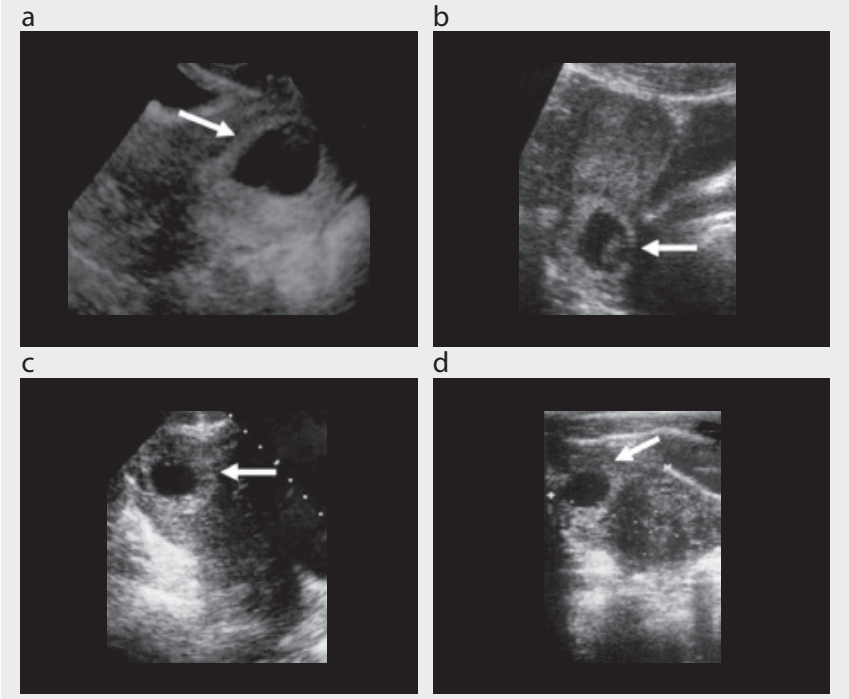

The diagnostic signs of an ectopic pregnancy can be direct or indirect:

Direct sign: visualization of the ectopic sac with or without a yolk sac and embryo (detected in 9–64% of cases) (Fig. 2.17);

Indirect signs: non-visualization of an intrauterine sac (empty uterus) with the hCG level greater than the discriminatory zone (1500–2000 IU/l); pseudogestational sac inside the uterus (detected in 10–20% of cases); complex, poorly defined, extra-ovarian adnexal mass (80%); tubal ring (echo-free structure inside the tube, 68–78%); abnormal tubal content (due to clots [haematosalpinx] and ovular material); intra-peritoneal free fluid collection (Douglas pouch, pelvis or abdomen, 60%) (Fig. 2.18).

A differential diagnosis must be made from other tubal pathological conditions (hydrosactosalpinx) sometimes associated with ectopic pregnancies, or from normal structures, such as a luteal body or bowel. The accuracy of ultrasound for detecting an ectopic gestation is about 80–85%, with a specificity of 96% and a false-positive rate of 0.5–1%.

Fig. 2.17. Tubal ectopic pregnancies. (a) Transvaginal ultrasound: tubal ring (arrow) at 6 weeks' gestational age. (b) Transabdominal ultrasound: ectopic pregnancy at 7 weeks with a visible embryo inside the sac (arrow). (c) Transvaginal ultrasound: tubal gestational sac at 5 weeks (arrow), with the whole tube visible (dotted arrow on the ampulla)

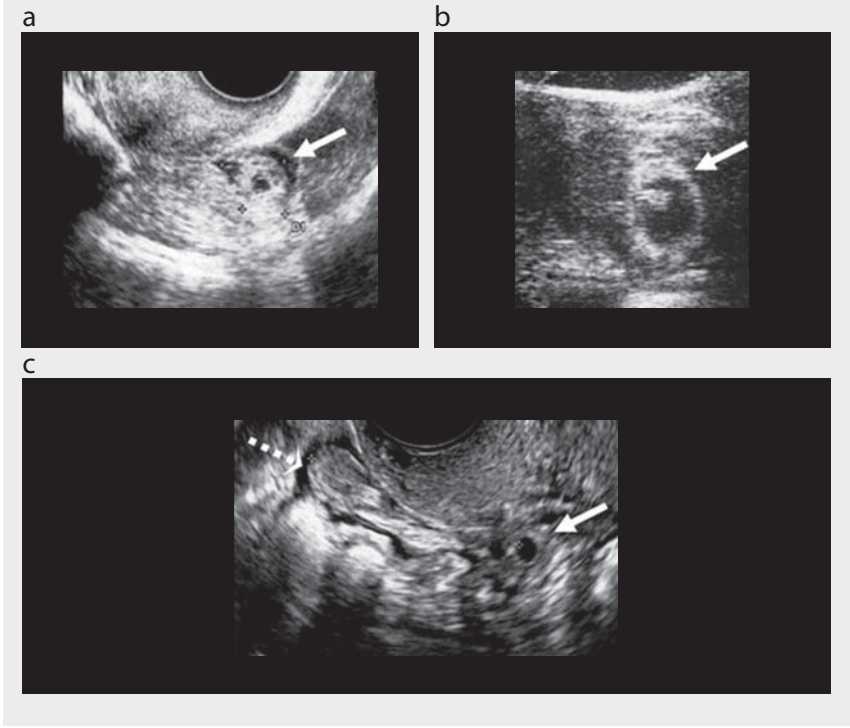

Fig. 2.18. Transvaginal ultrasound in cases of tubal ectopic pregnancy. (a) Large pseudogestational sac inside the uterine cavity (arrow), with the ectopic gestational sac containing an embryo (dotted arrow) visible inside a hydrosalpinx. (b) Complex mass (dotted arrow) and fluid collection in the cul-de-sac (arrow). (c) Small pseudogestational sac in the middle of the uterine cavity (arrow)

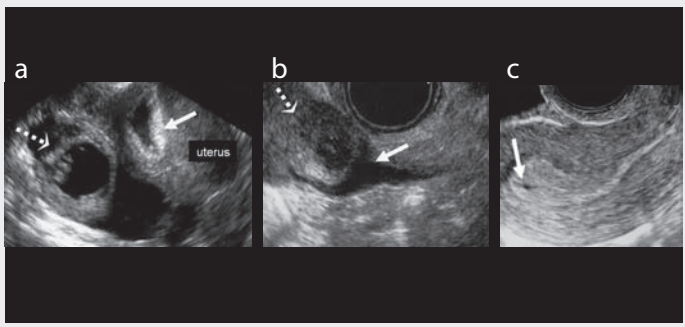

Gestational trophoblastic disease

Gestational trophoblastic disease is a spectrum of conditions, including hydatidiform mole, invasive mole and chorioncarcinoma. First-trimester bleeding is often the commonest clinical presentation of these disorders, with excessive, rapidly growing uterine size, exceeding the normal size for gestational age. Other clinical features are hyperemesis gravidarum or pre-eclampsia before 24 weeks. Maternal blood contains excessive hCG due to abnormal proliferation of trophoblastic tissue.

Hydatidiform mole (molar pregnancy)

Hydatidiform mole is a gestational complication that occurs in 1 out of 1000–2000 pregnancies. Complete and partial molar pregnancies have been described. **Complete hydatidiform mole** is the commonest trophoblastic disease, resulting from fecundation of an egg with no active nucleus: all the chromosomes present in the product of conception are of paternal origin (complete hydatidiform mole is also known as uniparental disomy, with a 46,XX karyotype in 90% of cases). The uniparental disomy causes early embryonic demise and proliferation of trophoblastic tissue, with the gross pathological appearance of a complex multicystic mass, shown as a snowstorm pattern with the oldest ultrasound equipment. The current ultrasound appearance of a complete hydatidiform mole is a heterogeneous echogenic endometrial mass with multiple cysts of variable size and necrotic–haemorrhagic areas. Doppler examination reveals increased uterine vascularity with high velocities and a low resistance index in the uterine arteries. In 50% of cases of complete hydatidiform mole, theca lutein cysts are present in the adnexa, resulting from hCG stimulation of the ovaries. On ultrasound, theca lutein cysts appear as multiple, large, bilateral, multiseptated ovarian cysts, sometimes haemorrhagic or complex, described as clusters of grapes (Fig. 2.19).

Partial hydatidiform moles result from fecundation of a normal egg with two spermatozoa or a diploid sperm, known as diandry (extra haploid set from the father). The abnormal karyotype is triploid (69,XXY) or tetraploid (92,XXXY). In partial moles, the triploidy is always paternal. In cases of maternal triploidy (digyny, an extra haploid set from the mother), other disorders, such as intrauterine growth retardation or spontaneous abortion, occur, with a non-molar placenta. In partial molar pregnancy, the ultrasound scan shows a gestational sac containing a fetus and an enlarged placenta with focal areas of multiple cysts. Often, the fetus coexisting with a molar pregnancy shows growth retardation and congenital anomalies (Fig. 2.20).

The differential diagnosis of a partial mole includes:

- twin pregnancy with one normal fetus and placenta and an accompanying complete hydatidiform mole; in this case, the fetal growth and anatomy are normal;
- fetal demise with hydropic degeneration of the placenta; the ultrasound presentation can be identical to that of a partial molar pregnancy, and pathological diagnosis is needed;
- placental pseudomole, due to mesenchymal dysplasia with villous hydrops, seen in pre-eclampsia. This placental pathology is rare in the first trimester.

Fig. 2.19. Complete hydatidiform mole. (a) Transvaginal ultrasound showing ovarian theca lutein cysts. (b), (c) Transabdominal ultrasound showing cystic villus degeneration (dotted arrows) and necrotic–haemorrhagic areas (arrows)

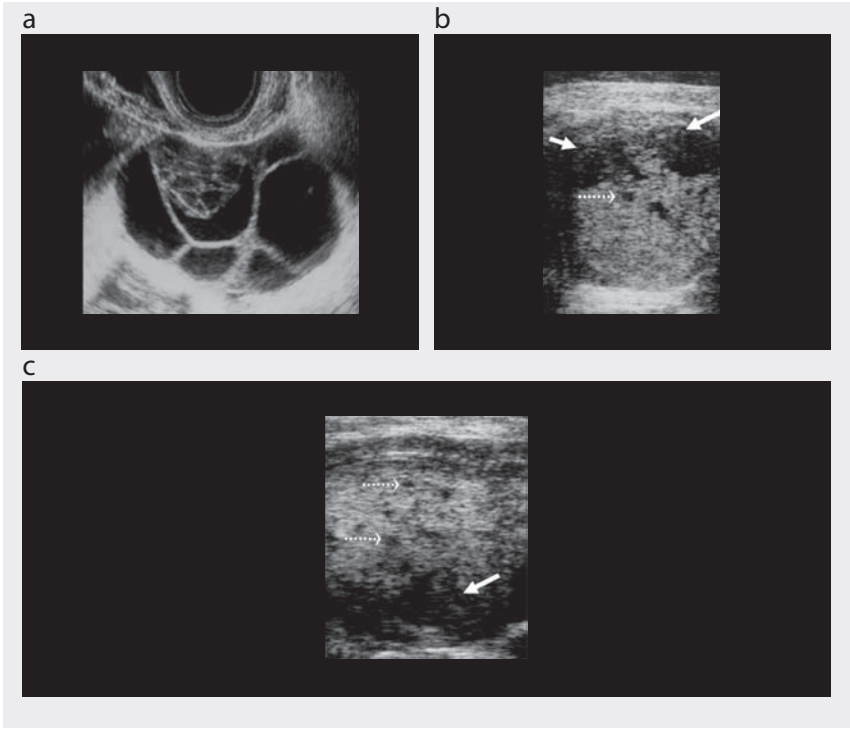

Fig. 2.20. Partial hydatidiform mole. (a), (b) Transabdominal ultrasound showing cystic degeneration of the placenta associated with a gestational sac and a non-living embryo (arrows)

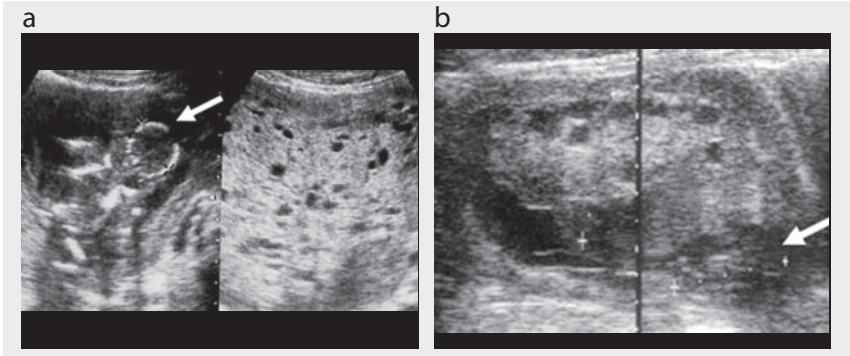

Invasive mole and chorioncarcinoma

Invasive mole presents as a deep growth into the myometrium and beyond, sometimes with penetration into the peritoneum and parametria. This tumour is locally invasive and rarely metastasizes, in contrast to chorioncarcinoma, which typically metastasizes extensively to the lung and pelvic organs. Of these tumours, 50% derive from a molar pregnancy, 25% from an abortion and 25% from an apparently normal pregnancy. A diagnosis is made when hCG levels remain elevated after evacuation of a pregnancy or after a delivery. Ultrasound may show the presence of a uterine mass similar to a complete hydatidiform mole and sometimes myometrial trophoblastic invasion. Haemorrhagic areas are often present inside the molar tissue, giving a complex aspect, mainly in chorioncarcinoma. Doppler shows increased myometrial flow, with abnormal vessels and shunts.

Computed tomography (CT) is useful for detecting metastases, and magnetic resonance imaging (MRI) demonstrates myometrial and vaginal invasion.

Embryo–fetal anomalies

Although many congenital anomalies cannot be diagnosed with confidence until the middle of the second trimester, imaging of the embryo has improved with continued technological advances, and many major fetal defects (such as acrania or anencephaly, large encephalocoele, holoprosencephaly, ventral wall defects, megacystis and conjoined twins) can be detected in the latter part of the first trimester. By 10 weeks' gestational age, the fetal cranium, brain, trunk and extremities can be visualized.

Anencephaly is characterized by the absence of the cranial vault (acrania), with dystrophic brain tissue exposed to the amniotic fluid: the fetal head has an irregular shape, and no cranial bones are visible (Fig. 2.21a).

Hydranencephaly is a lethal condition caused by complete occlusion of the internal carotid artery and its branches, resulting in the absence of cerebral hemispheres. This condition in early pregnancy appears as a large head with a fluid-filled (echo-free) intracranial cavity and no midline echo. Severe cases of ventriculomegaly (**hydrocephaly**) can be diagnosed during the first trimester (Fig. 2.21b).

Large **meningo-encephalocoele** is due to a defect in the skull, usually in the occipital region, through which the intracranial contents herniate. Either meninges (meningocoele) or both meninges and brain tissue (encephalocoele) protrude through this opening. This defect can be diagnosed in early pregnancy, but the diagnosis is difficult before ossification of the cranial vault (Fig. 2.21c).

In **alobar holoprosencephaly**, the prosencephalon fails to cleave into the two cerebral hemispheres. A large central cystic space is present inside the head and the falx and choroid plexus are absent. In 30% of cases, this condition is associated with trisomy 13 or 18 (Fig. 2.21d).

Cystic hygromas are large fluid collections behind or lateral to the fetal head, neck and trunk, sometimes associated with generalized hydrops. Hygromas can be septated or not and of variable size; they are associated in 70–90% of cases with Turner syndrome and trisomy 13, 18 or 21 (Fig. 2.22).

Fig. 2.21. Transvaginal ultrasound of central nervous system anomalies. (a) Acrania at 11 weeks' gestational age: meninges (arrow) without skull covering the abnormal brain tissue. (b) Hydrocephaly of the posterior horns of the lateral ventricles. (c) Occipital cephalocoele (arrow). (d) Holoprosencephaly

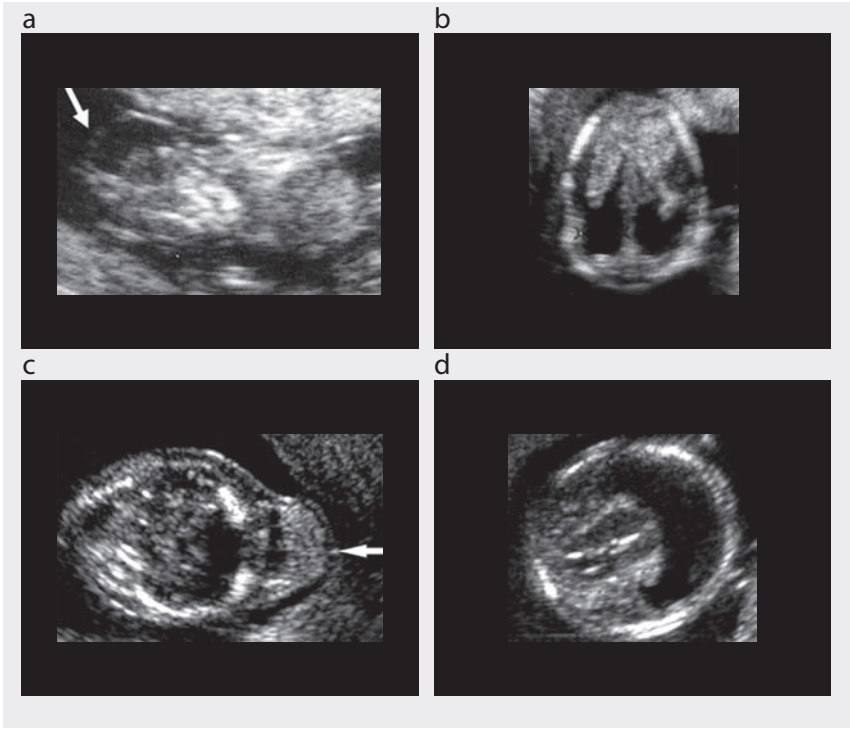

Large ventral wall defects, such as **omphalocoele (exomphalos)** and **gastroschisis**, should be differentiated from physiological bowel herniation, a normal finding up to 12 weeks' gestational age. Before 12 weeks, if the mass protruding outside the ventral wall is greater than 7 mm, a ventral wall defect should be suspected. In exomphalos, the extruded abdominal content is covered by a peritoneal membrane and has a smooth, rounded contour. In 60% of cases, exomphalos is associated with chromosomal anomalies (mainly trisomy 18). Gastroschisis results from a defect involving the entire thickness of the abdominal wall and is usually located to the right of the umbilical cord insertion. In gastroschisis, the protruding small bowel loops are not covered by a membrane, and the contour of the lesion is irregular; the cord insertion is normal. This condition is not associated with an increased risk for aneuploidy (Fig. 2.23a, b).

Megacystis is diagnosed when the fetal bladder length exceeds the normal value of 6 mm at 11–14 weeks' gestational age. Megacystis with a longitudinal bladder diameter of 7–15 mm is associated in 20% of cases with trisomy 13 or 18. If the bladder is more than 15 mm long, the incidence of chromosomal defects is only 10%, but there is a strong association with progressive obstructive uropathy (Fig. 2.23a–c).

Fig. 2.22. Transvaginal ultrasound in cases of cystic hygroma. (a) Trisomy 21 fetus: left, longitudinal scan showing nuchal translucency enlargement (calipers) and neck hygroma; right, echo-rich bowel (dotted arrow) and hypoplastic middle phalanx of the fifth digit (arrow) in the same fetus. (b) Transverse section of the neck with septated bilateral cystic hygromas. (c) Longitudinal scan of a fetus with large cystic hygromas and generalized hydrops

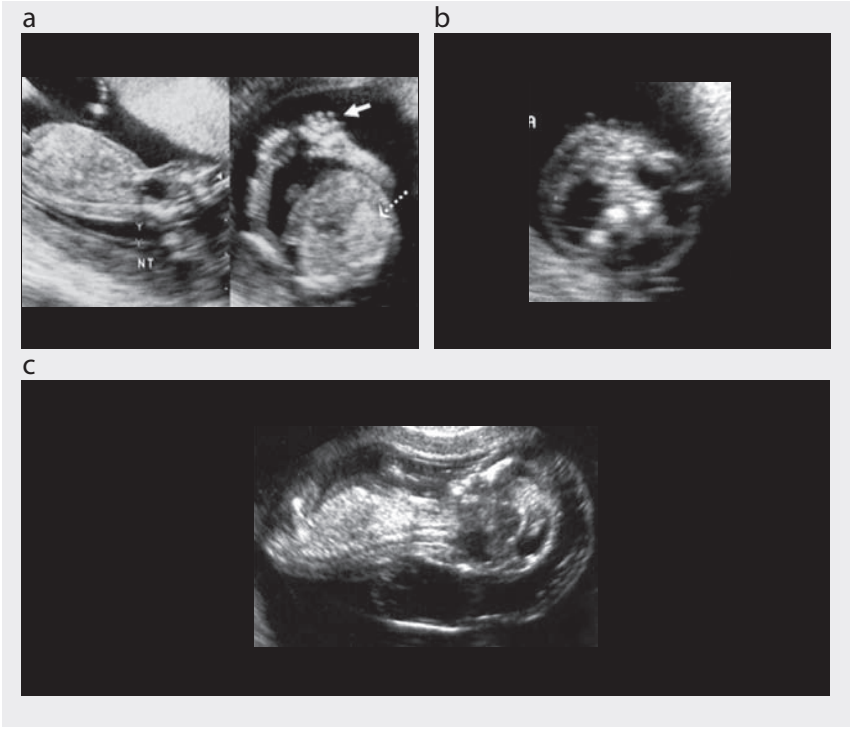

Conjoined twins are a complication of a monoamniotic monochorionic twin pregnancy and are due to an abnormality of monozygotic twinning, with incomplete division of an embryonic cell mass. Conjoined twins are sporadic and rare (one of 30 000–100 000 live births). They are, however, frequent in fetal life, because this condition is associated with a high rate of spontaneous abortion and stillbirth. Early in pregnancy, it can be difficult to differentiate conjoined twins from two separated but close monoamniotic twins; by the end of the first trimester, as the amniotic cavity enlarges, such differentiation becomes possible (Fig. 2.24).

Cardiac defects can be detected even in the first trimester of pregnancy due to improvements in the resolution of ultrasound machines. Increased nuchal translucency is known to be associated with all types of heart lesions, the prevalence of major cardiac defects being 1% with a nuchal translucency of 2.5–3.4 mm and 30% with a nuchal translucency of 6.5 mm or more. For fetuses with a nuchal translucency above the 99th centile, echocardiography is recommended. An echocardiogram, whether in the first trimester or later, must be done by an expert sonographer who has received specific training.

Fig. 2.23. (a) Transvaginal ultrasound in a 13-week + 4-day fetus with omphalocoele (arrow) and megacystis (dotted arrow). (b) Transvaginal ultrasound in a case of large gastroschisis with protrusion of bowel loops (arrow) at 14 weeks' gestational age. (c) Megacystis (arrow) at 14 weeks

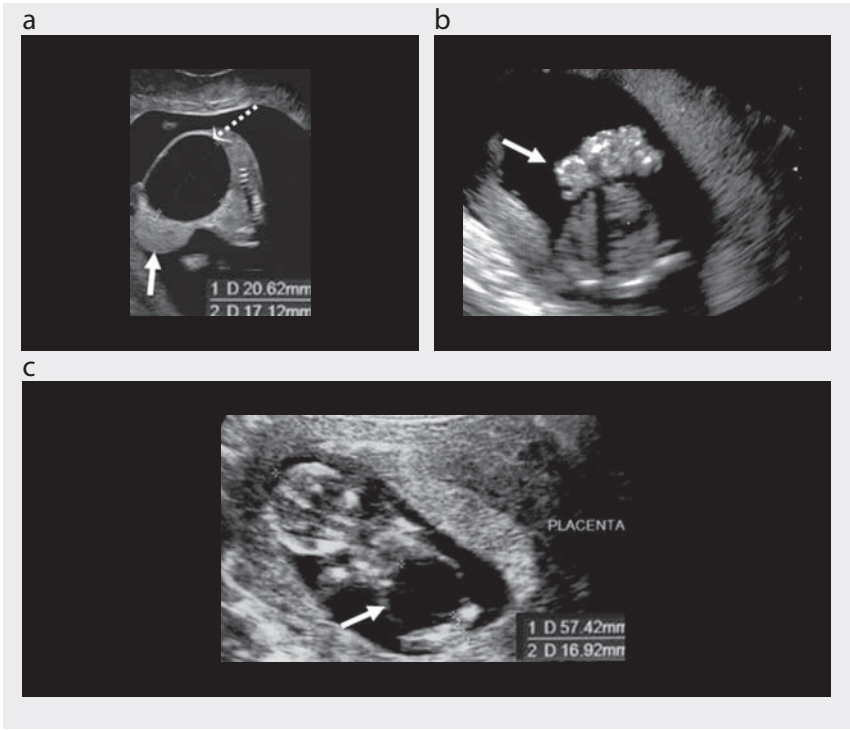

Fig. 2.24. Transabdominal ultrasound of monoamniotic conjoined twins. (a) Two fetuses close within the same sac. (b) Conjunction between the two fetal abdomens (arrow)

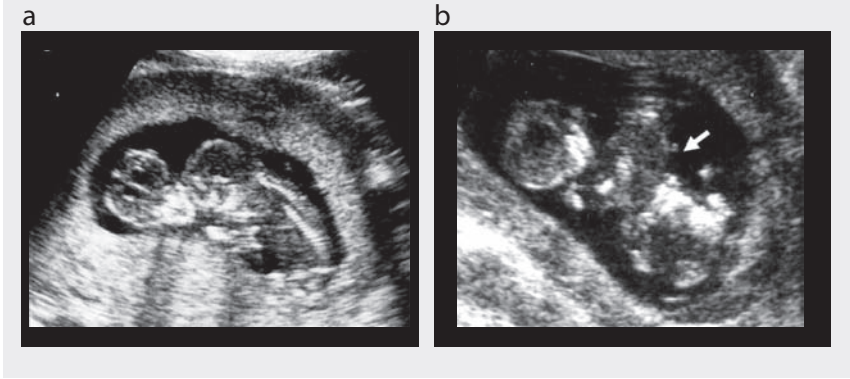

Second trimester

Indications

Sonographic examination in the second trimester of pregnancy should include: evaluation of the situation, presentation and cardiac activity of the fetus; placental localization (Fig. 2.25); assessment of the amniotic fluid; fetal biometrics; and assessment of fetal anatomical structures and movements. Sonography in the second trimester is also recommended in cases of vaginal bleeding, risks for fetal malformations and requests for invasive antenatal diagnosis.

Fig. 2.25. Placental localization. Sagittal scan of the uterus shows the anterior placenta, with its distal margin reaching the internal uterine orifice, and the fetus in a breech position

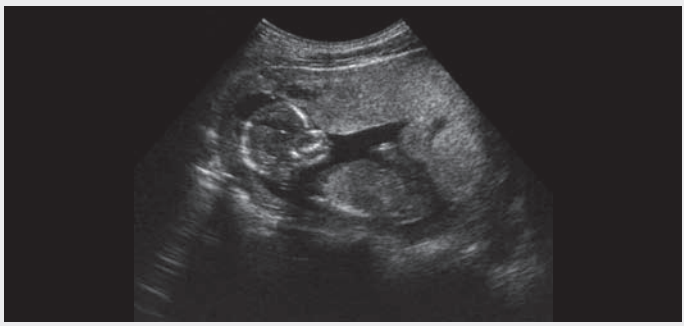

Estimation of gestational age

Gestational age (dating of pregnancy), unless already estimated in the first trimester, is based on the biparietal diameter and other biometric parameters (femur length, cranial circumference, transverse diameter of cerebellum). All these parameters should be compared to reference curves. If the discrepancy between anamnestic (i.e. menstrual) gestational age and ultrasound-derived gestational age is ≥ 2 weeks, the pregnancy should be re-dated.

Assessment of fetal morphology

Fetal morphology should be studied between 19 and 21 weeks to exclude the most serious malformations. It requires systematic scanning of the head, chest, abdomen and extremities, with assessment of placental and amniotic fluid volume.

Head

This study includes measurement of the biparietal diameter and cranial circumference, the thickness of the atrium (atrial width) of the lateral ventricles and the transverse

diameter of the cerebellum; the morphology of the orbits must also be demonstrated (Fig. 2.26, Fig. 2.27). The fetal brain should be scanned in at least four planes (transthalamic, transventricular, transcerebellar, transorbital), in which the examiner should measure the above-mentioned structures and identify all relevant cerebral structures, such as the falx, the ventricular walls, the cisterna magna, the septum pellucidum, the thalami, the brain peduncles, the cerebellar hemispheres and the vermis.

Transthalamic scanning (Fig. 2.27) is recommended for measuring the biparietal diameter, the frontal-occipital diameter and the cranial circumference (derived from the previous two measurements by means of the ellipsoid formula or traced directly on the ultrasound monitor). The cerebral structures to be assessed in this plane are the cavum septi pellucidi, the third ventricle, the thalami and the Sylvian fissures; when these structures are normal, many conditions can be excluded.

Fig. 2.26. Left, width (caliper 1) of the atrium of the lateral cerebral ventricles (atrial width). Right, transverse diameter of cerebellum (caliper 2) and anteroposterior diameter of the cisterna magna (caliper 3)

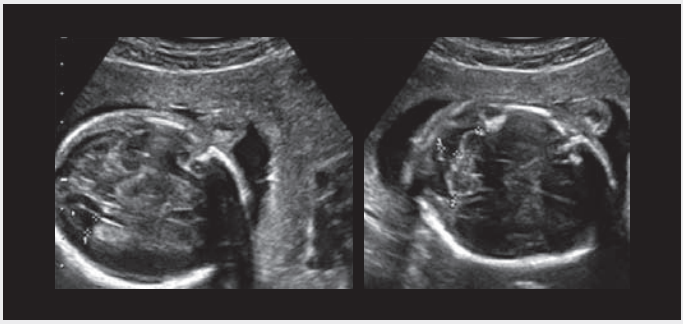

Fig. 2.27. Transthalamic scanning plane: biparietal diameter (caliper 1) and frontal–occipital diameter (caliper 2), from which the cranial circumference can be calculated

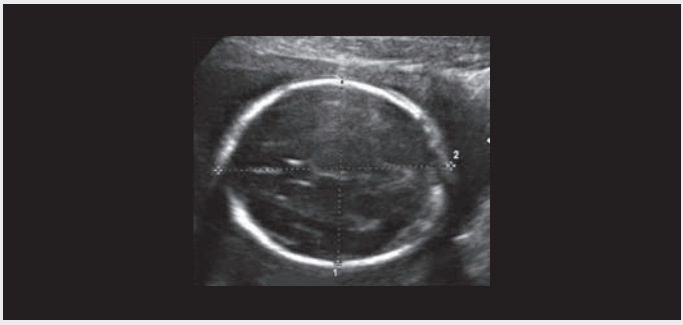

Transventricular scanning is done at a plane slightly higher than the previous one, allowing visualization at the median line of the same structures and the front and rear of the ventricular cavities. The atrial width of the frontal horns must be measured and reported at each examination: its average value is 7.5 ± 0.5 mm and its maximum value is 10 mm. After the 30th week, the cavity of the frontal horns can no longer be seen in the normal fetus.

Transcerebellar scanning (Fig. 2.28) allows a clear view of the cerebellum, the vermis, the cisterna magna (depth range: 4 to 10 mm) and the fourth ventricle.

Transorbital scanning (Fig. 2.29) can show the orbits, which should be symmetrical and of equal size.

Fig. 2.28. Transcerebellar scanning plane: cavum septi pellucidi and cerebellar hemispheres (calipers)

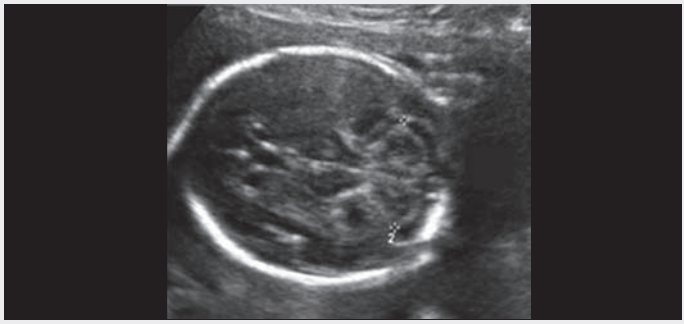

Fig. 2.29. Transorbital scanning plane

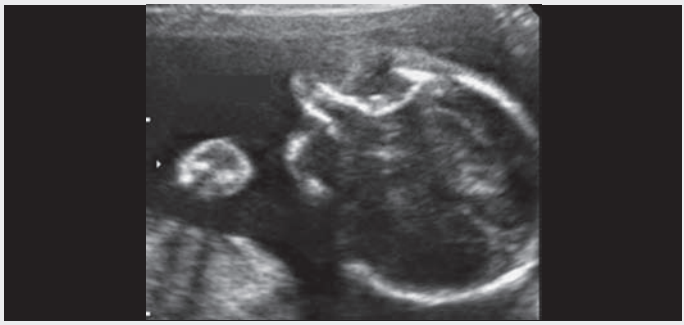

Vertebral column

Study of the vertebral column requires a longitudinal scan along the entire column (Fig. 2.30).

Fig. 2.30. Vertebral column. Longitudinal scans of the cervical and upper thoracic spine (a) and lower thoracic and lumbar spine (b)

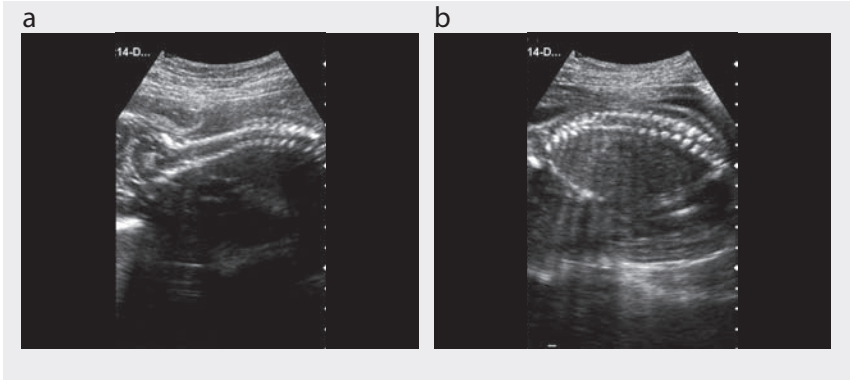

Chest

The examiner must obtain a display of the lungs, cardiac situs, four cardiac chambers (Fig. 2.31, Fig. 2.32) and left and right outflows (Fig. 2.33, Fig. 2.34). A scanning plane that shows the four cardiac chambers is best for assessing the chest anatomy.

Fig. 2.31. Chest. Sagittal (a) and transverse (b) scans of the chest, showing heart, lungs, diaphragm and fluid-filled stomach (a), and heart (view of four chambers), ribs, and spine (b)

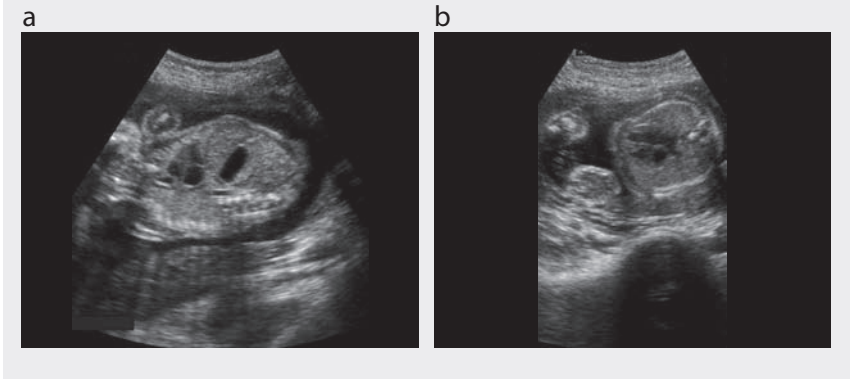

Fig. 2.32. Four cardiac chambers

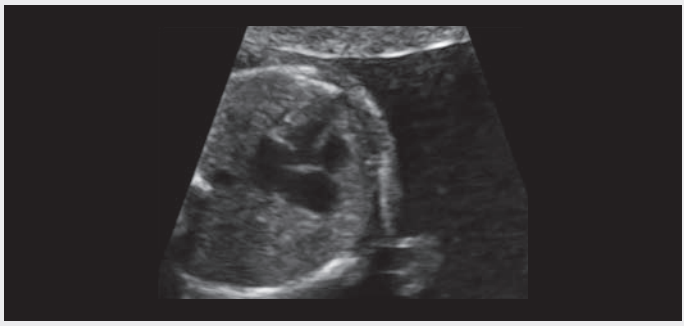

Fig. 2.33. Right outflow

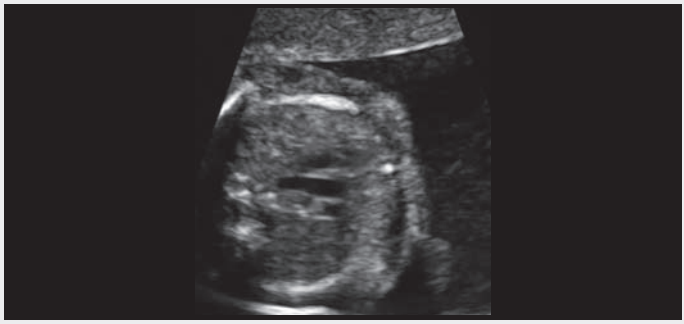

Fig. 2.34. Left outflow

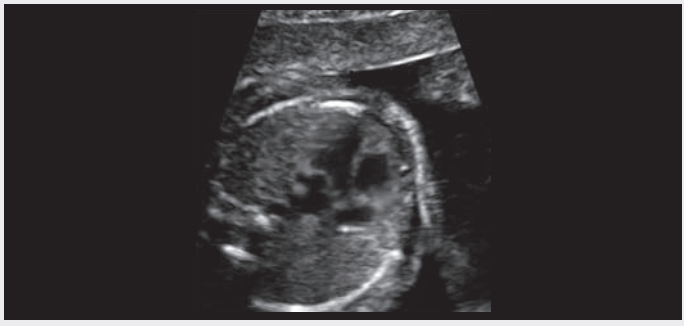

Abdomen

This study requires measurement of the abdominal circumference and visualization of the stomach, anterior abdominal wall, bladder and kidneys. The best plane for measuring the abdominal circumference is that in which the portal vein is visualized on a tangential section; the plane in which the stomach is visualized is also acceptable (Fig. 2.35). With accurate measurement of the abdominal circumference, the examiner will be able to obtain an accurate estimate of fetal weight, which is essential for assessing intrauterine fetal growth.

The stomach appears as a round, echo-free structure located in the upper part of the left abdomen. The shape and volume of the stomach are highly variable according to the degree of filling and peristalsis. If this organ is not visualized, the examination should be repeated later.

Assessment of urinary morphology requires a systematic sequential study to establish the location, volume and echogenicity of both kidneys; identification of renal vessels may be helpful in the assessment of congenital anomalies of the kidneys (Fig. 2.36 and Fig. 2.37). Ultrasound has an indirect role in the evaluation of renal function, from the measurement of amniotic fluid, the presence of urine in the bladder, the relation between abdominal and renal circumference and the cortical thickness of the kidneys.

Fig. 2.35. Abdominal circumference. Axial scan of the fetal abdomen showing the correct plane for measuring the transverse abdominal diameter and abdominal circumference: the portal vein (on a tangential section) and the fluid-filled stomach are both visualized

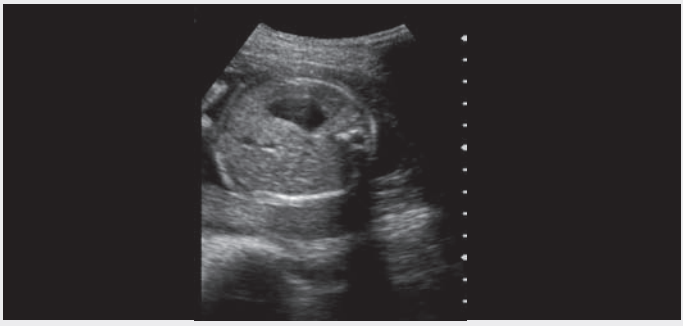

Fig. 2.36. Sagittal scan of the kidney (calipers)

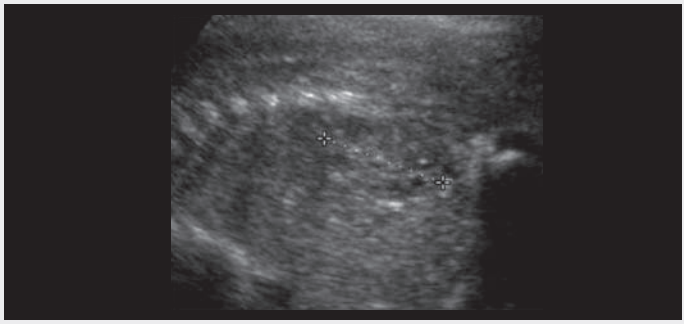

Fig. 2.37. Coronal plane (colour Doppler), with the kidneys, aorta and renal vessels (arrowheads)

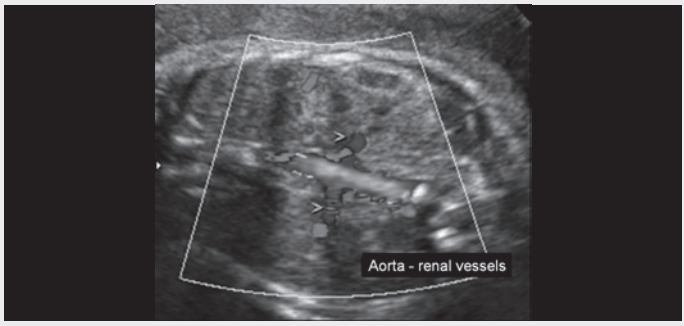

Extremities

The examiner must obtain a display of the long bones of the four limbs and of the distal extremities (hands and feet) to determine their presence. The femur length must be measured (Fig. 2.38), and the length, morphology and echogenicity of the limbs must be assessed (Fig. 2.39).

By convention, measurement of femur length (Fig. 2.38) is considered accurate only when the femoral bone on the image shows two blunted ends. The extension to the greater trochanter and the head of the femur should not be included. The measurement is also considered inaccurate when the femur image is at an angle of over 30° to the horizontal.

Fig. 2.38. Lower limbs: femur length (FL; calipers)

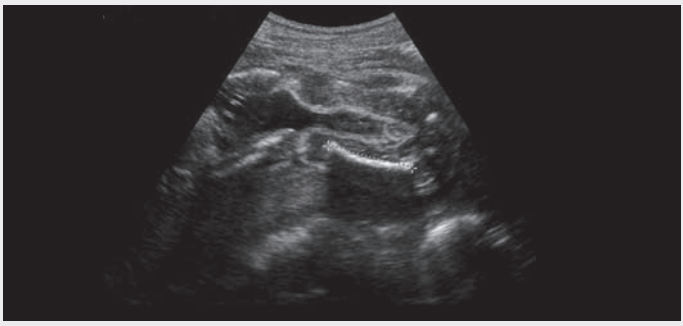

Fig. 2.39. Upper limb: hand, wrist, forearm and elbow

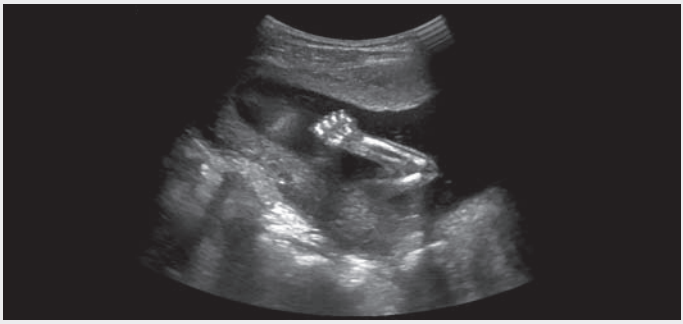

Amniotic fluid volume

Both a subjective evaluation and more objective estimates of the quantity of amniotic fluid can be made. The amniotic fluid index is calculated by measuring the deepest pocket of fluid in each of the four quadrants that ideally divide the uterus and by adding the four values; polydramnios is indicated if the resulting value is > 20 cm, and oligohydramnios is indicated if it is < 5 cm. The size of the greatest vertical pocket of fluid can also be measured. The normal values are 2–8 cm; a pocket measuring < 2 cm indicates oligohydramnios, while one > 8 cm indicates polydramnios (see section below on Amniotic fluid).

Placenta

The examiner should identify the location of the placenta and assess the normality of the umbilical cord and of the placental implant and its relation to the internal uterine orifice (see section below on Placenta). (Fig. 2.25, Fig. 2.40).

Fig. 2.40. Normal umbilical cord and placenta. Sagittal scans in different pregnancies show normal anterior (a)and posterior (b) localization of placenta; normal umbilical cord (arrows), with two arteries and one vein

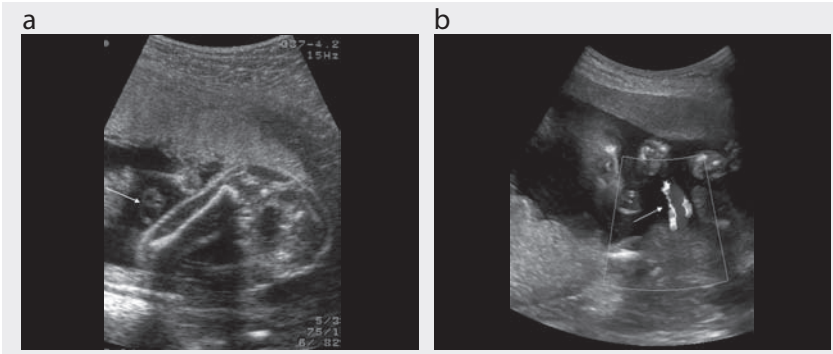

Third trimester

Introduction

Fetal biometry is an important part of routine examinations in the third trimester of pregnancy. Fetal measurements can be combined to estimate fetal weight or can be compared with previous measurements in the same fetus to evaluate growth longitudinally. The growth kinetics of normal fetuses has been studied extensively with ultrasound, to track parameters such as head and abdominal diameter and limb dimensions. The progression in growth of the fetal head and body is variable and the changes in fetal morphological characteristics are dynamic, responding to a complex array of environmental and genetic factors. The growth of these parameters appears to be different in the different periods of normal pregnancy and to vary even more in relation to pathological conditions that can affect fetal growth. Most measurements are plotted on reference charts for gestation to compare the measurements with the normal distribution. Growing interest in adjusting fetal size charts for genetic influence has resulted in publications on race-adjusted or customized fetal size charts.

Biometric parameters

The most important biometric parameters evaluated in the third trimester of pregnancy are head measurements (biparietal diameter and head circumference), abdominal circumference and limb dimensions (femur and humerus length).

Head measurements

The biparietal diameter is measured by positioning the calipers at the outer limits of the proximal and distal borders of the fetal skull (Fig. 2.41). All reports on biparietal diameter have shown it to be an accurate predictor of menstrual age before 20 weeks,

with a variation of ± 1 week (2 standard deviations [SD]). Virtually all studies showed a progressive increase in variation between 20 weeks and term, but the variation increases by ± 2 to ± 3.5 weeks (2 SD) in the late third trimester of pregnancy.

The head circumference (Fig. 2.41) and the abdominal circumference are measured directly with the ellipse facility around the perimeters of the head and abdomen. Head measurements are taken on the classic axial plane of the fetal head, identified from the cerebral peduncles, the thalami and the cavum septum pellucidum, which interrupts the continuous midline echo in its anterior third. Head circumference can be derived from measurements of the occipito-frontal diameter and the biparietal diameter from the formula $\pi (d_1 + d_2)/2$. Several authors have reported that head circumference is one of the most reliable parameters for estimating menstrual age because of its shape independence, its ease of measurement (and therefore accuracy) and its predictive value for gestational age. It can predict menstrual age to within 1 week (2 SD) before 20 weeks' gestation to 3.8 weeks (2 SD) in the late third trimester.

Fig. 2.41. Measurement of biparietal diameter (BPD; calipers) and head circumference (dotted ellipse). GA, gestational age; OFD occipito-frontal diameter; CC head circumference

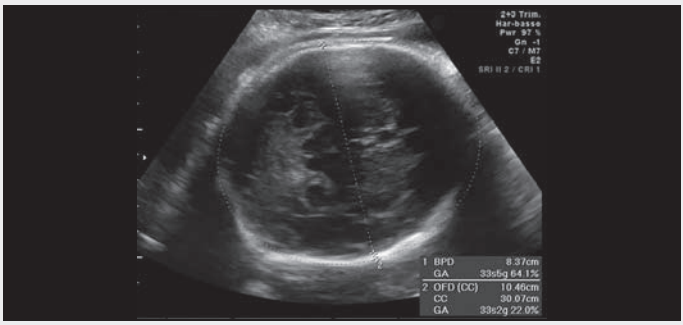

Abdominal measurements

The abdominal circumference is measured in a location that allows an estimate of liver size. The liver is the largest organ in the fetal torso, and its size reflects aberrations of growth, both restriction and macrosomia. The fetal abdominal circumference is measured at the position where the transverse diameter of the liver is greatest, which corresponds sonographically to the plane at which the right and left portal veins are continuous. The abdominal circumference is obtained on a transverse circular section of the fetal abdomen, identified by the stomach and the intrahepatic tract of the umbilical vein, just above the level of the umbilical cord insertion (Fig. 2.42).

Of the basic ultrasound measurements, abdominal circumference is reported to be the most variable, partly because it is more acutely affected by growth disturbances, but this variation is probably due more to measurement error than to biological differences. Furthermore, measurements of abdominal circumference are

the most difficult to obtain. Variability in predicting menstrual age from abdominal circumference increases as pregnancy advances, reaching a peak of approximately 4.5 weeks (2 SD) in the late third trimester of pregnancy.

Fig. 2.42. Measurement of the transverse diameters (calipers) and circumference (dotted circle) of the fetal abdomen. APAD, anteroposterior abdominal diameter; TAD, transverse abdominal diameter; CA, abdominal circumference; GA, gestational age; EFW, estimated fetal weight

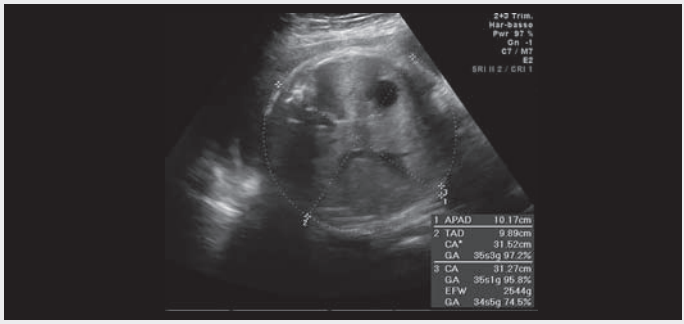

Limb measurements

Femur length is measured on a longitudinal scan showing the whole femur diaphysis, imaged on a plane as close as possible at right angles to the sonographic beam. The measurement is taken from one end of the diaphysis to the other (Fig. 2.43). The same technique is used to measure the length of other bones, such as the humerus, tibia, fibula, ulna and radium (Fig. 2.44).

Fig. 2.43. Femur length (FL; calipers). GA, gestational age

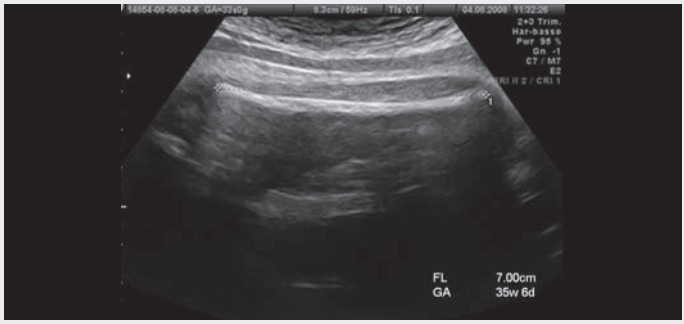

Fig. 2.44. Longitudinal measurement (calipers) of the humerus (left) and femur (right)

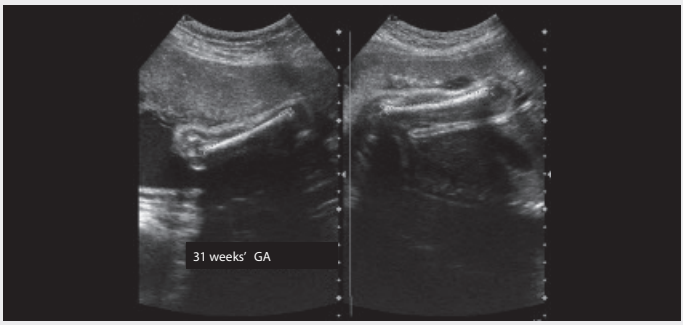

Most studies suggest that the femur length is an accurate predictor of menstrual age in the early second trimester, with a variation of ± 1 week (2 SD). Again, however, variation increases as pregnancy advances, reaching a peak of approximately 3.5 weeks in the late third trimester. It is important to emphasize that the variability of head and femur measurements is small early in gestation.

Biometric charts of size or volume have been obtained for some fetal organs, such as the orbits, cerebellum, liver, kidney and heart, which can be useful for suspected or diagnosed malformations. Kidney volume is reported to be linked with all fetal growth parameters in late pregnancy (Fig. 2.45).

Fig. 2.45. Kidneys. Sagittal (left) and axial (right) scan of the fetal abdomen showing normal kidneys

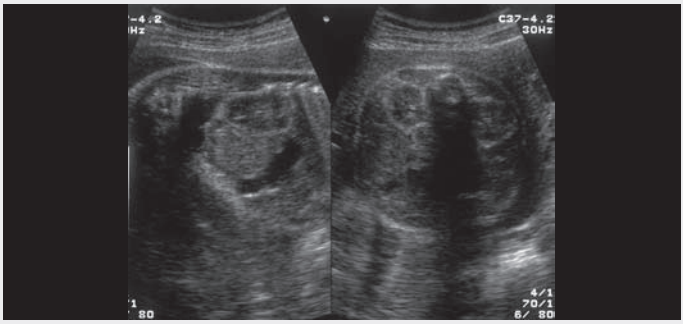

Amniotic fluid

Evaluation of amniotic fluid is now considered an integral, important part of the ultrasound evaluation of gravid women, particularly in situations such as intrauterine growth restriction or post-term pregnancy. Several subjective and objective methods are available. Subjective assessment of amniotic fluid volume involves comparing the echo-free fluid areas surrounding the fetus with the space occupied by the fetus and placenta (Fig. 2.46). The most commonly used objective methods are measurement of the single deepest amniotic fluid pocket free of umbilical cord and fetal parts (maximum vertical pocket), and the amniotic fluid index, which is the sum of the deepest amniotic fluid pockets measured in the four quadrants of the gravid uterus (see section below on Amniotic fluid).

Many studies have shown that the amniotic fluid index is more closely related to the amniotic fluid volume found in dye-dilution studies and, in many cases, is more accurate than measuring a single pocket. Other investigators do not agree. Neither fetal movements nor maternal position seem to adversely affect the assessment of amniotic fluid volume; however, fetal position may influence measurements. Similarly, excessive transducer pressure on the maternal abdomen can affect measurements of the amniotic fluid index. Other potential pitfalls exist. An umbilical cord-filled amniotic fluid pocket should not be used in assessing amniotic fluid volume. Colour Doppler flow imaging is often useful in identifying the umbilical cord. Obese women may appear to have significantly less fluid because of artefactual echoes into the amniotic fluid. This problem can be overcome by using a lower-frequency transducer. Similarly, in the third trimester, free-floating particles, perhaps resulting from vernix, can make the true amniotic space less conspicuous.

Amniotic fluid volume begins to decline near term and may do so precipitously in post-term women. This could be related to placental insufficiency, such as in cases of intrauterine fetal growth restriction, due to redistribution in cardiac blood flow such that renal perfusion is decreased, whereas cerebral blood flow is increased.

Fig. 2.46. Amniotic fluid. Normal amount of amniotic fluid subjectively assessed in comparison with fetus and placenta

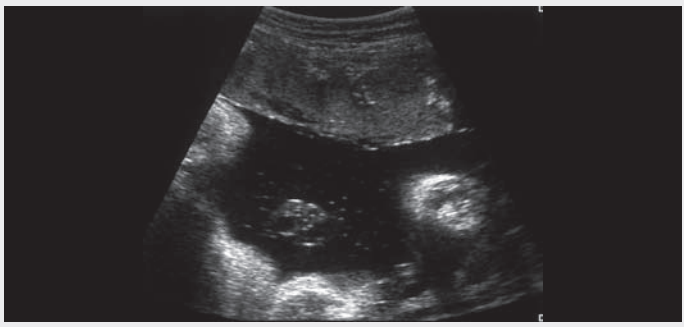

Estimation of fetal weight with ultrasound

Fetal biometrics can be used alone or in combination with mathematical formulas to predict fetal weight. Many formulas, broadly classified as linear or exponential, are used to estimate fetal weight in clinical practice (Table 2.3). In exponential formulas, the logarithm of the weight is expressed as a polynomial function of the ultrasound parameters. Early formulas used to predict birth weight with ultrasound were based on measurements of abdominal circumference alone or abdominal circumference and biparietal diameter. The model that included the two parameters predicted fetal weight to within 10% of the actual weight in 85% of cases; by incorporating another fetal parameter, the random error in estimating fetal weight was reduced by 15–25%. Use of three variables repetitively in the same formula is, however, cumbersome and sometimes requires multiple mathematical manipulations, which could limit its clinical usefulness.

The population-based reference ranges used to assess fetal growth have some limitations. Moreover, most of the formulas are based on a general fetal population, which includes a wide range of birth weights at term or close to term. For these reasons, some authors have suggested that these formulas are not relevant to very preterm fetuses. As preterm labour is often triggered by pathological conditions that affect growth, preterm birth weights are significantly lower than those of fetuses delivered at term. Individualized growth models have therefore been proposed: by defining a growth curve specific to a particular fetus, the obvious limitations of population-based growth charts should be eliminated. In a normal fetus, growth before 28 weeks' gestation predicts its subsequent growth pattern. In this approach, each fetus acts as its own control. The method is limited, however, by its dependence on normal second trimester growth and is useful when a growth abnormality occurs in the third trimester.

Another complex weight prediction formula has been proposed, which includes not ultrasound parameters but length of gestation, the sex of the fetus, the height of the mother, third-trimester maternal weight-gain rate and parity. This equation could be used when a fast, approximate estimation is required. Not all physicians are skilled in ultrasound biometry, and the cost of an ultrasound examination is much greater than the cost of this complex weight prediction method, which can be performed even by women themselves.

Accurate assessment of fetal weight is an integral part of obstetrics practice. It is well known that both low birth weight and excessive fetal weight are associated with increased risks for complications in the newborn during labour and puerperium. The optimal range of birth weights is considered to be 3000–4000 g. Exact estimation of birth weight is important, particularly for fetuses with an inappropriate weight, such as small-for-gestational age or macrosomic fetuses. Most universally applicable formulas were derived in studies in which few small or macrosomic infants were included. In contrast, targeted formulas derived specifically for these infants are generally based on small numbers of cases. Moreover, small-for-gestational age fetuses are frequently delivered extremely prematurely.

Table 2.3. Biparietal diameter (BPD), head circumference (HC), femur length (FL), abdominal circumference (AC), estimated fetal weight (EFW), birth weight (BW), mean abdominal diameter (mAD), calculated as the mean of anteroposterior and transverse abdominal diameters

Reference	Parameter	Regression equation
Warsof, 1977	AC	$\text{Log}_{10}\text{EFW} = -1.8367 + 0.092(\text{AC}) - \frac{0.019(\text{AC} \times \text{AC} \times \text{AC})}{1000}$
Hadlock, 1984	AC	$\log_e\text{EFW} = 2.695 + 0.253(\text{AC}) - 0.00275\ (\text{AC} \times \text{AC})$
Campbell & Wilkin, 1975	AC	$\log\ \text{EFW} = -4.564 + 0.282(\text{AC}) - 0.00331(\text{AC})^2$
Eik-Nes, 1982	BPD/AC	$\log\ \text{BW} = 1.85628(\log\ \text{BPD}) + 1.34008(\log\ \text{mAD}) - 2.8442$
Warsof, 1977	BPD/AC	$\log_{10}\text{EFW} = -1.599 + 0.144(\text{BPD}) + 0.032(\text{AC}) - \frac{0.111(\text{BPD} \times \text{BPD} \times \text{AC})}{1000}$
Shepard, 1982	BPD/AC	$\log_{10}\text{EFW} = -1.7492 + 0.166(\text{BPD}) + 0.046(\text{AC}) - \frac{2.646(\text{AC} \times \text{BPD})}{1000}$
Birnholz, 1986	BPD/AC	$\text{BW} = \frac{3.42928(\text{BPD} \times \text{mAD} \times \text{mAD})}{1000} + 41.218$
Vintzileos, 1987	BPD/AC	$\log_{10}\text{BW} = 1.879 + 0.026(\text{AC}) + 0.084(\text{BPD})$
Hadlock, 1984	AC/FL	$\log_{10}\text{BW} = 1.304 + 0.05281(\text{AC}) + 0.1938(\text{FL}) - 0.004(\text{AC} \times \text{FL})$
Warsof, 1977	AC/FL	$\log_n\text{BW} = 2.792 + 0.108(\text{FL}) + 0.000036(\text{AC}^2) - 0.00027(\text{FL} \times \text{AC})$
Nzeh, 1992	BPD/AC/FL	$\log_{10}\text{BW} = 0.470 + 0.488(\log_{10}\text{BPD}) + 0.554(\log_{10}\text{FL}) + 1.377(\log_{10}\text{AC})$
Hill, 1985	BPD/AC/FL	$\text{BW} = -3153.1 + 13.645(\text{AC} \times \text{BPD}) + 2753.97(\text{FL/BPD})$
Ott, 1986	BPD/AC/FL	$\log\ \text{BW} = 0.04355(\text{HC}) + 0.05394(\text{AC}) - 0.0008582(\text{HC} \times \text{AC}) + 1.2594(\text{FL/AC}) - 2.0661$
Hadlock, 1985	BPD/AC/FL	$\log_{10}\text{EFW} = 1.5662 - 0.0108(\text{HC}) + 0.0468(\text{AC}) + 0.171(\text{FL}) + 0.00034(\text{HC} \times \text{HC}) - 0.003685(\text{AC} \times \text{FL})\ln(\text{BW}) = 0.143(\text{BPD} + \text{mAD} + \text{FL}) + 4.198$
Sabbagha, 1989	BPD/AC/FL	$\text{EFW} = -55.3 - 16.35(\text{GA} + \text{HC} + 2\text{AC} + \text{FL}) + 0.25858((\text{GA} + \text{HC} + 2\text{AC} + \text{FL}) \times (\text{GA} + \text{HC} + 2\text{AC} + \text{FL}))$
Hadlock, 1985	BPD/AC/FL	$\log_{10}\text{BW} = 1.3596 + 0.00386(\text{AC} \times \text{FL}) + 0.0064(\text{HC}) + 0.00061(\text{BPD} \times \text{AC}) + 0.0424(\text{AC}) + 0.174(\text{FL})$
Rose & McCallum, 1987	BPD/AC/FL	$\log_n\text{BW} = 0.143(\text{BPD} + \text{mAD} + \text{FL}) + 4.198$

Fetal macrosomia

Macrosomic fetuses, defined as fetuses with a birth weight over 4000 g, represent about 10% of all newborns, but the percentage has been increasing over the past few decades in western countries because of nutrient supplements and better nutrition. During the past 2–3 decades, an overall 15–25% increase in the proportion of women giving birth to large infants has been found in various populations around the world, with a few exceptions, such as the United States. Fetal macrosomia is frequently associated with neonatal morbidity and traumatic birth, and the complications associated with this condition include increased maternal and fetal trauma, shoulder dystocia with resulting Erb palsy, perinatal asphyxia, meconium aspiration, increased frequency of labour disorders, postpartum atonia and haemorrhage, lacerations of the birth canal and haematomas.

Weight prediction by ultrasound gives adequate results for the general fetal population, but the results are less satisfactory for the macrosomic population. Nevertheless, sonographically estimated fetal weight, obtained with models that include abdominal circumference and femur length, remains a useful method for evaluating women at risk for macrosomia.

Many methods for ultrasound determination of fetal weight have been reported; in most, the predictive accuracy declines as the fetal weight approaches 4000 g. A major problem in the estimation of macrosomic fetal weight with ultrasound is the high degree of inherent error. Moreover, most formulas for estimating fetal weight are derived from cross-sectional data on unselected patient populations, a minority of whom probably have diabetes. The proposed ultrasound methods do not appear to differ substantially in terms of accuracy in predicting macrosomia. The mean absolute percentage error in predicting fetal birth weight was about 7%, but the sensitivity of ultrasound in detecting macrosomia was only 65%.

As clinical and ultrasound methods have similar limited power to predict fetal weight greater than 4000 g, the American College of Obstetricians and Gynecologists cited a third method, namely the mothers' own estimate of fetal size. The probability that this method could predict macrosomia is similar to that of clinical and ultrasound methods.

Because fat is less dense that lean mass and because of the disproportionate increase in the fetal fat component of infants of women with diabetes, the weight of their fetuses, especially those with excessive birth weight, may be systematically overestimated by ultrasound with these formulas. The results of studies addressing this issue are, however, inconsistent. Because of the increased contribution of fat mass to the fetal weight of infants of women with diabetes, formulas based exclusively on soft tissue measurements might be more accurate than those with measures of both fat and lean tissue. Although a good correlation has been found between ultrasound measures of fetal body composition and those taken at birth, the usefulness of the approach of measuring fetal fat for detecting macrosomic newborns was not confirmed, and its clinical use in comparison with other predictors remains to be defined.

Fetal body configuration may be more important than an arbitrarily defined birth weight threshold. Macrosomic fetuses are in fact characterized by larger trunk and chest circumference and an increased bisacromial diameter as fetal weight increases. Macrosomic infants of diabetic mothers are also characterized by larger shoulder and extremity circumferences, a decreased head-to-shoulder ratio, significantly higher percentages of body fat and thicker upper extremity skin folds than controls of similar birth weight and length. Use of other, nonstandard ultrasound measurements, such as humeral soft tissue thickness, ratio of subcutaneous tissue to femur length and cheek-to-cheek diameter, to estimate fetal weight does not, however, significantly improve the predictive value of obstetric ultrasound for birth weight.

In normal pregnancies, fetal abdominal subcutaneous tissue thickness at term is positively associated with birth weight. With increasing thickness, the likelihood of operative vaginal and Caesarean delivery increases; however, this measure is not associated with perinatal outcome.

Advancements in ultrasound technology have not changed this situation. The introduction of three-dimensional ultrasound led some authors to propose new formulas that incorporate volumetric data on fetal limbs. Application of these techniques was generally limited by the excessive time required for measuring volume and by the need for a three-dimensional machine with specific software. Similarly, the clinical usefulness of MRI to estimate fetal weight requires further documentation.

Clinical indications for ultrasound examination: placenta praevia and accreta

In late pregnancy, diagnostic ultrasound is used selectively for specific clinical indications, and the value of routine ultrasound screening during late pregnancy in unselected populations is controversial. The Cochrane Database used existing evidence to conclude that routine ultrasound in late pregnancy in low-risk or unselected populations provided no benefit for the mother or the infant. Information is lacking about the potential psychological effects of routine ultrasound in late pregnancy and the effects on both short- and long-term neonatal and childhood outcomes. Ultrasound examination could be useful in certain situations, such as a suspected anomalous placental location (placenta praevia) or adherence (placenta accreta–percreta).

Placenta praevia

While clinical judgement remains crucial in suspecting and managing placenta praevia, a definitive diagnosis of most low-lying placentas is now achieved with ultrasound imaging. Clinical suspicion should, however, be raised in any case of vaginal bleeding. Transvaginal ultrasound, if available, can be used to investigate placental location at any time in pregnancy and in particular in the third trimester, if the placenta is thought to be low-lying. The transvaginal approach is significantly more accurate than transabdominal ultrasound

and is highly recommended, especially in the case of a posteriorly situated placenta, with the additional benefit of reduced scanning time. Its safety is well established, as confirmed in numerous prospective observational studies in which transvaginal ultrasound scanning was used to diagnose placenta praevia with no haemorrhagic complications.

In 60% of women who undergo transabdominal ultrasound, the placental position may be reclassified when they undergo transvaginal scan. On the basis of the increased prognostic value of a transvaginal ultrasound diagnosis, sonographers are encouraged to report the actual distance between the placental edge and the internal cervical os at transvaginal scan, using the standard terminology of millimetres from the os or millimetres of overlap (a placental edge that reaches exactly the internal os is described as 0 mm).

Placenta accreta

Placenta accreta are abnormal adherences of the placenta to the uterus, with subsequent failure to separate after delivery of the fetus. The most frequent predisposing conditions are previous Caesarean section and placenta praevia. The type of accreta varies according to the depth of invasion: villi penetrate the decidua but not the myometrium (accreta); villi penetrate and invade the myometrium but not the serosa (increta); and villi penetrate the myometrium and may perforate the serosa, sometimes into adjacent organs (percreta).

The diagnosis can be made by ultrasound. The features of placenta accreta include irregularly shaped placental lacunae (vascular spaces) with turbulent internal flow shown by Doppler, thinning of the myometrium overlying the placenta, loss of the retroplacental echo-poor clear zone, absence of a decidual interface with normal placental echogenicity, interruption or increased vascularity of the uterine serosa–posterior bladder wall interface, and apparent bulging or protrusion of the placenta into the bladder (Fig. 2.47).

Fig. 2.47. Placenta accreta: the placenta appears heterogeneous with prominent vascular spaces (Swiss-cheese appearance) and loss of the retroplacental echo-poor zone

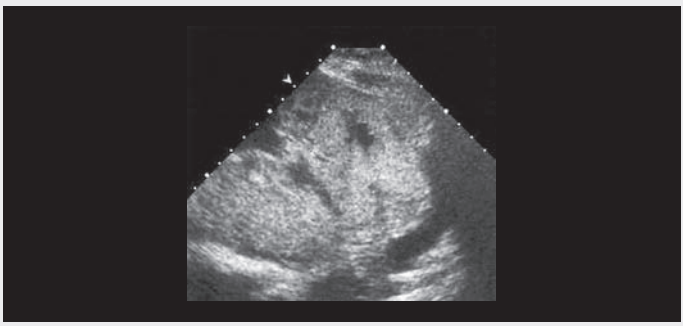

In addition to grey-scale ultrasound findings, targeted Doppler assessment should be performed. Sometimes, MRI may be considered in this evaluation, as it can provide additional diagnostic information in equivocal cases or when the placenta is in a posterior location.

Fetal growth restriction

Fetal growth depends on genetic, placental and maternal factors. Each fetus has an inherent growth potential which, under normal circumstances, yields a healthy newborn of appropriate size. The maternal–placental–fetal unit acts in harmony to provide the needs of the fetus while supporting the physiological changes of the mother. In normal pregnancy, the fetus and the placenta grow at different rates. The placenta expands early and develops into a large tertiary villus structure, with maximum surface area and thus functional activity for exchange peaking at about 37 weeks' gestation; at this time, it weighs about 500 g. From then until delivery, its surface area decreases slightly as microinfarctions occur. The placenta partially regulates fetal growth. The fetus grows throughout pregnancy, but the rate of weight increase per week begins to slow from the 36th week of gestation.

The fetus requires three kinds of substrate for its growth. Glucose freely crosses the placental barrier by facilitated diffusion, while maternal amino acids are actively transported to the fetus, so that their concentration is higher in fetal blood that in the maternal circulation. Oxygen passes to the fetal circulation by simple diffusion. Glucose is burnt with oxygen to produce energy and to convert amino acids into structural proteins: the result is a normally growing fetus. Regulation of the fetal growth rate depends not only on the availability of substrates from placental transfer but also on the activity of fetal hormones, such as insulin and insulin-like growth factors.

Causes of intrauterine growth restriction

The causes of intrauterine growth restriction (Table 2.4) can be grouped into three categories on the basis of substrate availability and consumption:

- **Maternal substrate availability**: Maternal nutrition before and during pregnancy is crucial for normal fetal development. Abnormalities may occur if the mother has chronic disorders that reduce substrate availability, e.g. chronic lung disease for oxygen supply or malabsorption syndromes.
- **Placenta group**: Women may have poor uterine blood flow or a small placental surface-active area. Even cigarette smoking can affect this area, because it both causes endothelial damage and releases vasospastic modulators that reduce uterine and placental blood flow. The commonest clinical symptom of constricted uterine vessels is maternal hypertension, and this is also the commonest maternal factor associated with intrauterine growth restriction.

- **Fetal group**: In some fetuses, substrate consumption is impaired due to a genetic disorder, major congenital anomalies, metabolic disorders or accelerated metabolism and impaired growth caused by congenital intrauterine infection.

Table 2.4. Causes of intrauterine growth restriction

Maternal causes	Fetal causes
Disease	
Poor nutritional status	Genetic disorders
Cardiovascular disease	Malformations
Diabetes	Infections
Placental insufficiency	
Idiopathic	
Pre-eclampsia and other hypertensive disorders of pregnancy	
Abnormal placentation	
Substance abuse (smoking, alcohol, drugs)	Metabolic disorders
Multiple pregnancy	
Cord anomalies	
Autoimmune diseases	

Diagnosis and definition

Intrauterine growth restriction refers to conditions in which a fetus is unable to achieve its inherent growth potential. This functional definition applies to fetuses at risk for various poor outcomes. It intentionally excludes fetuses who are small for gestational age, i.e. at or below the 10th percentile for weight of normal fetuses of the same gestational age, but not pathologically small. A certain number of fetuses at or below the 10th percentile may be constitutionally small. In these cases, maternal or paternal features, the neonate's ability to maintain its own growth rate even if at a low centile, and the absence of other signs of uteroplacental insufficiency (e.g. oligohydramnios, abnormal Doppler findings) can be reassuring. Some fetuses who are pathologically growth-restricted may nevertheless be over the 10th percentile of estimated fetal weight. An estimated fetal weight at or below the 10th percentile is therefore used only to identify fetuses at risk.

The incidence of intrauterine growth restriction in the general obstetric population is estimated to be approximately 5%. Identification of this condition is crucial because proper evaluation and management can result in a favourable outcome. Certain pregnancies are at high risk for growth restriction, although a substantial percentage of cases occur in the general obstetric population. Accurate dating early in pregnancy is essential for a diagnosis; ultrasound biometry on serial longitudinal evaluation is the gold standard for determining fetal size and the amount of amniotic fluid, while Doppler assessment of fetal circulation may be of value in determining fetal status and assessing well-being.

In 1977, Campbell and Thoms introduced the concept of symmetric versus asymmetric growth-restriction. Symmetric growth restriction results in a fetus whose entire body is proportionally small, often due to a condition occurring in the first trimester, such

as a congenital anomaly, a genetic disorder or congenital infection. Asymmetric growth restriction results in a fetus who is undernourished and is directing most of its energy to maintaining the growth of vital organs, such as the brain and heart, at the expense of other structures, such as muscle, fat and the abdomen, especially its storage organ, the liver. This type of growth restriction is usually the result of placental insufficiency.

This differentiation has been questioned, because intrauterine growth restriction due to placental causes that have been present for a long time may present as symmetric growth impairment, as even brain development may be adversely affected. In growth-restricted hypoxic fetuses, redistribution of well-oxygenated blood to vital organs, such as the brain, heart and adrenal glands, is a compensatory mechanism to prevent fetal damage. When the reserve capacity of circulatory redistribution reaches its limit, fetal deterioration may occur rapidly. The most widely used definition of intrauterine growth restriction is now a fetus whose estimated weight is below the 10th percentile for gestational age and whose abdominal circumference is below the second percentile.

Accurate dating in early pregnancy is essential in diagnosing intrauterine growth restriction. The most reliable dating method is an ultrasound examination performed during the first trimester and no later than 20 weeks' gestation. Pregnancy can be re-dated by ultrasound scanning if the difference between menstrual age and ultrasound parameters is 7 days or more in the first trimester or 2 weeks or more in the second trimester. Re-dating during the second trimester should be avoided if an ultrasound scan from the first trimester is available. A woman's due date should never be changed on the basis of a third-trimester sonogram.

Ultrasound biometry

Ultrasound biometry of the fetus from measurements of the biparietal diameter, head circumference, abdominal circumference and femur length is now the gold standard for assessing fetal growth (Fig. 2.48). The percentiles have been established for each of these parameters, and fetal weight can be calculated.

In the presence of normal head and femur measurements, an abdominal circumference measurement less than 2 SD below the mean is considered a reasonable cut-off for considering a fetus to be asymmetric. The most sensitive indicator of symmetric and asymmetric intrauterine growth restriction is the abdominal circumference, which has a sensitivity of over 98% if the measurement is below the 2.5th percentile and has the lowest positive predictive value (36.3%). It may also be useful to calculate the ratio of the head circumference to the abdominal circumference. Between 20 and 36 weeks of gestation, this ratio normally drops almost linearly from 1.2 to 1.0. It is normal in a fetus with symmetric growth restriction and increased in asymmetric growth restriction.

Evidence of a hostile intrauterine environment can be obtained by looking specifically at the amniotic fluid volume. A decreased volume is strongly associated with intrauterine growth restriction. Significant morbidity has been found in pregnancies

with an amniotic fluid index of less than 5 cm, and a decreased index may be an early marker of declining placental function. The combination of oligohydramnios and intrauterine growth restriction portends a less favourable outcome, and early delivery should be considered. Generally, if the pregnancy is at 36 weeks or more, the high risk for intrauterine loss may mandate delivery.

Fig. 2.48. Asymmetric growth restriction. Ultrasound biometry in a 33-week fetus shows severe growth restriction, as demonstrated by the measurements of the biparietal diameter (top left), femur length (top right), and abdominal circumference (bottom left), all below –2 SD, and by the abnormally increased ratio of the head circumference to the abdominal circumference (bottom right; upper, middle, lower lines: 95th, 50th, 5th percentiles)

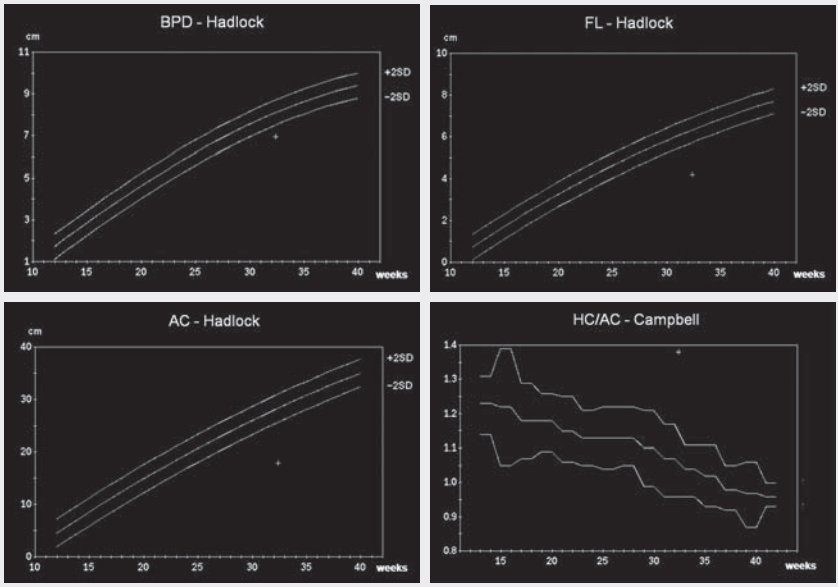

Haemodynamic modifications

During the past few years, technological advances in ultrasound have made it possible to study haemodynamic modifications in both physiological and pathological pregnancies. Both arterial and venous Doppler have been used to identify fetuses with intrauterine growth restriction and also to obtain additional information for planning delivery of fetuses at risk.

Placental insufficiency can be quantified on the basis of a reduction in end-diastolic Doppler flow velocity. Umbilical artery resistance decreases continuously in normal pregnancies but not in fetuses with uteroplacental insufficiency. The commonest measure of gestational age-specific umbilical artery resistance is systolic:diastolic

flow, which increases from baseline with worsening disease. As the insufficiency progresses, end-diastolic velocity is lost and, finally, reversed (Fig. 2.49).

Fig. 2.49. Umbilical artery: normal impedance to flow (a) and absent end-diastolic flow (b)

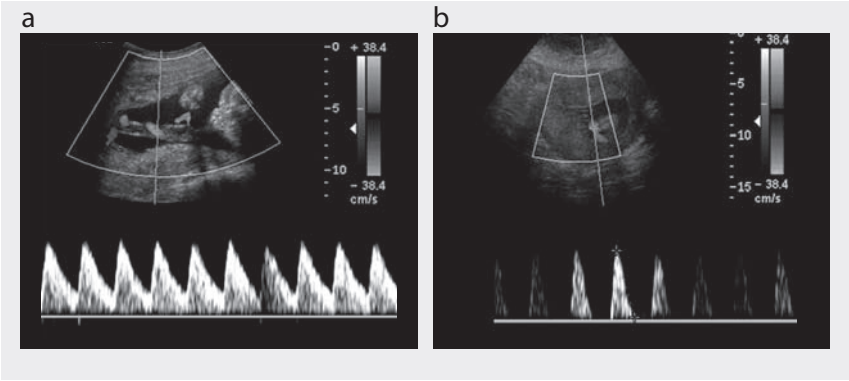

Fetuses with intrauterine growth restriction due to uteroplacental insufficiency are characterized by selective changes in peripheral vascular resistance, the so-called brain-sparing effect (Fig. 2.50), with increased blood supply to the brain, heart and adrenal glands and reduced perfusion of the kidneys, gastrointestinal tract and lower extremities. This mechanism allows preferential delivery of nutrients and oxygen to the vital organs, thereby compensating for diminished placental resources. Compensation through cerebral vasodilatation is, however, limited, and the maximum vascular adaptation to hypoxaemia precedes critical impairment of fetal oxygenation. In a series of intrauterine growth-restricted fetuses, examined longitudinally, a curvilinear relation was described between impedance in cerebral vessels and the state of fetal oxygenation; the progressive fall in impedance reached a nadir 2 weeks before the onset of late fetal heart rate deceleration.

Secondary to the brain-sparing condition, selective modifications occur in cardiac afterload, with a decreased left ventricle afterload due to cerebral vasodilation and an increased right ventricle afterload due to systemic and pulmonary vasoconstriction. In the first stages of the disease, the intrinsic myocardial function takes part in compensation for intrauterine growth restriction after establishment of the brain-sparing effect, as the supply of substrates and oxygen can be maintained at near-normal levels despite an absolute reduction in placental transfer.

The next phase of the disease is abnormal reversal of blood velocity, first in the inferior vena cava and then in the ductus venous, increasing the ratio of peak systolic velocity to end-diastolic velocity, mainly due to a reduction in the atrial component of the velocity waveforms (Fig. 2.51).

Fig. 2.50. Middle cerebral artery. Colour flow imaging (top) and spectral Doppler (bottom) in a normal fetus (bottom left) and in a growth-restricted fetus (bottom right). Normal (bottom left) and low (bottom right, with brain-sparing effect) impedance to flow

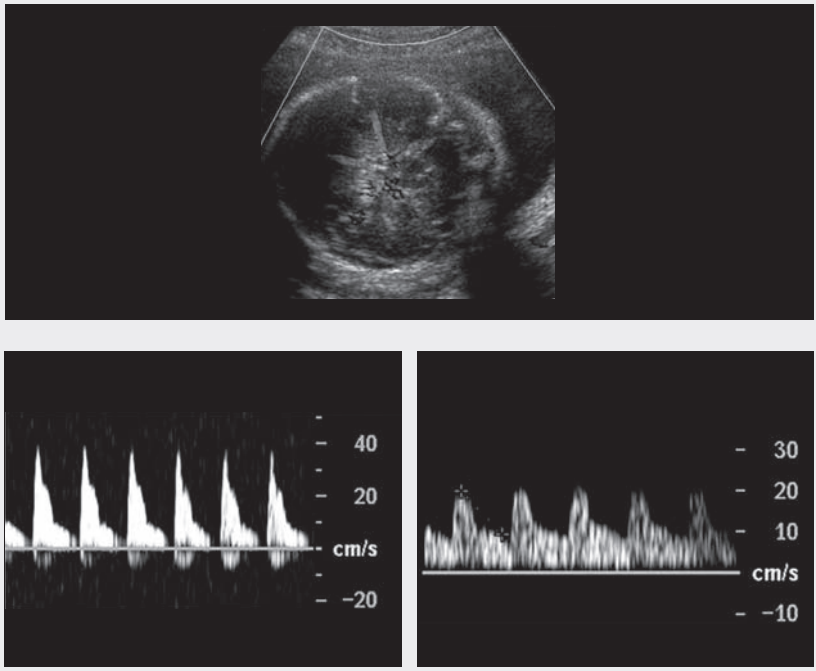

The high venous pressure induces a reduction in velocity at end diastole in the umbilical vein, causing typical end-diastolic pulsations. Development of these pulsations occurs close to the onset of fetal heart rate anomalies and is frequently associated with acidaemia and fetal endocrine changes. At this stage, reduced or reverse end-diastolic velocity may also be present in pulmonary veins, and coronary blood flow can be seen to be faster than in normal third-trimester fetuses. If the fetuses are not delivered, intrauterine death may occur after a median of 3.5 days.

Fig. 2.51. Ductus venous (top). Normal flow waveform (bottom left) and reversal of blood flow during atrial contraction (bottom right)

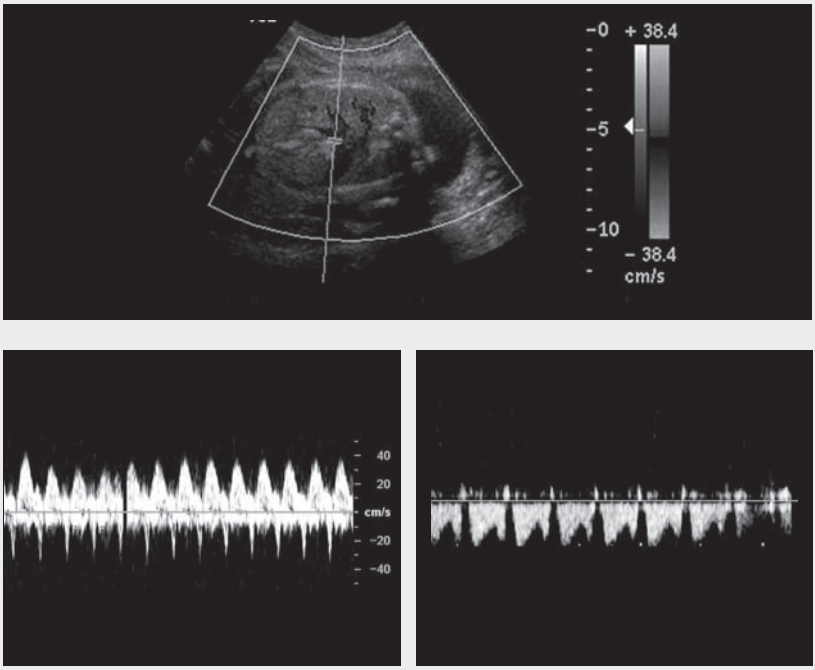

Management and delivery planning

Once a small-for-gestational age fetus is identified, intensive efforts should be made to determine whether there is growth restriction and, if so, its cause and severity, first by excluding structural or chromosomal abnormalities and possibly congenital infections.

Proper clinical management of intrauterine growth restriction requires maternal hospitalization and strict fetal surveillance, including a non-stress test (depending on gestational age) and serial Doppler velocity waveform measurements. For severely growth-retarded fetuses remote from term, the timing of delivery depends on an evaluation of the risk presented by intrauterine stay as compared with that of a very preterm birth. As no effective treatment of intrauterine growth restriction is available, the goal of management is to deliver the most mature fetus in the best physiological condition possible, while minimizing the risk to the mother. This requires antenatal testing to identify intrauterine growth restriction before acidosis.

Numerous protocols have been suggested for antenatal monitoring of such fetuses, including the non-stress test, amniotic fluid volume determination, biophysical profiles, venous and arterial Doppler measurements and fetal heart rate.

Harman and Baschat suggested a strategy for monitoring intrauterine growth restriction, which integrates fetal testing for increasing orders of severity, from 1 to 5.

Step 1

- *Test results*: abdominal circumference less than the fifth percentile, low abdominal circumference growth rate, high ratio of head circumference to abdominal circumference; biophysical profile score ≥ 8 and normal amniotic fluid volume; abnormal umbilical artery or cerebroplacental ratio; normal middle cerebral artery;
- *Interpretation*: intrauterine growth restriction diagnosed, asphyxia extremely rare, increased risk for intrapartum distress;
- *Recommended management*: intervention for obstetric or maternal factors only, weekly biophysical profile score, multivessel Doppler every 2 weeks.

Step 2

- *Test results*: intrauterine growth restriction criteria met, biophysical profile score ≥ 8, normal amniotic fluid volume, umbilical artery with absent or reversed end-diastolic velocities, decreased middle cerebral artery;
- *Interpretation*: intrauterine growth restriction with brain sparing, hypoxaemia possible and asphyxia rare, at risk for intrapartum distress;
- *Recommended management*: intervention for obstetric or maternal factors only; biophysical profile score three times a week; weekly umbilical artery, middle cerebral artery and venous Doppler.

Step 3

- *Test results*: intrauterine growth restriction with low middle cerebral artery pulsatility index; oligohydramnios; biophysical profile score ≥ 6; normal inferior vena cava, ductus venous and umbilical vein flow;
- *Interpretation*: intrauterine growth restriction with significant brain sparing, onset of fetal compromise, hypoxaemia common, acidaemia or asphyxia possible;
- *Recommended management*: if at more than 34 weeks' gestation, deliver (route determined by obstetric factors); if at less than 34 weeks' gestation, administer steroids to achieve lung maturity and repeat all testing after 24 h.

Step 4

- *Test results*: intrauterine growth restriction with brain sparing, oligohydramnios, biophysical profile score ≥ 6, increased inferior vena cava and ductus venous indices, umbilical vein flow normal;
- *Interpretation*: intrauterine growth restriction with brain sparing, proven fetal compromise, hypoxaemia common, acidaemia or asphyxia likely;
- *Recommended management*: if at more than 34 weeks' gestation, deliver (route determined by obstetric factors and oxytocin challenge test results); if at less

than 34 weeks' gestation, individualize treatment with admission, continuous cardiotocography, steroids, maternal oxygen or amnioinfusion, then repeat all testing up to three times a day, depending on status.

Step 5

- *Test results*: intrauterine growth restriction with accelerating compromise, biophysical profile score ≤ 6, abnormal inferior vena cava and ductus venous indices, pulsatile umbilical vein flow;
- *Interpretation*: intrauterine growth restriction with decompensation, cardiovascular instability, hypoxaemia certain, acidaemia or asphyxia common, high perinatal mortality, death imminent;
- *Recommended management*: if fetus is considered viable by size, deliver as soon as possible at tertiary centre (route determined by obstetric factors and oxytocin challenge test results); fetus requires highest level of natal intensive care.

In all cases, a diagnosis of intrauterine growth restriction before 32 weeks' gestation is associated with a poor prognosis. Therapy must be highly individualized. Several studies have shown that the ductus venous pulsatility index and short-term variation in fetal heart rate are important indicators for the optimal timing of delivery before 32 weeks' gestation. Delivery should be considered if one of these parameters is persistently abnormal, and it should be delayed for 48 h to allow maximum fetal benefit of maternal administration of glucocorticoids. Worsening of the mother's condition because of the pregnancy must be considered in deciding on the delivery of a severely growth-retarded fetus.

Perinatal and long-term sequelae

As the likelihood of severe distress in growth-retarded fetuses during labour is considerably increased, they should be monitored closely and Caesarean section should be considered. Moreover, the lack of amniotic fluid predisposes to cord accidents and their consequences. Growth-retarded newborns are also susceptible to hypothermia and other metabolic effects, such as serious hypoglycaemia. Polycythaemia and blood hyperviscosity (due to chronic hypoxia in utero) may occasionally cause cardiac heart failure at birth.

Most infants who have growth restriction in utero have normal rates of growth in infancy and childhood, although at least one third of them may show impaired growth and neurological development of various degrees. Many of these infants are also born prematurely, with additional morbidity. Children with a history of intrauterine growth restriction have been found to have attention and performance deficits. Minimizing hypoxic episodes during labour and delivery and intensive neonatal care at birth are mandatory for the best outcome.

Future directions and prevention

Prevention of intrauterine growth restriction is highly desirable. Investigators have suggested altering the thromboxane:prostacyclin ratio by administering aspirin with or without dipyridamole to mothers of fetuses with intrauterine growth restriction. Despite the theoretical benefit of aspirin, its role in preventing intrauterine growth restriction is still unclear. A large randomized controlled trial with a standardized high-risk population and a standardized treatment regimen could better answer this question.

Placenta, umbilical cord, amniotic fluid

Placenta

Normal findings

The echo pattern of the placenta changes during pregnancy. The intervillous spaces appear as lacunae 10–13 days after ovulation. Until 10–12 weeks, because of the proliferation of villi, the placenta appears as a hyperechoic rim of tissue around the gestational sac. At 12–16 weeks, the chorion normally apposes with the amnion. By 14–15 weeks, the placenta appears as a prominent echo-poor area. At 16–18 weeks, small intraplacental arteries may be visible. In the third trimester, the placenta is a highly vascularized organ.

Sonographic evaluation of the placenta begins with localization, but ultrasound can also be used to assess placental size, thickness and echo texture. The normal at-term placenta measures 15–20 cm in diameter, with a volume of 400–600 ml. The normal placental thickness is approximately 1 mm per week of gestation (at term 45 mm). Common causes of homogeneous thickening are diabetes mellitus, anaemia, hydrops, infection and aneuploidy.

Abnormalities

Placenta bipartita or bilobata: The placenta is separated into lobes, but the division is incomplete and the fetal vessels traverse the membranes, extending from one lobe to the other, before uniting to form the umbilical cord (Fig. 2.52).

Placenta succenturiata: In this condition, one or more small accessory lobes develop in the membranes at a distance from the main placenta and can be recognized on ultrasound as a distinct, apparently separate mass of placental tissue. There is a strong association with placental infarction and velamentous insertion of the umbilical cord.

Placenta circumvallata: The chorionic plate, on the fetal side of the placenta, is smaller than the basal plate, on the maternal side; the fetal surface of the placenta presents a central depression, surrounded by a thickened ring composed of a double fold of amnion and chorion. The fetal surface presents the large vessels that terminate at the margin of the ring.

Placenta circummarginata: The chorionic plate, on the fetal side of the placenta, is smaller than the basal plate, on the maternal side, but the ring does not have

Fig. 2.52. At 27 weeks, a bilobate placenta (large arrowhead shows separation of the two lobes), with the two lobes (small arrowheads) originating from the anterior and posterior wall of the uterus

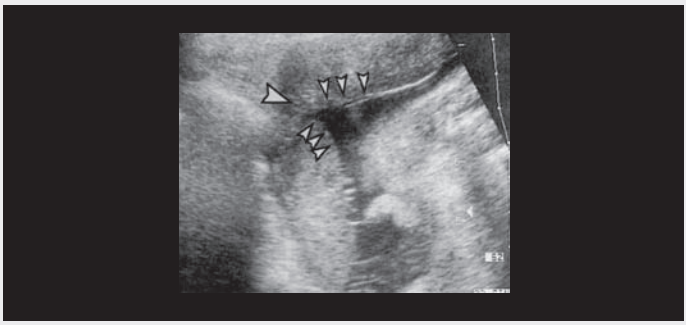

a central depression with the fold of membranes seen in placenta circumvallata, and the fetal membrane insertion is flat.

Placental calcifications

The placenta can mature and calcify. Although there is a system for grading placentas in utero, only premature or accelerated placental calcification has been associated with maternal or fetal disorders, such as hypertension and intrauterine growth restriction.

Focal lesions

Focal lesions, which are often of no clinical significance, can be cystic or echo-poor. They may result from intervillous thrombus, decidual septal cysts or perivillous fibrin deposition and are usually < 3 cm in diameter (Fig. 2.53).

Fig. 2.53. Placental cyst (arrowheads) centrally located and situated below the chorionic plate, at 24 weeks. Colour Doppler velocimetry failed to demonstrate flow within the echo-poor area

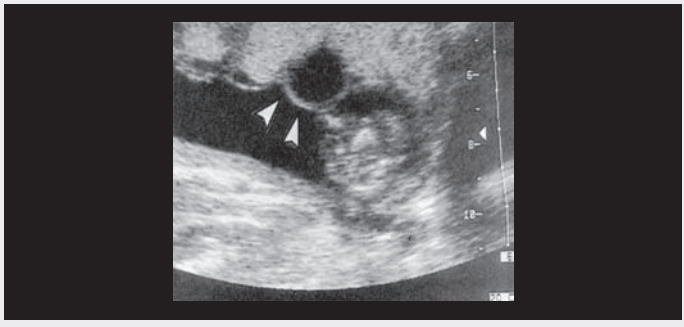

Vascular abnormalities

Placental infarct: A placental infarct is a localized area of ischaemic villous necrosis, more commonly at the periphery of the placenta. In almost 90% of cases, it is located at the placental margin and is < 1 cm. This type of limited infarction results from occlusion of the maternal uteroplacental circulation and usually represents normal ageing. Placental infarcts can be an incidental, normal finding, but placental insufficiency may develop if they are numerous.

Most placental infarcts are not readily detectable by ultrasound because they are isoechoic with adjacent placental tissue; in rare instances, an acute placental infarct may be visible as a slightly echo-rich region. Most infarcts are small and are not clinically significant. When they are thick, centrally located and randomly distributed, they may be associated with pre-eclampsia or lupus anticoagulant.

Maternal floor infarct: This uteroplacental vasculopathy differs from the previously described infarcts in that there are no large areas of villous infarction. Instead, fibrinoid deposition occurs within the decidua basalis, usually confined to the placental floor. These lesions are not detectable by antenatal ultrasound.

Haematomas

The location, cause, sonographic findings and clinical impact of haematomas should be determined. Subchorionic or marginal haematomas are located at the lateral margin of the placenta. Retroplacental haematomas, which can manifest as placental abruption, are of the greatest clinical consequence. When the placenta is imaged, the retroplacental echo-poor complex, composed of uteroplacental vessels (veins) and myometrium, should be observed. When this region appears thicker, the possibility of retroplacental haemorrhage should be considered.

Placental abruption

The clinical condition (abruption) and the pathological condition (haematoma) both involve abnormal accumulation of maternal blood within or above the placenta or membranes. The sonographic appearance of retroplacental haemorrhage depends on age and location of bleeding. Characteristically, haemorrhage may be hyperechoic acutely (0–48 h), isoechoic at 3–7 days and hypoechoic at 1–2 weeks. After 2 weeks, portions of the clot may become echo-free.

Placenta praevia

In placenta praevia, the placenta is located over or very near the internal os (Fig. 2.54). Four degrees of this abnormality have been recognized:

- **Total placenta praevia**: the internal cervical os is completely covered by placenta.
- **Partial placenta praevia**: the internal os is partially covered by placenta.
- **Marginal placenta praevia**: the edge of the placenta is at the margin of the internal os.

Fig. 2.54. Placenta praevia

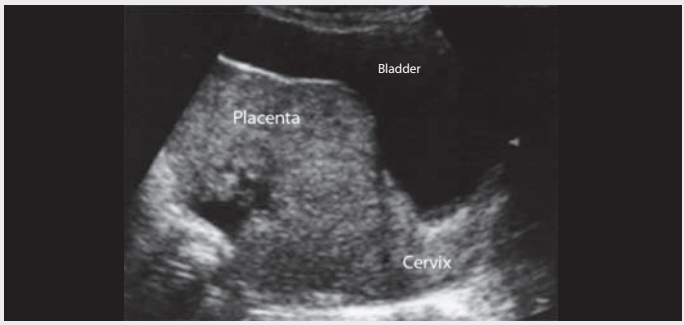

- **Low-lying placenta**: the placenta is implanted in the lower uterine segment such that the placental edge does not reach the internal os but is in close proximity to it.

Sonographic evaluation of the placental location with respect to the internal cervical os is reliable, and a diagnostic accuracy of 90–95% has been reported. Placenta praevia can also be diagnosed transvaginally, particularly for a posteriorly implanted placenta. The positive predictive value is 71% with the transvaginal approach and 31% with the transabdominal approach. The high false-positive rate with transabdominal ultrasound may be due to technical reasons. Excessive distension of the urinary bladder can result in approximation of the anterior and posterior lower segments, creating a false impression of placenta praevia. Therefore, the evaluation should be performed with the bladder partially full and not overdistended. A laterally implanted placenta, in conjunction with normal uterine rotation and a distended bladder can also lead to a false diagnosis. It is important to identify the cervix. Parasagittal evaluation of a laterally located placenta or isolated contractions of the lower segment in conjunction with a distended bladder can lead to a false diagnosis.

Accurate diagnosis of placenta praevia thus requires knowledge of the location of the cervix, the internal cervical os and the placenta. The diagnosis should be confirmed by sonographic examinations with the urinary bladder both filled and partially empty. A careful transvaginal technique can confirm the diagnosis.

Placenta accreta

The term 'placenta accreta' is used to describe any placental implantation in which there is abnormally firm adherence to the uterine wall. Placenta praevia can be associated with placenta accreta or one of its more advanced forms, placenta increta or

Fig. 2.55. Placenta accreta: longitudinal power Doppler sonogram in the 19th week of gestation shows arcuate and radial arteries within the bladder muscle layer. P, placenta; U, urinary bladder

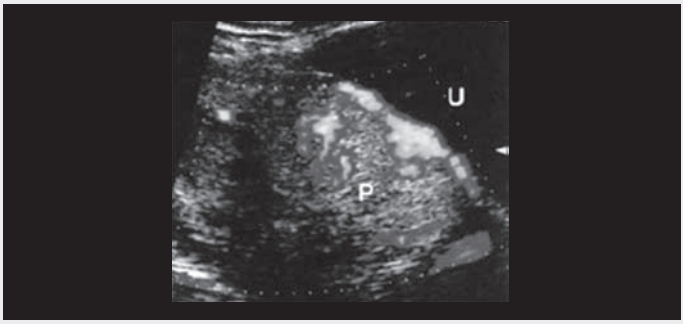

percreta (Fig. 2.55). As a consequence of the partial or total absence of the decidua basalis and imperfect development of the fibrinoid layer, placental villi are attached to the myometrium in placenta accreta and actually invade the myometrium in placenta increta or penetrate through the myometrium in placenta percreta.

Ultrasound is only 33% sensitive for detecting placenta accreta; however, with ultrasound Doppler colour flow mapping, two factors are highly predictive of myometrial invasion: a distance < 1 mm between the uterine serosal bladder interface and the retroplacental vessels and the presence of large intraplacental lakes.

Tumours

Chorioangioma (haemangioma): Chorioangiomas are unique, non-trophoblastic placental tumours, which are present in approximately 1% of all placentas examined. Antenatal diagnosis is possible. Morphologically, they appear most commonly on the fetal surface of the placenta but can occur within the substance. The sonographic features are complex. Colour flow Doppler can reveal highly turbulent flow or low flow. Small chorioangiomas are often benign, whereas large tumours have been associated with polyhydramnios in 15–30% of cases.

Gestational trophoblastic neoplasia: Benign gestational trophoblastic neoplasia is commonly referred to as hydatidiform mole (Fig. 2.56). The clinical course is benign in 80–85% of cases. The sonographic features of hydatidiform mole are distinctive and characteristic at advanced gestational ages. Sonographically, the uterus is usually filled with multiple isoechoic-to-hyperechoic areas which are highly correlated with the presence of vesicles, the size of which depends on gestational age. During the first trimester, the vesicles are not easily delineated and the uterine cavity appears echo-rich, generating the classical snowstorm appearance seen in the old B-mode static scanning. This appearance may not be as evident using current ultrasound technology. The diameter of the vesicles can reach 10 mm during the second

Fig. 2.56. Hydatidiform mole (Doppler signals in white)

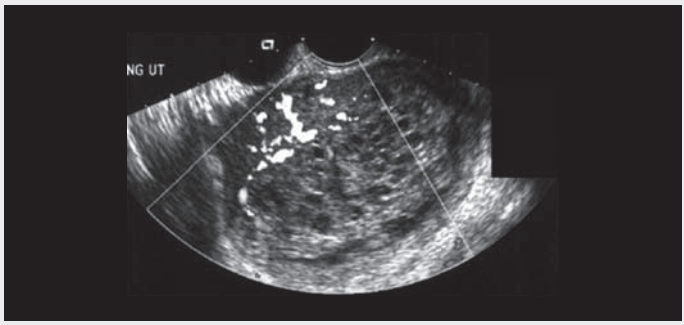

trimester. Areas of haemorrhage can also be seen. Theca lutein cysts of the ovaries can be demonstrated sonographically. Other gynaecological conditions that can be mistaken for a molar pregnancy on ultrasound examination are embryonic demise, anembryonic pregnancy, leiomyoma and retained products of conception associated with an incomplete abortion.

A coexisting fetus, which is often dead, is seen in approximately 2% of cases. It is thought that this association is probably the result of molar transformation of one placenta in a dizygotic twin pregnancy. The hydatidiform mole frequently has a parental 46,XX (dispermy) karyotype, while the coexisting fetus generally has a normal karyotype. Fetal karyotypic analysis of this twin is recommended if the woman wishes to continue the pregnancy. It is important to distinguish between a partial hydatidiform and a molar pregnancy with a coexisting fetus, as a partial mole is considered to have less malignant potential than a complete hydatidiform mole.

The sonographic characteristics of a partial mole include a large, thickened placenta containing cystic spaces and a gestational sac with a fetus. If the fetus is alive, it is often severely growth-restricted. Fetal triploidy is characterized by severe growth restriction, oligohydramnios, hydrocephaly and hydropic placental changes.

Umbilical cord

The umbilical cord is first visualized by ultrasound at 8 weeks, when the length of the cord is approximately equal to the crown–rump length; it usually remains at the same length as the fetus throughout pregnancy. The diameter of the umbilical cord is normally < 2 cm. It usually contains two arteries and one vein; early in development, there are two umbilical veins, but the right vein atrophies and the left vein persists. The presence of two umbilical arteries can be confirmed on a short axis view or by visualizing vessels on each side, lateral to the fetal bladder (Fig. 2.57, Fig. 2.58).

The average length of the umbilical cord is 59 cm (range, 22–130 cm). The two factors that determine its length are sufficient space in the amniotic cavity for

movement and the tensile force applied to the cord during fetal movement. The vessels of the cord are surrounded by Wharton jelly, a gelatinous connective tissue that protects the umbilical vessels from compression.

The commonest abnormality of the umbilical cord is a single umbilical artery, which may occur as aplasia or as the consequence of atrophy of one artery secondary to thrombosis. Normally, the umbilical cord has a central insertion within the placenta. In 7% of pregnancies, there is an insertion of the cord at the margin of the placenta. Insertion of the cord beyond the placental edge into the free membranes is referred to as a velamentous insertion. Focal abnormalities within the umbilical cord may be seen incidentally during routine ultrasound. Single or multiple cysts are occasionally seen, whereas focal masses are rare and include tumours, haematomas, varices and aneurysms.

Fig. 2.57. Two vessels in an umbilical cord (short axis view of the cord)

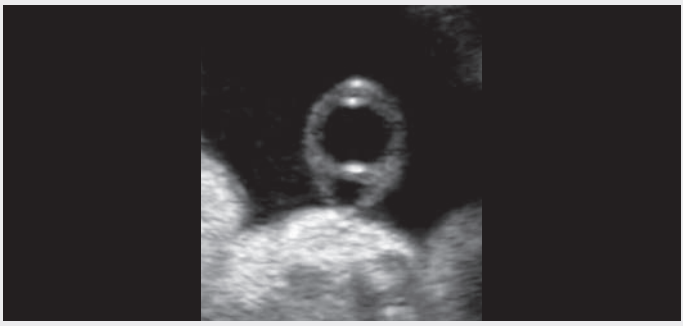

Fig. 2.58. Two vessels in an umbilical cord. Sagittal scan lateral to the fetal bladder (left); long axis view of the cord (right). RT UMB ART, right umbilical artery; BL, urinary bladder; 2VC, two-vessel cord

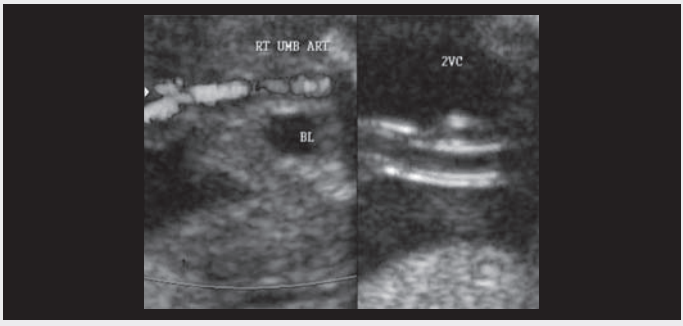

Amniotic fluid

Over the past two decades, estimation of amniotic fluid volume has become part of the standard evaluation in antenatal surveillance and intrapartum management in both normal and high-risk pregnancies. Although progressive improvement of ultrasound techniques and of clinical expertise has led to sophisticated methods for quantifying amniotic fluid volume with highly reproducible accuracy, there is still no unanimous agreement on which method of measuring the fluid is the best prognostic indicator of pregnancy outcome.

Methods for evaluating amniotic fluid

Today, ultrasound visualization of amniotic fluid pockets allows both subjective and objective estimates of amniotic fluid volume, the former being closely dependent on the sonographer's experience and the latter providing more accurate trends in volume over time and comparison with standard values. Semiquantitative methods are described below.

Single deepest pocket technique: The concept of estimating amniotic fluid volume from the depth of the maximum vertical pocket observed with ultrasound was first introduced in 1984 by Chamberlain. This technique consists of measuring the deepest clear amniotic fluid pocket (free from umbilical cord and small fetal parts) in its anteroposterior diameter within the uterus. **Oligohydramnios** is a pocket < 1 cm in depth, while a reduced fluid volume is a pocket measuring 1–2 cm. Measured pockets deeper than 8 cm are classified as **hydramnios**. Although the criteria for normal amniotic fluid volume in the study of Chamberlain were based on a population of high-risk, post-date pregnancies, this technique has the virtues of simplicity, reproducibility and a large body of experience; moreover, it is probably the best method for estimating amniotic fluid volume in the sacs of multifetal pregnancies.

Amniotic fluid index: The amniotic fluid index was used for the first time in 1987 by Phelan. It is obtained by summing the maximum vertical pocket in each of four quadrants of the uterus; the uterine quadrants are defined sagittally by the linea nigra for left and right and by the umbilicus for the upper and lower. When taking the measurements, the ultrasound transducer should be positioned parallel to the woman's sagittal plane and perpendicular to the coronal plane (not angled following the uterine curvature), and the pockets should be clear of umbilical cord and small fetal parts. To allow use of the amniotic fluid index in preterm pregnancies, the upper and lower quadrants are divided at half the fundal height, regardless of umbilical position.

The range and distribution of amniotic fluid indexes were more rigorously defined by Moore and Cayle (1990) in a group of normal pregnancies. These authors found that the mean amniotic fluid index in term pregnancies (40 weeks) was 12 cm, in hydramnios it was 21 cm (95th percentile) and in oligohydramnios it was 7 cm (5th percentile). Huge variations in amniotic fluid index were noted at different gestational ages, the median index varying from approximately 15 cm at mid-trimester to < 11 cm after 42 weeks.

Moore evaluated the interobserver and intraobserver variation in multiple measurements of the amniotic fluid index in the same woman and found an intertest variation of approximately 1 cm, which represents a variation of > 15% at low amniotic fluid indexes (< 7 cm). To obtain optimal accuracy with this technique, taking the average of three measurements at the same ultrasonographic session has been recommended.

Two-diameter pocket: In this method, the depth of the maximum vertical pocket in the uterus is multiplied by its largest horizontal diameter (again, the pocket must be free of cord or fetal extremities). With this technique, the normal amniotic fluid volume is defined as 15–50 cm^2, hydramnios as > 50 cm^2 and oligohydramnios as 0–15 cm^2.

Amniotic fluid volume in multiple pregnancies

Estimating amniotic fluid volume in multiple pregnancies is challenging, as the cavity occupied by each fetus is irregular and the position and limits of the intervening membranes may be difficult to discern. The three methods described above were evaluated and found to be approximately equivalent (80–98% accurate) when the amniotic fluid volume was in the normal range. When the volume measured with the dye infusion technique was < 500 ml (oligohydramnios), however, the accuracy of all three techniques fell to 3–57%. This finding, as for singleton gestations, confirms the difficulty of identifying oligohydramnios with ultrasound in multiple pregnancies.

Because of the convoluted position of the dividing membranes, the rapidly changing fetal position and pressure and volume differences within each sac, the four-quadrant approach (based on several angle-dependent measurements) might be even less accurate for multifetal gestations than for singletons.

Given the simplicity of the maximum vertical pocket and the two-diameter techniques, either will provide the most accurate and reproducible assessment of amniotic fluid volume in multiple pregnancies. Oligohydramnios should be suspected if no pocket at least 3 cm in depth can be measured in an individual sac, and hydramnios should be suspected if a single pocket exceeds 8 cm.

Cervix

The main aim of ultrasonographic evaluation of the cervix is to identify women at risk for preterm labour. It can also be used before medical induction of labour, with a clinical examination, to evaluate the probability of successful induction. A study with transvaginal ultrasound of the relation between placental insertion and uterine internal os is recommended in all cases of placenta praevia or low-lying placenta suspected on transabdominal ultrasound. For a differential diagnosis of complete placenta praevia, incomplete placenta praevia and low-lying placenta, transvaginal ultrasound of the uterine neck and its relation to the lower placental edge is advised between 32 and 37 weeks' gestational age in all cases suspected earlier (Fig. 2.59). If

Fig. 2.59. Transvaginal ultrasound in cases of placenta praevia. (a) 32 weeks: the inferior placental edge (dotted arrow) does not cover the internal uterine os (arrow). (b) 28 weeks: the placenta praevia covers the internal os (arrow); IUO, internal uterine os

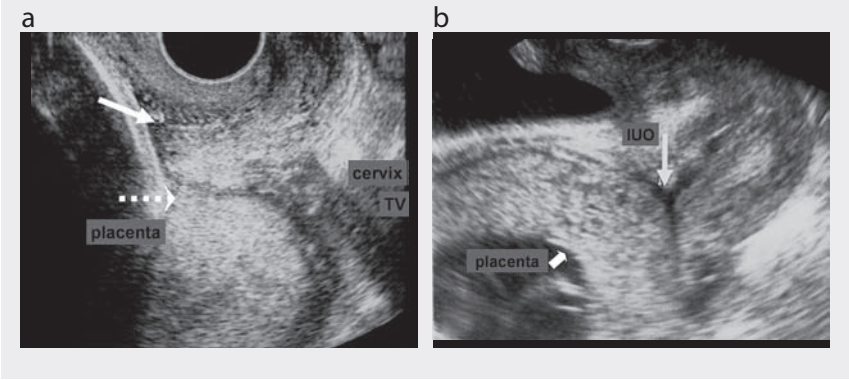

bleeding occurs, transvaginal ultrasound can be used at any time during gestation, but the diagnosis must be confirmed after 32 weeks.

Indication

Evaluation of the uterine cervix is indicated for women at risk for a preterm birth based on a previous history, women with symptoms of preterm labour and follow-up of women after cervical cerclage positioning. Evaluation is not indicated for low-risk populations, i.e. in screening to predict preterm labour. The value of ultrasound cervical examination in predicting the success of labour induction and mode of delivery is still being investigated.

Preparation

For transabdominal ultrasound, the woman should have a full bladder. To fill her bladder, the woman should drink 1 l (four glasses) of water 0.5–1 h before the procedure. If she cannot drink, the bladder can be filled with a saline solution through a Foley catheter. For transvaginal or transperineal ultrasound, the woman should void her bladder immediately before the procedure.

Examination techniques

For transabdominal, transperineal (translabial), or transvaginal ultrasound, the woman should lie on the examination bed on her back, with extended or flexed legs.

For **transabdominal ultrasound**, ultrasonographic gel is applied to the woman's skin, and the ultrasonographic probe is used to examine the pelvis and the lower part of the abdomen through horizontal (transverse), vertical (sagittal) and oblique

scanning planes. Unfortunately, this technique is not sufficiently reliable or valid, because bladder filling often elongates the cervix and masks the funnelling of the internal os; fetal parts can obscure the cervix, especially after 20 weeks; and the distance between the probe and the cervix degrades the image quality.

For **transperineal** (translabial) **ultrasound**, a gloved transducer in a sagittal orientation is positioned on the perineum, at the vaginal introitus between the labia majora, oriented in the direction of the vagina to visualize the uterine neck. This technique is well accepted by most women, as the transducer does not enter the vagina, avoiding pressure on the cervix; however, the technique is more difficult than transvaginal ultrasound, and gas in the rectum can impede satisfactory visualization of the uterine neck.

For **transvaginal ultrasound** (Fig. 2.60), a clean transvaginal probe, placed in an aseptic probe cover (condom) filled with ultrasonographic gel, is inserted into the anterior fornix of the vagina. The probe is close to the cervix, without the problem of obscuring bowel gas. This technique has become the preferred method of evaluating the cervix in all clinical settings. Recommendations for transvaginal ultrasound examination of the cervix are to:

- obtain a sagittal long-axis view of the endocervical canal, along its entire length;
- withdraw the probe until the image is blurred and apply just enough pressure to restore the image, avoiding excess pressure, which can elongate the cervix;
- enlarge the image so that the cervix occupies two thirds of the picture, with both the external and the internal os clearly visible;

Fig. 2.60. Transvaginal ultrasound of normal cervical length. (a) Uterine neck at 24 weeks: normal cervical length after cervical cerclage (arrowheads), internal os (arrow), external os (dotted arrow). (b) Normal cervix at 25 weeks: closed and curved endocervical canal from internal (arrow) to external os (dotted arrow); IUO, internal uterine os

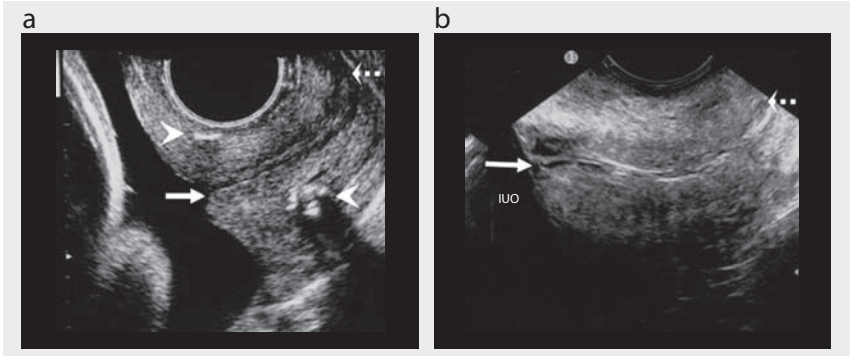

- measure the cervical length from the internal to the external os along the endocervical canal (take at least three measurements and record the shortest, best measurement in millimetres);
- apply transfundal pressure for 15 s and record the cervical length again;
- describe the presence of funnelling (opening) of the internal os and cervix and measure its length and width.

Normal findings

Transvaginal sonography has been shown to be superior to manual examination for evaluating the cervix. Various cervical parameters have been evaluated, but cervical length, measured from the internal os to the external os along the endocervical canal, is the most reproducible and reliable measurement. If the cervical canal is curved, the cervical length can be measured on a straight line between the internal and external os or as the sum of two straight lines that follow the curve.

The normal cervical length is 25–50 mm at 14–30 weeks' gestational age in singleton pregnancies. A cervical length > 25–30 mm is a reassuring finding. After 30 weeks, the cervix progressively shortens in preparation for term labour, so that a length of 15–24 mm can be physiological in asymptomatic women. In normal pregnancies, the internal os is flat, the cervical canal and the internal os are closed, and the length of the cervix is the only measurement to be made (Fig. 2.60). The length may change dynamically during a 5- to 10-min examination, and in some cases funnelling of the upper cervical canal may appear and resolve. This occurs in women having contractions, and, similarly, the cervix may shorten in response to transfundal pressure in an otherwise normal cervix.

In multiple pregnancies, cervical length measured at 14–19 weeks is similar to that in singleton pregnancies, but in multiple pregnancies the cervix is progressively much shorter, starting from 20 weeks' gestational age.

Pathological findings

Risk of preterm birth and patient with preterm birth

The changes in the cervix that lead to preterm or term labour, seen by transvaginal ultrasound, include: initial opening of the internal os of the cervix; progressive cervical shortening and widening along the endocervical canal (from the internal to the external os); and opening of the external os. A short cervical length (< 25 mm) is the best predictor of preterm birth at 16–24 weeks: the shorter the cervical length, the higher the risk for preterm birth. In high-risk women, preterm birth after the detection of a short cervix (< 10 mm) is often preceded by premature rupture of the membranes. When funnelling occurs, the internal os and the open part of the cervical canal have a triangular shape, and the total cervical length is the sum of the funnel (open portion of the cervix) length and the functional cervical length (closed portion of the endocervical canal). It is also possible to measure the internal os diameter (funnel width) (Fig. 2.61).

Fig. 2.61. Different degrees of cervical shortening and funnelling. (a) 31 weeks: cervical length, 36 mm, funnelling of the internal os, 4.5 mm (calipers). (b) 19 weeks: cervical length, 33 mm (calipers), evident funnelling. (c) 22 weeks: cervical length, 36 mm, funnel width, 11.3 mm (calipers). (d) 27 weeks: cervical length, 15 mm (calipers), broad funnelling

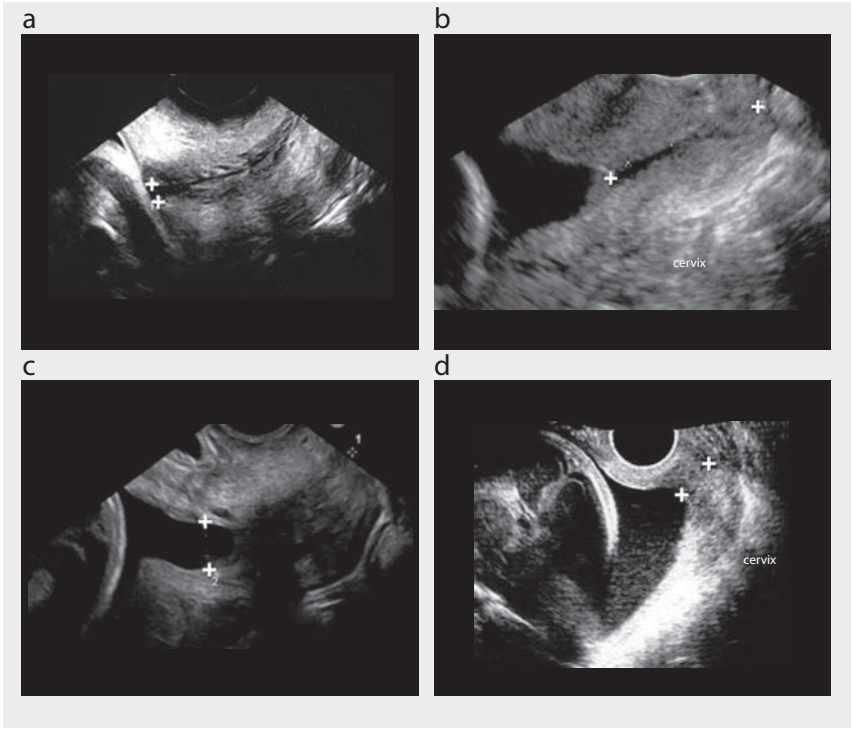

After measurement of a cervix < 25 mm before 24 weeks by transvaginal ultrasound, cervical cerclage is suggested in women with a singleton pregnancy and a previous preterm birth. The sensitivity of such measurements for predicting preterm birth in high-risk singleton pregnancies is often > 60%. Unfortunately, the sensitivity for predicting preterm births in low-risk women is low for singleton pregnancies (< 40%), twin pregnancies (30%) and triplet pregnancies (10%). Given these findings, routine screening for cervical length with transvaginal ultrasound is not recommended for all pregnant women.

Follow-up after cervical cerclage

Transvaginal sonography of the cervix has been evaluated in women with cerclage in place (indicated by history, physical examination or ultrasound). Evaluations of pre- and post-cerclage cervical length have shown that it usually increases after cerclage and that the increase is associated with a higher rate of term delivery. In women with cerclage, the best indicators for preterm birth are a cervical length < 25 mm and an upper cervix length (the closed cervical portion above the cerclage) < 10 mm.

Fig. 2.62. Ultrasound follow-up after cervical cerclage. (a) Transabdominal ultrasound, cerclage in place, 17 weeks; the two arrows show anterior and posterior views of the neck suture. (b) Transabdominal ultrasound, cerclage displacement, 24 weeks; left, longitudinal scan; right, transverse scan; the arrows show the suture displaced anteriorly with the protruding inferior pole of the membranes. (c) Transvaginal ultrasound, cerclage in place, 31 weeks; the arrows show the normal suture position

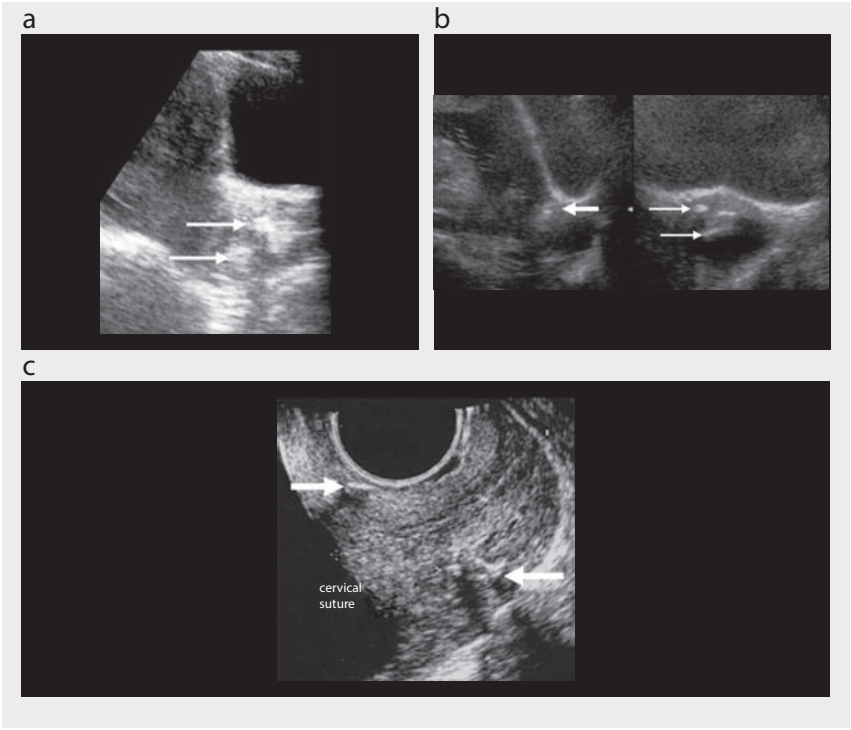

Transabdominal or transvaginal ultrasound or physical (manual, digital) examination can be used to detect cerclage displacement (Fig. 2.62).

Predicting the success of labour induction and mode of delivery

Some studies show that cervical length measured by transvaginal ultrasound at 37 weeks correlates with the mean gestational age at delivery: 38 weeks for women with a cervical length of 10 mm at 37 weeks, 41 weeks for women with a cervical length of 35 mm and > 41 weeks if the cervical length is > 40 mm. A short cervical length is associated with a short duration of labour and a higher incidence of vaginal delivery compared with a cervix measuring > 26–30 mm at the onset of labour. Caesarean delivery was recorded for only 4% of women in spontaneous labour with a cervical length < 20 mm but for 12% of women with a cervical length > 40 mm. The Bishop score parameter was less sensitive than transvaginal ultrasound for evaluating the need for intracervical prostaglandin treatment before oxytocin labour induction.

Multiple pregnancies

The incidence of multiple pregnancies is 3%. Over the past 20 years, the number of twin births has increased by 50% and the number of multiple deliveries by 400%, primarily because of the availability and increased use of ovulation-inducing drugs and assisted reproductive techniques. The increase is also related to advanced maternal age, with the rate of dizygotic twinning peaking between 35 and 40 years of age, mainly in multiparous women. Heredity and a maternal history of twinning (either dizygotic or monozygotic) are particularly important for twinning, while the father's history plays little or no part. Race is also a factor: the percentage of dizygotic twins is 1% in whites, lower in blacks and higher in Asians.

There are two kinds of twins. Dizygotic twins are the result of simultaneous fertilization of two different oocytes by two different spermatozoa. Monozygotic or identical twins result from duplication of a single conceptional product. As dizygotic twins originate from multiple ovulations, they reflect the incidence of genetic and ethnic factors, whereas monozygotic twins result from duplication of a single zygote, with a constant frequency in all ethnic groups. Dizygotic twins have two different placentas and amniotic membranes in two amniochorionic membranes (dichorionic twins). They are the same sex in 50% of cases. In monozygotic twins, who are always the same sex, placentation depends on the time of embryo duplication:

- within 3–4 days after conception: dichorionic diamniotic;
- between 3 and 9 days after conception: monochorionic diamniotic;
- between 9 and 12 days after conception: monochorionic monoamniotic;
- at ≥ 12 days after conception: Siamese or joined.

The placenta can be mono- or dichorionic. Fetal risks increase in relation to monochorionicity and monoamnionicity. Fetal mortality is three times greater among twins than among singletons. The fetal risk for cerebral palsy is eight times greater than in singletons and 47 times greater in triplets. Maternal risks, such as hypertension, postpartum haemorrhage and mortality, are twice as high as in a single pregnancy.

The purposes of management are to:

- prevent preterm birth;
- identify growth alterations in one or both twins;
- recognize correlated pathological conditions and, if necessary, treat them;
- determine the timing and type of delivery.

Indications

Early diagnosis of multiple pregnancy is possible from the 5th to 6th week by ultrasound scan. The final diagnosis, however, relies on embryo individuation, which is possible from week 6–7.

An ultrasound scan should be performed in the first trimester to:

- visualize ovular implants (or gestational sacs) in the uterus and their number;
- verify the presence of embryos or fetuses, their number and their cardiac activity;
- date the pregnancy.

In the case of multiple pregnancies, chorionicity and amniocity should be evaluated.

Preparation

Pregnancy can be evaluated with transabdominal or transvaginal probes. The main advantage of transvaginal scan is the significant improvement in image resolution. For transabdominal scanning, a probe of at least 3.5 MHz should be used to scan through the abdominal wall, with a full bladder, at an early gestational age. For the transvaginal scan, with an empty bladder, a high-frequency probe (at least 5 MHz) can be used because of the shorter distance between the transducer and the organ target, with a large increase in resolution. The two methods are, however, complementary. Transvaginal scan is preferred at early gestational ages (first trimester).

Normal findings

A twin pregnancy can be diagnosed from week 5 with a transabdominal or transvaginal probe to evaluate the number of intrauterine gestational sacs.

The main aims of ultrasound scanning in the first trimester are:

- pregnancy dating
- evaluation of the number of embryos or fetuses
- evaluation of fetal heartbeat
- diagnosis of amnionicity and chorionicity
- exclusion of early morphological anomalies
- cervix evaluation.

In the second trimester, ultrasound is used for morphostructural examinations, fetal growth evaluation and cervix evaluation; and in the third trimester, ultrasound is used for fetal growth evaluation and assessment of fetal well-being (Doppler).

In multiple pregnancies, the determination of chorionicity, as a distinction between monochorionicity and dichorionicity, will differentiate between monozygotic and dizygotic twins.

The accuracy of ultrasound scanning for diagnosing chorionicity is nearly 100% in the first trimester (14 weeks), but ultrasonographic determination is not always possible at an advanced gestational age, especially for a differential diagnosis of a

single or seemingly single placenta. This may require identification of typical signs, such as the lambda sign, or the interamniotic septum thickness.

Lambda sign: The chorial septum that separates the dichorionic gestational sacs in the first trimester becomes thinner during pregnancy but remains thicker in the portion next to the placenta. It can be seen as a triangular projection of chorial tissue at the base of the septum that separates the amniotic membranes of the twins. This feature, known as the lambda or twin peak sign, indicates a dichorionic pregnancy, with 94% sensitivity, 88% specificity, 97% positive predictive value and 78% negative predictive value. This part of the chorial tissue can, however, grow thin and become invisible in the second half of pregnancy.

Thickness of the interamniotic septum: This septum is thicker in cases of dichorionicity. Although there is no consensus on a cut-off, a 2-mm interamniotic septum indicates a dichorionic pregnancy. As septum thickness decreases in all pregnancies during the second trimester, the evaluation is subjective and the measurement is not reproducible.

In advanced pregnancies, a membrane between the two amniotic sacs is not always visible. When the insertion of the membranes on the uterine wall cannot be seen, the lambda sign is the index of a dichorionic twin pregnancy. While a diagnosis of chorionicity can be made reliably at the beginning of the second trimester with the lambda sign, its absence after the 20th week cannot exclude dichorionicity.

The type of twin pregnancy is determined in the first trimester as follows:

- **dichorionic, diamniotic**: Two chorions visible as two separate hyperechoic rings; the septum is thicker, with more intense echogenicity; four membranes (two chorions and two amnions) can be seen (Fig. 2.63);
- **monochorionic, diamniotic**: Only one hyperechoic chorionic ring, with two separate yolk sacs and two embryos separated by amniotic membranes; the septum is < 2 mm (Fig. 2.64, Fig. 2.65). In the early phases of gestation, only the two vitelline sacs are observed, before the embryos become visible;
- **monochorionic, monoamniotic**: Only one hyperechoic chorial sac, with two separate embryos; no membrane of separation between the twins is seen; the fetuses are free to move inside the uterine hollow; the amniotic fluid appears evenly distributed (Fig. 2.66, Fig. 2.67).

In the first trimester, a dichorionic pregnancy appears on an ultrasound scan as two separate hyperechoic rings in the endometrium. To confirm this diagnosis, a yolk sac and a fetus must be demonstrated in each chorionic sac.

Monozygotic pregnancies are identical to dizygotic ones. A monochorial diamniotic pregnancy appears on ultrasound as a single chorionic hollow containing two yolk sacs and subsequently two embryos, each with its own cardiac activity. Because of the unfavourable prognosis and greater incidence of malformations and complications in monoamniotic twins, the amnion must be identified. Identification of the amnion between the two fetuses has 100% predictive value for a diamniotic twin pregnancy.

Fig. 2.63. Dichorionic biamniotic twins: interamniotic septum (arrow)

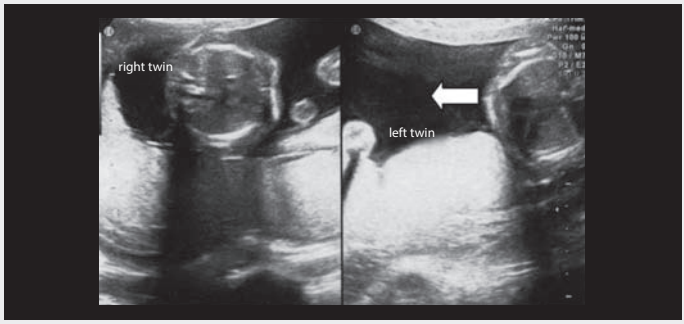

Fig. 2.64. Monochorionic biamniotic twins: ultrasound evaluation of cord insertions (arrows)

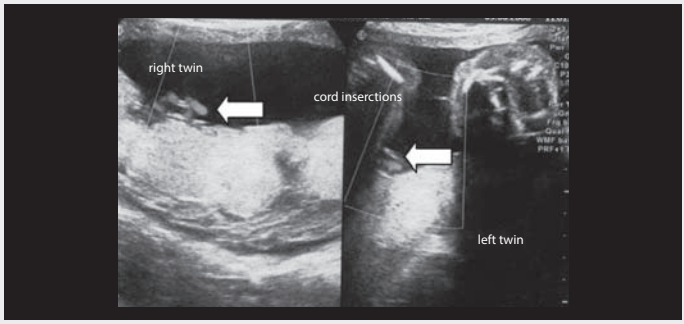

Fig. 2.65. Monochorionic biamniotic twins: ultrasound evaluation of twin sex (males)

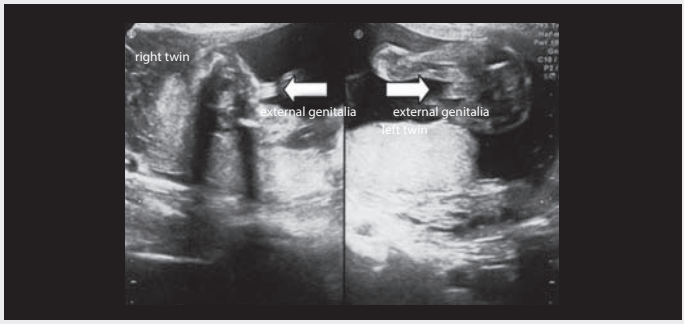

Fig. 2.66. Monoamniotic twins

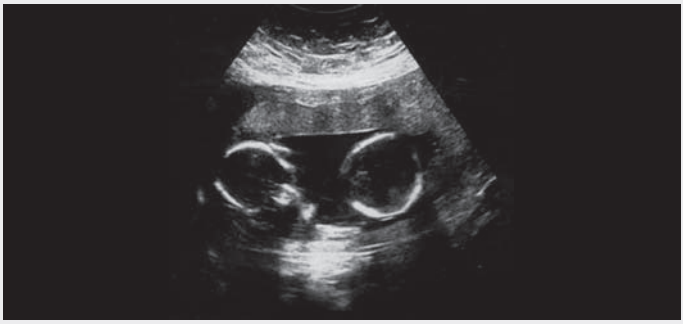

Fig. 2.67. Monoamniotic twins: measurement of BPD of each twin (calipers 1; calipers 2)"

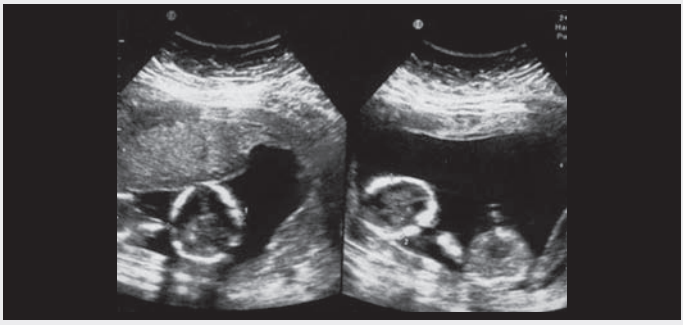

Mono- and dichorionic twins cannot be differentiated on the basis of identification of a membrane separating two fetuses after fusion of the amnion and the chorion from the 16th week. In monochorionic twins with a double amniotic sac, this membrane is composed of two layers, while in dichorionic twins it is formed from four layers: two chorions and two amnions. In both cases, the membranes can appear as a single echo-rich layer.

Biovular (dizygotic) twins have two different placentas, which, in cases of near ovular implant, can subsequently fuse. The chorion and amnion are always double. Monovular twins (monozygotic) generally have only one placenta, with a chorion containing one or two amniotic sacs. They can, however, have a fused placenta or two separate placentas, each with a chorion containing an amniotic sac. Therefore, it is not possible to establish whether one placenta indicates a mono- or a dichorionic pregnancy, unless the twins are of different sexes. When two placentas are observed,

the chorion–amniotic membrane extends sideways from the border of a placenta to the contralateral border. In the case of a single placenta, the chorion–amniotic membrane originates from the central portion of the placental implant. This typical aspect is useful for distinguishing it from the other membranes of the pregnancy, such as synechiae, the uterine septum and amniotic bands.

In early pregnancy, an intrauterine transonic area does not always indicate a gestational sac, unless an embryonic pole is seen, preferably with detectable cardiac activity. Similarly, not all hypoechoic areas near a gestational sac necessarily correspond to a second sac; they might, in fact, be due to a haematoma. If during the first trimester two amniotic sacs of different sizes are observed, it is reasonable to predict that the smaller sac is not viable and will be expelled or reabsorbed. Different growth rates of embryos in the early stage can be a sign of a malformation that will result in the death of the smaller twin.

Sonographic findings that can be misinterpreted as a second ovular sac are:

- an extracoelomatic space, visible up to 7–8 weeks in single pregnancies;
- subchorionic blood collection;
- pregnancy in a horn of a bicornate uterus and fluid collection in the other horn, or a pregnancy in a septated uterus with the septum mistakenly interpreted as a membrane separating two ovular sacs;
- a chorioangioma or a placental cyst.

Most authors agree that the pattern of growth in the first and second trimesters is the same in twins and in single fetuses. Various studies of fetal weight at birth have led to the hypothesis of a more rapid decrease in the growth curves of twins than of singletons between the 27th and the 37th week of pregnancy.

A decrease in the weight of fetal organs can be seen in cases of twins from the 30th week onwards. Some studies have shown a decrease in the rate of growth of the biparietal diameter of one of the two fetuses after week 31–32 and of the abdominal circumference after week 33–34, but no alteration in the rate of femoral growth in comparison with single fetuses.

The occurrence of a polydramnios is relatively frequent in twin pregnancies, especially if they are monovular. Any difference in growth between twins poses a risk for the smaller fetus. An apparent difference in the growth of the two biparietal diameters can be observed when one twin is in vertex and the other in breech presentation, a situation that provokes marked dolichocephaly. In such cases, the biparietal diameter is smaller, but the cranial circumference is in fact normal.

Serial measurements must be made of the growth parameters of twins in the second and third trimesters to detect and monitor intrauterine growth restriction or to identify serious pathological conditions such as the twin–twin transfusion syndrome.

Pathological findings

In modern obstetrical care, clinical management of a multiple pregnancy depends on sonography, which is irreplaceable for monitoring fetal growth and amniotic fluid volume. The frequency of monitoring is defined on the basis of chorionicity: monochorionic pregnancies should be monitored every 2 weeks, while monthly scans until birth are adequate for dichorionic pregnancies.

From the 16th week onwards, all monochorionic pregnancies should be examined to identify signs of twin–twin transfusion syndrome. All twin pregnancies should have a morphological ultrasound scan at the 20th week. Doppler velocimetry should be conducted in cases of a twin pregnancy with discordant growth. Transvaginal sonographic evaluation of the uterine cervix (length and funnelling) is also advisable. A cervix that is < 25 mm at the 24th week is strongly predictive of preterm birth before week 32.

Antenatal diagnosis of congenital anomalies

Increased maternal age enhances the risks for both aneuploidy and twin pregnancy. The general risk for aneuploidy in each twin depends on the zygosity. For dizygotic twins, who are genetically independent, the risk (related to maternal age and familial factors) is the same as that of a single fetus. Therefore, the risk that at least one fetus has a chromosomal anomaly is increased as many times as the number of fetuses, while the risk that both twins are affected is the same as that of a single fetus squared (or cubed if there are three or more fetuses).

The incidence of malformations is greater in twin pregnancies than in single pregnancies, particularly in monozygotic pregnancies. The risk is approximately doubled for major malformations (cardiac, central nervous system, intestinal; 2.12%) and a little less than doubled (4.13%) for minor malformations. Each fetus in a dizygotic pregnancy has the same risk as a single fetus, and the higher incidence of structural anomalies is attributable to defects in monozygotic twins. The most frequent anomalies are defects of the median line (holoprosencephaly), defects of the neural tube and cloacal exstrophy. Cardiac defects account for about 3.8% of defects in monozygotic pregnancies and 0.56% in dizygotic pregnancies.

Monozygotic twins have the same karyotype, and the risk for aneuploidy in relation to maternal age is identical to that of singletons. In dizygotic pregnancies, the risk for aneuploidy is twice that of single pregnancies at the same maternal age.

Defects that occur specifically in monozygotic twins are due to asymmetrical separation during division (joined twins) and the presence of placental anastomosis, which creates unbalanced perfusion of the two fetuses (twin–twin transfusion syndrome or twin reversed arterial perfusion). As zygosity cannot always be established, the probability that one or both fetuses are affected can be estimated from the chorionicity, keeping in mind that the risk is the same as that of a single pregnancy for 10% of monozygotic dichorionic pregnancies.

In twin pregnancies, invasive and noninvasive antenatal tests can be used. The best method for trisomy screening in twin pregnancies is evaluation of nuchal

translucency at 10–14 weeks. Serological screening has a low detection rate. The rate obtained by evaluation of nuchal translucency is similar to that in single pregnancies, but the percentage of false positives is higher (8% in monochorionic pregnancies). Evaluation of nuchal translucency in combination with serological screening increases the detection rate, but it is nevertheless 10% lower than in singleton pregnancies.

Invasive antenatal diagnosis, such as amniocentesis and villocentesis, is also possible. There is no agreement about the risk for fetal loss associated with diagnostic amniocentesis in the second trimester in twin pregnancies, and the issue must be discussed carefully with the couple. For expert operators, the risks associated with villocentesis are the same as those for amniocentesis.

Fetal growth

Twins weigh less at birth than infants born of single pregnancies, due to deceleration of the rate of intrauterine growth and to premature birth: a birth weight of < 2500 g is found in 50% of infants born of twin pregnancies and 5% of singletons. The intrauterine growth rate of twins is similar to that of single fetuses up to 30 weeks but then slows.

The growth of twins can differ in each trimester. When discordance occurs during the first trimester, it could indicate congenital anomalies in the smaller twin. A reduction in the growth of twins can also be detected at the end of the second trimester and at the beginning of the third. The percentage of discordance is assessed from a formula in which the difference in weight between twins is divided by the weight of the heavier twin. The greater the discordance in weight between two twins, the greater the risk for perinatal mortality. Although there is no agreement on a clinically relevant reference value, a discordance in weight of 20–25% is generally considered indicative of a worse perinatal outcome.

When there is both growth discordance and monochorionicity, the presence of unbalanced transfusion between the fetuses must be excluded. In dichorionic placentation, the fetuses may have different genetic codes, and the growth discordance might be due to subjective differences in each twin. The presence of two placentas could limit the uterine surface, with consequent suboptimal implantation of one, potentially detectable by spectral Doppler examination. In the case of dichorionic twins with discordant weights, the spectral Doppler reference point is the pulsatility index in the umbilical artery and its progressive increase, while in the case of monochorionicity, the spectral Doppler reference point is the increase in peak velocity of the cardiac outflow, a sign of anaemia in the smaller twin.

Intrauterine growth restriction

Intrauterine growth restriction is one of the most important causes of perinatal mortality in twins. The prevalence in twins is about 25%, 10 times greater than in single pregnancies. Generally, a difference of 20–25% in fetal weight between the two twins is considered clinically relevant. On the basis of the curves for fetal growth in single pregnancies, intrauterine growth restriction of one twin (rarely both) is found in

about one of three twin pregnancies. Such growth discordance is due mainly to the reduced space available in the uterine hollow or to fetal anomalies. In dichorionic pregnancies, intrauterine growth restriction can be due to differences in the growth potential of the twins or to different blood flow in the placentas. In monochorionic pregnancies, it can derive from unequal division of the initial cellular mass between the two embryos or from the presence of vascular communications in monochorionic placentas that causes imbalances in nutrition.

Criteria that can be used to diagnose differential growth in two fetuses include:

- a difference in the estimated weight of the two fetuses of at least 500 g;
- a difference in the estimated weight of the two fetuses of 15–20%;
- a difference in the abdominal circumference of the two fetuses of at least 2 mm.

The most useful measurements are abdominal circumferences and fetal weight. This method is sensitive (80%) and has a high negative predictive value (93%); furthermore, it can be combined with information on the amniotic fluid volume and a Doppler examination of fetal flows. This examination is necessary even though concordant intrauterine growth restriction is rare.

In monochorionic pregnancies, growth discordance can indicate either the presence of intrauterine growth restriction or twin–twin transfusion syndrome, which must be sought by suggestive signs.

Complications related to monochorionicity

Monochorionic twin pregnancies are associated with a fivefold greater risk for fetal and perinatal loss, a 10-fold greater risk for antenatally acquired cerebral paralysis and at least double the risk for intrauterine growth restriction in comparison with dichorionic pregnancies.

Twin–twin transfusion syndrome (imbalanced fetus–fetus transfusion) complicates 10–15% of monochorionic twin pregnancies. Generally, it is seen during the second trimester of pregnancy. The natural history of this syndrome results in approximately 80% mortality without treatment and severe newborn outcome. The demonstration of vascular anastomoses suggests that the physiopathology of this syndrome is based on impaired haematic exchange between the two fetuses. The donor twin generally appears hypovolaemic and, at times, anaemic, with delayed growth and a marked reduction in the amniotic fluid volume (oligoamnios; bladder poorly distended or not visualized; Fig. 2.68, Fig. 2.69, Fig. 2.70, Fig. 2.71). In contrast, the receiving fetus already appears hyperperfused and polyuric (polydramnios and hyperexpanded bladder), and signs of cardiac overload (cardiomegaly, fetal hydrops, myocardial hypertrophy) can be detected.

In the most serious cases, the donor twin is completely deprived of amniotic fluid, cannot move, leans against the uterine wall (stuck twin) and can have impaired

Fig. 2.68. Monochorionic biamniotic pregnancy complicated by twin–twin transfusion syndrome: different fetal growth and different amniotic fluid volume, with polyhydramnios of the recipient twin and oligoamnios of the donor twin

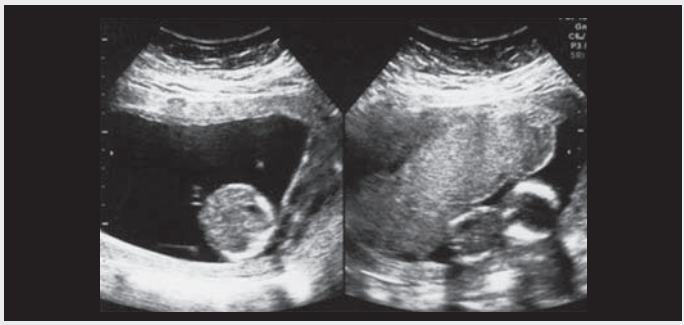

Fig. 2.69. Normal monochorionic biamniotic twins: no differences in bladder volumes (arrows)

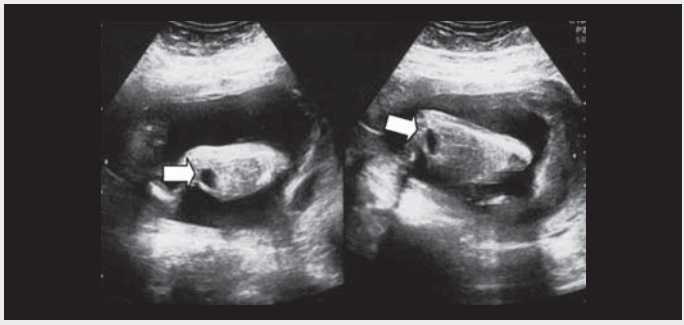

Fig. 2.70. Twin–twin transfusion syndrome: different bladder volumes (arrows)

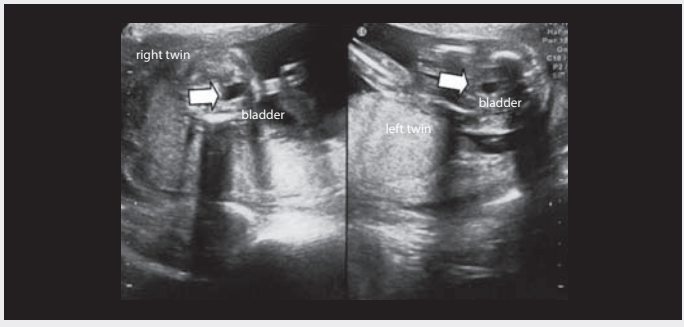

Fig. 2.71. Twin–twin transfusion syndrome: different amniotic fluid volume with hydramnios in the recipient twin and death of donor twin (stuck twin)

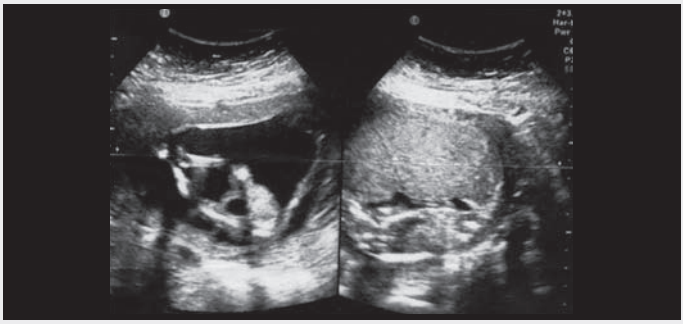

or pathological arterial flow. The resulting chronic hypoxia can induce cerebral lesions or bring about exitus in utero. The receiver twin shows signs of serious cardiac failure (tricuspid regurgitation, fetal hydrops, pathological venous flow), which can also bring about exitus in utero. The death in utero of one of the twins exposes the other to a 50% higher risk for death or at least results in neurological ischaemic injuries, as the surviving twin suffers acute hypovolaemia when part of its circulating mass is recalled into the dilated vessels and low pressure circle of the dying twin.

Antenatal ultrasound diagnosis of twin–twin transfusion syndrome is based on the following observations:

- a single placenta;
- a difference in the quantity of amniotic fluid: polydramnios in the receiving and oligoamnios in the donor twin;
- a difference in the degree of bladder filling: bladder hyperextended in the receiving twin and small or not visualized in the donor twin.

Additionally:

- hydrops in both fetuses or signs of congestive failure in the transfused fetus;
- weight discrepancy between the twins (on ultrasound);
- difference in haemoglobin levels between the two fetuses (on cordocentesis);
- differences in the dimensions or number of vases of the umbilical cords;
- pathological Doppler velocimetry (venous duct, umbilical vessels, fetal cerebral vessels).

Of the treatment options proposed, serial amnioreductions, septostomy, laser ablation and selective feticide are those most frequently practised. Fetus–fetus transfusion

can also occur acutely during labour. One of the two newborns will appear plethoric and the other strongly anaemic in a pregnancy without complications.

Fetal mortality in monoamniotic pregnancies is mainly due to twisting of the umbilical cord, which leads to fetal asphyxia. As fetal death is sudden and unpredictable, close sonographic checks are necessary to verify fetal comfort, especially if the cords are already entangled. Twisting of the umbilical cords occurs early in pregnancy, during the first or second trimester, when the fetuses can move freely within the uterus. In monochorionic monoamniotic pregnancies, in which the cords have a close placental insertion and there may be some large-calibre vascular anastomoses between the two fetal circulations, acute episodes of haemodynamic failure can also occur.

Intrauterine twin death

The incidence of death in twin pregnancies is greater in the first trimester than at birth. It has been estimated that about 12% of pregnancies are multiple at conception but only 2% evolve to twin births. About 20–70% of pregnancies diagnosed as twin in the first trimester result in a vanishing twin. In such cases, the prognosis of the surviving twin is good, although the risk for miscarriage is greater, particularly in monochorionic pregnancies.

The outcome of the surviving twin is poorer if one fetus is lost at a more advanced stage of pregnancy, particularly in the third trimester. The risk is estimated to be about 6% (about 8% in monochorionicity and about 4% in dichorionicity). The risk of death for the surviving twin reaches 30% and the risk for cerebral paralysis has been estimated variously to be 10–46% in monochorionic twins; in dichorionic twins, the outcome is favourable except for cases of congenital anomalies. The mechanism of the damage in the surviving twin is acute haemodynamic failure (hypotension and ischaemia) consequent to the passage of blood towards the vascular bed of the dead twin through the placental anastomosis.

Clinical management of such pregnancies is not simple. The most important elements are chorionicity and gestational age. In cases of dichorionicity, an immediate intervention is not necessary if the cause is established, and wait-and-see management associated with careful maternal and fetal monitoring shows no significant differences in terms of weeks and weight at birth of the surviving twin from interventional management. Moreover, in the presence of acute twin–twin transfusion syndrome, delivery immediately after the death of a twin does not prevent the ischaemic complications for the central nervous system of the surviving twin. Management greatly depends on gestational age, as delivery of the healthy twin at an early stage of pregnancy has little justification. If the cause of a twin's death in utero might also compromise the other (for instance, pre-eclampsia or chorioamniotitis), management must be adapted to avoid loss of the survivor. In monochorionic twin pregnancies, the risk for neurological damage can be monitored during the pregnancy with ultrasound or MRI. Evidence of a serious anaemic state is a poor prognosis, but the advantages of transfusion in utero through cordocentesis have not been clearly

demonstrated. Doppler measurement of peak velocity in the middle cerebral artery has been proposed as a noninvasive index for evaluating fetal anaemia.

Twin reversed arterial perfusion sequence

The twin reversed arterial perfusion sequence, also called the acardiac twin syndrome, is a rare disease that occurs in about 1% of monochorionic pregnancies. It is considered to be an extreme example of haemodynamic anomaly in a twin pregnancy with a single placenta: the acardiac twin receives blood into the umbilical artery through a large arterio-arterial anastomosis that allows the passage of blood from the umbilical artery of the twin cardiac donor (pump twin).

On colour Doppler, the cord of the perfused twin is composed of only two vessels, a single artery and a vein (there are only rarely two arteries), for arterial flow from the placenta to the fetus and venous flow from the fetus to the placenta. The perfused twin receives poorly oxygenated blood, which is distributed particularly to the iliac district; the affected twin's organs show anomalies that are probably due to hypoxic injuries, and the heart is completely absent or rudimentary. The cephalic extremity is usually absent (acardiac–acephalus twin), as are the upper extremities, while the lower part of the trunk is usually present. The acardiac twin often develops oedema and appears to be double the size of the other. Due to congestive cardiac failure and hydrops or as a result of prematurity induced by polydramnios, up to 50% of cardiac twins die during the perinatal period.

Joined twins

Joined twins occur in one of every 50 000 pregnancies. The cause is late, incomplete division of the embryonic disc around day 15–17 after conception. The twins are always monozygotic, monochorionic and monoamniotic. A diagnosis is based on the finding of a monochorionic monoamniotic pregnancy without separation of the vascular systems of the two fetuses.

If the two fetal heads are close to one another, there is a strong probability of Siamese twins, although the absence of this finding does not exclude the diagnosis. When the two twins are almost entirely formed, the point of union is often the anterior surface of the chest (thoracopagus) or more rarely the abdomen (omphalopagus), the back (pygopagus), the skull (craniopagus) or the pelvis (ischiopagus). When the duplication is less complete, the point of union is often lateral.

The survival of such twins is related to the gestational age at birth and the type of connection between the fetuses. In cases of extensive cardiovascular connections, the death of at least one twin is inevitable (Fig. 2.72).

Fig. 2.72. Monoamniotic twins (18 weeks' gestational age): conjoined twins with early death of one twin (arrow) (calipers: abdominal diameters of the dead twin)

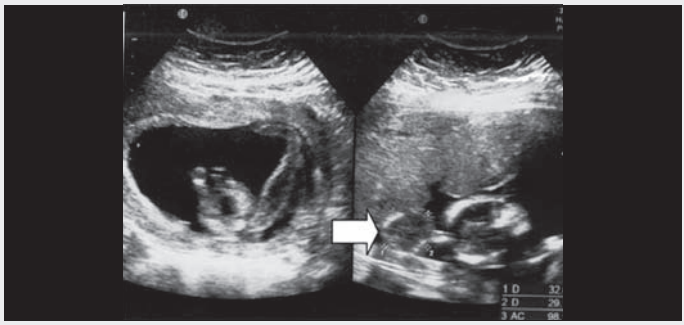

Fetus papyraceus is a dead twin pressed onto the uterine wall by the expanding amniotic hollow of the other twin. The dead fetus appears to be enclosed in its own membranes but with no amniotic fluid. The hydric content of the dead fetus is slowly reabsorbed, with further reduction of fetal size.

Fetus in fetu is a rare anomaly in which a parasitic twin is included in the retroperitoneum of the superior abdomen of the carrier fetus. The included fetus has a well-developed vertebral system, which is a distinctive sign for differential diagnosis with teratoma.

Fetal malformations

Antenatal ultrasound diagnosis of fetal malformations is the most difficult task of sonographers and sonologists in the field of obstetrics. The number of fetal malformations detectable by ultrasound is high and increasing with the development of technology and interest in the field of antenatal medicine. Fetal malformations are usually an unexpected finding during sonographic examination of an apparently healthy pregnant woman, as in most cases they are found in women with no risk factors. For this reason, in developed countries, ultrasonic examination of fetal anatomy has become a standard screening procedure, usually between 19 and 22 gestational weeks. This short interval has been chosen because: the development of fetal organs is almost complete; the amount of amniotic fluid is higher than the fetal body, allowing a good acoustic window for penetration of the ultrasound beam; and, if a fetal malformation is detected, it is still possible to plan other diagnostic procedures, such as amniocentesis, or offer the woman the option of terminating the pregnancy in the case of a severe anomaly.

If screening with ultrasound is accepted, a detailed survey of the fetal anatomy must be performed during the second trimester. The diagnostic results reported

in the literature for such a screening procedure vary widely in different countries, operators' skills and instrument characteristics. The most recent European multicentre trial showed a sensitivity of 60%. The aim of this section is not to describe how to diagnose all fetal congenital malformations (several textbooks are available on this topic) but how to suspect a malformation during a fetal anatomical survey. We therefore describe the findings suggesting malformations.

Fetal head

Evaluation of the fetal head requires visualization and measurement of the biparietal diameter and head circumference, measurement of the atrial width and transverse cerebellar diameter and visualization of the orbits (Fig. 2.73).

In cases of failed or abnormal measurement of biparietal diameter and head circumference, the malformations described below can be detected.

Fig. 2.73. Evaluation of a normal fetal head. (a) Transthalamic axial scan, in which the biparietal diameter and head circumference are measured. (b) Transventricular scan, in which the atrial width is measured (arrows). (c) Transcerebellar scan, in which the transverse cerebellar diameter (arrows) is measured. (d) Transorbital scan. CSP, cavum septum pellucidum; FH, frontal horns of lateral ventricles; T, thalamus; open arrow, insula

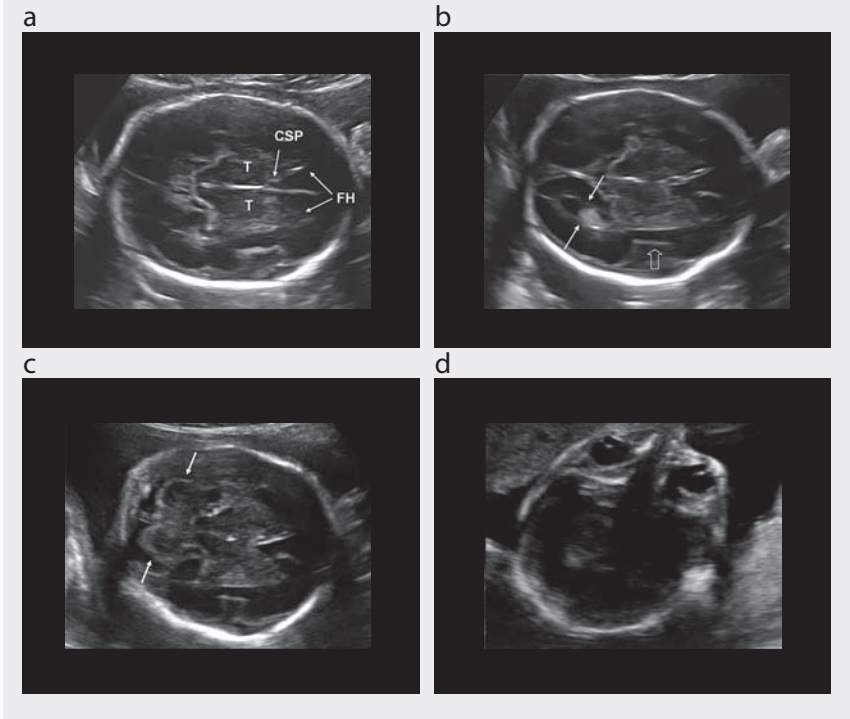

Anencephaly: severe anomaly incompatible with postnatal life, easily detectable from the first trimester by the absence of the fetal calvaria (Fig. 2.74).

Microcephaly: fetal head and brain smaller than normal. The diagnosis is difficult and frequently late. It is important to compare the head size with the abdominal circumference and femur length in order to confirm the diagnosis (Fig. 2.75).

Macrocephaly: an enlarged fetal head, usually due to severe hydrocephaly or the presence of intracranial masses such as tumours or cysts (Fig. 2.76). The brain anatomy is completely distorted by the severely enlarged ventricles in the first case, by a prevalently solid mass in the second case and by a prevalently cystic mass in the third one. In rare conditions, there is a large head with normal anatomy, which has a good prognosis but is sometimes a sign of severe neuronal migration disorder.

Fig. 2.74. Anencephaly. The fetal calvaria cannot be visualized

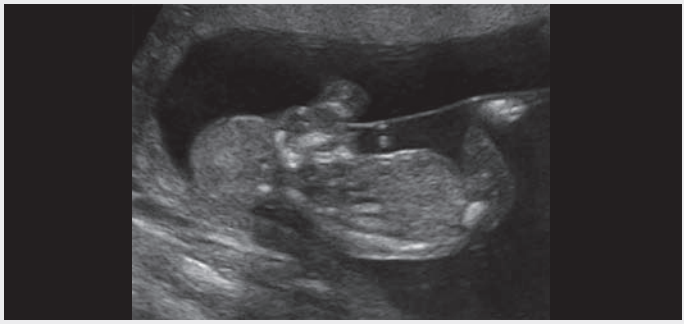

Fig. 2.75. Microcephaly. The fetal head is small in comparison with the face

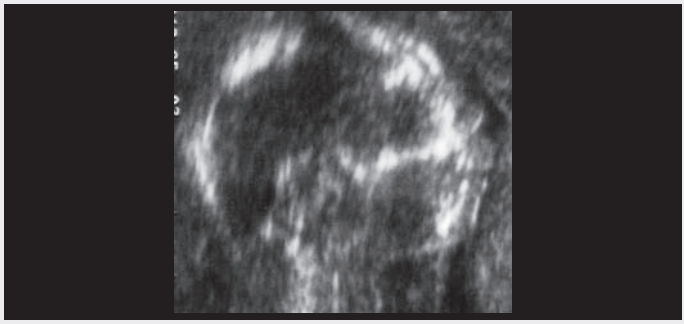

Fig. 2.76. Macrocephaly due to severe hydrocephaly (a), brain teratoma (b) and arachnoid cyst (c)

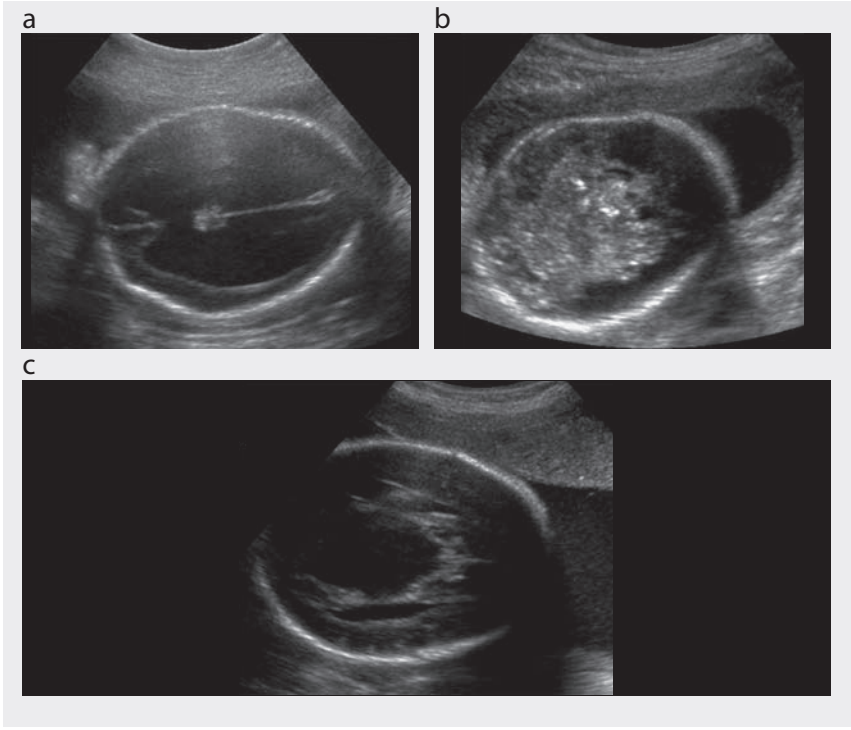

Cephalocoele: protrusion of meninges alone (meningocoele) or meninges and brain tissue (encephalomeningocoele) through a bony defect, usually located in the occipital pole (Fig. 2.77)

Fig. 2.77. Occipital cephalocele. A complex mass protrudes through a bony defect of the calvaria in the occipital pole

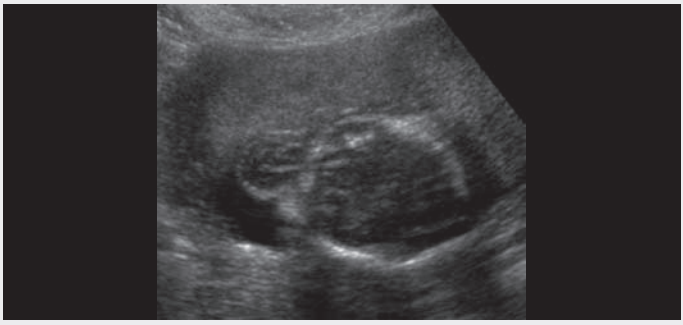

Abnormal findings and measurement of the atrium allow recognition of other malformations.

Ventriculomegaly: the ventricular size is considered normal when the atrial width is < 10 mm, independently of gestational age. Measurements of 10–15 mm are defined as borderline ventriculomegaly; dilatation > 15 mm is considered severe ventriculomegaly (Fig. 2.78). In cases of borderline ventriculomegaly, the prognosis depends mainly on the presence of associated anomalies; it is good in 90% of cases, particularly when the dilatation is 10–12 mm. In cases of severe ventriculomegaly (frank hydrocephalus), the prognosis is usually worse and depends mainly on the cause of the ventricular dilatation and the presence of associated anomalies.

Choroid plexus cysts are small fluid collections, usually bilateral, within the choroid plexus and are easily recognizable within the atrium (Fig. 2.79). In most cases, they are a transient finding and disappear by the end of the second trimester. If isolated, they have no clinical consequence; when associated with other anomalies, they may be a sign of chromosomopathy and especially trisomy 18.

Holoprosencephaly is the consequence of failed division of the prosencephalon into the two telencephalic vesicles in the early stages of brain development. They are classified according to the severity of the defect into alobar, semilobar and lobar. The first is easily detectable by the typical horse-shoe appearance of the single ventricular cavity with fused thalami (Fig. 2.80). In the semilobar variety, the frontal horns are fused, and abnormal occipital horns are present. The lobar variety is extremely difficult or impossible to diagnose, as the defect is limited to the area of septum pellucidum and olfactive tracts. Alobar and semilobar forms are frequently associated with other anomalies, mainly at the level of the face, such as cyclopia, hypotelorism, cleft palate (Fig. 2.80) and proboscis. In these cases, trisomy 13 or 18 should be suspected.

Abnormal findings and measurement of the cerebellum allow the detection of further anomalies.

Fig. 2.78. Borderline (a) and severe (b)ventriculomegaly

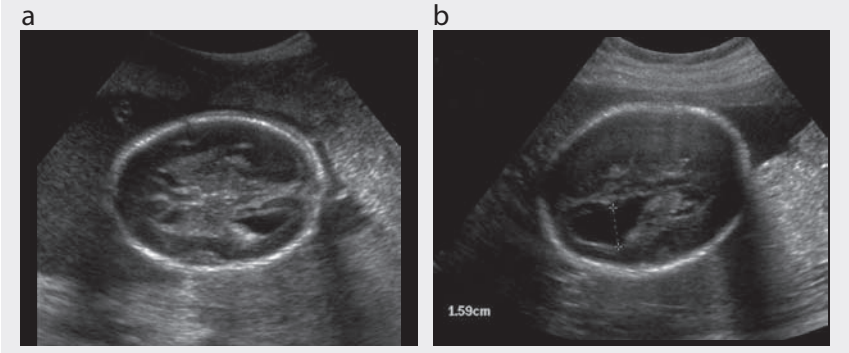

Fig. 2.79. Choroid plexus cyst

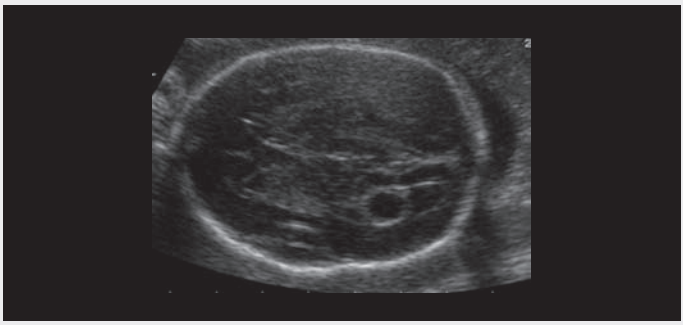

Fig. 2.80. Alobar holoprosencephaly: the single horse-shoe-shaped ventricular cavity (a) and the associated cleft palate (b, arrow) can be seen

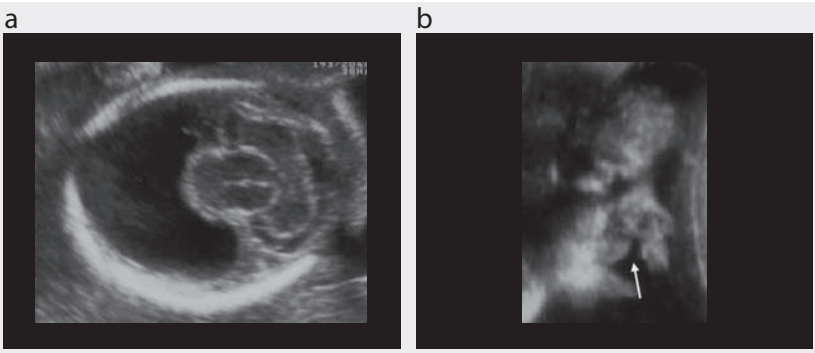

Dandy-Walker complex: This term covers anomalies characterized by various degrees of hypoplasia of the cerebellar vermis. In the classic Dandy-Walker malformation, the cerebellar vermis is severely hypoplastic and rotated upwards by an extremely enlarged fourth ventricle, which appears as a cyst in the posterior fossa; hydrocephaly is frequently associated (Fig. 2.81). In the so-called Dandy-Walker variant, the vermis is hypoplastic but still present and the enlarged fourth ventricle appears as a key-hole cystic structure between the two cerebellar hemispheres (Fig. 2.81). In this case, a difficult differential diagnosis is made from the Blake pouch cyst, which is a digit-like posterior protrusion of the fourth ventricle below a normal vermis. This condition usually has a better prognosis than Dandy-Walker complex.

Mega cisterna magna: The cisterna magna is considered enlarged when the anteroposterior diameter at the level of the cerebellar vermis is > 10 mm (Fig. 2.82). In these cases, a careful survey of fetal anatomy should be performed to rule out associated anomalies. The prognosis of the isolated forms is usually good.

Fig. 2.81. Dandy-Walker complex. Classical (a) and variant (b) malformations

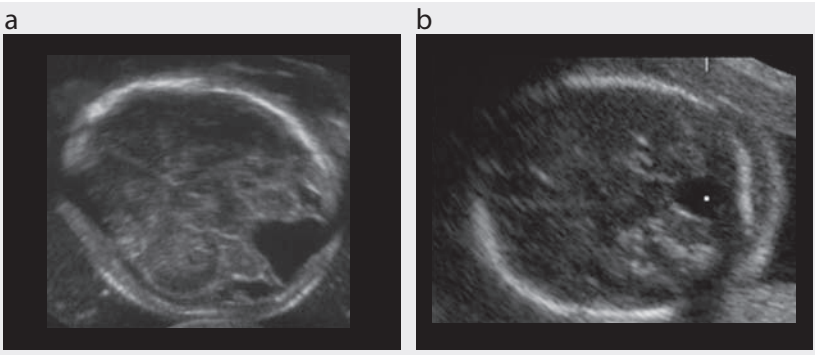

Fig. 2.82. Mega cisterna magna (calipers)

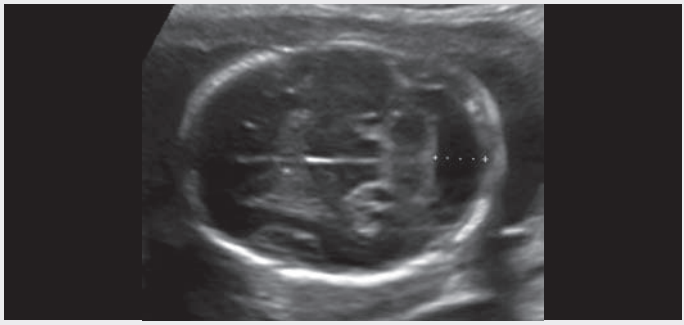

Fig. 2.83. Chiari II malformation. (a) Small cerebellum with effaced cisterna magna, 24 weeks' gestation. (b) Abnormal shape of the calvaria (lemon sign), 20 weeks' gestation

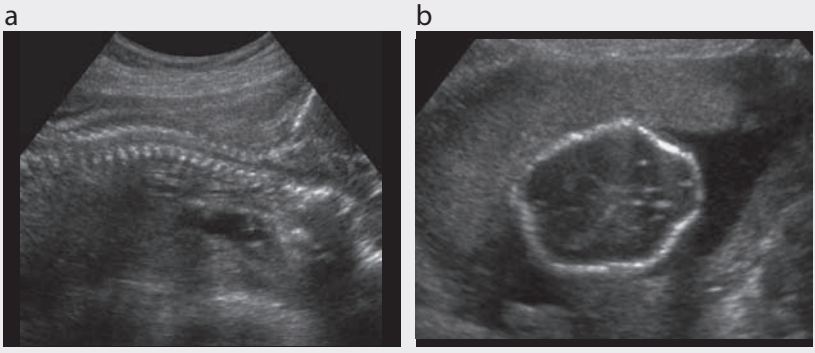

Fig. 2.84. Abnormal findings at the level of the orbits. Hypotelorism (a), cyclopia (b), unilateral microphthalmia (arrow) (c)

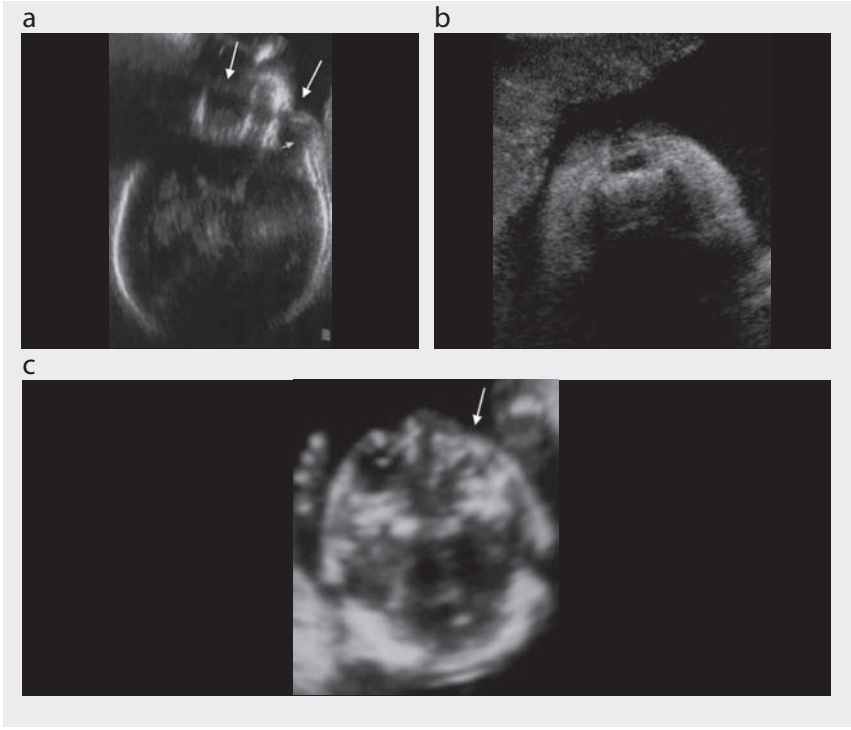

Chiari II malformation: The posterior fossa is small, the cerebellum shows a typical banana shape and the cisterna magna is effaced (Fig. 2.83a). Sometimes, the calvaria assumes a lemon shape (Fig. 2.83b). An open spina bifida is almost always associated.

Abnormal findings at the level of the orbits include hypotelorism, cyclopia, hypertelorism, microphthalmia and anophthalmia (Fig. 2.84).

Fetal spine

Routine examination of the fetal spine should include evaluation of its longitudinal view, to demonstrate the integrity of the spinal canal. In the transverse view, the spinal canal is delimited anteriorly by the ossification centre of the vertebral body and posteriorly by the ossification centres of the laminae (Fig. 2.85).

An abnormal appearance of the fetal spine may be due to several anomalies.

Spina bifida: In the longitudinal view, the spinal canal shows an enlargement at the level of the vertebral defect; the axial view at the same level shows lateral displacement of the laminae. The meningocoele protruding from the vertebral defect appears as a cystic structure of variable size (Fig. 2.86). Small spinal defects, however, can easily be missed; for this reason, it is easier to screen for open neural tube defects by

Fig. 2.85. Normal appearance of the fetal spine in the longitudinal (a) and axial (b) views

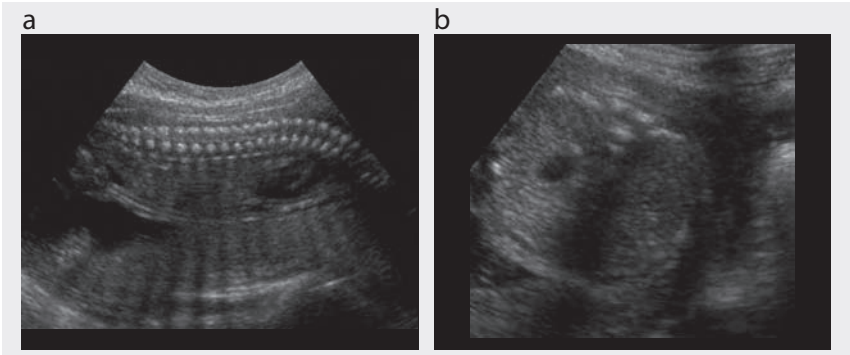

Fig. 2.86. Examples of spina bifida: in the axial view, the laminae are displaced laterally (arrow) (a). In the longitudinal view, the spinal canal shows an enlargement at the level of the vertebral defect (arrows) (b). The meningocoele appears as a cystic structure protruding from the defect (arrow) (c) and (d)

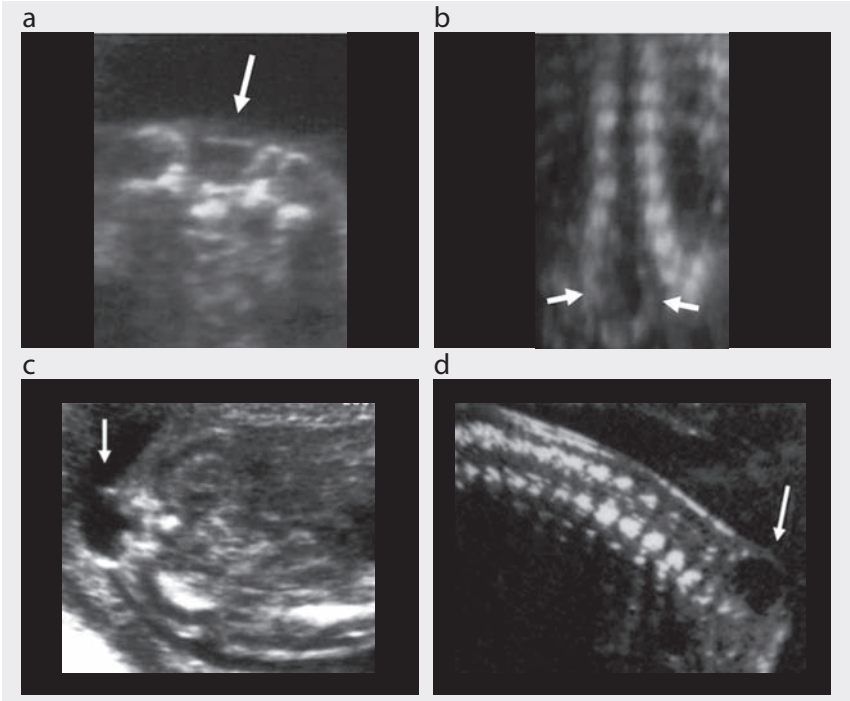

searching for the associated cranial signs typical of the Chiari II malformation, i.e. a small cerebellum with effaced cisterna magna (banana sign) and abnormal shape of the calvaria (lemon sign) (Fig. 2.83).

Fetal lungs

The fetal lungs are usually examined routinely in the axial view of the fetal chest, at the same level at which the four chambers of the fetal heart are visible. They appear as two echogenic wings surrounding the heart (Fig. 2.87).

Fig. 2.87. Axial view of the fetal chest at the level of the four cardiac chambers. The lungs (L) are the echogenic wings surrounding the fetal heart

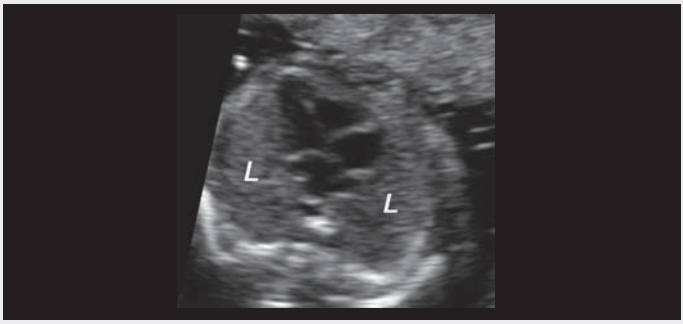

An abnormal appearance of the lungs in this axial view allows detection of several anomalies.

Cystic adenomatoid malformation: The lesion is usually unilateral. Part of the lung is replaced by dysplastic cystic tissue, defined as microcystic or macrocystic depending on the size of the cysts (Fig. 2.88). In the former, the cysts are too small to be visualized by ultrasound, and the lesion appears as an echogenic area of variable size; in the latter, the cystic lesions are clearly recognized. Small lesions may undergo spontaneous regression during pregnancy or after delivery. Large lesions cause mediastinal shift and can be complicated by pleural effusion. Cystic adenomatoid malformation should be differentiated from **pulmonary sequestration**, which is an abnormal solid pulmonary structure that does not communicate with the normal bronchial tree or the pulmonary vessels. Colour Doppler can be used to visualize the feeding vessel of the lesion, which originates directly from the descending aorta.

Pleural effusion: A collection of fluid in the pleural cavity is easily recognizable as an echo-free area compressing the fetal lung. It can be uni- or bilateral (Fig. 2.89). The unilateral lesion is usually a chylothorax; bilateral lesions can be caused by heart malformations, infection or lung malformations, for example, or can be part of generalized hydrops.

Diaphragmatic hernia: In this anomaly, abdominal organs (stomach, gut or even liver) protrude into the mediastinum through a diaphragmatic defect. The commonest site of the defect is in the left posterior area. In the axial view of the fetal chest, the heart is shifted to the right and the lungs are compressed by the herniated abdominal structures (Fig. 2.90). As a consequence of the persisting compression, lung hypoplasia may develop, which is the main cause of neonatal death.

Fig. 2.88. Cystic adenomatoid malformation of the lung: microcystic (a) and macrocystic (b)

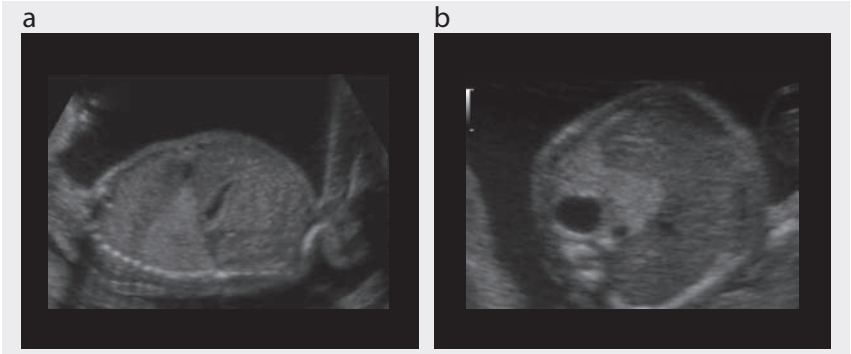

Fig. 2.89. Bilateral pleural effusion in the axial (a) and sagittal (b) view of the chest

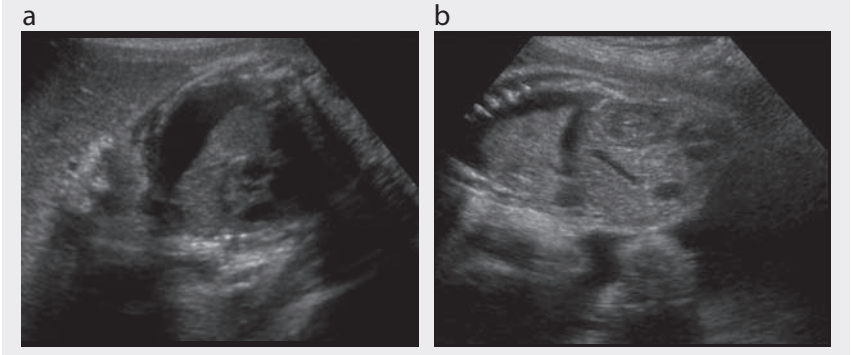

Fig. 2.90. Diaphragmatic hernia: the heart is shifted to the right and the lungs are compressed by the herniated abdominal structures; the herniated stomach is easily recognized as a cystic structure on the left side of the heart

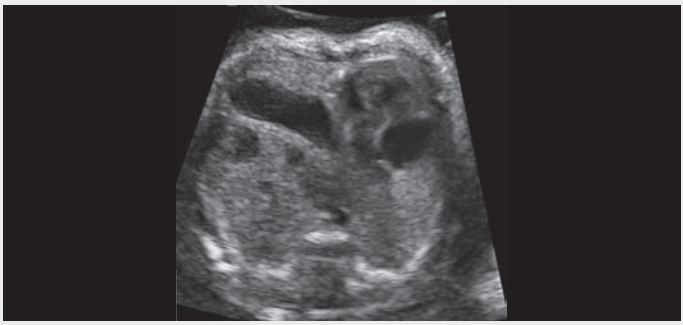

Fetal heart

Sonographic examination of the fetal heart is the most complicated part of the fetal morphological evaluation. The sensitivity of ultrasound in screening for cardiac anomalies depends on the scanning planes used. The simplest screening procedure is based on the four-chamber view of the heart. It can be apical when the apex of the fetal heart points anteriorly towards the transducer (Fig. 2.91) and transverse when the cardiac axis is perpendicular to the ultrasonic beam. Correct acquisition of the four-chamber view requires the following: (i) the situs is normal in relation to the location of the stomach; (ii) two thirds of the heart is in the left half of the thorax; (iii) the apex is pointing to the left (laevocardia); (iv) at least two pulmonary veins can be seen opening into the left atrium; (v) the atria are the same size; (vi) the atrial septum is interrupted by the foramen ovale; (vii) the tricuspid valve is inserted slightly lower than the mitral valve; (viii) the ventricles are almost the same size but have a different shape (the left ventricle is elongated and reaches the apex and the right ventricle is circular due to the presence of the moderator band); (ix) the thickness of the walls is similar in the two ventricles; and (x) the interventricular septum is continuous.

Starting from the four-chamber view and rotating the transducer slightly towards the right fetal shoulder, it is possible to visualize the left outflow tract, with the ascending aorta originating from the left ventricle (Fig. 2.91). With a similar movement towards the left fetal shoulder, the right outflow tract is obtained, with the pulmonary artery emerging from the right ventricle and crossing the aorta (Fig. 2.91).

A further useful section plane is the three-vessel plane, which is obtained simply by starting from the four-chamber view and moving the transducer upwards. It shows the axial section of the superior vena cava, aorta and pulmonary artery located posterior to the thymus (Fig. 2.92).

Fig. 2.91. Apical four-chamber view of the fetal heart (a); visualization of the left (b) and right (c) outflow tracts

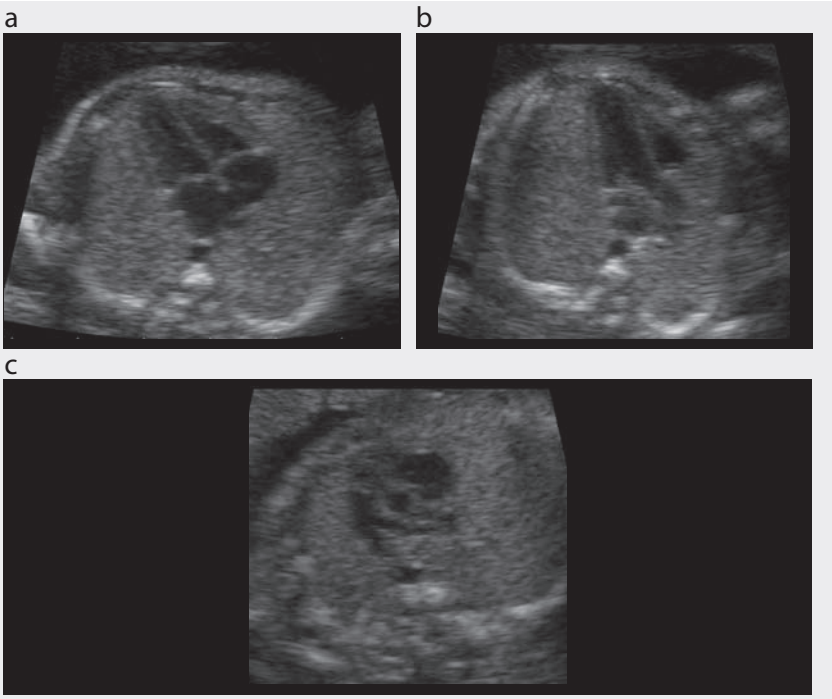

Fig. 2.92. Three-vessel view, showing, from right to left, the superior vena cava, aorta and pulmonary artery

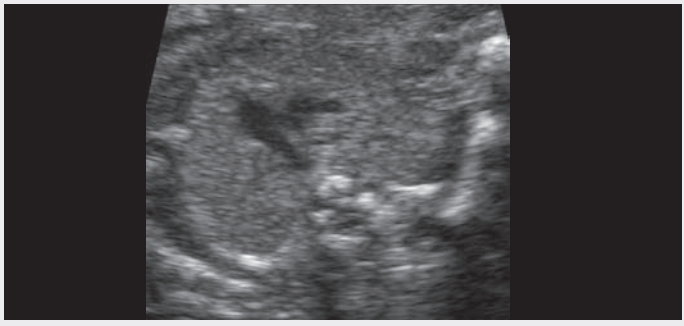

With only the four-chamber view, the sensitivity of ultrasound for detecting fetal cardiac anomalies is less than 50%; this rises to 70% when the outflow tracts are included in the screening procedure.

The number of congenital heart defects is high and their correct diagnosis requires skill and accurate knowledge of the haemodynamic of each disease, so that the mother can be counselled properly. For these reasons, fetal echocardiography is considered a specialized part of antenatal ultrasonography. In this section, we list only the main cardiac malformations that may be suspected during screening.

Anomalies detectable with the four-chamber view

Atrial anomalies: A single atrium is seen in most cases of complete atrioventricular canal (single atrium, single atrioventricular valve, wide ventricular septum defect) (Fig. 2.93). Interatrial defects with normal atrioventricular valves may be missed. An enlarged right atrium may be associated with Ebstein anomaly (low insertion of the tricuspid valve in the right ventricle (Fig. 2.94) or tricuspid valve dysplasia (Fig. 2.95). In both cases, pulsed and colour Doppler demonstrate valvular regurgitation. Dilatation of the left atrium is rarer and is due to mitral insufficiency secondary to critical aortic stenosis.

Septal defects*:* In the four-chamber view, large muscular defects or inlet defects of the perimembranous area can be visualized (Fig. 2.96). Small muscular defects and outlet defects of the perimembranous area cannot be detected.

Ventricular disproportion: A small, sometimes virtual left ventricle associated with mitral atresia is typical of hypoplastic left heart syndrome (Fig. 2.97). A small right ventricle can be seen in association with tricuspid atresia. In this case, a small interventricular septum defect is present. The presence of hypertrophy of the right ventricular walls raises suspicion of coarctation of the aorta (Fig. 2.98), although this finding can be benign and disappear after delivery. Severe dilatation of the left ventricle with increased echogenicity and reduced contractility of the muscular wall is typical of critical aortic stenosis (Fig. 2.99).

Fig. 2.93. Complete atrioventricular canal: the four-chamber view shows a single atrium, a single atrioventricular valve and a wide ventricular septal defect

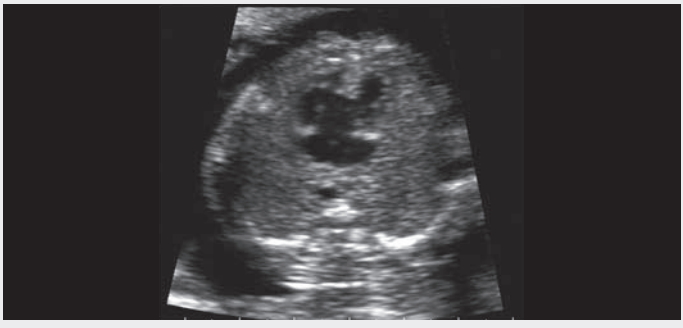

Fig. 2.94. Ebstein anomaly: the right atrium is extremely enlarged and the tricuspid valve has a low insertion

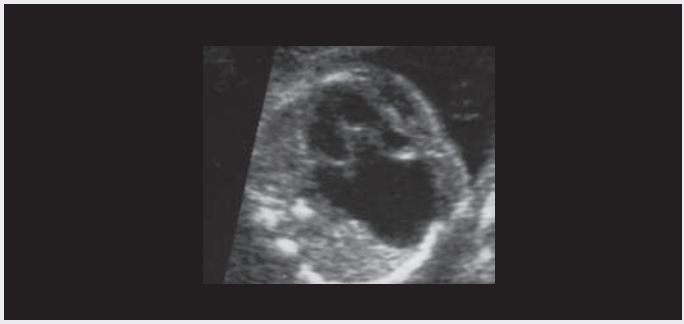

Fig. 2.95. Dilatation of the right atrium in tricuspid valve dysplasia

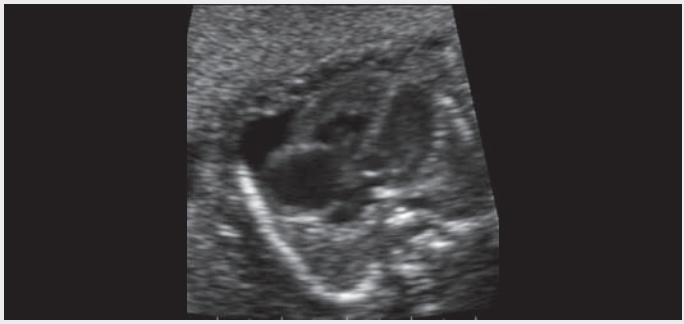

Fig. 2.96. Inlet interventricular defect of the membranous area

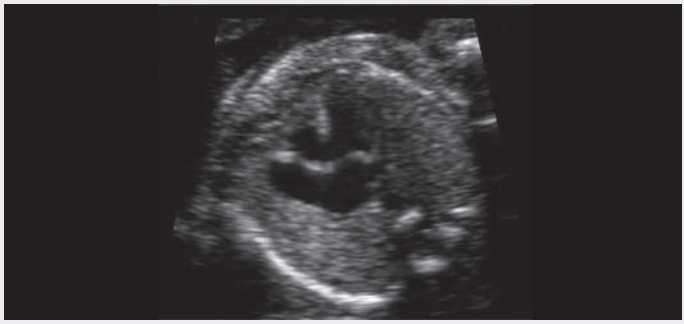

Fig. 2.97. Mitral atresia with small ventricular cavity (hypoplastic left heart syndrome)

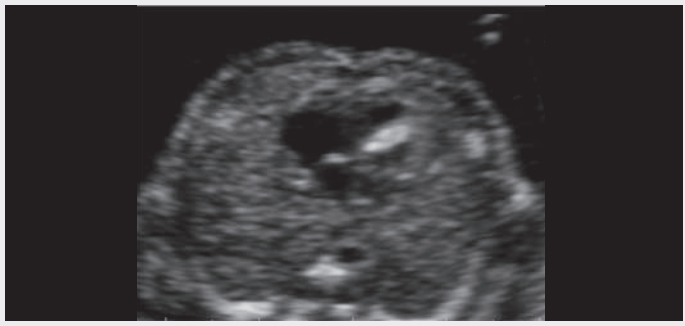

Fig. 2.98. Hypertrophy of the right ventricular walls, raising suspicion of coarctation of the aorta

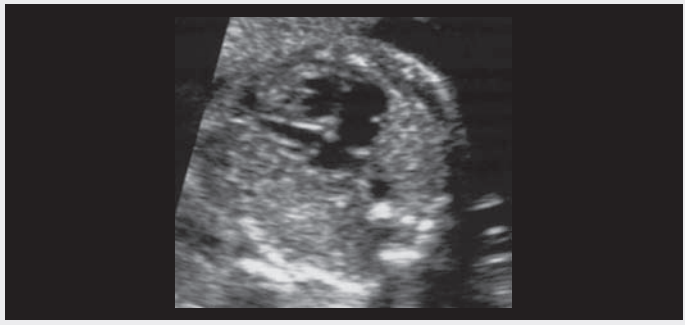

Fig. 2.99. Severe dilatation of the left ventricle with reduced contractility of the ventricular wall, typical of critical aortic stenosis

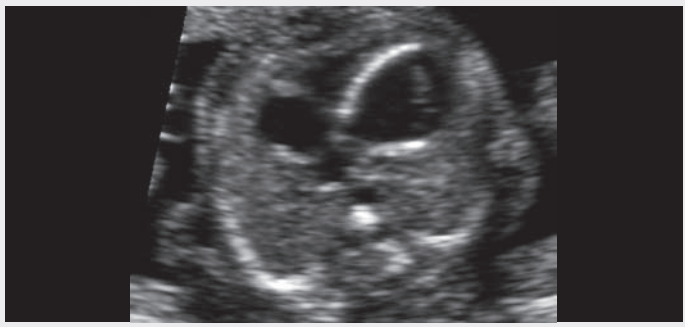

Anomalies detectable in the outflow tract

Septal anomalies: Interventricular septum defects can be recognized in the left outflow tract. When the emerging aorta overrides the defect, several conotruncal anomalies can be suspected; in these cases, it is important to evaluate the right outflow tract. A small pulmonary artery is typical of the tetralogy of Fallot (Fig. 2.100). When the pulmonary artery rises directly from the aorta, a common arterial truncus is suspected.

Anomalies of vessel crossing: When two parallel vessels are seen on the left outflow tract which do not cross each other, complete transposition of the great arteries is suspected if each vessel originates from separate ventricles (Fig. 2.101); double outlet right ventricle is suspected if both vessels originate from the anterior ventricle.

Fig. 2.100. Interventricular septal defect with overriding aorta in a case of tetralogy of Fallot

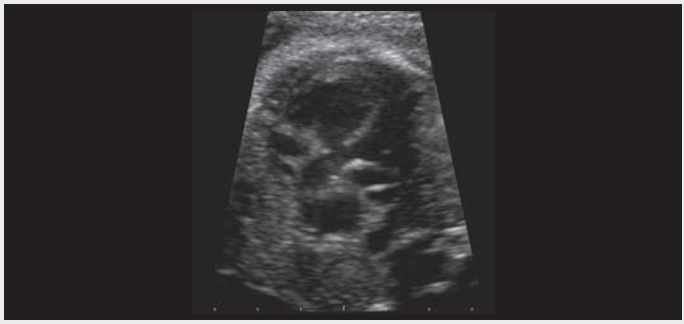

Fig. 2.101. Complete transposition of the great vessels: the aorta (ao) and pulmonary artery (p) are parallel and do not cross each other

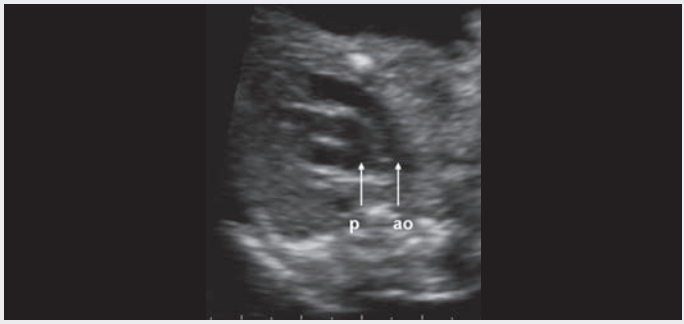

Anomalies of vessel size: A small aortic annulus associated with a dilated left ventricle is typical of critical aortic stenosis. A thin pulmonary artery is typical of pulmonary atresia and is usually associated with a small right ventricle and an interventricular septum defect. A severely dilated pulmonary artery is observed in cases of tetralogy of Fallot, with absent pulmonary valves (Fig. 2.102).

Fig. 2.102. Severe dilatation of the pulmonary artery (P) in tetralogy of Fallot with absent pulmonary valve

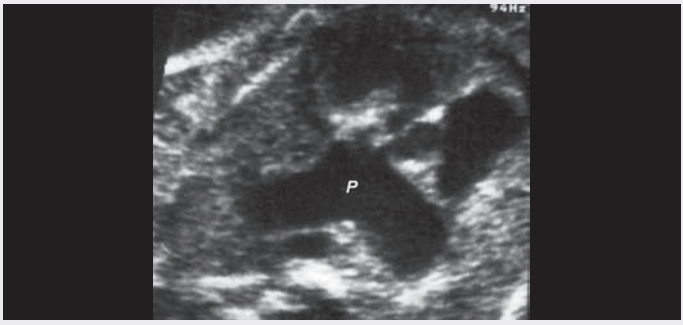

Fetal gastrointestinal tract

Routine examination of the fetal gastrointestinal tract is performed in the axial view of the fetal abdomen. In the upper axial view, the echo-free stomach and the echogenic liver can be visualized with the intrahepatic tract of the umbilical vein (Fig. 2.103a) and the gall bladder (Fig. 2.103b). At a lower level, the echogenic bowel can be seen (Fig. 2.103c).

Bowel obstruction results in different findings depending on the level of obstruction. In **oesophageal atresia**, lack of visualization of the stomach is associated with polyhydramnios secondary to failure of fetal swallowing of amniotic fluid (Fig. 2.104); however, in 90% of cases, oesophageal atresia is associated with tracheo-oesophageal fistula, which allows partial filling of the stomach even in the presence of polyhydramnios. In the longitudinal view, the dilated proximal portion of the oesophagus can be seen during fetal swallowing (Fig. 2.104).

In **duodenal atresia**, dilatation of the stomach and proximal duodenum produces the typical double-bubble sign and polyhydramnios (Fig. 2.105); this condition is frequently associated with trisomy 21.

Dilatation of the intestinal lumen secondary to **ileojejunal obstruction** produces multiple cystic areas in the abdomen below the liver (Fig. 2.106); in this case, polyhydramnios is usually a late occurrence. Severe dilatation may be complicated by bowel perforation and ascites.

Fig. 2.103. Normal gastrointestinal organs. (a) Stomach (S), liver (L) and intrahepatic tract of the umbilical vein (UV). (b) Gall bladder (G). (c) echogenic bowel

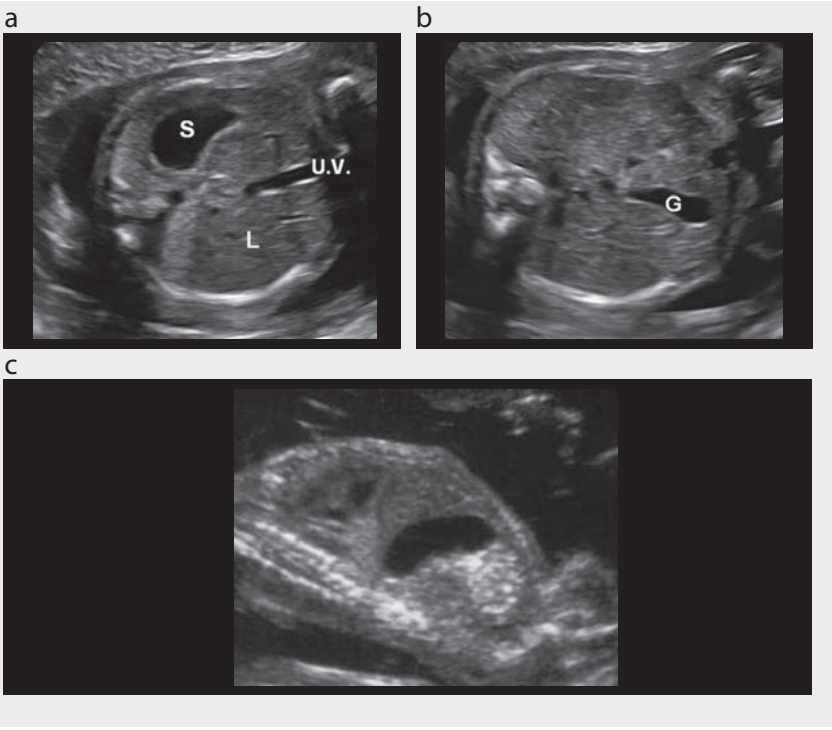

Fig. 2.104. Oesophageal atresia suspected from lack of visualization of the stomach in association with polyhydramnios (a). In the longitudinal view (b), the dilated proximal oesophagus can be seen

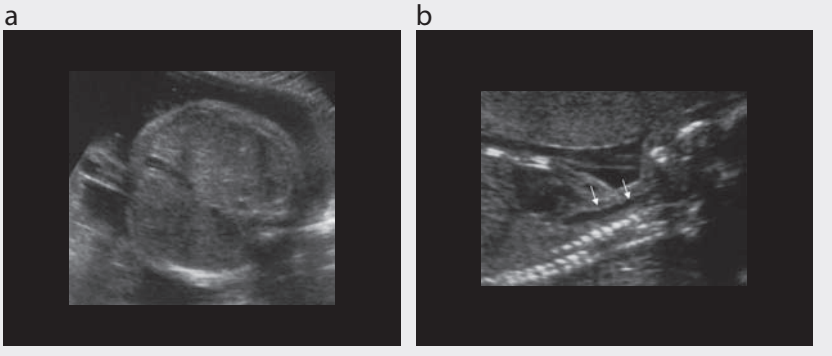

Fig. 2.105. Duodenal atresia: dilatation of the stomach and proximal duodenum produces the typical double-bubble sign

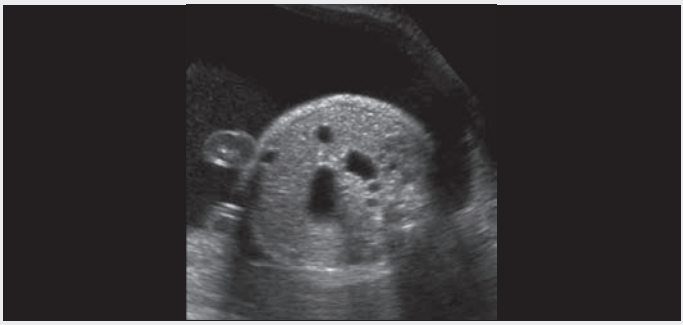

Fig. 2.106. Jejunal obstruction: the dilated bowel produces multiple fluid-filled cystic or tubular areas in the abdomen ((a) sagittal view; (b) axial view)

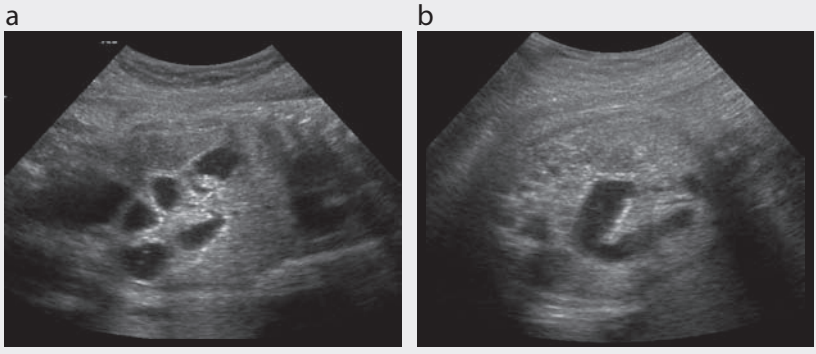

An abnormal shape of the fetal abdomen is produced by **omphalocoele** and **gastroschisis**. In cases of omphalocoele, the abdominal defect is at the level of insertion of the umbilical cord. Intestinal loops or even the stomach and part of the liver (Fig. 2.107) may protrude through the defect and be covered by an amnio-peritoneal membrane. This condition is frequently associated with chromosomopathy.

In cases of gastroschisis, the defect is on the right side of the umbilical cord insertion and is not covered by a membrane; therefore, the herniated bowel loops float freely in the amniotic cavity (Fig. 2.108).

Another anomaly that is easily recognizable on the axial scan of the fetal abdomen is **ascites**, which can have various causes, including cardiac disease, infections, bowel perforation and autoimmune diseases. In these cases, the abdominal circumference is increased and the abdominal cavity is filled with fluid (Fig. 2.109). The ascites can be isolated or be part of general **hydrops** with pleural effusion and soft tissue oedema.

Fig. 2.107. (a) Small and (b) huge omphalocoeles. In the former, only bowel loops are herniated and are covered by a membrane; in the latter, part of the liver may be observed

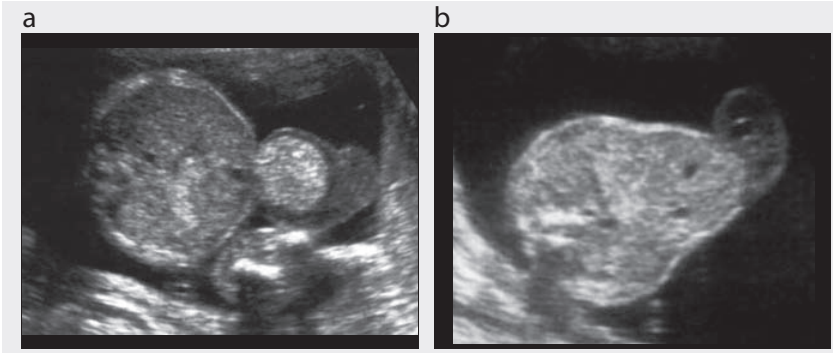

Fig. 2.108. Gastroschisis: herniated bowel loops are floating freely in the amniotic cavity

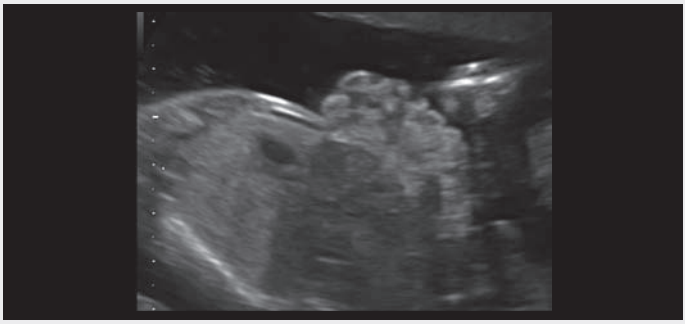

Fig. 2.109. Fetal ascites. (a) Axial and (b) longitudinal views

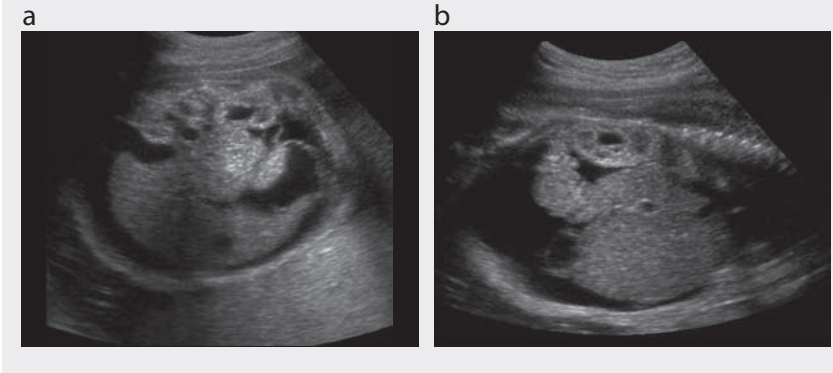

Urinary tract anomalies

Routine evaluation of the fetal urinary tract requires visualization of both kidneys and bladder (Fig. 2.110). The kidneys are usually examined in the axial view of the fetal abdomen, lateral to the spine, sometimes with mild dilatation of the pelvis, which is considered normal up to 5 mm in the second trimester and up to 8 mm in the third trimester.

Fig. 2.110. Normal right kidney in the (a) sagittal and (b) axial views. The renal pelvis (b) (calipers: 3 mm) is not dilated.(c) Normal bladder, axial view, with power Doppler depiction of hypogastric arteries

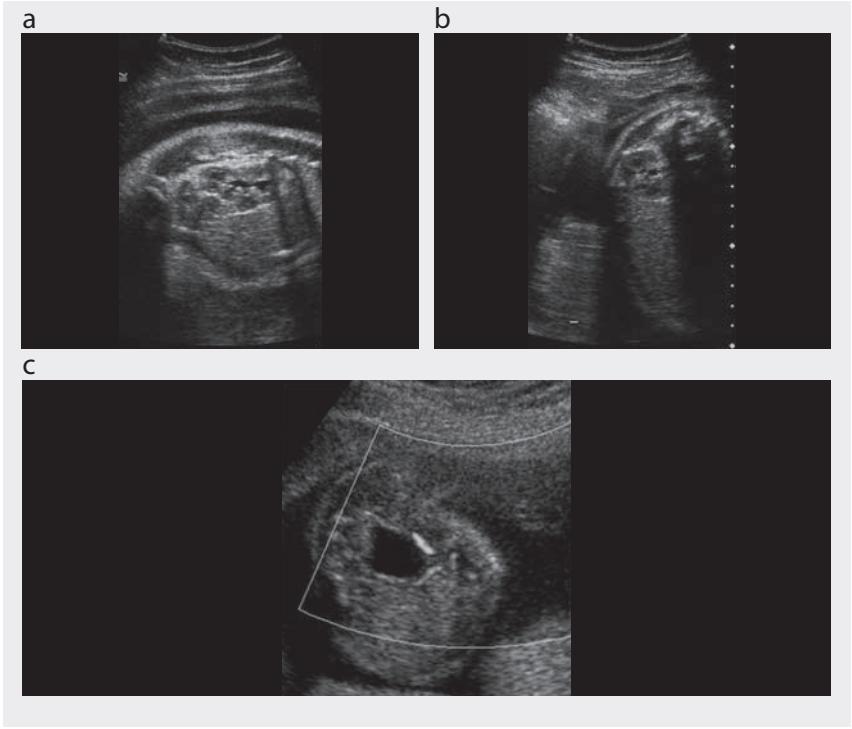

In **bilateral renal agenesis**, the kidneys and bladder cannot be visualized and severe oligohydramnios is present due to lack of fetal urine production (Fig. 2.111). The diagnosis is not easy as the oligohydramnios affects image quality; furthermore, the adrenal glands may mimic the presence of the kidneys. The inability to visualize the renal arteries with colour Doppler may be a helpful sign. This technique also helps to confirm a diagnosis of **unilateral renal agenesis** or **ectopic kidney** (Fig. 2.112).

In **polycystic kidney disease**, both kidneys are enlarged and uniformly hyperechoic; the bladder is absent, and severe oligohydramnios is present (Fig. 2.113). This condition may be part of the Meckel-Gruber syndrome in association with cephalocoele and polydactyly.

Fig. 2.111. Bilateral renal agenesis. The kidneys cannot be visualized; severe oligohydramnios is present

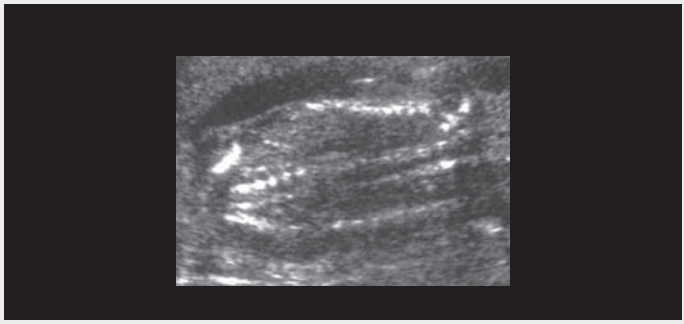

Fig. 2.112. Colour Doppler visualization of the aorta and renal arteries in a normal fetus (a), bilateral renal agenesis (b) and unilateral renal agenesis (c)

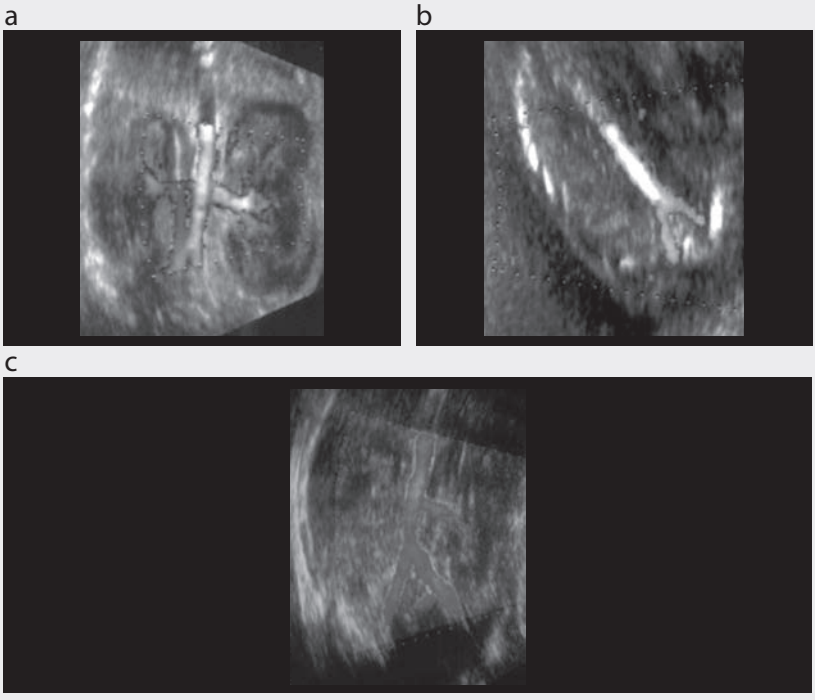

Fig. 2.113. Polycystic kidney disease. Both kidneys are symmetrically enlarged and uniformly echo-rich; severe oligohydramnios is present

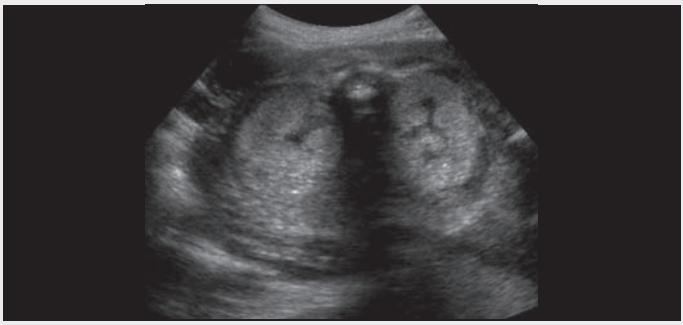

Fig. 2.114. Unilateral multicystic kidney disease. The affected kidney (arrows: (a) transverse view; (b) sagittal view) is enlarged compared with the normal contralateral kidney due to the presence of multiple cysts of variable size

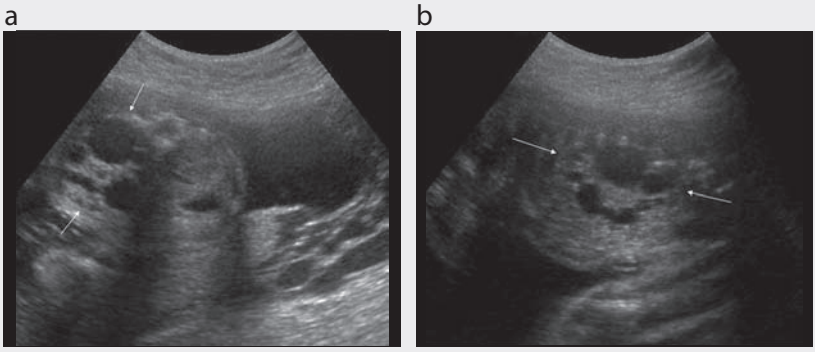

In **multicystic kidney disease**, which is usually unilateral, the affected kidney is enlarged due to the presence of multiple cysts of variable size (Fig. 2.114) as a consequence of early-onset dysplasia of the developing kidney.

Urinary tract obstruction causes different sonographic findings depending on the level of the obstruction. **High-level obstruction**, such as ureteropelvic stenosis, causes dilatation of the renal pelvis and calyces of variable degrees, leading to thinning of the kidney parenchyma (Fig. 2.115).

In **middle-level obstruction**, such as uretero-vesical stenosis, vesico-ureteral reflux and primitive megaureter, the dilated ureter appears as an irregular cystic tubular structure with associated pyelectasis of variable degrees (Fig. 2.116).

Lower urinary tract obstruction can include posterior urethral valves and urethral atresia. In these conditions, the prominent sonographic sign is severe bladder

Fig. 2.115. Moderate (a) and severe (b) unilateral hydronephrosis (calipers: renal pelvis). The renal parenchyma is normal

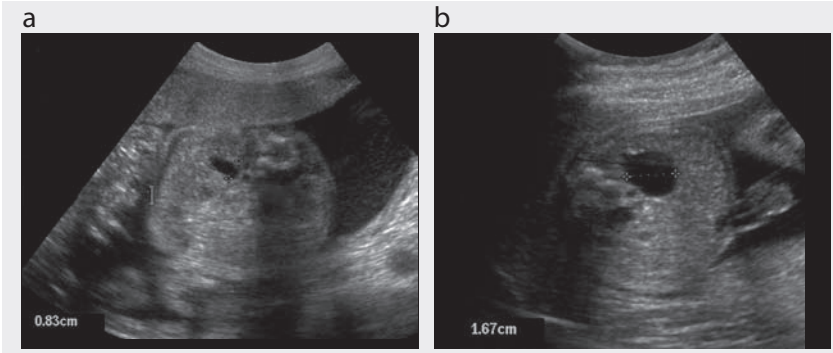

Fig. 2.116. Vesico-ureteral obstruction leading to dilatation of the ureter (U) and pelvis (P). B, bladder

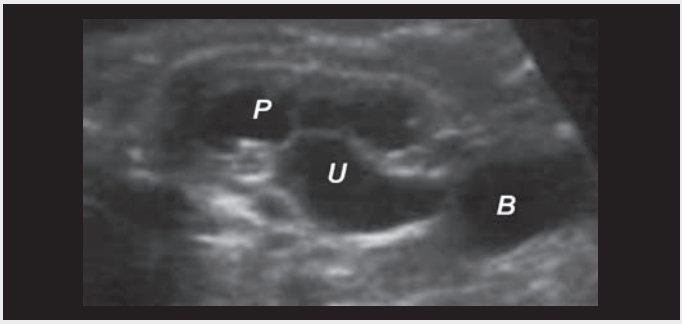

dilatation. In cases of posterior urethral valves, the proximal dilated urethra can also be visualized, forming the typical key-hole appearance of the bladder (Fig. 2.117). As a consequence of the obstruction, bilateral hydronephrosis and subsequent renal dysplasia occur; renal dysplasia should be suspected in the presence of uniformly hyperechoic kidneys (Fig. 2.118) or multiple small cortical cysts. In the most severe forms, the dilated bladder may occupy the entire fetal abdomen, with compression of the diaphragm and lungs.

Fig. 2.117. Severe bladder dilatation in posterior urethral valves. The dilated proximal urethra causes the typical key-hole appearance of the bladder

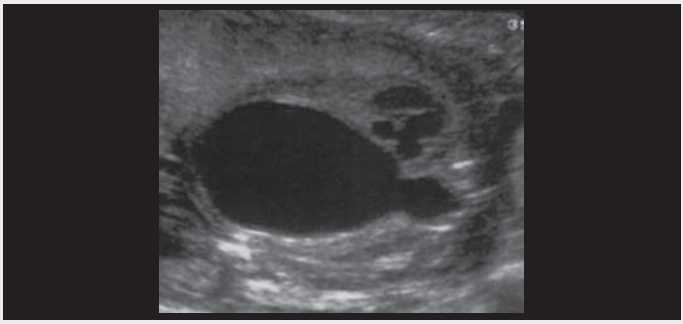

Fig. 2.118. Hyperechoic dysplastic kidney

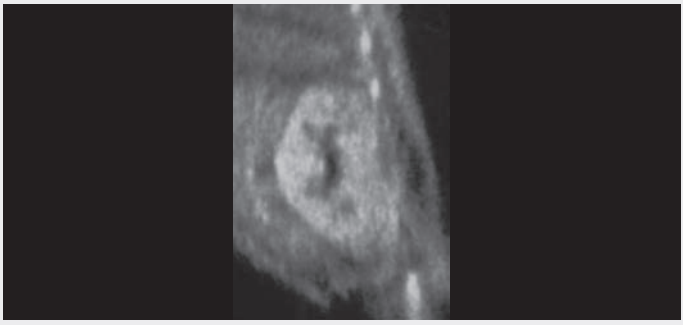

Fetal skeletal system

Sonographic evaluation of the fetal skeleton includes examination of the long bones and extremities, the spine and chest, the head, the degree of mineralization and abnormal contractures.

Long bones and extremities*:* In evaluating the long bones and extremities, the ratio between the rhizomelic (femur:humerus), mesomelic (tibia:fibula, radius:ulna) and acromelic (hand:foot) portions of the limbs must be considered (Fig. 2.119).

Hypoplasia of a single segment is defined as rhizomelia, mesomelia or micromelia, depending on the segment. If the limb is totally hypoplastic, the term 'micromelia' is used (Fig. 2.120).

Fig. 2.119. Normal upper and lower limbs: visualization of the shoulder, arm, forearm, and hand (a) and of the thigh, calf, and feet (b) at 21 weeks' gestational age; hands (c) and foot (d) at 25 weeks' gestational age

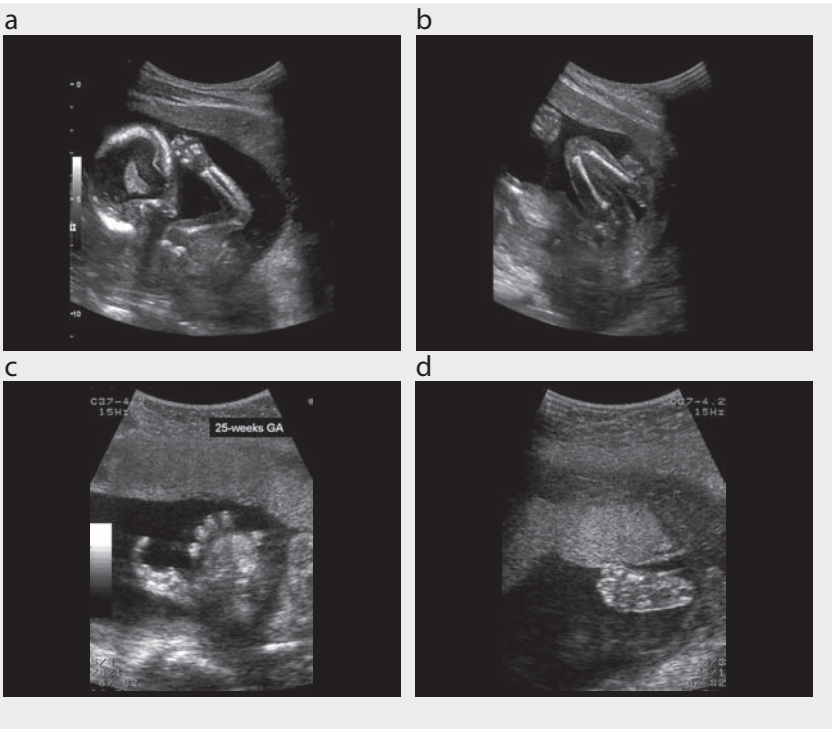

Fig. 2.120. Micromelia of the lower limbs, short and abnormal in shape

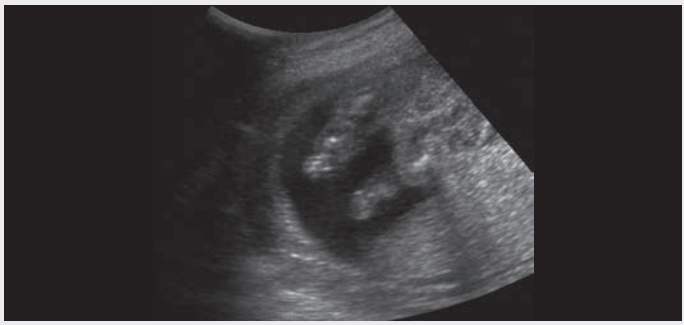

Abnormal shape and fractures of the long bones can also be seen (Fig. 2.121). Abnormal positions of the extremities include club foot (Fig. 2.122) and ulnar deviation of the hand.

Fig. 2.121. Abnormally curved, hypoplastic femur

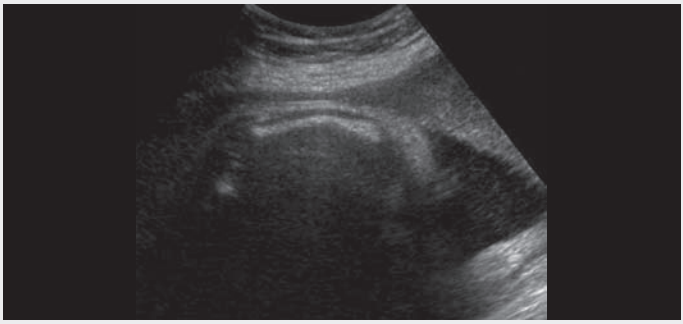

Fig. 2.122. Club foot

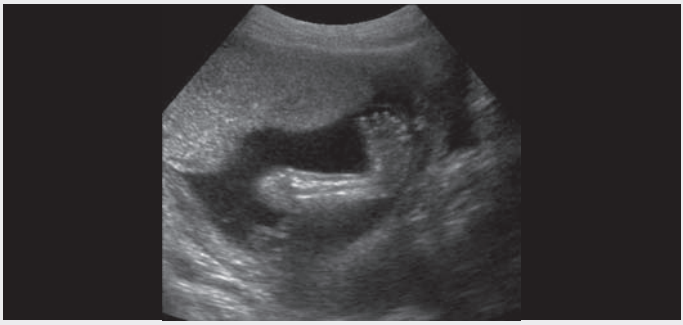

Spine and chest: An abnormally shaped spine can be due to scoliosis or hemivertebra. A hypoplastic chest is common to various skeletal dysplasias and can cause neonatal death as a consequence of the associated lung hypoplasia (Fig. 2.123).

Head: An abnormally shaped head is most commonly due to synostosis. The characteristic sign is the cloverleaf skull, which is typical of thanatophoric dysplasia (Fig. 2.124). Other abnormalities include frontal bossing (Fig. 2.125) and micrognathia.

Degree of mineralization: Thin and transparent skull bones are signs of hypomineralization, which is commonly observed in association with osteogenesis imperfecta (Fig. 2.126) and hypophosphatasia.

Fig. 2.123. Severe hypoplasia of the chest and achondrogenesis in a 22-week fetus

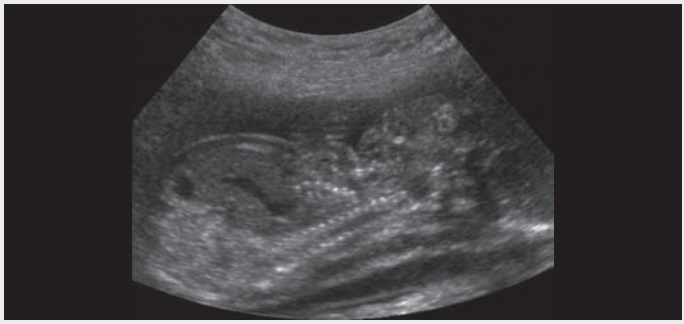

Fig. 2.124. Cloverleaf skull typical of thanatophoric dysplasia

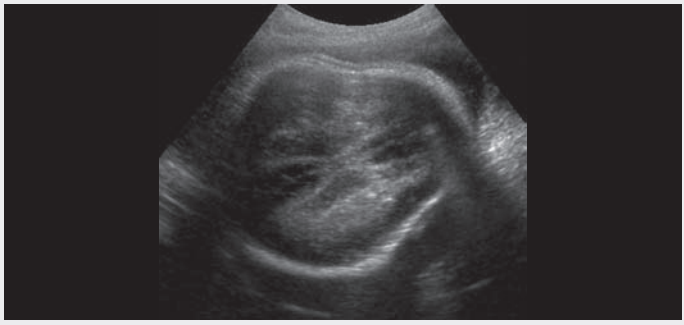

Fig. 2.125. Frontal bossing

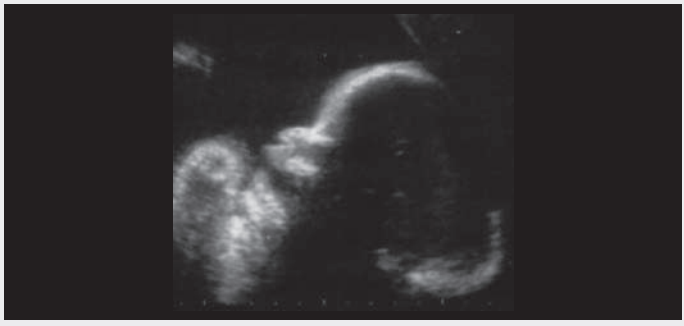

Fig. 2.126. Thin and transparent skull bones (arrowheads): a sign of hypomineralization in osteogenesis imperfecta

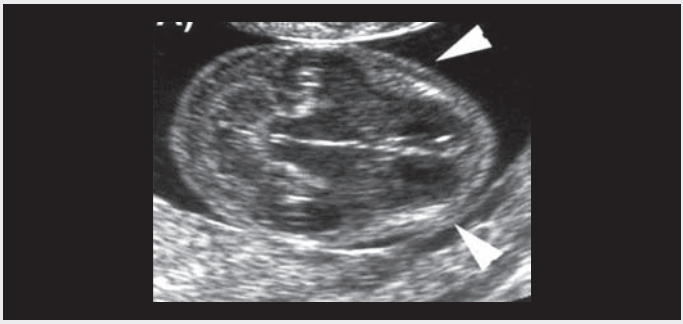

Abnormal contractions: Abnormal contractions of the limbs are typical of arthrogryposis, akinesia deformation syndrome, multiple pterygium syndrome and trisomy 18.

The abnormal sonographic findings described are typical of various skeletal dysplasias, and the antenatal diagnosis is not specific in most cases. By combining the different signs, however, it is possible to make a differential diagnosis or limit the number of possible diagnoses (Table 2.5).

Table 2.5. Differential diagnoses on the basis of main and associated signs

Main sign	Associated signs	Diagnosis
Micromelia	Hypoplastic chest, cloverleaf skull	Thanatophoric dysplasia
	Multiple fractures, hypomineralization	Osteogenesis imperfecta
	Severe diffuse hypomineralization	Hypophosphatasia
	Hypoplastic chest, cardiac defect, polydactyly	Short rib polydactyly syndrome
Rhizomelia	Frontal bossing, macrocrania	Achondroplasia
	Hypoplastic chest, renal anomalies	Jeune syndrome
	Exadactyly, cardiac defect	Chondroectodermal dysplasia
Hypoplastic chest	Micromelia, cloverleaf skull	Thanatophoric dysplasia
	Rhizomelia, renal anomalies	Jeune syndrome
	Micromelia, hypomineralization	Achondrogenesis
	Micromelia, cardiac defect, polydactyly	Short rib polydactyly syndrome

Use of Doppler in obstetrics

Assessment of fetal circulation is essential for better understanding of the pathophysiology of a wide spectrum of pathological pregnancies and their clinical management. This section is intended as a brief description on how to use Doppler application in obstetrical clinical practice. The first part describes the basic concepts of Doppler

sonography, which are essential for understanding its diagnostic uses. The second focuses on the primary clinical applications of Doppler techniques in obstetrics and in assessing fetal health status in pregnancies complicated by placental insufficiency.

Doppler ultrasound: principles and practice

Doppler principles

Competent use of Doppler ultrasound techniques requires an understanding of three components: the capacity and limitations of Doppler ultrasound, the parameters that contribute to a flow assessment and the features of blood flow in arteries and veins.

Ultrasound images of flow are obtained by measuring moving fluids. In ultrasound scanners, a series of pulses is transmitted to detect the movement of blood; echoes from moving scatterers determine slight differences in the time for return of the signal to the receiver. These differences can be measured as direct time differences or, more often, in terms of a phase shift from which the Doppler frequency is obtained (Fig. 2.127). They are then processed to produce a colour flow display or a Doppler sonogram.

Fig. 2.127. Doppler effect

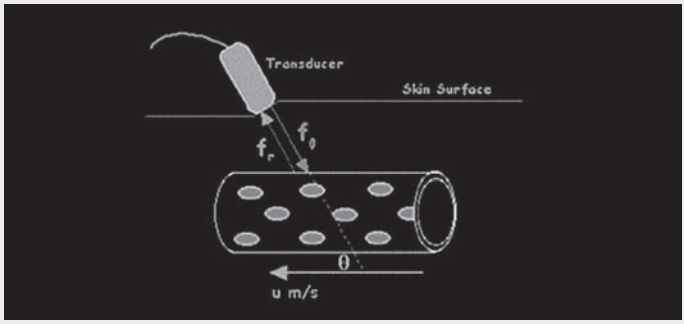

Fig. 2.127 shows the Doppler transducer scanning at an angle θ to a blood vessel, in which blood flows at a velocity of u m/s. The ultrasound waves are emitted by the transducer at a frequency f_o and are directed back to the transducer by moving reflectors in the blood (red blood cells) at a different frequency f_r. The difference between the transmitted and received frequencies, Δf, is related to the velocity of the flowing blood, u, and the speed of sound in tissue, v, according to the equation:

$$\Delta f = f_o - f_r = \frac{2 f_o u \cos \theta}{v}$$

There has to be motion in the direction of the beam to obtain Doppler signals; this does not happen if the flow is perpendicular to the beam.

The magnitude of the Doppler signal depends on:

- blood velocity;
- ultrasound frequency: the higher the ultrasound frequency, the higher the Doppler frequency. As in B-mode, lower ultrasound frequencies have better penetration; the choice of frequency is therefore a compromise between better sensitivity and better penetration;
- the angle of insonation: the Doppler frequency increases as the angle between the beam and the direction of flow becomes smaller.

The two main types of Doppler systems in common use today are **continuous wave** and **pulsed wave**. They differ in transducer design, operating features, signal processing procedures, and the types of information provided.

Doppler practice

Continuous-wave Doppler requires continuous generation of ultrasound waves with continuous ultrasound reception. A two-crystal transducer has this dual function, with one crystal for each function. The main advantage of continuous-wave Doppler is for measuring high blood velocities accurately; its main disadvantage is the lack of selectivity and depth discrimination. As continuous-wave Doppler is constantly transmitting and receiving from two different transducer heads (crystals), there is no provision for imaging or range gating to allow selective placing of a given Doppler sample volume in space.

Pulsed-wave Doppler systems have a transducer that alternates transmission and reception of ultrasound in a way similar to the M-mode transducer. The main advantage of pulsed Doppler is that Doppler shift data are produced selectively from a small segment along the ultrasound beam, referred to as the sample volume, the location of which is controlled by the operator. An ultrasound pulse is transmitted into tissues and travels for a given time (time X) until it is reflected back by a moving red cell. It then returns to the transducer over the same interval but at a shifted frequency. The total transit time to and from the area is 2X. This process is repeated alternately through many transmit–receive cycles each second. The range gating therefore depends on a timing mechanism that samples the returning Doppler shift data from only a given region. All other returning ultrasound information is essentially ignored. The main disadvantage of pulsed-wave Doppler is that high blood flow velocities cannot be measured accurately.

Aliasing effect: Pulsed-wave systems have a fundamental limitation. When pulses are transmitted at a given sampling frequency (pulse repetition frequency), the maximum Doppler frequency that can be measured is half of that frequency. Therefore, if the Doppler frequency is greater than half the pulse repetition frequency,

the Doppler signal is ambiguous. This condition is known as *aliasing*. The interval between sampling pulses must be sufficient for a pulse to go away and come back to the transducer. If a second pulse is sent before the first is received, the receiver cannot correctly discriminate between the two. The deeper the sample volume, the longer the pulse's journey, so that the pulse repetition frequency must be reduced for unambiguous ranging. The result is that the maximum measurable Doppler frequency decreases with depth.

Ultrasound Doppler modes: colour flow imaging and spectral Doppler

Colour flow imaging produces a picture of a blood vessel by converting the Doppler data into colours, which are overlaid onto the B-mode image of the blood vessel and represent the speed and direction of blood flow through the vessel. It is useful for identifying the vessels under examination, verifying the presence and direction of flow and finding the correct angle of insonation for velocity measurements.

Power Doppler is a newer ultrasound technique that is up to five times more sensitive in detecting low blood flow than standard colour Doppler. The magnitude of the flow output rather than the Doppler frequency signal is shown. Power Doppler can obtain some images that are difficult or impossible to obtain with standard colour Doppler.

Spectral Doppler (pulsed-wave Doppler) is used to provide a sonogram of a vessel in order to measure the distribution of flow velocities in the sample volume. The Doppler signal is processed in a Fourier spectrum analyser. The amplitudes of the resulting spectra are encoded as brightness, and these are plotted as a function of time (horizontal axis) and frequency shift (vertical axis) to give a two-dimensional spectral display. With this technique, a range of blood velocities in a sample volume will produce a corresponding range of frequency shifts on the spectral display.

To obtain proper images and measures, the operator should:

- identify the vessel (possibly by colour flow imaging);
- adjust the gain so that the sonogram is clear and free of noise;
- place the Doppler cursor on the vessel to be investigated (sample volume) and set the correct size;
- obtain a proper angle of insonation (60° or less);
- adjust the pulse repetition frequency to suit flow conditions and avoid aliasing.

Flow waveform analysis: Doppler waveform analysis is often used for diagnosis in the clinical assessment of disease. The complex shapes of Doppler waveforms can be described by relatively simple indices, which have been used to evaluate fetal health and organ blood flow. Common indices are the pulsatility index (PI), resistance index (RI) and the ratio of systolic to diastolic (S/D or A/B).

$$\mathrm{PI} = \frac{f_{\max} - f_{\min}}{f_{\mathrm{mean}}}$$

$$RI = \frac{f_{max} - f_{min}}{f_{max}}$$

$$S/D = \frac{f_{max}}{f_{min}}$$

where f_{max} is the maximum systolic frequency, f_{min} is the minimum diastolic frequency, and f_{mean} is the time-averaged frequency (Fig. 2.128).

An advantage of these waveform indices is that they consist of ratios of Doppler shift frequencies and are thus independent of transmission frequency and Doppler angle. Generally, low- and high-pulsatility waveforms occur in low- and high-resistance vascular beds, respectively. In addition to these indices, the flow waveform can be described or categorized by the presence or absence of a particular feature, for example the absence of end-diastolic flow and the presence of a post-systolic notch.

Fig. 2.128. Doppler waveform indices (for abbreviations, see text)

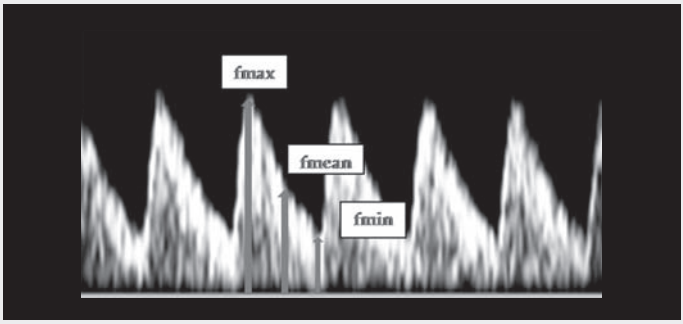

Doppler assessment of placental and fetal circulation

Placental insufficiency is the primary cause of intrauterine growth restriction in normal fetuses. The use of Doppler during antenatal fetal surveillance involves assessment of umbilical arterial and venous flow velocity waveforms, the fetal cerebral circulation and the fetal venous circulation, in particular the ductus venosus.

Assessment of placental function with umbilical artery Doppler velocimetry

The yolk sac develops 7–16 days after conception, and early development of the primary chorionic villi takes place. Thereafter, the chorioallantoic placenta develops in stages, consisting of invasion of the spiral arteries by an endovascular cytotrophoblast,

followed by a second wave of invasion that extends into the myometrium. Spiral arteries invaded by cytotrophoblastic cells are converted into uteroplacental arteries characterized by a dilated and tortuous lumen, with complete absence of muscular and elastic tissue and no continuous endothelial lining. The placental villi development leads to a progressive increase in the vessel diameter lumen and to the growth of a complex capillary network: the terminal villi will have small calibre (40–100 μm) but reach an extensive surface area (>10 m^2), thus reducing impedance to flow and optimizing feto-maternal exchange in the intervillous space.

The basic organization of the human placenta is present by approximately day 20 of pregnancy. Further refinement of the basic structure continues until term, at which time there are approximately 50–60 primary fetal stem villi branching into several terminal or tertiary villi. The branching of the stem villi is responsible for the low vascular resistance, the increased placental blood flow and the increased transplacental gas exchange that characterize human placentation. The low umbilical-placental vascular resistance also allows increased end-diastolic blood flow velocity in the umbilical artery during the third trimester of a normal pregnancy. Impaired placentation results in abnormally high umbilical-placental vascular resistance, reduced umbilical blood flow and chronic fetal hypoxaemia.

With increased downstream placental vascular resistance, the velocity of the end-diastolic flow in the umbilical cord artery is reduced, while the peak-systolic component is not significantly affected (Fig. 2.49).

To obtain umbilical artery Doppler waveforms with a pulsed-wave Doppler system, an ultrasound scan is first made, a free-floating portion of the cord is identified and the Doppler sample volume is placed over an artery and the vein. The angle of the fetal Doppler insonation should be kept at < 45° for optimal recording.

Several factors affect the umbilical artery Doppler waveform, independently of changes in placental vascular resistance:

- **Gestational age**: With advancing gestation, umbilical arterial Doppler waveforms show a progressive rise in end-diastolic velocity and decreased impedance indices. Gestational age-dependent nomograms are necessary for accurate interpretation of umbilical cord artery velocimetry.
- **Fetal heart rate**: When the heart rate drops, the diastolic phase of the cardiac cycle is prolonged and the end-diastolic frequency shift declines. The change is of no clinical significance when the heart rate is within the normal range.
- **Fetal breathing movements**: During fetal breathing, the shape of the flow velocity waveforms varies. Therefore, Doppler examinations should be conducted only during fetal apnoea and in the absence of excessive fetal movement.
- **Location of sample volume**: The impedance indices are significantly higher at the fetal end of the cord than at the placental end. It is recommended that umbilical artery Doppler waveforms be measured within 5 cm of the umbilical cord insertion.

Table 2.6. Umbilical artery pulsatility index at the fetal end of the umbilical cord based on 513 observations in 130 low-risk pregnancies

Gestational age (weeks)	Percentile				
	5th	25th	50th	75th	95th
24	0.94	1.11	1.24	1.38	1.59
25	0.91	1.08	1.21	1.34	1.55
26	0.87	1.04	1.17	1.31	1.51
27	0.84	1.01	1.14	1.27	1.48
28	0.81	0.98	1.11	1.24	1.45
29	0.78	0.95	1.08	1.21	1.42
30	0.75	0.92	1.05	1.18	1.39
31	0.73	0.89	1.02	1.16	1.36
32	0.70	0.87	0.99	1.13	1.34
33	0.67	0.84	0.97	1.11	1.32
34	0.65	0.82	0.95	1.08	1.30
35	0.62	0.79	0.92	1.06	1.28
36	0.60	0.77	0.90	1.04	1.26
37	0.58	0.75	0.88	1.02	1.24
38	0.56	0.73	0.86	1.00	1.23
39	0.54	0.71	0.84	0.98	1.21
40	0.52	0.69	0.82	0.97	1.20
41	0.50	0.67	0.80	0.95	1.18

Modified from Acharya et al. (2005)

In high-risk pregnancies complicated by maternal hypertension, intrauterine growth restriction or multiple pregnancy, umbilical artery Doppler studies should be part of antenatal assessment (Table 2.6). Placental insufficiency can be classified on the basis of the reduction in end-diastolic Doppler flow velocity into reduced, absent and reversed end-diastolic flow velocity. The risk for perinatal mortality increases up to 60% with increasing severity of reduced to reversed end-diastolic flow velocity. As there is no evidence that use of umbilical artery Doppler is of value in low-risk pregnancies, it should not be used for routine screening.

Prediction of fetal hypoxaemia from the fetal middle cerebral artery

With increased downstream placental vascular resistance, the velocity of the end-diastolic flow in the umbilical cord artery is reduced. In fetal hypoxaemia, there is an increased blood supply to the brain, myocardium and adrenal glands and reduced perfusion of the kidneys, gastrointestinal tract and lower extremities. This mechanism allows a preferential supply of nutrients and oxygen to vital organs. The phenomenon has been described as brain sparing. Chronic hypoxia with increased pCO_2 or reduced pO_2 will increase the fetal cerebral arterial Doppler end-diastolic flow velocity, probably related to cerebral vasodilatation (Fig. 2.50 and Table 2.7).

Compensation through cerebral vasodilatation is limited. In a series of intrauterine growth-restricted fetuses, longitudinally examined, a curvilinear relationship

Table 2.7. Longitudinal reference ranges for the middle cerebral artery pulsatility index based on 566 observations in 161 low-risk pregnancies

Gestational age (weeks)	Percentile				
	5th	25th	50th	75th	95th
24	1.38	1.64	1.86	2.10	2.52
25	1.44	1.71	1.94	2.19	2.62
26	1.50	1.78	2.01	2.26	2.71
27	1.55	1.83	2.06	2.33	2.78
28	1.58	1.88	2.11	2.38	2.84
29	1.61	1.91	2.15	2.42	2.88
30	1.62	1.92	2.16	2.44	2.90
31	1.62	1.92	2.16	2.43	2.90
32	1.61	1.90	2.14	2.41	2.87
33	1.58	1.87	2.10	2.37	2.82
34	1.53	1.81	2.04	2.30	2.74
35	1.47	1.74	1.96	2.21	2.64
36	1.39	1.65	1.86	2.11	2.52
37	1.30	1.55	1.75	1.98	2.38
38	1.20	1.44	1.63	1.85	2.22
39	1.10	1.32	1.49	1.70	2.05

Modified from Ebbing C et al. (2007)

was found between impedance in cerebral vessels and the status of fetal oxygenation; the progressive fall in impedance reached a nadir 2 weeks before the onset of late fetal heart rate decelerations. Middle cerebral artery Doppler velocimetry is thus unsuitable for longitudinal monitoring of growth-restricted fetuses. Venous velocity waveforms give more information regarding fetal status.

The middle cerebral artery parameters that are mainly taken into account are pulsatility index and cerebroplacental ratio (middle cerebral artery pulsatility index/umbilical artery pulsatility index). A low cerebroplacental ratio reflects redistribution of the cardiac output to the cerebral circulation and has been shown to improve accuracy in predicting adverse outcomes over that obtained with the middle cerebral artery or umbilical artery Doppler alone.

To conduct appropriate scanning of the middle cerebral artery, a transverse section of the fetal brain is obtained at the level of the biparietal diameter and the transducer is slightly moved towards the base of the skull. With colour flow imaging, the middle cerebral artery can be seen as a major lateral branch of the circle of Willis, dividing the anterior and the middle cerebral fossae (Fig. 2.50). The pulsed Doppler sample volume is obtained from the middle part of the vessel. During the examination, care should be taken to avoid high pressure on the maternal abdomen, as fetal head compression is associated with alterations of intracranial arterial waveforms.

The same factors that affect umbilical artery Doppler waveforms can also affect fetal cerebral artery Doppler waveforms.

Prediction of fetal hypoxaemia with fetal venous Doppler

The fetal liver with its venous vasculature (umbilical and portal veins, ductus venosus and hepatic veins) and the inferior vena cava are the main areas of interest in investigating venous blood return to the fetal heart. The ductus venosus originates from the umbilical vein before it turns to the right, and it enters the inferior vena cava in a venous vestibulum just below the diaphragm. The diameter of the ductus venosus is approximately one third that of the umbilical vein. With colour Doppler, the ductus venosus is identified in a midsagittal or oblique transection as a vessel connecting the umbilical vein with the inferior vena cava and exhibiting the typical aliasing of high velocities when compared with the umbilical vein (Fig. 2.51).

In severe hypoxaemia, the umbilical venous blood is redistributed to the ductus venosus at the expense of the hepatic blood flow. Consequently, the proportion of umbilical venous blood contributing to the fetal cardiac output is increased to ensure an increase in umbilical venous-derived oxygen delivery to the myocardium and increased oxygen delivery to the fetal brain. Increased placental resistance and peripheral vasoconstriction, seen in fetal arterial redistribution, cause an increase in the right ventricular afterload, and thus ventricular end-diastolic pressure increases. This may result in highly pulsatile venous blood flow waveforms and umbilical venous pulsations due to transmission of atrial pressure waves through the ductus venosus. In the inferior vena cava, reverse flow during atrial contraction increases with progressive fetal deterioration, suggesting a higher pressure gradient in the right atrium.

The next step in the disease is extension of the abnormal reversal of blood velocities in the inferior vena cava to the ductus venosus, inducing an increase in the ratio of peak systolic velocity to end-diastolic velocity, mainly due to a reduction in the latter component of the velocity waveforms (Fig. 2.51). The main ductus venosus Doppler parameter that is taken into account is the pulsatility index for veins, PI, which is calculated as:

$$\mathrm{PI} = \frac{v_s - v_d}{v_m}$$

where v_s is peak systolic velocity, v_d is end-diastolic velocity and v_m is time-averaged maximum velocity.

The high venous pressure induces a reduction in velocity at end-diastole in the umbilical vein, causing typical end-diastolic pulsations. Umbilical venous pulsations, particularly double pulsations, have been associated with perinatal mortality rates of up to 16% with absent umbilical artery end-diastolic flow velocity and 60% with reversed umbilical artery end-diastolic flow velocity.

The ductus venosus pulsatility index and short-term variations in fetal heart rate are important indicators for the optimal timing of delivery before 32 weeks of gestation (Table 2.8). Delivery should be considered if one of these parameters is persistently abnormal. The interval may be as short as a few hours in late gestation

Table 2.8. Longitudinal reference ranges for the pulsatility index of veins of the ductus venosus based on 547 observations in 160 low-risk pregnancies

Gestational age (weeks)	Percentile				
	5th	25th	50th	75th	95th
24	0.27	0.38	0.47	0.68	0.83
25	0.27	0.37	0.47	0.67	0.83
26	0.27	0.37	0.46	0.67	0.82
27	0.26	0.36	0.46	0.67	0.82
28	0.26	0.36	0.45	0.66	0.81
29	0.25	0.35	0.45	0.65	0.81
30	0.25	0.35	0.44	0.65	0.80
31	0.24	0.34	0.43	0.64	0.79
32	0.23	0.33	0.42	0.63	0.78
33	0.22	0.32	0.41	0.62	0.77
34	0.21	0.31	0.40	0.61	0.76
35	0.20	0.30	0.39	0.60	0.75
36	0.19	0.29	0.38	0.59	0.74
37	0.18	0.28	0.37	0.58	0.73
38	0.17	0.27	0.36	0.57	0.72
39	0.16	0.26	0.35	0.56	0.71

Modified from Kessler et al. (2006)

and in women with pre-eclampsia; in contrast, during the second trimester, severely abnormal venous waveforms can be present several days before intrauterine death.

Clinical recommendations

- Umbilical artery Doppler should not be used for screening in healthy pregnancies.
- Doppler assessment of the placental circulation is important in screening for impaired placentation and its complications of pre-eclampsia, intrauterine growth restriction and perinatal death.
- In these conditions, abnormal umbilical artery Doppler velocimetry is an indication for accurate evaluation of fetal health status. Doppler investigation of fetal middle cerebral artery and ductus venosus is recommended.
- Measurements must be taken and interpreted by expert operators with appropriate instruments and technique to avoid inappropriate clinical decisions.

Recommendations on reporting of obstetrical ultrasound examinations

A report should be written at the end of every sonographic examination.

First trimester

In the first trimester of pregnancy, the report must contain:

- the reason for the examination;
- the position and number of gestational sacs;
- the number of embryos and fetuses;
- the presence or absence of cardiac activity;
- chorionicity and amnionicity in cases of multiple pregnancy;
- the mean diameter of the gestational sac;
- craniocaudal length (crown–rump length) or biparietal diameter of the embryo or fetus.

The measurements of all parameters must be compared to reference curves in order to assess whether the sonographic age coincides with the anamnestic (i.e. menstrual) gestational age. The report should mention whether the pregnancy is to be re-dated.

The report should also include:

- possible uterine or adnexal anomalies;
- suggestions on the need and timing of further sonographic examinations (between 20 and 22 weeks and 30 and 34 weeks or, on particular indications, at other times);
- any limitations of the examination (maternal obesity, unfavourable position of the fetus);
- the device used: 3.5-MHz transabdominal probe or 7.5-MHz endovaginal probe;
- images;
- the date and signature of the operator.

Second trimester

In the second trimester of the pregnancy, the report must contain:

- number of fetuses and presence or absence of cardiac activity
- results of the anatomical evaluation
- results of the biometric evaluation
- chorionicity and amnionicity in cases of multiple pregnancy
- the position of the placenta.

The measurements of all parameters and morphological aspects must be compared to reference curves in order to assess whether the sonographic age coincides with the anamnestic gestational age. The report should mention whether the pregnancy is to be re-dated.

The report should also include:

- any limitations of the examination (maternal obesity, unfavourable position of the fetus, oligoamnios) that hindered or limited morphological study of the fetus;
- suspect or pathological features requiring further diagnostic investigations;
- suggestions on the need and timing of further sonographic examinations (between 30 and 34 weeks or, on particular indications, at other times);
- images;
- the date and signature of the operator.

Third trimester

In the third trimester of the pregnancy, the report must contain:

- the number of fetuses and the presence or absence of cardiac activity;
- the situation and presentation of the fetus;
- the position of the placenta;
- the quantity of amniotic fluid;
- the estimated fetal weight;
- all biometric parameters and morphological aspects, particularly the thickness of the atrium (atrial width) of the cerebral ventricles, fetal cardiac activity, both kidneys and the bladder; and the curve of fetal growth, reported on a reference curve;
- suggestions about the need and timing of further sonographic examinations;
- any limitations of the examination (maternal obesity, unfavourable position of the fetus, oligoamnios);
- images;
- the date and signature of the operator.

Chapter 3

Gynaecology

3

Gynaecology
Uterus and ovaries

Gynaecological ultrasonography is a non-invasive imaging technique that can be used:

- in the diagnostic work-up of pelvic masses suspected on the basis of history and pelvic clinical examination;
- in the diagnostic work-up of dysfunctional or infective diseases that involve or can involve the pelvis;
- in the differential diagnosis of other acute abdominopelvic diseases (appendicitis, diverticulitis, inflammatory bowel diseases);
- in the peri- and postmenopausal diagnostic evaluation of women with atypical uterine bleeding, in order to define the macroscopic characteristics of the endometrium and uterine cavity;
- in ovarian and endometrial surveillance of women at high-risk for ovarian and endometrial cancer (familial, drugs);
- in monitoring spontaneous or drug-induced ovulation;
- in monitoring therapy and surgery.

Sonography plays an important role in the detection of gynaecological disorders and is used widely with clinical examinations but also for first-line imaging to give an accurate indication for more sophisticated diagnostic techniques or more invasive endoscopic procedures. Technological advances have made it possible to use transabdominal (suprapubic) sonography with transvaginal or transrectal scanning.

The choice of an ultrasound examination should be guided by clinical indications, but the widespread availability of ultrasound equipment leads many specialists to request an ultrasound scan on almost all women, to complete their clinical examination.

Transvaginal scanning is now the examination technique of choice. Some conditions do not allow or limit transvaginal scanning: the integrity of the hymen, women's refusal to undergo an imaging technique that they consider invasive, or the presence of phlogistic and cicatricial processes involving the vaginal walls that could make the transducer's movements painful or limit them. Uterine bleeding is not a contraindication for ultrasound examination, even for suspected miscarriage.

In such cases, women should be reassured that transvaginal scanning is a harmless imaging technique that can help to clarify the causes of bleeding.

Transabdominal ultrasound should be considered for use with transvaginal scanning in abdominopelvic neoformation that cannot be explored completely with transvaginal ultrasound and when a woman's condition does not allow endovaginal access.

Transrectal scanning is seldom used but may be useful when transvaginal scanning cannot be performed or to study the vaginal walls, the cervix, the parametria and the vaginal cuff after hysterectomy.

Preparation and scanning techniques

The techniques of choice for studying the uterus and ovaries are transabdominal and transvaginal ultrasound.

Transabdominal ultrasound

Transabdominal examination is performed with real-time, 2.5- to 5-MHz convex or sectoral transducers, depending on the woman's age and body. Modern devices with multi-frequency transducers allow optimization of the ultrasound frequency to the woman's body size and the structures to be studied. Convex transducers are widely used, although sectoral transducers may be better in some cases, such as abundant subcutaneous fat or a pendulous abdomen.

The examination should be performed with optimal bladder filling, generally obtained when the bladder covers the uterine fundus. A full bladder is needed as an acoustic window to displace the intervening bowel but also to decrease uterine physiological anteversion, bringing it into a better position for ultrasound scanning (Fig. 3.1). Scant filling is unfavourable, but hyperdistention of the bladder must be avoided as well because the uterus and adnexa are compressed and displaced into a deep location far from the skin plane. Hyperhydration is also to be avoided, because some fluid effusion may collect in the pelvis and simulate a disease state, and bowel loops may appear distended by fluid.

When appropriate bladder filling has been obtained, the operator performs longitudinal scans along the cervix–fundus of uterus axis and transversal scans along axial planes. The ovaries have a variable position and should be sought with appropriate paramedian-oblique ultrasound scans. Hypogastric vessels are important landmarks for the ovaries, because they run back and lateral to them (Fig. 3.2). The operator should be able to recognize possible artefacts, for example acoustic shadowing by enteric gas, that can create empty signal areas and simulate cysts; furthermore, a hyperdistended loop of bowel could simulate adnexal disease.

If the uterus is retroverted, its fundus is situated in a back position, far from the transducer and with an adverse ultrasound incidence. The fundus might thus appear less echogenic than the remaining myometrium, simulating a fibroid. The operator should distinguish these false aspects from real disease on the basis of his or her experience, perhaps repeating the examination or performing transvaginal scanning.

Fig. 3.1. Structures scanned by ultrasound during a pelvic transabdominal examination

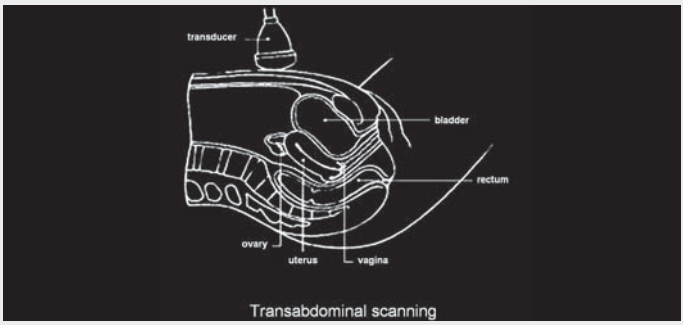

Fig. 3.2. Transabdominal (a) and transvaginal (b) examinations of the right adnexal region (different patients), showing the relation between the ovary and uterus (a) and the ovary and iliac vessels (b)

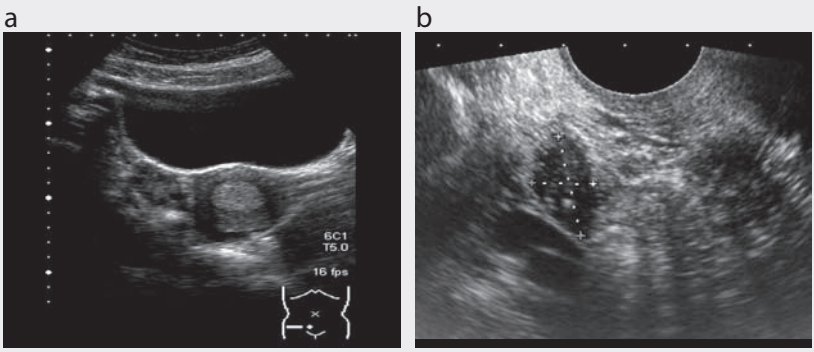

Transvaginal ultrasound

Transvaginal scanning is the best method for studying the uterus and adnexa. The woman must have an empty bladder, which will result in a shorter wait and less discomfort. The operator can also perform transabdominal scanning before a transvaginal scan.

Unlike transabdominal scanning, where the bladder must be filled or the bowel opportunistically cleaned, in transvaginal scanning no particular preparation is requested. The only advice is to empty the bladder soon before starting the examination, if it has been preceded by a transabdominal study. In this way, the woman's discomfort is reduced and the transducer is not too far from the pelvic structures that are to be examined. Moreover, a full bladder can displace or compress adjacent organs, inducing distortions that can lead to an erroneous diagnosis. While the transabdominal technique is characterized by wide transducer inclination along

various angles and allows the examiner to visually assess the scan plane, during transvaginal scanning the transducer's movements are limited and consist mainly of shifting the transducer along the sagittal and transverse axis or rotation.

The examination is done with the woman in the gynaecological position, ideally on a suitable bed with leg rests. If this is not available, the woman should remain supine with raised knees, legs wide apart and with the pelvis raised by a pillow, so that the bed does not stop the transducer's movements. The abdomen and genitals should be covered with a sheet to reduce psychological discomfort. In this position, the Douglas cavity is no longer the most declivous site in the abdomen, so any free fluid can move upwards and may not be detected; to avoid this, it is useful to bend the back by about 30°.

Convex transducers with a high frequency (5–7.5 MHz) are used, with crystals set in the extremity. Before the transducer is inserted into the vagina, its distal extremity should be spread with ultrasound gel and then fitted into a sterile cover (a latex glove or a condom) also sprinkled with gel in order to aid ultrasound transmission and to lubricate the vaginal walls. Air bubbles should not be left between the transducer and the cover because they prevent ultrasound propagation. Should the condom break, and always at the end of each examination, the transducer should be sterilized and disinfected by bathing it in 2–3% glutaraldehyde and rinsed in sterile water.

The operator should start by scanning along the axial planes to obtain transversal uterine corpus sections (Fig. 3.3); then the transducer should be rotated to the right about 90° in order to obtain sagittal uterine scans. In this way, the uterus is visualized from the cervix to the fundus. For optimal cervix visualization, the transducer can be drawn back slightly. To observe the adnexa, the transducer should then be moved towards the lateral fornices and angled laterally.

The decreased distance between the transducer and the structures being examined, the possibility of using high-frequency transducers and the lack of interference from bowel gas make it possible to obtain better anatomical detail. Furthermore, transvaginal transducers allow a detailed colour Doppler examination, which

Fig. 3.3. Structures scanned by ultrasound during a pelvic transvaginal examination, on a sagittal scan

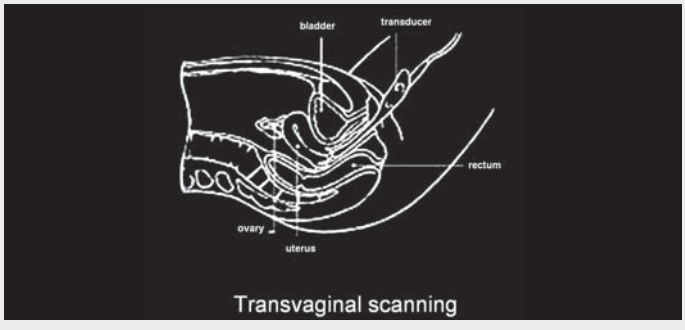

provides important functional information, either for monitoring physiological flow variations associated with ovulation or to recognize signs of malignant neoangiogenesis and thus help characterize uterine or ovarian masses (Fig. 3.4). A major limitation of transvaginal scanning is the lack of a panoramic view, preventing adequate study of large masses and processes occupying space in the upper pelvis.

Fig. 3.4. Doppler techniques. Colour Doppler sagittal scan of the uterus, periovulatory phase (a). Pulsed Doppler scans of the intramyometrial uterine arteries ((b), transverse plane of the uterine corpus) and venules ((c), sagittal plane) and of the intraovarian arterial branches (d). Note the higher velocities and arterial resistance for the uterine branches (a) compared with the intraparenchymal ovarian branches (d).

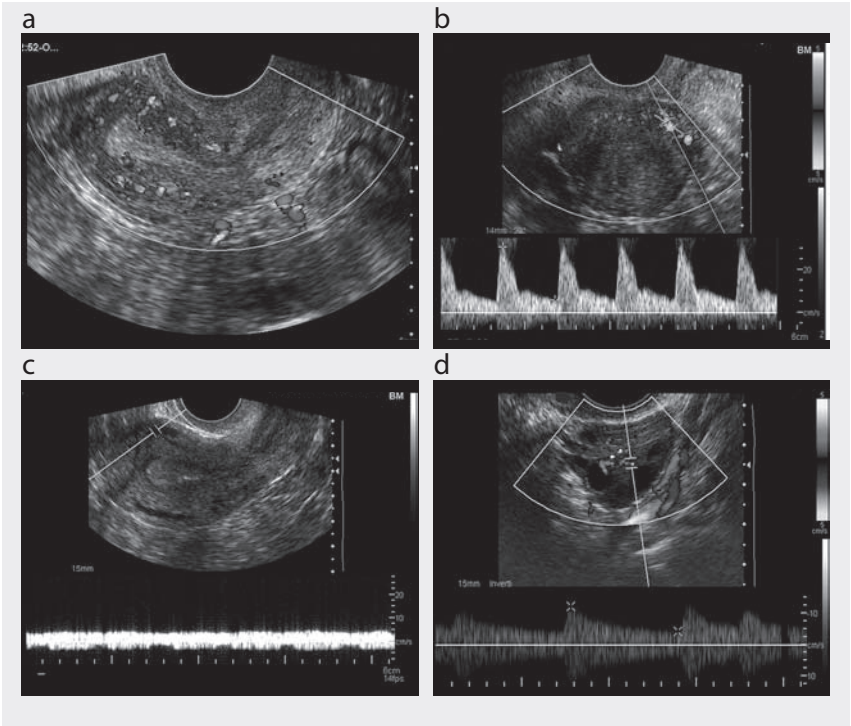

Normal findings

Uterus

Anatomy and measurements

The uterus is located in the middle pelvis, in the space between the bladder and the rectum. It is situated medially to the Fallopian tubes, over the vagina and below the bowel loops. It is cone-shaped, with the base at the top and the apex sunk in the vagina. A circular narrowing in its inferior portion divides the uterus into two: the superior part is the uterine corpus and the inferior one is the uterine cervix, which

is shorter and cylindrical. The boundary between the corpus and the cervix is called the isthmus, which is very marked in female children, decreases in prepuberal girls and almost disappears in pluriparous women.

The superior extremity, called the fundus, is the widest part of the uterus. It has a concave profile at paediatric ages, is straight in nulliparous women and is convex in pluriparous women. Laterally, it forms two angles from which the Fallopian tubes originate. The uterus measures 6–7 cm in length, 4 cm in width and 3 cm in thickness; these dimensions increase by 1–2 cm in pluriparous women. The dimensions of the uterine corpus and cervix change with age (Table 3.1). In children, the uterine cervix is more prominent than the corpus, representing about three fifths of the total uterine length. At puberty, the uterine corpus becomes larger and longer; and in adult women it is longer than the cervix. In pluriparous women, the corpus is even larger, and its length represents about three fifths of the total. After menopause, the uterus becomes atrophic, with maximum volumetric reduction in the first 10 years.

Table 3.1. Uterine diameters at different ages

Age	Length (cm)	Width (cm)	Thickness (cm)	Volume (ml)
Prepuberty	1–3	0.5–1.0	0.5–1.0	10–20
Pluriparous women	8	4	5	60–80
Nulliparous women	6–8	3–4	3–4	30–40
Postmenopausal women	4–6	2–3	2–3	14–17

When the bladder is empty, the uterus and vagina are oriented at an angle of about 90° (version angle); the uterine corpus is flexed towards the cervix at a variable angle of 140–170° (flexion angle), as seen by transvaginal scanning. When the bladder is filled (an indispensable condition for a transabdominal ultrasound scan), the uterus is pushed back, and the version and flexion angles increase (Fig. 3.5). In many women, the uterus tilts to the right or left but usually the right.

Fig. 3.5. (a) Anteverted uterus (cursors: endometrium). (b) Retroflexed uterus (cursors: endometrium). (c) Retroverted uterus

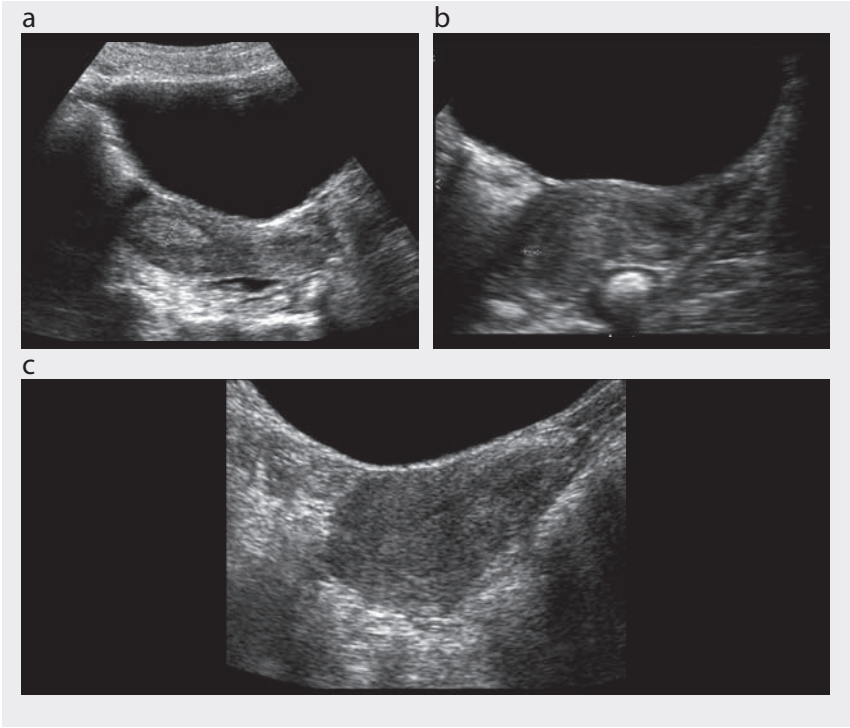

Structural features

The uterus is composed of three superimposed layers: the peritoneal serosa, the muscular layer, called the myometrium, which represents almost the entire uterine wall, and the mucosal layer, or endometrium.

The **myometrium** is composed of three layers, which can be distinguished by ultrasound:

- external, somewhat less echogenic than the intermediate layer, from which it is separated by arcuate vessels;
- intermediate, the thickest layer, with a homogeneous echo pattern and low-to-moderate echogenicity;
- internal, compact and hypovascular, hypoechoic and surrounds the relatively echoic endometrium (subendometrial halo).

Altogether, the uterus has an intermediate homogeneous echo pattern; in some cases, small ectatic vessels are visible in the most external myometrium. In older women, minute hyperechoic spots with a circumferential disposition are sometimes identifiable, representing parietal arteriolar calcifications. Within the uterine cervix,

small anechoic sub-centimetric formations, called Naboth cysts, can often be seen, which are due to occlusion and stretching of cervical glands by their secretion.

The **endometrium** looks like a central line with varied echogenicity and appearance, depending on the phase of the menstrual cycle (Table 3.2). The endometrium undergoes large changes in thickness and echogenicity due to the serum levels of estrogen and progesterone, which are detectable on either transabdominal or transvaginal scanning, which is the best technique for studying the uterus and adnexa. The cervical canal appears as an echoic linear stripe, and its aspect and thickening do not undergo significant variation during the menstrual cycle.

Table 3.2. Endometrial thickness and ultrasound pattern

Menstrual phase	Hyperechoic, linear
Proliferative phase	Hypoechoic, 4–8 mm
Periovulatory phase	Three-layer stratified endometrium, 6–10 mm
Secretory phase	Hyperechoic, 7–14 mm
Postmenopause	Hyperechoic, thin < 5 mm
Postmenopause with hormonal therapy	Variable ultrasound patterns, thickness 4–8 mm

In the menstrual phase, the endometrium is extremely thin, formed from only the basal layer, and appears as a hyperechoic line, due to the interface between the anterior and posterior uterine walls. In the proliferative phase, the endometrium becomes progressively thicker and shows three concentric layers, consisting from the centre to the exterior of a central hyperechoic stripe due to the interface of the two endometrial surfaces, a hypoechoic intermediate layer due to the physiologically thickened functional stratum and an external echoic layer, which represents the basal stratum. Peripherally, there is a thin hypoechoic subendometrial halo, corresponding to the inner, less vascularized part of the myometrium. In the secretory phase, the endometrium appears homogeneously hyperechoic, because of vascular changes and glandular hyperplasia (Fig. 3.6).

The endometrial thickness is about 5 mm in the early proliferative phase and reaches 10–12 mm in the ovulatory phase. After menopause, the endometrium becomes atrophic and appears as a thin echoic stripe (maximum thickness, 3–4 mm) (Fig. 3.6). Only scant fluid is sometimes found within the uterine cavity, due to transitory staunching of secretion; it has no pathological significance. The endometrial thickness at menopause is used to classify benign and malignant diseases: a value of 5 mm is commonly accepted as the threshold, under which it is possible to exclude a tumoural pathology. For women of postmenopausal age who take hormonal therapy, varying patterns of endometrial thickening are seen, related to the type and phase of the hormonal treatment. In these women, an endometrial thickness > 5 mm is still acceptable.

Fig. 3.6. Changes in endometrial thickness with phases of the menstrual cycle and with age. (a) Early proliferative phase. (b) Late proliferative phase. (c) Secretory phase (cursors: endometrium). (d) Postmenopausal atrophic endometrium

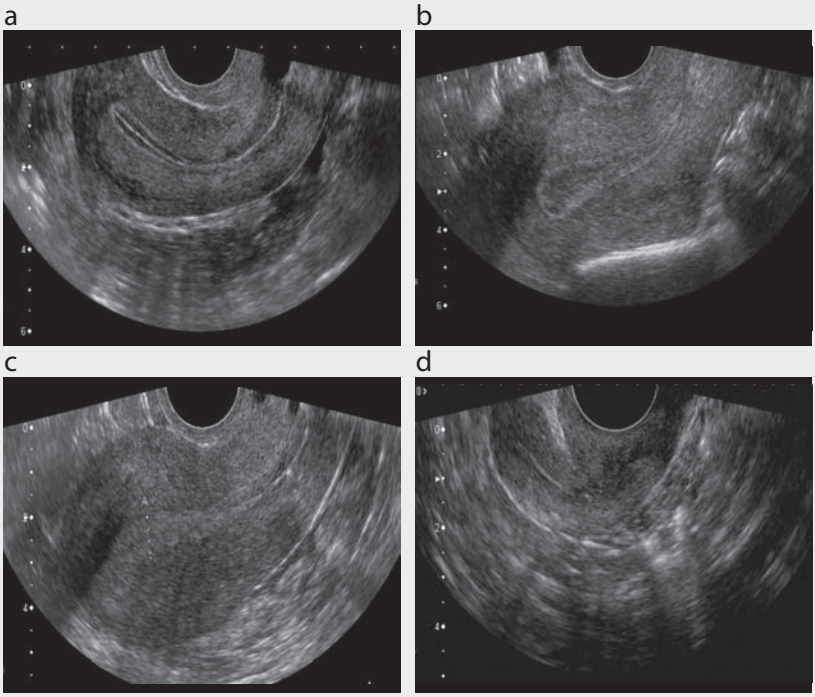

Ovaries

Anatomy and measurements

The ovaries are ellipsoid and are located in most cases in the superior-lateral part of the retrouterine hollow. The ovaries juxtapose the lateral walls of the pelvis in Waldeyer fossae, delimited in the back by epigastric vessels and the ureter, in the front by the insertion of the large ligament and in the upper part by the external iliac vessels. The position of the ovaries is, however, often asymmetric, and, in spite of numerous connective ligaments, they are very mobile.

The best, most careful dimensional evaluation of the ovary is by volume calculation, by applying the ellipsoid formula: length × width × thickness / 2. The ovarian volume is relatively stable until 5 years of age, when progressive proportional growth is seen. In adult women, the ovary generally measures 3 × 2 × 1 cm. The ovarian volume varies from 2–3 ml in children to 4–5 ml in adolescents and 6–8 ml in adults. At menopause, the mean volume is reduced to about 3.7 ml, and the ovaries are difficult to see, even on transvaginal examination.

Structural features

The ovary has two morphologically and structurally defined areas: the medulla, which spreads from the hilum to the centre, and the cortex, which surrounds the medulla. The medulla is made up of vessels in connective and muscular tissue; sonographically, it is somewhat more echoic than the myometrium. The cortex contains the essential ovarian elements, the follicles, which differ in number and dimensions depending on the woman's age and the phase of the menstrual cycle. On ultrasound scanning, the follicles appear as roundish or oval anechoic structures, with well-defined borders. At paediatric ages, small follicles, measuring a few millimetres, can already be seen.

In adult women, the ovary is an extremely dynamic structure, and its ultrasound pattern varies according to the phase of the cycle. In the estrogenic phase, some follicles begin to develop (Fig. 3.7), but only one will mature completely (the dominant follicle). This follicle (Fig. 3.8) grows linearly, from the 5th or 6th day until ovulation, at a mean growth of 2–3 mm a day.

Fig. 3.7. Multifollicular ovary

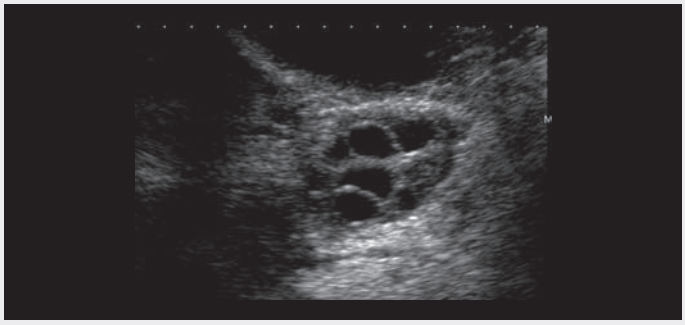

Fig. 3.8. Dominant follicle. Transvaginal scan of the ovary at day 13 of the menstrual cycle shows the dominant follicle as a rounded echo-free structure (about 15 mm in size).

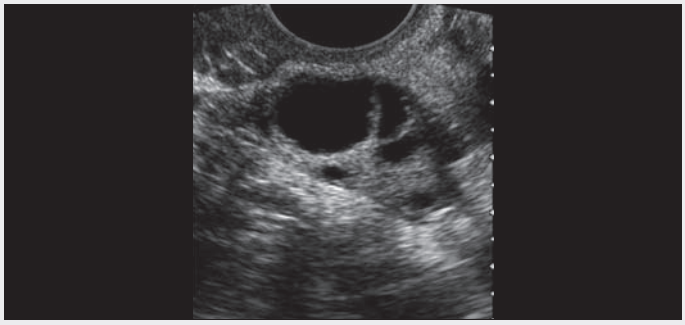

The mean diameter of the dominant follicle at ovulation is 20 mm, with a range of 17–26 mm; this wide range limits the use of follicular diameter as a predictor of ovulation. After the follicle bursts and releases the oocyte, the residual cavity becomes virtual and partially occupied by haematic material, which is then replaced by proliferating thecal cells, thus forming the corpus luteum. The ultrasound morphology of the corpus luteum is variable; typically, it appears as a small cystic formation, with irregular borders and internal echoes due to its haematic contents, often with prominent peripheral vascular signals and typical low-resistance flow (Fig. 3.9). In some cases, the follicle collapses and the corpus luteum is not identifiable. In other cases, a larger, sometimes haemorrhagic luteal cyst forms but tends to resolve in subsequent cycles.

Fig. 3.9. Corpus luteum. Transvaginal scans show an inhomogeneous area within the left ovary (a), with peripheral vascular signals on power Doppler (b) and low-resistance flow on pulsed Doppler (c)

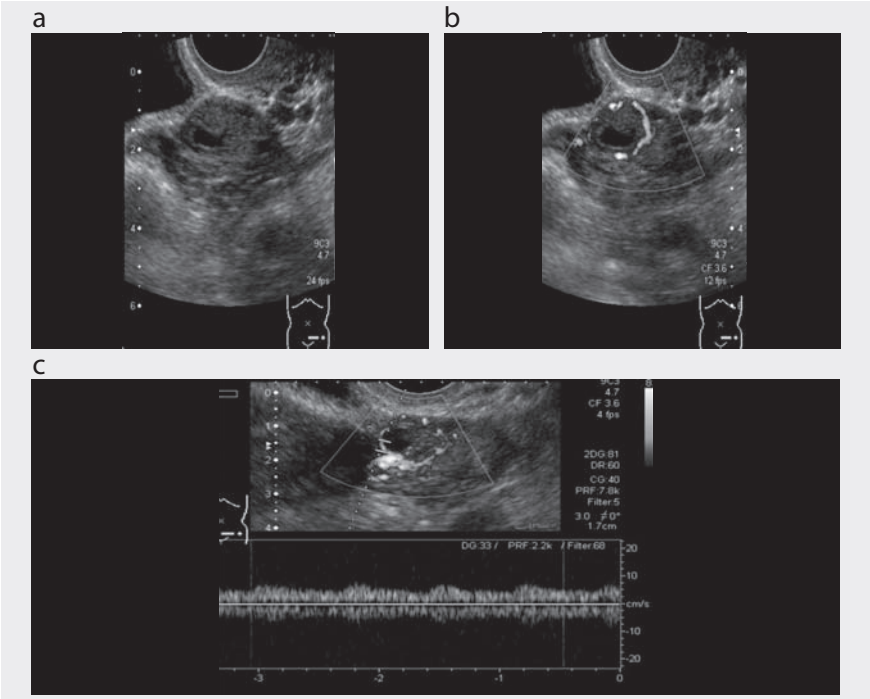

The ovarian structure and modification of the follicles during the menstrual cycle can be seen better with transvaginal transducers, although they can also be identified by transabdominal scanning. Appraisal of modifications of ovarian structure and follicles during the menstrual cycle is an integral part of gynaecological echographic examinations, because they give useful functional information.

During menopause, the follicles are no longer identifiable and the ovaries show a hypoechoic, uniform structure sonographically (Fig. 3.10); in 14.8% of cases, benign, simple cysts (< 5 cm) can be seen.

Fig. 3.10. Postmenopausal ovaries (between calipers). RT ov, right ovary; EIV, external iliac vein; LT ov, left ovary

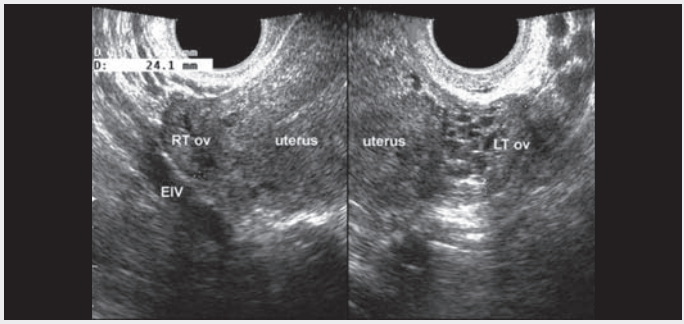

Ovarian dysfunction: polycystic ovary syndrome

Polycystic ovary syndrome is the commonest endocrine disorder in women of reproductive age. There is no internationally accepted definition of this syndrome, and the criteria for its diagnosis have yet to be standardized. The symptoms are heterogeneous and highly variable. In its classic form, polycystic ovary syndrome is characterized by chronic anovulation, irregular menses and hyperandrogenism, which may be associated with hirsutism, acne, seborrhoea and obesity. Polycystic ovary syndrome is considered to be present when at least two of the following are present:

- oligo-amenorrhoea or anovulation;
- clinical or biochemical signs of hyperandrogenism, in particular a ratio of luteinizing hormone: follicle-stimulating hormone > 2.5, increased levels of testosterone or an elevated free androgen index;
- sonographic evidence of polycystic ovaries.

Pelvic ultrasound can make a valuable contribution to the diagnosis of polycystic ovary syndrome, but it must be supplemented with a careful history and laboratory work-up. The ultrasound features of a polycystic ovary are (Fig. 3.11):

- multiple (≥ 8), small (mean diameter, 2–8 mm) follicles within the ovarian cortex;
- increased stromal density in the central cortex;

- increased ovarian volume (≥ 10 ml), calculated according to the formula: $\pi / 6 \times A \times B \times C$), where A, B and C represent the longitudinal, anteroposterior and transverse diameters of the ovary, respectively.

Fig. 3.11. Micropolycystic ovary, with increased stroma and microfollicles

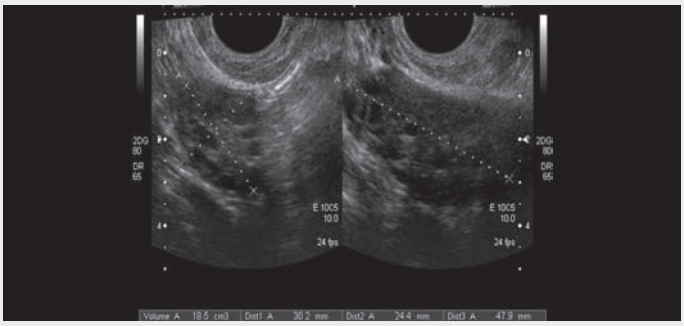

Abnormal ultrasound findings are generally present in both ovaries. Recent reports suggest that the transvaginal approach is preferable to the transabdominal, when possible.

A differential diagnosis of polycystic ovary syndrome includes multifollicular ovaries, which are associated with the presence of normal or mildly enlarged ovaries containing multiple follicles (Fig. 3.6). The follicles are distributed throughout the ovarian section and are often larger than those in polycystic ovary syndrome. Unlike polycystic ovary syndrome, multifollicular ovaries are not associated with accentuation of the stromal component.

Addition of colour Doppler greatly improves the diagnostic efficacy of transvaginal ultrasound, as it provides morphological and pathophysiological data on the flow dynamics in ovarian and pelvic vessels. In polycystic ovary syndrome, the pulsatility index of the uterine arteries is increased and vascularization is reduced, with a decrease in the resistivity index of the intraovarian arterioles, indicative of enhanced stromal vascularization.

Encouraging results have been obtained with three-dimensional transvaginal ultrasound, which provides more reliable estimates of organ volumes and blood flow and, most importantly, leads to standardization of ultrasound examinations. Introduction of this advanced technique has improved the precision and reproducibility of ovarian measurements. The stromal volume can be calculated as the difference between the total ovarian volume and the total follicle volume. This approach also allows quantitative assessment of the ovarian vasculature by quantification of Doppler signals.

Uterine disorders

Congenital abnormalities

Congenital uterine abnormalities due to developmental defects of the Müllerian ducts are clinically important because they are associated with higher rates of spontaneous abortion, premature birth and abnormal fetal position at delivery. Estimates of their frequency vary widely, but the overall data indicate a prevalence of about 1% in the general population and > 3% in women with recurrent pregnancy loss. As the urinary and genital systems arise from common embryonic structures, abnormal differentiation of the uterovaginal canal is frequently associated with renal anomalies (e.g. unilateral renal agenesis and crossed renal ectopy). The ovaries develop separately and are therefore not usually involved.

The most widely accepted classification (American Fertility Society, 1988) separates Müllerian duct anomalies into classes with similar clinical features, but complex and associated obstructive anomalies may also occur. Incomplete or absent fusion and resorption of the Müllerian ducts result in a didelphys, bicornuate or septate uterus. **Septate uterus** is the commonest Müllerian duct anomaly (approximately 55%) and is associated with the highest rate of recurrent spontaneous abortions. On ultrasound, the external configuration of the uterus is almost normal, but the endometrial stripe near the fundus is partially split into two symmetrical endometrial complexes by a septum isoechoic to the myometrium; the longitudinal extension and degree of vascularity of the septum can be assessed by ultrasound (Fig. 3.12). In the **bicornuate uterus**, there is incomplete fusion at the level of the fundus, with an intervening fundal cleft of variable length; two divergent uterine horns are fused caudally, with two endometrial cavities communicating inferiorly or two separate endometrial cavities and cervical canals. In **uterus didelphys**, two separate, divergent uteri can be seen, each with its endometrial cavity and cervix. There is only partial fusion at the level of the cervices and no communication between the two endometrial cavities.

Abnormal development of the Müllerian ducts before fusion results in **agenesis** or **hypoplasia** of the uterus and vagina**,** such as in Mayer-Rokitansky-Küster-Hauser syndrome (vaginal agenesis associated with uterine agenesis or an obstructed or rudimentary uterus)**.** A **unicornuate uterus** results when only one Müllerian duct develops normally (approximately 20%).

The features of different Müllerian duct anomalies may be further complicated by obstruction due to vaginal agenesis or transverse vaginal septa. If functional endometrial tissue is present, the condition may be suspected at menarche, with cyclic pelvic pain and a pelvic mass due to progressive accumulation of menstrual blood with or without primary amenorrhoea, depending on whether there are concurrent duplicate anomalies. On ultrasound the vagina and the endometrial cavity are distended by fluid and usually appear as a cystic mass; the contents may be hypoechoic, the low-level echoes being due to retained menstrual blood (haematocolpos or haematometrocolpos), or anechoic, due to mucous secretions in neonates (hydrocolpos or hydrometrocolpos) (Fig. 3.13).

Fig. 3.12. Septate uterus. Transverse transvaginal scan in the progestin phase of the menstrual cycle demonstrates a hypoechoic septum separating two paired echogenic endometrial stripes (EN)

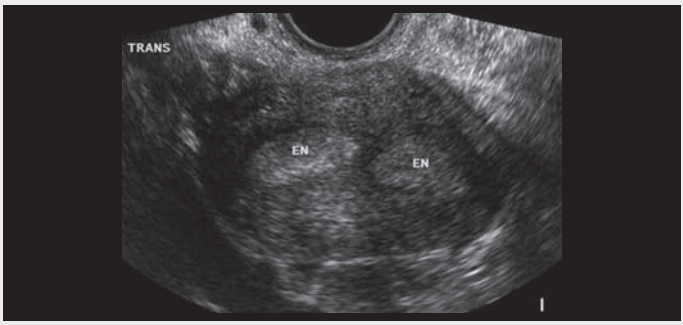

Fig. 3.13. Hydrometrocolpos in a neonate due to a vaginal septum; sagittal scan with a high-resolution 7.5-MHz linear probe. The vagina (VA) and to a lesser extent the uterine cavity (on the left of the image) are filled with anechoic fluid; some corpusculated material (S) is seen along the posterior vaginal wall

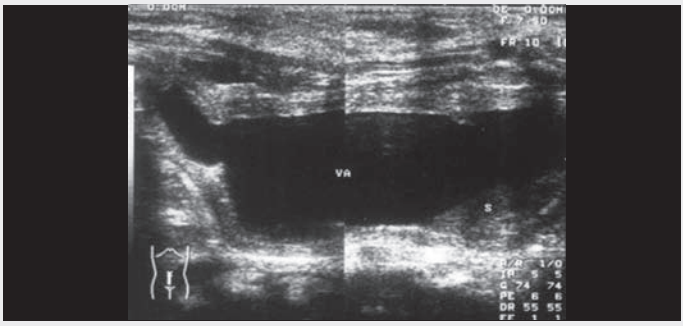

In order to evaluate congenital anomalies, the ultrasound examination should be performed during the secretory phase of the menstrual cycle (Fig. 3.12), as the echogenic endometrium is more easily recognized at this time. The purpose of the ultrasound examination should be to evaluate the morphology not only of the uterine cavity but of the external fundal contour (convex, flat, with an indentation or cleft). This information is crucial, as therapeutic modalities vary widely depending on the underlying anomaly. Three-dimensional ultrasound, which allows coronal reconstruction and better delineation of the external contour and volume of the uterus, is the most effective for demonstrating such anomalies, with higher sensitivity and specificity than conventional ultrasound. In complex anomalies, however, ultrasound may not allow adequate analysis of the uterovaginal anatomy. Magnetic resonance

imaging (MRI), although more expensive than ultrasound, is reported to be the most accurate for evaluating Müllerian duct anomalies. When uterine anomalies are detected, the ultrasound examination should be extended to the kidneys because of the frequent association with renal anomalies (reported in up to 31% of cases).

Benign endometrial disease

In diagnostic work-up of endometrial disease, the examiner must remember that the appearance of the endometrium is determined by many factors (the woman's age, the phase of the menstrual cycle, hormonal replacement or tamoxifen therapy), all of which must be taken into account with the clinical history and the findings of the physical examination. The main ultrasound sign of disease is increased endometrial thickness that is not consistent with age or menstrual phase. Increased thickness is, however, a nonspecific finding, which can be seen in several benign and malignant conditions. In order to make a correct diagnosis, the ultrasound evaluation must therefore include other features, such as echo texture, the endometrial–myometrial interface and the degree of vascular signals. Sonohysterography, in which the endometrial cavity is distended with saline, reliably distinguishes focal from diffuse abnormalities and characterization of most endometrial lesions.

Endometritis

Endometritis is often an early stage of pelvic inflammatory disease (when infection from the lower genital tract extends upwards to the Fallopian tubes and peritoneal cavity), or it may follow puerperal or post-abortion complications or insults due to instrumentation or intrauterine contraceptive devices. The endometrium may appear almost normal in mild cases, diffusely hypoechoic or thickened and heterogeneous. Prominent vessels may be seen within the myometrium, secondary to hyperaemia. Scant intracavitary collections of fluid may simulate an intrauterine abortion or a pseudogestational sac; larger echogenic fluid collections are a sign of more severe disease (pyometra, abscess). Intrauterine air pockets (due to gas-producing bacteria) are a more specific but rare sign of infection (Fig. 3.14). In genital tuberculosis, the endometrium is affected in 60–90% of cases, and the uterus may be enlarged due to filling and expansion of the endometrial cavity by caseous material.

Fig. 3.14. Endometritis. In the transabdominal sagittal scan, the central portion of the uterus is filled with bright echoes and dirty shadowing, consistent with gas in the uterine cavity

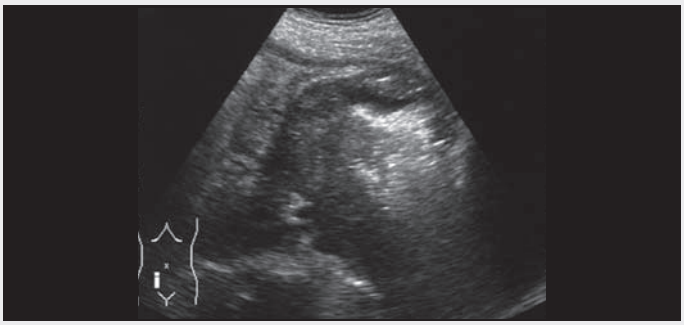

Endometrial hyperplasia

Diffuse proliferation of endometrial stroma and glands is defined as hyperplasia. It is prevalent in women around menopause and in conditions of unbalanced estrogenic stimulation. Because of the increase in glandular mass, hyperplasia is most often seen as a diffuse, smooth thickening of the whole endometrium (Fig. 3.15), similar to that seen during the secretory phase. The endometrial thickness must thus always be compared with normal values and the appearance expected for the menstrual phase or age of the woman. Smaller sonolucent areas in the thickened endometrium, or focal thickening, although less common, are occasionally seen.

Fig. 3.15. Endometrial hyperplasia. Sagittal transvaginal scan in a postmenopausal woman reveals a diffusely thickened endometrium, which is symmetrical and homogeneous. The separation between the endometrium and myometrium is clear

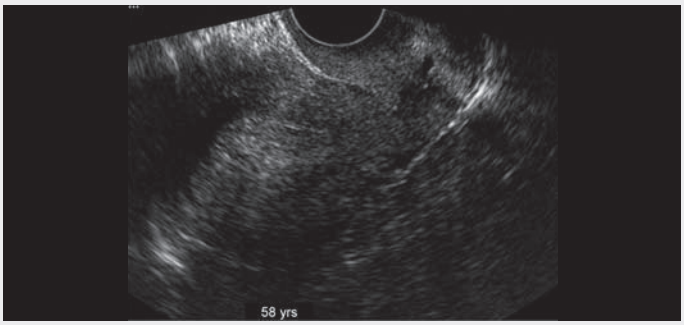

The separation between the endometrium and myometrium is always present. An endometrium with an inhomogeneous texture is probably due to other abnormalities (large polyps, submucosal fibroids, cancer) and is best assessed by sonohysterography or biopsy if there is a clinical suspicion of malignancy.

Endometrial polyps

Endometrial polyps are a common cause of abnormal vaginal bleeding, although they may be asymptomatic and found incidentally. They are most frequent in perimenopausal women or in women receiving tamoxifen as adjunct therapy for breast cancer. Most polyps are echogenic and are therefore best identified during the estrogenic phase of the menstrual cycle, appearing as small, well-defined, homogeneous lesions surrounded by the hypoechoic proliferative endometrium (Fig. 3.16). Polyps may also be isoechoic and blend into the surrounding endometrium, resulting in nonspecific endometrial thickening with preservation of the endometrial–myometrial interface. Larger or complicated polyps (due to haemorrhage, infarction or inflammation) may be more heterogeneous or show tiny cystic spaces (Fig. 3.17).

Colour Doppler can usually demonstrate the feeding vessels in the stalk of the polyp, thus helping to differentiate polyps from hyperplasia (Fig. 3.18). Sonohysterography allows easy, reliable diagnosis of polyps, as they appear as smooth or irregular, broad-based or pedunculated masses, well outlined by the saline solution instilled in the uterine cavity.

Fig. 3.16. Endometrial polyps in a premenopausal asymptomatic woman. Transvaginal sagittal scan of the uterus in the estrogenic phase of the menstrual cycle shows two smooth rounded masses, slightly echogenic compared with the surrounding hypoechoic proliferative endometrium

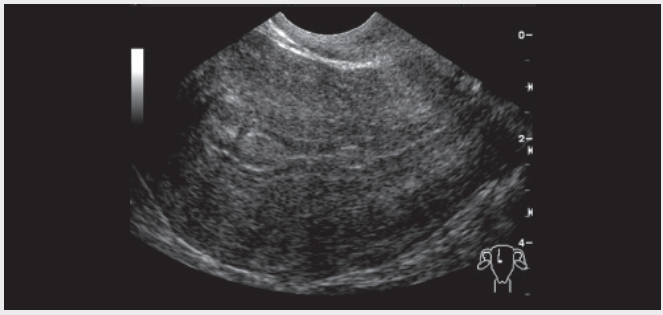

Fig. 3.17. Endometrial polyp and calcified fibroids in a postmenopausal woman. Transverse transvaginal scan shows two hyperechoic irregular masses with acoustic shadowing, due to calcified fibroids in a subserosal location along the right and posterior uterine walls. The uterine cavity is entirely occupied by an endoluminal mass, echogenic with large cystic spaces, consistent with an endometrial polyp

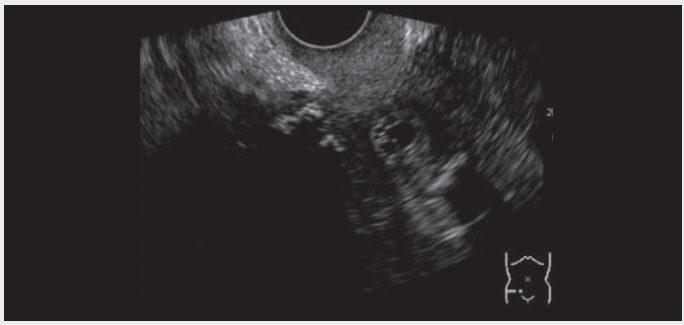

Fig. 3.18. Endometrial polyp. Transvaginal sagittal scans of a retroverted uterus in the periovulatory phase show a slightly hyperechoic lesion embedded posteriorly within the endometrial layer (a). A power Doppler image (b) shows the vascular pedicle at the base of the attachment of the polyp and the remaining hypovascular endometrium

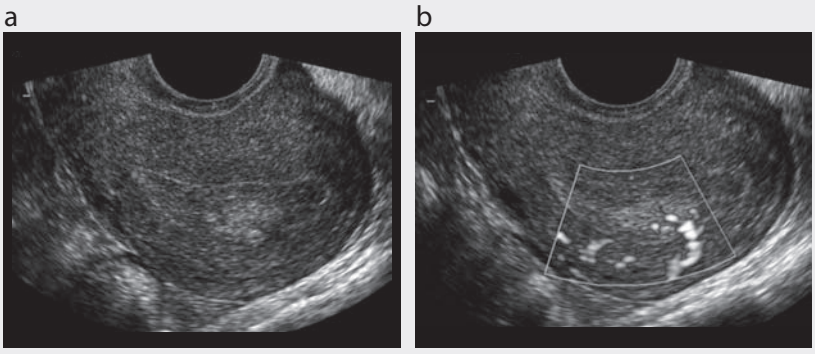

Tamoxifen therapy, intrauterine fluid collections and adhesions

Tamoxifen, widely used in former years as adjunct therapy in breast cancer patients, has a weak estrogenic effect on the endometrium, increasing the prevalence of endometrial hyperplasia, polyps and carcinoma. In women under tamoxifen therapy, the endometrium may appear thickened and irregular and show multiple cystic spaces (so-called cystic atrophy) in a subendometrial location, as shown by sonohysterography.

During the menstrual phase and in postmenopausal women, the finding of scant fluid within the uterine cavity is not rare and may be considered normal. Larger fluid collections are abnormal, as they are often associated with uterine malignancies. Congenital obstructive malformations of the uterus and vagina (such as cervical atresia, vaginal septa and imperforate hymen) in prepubertal children and even in neonates may lead to the accumulation of large fluid volumes within the endometrial canal or the vagina (hydro- or haematometrocolpos) (Fig. 3.13). The fluid accumulated within the uterine cavity may be echo-free (mucin) or hypo- to hyperechoic (serum or blood).

Endometrial adhesions, or synechiae, may develop as a result of endometrial injury (due to dilatation and curettage, caesarean delivery, evacuation of a hydatidiform mole or pelvic tuberculosis) and may be associated with infertility, recurrent pregnancy loss or amenorrhoea. Ultrasound examination requires fluid distension of the endometrial cavity by means of sonohysterography, which can demonstrate adhesions as echogenic bands crossing the uterine cavity; they may be mobile and thin, thick and broad-based or, occasionally, completely obliterating the endometrial cavity.

Benign myometrial disease

Fibroids

Uterine leiomyomas (also referred to as myomas or fibroids) are common benign soft-tissue tumours, frequently multiple, composed of smooth muscle and connective tissue, affecting nearly one fourth of women of reproductive age. Depending on their size and location, the symptoms include abnormal uterine bleeding, dysmenorrhoea, mass effect (bladder and rectal pressure) and pelvic and back pain. Owing to their estrogen sensitivity, fibroids tend to increase in size and number with age up to menopause, sometimes with periods of growth acceleration (e.g. in early pregnancy) or, conversely, involution (in menopause or puerperium) and may therefore undergo necrosis and degenerative changes (haemorrhage, infarction, calcification, fatty degeneration). They commonly appear as rounded, hypoechoic, solid masses, but may be heterogeneous or also hyperechoic, and show acoustic shadowing (due to calcifications) or cystic areas (Fig. 3.17, Fig. 3.19, Fig. 3.20, Fig. 3.21). Transvaginal examination may show whorls, with multiple discrete shadows originating from within the mass (recurrent shadowing), and this typical pattern can be useful in cases of diagnostic ambiguity (Fig. 3.19, Fig. 3.22). Colour Doppler can show the peripheral blood supply of fibroids, the vessels mainly coursing around the fibroid with scant central flow (Fig. 3.22). In large fibroids with necrotic or degenerative changes, increased blood flow and an inhomogeneous texture may even mimic uterine sarcomas, on both grey-scale and colour Doppler.

Depending on their location, fibroids are referred to as **intramural** when located within the myometrium (Fig. 3.21), **subserosal** when they are external and distort the uterine contour (Fig. 3.19), **submucosal** when they distort or extend into the endometrial cavity (Fig. 3.20) or **pedunculated** in a serosal or submucous location. Exophytic pedunculated fibroids can be misdiagnosed as they can mimic adnexal and other pelvic disorders. Submucosal fibroids may distort the uterine cavity or be almost entirely endoluminal. The degree of protrusion of the fibroid into the endometrial cavity is important information for surgical management and is best determined by sonohysterography.

Fig. 3.19. Fibroids. Transabdominal (a) and transvaginal (b) sagittal scans in a premenopausal woman show increased volume of the uterus and irregular appearance of its external configuration due to multiple hypo- and isoechoic fibroids, some with acoustic shadowing. Because of impaired transmission and poor visualization of endometrial echoes, the exact number, size and location of fibroids are difficult to determine accurately

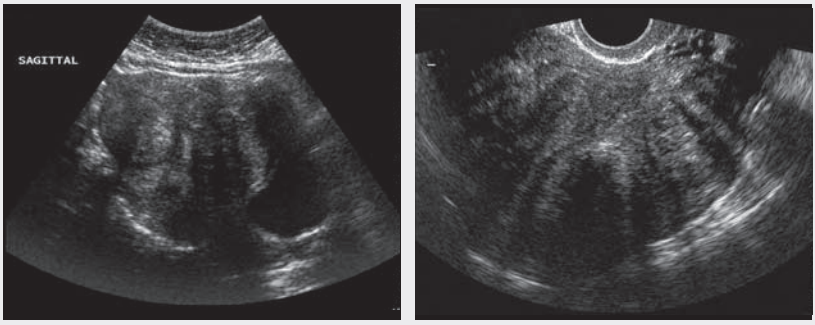

Fig. 3.20. Submucosal fibroid. Axial transvaginal sonogram shows a hyperechoic inhomogeneous fibroid (cursors) with minimal distortion on the overlying endometrium

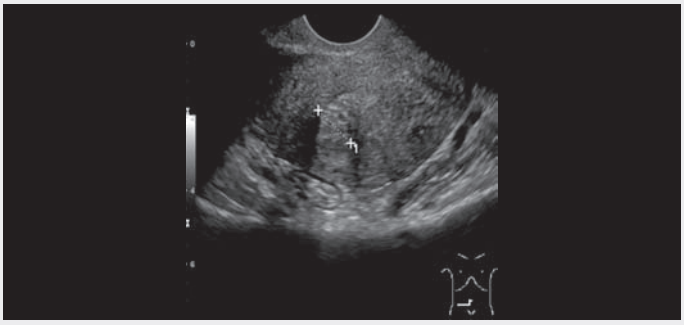

Fig. 3.21. Intramural fibroid, menstrual phase: transverse transvaginal sonogram shows a rounded isoechoic fibroid (cursors) and scant fluid within the endometrial cavity

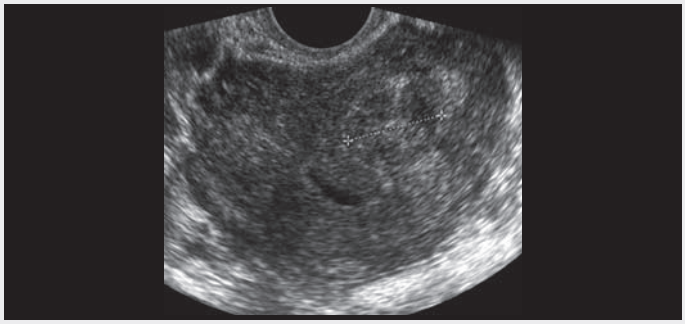

Fig. 3.22. Intramural submucosal fibroid. (a) Axial transvaginal sonogram shows a hypo-isoechoic fibroid (cursors) distorting the endometrial stripe, with recurrent shadowing. (b) Power Doppler demonstrates vessels typically running peripheral to the fibroid

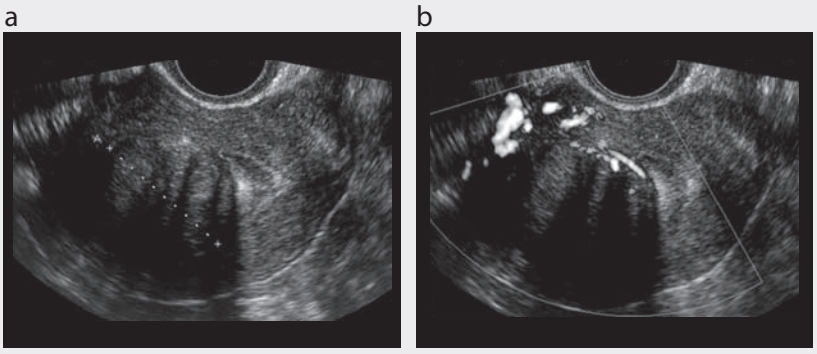

Although fibroids are usually easily identified and diagnosed by ultrasound, technical limitations may impair the examination. MRI can be helpful, as it allows accurate assessment of the total number and location of fibroids and the presence of concurrent adenomyosis or other uterine or ovarian disorders.

Adenomyosis

Uterine adenomyosis is defined as the presence of endometrial glands and stroma in the myometrium beneath the endometrial–myometrial junction, with accompanying smooth muscle hyperplasia. With diffuse involvement, the uterus is enlarged, with thickening and asymmetry of the walls, pseudo-widening of the endometrium, poor definition or shaggy appearance of the endo–myometrial junction and small

cyst-like areas of fluid (usually < 5 mm) within the myometrium (Fig. 3.23). With focal involvement, the myometrium is thickened and heterogeneous, with echogenic linear striations, poorly defined echogenic nodules or circumscribed hypoechoic nodules resembling a fibroid but with ill-defined margins and minimal mass effect. In contrast to fibroids, the adenomyosis nodules have blood flow (raindrop appearance).

Notwithstanding these many signs, the ultrasound detection of adenomyosis, and especially differential diagnosis from fibroids, can be difficult, so that this condition is frequently overlooked, especially when uterine fibroids coexist. As the therapeutic options differ, equivocal ultrasound findings (fibroids or adenomyosis) can be resolved by MRI to assess both adenomyosis and pelvic endometriosis with greater accuracy.

Fig. 3.23. Adenomyosis. Transvaginal transverse (a), (b) and sagittal (c) sonograms in different patients. (a) Diffusely heterogeneous myometrium and poorly defined endometrium, with a tiny cystic space posteriorly at the endo–myometrial junction. (b) Diffusely heterogeneous myometrium with multiple ill-defined and irregular hypoechoic areas scattered throughout the posterior uterine wall; note the enhanced transmission near the hyperechoic secretory endometrium. (c) Marked distortion of the endometrial stripe, with poor definition of the endo–myometrial junction anteriorly and tiny cystic spaces within the anterior myometrium

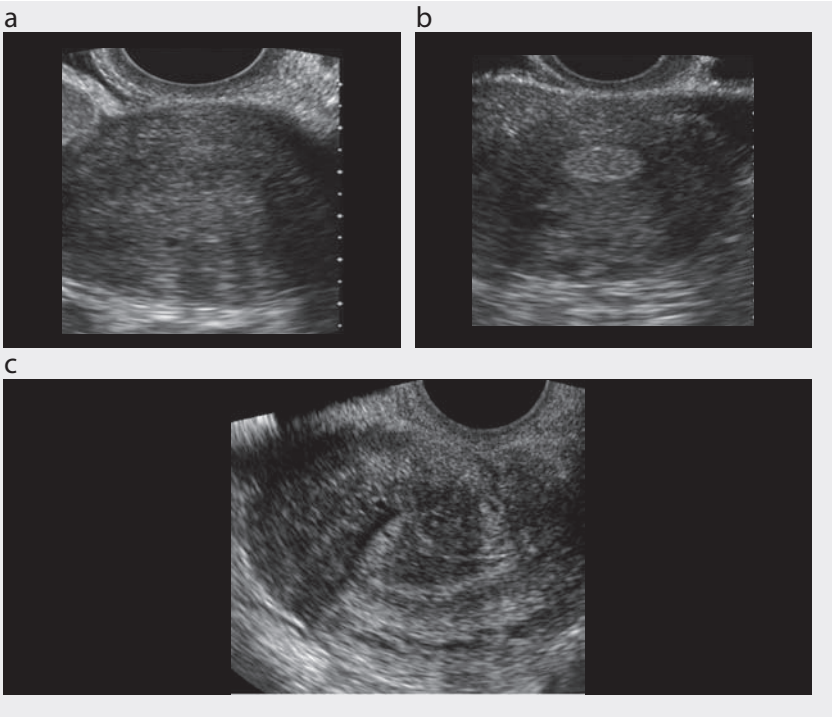

Neoplasms

Atypical vaginal bleeding (i.e. between menstrual cycles or in the postmenopausal period) is of great concern as it is the common presenting sign of endometrial and cervical cancers. Although the causes of bleeding are usually benign (postmenopausal atrophy, endometrial polyps and hyperplasia, submucosal fibroids), about 10% of all postmenopausal bleeding is due to endometrial carcinoma. In postmenopausal women, the ultrasound finding of an endometrium measuring ≤ 5 mm (double-layer thickness), which is smooth and homogeneous in the absence of any focal thickening, is consistent with atrophy and excludes any significant disease, such as endometrial cancer. The criteria may vary if the woman is receiving hormonal replacement therapy, as the expected thickness of the endometrium is increased. In the presence of postmenopausal bleeding, any abnormal increase in thickness or focal structural abnormality of the endometrium should be investigated further, possibly by sonohysterography or hysteroscopy, as blind endometrial sampling can yield false-negative results if the abnormality is focal and not sampled.

Endometrial carcinoma

Endometrial cancer is the commonest gynaecological malignancy (about 6% of all cancers in women). Abnormal or postmenopausal bleeding is the earliest, most frequent presenting symptom. The main ultrasound sign is nonspecific thickening of the endometrium, which is usually diffuse but can be polypoid in early cases. Endometrial tumours are usually more heterogeneous than hyperplasia or polyps and appear as a marked irregular or mass-like thickening, of varying echogenicity, and are often difficult to distinguish from the myometrium because of irregularity or focal effacement of the endometrial–myometrial border (Fig. 3.24, Fig. 3.25, Fig. 3.26). Corpusculated fluid may accumulate in the endometrial cavity due to cervical stenosis.

The tumour tissue may show abnormal flow signals on colour and power Doppler imaging, indicating high-velocity, low-resistance arterial flow (Fig. 3.24, Fig. 3.25, Fig. 3.26).

Treatment and prognosis are based mainly on tumour extent (depth of myometrial invasion, cervical and nodal involvement), as well as individual and histological factors. An indistinct or disrupted endometrial–myometrial interface is a sign of myometrial invasion. The depth of invasion (deepest point reached by the tumour inside the myometrium wall) is rated as superficial if only the inner half of the myometrium is involved or deep if it involves the outer half of the myometrium and beyond, also depending on whether the residual uterine wall is more or less than 1 cm (Fig. 3.24). Technical limitations (acoustic shadowing from fibroids, adenomyosis, uterine size, thinning of uterine walls due to distension from a clot, fluid or polypoid tumour) may reduce the accuracy of ultrasound.

Contrast-enhanced MRI is currently seen as the most reliable technique for evaluating myometrial invasion, with significantly better performance than non-enhanced MRI, ultrasound and CT. Cervical invasion is difficult to assess with

Fig. 3.24. Endometrial carcinoma. Transabdominal coronal (a) and sagittal (b) scans show a diffusely enlarged uterus and complete disruption of the endometrial–myometrial junction by irregular echogenic tissue, almost reaching the serosa posteriorly (b). (c) On Doppler examination, abnormal endometrial vessels and low-impedance arterial flow are seen

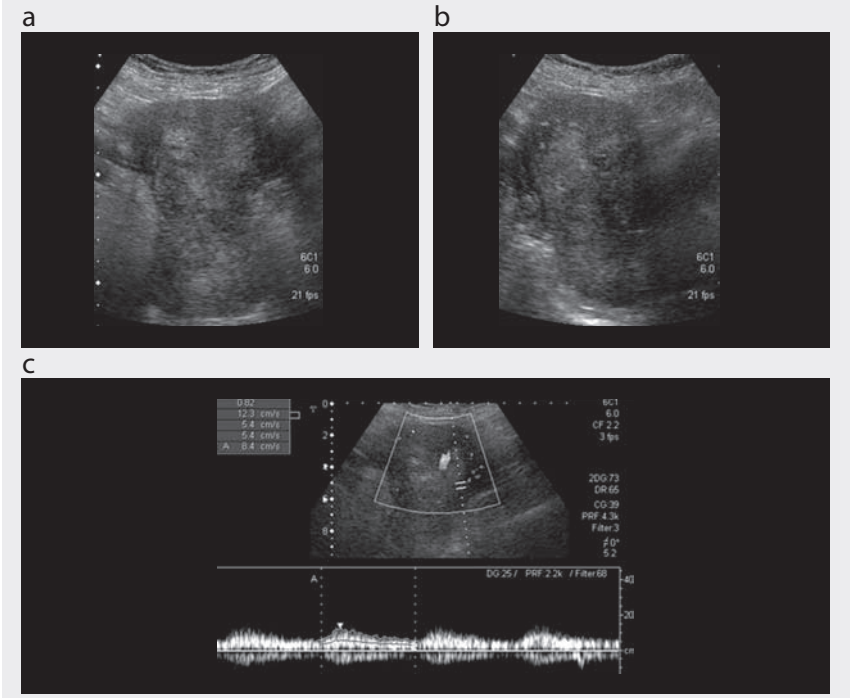

Fig. 3.25. Endometrial carcinoma in an 80-year-old woman. Transabdominal sagittal scans show (a) a markedly enlarged, hypoechoic endometrial stripe (cursors) and increased uterine size. On colour Doppler imaging (b), note increased blood flow and multiple vessels peripheral to and within the tumour

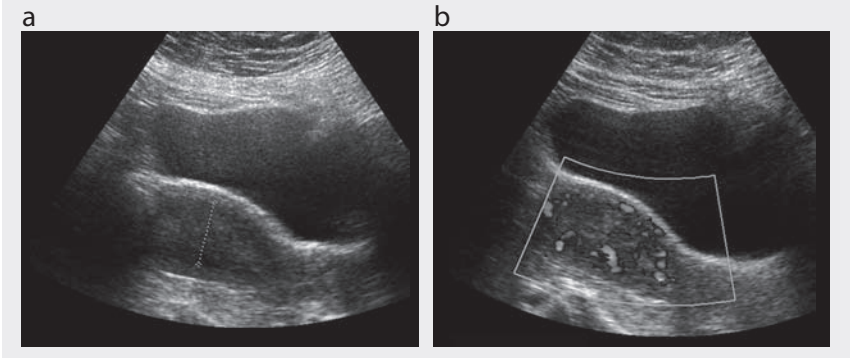

Fig. 3.26. Endometrial carcinoma. On transvaginal sagittal scans, the uterine cavity is largely filled by a large heterogeneous endometrial mass (a), with increased colour signals (b) and low-impedance intratumoral blood flow (c)

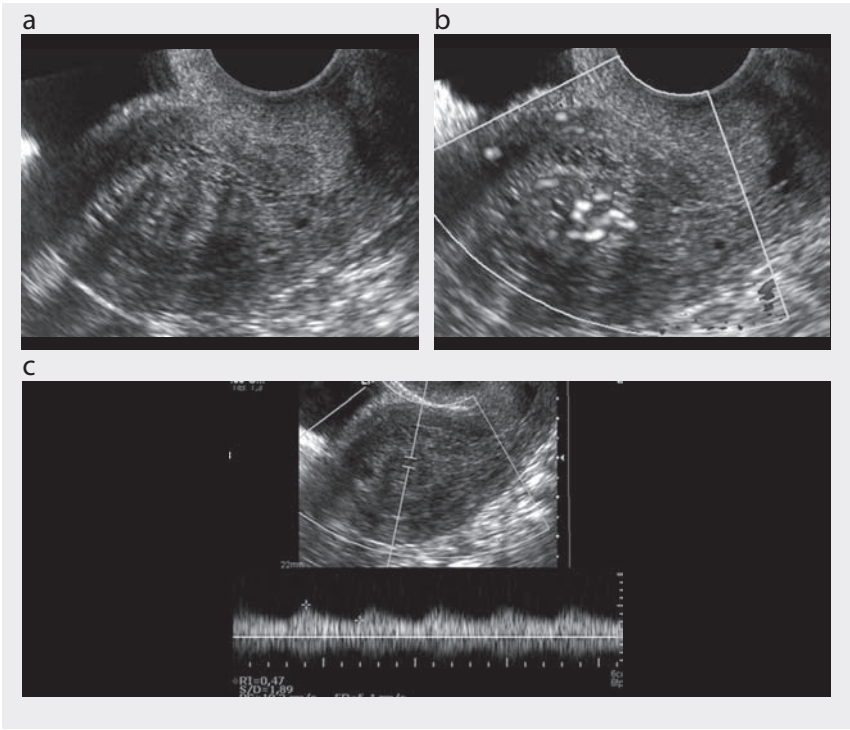

ultrasound or computed tomography, whereas it is accurately depicted by MRI. Para-aortic and pelvic lymphadenopathies are often not detected by sonography and are more reliably shown by MRI and CT.

The ultrasound features of endometrial cancer can be difficult to differentiate from endometrial hyperplasia and polyps. The thickness of the endometrium is often similar in benign and malignant conditions. Malignancy should be suspected in the presence of a very thick or irregular endometrial stripe or when the endometrial–myometrial interface is disrupted. Contrast-enhanced MRI is considered the most reliable technique for evaluating myometrial invasion.

Cervical carcinoma

Cervical carcinoma is the commonest gynaecological malignancy in premenopausal women, spreading by direct local invasion or through the lymphatic system. The most significant prognostic factors are tumour size and the status of the para-aortic lymph nodes; staging variables include extension into the vagina, parametria or pelvic walls, invasion of the bladder or rectum and spread to distant organs. In early

stages, the diagnosis is clinical rather than by imaging techniques, which are necessary for correct staging of more advanced tumours.

On transabdominal sonography, the cervix may be diffusely enlarged by a hypo- or isoechoic mass, and the uterine cavity may be distended by fluid and debris (haematometra). On transvaginal or transrectal sonography, the tumour may appear as a hypoechoic or isoechoic (relative to normal uterine muscle and the cervical stroma), poorly defined lesion within an enlarged cervix (Fig. 3.27, Fig. 3.28), asymmetrical and prolonging laterally when parametrial invasion occurs, or disrupting the vesical or rectal wall (Fig. 3.29, Fig. 3.30). Transvaginal or transrectal sonography can be used to evaluate the size of the cervix but not consistently the size of the tumour, because of poor discrimination between normal cervical stroma and tumour tissue.

Fig. 3.27. Cervical carcinoma, stage I. Transvaginal sagittal scan shows a superficial tumour of the cervix as an ill-defined, hypoechoic area (cursors) effacing the central linear echo of the cervical canal

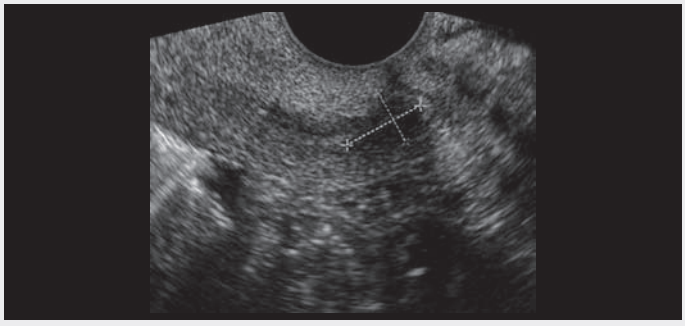

Fig. 3.28. Cervical carcinoma, stage II. Transrectal sagittal scan shows enlargement of the cervix (cursors) by the tumour, with effacement of the cervical canal

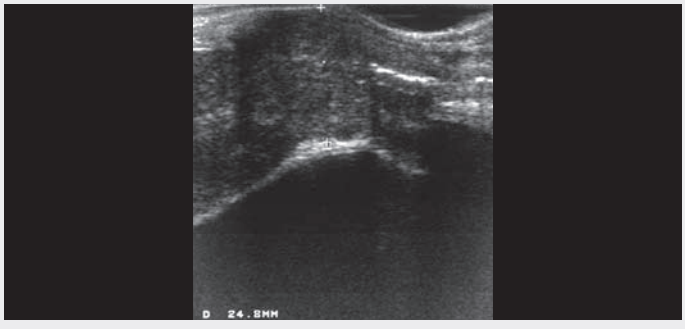

Myometrial and vaginal involvement can be detected, although not consistently, by an upwards extension of the cervical lesion or by irregular thickening of the anterior or posterior vaginal wall, respectively, continuous with the cervical lesion. Increased intratumoral blood flow may be found on colour Doppler in larger lesions; this finding appears to be related to the aggressiveness of the tumour and the likelihood of nodal invasion.

The limitations of transrectal and, to a lesser extent, transvaginal scans are that it is difficult to evaluate tumour extension to the pelvic wall or to scan large tumours when the leading edge of the tumour is beyond the range of the probe. Bladder and rectal invasion are accurately detected by transvaginal or transrectal sonography as the loss of intervening fat planes and by hypoechoic thickening and loss of the normal layered pattern of the vesical and rectal walls (Fig. 3.29, Fig. 3.30). Transabdominal sonography can readily detect obstruction of the urinary tract (due to parametrial invasion with ureteral obstruction), gross bladder invasion and liver metastases in advanced disease, but has a limited role in identifying enlarged pelvic or para-aortic lymph nodes, which are more reliably detected by CT and MRI. MRI appears to be the single most accurate technique for local staging of cervical carcinoma.

Sonography can be useful in local staging of cervical cancer, especially with a transvaginal or transrectal technique, but has limitations, especially in assessing lymph node involvement and extension to the pelvic walls. Accurate local staging is best accomplished with MRI, whereas both CT and MRI can be used to assess extrapelvic disease.

Fig. 3.29. Cervical carcinoma, stage IVa. Transabdominal sagittal and transverse scans show a bulky hypoechoic lesion replacing the uterine cervix and body, with associated fluid collection within the upper uterine cavity. The tumour mass disrupts the uterovesical septum and invades the bladder

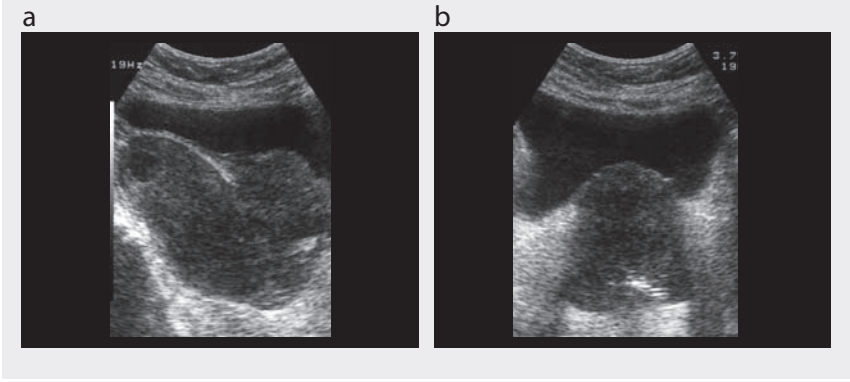

Fig. 3.30. Advanced cervical carcinoma, stage IVa. Transrectal sagittal scan shows an inhomogeneous and grossly enlarged cervix. Invasion of the rectal wall is shown by loss of the intervening fat plane between cervix and rectum. The adjacent bladder wall is focally disrupted by the tumour; hypoechoic material between the bladder wall and the vesical catheter represents tumour tissue and blood clots

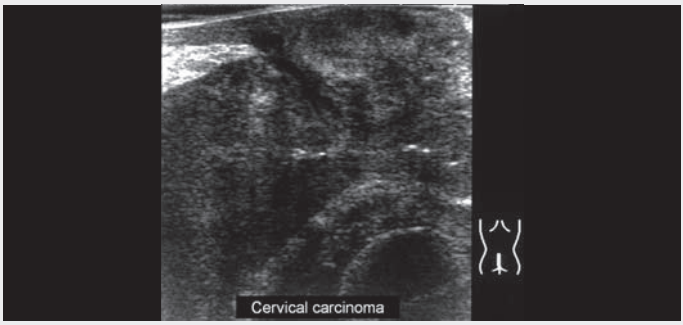

Sarcoma and chorioncarcinoma

Leiomyosarcoma is an aggressive tumour, often diagnosed only histologically after hysterectomy or clinically suspected by its rapid growth, metrorrhagia and pelvic pain. Although signs of necrosis and markedly increased intratumoral blood flow have been described on sonography and Doppler, leiomyosarcoma is difficult to distinguish from leiomyoma, unless its rapid growth raises clinical suspicion or there is evidence of local invasion or metastasis.

In **chorioncarcinoma** (gestational trophoblastic neoplasia), multiple hypoechoic areas surrounded by irregular echogenic areas and abundant intramyometrial vascularity with low resistance flow may be seen on grey-scale and colour Doppler sonography.

Recurrent disease

Local recurrence of gynaecological malignancies on the vaginal cuff or within the central pelvis is relatively frequent in women who have undergone radical hysterectomy. Larger recurrences can be detected even on transabdominal scans as space-occupying lesions, centrally located and continuous with the vaginal cuff. Transrectal and transvaginal sonography allow more detailed visualization of the vaginal cuff and central pelvis and are therefore useful for accurate detection or exclusion of tumour recurrence. Focal enlargement, structural abnormalities or true masses, usually with increased vascularity, can be seen in cases of early and more advanced recurrences (Fig. 3.31, Fig. 3.32); possible infiltration of the parametrial tissues or of the recto-vaginal or vesico-vaginal septa can also be assessed.

Fig. 3.31. Vaginal recurrence of endometrial carcinoma. (a) Transabdominal examination shows a solid mass continuous with the vagina. (b) Follow-up transrectal sagittal scan after radiotherapy shows a reduction in the size of the lesion (R); the recto-vaginal septum and rectal wall are normal. VA, vagina; BL, bladder

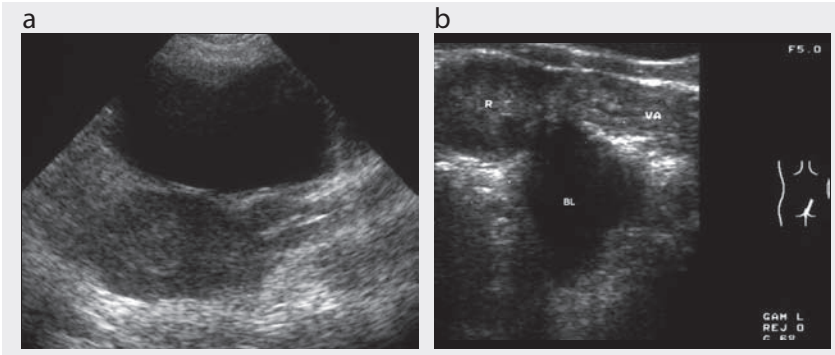

Fig. 3.32. Vaginal recurrence of cervical carcinoma. Transrectal sagittal scans ((a), along the right and (b), along the left aspect of the vagina) show a vaginal cuff of normal size; however, a small inhomogeneous hypoechoic area with irregular borders (cursors) is seen in its right portion, due to a small recurrence. Note normal rectal wall and recto-vaginal septum

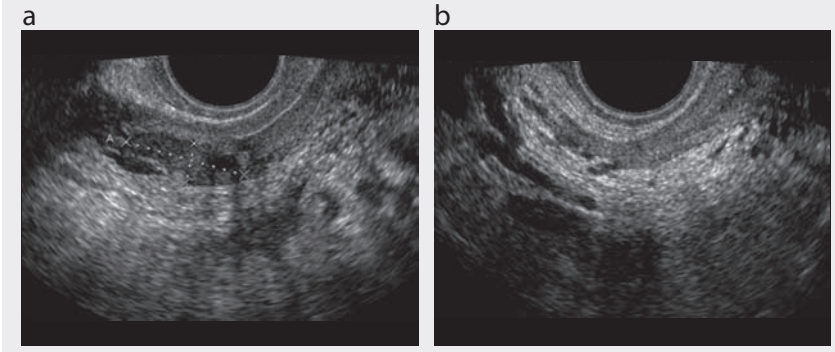

Adnexal lesions

Ovarian masses: the importance of ultrasound

Ultrasound examination is clearly the most informative means of studying ovarian neoformations, i.e. structures inconsistent with the normal physiology of this organ. These should be distinguished from the numerous functional formations detected in the ovarian parenchyma during the menstrual cycle, such as follicles, corpora lutea and luteal cysts, which are not classified as pathological formations.

Ultrasound allows analysis in vivo of all the characteristics evaluated by surgeons and anatomical pathologists. Both anatomical pathologists and ultrasound operators can suspect a diagnosis on the basis of the morphological characteristics of a lesion, such as its complexity, the presence of solid portions and irregularity. Ultrasound examination also allows evaluation of additional parameters, such as vascularization, the relation of the lesion to nearby organs and tenderness on pressure. These characteristics make ultrasound an accurate diagnostic tool for discriminating between malignant and benign ovarian masses and, in many cases, for making a specific diagnosis.

Classification systems

Differentiation of ovarian masses into benign and malignant masses is based on many morphological parameters. Transvaginal ultrasound investigation of any adnexal mass (or either transabdominal ultrasound for larger masses) provides information on its **location** in the pelvis, its **laterality** and its relation with the ovarian parenchyma and with the adjacent organs. It also allows a quantitative assessment of the **size** of both ovaries and the lesions, measured by taking the three largest diameters in two perpendicular planes (Fig. 3.33).

Transvaginal ultrasound investigation provides information on the *morphology* of the mass, classified into unilocular, multilocular, unilocular–solid, multilocular–solid, solid or unclassifiable (Table 3.3).

Fig. 3.33. Measurement of (a) the ovary and (b) an ovarian cyst from the three largest diameters in two perpendicular planes

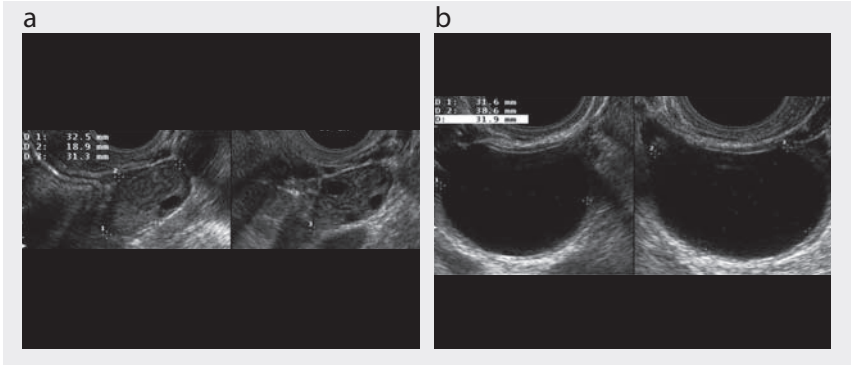

Table 3.3. Morphology of ovarian masses

Unilocular cyst		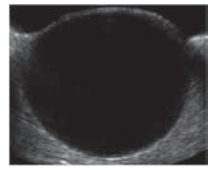
Unilocular–solid cyst		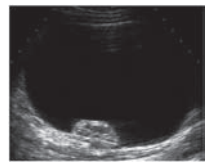
Multilocular cyst		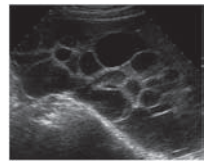
Multilocular–solid cyst		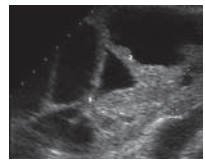
Solid		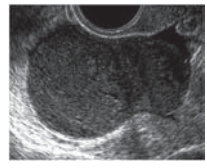

Information can also be obtained if a **septum** or multiple septa are present. (Fig. 3.34) shows a complete (thin strand of tissue running across the cyst cavity from one internal surface to the contralateral side) and an incomplete septum (which is not complete in some scanning planes). The thickness is measured where it appears to be at its widest.

Solid papillary projections are any solid projections into the cyst cavity from the cyst wall with a height ≥ 3 mm (smooth or irregular). The height and base of the largest projection are measured. The number of separate papillary projections and whether blood flow can be detected are also recorded (Fig. 3.35).

Fig. 3.34. Septa. (a) Complete septum. (b) Measurement of a septum. (c) Incomplete septum

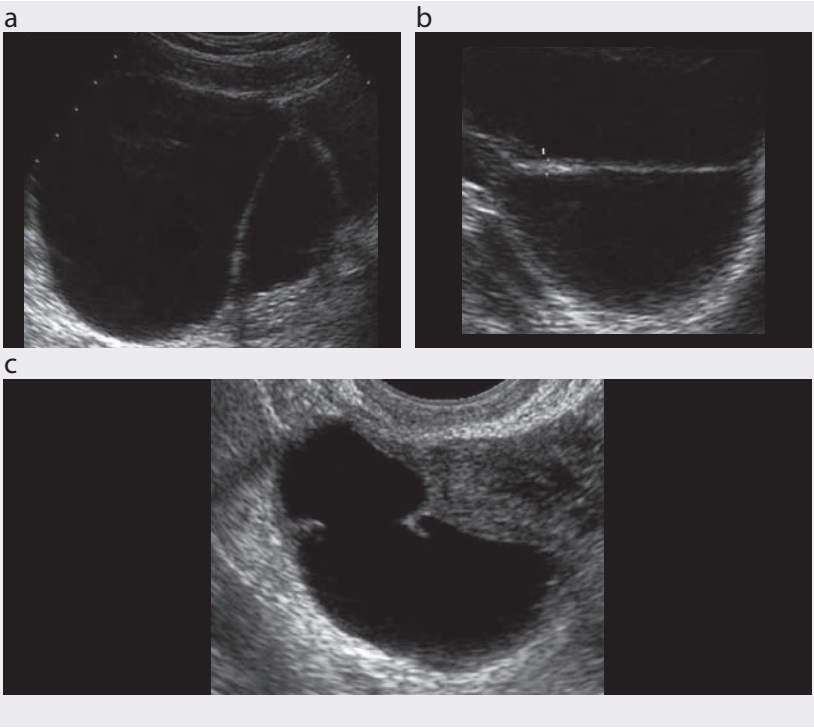

Fig. 3.35. (a), (b) Solid papillary projection

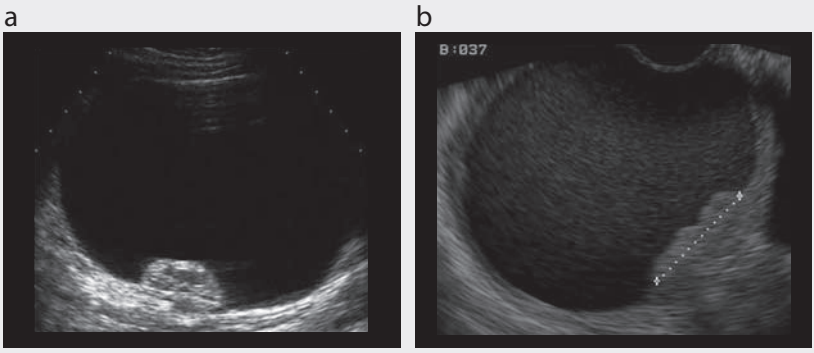

The **cystic contents** can be anechoic (black), have homogeneous low-level echogenicity (as seen in mucinous tumours or an appearance similar to amniotic fluid), have a ground-glass appearance (homogeneously dispersed echogenic cystic contents, as seen in endometriotic cysts), be haemorrhagic (internal thread-like structures, representing fibrin strands; star-shaped, cobweb-like, jelly-like) or mixed (as often seen in teratomas) (Fig. 3.36).

Acoustic shadows are seen as a loss of acoustic echo behind a sound-absorbing structure (Fig. 3.37).

Fig. 3.36. Cystic contents. (a) Anechoic. (b) Low-level. (c) Ground glass. (d) Haemorrhagic. (e) Mixed

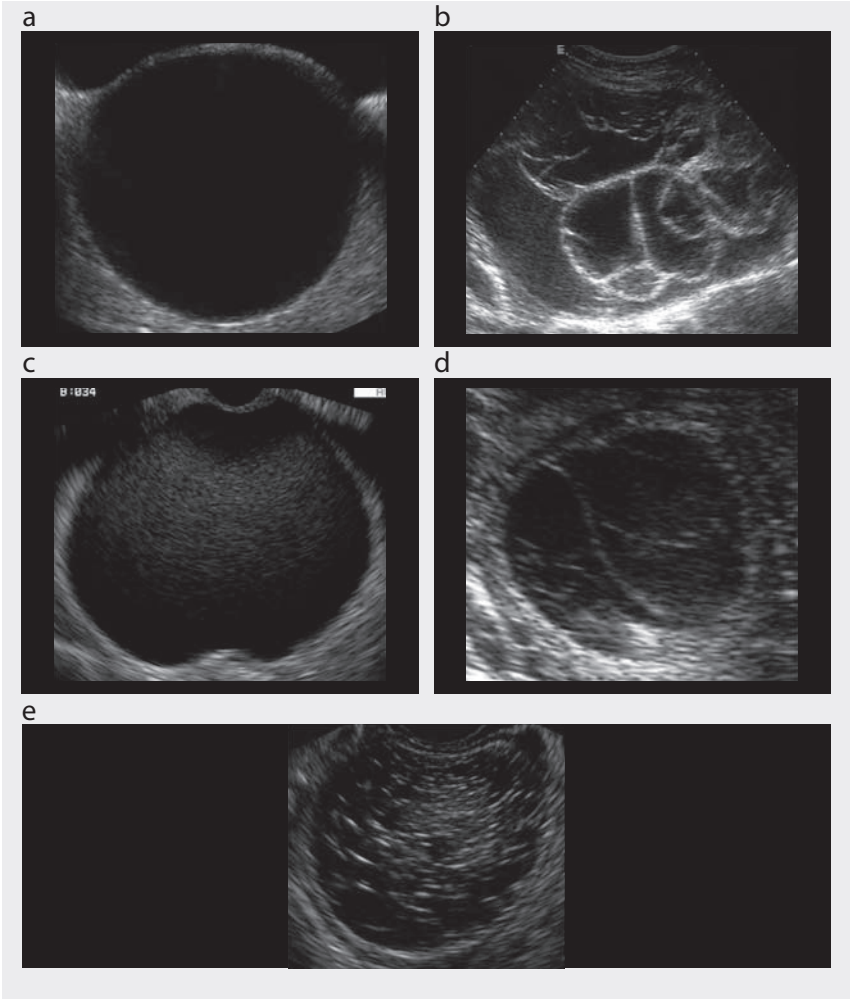

Fig. 3.37. Acoustic shadow

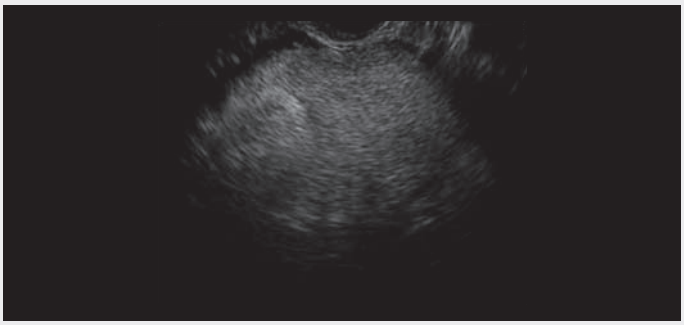

A subjective, semiquantitative assessment of **vascularization** (within a septum or papillary projections) can be made by means of colour Doppler analysis and given a colour score from 1 (absence of flow) to 4 (hypervascularization).

Ultrasound investigation can also demonstrate **fluid** in the pouch of Douglas or ascites (fluid outside the pouch of Douglas).

Clinical data (family history of gynaecological neoplasms, age, parity, menopausal state, hormonal therapy, pain) and serological data (presence of CA-125 protein) are then linked to the ultrasound findings. The International Ovarian Tumor Analysis Group analysed all the parameters described above to identify significant differences between benign and malignant masses. On the basis of the morphology of the lesion, the prevalence of malignancy was 0.6% in unilocular neoformations, 10% in multilocular, 33% in solid–unilocular, 41% in solid–multilocular and 62% in solid formations. With logistic multivariate regressive analysis, the parameters that were significantly independent predictors of malignancy were: the woman's age, a positive history of ovarian carcinoma, the diameter of the largest lesion, the diameter of the solid component, the presence of ascites, the presence of solid vascularized tissue, a completely solid aspect of the lesion and the colour score. Factors that indicated a reduced risk for malignancy were: cone shadow, pelvic pain during examination and hormonal therapy. The variables were used to elaborate a mathematical model to predict risk for malignancy. The applicability and accuracy of this model are being studied in centers that were not involved in its development, before it may be used to evaluate risk in the general population. The International Ovarian Tumor Analysis Group has also drawn up simple rules, which, if applicable, will predict whether an ovarian mass is benign or malignant (Table 3.4).

Table 3.4. Rules for predicting whether an ovarian mass is benign or malignant

Classification	Characteristic
Benign (B rules)	
B1	Unilocular
B2	Presence of solid components, of which the largest has a diameter < 7 mm
B3	Presence of acoustic shadows
B4	Smooth multilocular tumour with the largest diameter < 100 mm
B5	No blood flow (colour score, 1)
Malignant (M rules)	
M1	Irregular solid tumour
M2	Presence of ascites
M3	At least four papillary structures
M4	Irregular multilocular solid tumour with the largest diameter ≥ 100 mm
M5	Very strong blood flow (colour score, 4)

Adapted from International Ovarian Tumor Analysis Group (2005)

If one or more M rules apply in the absence of a B rule, the mass is classified as malignant; if one or more B rules apply in the absence of an M rule, the mass is classified as benign; if both M rules and B rules apply, the mass cannot be classified; if no rule applies, the mass cannot be classified. In the published study, the rules were applicable for 76% of the tumours, with a sensitivity of 95% and a specificity of 91%.

Specific diagnosis

Once detected, an ovarian lesion should be evaluated for the risk for malignancy, and the ultrasound examiner should express a specific diagnosis. It is therefore important to distinguish between physiological structures in the ovary (e.g. follicles and corpus luteum), abnormal but functional masses (e.g. due to ovarian hyperstimulation or a haemorrhagic corpus luteum) and clearly pathological structures.

Physiological structures and functional lesions

The follicles are recognized by ultrasound as anechoic rounded formations with a thin regular wall and a diameter ranging from a few to 18–20 mm (Fig. 3.38). The corpus luteum can assume various morphological aspects: it generally has a starry aspect due to deflation of the follicular wall after ovulation, with cobweb content. It may also contain haematic clots, which can be mistaken for papillary projections or solid components even by expert operators. A peripheral vascular ring is a typical finding on colour Doppler evaluation (Fig. 3.38).

Fig. 3.38. (a) Normal ovary with follicles. (b) Ovary with corpus luteum. (c) Vascular ring in a corpus luteum

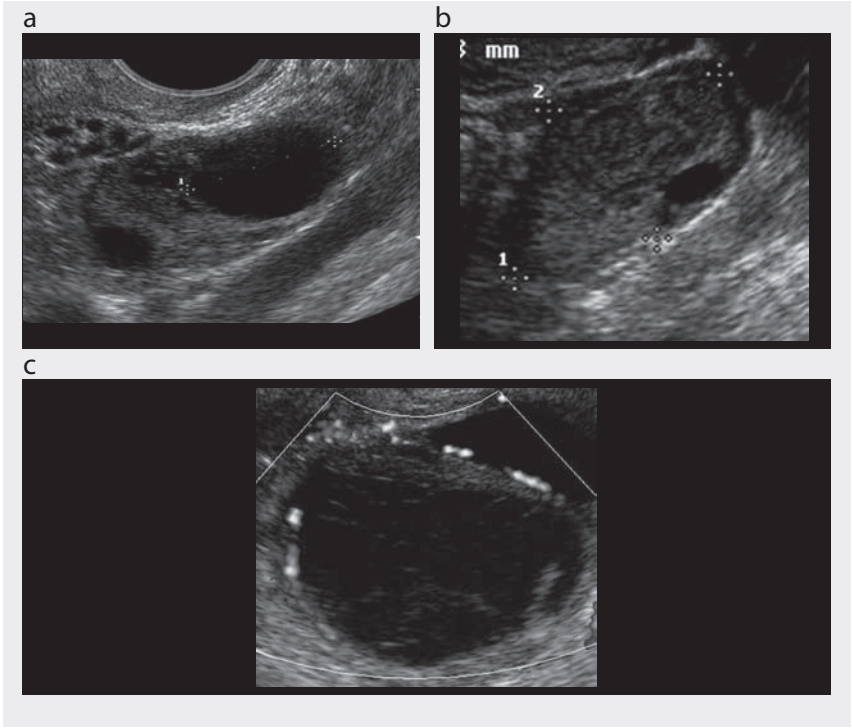

Adnexal tumours

In order to diagnose ovarian neoformations accurately, it is important to review the structures that make up the ovarian parenchyma: the ovarian epithelium, from which all epithelial formations arise (benign, borderline and malignant); the germinal cells, from which teratoma cysts and the corresponding malignant neoformations arise; the stroma (fibroblast, vessels), in which the corresponding benign and malignant stromal tumours arise (ovarian fibromas, fibrothecomas and fibrosarcomas, granulosa-cell tumours, Sertoli-Leydig cell tumours). The ovary can also be the site of metastases originating from tumours in other organs.

Benign epithelial neoformations

Simple ovarian cysts

This group consists of unilocular cysts measuring up to 10–14 cm, which are anechoic, with sharp margins and no solid component. As smaller cysts are not distinguishable from ovarian follicles on ultrasound examination, in women of child-bearing age only those fluid images measuring > 3 cm are referred to as cysts. These lesions occur in 40% of cases of cystadenoma. This type of lesion should be followed up by ultrasound. Removal of these cysts is indicated when they appear as solid coins or when they are large.

Endometriotic cysts

Endometriotic ovarian cysts present highly typical ultrasound features and clinical symptoms, and diagnosis is usually easy. They are unilocular, with regular margins and a ground-glass or densely homogeneous content. Doppler examination reveals scant pericystic vascularization and no central vascularization. In some endometriotic cysts, septa are seen, which may be faintly vascularized. An ultrasound feature that is seen in 20% of cases, which is useful for differential diagnosis, is the presence of hyperechoic wall foci. Although they can be mistaken for papillae, they are accumulations of haemosiderin–fibrin or clots (Fig. 3.39).

Fig. 3.39. (a) Endometriotic ovarian cysts. (b) Accumulation of haemosiderin

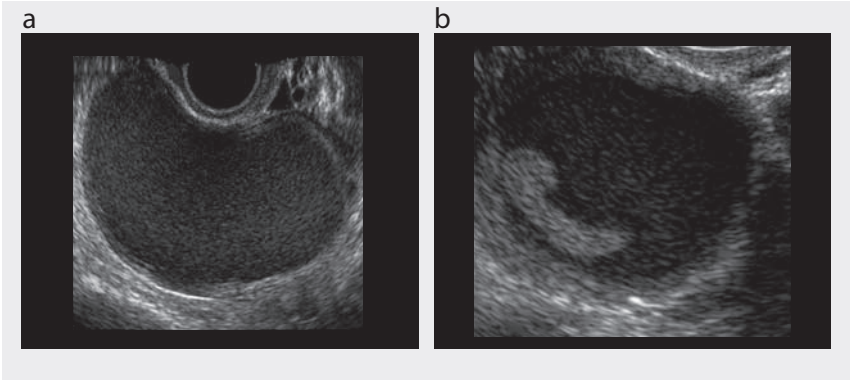

Epithelial borderline neoformations and invasive carcinomas

Borderline ovarian tumours

Borderline ovarian tumours constitute 10–15% of all malignant neoplasms. They are considered to be one of the most difficult groups of masses to classify correctly, and numerous studies have been conducted to identify ultrasound characteristics that distinguish borderline ovarian tumours from primitive ovarian tumours.

Borderline ovarian tumours are characterized histologically as serous and mucinous and the latter as endocervical and intestinal type. On ultrasound examination, the morphological characteristics of mucinous endocervical borderline ovarian tumours are similar to those of serous tumours: both are frequently unilocular–solid lesions with papillary projections. On the contrary, the mucinous intestinal-type borderline ovarian tumors have different morphology: mucinous intestinal-type lesions are greater than endocervical-type lesions, and are frequently multilocular with regular septa and a large number of concamerations (Fig. 3.40).

Fig. 3.40. (a) Serous borderline ovarian tumour. (b) Mucinous borderline ovarian tumour, endocervical type. (c) Mucinous borderline ovarian tumour, intestinal type

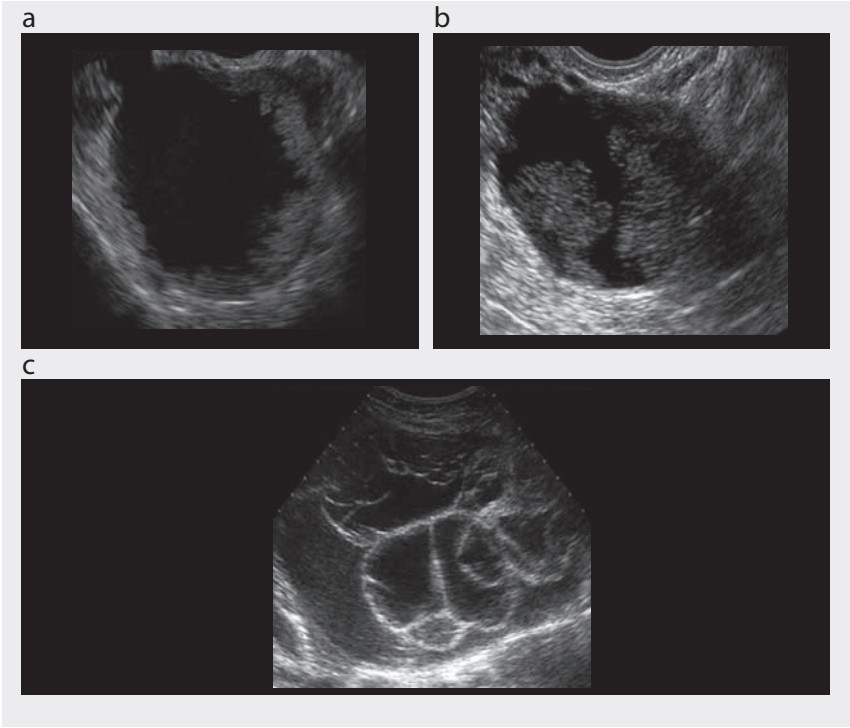

Epithelial ovarian carcinomas

Early-stage borderline tumours and ovarian carcinomas have numerous ultrasound characteristics in common. The solid tissue of the neoplasm increases in proportion with degree of malignancy, from borderline to the various stages of ovarian carcinoma, and becomes progressively more echogenic, with more irregular borders. Borderline ovarian tumours and the first stages of ovarian carcinoma have a similar percentage of papilla formation, which is significantly higher in advanced cases, with a significantly lower percentage of solid neoformations.

Germinal ovarian tumours

Cystic teratoma

Cystic teratoma (dermoid) is a benign neoformation which originates from the three embryonic membranes, the ectoderm, the mesoderm and the endoderm. It is constituted mainly of sebaceous material and piliferous structures, often with teeth, bones and muscular tissue inside. On ultrasound, the lesions appear unilocular, with an inhomogeneous content or with horizontal hyperechoic stria, due to hair. The piliferous content sometimes concentrates inside the formation to form the Rokitansky

nucleus, which, on ultrasound, has the appearance of a hyperechoic, roundish formation (white ball); it should not be mistaken for solid parenchymal tissue. A prevalently cystic echo pattern is seen in 9–18% of dermoids (Fig. 3.41).

Fig. 3.41. Ultrasound features (a) and macroscopic aspect (b) of a dermoid cyst

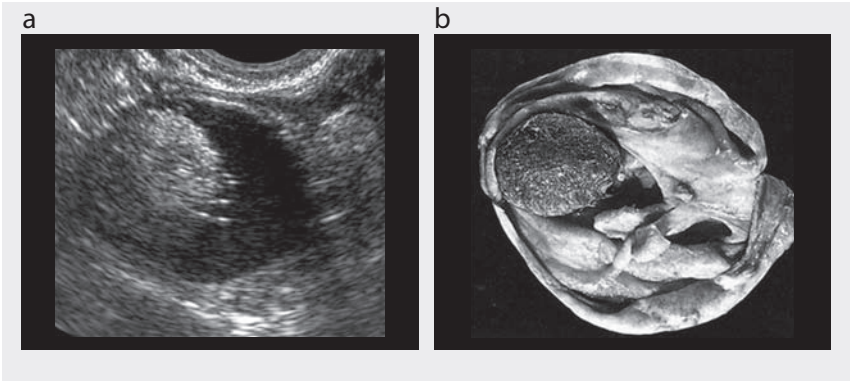

Malignant germinal tumours

The rare malignant germinal tumours can be divided into dysgerminomas, yolk sac tumours and choriocarcinomas. Given the rarity of these neoplasms, there are no characteristic ultrasound markers; they are usually seen as large, multilocular, solid lesions, with rich vascularization.

Stromal tumours

Fibromas, fibrothecomas and Brenner tumours

Most stromal tumours are benign. Ovarian fibromas and fibrothecomas are often considered to be difficult to diagnose by ultrasound. Ovarian fibromas often have characteristic features that may suggest a diagnosis, such as a solid spherical or ovoidal structure and hypo- or anechoic stria arranged like a halo (stripy echogenicity). The ultrasound characteristics of fibrothecomas, however, are not well defined. They are solid, often with cystic concamerations, but their inner structure is sometimes so inhomogeneous that it is difficult to differentiate them from malignant ovarian masses.

Granulosa-cell tumours and Sertoli-Leydig tumours

Stromal tumours also include neoplasms arising from the mesenchymal tissues, from granulosa cells and from Sertoli-Leydig cells. Granulosa-cell tumours and Sertoli-Leydig tumours are rare lesions, and few studies have been conducted on ultrasound markers. In a multicentre study, granulosa-cell tumours were reported to be large tumours (median largest diameter, 102 mm; range, 37–242 mm), with moderate or high colour content on colour Doppler examination (colour score 3 in 57%, 4 in

35%). They appear as multilocular–solid in 52%, purely solid in 39%, unilocular–solid in 4% and multilocular in 4% of cases. Multilocular and multilocular–solid cysts typically contain large numbers of small locules (> 10). The echogenicity of the cyst content is often mixed (38%) or low (44%). Papillary projections are found in 17% of cases.

Metastatic ovarian tumours

Ovarian masses are metastases in 4–5% of cases. Most originate from neoplasms in the intestinal tract or breast. Anatomopathologically, ovarian metastases may appear as bilateral lesions or as multiple solid nodules within the ovary, partly cystic or, less frequently, totally cystic lesions. Extensive areas of necrosis or haemorrhage are commonly seen inside these lesions. Krukenberg tumours are typically solid, with a lobulated external surface (Fig. 3.42).

Fig. 3.42. Krukenberg tumour. (a) Ultrasound features. (b) Macroscopic section

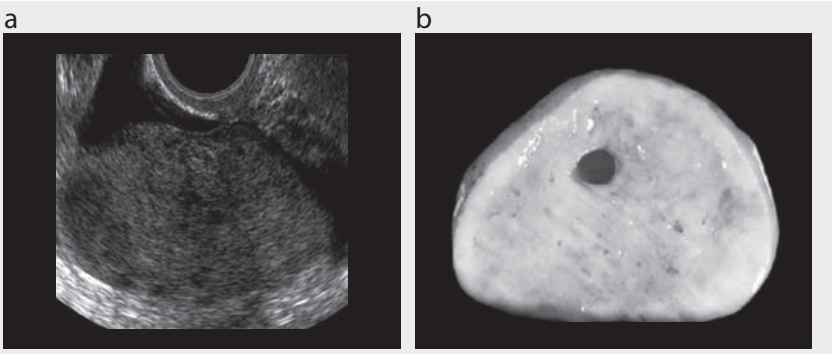

The ultrasound characteristics of histologically diagnosed ovarian metastatic tumours in 67 women were examined in a multicentre study. Nearly all the tumours (93%) deriving from primary malignancies of the stomach, breast or uterus or from lymphoma were solid, while metastases deriving from primary malignancies of the colon or rectum, appendix and biliary tract were multilocular or multilocular–solid.

Paraovarian cysts

Paraovarian cysts constitute 5–20% of pathological adnexal findings; they develop from embryonic ducts (mesothelial, mesonephric or paramesonephric) and are located between the Fallopian tube and the ovary. On ultrasound examination, paraovarian cysts usually appear as unilocular formations, with regular margins, round or oval, near to but separated from the ovarian ipsilateral parenchyma. The median diameter is variable, ranging from 15 to 120 mm. The contents can be anechoic or

finely corpuscular; in a high percentage of cases, the interior wall is irregular, due to the presence of papillary projections. According to some authors, papillae may be observed in 33% of paraovarian cysts; a large number of projecting papillae may be related to a histopathological borderline diagnosis.

Peritoneal pseudocysts

Peritoneal pseudocysts (or pelvic inclusion cysts) are loculated fluid collections resulting from fluids entrapped by adhesion strands, formed in the course of an inflammatory process in the peritoneal cavity or as a consequence of surgery. At times, they are observed as cystic formations, oval or roundish, but more often appear as anechoic collections modelled on the pelvic wall outline. The ovarian parenchyma may appear to be suspended between the adhesions in a central or peripheral region of the cyst. The cystic content can be anechoic or finely corpuscular, and the cyst may contain septa or papillary projections. Septa are present in about 80% of cases; they are often mobile when pressure is exerted by the endovaginal probe, producing the typical flapping sail movement.

Fallopian tubes

Normal Fallopian tube

The Fallopian tubes vary in length between 7 and 12 cm. Both tubes are situated in the superior free margin of the large ligament, covered by peritoneum. The different anatomical parts of the salpinges can be distinguished as the interstitial, the isthmic, the infundibular and the ampullar (Fig. 3.43).

Fig. 3.43. Segments of the Fallopian tube: (1) interstitial, (2) isthmic, (3) infundibular, (4) ampullar

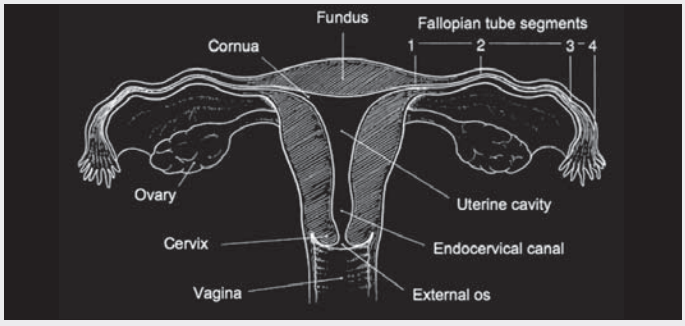

The interstitial part is the thinnest, lying within the muscle layer of the uterus and measuring 1–2 cm. This tract can be visualized by transvaginal ultrasound in a transversal scan of the uterus at the level of the fundus, following the

endometrial echoes in a lateral direction (Fig. 3.44). It appears as a thin hyperechogenic streak that begins in the endometrium and runs towards the external profile of the uterus.

Fig. 3.44. Interstitial part of the Fallopian tube visualized on a transversal section at the level of the fundus as a thin echogenic line (arrows) through the right and left aspect of the uterine wall

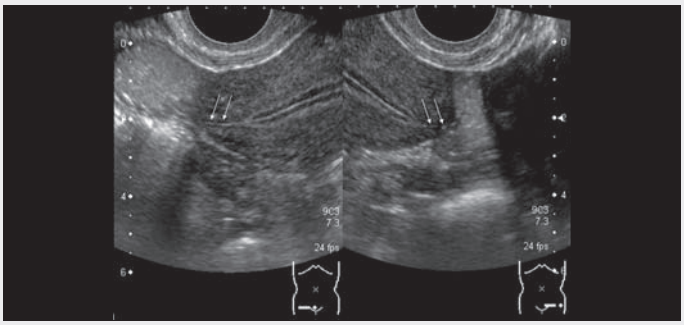

The isthmic part is thin and tubular and runs adjacent to the lateral margin of the uterus for several centimetres. The infundibular section is longer and larger. The distal (ampullar) extremity opens freely into the abdominal cavity, ending with the fimbriae, thin fringe-like structures that surround the abdominal orifice of the tube.

The salpinges are difficult to visualize with ultrasound, except when there is a moderate amount of free fluid in the abdomen, which surrounds the tube and acts as an ultrasound contrast agent (Fig. 3.45, Fig. 3.46).

Fig. 3.45. Free fluid in the pouch of Douglas and visualization of the tubal infundibular and ampullar tract

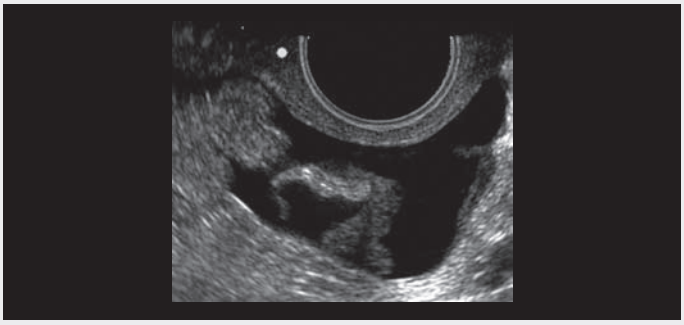

Fig. 3.46. Free fluid in the pelvis and bilateral visualization of the tubal ampullar tract

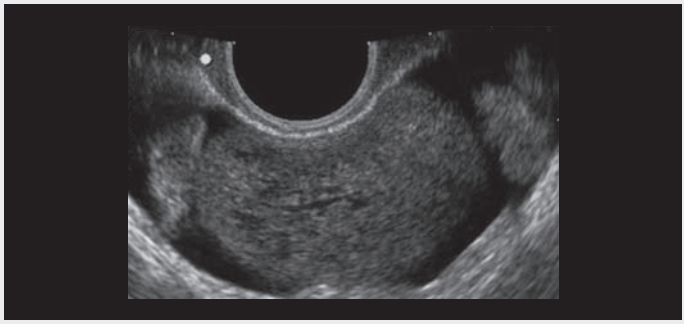

Paraovarian and paratubal cysts

Paraovarian and paratubal cysts account for about 10% of all adnexal cysts. They are distinguished as mesonephric (Wolffian ducts), paramesonephric or tubal (Müllerian ducts) and mesothelial on the basis of their origin. These cysts have common ultrasound characteristics, independently of their histological origin. They are usually anechoic cysts, with thin walls and well-defined margins. They rarely contain septa or papillae, with a few vessels. Useful diagnostic criteria for paraovarian cysts are visualization of a close but distinct ipsilateral ovary, the absence of a pericystic ovarian parenchyma and movement of the cyst from the contiguous ovary when light pressure is exercised with the vaginal probe (Fig. 3.47, Fig. 3.48).

Fig. 3.47. Paraovarian cyst, close but distinct from the ovary, with no pericystic ovarian parenchyma

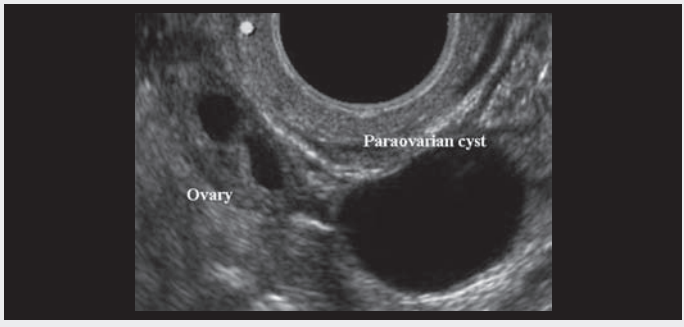

Fig. 3.48. Paratubal cyst: free fluid in the pelvis and visualization of the tubal infundibular and ampullar tract and a small cyst close to the tube

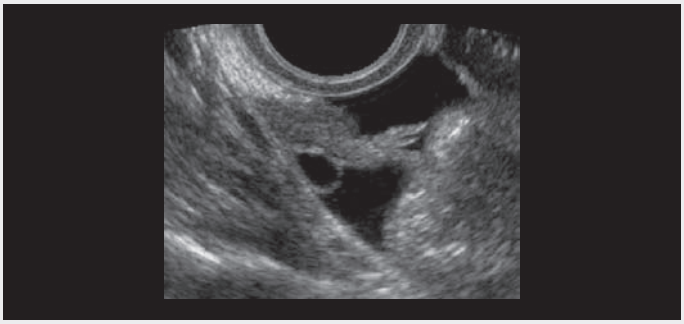

Adhesions

Adhesions are suspected if palpation with the probe or abdominal palpation with the hand indicates that the ovaries or the uterus are adhering to adjacent structures (broad ligament, pouch of Douglas, bladder, rectum or parietal peritoneum). Sometimes, in the presence of pelvic fluid, fine septa (adhesions) can be seen between the ovary and the uterus or the peritoneum of the pouch of Douglas.

The sonographic sign of adhesions are:

- the presence of thin septa in pelvic fluid between organs (Fig. 3.49), with no or little vascularization in the septa and movement of these thin septa (filmy adhesions) by manual or probe palpation, looks like a sail;

Fig. 3.49. Pelvic fluid and fine, thin septa (adhesions) can be seen between the uterus (a) and the peritoneum of the pouch of Douglas (b)

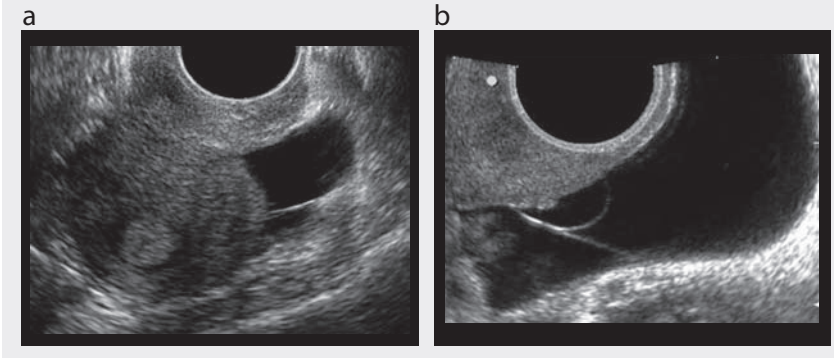

- the presence of a pelvic peritoneal inclusion cyst, with fluid accumulation in the cul-de-sac or pelvis, walls identical to the pelvic wall and thin septa;
- fixed organs, whereby the uterus and ovaries, which are normally mobile and not adherent to the surrounding tissues by palpation with a probe or by abdominal palpation with the hand, appear to be fixed to each other.

Tubal diseases

Inflammatory disease

Inflammatory processes of the Fallopian tubes, or pelvic inflammatory disease, are a frequent and serious yet treatable disease that can lead to abscess formation or pelvic fluid accumulation. Over the years, it has become clear that the transvaginal ultrasound appearance of tubal inflammatory disease is typical and reproducible. Various ultrasound markers of tubal disease have been identified and placed in the context of the pathogenesis. Correct identification of the chronic sequelae resulting from previous inflammatory disease enables the observer to differentiate these ultrasound markers from unrelated diseases of the bowel, cystic ovarian neoplasia with papillary formation and other malignancies of the ovaries.

Sonographic markers of tubal inflammatory disease

Tubal inflammatory disease was identified with transvaginal ultrasound on the basis of shape, wall structure, wall thickness, extent of ovarian involvement and the presence of fluid (Timor-Tritsch, 1998).

Shape: on a longitudinal section, a pear-shaped, ovoid or retort-shaped structure containing sonolucent fluid or, sometimes, low-level echoes (Fig. 3.50).

Wall structure:

- incomplete septa (Fig. 3.50, Fig. 3.51), defined as hyperechoic septa that originate as a triangular protrusion from one of the walls but do not reach the opposite wall;
- cogwheel sign, defined as a sonolucent cogwheel-shaped structure visible in the cross-section of the tube, with thick walls (Fig. 3.52); or
- beads-on-a-string sign, defined as hyperechoic mural nodules measuring 2–3 mm and seen on the cross-section of the fluid-filled distended structure (Fig. 3.53).

Wall thickness: considered thick if ≥ 5 mm (Fig. 3.51 and 3.52) or thin if < 5 mm (Fig. 3.53).

Fig. 3.50. Longitudinal section of a hydrosalpinx, seen as a fluid-filled convoluted structure containing low-level echoes

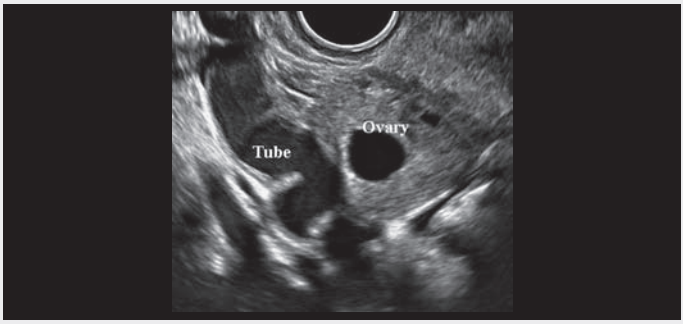

Fig. 3.51. Acute salpingitis with incomplete septa and thick wall (> 5 mm)

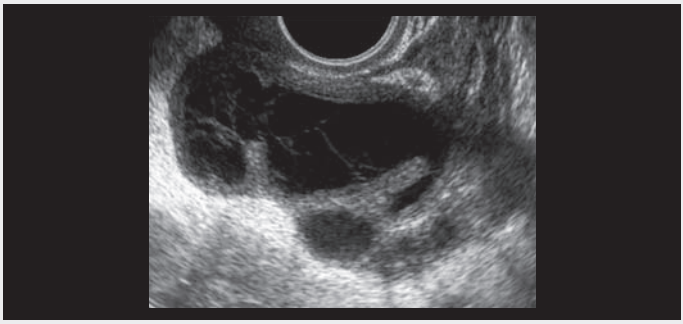

Fig. 3.52. Transverse section of acute salpingitis: a sonolucent cogwheel-shaped structure is visible in the cross-section of the tube, with thick walls

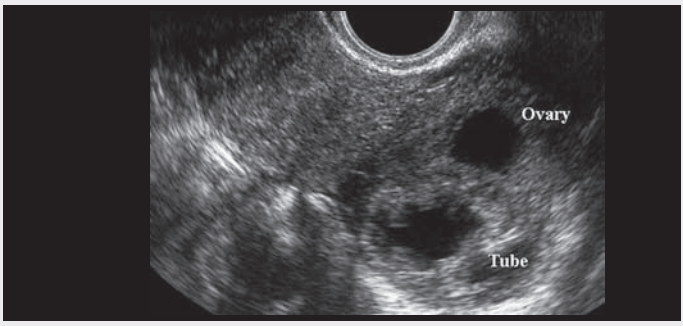

Fig. 3.53. Hydrosalpinx: beads-on-a-string sign. (a) Ultrasound features, (b) Doppler features

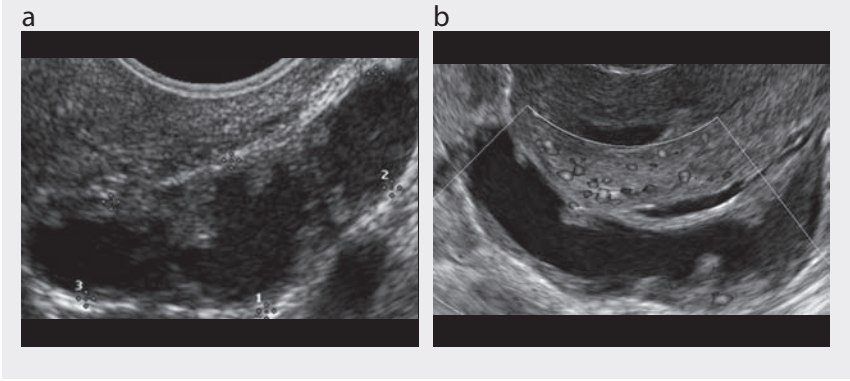

Extent of ovarian involvement:

- none if the ovary appears normal and can be distinctly identified (Fig. 3.54);
- tubo-ovarian complex (Fig. 3.50) in which the ovaries and tubes are identified and recognized (Fig. 3.52), but the ovaries cannot be separated by pushing the tube with the vaginal probe; the woman also has the clinical signs and symptoms of acute pelvic inflammatory disease (Fig. 3.55, Fig. 3.56);
- tubo-ovarian abscess, in which an acutely ill patient with marked tenderness at the touch of the ultrasound probe shows total breakdown of the normal architecture of one or both the adnexa, with formation of a conglomerate in which neither the ovary nor the tubes can be separately recognized as such (Fig. 3.57). The classical pelvic abscess formation with total breakdown of separately identifiable tissues and speckled fluid is also regarded as a tubo-ovarian abscess.

Presence of fluid: free or in a pelvic peritoneal inclusion cyst. The latter is a sonolucent, fluid-filled accumulation in the cul-de-sac, the walls of which are identical to the pelvic wall, with thin adhesions between the organs in the pelvis (Fig. 3.49); the process is not acute, i.e. there is no tenderness upon touch with the vaginal probe or clinical signs and symptoms of an acute illness.

Fig. 3.54. Acute salpingitis: ovary is clearly seen and separate from the tube with thick walls

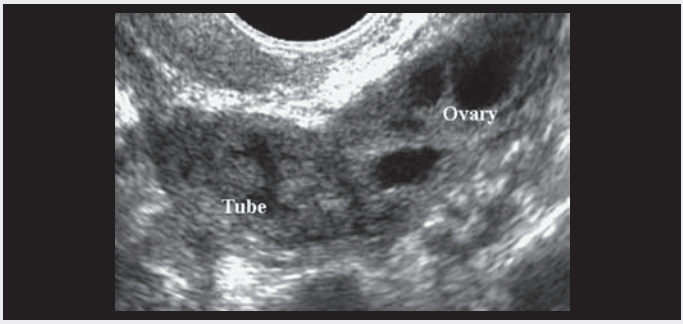

Fig. 3.55. Acute salpingitis: the ovary (OV) is clearly seen but adherent to the tube (TU), with thick walls, incomplete septa and fluid dense content

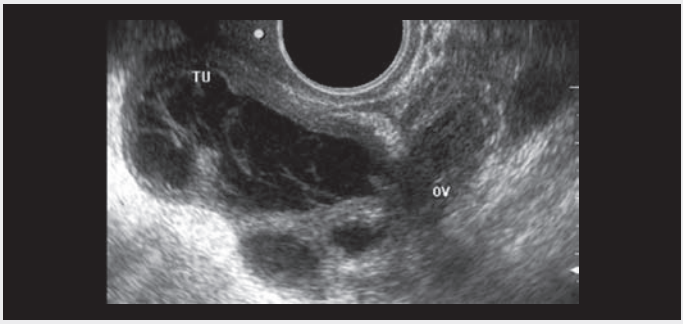

Fig. 3.56. Tubo-ovarian complex: the ovary is clearly seen and is adherent to the tube, with purulent exudate filling the lumen

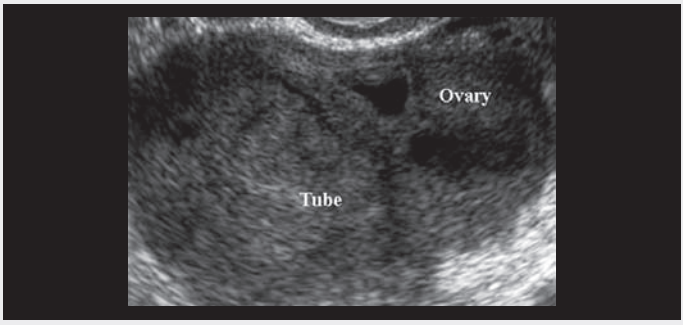

Fig. 3.57. Tubo-ovarian abscess in which neither the ovary nor the tubes can be separately recognized (a). Tube with incomplete septa and thick walls with marked vascularization (b)

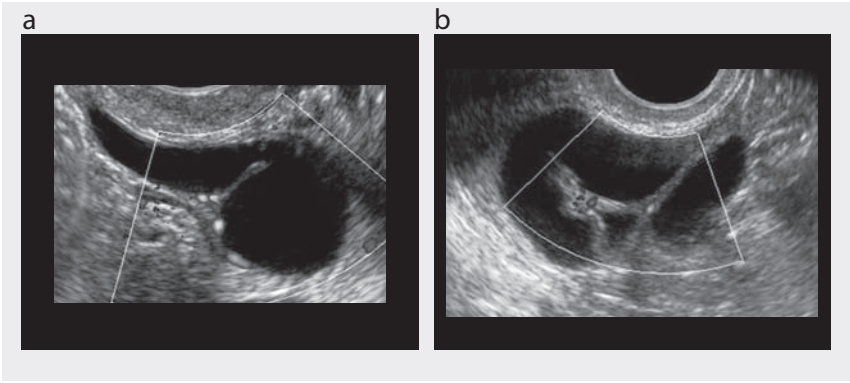

Correlation between ultrasound image and acute or chronic pelvic inflammatory disease

In a number of studies, the ultrasound images are classified as acute or chronic and, in each of these categories, one section depicts wall thickness, incomplete septa and wall structure. Once ovarian involvement is suspected or detected, the acute and chronic involvement of the pelvic organs is classified as tubo-ovarian complex or tubo-ovarian abscess. Late sequelae of possible inflammatory disease, such as pelvic peritoneal inclusion cyst or fluid, are frequent in women with a history of pelvic inflammatory disease.

Wall thickness: Women with acute disease have thick Fallopian tube walls (Fig. 3.51, Fig. 3.52, Fig. 3.54, Fig. 3.55), whereas overwhelmingly more women with chronic disease have a thin wall (Fig. 3.53, Fig. 3.58, Fig. 3.59).

Wall structure: Women with acute disease have the cogwheel sign, whereas the beads-on-a-string sign is present in women with chronic disease (Fig. 3.53, Fig. 3.59). Incomplete septa are present in both chronic and acute cases (Fig. 3.50, Fig. 3.51, Fig. 3.55, Fig. 3.58, Fig. 3.59).

Tubo-ovarian complex is common in women with acute disease and rare in women with chronic disease.

Cul-de-sac fluid is more commonly seen in acute cases.

Palpable findings are common in both acute and chronic cases. The bimanual palpatory pelvic examination before the scan or palpation with the probe often cause tenderness and pain in acute cases but sometimes also in chronic cases.

Differentiation between tubo-ovarian complex and tubo-ovarian abscess

These two entities are not only sonographically distinct, but also clinically different and require different therapeutic approaches. The tubo-ovarian complex is a first step in a process that may lead to abscess formation. A tubo-ovarian complex should be diagnosed if transvaginal ultrasound shows clear inflammatory features in tubal

and ovarian structures (e.g. thick wall, cogwheel sign) (Fig. 3.51, Fig. 3.52, Fig. 3.55, Fig. 3.56). The term 'tubo-ovarian abscess' should be reserved for a later phase in this process, when total breakdown of the adnexal structures on one or both sides is seen (Fig. 3.57). At times, the presence of loculated, speckled fluid above the rectum (in the cul-de-sac) can be detected sonographically. This is consistent with pus and is probably due to debris from white blood cells, fibrin and degrading tissue.

Natural course of tubal inflammatory disease and ultrasound findings

The ultrasound classification of tubal inflammatory disease is based on its natural course. During the acute phase, if the tubal mucosa is involved in the inflammatory process, the tubal wall becomes thick and oedematous, and purulent exudate fills the lumen (Fig. 3.50, Fig. 3.51). Some exudate may also spill into the cul-de-sac through the fimbrial end of the tube. The ultrasound image reflects these pathological changes as the cogwheel sign, with a tubal wall that is ≥ 5 mm thick and highly vascularized (Fig. 3.52, Fig. 3.55, Fig. 3.56, Fig. 3.57). These are pathognomonic signs of acute tubal inflammation.

Fig. 3.58. (a), (b) Convoluted, retort-shaped tubes and presence of an incomplete septum

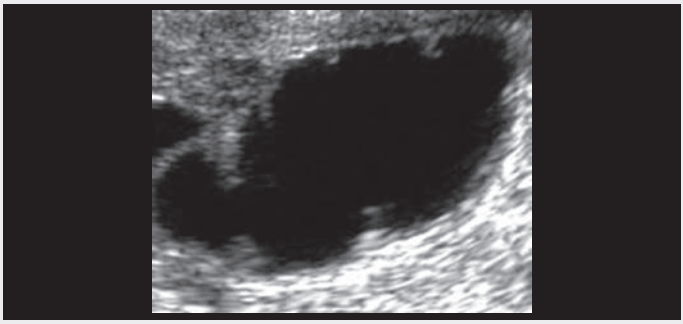

If the tubes become occluded at the fimbrial or the cornual end, mucus or pus will fill and distend the tubes, leading to entities called hydrosalpinx and pyosalpinx, respectively (Fig. 3.50, Fig. 3.51). The tubes become convoluted and both in situ and on ultrasound resemble the glass retorts used in laboratories, due to the presence of an incomplete septum; they are therefore known as retort-shaped tubes (Fig. 3.58, Fig. 3.60).

The progressive filling and ballooning of the occluded tube leads to a doubling-up or kinking of the hydro- or pyosalpinx (Fig. 3.60). The ultrasound equivalent of this process is the incomplete septum seen in both acute and chronic tubal disease (Fig. 3.58).

If the tube does not become occluded, some of the infectious pathogens spill into the pelvis and take advantage of ovulation, at which time a small defect on the ovary itself is obvious at the site of the ovulation. Bacteria invade during this incipient stage, usually only the ovary and the tube on one side. At first, the anatomy is

Fig. 3.59. Chronic hydrosalpinx: dilated tube with thin wall and beads-on-a-string sign

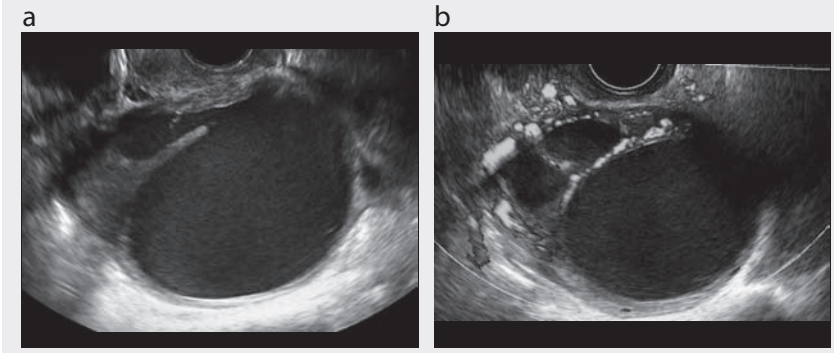

Fig. 3.60. (a)–(d) Three-dimensional evaluation and inverse mode of a retort-shaped hydrosalpinx

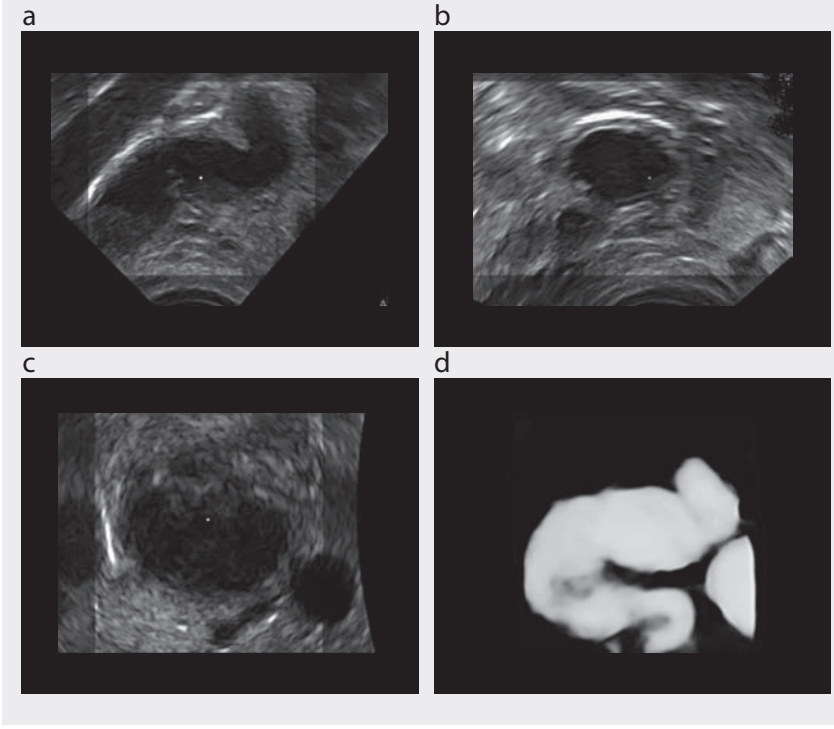

not broken down, and, if a laparoscopy or a laparotomy is performed at this stage, an inflammatory conglomerate is seen, with the ovary and the tube still recognizable as separate entities by transvaginal ultrasound (Fig. 3.54, Fig. 3.55, Fig. 3.56).

If treatment fails or is not applied, the acute inflammatory process progresses to its most severe phase, resulting in a full-blown tubo-ovarian abscess (Fig. 3.57). Only at a relatively later stage (days) does the process spread to the other side to involve the contralateral ovary and Fallopian tube. Therefore, an out-of-phase appearance of the two adnexa may be seen: one in which the process has advanced to the tubo-ovarian abscess stage and the contralateral one which lags behind, exhibiting all the signs of a tubo-ovarian complex in which the anatomy has not yet broken down.

The process may enter a chronic phase, characterized by a completely blocked tube in which fluid accumulates, distending the wall and rendering it very thin. The endosalpingeal folds almost disappear or become flattened and extremely fibrous. On cross-section of the tube, the pathological specimen and histological sections show these remnants of the fibrosed endosalpingeal folds (Fig. 3.53). Ultrasound examination also shows the typical dilated, thin-walled structure, studded with the echogenic remnants of the endosalpingeal structures, known as beads-on-a-string (Fig. 3.53, Fig. 3.58, Fig. 3.59). This ultrasound sign is a reliable marker of chronic tubal disease, e.g. hydrosalpinx. Hydrosalpinx can be the result of previous acute salpingitis and has also been described in women with a history of pelvic inflammatory disease or salpingitis or even hysterectomy. Hydrosalpinx can also develop in tubes occluded previously by ligation or cauterization. The ultrasound finding of a thin-walled, fluid-filled tube with the characteristics described here in women who have undergone hysterectomy or tubal sterilization is harder to explain; however, there is evidence that, in these cases, the fimbrial end of the tube may already have been occluded or give the typical ultrasound picture of a hydrosalpinx.

In the acute phase, a small amount of fluid may accumulate in the cul-de-sac or in other parts of the pelvis and persist for a variable length of time. Adhesions between various organs in the pelvis, formed during the acute phase of the inflammatory disease, may persist for months or even years (Fig. 3.49).

Tubal inflammatory disease and differential diagnosis from ovarian lesions

It is critical to differentiate tubal inflammatory disease from an ovarian tumour, whether benign or malignant. In the case of an acute inflammatory process, this is relatively easy, determined by the acute inflammatory features of the pelvic disease. Differentiation is more difficult when a diagnosis of chronic tubal disease with the beads-on-a-string sign and some septations must be differentiated from that of an ovarian cystic structure with small internal papillations and septa. In the case of a chronic hydrosalpinx, the mural lesions (beads-on-a-string) are small, almost equal in size and distributed around the thin wall, whereas papillary formations of an ovarian tumour are usually dissimilar in size and located along the wall, which may show variable thickness. If incomplete septa are present, these almost always indicate a Fallopian tube as the true septa of ovarian tumours are very seldom, if ever, incomplete.

For an accurate differential diagnosis of other adnexal lesions, each case must be placed in its appropriate clinical context. By combining the information provided by

the woman with the transvaginal ultrasound work-up of the pelvis, valuable ultrasound markers of inflammatory disease of the tubes and the ovary can be recognized and the appropriate diagnosis established.

Tubal carcinoma

Tubal carcinomas are the rarest tumours of the female reproductive system, with an incidence of 0.5% of all gynaecological tumours. Only about 1500 cases have been reported in the literature. The clinical characteristics and the response to cytostatic therapy are similar to those of ovarian cancer, but their ultrasound appearance may be different. Preoperative diagnosis of tubal cancer is difficult and is based on visualization of both ovaries, of normal dimensions and morphology, and an adnexal mass with malignant ultrasound characteristics, separated and distinct from the ovaries. These neoplasms often have an elongated oval shape (sausage-like); the cystic component is generally hypoechoic, and its appearance is similar to that of an adnexal inflammation at an advanced stage or a tubo-ovarian abscess.

Tumour markers (e.g. CA-125) may be only moderately increased. The persistence of the mass, its growth over a brief period and a lack of response to antibiotics should guide a differential diagnosis. Ultrasound features of peritoneal carcinomatosis are found in 30–40% of patients with tubal cancer at diagnosis. Otherwise, it appears as a uni- or bilateral adnexal mass, with a complex echotexture and extensive, richly vascularized solid areas that can be visualized with transvaginal ultrasound.

Tubal patency

Tubal occlusion is the single most common cause of female infertility. Some degree of tubal disease, resulting in occlusion of one or both tubes, is found in one of three infertile women (30–50%), and the proportion is considered to be increasing. Evaluation of tubal status is generally the first step in an investigation of infertility factors in women. The usual methods for assessing tubal patency are hysterosalpingography and laparoscopic dye chromopertubation (lap-and-dye). The lap-and-dye test is the gold standard for tubal investigations; however, it involves anaesthesia and surgery, is expensive and often involves delays, as it is an inpatient procedure. Hysterosalpingography can be performed on outpatients but involves gonadal exposure to X-ray irradiation, may produce a hypersensitivity reaction to iodinated contrast medium and is 80–90% as accurate as lap-and-dye.

Hysterosalpingo-contrast sonography

Transvaginal hysterosalpingo-contrast sonography (HyCoSy) can be used to evaluate tubal patency. It involves the introduction of saline solution into the uterine cavity and the Fallopian tubes during transvaginal ultrasound; when free fluid is found in the pouch of Douglas, the patency of at least one tube can be deduced. Saline solution has the advantage of being completely safe and inexpensive. Although it is a useful negative contrast medium for visualizing intrauterine disease (sonohysterography),

saline is not an accurate medium for evaluating the state and patency of the Fallopian tubes. Combination of transvaginal ultrasonography with colour Doppler or ultrasound positive contrast media has increased the accuracy of this method.

To examine the Fallopian tubes, a positive contrast medium, such as air or albumin or galactose with micro-air bubbles, is used. These agents outline the lumina of the Fallopian tubes, giving a hyperechoic appearance. Use of contrast media (such as Echovist, Levovist and Infoson) facilitates evaluation of tubal patency by hysterosalpingo-contrast sonography; however, these contrast media are expensive, not available in many countries and not always accepted by women. The most readily available, least expensive contrast medium is saline solution mixed with air; when this solution is shaken, it produces a suspension of air bubbles which are easily seen when injected into the uterine cavity and the Fallopian tubes.

Hysterosalpingo-contrast sonography is performed as an outpatient procedure after a preliminary scan to detect the position of the ovaries and the interstitial part of the tubes. After insertion of a speculum, a 5-French salpingographic balloon catheter is placed in the uterine cavity and filled with 1–2 ml of air. This step ensures that the cervical canal is closed, prevents leakage of saline solution and air and keeps the catheter in position. A 20-ml syringe containing 15 ml of saline solution and 5 ml of air is prepared and shaken immediately before injection.

A vaginal ultrasound probe is then inserted, and a transversal section of the uterus is taken to localize the interstitial part of the tube. Saline solution is injected slowly and continuously through the catheter, and any resistance during injection is noted. Power Doppler can be used to locate the tubal area. Although colour Doppler imaging is not essential for evaluation of tubal patency, it might facilitate visualization of the passage of saline solution and localization of the tube. When the saline solution and air are injected, a flow of air bubbles through the tubes can be seen. The tube is followed as distally as possible by moving the probe slowly.

The salpinges should be sought and scanned methodically and continuously during injection, starting at the uterine cornu in a plane that also shows the interstitial part of the tube, and then scanning laterally to identify for the flow of air bubbles throughout the tube and near the ovaries. Each salpinx must be examined separately.

If the procedure becomes painful, the examination can be interrupted for a short time to allow any tubal spasm to pass. Hard pressure felt during injection of air and fluid is regarded as a sign of tubal spasm or occlusion. If the pressure does not decrease and no air bubbles are seen to flow from the tube, it is considered to be obstructed.

The criteria for tubal patency on hysterosalpingo-contrast sonography with saline and air contrast media are:

- the passage of air and saline through the interstitial part of the tube;
- detection of air bubbles moving around the ovary, even without visualization of the passage through the tube;
- detection of the solution and air bubbles in the pouch of Douglas;
- power Doppler evidence of the passage of saline solution.

Transvaginal hysterosalpingo-contrast sonography with saline and air solution is a relatively simple, safe, inexpensive, rapid, well-tolerated outpatient technique for determining tubal patency. Furthermore, transvaginal ultrasound accurately demonstrates various pelvic conditions that may be responsible for infertility, so that, in the same setting and at the same time, more information on the pelvis and tubal patency can be obtained**.** The accuracy and advantages of hysterosalpingo-contrast sonography over hysterosalpingography and lap-and-dye have been demonstrated, especially when the tubes are patent; poorer accuracy has been found in cases of tubal occlusion, especially when it is unilateral.

Several studies have suggested that hysterosalpingo-contrast sonography could be used in initial screening of infertile women; however, a reported false occlusion rate of 5–15% raises some concern. In contrast to hysterosalpingography, hysterosalpingo-contrast sonography does not allow imaging of the entire tube and its course. Use of ultrasound contrast media has been proposed to improve evaluation of tubal occlusion and for visualization of the tubal course. Ultrasound contrast media create an image because of the vibration of the bubbles caused by the ultrasound beam at low acoustic pressure. Even with contrast media, however, the false-positive rate for tubal occlusion is still 5–10%, because it is not always possible to visualize the entire tube due to either tubal spasm, only partial occlusion or overlapping by the ultrasound images of other organs (uterus, ovaries, intestine).

The contrast media generally used produce a contrast response, with an overlap between the tissue and the contrast response. To ensure that a signal is received only from the contrast medium, application of dedicated software to the vaginal probe and new contrast media have been proposed. This technique optimizes the use of ultrasound contrast media by means of low acoustic pressure and allows detection of the contrast medium by selecting the harmonic response of the microbubbles of the medium from the signals coming from insonated organs. The image displayed with this technique is due only to harmonic signals produced by contrast media microbubbles; broadband ultrasonic signals from surrounding tissue are filtered out completely, therefore obviating any overlap between the tissue and the contrast response.

When intrauterine injection of contrast medium is visualized by ultrasound with low acoustic pressure, the contrast medium is first seen in the tube, if it is patent proximally, and then spills into the abdominal cavity if the tube is distally and totally patent. Tubal occlusion can be assumed when the contrast medium remains concentrated within the uterus or the tubes and does not spill into the abdominal cavity, which remains hypoechoic (Fig. 3.61).

As the contrast medium is extremely hyperechogenic and can be visualized for several minutes, it is possible to study the tubal course and shape (Fig. 3.62).

Hysterosalpingo-contrast sonography associated with transvaginal scanning can be used for primary investigation of infertility in women on an outpatient basis. Hysterosalpingo-contrast sonography performed with a combination of air and saline is a quick, inexpensive, well-tolerated method for determining tubal patency, but it requires some experience. One of the most important advantages

Fig. 3.61. Hysterosalpingo-contrast sonography with low acoustic pressure and new ultrasound contrast media. (a) Patent tube; the hyperechoic contrast agent is seen on the left in the uterine cavity, in the tube (note visualization of the tubal course), and on the right around the ovary. (b) Tubal occlusion; the hyperechoic contrast medium is seen only in the uterine cavity and not laterally to the uterus nor in the pelvis, which is anechoic

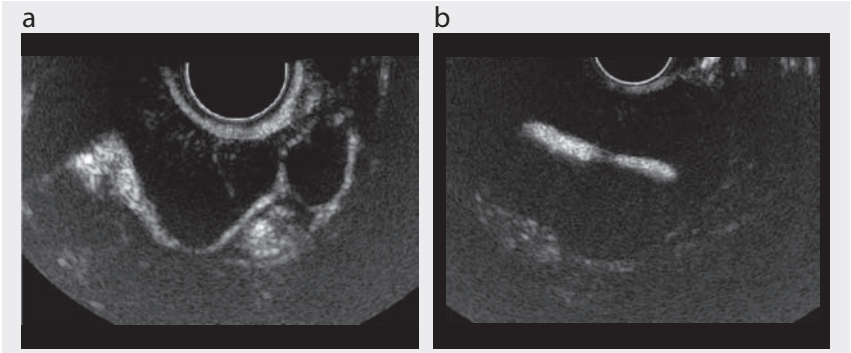

Fig. 3.62. Patent tubes on hysterosalpingo-contrast sonography with low acoustic pressure and new ultrasound contrast media. The hyperechoic contrast clearly shows the course of the tubes; the organs beneath the tubes are excluded from the image due to the harmonic signal response of the contrast medium microbubbles and to the broadband ultrasonic signals from surrounding tissue filtered out by the software. (a) Tube with an angle. (b) Tortuous tube

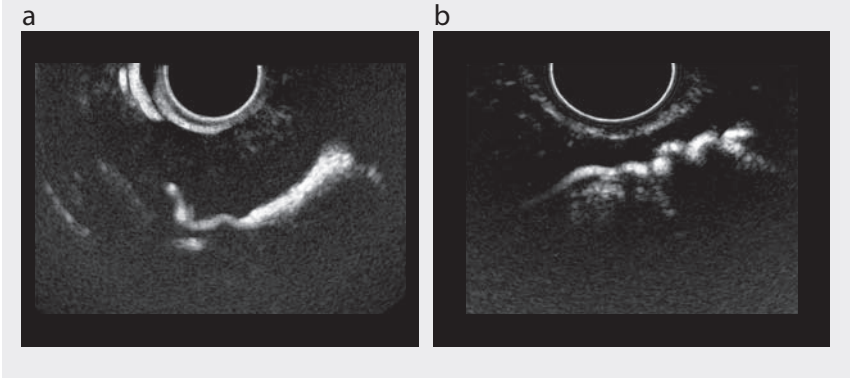

of this technique is that information on tubal status and the uterine cavity can be obtained at the same time as the transvaginal ultrasound scan. Hysterosalpingo-contrast sonography performed with dedicated ultrasound contrast media and low acoustic pressure is an accurate method for obtaining information on tubal status and, in particular, on tubal occlusion. When combined with a transvaginal scan, it can replace a hysterosalpingogram and does not require a high degree of experience. If tubal occlusion is diagnosed by hysterosalpingo-contrast sonography, laparoscopy should be considered as the second-line procedure.

Chapter 4

Breast

4

Breast

Normal anatomy, basic examination and biopsy technique

Indications

Breast ultrasound is a non-invasive imaging technique for diagnosing breast disease. Mammography is a well-established imaging tool for screening breast cancer in order to reduce its inherent mortality by an early diagnosis. Even so, mammograms do not detect all breast cancers: some breast lesions and abnormalities are not visible or are difficult to interpret on mammograms. In dense breasts (a lot of breast tissue and less fat), many cancers can be hard to see on mammography.

Breast ultrasound can be used in several ways. The commonest application is for investigating an area of the breast in which a problem is suspected. A palpable lump or a lump or density discovered by X-ray imaging (mammogram) can be evaluated further by ultrasound. This is especially helpful for distinguishing between a fluid-filled cyst and a solid mass.

Breast ultrasound is often the first examination performed to evaluate masses in women under 35 years of age, whose mammograms can be difficult to interpret because of the density of their breast tissue. Ultrasound may also be used in women for whom radiation is contraindicated, such as pregnant women, young women and women with silicone breast implants.

Breast ultrasound is also used to observe and guide a needle in several interventional procedures, including cyst aspiration, fine-needle aspiration, large-core needle biopsy and needle localization in surgical breast biopsy. Biopsies guided by ultrasound have distinct advantages: they are generally less costly than surgical biopsies, and, if the abnormality to be sampled can be seen on both a mammogram and ultrasound, an ultrasound-guided biopsy is often more comfortable for the woman, as no compression is necessary.

Preparation

The ultrasound unit should be on the woman's right. The radiologist takes images with the right hand and operates the machine with the left hand. The woman is in a supine position with a raised arm, and the examiner sits at her level. A raised arm

flattens and immobilizes the breast on the chest wall by tension on the pectoral muscles. This position is the same as that used for breast operation and ensures the reproducibility of the examination. Larger breasts shift laterally, creating non-uniform tissue distortion. In this case, the radiologist should ask the woman to roll to allow study of the lateral quadrants. Asking the women to assume a sitting position might help the examiner to localize the lesion if a palpable mass cannot be found when she is in the supine position.

Before the procedure, clear gel is applied to the woman's skin to allow smooth movement of the transducer over the skin and to eliminate air between the skin and the transducer. The transducer is held at the base, in maximum contact with the fingers and palm. The examiner's forearm rests lightly on the woman's torso, and the movement of the transducer is controlled by the wrist, not the entire arm.

Examination technique

Real-time hand-held scanners should include a linear array and a high-frequency transducer operating at a frequency of 7.5–10 MHz or more, which provides good tissue penetration to 4–5 cm. The depth of focus is placed at ≤ 3 cm. The time-compensated gain curve should be adjusted so that fat is uniformly grey, from the subcutaneous tissue to the chest wall. Improper adjustment of technical parameters can lead to suboptimal images and produce artefactual echoes that can result in misdiagnosis. Routine calibration of the unit and evaluation of the unit's performance with a breast phantom help prevent technical errors.

To ensure that the field of view includes all the breast tissue, from the skin surface to the chest wall, the operator should see the pectoral muscles and the chest wall at the bottom of the screen. In order to reduce reflective and refractive attenuation, the transducer should be kept parallel to the breast surface and the ultrasound beam perpendicular to the breast tissue by applying gentle, uniform pressure. Use of a Doppler probe during an ultrasound procedure allows assessment of blood flow within the breast.

The breast is moveable and contains few anatomical landmarks. In order to achieve complete coverage, a systemic scanning pattern is needed, involving sagittal, transverse, radial and tangential scans. Radial scanning is critical for detecting intraductal mammary lesions. If it is not viewed along the long axis of the duct, a mass will be difficult to detect; it is relatively easy to see a mass in the duct when the transducer is aligned along it.

An ultrasound examination should always be complemented by a study of the axillary regions.

Palpation during scanning allows precise localization of palpable abnormalities. It enables the examiner not only to find subtle lesions, but also to determine

whether normal structures, such as fat lobules and thickened Cooper ligaments, are responsible for a palpable abnormality.

Once an area of interest or a mass is identified, the image should be large enough to fill the monitor or screen, so that its important features can be evaluated. The focal zone, the time-compensated gain curve and the depth-compensated gain curve should be reset on the lesion. Each image should be labelled as pertaining to the right or left breast, the quadrant or clock position, the scanning plane (radial, longitudinal or transverse) and the number of centimetres from the nipple.

A good ultrasound study is difficult to obtain if the woman cannot remain quietly in one position. Obesity and excessively large breasts may interfere with breast ultrasound.

The examination may take from 20 to 40 min.

Normal findings

Each breast has 15–20 sections, called lobes, which are arranged in a radial fashion from the nipple. Each lobe is triangular and has one central excretory duct that opens into the nipple. Each lobe has many smaller lobules, and the spaces between the lobules and ducts are filled with fat. Fibrous strands of connective tissue (Cooper ligaments) extend from the skin to the underlying pectoralis fascia and are arranged in a honeycomb-like structure surrounding the breast ducts and fat (Fig. 4.1). The most superficial lobes are attached by their summit to the superficial layer of the fascia and constitute the Duret crests. The deepest crests connect the anterior lobes to the deep layer through the suspensory Cooper ligament. The ratio of supporting stroma to glandular tissue varies widely in the normal population and depends on the woman's age, parity and hormonal status. In young women, breast tissue is composed mostly of dense glandular tissue; with age, the dense tissue turns into fat. Each breast also contains blood vessels and vessels that carry lymph.

Fig. 4.1. Anatomical drawing of the breast

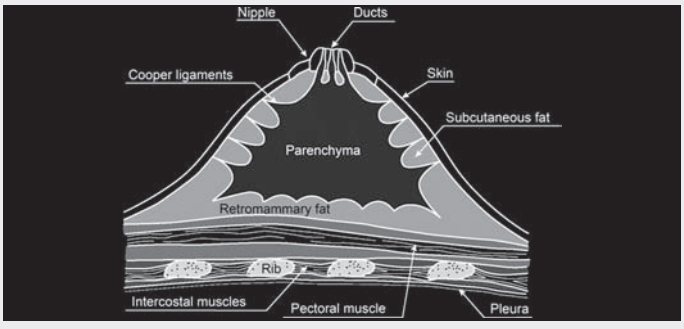

Skin

The skin line is a bright linear echo immediately under the transducer (at the top of the image). The skin line is normally 2–3 mm thick and has an echo-poor layer of subcutaneous fat immediately beneath it (Fig. 4.2, Fig. 4.3).

Fig. 4.2. Sonographic breast anatomy: longitudinal scan of the left breast. The field of view includes all breast tissue, from the skin surface to the chest wall (pleura and ribs are visible at the bottom of the screen)

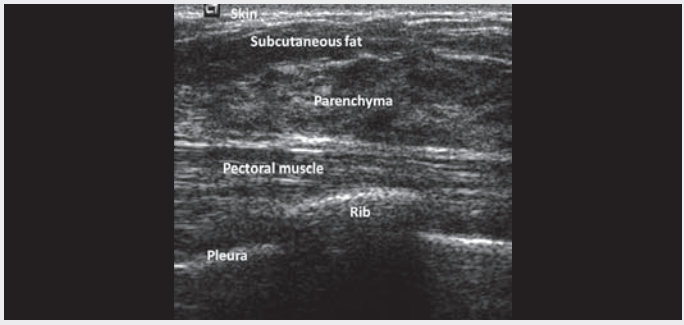

Fig. 4.3. Cooper ligaments: thin linear echogenic structures that support the surrounding fat and glandular elements

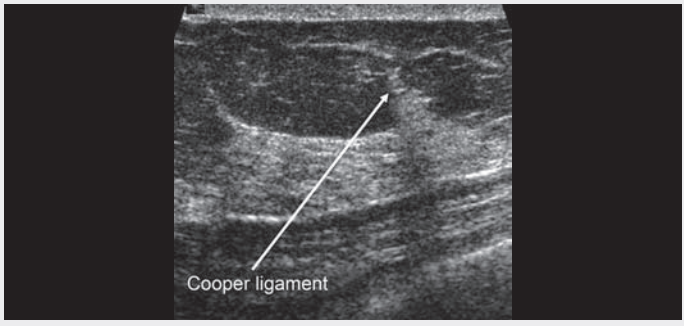

Subcutaneous fat

Fat in the breast appears dark or echo-poor. The only exception to echo-poor fat in the breast is echogenic fat in the lymph node hilum. Subcutaneous fat lies between the skin and the breast parenchyma; it is homogeneous and variable in quantity (Fig. 4.2, Fig. 4.3).

Cooper ligaments

Cooper ligaments are thin, linear, echogenic structures that support the surrounding fat and glandular elements. Attenuation of ultrasound by Cooper ligaments (especially in the subcutaneous fat region) may be mistaken for a lesion. The examiner should change the angle of the transducer or compress it over the area to exclude a lesion (Fig. 4.1, Fig. 4.3).

Parenchyma

Breast parenchyma appears echogenic, with intermediate echogenicity between the echo-rich connective tissue and the lower echogenicity of fat tissue, and lies beneath the subcutaneous fat. The pattern of parenchymal echogenicity (mixed) depends on age, glandular density, menstrual cycle phase, pregnancy and lactation (Fig. 4.4, Fig. 4.5).

Fig. 4.4. Dense breast: high echogenicity of parenchyma

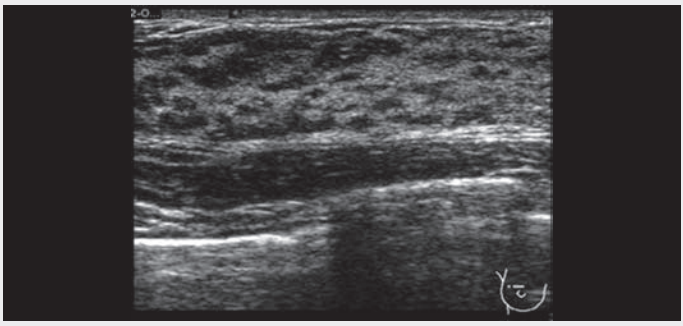

Fig. 4.5. Fatty breast: low echogenicity of parenchyma

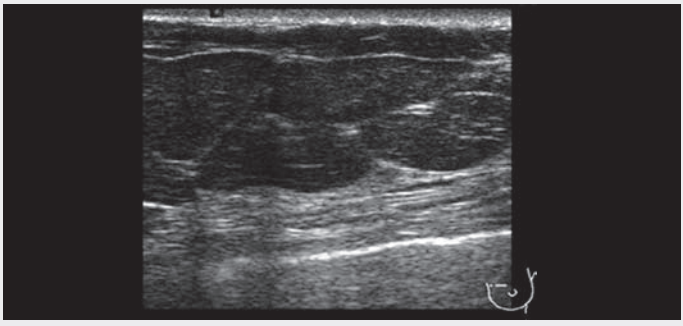

Retromammary fat

The retromammary fat is posterior to parenchyma (Fig. 4.1).

Pectoral muscle

The pectoral muscle (anterior to the ribs) is an echo-poor structure of varying thickness that contains thin lines of supporting stroma coursing along the long axis of the muscle (Fig. 4.1, Fig. 4.2).

Ribs

The ribs, contained in the intercostal muscles, are round or oval in cross-section and cause an intense acoustic shadow due to bone attenuation. High-resolution transducers may display calcifications in the anterior portions of cartilaginous elements of the ribs (Fig. 4.1, Fig. 4.2, Fig. 4.6).

Fig. 4.6. Ribs are visualized in cross-section as round or oval structures; calcifications can be seen in the anterior portion

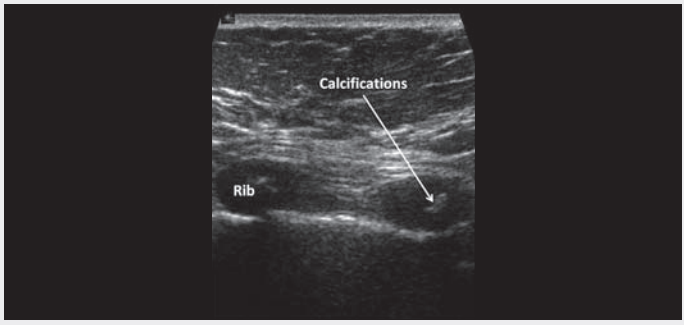

Pleura

The pleura gives echogenic lines deep to the ribs that move with respiration (Fig. 4.1, Fig. 4.2).

Nipple

The nipple is an echo-poor structure consisting of dense connective tissue and subareolar ducts, which can cause posterior acoustic shadowing. Sound attenuation by the nipple improves with pressure (Fig. 4.1, Fig. 4.7).

Ducts

Ducts are tubular branching structures leading to the nipple (Fig. 4.1, Fig. 4.7).

Fig. 4.7. The nipple is an echo-poor, oval structure that can cause posterior acoustic shadowing; the ducts are tubular echo-free structures leading to the nipple

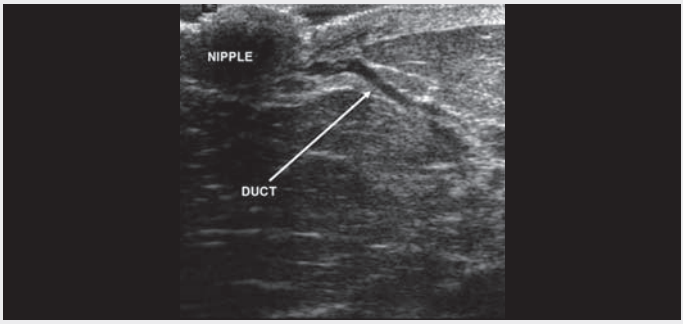

Lymph nodes

Lymph nodes appear as solid, oval structures with a thin, homogeneous, echo-poor cortex and an ovoid, echogenic, fatty hilum. Lymph nodes are generally visualized in the axilla region (Fig. 4.8). Small lymph nodes with normal findings can also be detected within the breast (Fig. 4.9).

Fig. 4.8. Axillary lymph node (arrows)

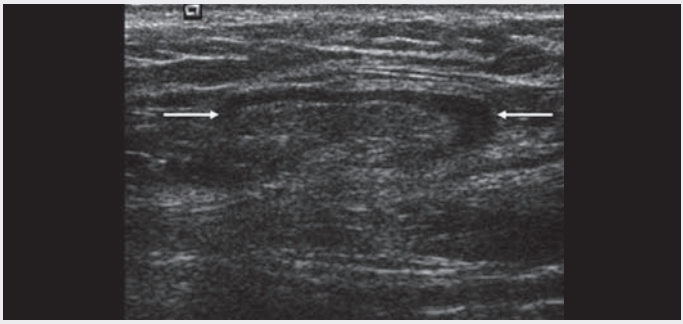

The accuracy of ultrasound depends on the operator, and considerable observer variation in the descriptions and assessments of breast lesions have been reported. Referring physicians, other radiologists and women would benefit from standardization of the terms for characterizing and reporting lesions. Therefore, a lexicon of descriptors and assessment categories has been drawn up by the American College of

Radiology to promote the clinical efficacy of breast ultrasound. The lexicon (Breast Imaging Reporting and Data System) includes ultrasound descriptors for shape, orientation, margins, lesion boundary, echo pattern, posterior acoustic features and alterations to surrounding tissue. On the basis of these descriptors, each lesion was assigned an assessment category associated with the most appropriate clinical management of the woman (Table 4.1).

To perform a correct breast ultrasound examination, the following diagnostic algorithm can be used:

1. scanning of the entire breast
2. detection of lesion
3. adjustment of technical parameters
4. study of lesion
5. classification of lesion
6. referral.

Fig. 4.9. Intramammary lymph node (arrows)

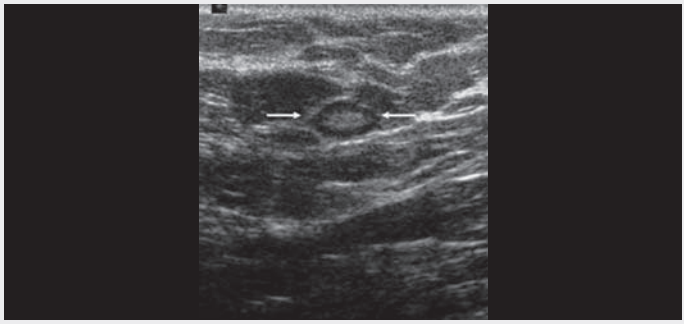

Table 4.1. Breast Imaging Reporting and Data System, final assessment categories

Category	Assessment
0	Need additional imaging
1	Negative
2	Benign finding(s)
3	Probably benign finding; short-interval follow-up suggested
4	Suspected abnormality; biopsy should be considered
5	Highly suggestive of malignancy; appropriate action should be taken
6	Biopsy-proven malignancy; appropriate action should be taken

Biopsy

Pre-biopsy work-up

Non-palpable, sonographically detected breast lesions are amenable to preoperative localization or percutaneous biopsy. Informed consent is an important part of these procedures: the woman should be informed about the risks, benefits and alternatives to biopsy. Possible risks include inability to sample the lesion, haematoma, bleeding, pneumothorax and breast infection. Local anaesthesia is routinely used for breast biopsy and preoperative needle localization. A common local anaesthetic for percutaneous breast procedures is lidocaine or Carbocaine, which is injected through a 25-gauge needle. Sterile technique is always recommended.

Biopsy technique

Preoperative needle localization

With the woman in the supine position, the radiologist rolls her until the needle path is directed safely away from the chest wall. Under direct ultrasound visualization, the radiologist plans the path of the needle to the lesion. Once the needle is within the lesion, the hook-wire is placed and the needle is removed.

Fine-needle aspiration or core-needle biopsy

For fine-needle aspiration, the radiologist introduces a needle (generally 21–25 gauge) in the plane of the transducer under direct visualization to show the entire shaft of the needle and the lesion to prevent pneumothorax. Once the needle is within the lesion, the material for cytological evaluation is aspirated with a to-and-fro movement.

For core biopsy, the radiologist determines whether the lesion is in a safe location (away from the chest wall) and calculates the needle throw to ensure that the core trough is in the middle of the lesion. In a core biopsy (generally with an 18- to 14- or 11-gauge needle in the case of vacuum-assisted biopsy), the skin is sterilized, and the core needle track is anaesthetized under ultrasound with a fine needle that reproduces the core biopsy trajectory. A scalpel is used to make a skin nick to introduce the large-core biopsy needle. Under direct ultrasound, the large-core biopsy needle is introduced into the breast to the edge of the lesion, and the biopsy core needle is used. The core is harvested, and direct pressure is exerted on the breast.

New ultrasound techniques

New ultrasound techniques, such as tissue harmonic imaging, spatial compound, ultrasound elastography and three-dimensional ultrasound, have improved the quality of ultrasound breast images and show promise for diagnosing cancerous breast lesions in a non-invasive manner.

In **harmonic imaging**, the ultrasound machine scans images at twice the frequency transmitted. This can suppress reverberation and other near-field noise, but it may limit the depth of penetration. Harmonic imaging reduces the possible number

of complex cysts or solid masses seen on breast ultrasound and increases the examiner's confidence that a lesion is in fact truly cystic and benign. The procedure may also better define the boundaries of lesions, which is important for distinguishing benign from malignant lesions.

In **spatial compound imaging**, information is obtained from several different angles of insonation and is then combined to produce a single image at real-time frame rates. Because images are averages from multiple angles, the image artefacts inherent to conventional ultrasound are reduced. Spatial compound imaging has also been shown to reduce speckle artefacts, improve visualization of low-contrast lesions, enhance tumour margins and improve images of the internal architecture of solid lesions and microcalcifications.

Elastography is a low-frequency vibration technique used to evaluate the elastic properties of tissues. It is performed by applying slight compression and comparing images obtained before and after compression.

Three-dimensional ultrasound: Two-dimensional transducer arrays can now produce three-dimensional ultrasound images, which have the advantage of being more rapid and reproducible and may solve the problem of screening ultrasound. Screening ultrasound has great potential, but screening the entire breast sonographically is labour-intensive and time-consuming for radiologists. A screening test should be simple, relatively cheap and, ideally, not require the presence of a physician. Screening by a technician or sonographer with three-dimensional ultrasound would permit a radiologist or another physician to review the data set in multiple scan planes, including radial planes.

Benign lesions

Cysts

Cysts are the commonest benign diseases of the breast found on ultrasound study. They are most often observed in pre-and perimenopausal women but sometimes occur in postmenopausal women, particularly in those receiving hormonal replacement therapy (estrogens). Under ideal conditions with suitable equipment, ultrasound can identify even 2- to 3-mm cysts and differentiate them from solid lesions with 95–100% accuracy. Differentiation between fluid-filled and solid lesions is the major function of sonography.

Simple cysts (Fig. 4.10) are defined by precise ultrasound characteristics. They are echo-free, roundish or oval, with well-defined anterior and posterior margins and posterior enhancement. A lesion with these features can be classified as a simple cyst and thus considered a benign lesion not requiring additional assessment, interventional procedures or follow-up. Ultrasound study of a simple cyst can, however, present a number of difficulties. In 25% of cases, posterior enhancement is not seen, especially in deeply located cysts, as the acoustic attenuation caused by adjacent

Fig. 4.10. Simple cyst, seen as an echo-free lesion with well-defined anterior and posterior margins and posterior enhancement

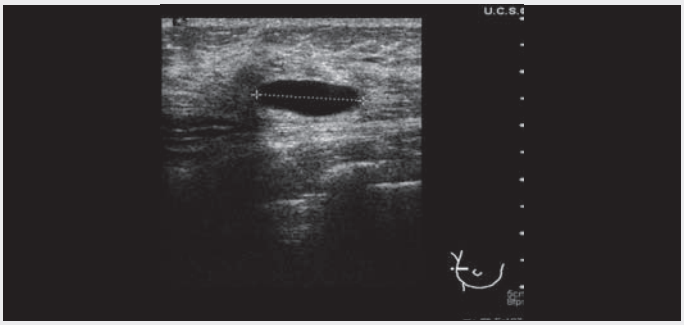

muscles and costal cartilage modifies the posterior enhancement usually associated with a fluid structure. The problem can often be overcome by scanning from different angles, by changing the woman's position or by probe compression.

Sometimes there is posterior beam attenuation behind the central portion of the cyst, due to the presence of calcifications deposited along the cystic wall. This artefact is typical of long-standing formations. Calcifications within the cyst (milk of lime) appear as structured echoes, which are mobile with changing posture and often lack the characteristic posterior attenuation of the beam. Inner echoes can be due to reverberation artefacts, which tend to involve the anterior margin of the lesion while the posterior margin remains evident and well defined. Careful equipment setting, such as precise focusing and correct gain adjustment, will optimize the diagnostic information.

Most lesions with inner echoes, sepimentations and posterior enhancement are **complex cysts** (Fig. 4.11), which are filled with protein or debris, mostly secondary to haemorrhagic or inflammatory phenomena. Ultrasound-guided aspiration of the lesion's content confirms the diagnosis and leads to cyst resolution (Fig. 4.12, Fig. 4.13) with no need for surgical excision. Each detail of a cyst should be carefully evaluated: markedly thickened walls and papillary lesions vegetating within the lumen can indicate a suspected malignant lesion, such as an intracystic carcinoma or a carcinoma with central necrosis (Fig. 4.14, Fig. 4.15). In these cases, surgical excision may be indicated, as cytological examination of the inner fluid is not always diagnostically reliable.

Sebaceous cysts can also occur in the breast, although they are much commoner in the back and neck. These benign lesions, containing keratin and with a capsule of squamous epithelial cells, often appear to be solid, both clinically and at mammography. On ultrasound, they appear as well-marginated formations containing uniformly distributed low-level echoes with evident posterior enhancement.

Fig. 4.11. Complex cyst: lesion with inner echoes, well-defined margins and posterior enhancement

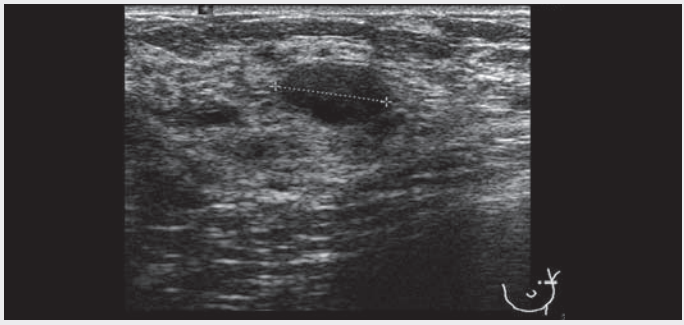

Fig. 4.12. Ultrasound-guided aspiration of echo-poor lesion (complex cyst)

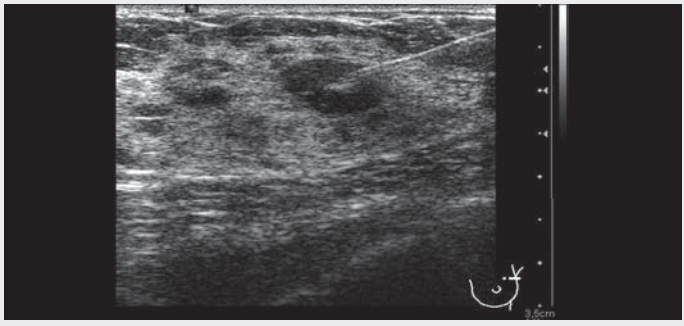

Fig. 4.13. Disappearance of the lesion content leads to cyst resolution and confirms the diagnosis

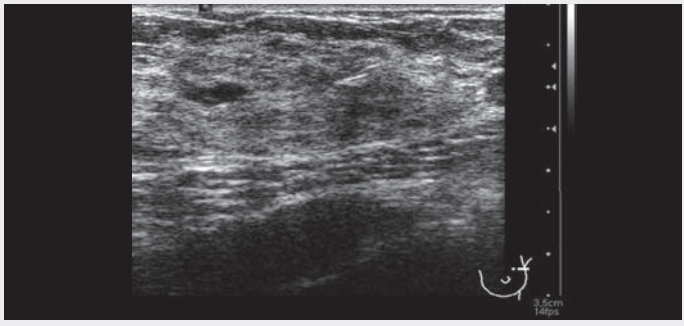

Fig. 4.14. Intracystic cancer seen as a papillary irregular lesion vegetating within the lumen of a cyst

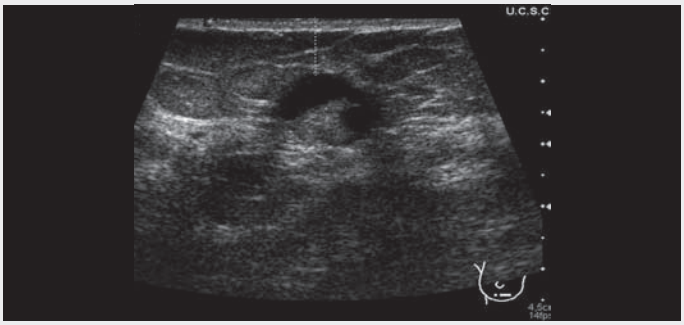

Fig. 4.15. Colour Doppler showing a large vascular spot in the solid part of the lesion

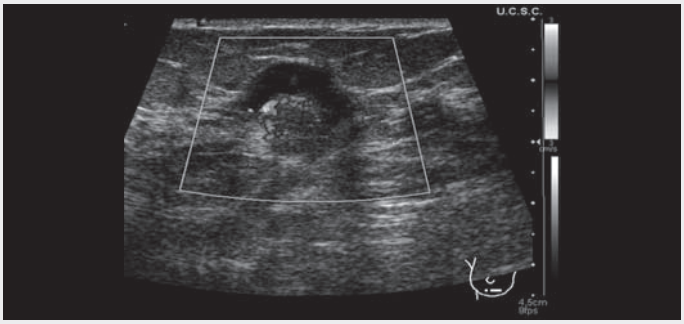

Acute mastitis and abscesses

Acute mastitis, although most common in breastfeeding women, can also affect other women. In most cases, the diagnosis is clinical. In women who do not respond adequately to even prolonged antibiotic therapy, the presence of an abscess should be excluded, because in these cases the elective treatment is surgery.

On ultrasound, **uncomplicated mastitis** appears as an echo-rich area with blurred margins and an inhomogeneous echoic structure (Fig. 4.16, Fig. 4.17). **Abscesses** appear as fluid-filled focal lesions. Their overall morphology varies from echo-free to echo-poor. Inner echoes, sometimes with fluid–fluid or fluid–debris levels, inner sepimentations and posterior enhancement, are frequent. An abscess cannot, however, be distinguished definitively on sonography from a non-infectious fluid collection. Ultrasound can be used to guide aspiration or definitive drainage.

Fig. 4.16. Uncomplicated mastitis, seen as an area with blurred margins and mixed structure

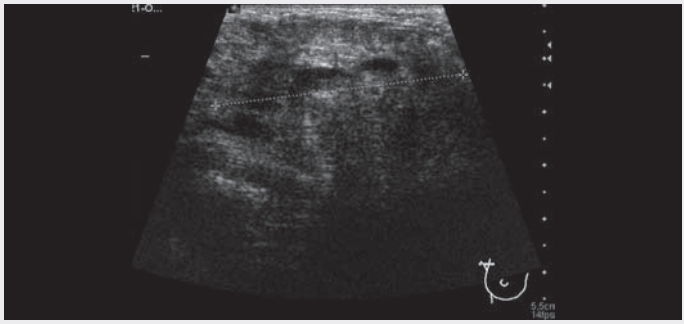

Fig. 4.17. Uncomplicated mastitis (in another patient), seen as an inhomogeneously echo-poor structure

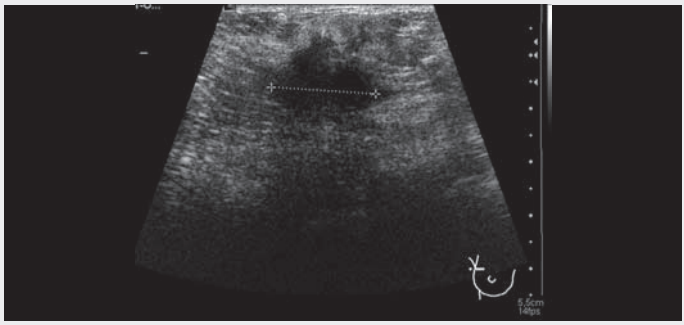

A differential diagnosis of inflammatory carcinoma is not always possible, as some have features that are similar to or even indistinguishable from those of mastitis or abscess (Fig. 4.18), both clinically (diffuse cutaneous thickening, reddening, erythema and generalized oedema) and sonographically.

Fig. 4.18. Inflammatory fluid collection: an echo-free, irregular area with internal sepimentation and an echo-poor lesion along the anterior wall

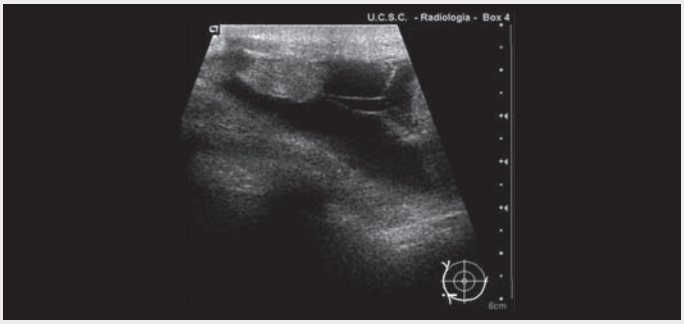

Haematoma

Breast haematoma may occur after an intervention or breast trauma. On ultrasound, it appears as an echo-rich to echo-free, well-marginated lesion, depending on its age and organization (Fig. 4.19).

Fig. 4.19. Breast haematoma, seen as an inhomogeneously echo-poor, well-marginated lesion

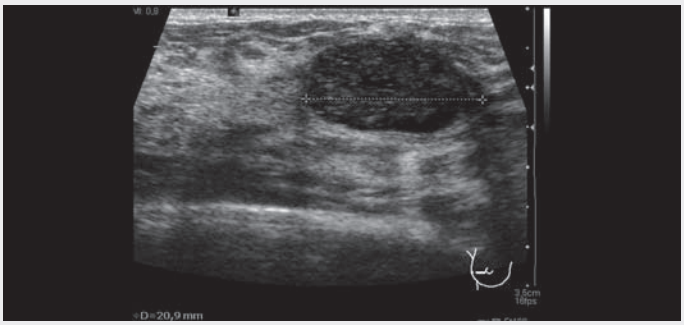

Fibroadenoma

Fibroadenomas are the most frequent solid lesions in women of premenopausal age. They are composed of epithelial cells and fibrocytes. Most are single lesions, but in 10–20% of cases they are multiple or bilateral. Fibroadenomas usually stop growing once they reach 2–3 cm (maximum diameter), unless there is abnormal hormonal stimulation, such as during pregnancy or in postmenopausal women under replacement therapy. Usually, they regress or undergo hyaline degeneration after menopause.

While not pathognomonic, the ultrasound features are a homogeneously echo-poor oval or roundish formation with regular or multilobular margins and no posterior beam attenuation or posterior enhancement (Fig. 4.20). These four features are present in only a small percentage (about 16%) of cases: 15–31% of lesions show multilobular margins and 25–58% show irregular margins. In over 11% of fibroadenomas, the pattern of inner echoes ranges from echo-rich to isoechoic, and inner echoes of inhomogeneous distribution are present in 12–52% of lesions, probably indicating the presence of hyaline necrosis, calcifications and fibrosis. In 9–11% of cases, there is posterior beam attenuation.

Fig. 4.20. Fibroadenoma: a homogeneously echo-poor, oval formation with regular margins and no posterior beam attenuation or posterior enhancement

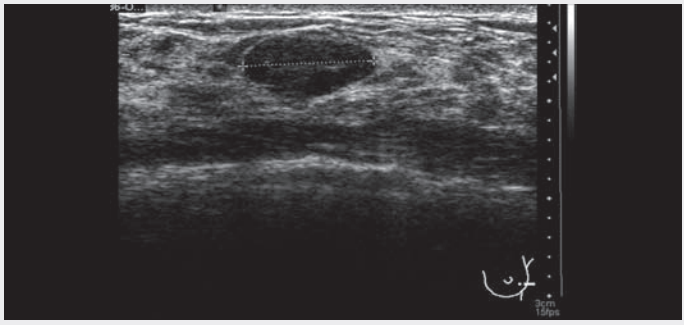

A definitive differential diagnosis of a fibroadenoma from a malignant lesion cannot be established on the basis of ultrasound criteria alone. In 10–25% of cases, breast tumours have circumscribed margins and benign ultrasound features. Use of the ratio between the axial diameter and the anteroposterior diameter of the lesion has been proposed as a fairly reliable criterion for differential diagnosis, with a suggested cut-off of 1.4. Higher ratios have been observed for most fibroadenomas but only rarely for tumours. Fibroadenomas can be difficult to identify in predominantly fibroadipose breasts, and use of high-frequency probes and the second harmonic may increase the detection rate.

Phyllodes tumour

Phyllodes tumour is a rare fibroepithelial tumour accounting for 0.3–1.5% of all breast tumours and 2.5% of all fibroepithelial tumours. Its relation to fibroadenoma is not clear. They show high cellularity, a sarcoma-like stroma and often contain fluid areas; they have a higher cell count, and the myxoid stroma is more evident than in normal fibroadenomas. These tumours are found mainly in women in the 5th to 6th decade of life and rarely in women < 20 years. Most phyllodes tumours are benign, but the differential diagnosis between benign, malignant and borderline lesions is based on histological appearance. Clinically, most phyllodes tumours are palpable large masses with alternating periods of rapid growth and remission. On ultrasound, they are solid, well-marginated, oval or lobulated formations. Smaller lesions are practically indistinguishable from fibroadenomas. In larger lesions, the presence of small cyst-like fluid collections, while not pathognomonic, suggests the diagnosis (Fig. 4.21).

Fig. 4.21. Phyllodes tumour, seen as a large mass with complex echo structure and small internal cyst-like fluid collections

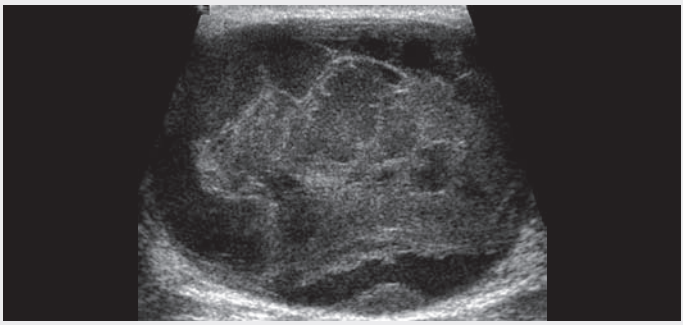

Intraductal papilloma

Intraductal papillomas are benign lesions characterized by epithelial proliferation protruding into the ductal lumen around an axis of connective and vascular tissue of variable thickness. Solitary papillomas are usually retroareolar (Fig. 4.22, Fig. 4.23), affect the main lactiferous ducts and are often accompanied by disorders of the nipple (haemorrhagic or serohaemorrhagic secretion). Papillomas growing within the terminal ducts and lobules are usually peripheral and tend to be multiple.

On ultrasound, they are represented by solid formations (when sufficiently large to be visualized) protruding into a usually ectatic duct, which allows their visualization. Use of high frequencies helps detect smaller lesions.

Fig. 4.22. Intraductal papilloma affecting the main retroareolar ducts: a small, echo-poor formation protruding from the wall into the lumen of the ectatic ducts

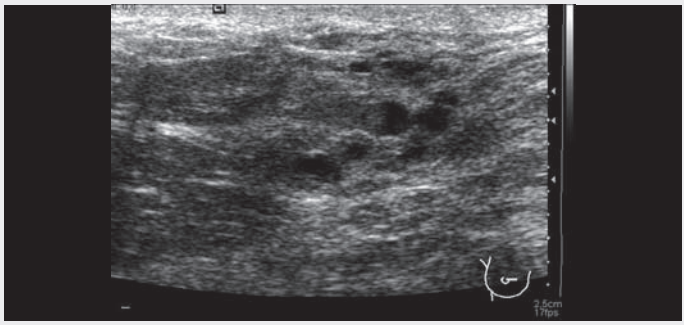

Fig. 4.23. Another case of intraductal papilloma affecting the main retroareolar ducts

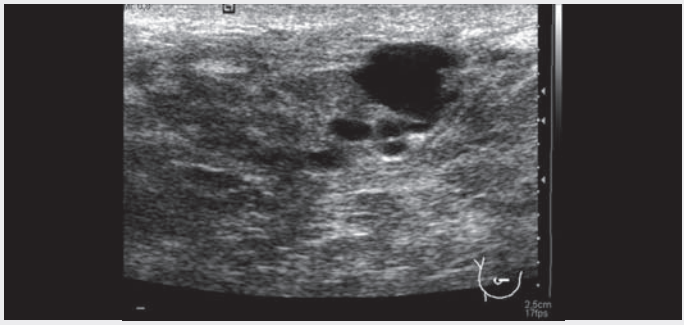

Intraparenchymal lymph nodes

Lymph nodes within the breast parenchyma are usually located in the upper external quadrants and may be palpable. On ultrasound, normal lymph nodes appear as well-circumscribed formations of roundish, oval or lobulated morphology, echo-poor to the surrounding parenchyma, often with an echo-rich centre representing the adipose hilum (Fig. 4.24). Pathological processes involving the axillary nodes can extend to the intraparenchymal nodes, which usually appear enlarged and destructured, that is, homogeneously echo-poor, globular, with a diffusely or focally thickened cortex in the absence of an echo-rich hilum (Fig. 4.25).

Fig. 4.24. Intraparenchymal lymph node seen as a well-circumscribed, oval formation, echo-poor, with an echo-rich centre representing the adipose hilum

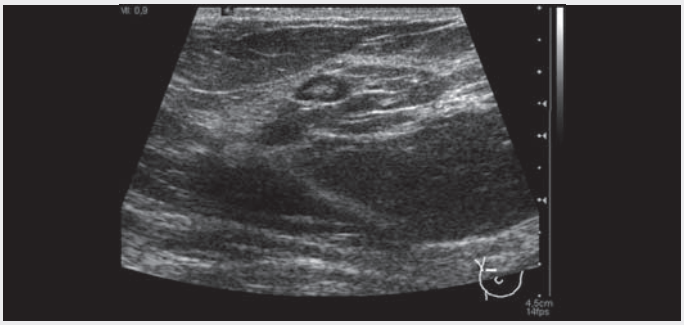

Fig. 4.25. Pathological intraparenchymal node, which appears enlarged and destructured, globular, with a diffusely thickened cortex and posterior beam attenuation

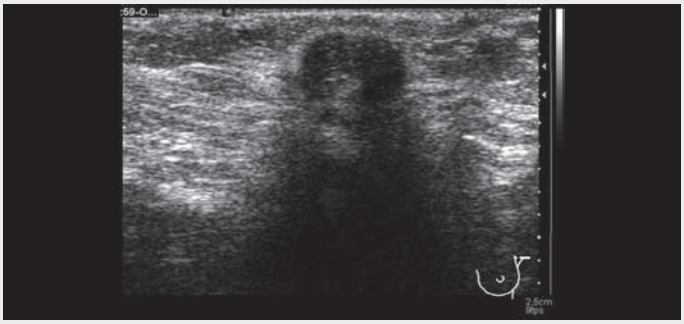

Fibrocystic alterations

Fibrocystic alterations are found clinically in 50% of women but histologically in about 90%. Histological abnormalities involving both the fibrous tissue and the glandular parenchyma include exuberant proliferation and growth of connective tissue, ductal cystic dilatation and ductal or lobular cell hyperplasia.

Fibrocystic mastopathy or **benign mammary dysplasia** occurs mainly in young women (25–45 years) and is characterized clinically by diffuse nodularity, palpable mainly in the upper external quadrants and associated with more pronounced pain during the menstrual cycle. On ultrasound, localized mastopathy appears as poorly marginated, echo-rich areas with inner cystic formations of variable dimensions, some with thickened and blurred walls indicating inflammatory phenomena, occurring mainly during periods of high hormonal stimulation (Fig. 4.26).

Fig. 4.26. Localized fibrocystic mastopathy: seen as a poorly marginated, echo-rich area with inner cystic formations of variable dimensions

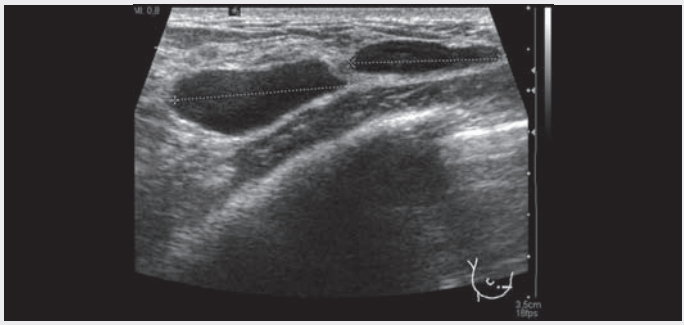

Sclerosing adenosis is a fibrocystic disorder characterized histologically by intralocular fibrosis and proliferation of small ducts or acini. On ultrasound, it can appear heterogeneous, depending on the predominant component involved in proliferation: as a large, solid formation with posterior beam attenuation when the fibrous component is widely involved, or as a macrocystic cluster with numerous acoustic interfaces and frequent calcium deposits along the walls when the fluid component is prevalent (Fig. 4.27).

Fig. 4.27. Sclerosing adenosis, seen as a large, solid, inhomogeneously echo-poor formation with indistinct margins and an echo-rich halo

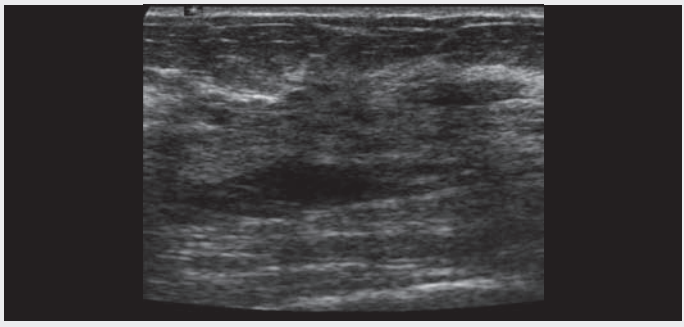

Fibrolipoadenoma

Fibrolipoadenoma is a rare benign tumour, also called a hamartoma, usually found in maturity. It consists of the contemporary presence of epithelial structures (such as lobules and ducts) and a mesenchymal component (represented by fibrous and adipose tissue). Fat, fibrous and glandular tissue can be present in various proportions, which determine the ultrasound appearance of the lesion. A well-defined nodular formation, often with gentle lobulated contours, of mixed, inhomogeneous appearance is seen, with echo-rich areas representing the fibroglandular component, and echo-poor areas representing the adipose component (Fig. 4.28).

Fig. 4.28. Fibrolipoadenoma, seen as a well-defined, oval formation with regular contours and mixed internal structure due to the contemporary presence of echo-rich and echo-poor areas representing fibroglandular and fatty components, respectively

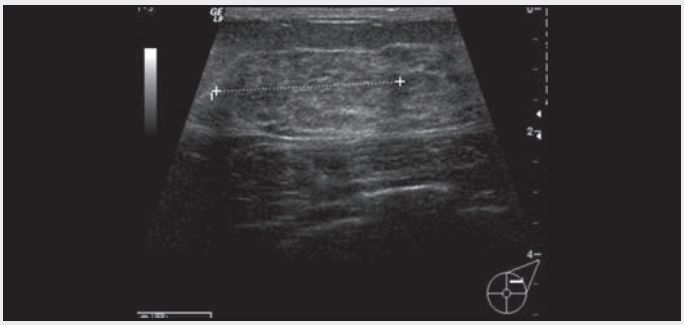

Galactocoele

Galactocoele is a benign cystic swelling that appears during breastfeeding or immediately after. It is due to obstruction of a lactiferous duct, with consequent stagnation of milk secretion and the appearance of a milk-containing pseudocyst. On ultrasound, it appears as a clearly marginated, roundish or oval formation of mixed echo-free–echo-poor morphology, representing the presence of inner, mostly unstructured, mobile and coarse echoes, depending on the degree of milk coagulation (Fig. 4.29). Chronic galactocoele may show marked ultrasound absorption and, consequently, clear posterior attenuation, due to the formation of a dense, absorptive inner precipitate.

Fig. 4.29. Galactocoele, seen as a clearly marginated, oval formation with an echo-poor pattern indicating the presence of inner, mostly unstructured, mobile and coarse echoes representing coagulated milk

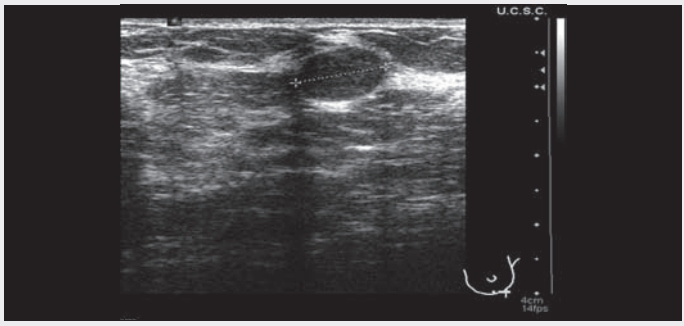

Adenoma

Tubular adenomas are benign tumours composed of numerous glandular formations clinging together, of uniform dimensions, lined with a single layer of epithelial cells. Adenoma of the nipple is a relatively rare benign lesion that affects mainly nulliparous women in their 40s to 50s. Clinically, on palpation, a retroareolar nodule is found, sometimes associated with nipple erosion, inversion and secretion. The nodule is a proliferation of glandular tubules involving the large retroareolar lactiferous ducts, which may show epithelial cell hyperplasia with a solid papillary architecture. Frequently, there is associated apocrine or squamous metaplasia and dense stromal fibrosis, with no evidence of a real capsule, sometimes with signs of

Fig. 4.30. Lactating adenoma, seen as a large, echo-poor area with blurred, poorly defined posterior margins, located behind the nipple and involving the main retroareolar ducts

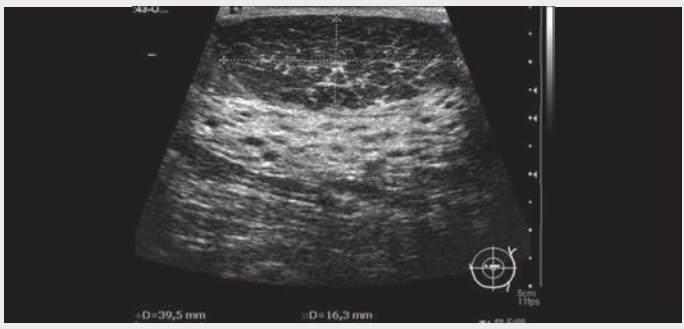

distortion and pseudo-infiltration of the ductal component (Fig. 4.30). On ultrasound, tubular adenomas appear as echo-poor areas with blurred, poorly defined margins, located immediately behind the nipple, often poorly distinguishable or differentiable from a malignant lesion, especially if there is abundant fibrosis causing posterior beam attenuation.

Liponecrosis

Liponecrosis is an infrequent disease, occurring mainly in obese and middle-aged women. It may be a consequence of rupture of dilated ducts or cysts but is most frequently traumatic or iatrogenic in origin (after breast surgery). The lesion is unilateral, and, if palpable, it appears as a small indolent nodule with a regular surface, poorly mobile, at times associated with skin retraction or an area of ecchymosis. It is caused by adipocyte necrosis and by the inflammatory reaction consequent to the release of lipid material through the cell membranes, typical of foreign body reactions, followed by the reparative phase, with formation of a capsule around the fatty material (lipophagic granuloma). As the process becomes chronic, a fibroelastic reaction occurs, with the formation of a scar and possible retraction of the overlying skin. At times, calcium salts may deposit as microcalcifications within the liponecrotic area.

On ultrasound, the appearance can be extremely heterogeneous. Liponecrosis can appear as a simple cyst, with typical posterior enhancement, as a complex cyst, roundish and echo-free, with small inner echogenic nodules (Fig. 4.31), as a straight or S-shaped band, or as an inhomogeneously echo-poor area with blurred margins, roundish or oval, at times with moderate posterior beam attenuation. Medical history and comparison with mammograms play major roles in differential diagnosis.

Fig. 4.31. Liponecrosis, seen as an inhomogeneously echo-poor area with blurred margins, irregularly roundish, with moderate posterior beam attenuation, located near a surgical scar

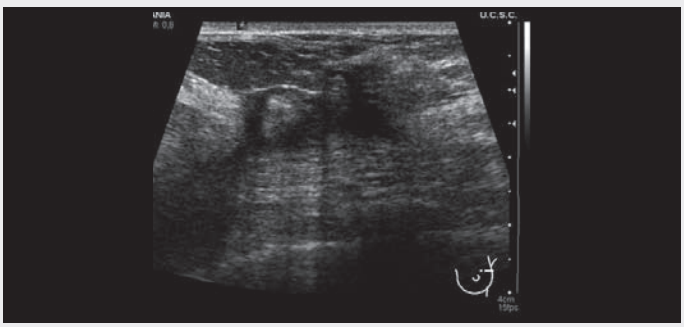

Male breast disease

The most frequent benign disease involving the male breast is so-called **gynaecomastia**, which is bilateral hyperplasia of the breast parenchyma. It should not be mistaken for pseudogynaecomastia, with an increased adipose component. This is readily observed on ultrasound, with the volumetric increase as well as with the typical diffuse echo-poor appearance of adipose breast. The incidence of gynaecomastia varies in relation to age, with a high prevalence in puberty and a peak (about 50% of cases) in adolescents up to 16 years. In most cases, it regresses spontaneously over some months. The prevalence increases again at older ages (> 50 years) due mainly to metabolic and pharmacological causes. The examination used preferentially is ultrasound, mainly to distinguish benign disease from male breast carcinoma.

Both on X-ray and ultrasound, three types of gynaecomastia are found: the nodular form, the dendritic form and the glandular form. The last is readily interpreted; it mimics the female breast in the florid phase, with the typical echo-rich appearance of parenchyma. The nodular form is usually retroareolar, echo-poor, with regular margins and contours, often accompanied by pain on palpation (Fig. 4.32).

Fig. 4.32. Nodular gynaecomastia, seen as a retroareolar, echo-poor, palpable mass with well-defined margins and contours

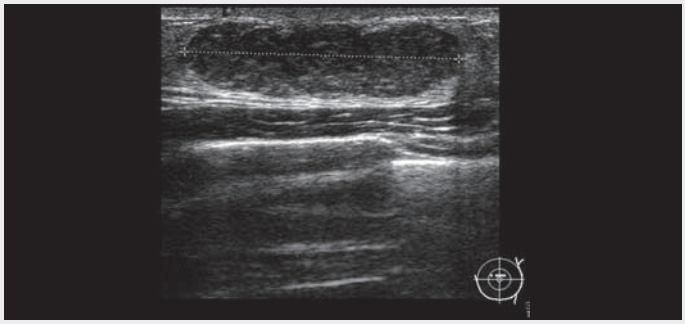

The dendritic form is typically echo-poor and is found in the retroareolar area (Fig. 4.33). It is often associated with echo-poor infiltration of the posterior tissue and is not readily distinguishable from a malignant neoplasm. In these cases, ultrasound can be used for a guided biopsy.

Fig. 4.33. Dendritic gynaecomastia, seen as an echo-poor, roundish lesion in the retroareolar area, with indistinct margins, associated with clear infiltration of the surrounding tissue

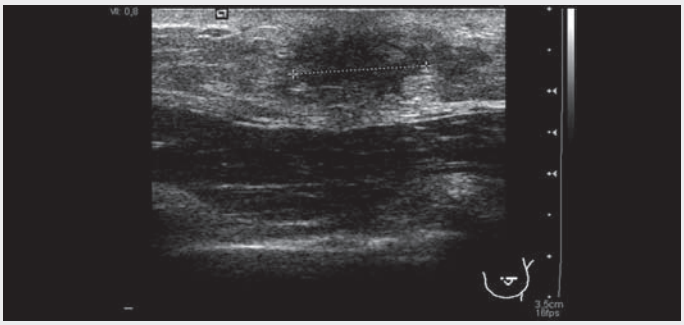

Malignant lesions

Breast cancer

Breast cancer is the most frequent malignant female cancer, occurring in 8–9% of women at some time in their lives. Epidemiological studies have shown a continuously increasing incidence of this disease, especially among women aged 45–65 years. Increases have also, however, been observed among older women, with the increase in natural human life, and, for unknown reasons, among younger women. The increase among women < 30 years is particularly worrying. Although the incidence of breast cancer is increasing linearly and continuously, mortality from this disease began to decrease from the second half of the 1980s as a result of early diagnosis and improved treatment.

Breast cancer is generally more frequent in urban than in rural populations and is 8–10 times more frequent in western and rich populations than in the poorest areas of the world. Several studies of lower-risk populations that have emigrated to countries with higher risk suggest that the reasons for the differences in incidences include the physical environment and cultural background. Notwithstanding knowledge about the risk factors for breast cancer, the reasons for the large international differences in the incidence of this disease are unknown, and, in countries with high incidences, it is not possible to identify subgroups of the population with a high concentration of cases on which to focus greater attention for early diagnosis.

The most useful criteria for identifying women at higher risk are age and family factors, such as a family history of breast cancer and a personal history of previous breast cancer. Despite the complex epidemiology of breast cancer, the list of further risk factors includes: null parity, higher age at first pregnancy, age at menarche, higher age at menopause, total calories consumed, postmenopausal obesity, alcohol

use, thorax irradiation, benign proliferative mastopathy, higher grade of education, use of hormonal replacement therapy, a higher level of low-density lipoprotein and a lower level of high-density lipoprotein and oxidative stress.

Role of ultrasound

Ultrasound examination of the breast is not an alternative to mammography but rather complementary, providing different information. It is particularly useful for examining young, dense breasts, for which mammography is less sensitive, and in pregnancy. Sometimes, ultrasound is the only means for understanding the nature of a mammographic abnormality or a palpable lesion, with adjunctive criteria, and can also be used as a guide during biopsy.

Ultrasound examination of the breast is conducted according to the criteria of the American College of Radiology. Accordingly, all signs of a suspected malignant lesion must be recorded: shape (irregular), orientation (not parallel to the skin), margins (not circumscribed), boundaries (echogenic halo), echo pattern (echo-poor), posterior acoustic features (shadowing), microcalcifications if present and vascularity (intra- and peri-lesional vascular spots on colour Doppler examination). The presence of these features, and particularly their association, supports a suspicion of a malignant lesion and thus the need for biopsy.

Breast lesions often represent benign conditions, such as cysts or fibroadenomas. If their diagnosis is verified, they are not a clinical problem for women.

Sonographic features

Premalignant lesions and in situ carcinomas

Epithelial malignant cancers account for 98% of all malignant breast neoplasms, including ductal carcinoma in situ, invasive ductal carcinoma and invasive lobular carcinoma. Differentiation of these forms is useful for defining the prognosis and therapy.

Ductal carcinoma in situ is constituted of a group of neoplastic cells inside the basal membrane, whereas the neoplasm becomes invasive if some neoplastic cells disrupt the membrane. The most frequent mammographic sign (60–80% of cases) of ductal carcinoma in situ is the presence of an isolated cluster of microcalcifications; in multifocal and multicentric forms, more than one cluster is located in the same or in different quadrants. Some microcalcifications, however, are associated with a nodular or spiculated mass (15–30%) or a nodular or spiculated opacity without microcalcification (10–15%). Generally, mammographic examination often underestimates the real extent of a ductal carcinoma in situ, particularly low-grade lesions. In these cases, ultrasound examination shows only the microcalcifications and does not identify their morphology clearly (as mammography does). Sometimes, a small, echo-poor lesion can be seen, with or without internal calcification. The distribution of the actual microcalcifications within a duct can sometimes be seen, especially when high-frequency ultrasound transducers are used.

Invasive carcinomas

Invasive ductal carcinoma is the most frequent malignant breast lesion; 3–5% of cases are multifocal and 10% of cases are multicentric. On ultrasound examination, an invasive ductal carcinoma is usually echo-poor, irregular, without circumscribed margins or shadowing. The size of the lesion measured by ultrasound correlates exactly with the actual size of the pathological sample, because ultrasound can distinguish the lesion from the desmoplastic reaction, which is the response of the surrounding tissues to tumour invasion (Fig. 4.34).

Fig. 4.34. Uncircumscribed echo-poor lesion, measuring 11 mm, with an echogenic halo representing the desmoplastic reaction of the surrounding tissues to tumour invasion

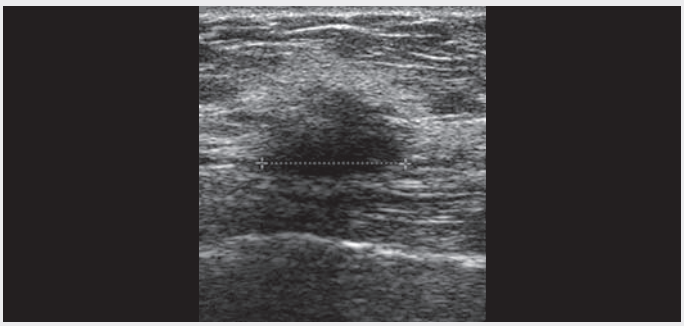

The typical ultrasound appearance of an invasive ductal carcinoma is a spiculated mass, but this feature is not specific, as it can also be associated with fibroadenomas, radial scars or fat necrosis. It may therefore be necessary to proceed to a biopsy to confirm the diagnosis. Sometimes, an invasive ductal carcinoma appears as a round or oval echo-poor mass with microlobulated or indistinct margins, with no echoic halo of a desmoplastic reaction (Fig. 4.35).

In smaller neoplasms, the margins are usually circumscribed and the structure appears more homogeneous. The neoplasm may be more echo-poor than the surrounding fibroglandular tissue or it may be isoechoic to the fat tissue; it is therefore difficult to identify these lesions in a fatty breast. The homogeneous or inhomogeneous appearance, which is well correlated with the homogeneity of the lesion on pathology, is due to the presence of sclerotic areas of fibrotic tissues (intense internal echoes) or necrotic areas (echo-poor areas or cystic components with internal echoes representing debris).

Microcalcifications are present in 40% of all breast cancers and are difficult to detect by ultrasound, especially when they are very small. Microcalcifications are more frequently visible if they are localized within a mass; outside lesions, they often look like echo-rich spots, frequently indistinguishable from the intense echoes produced by the interfaces of normal parenchyma (Fig. 4.36).

Fig. 4.35. Small (4-mm), solid, echo-poor mass with microlobulated margins. Histological examination revealed an invasive ductal carcinoma

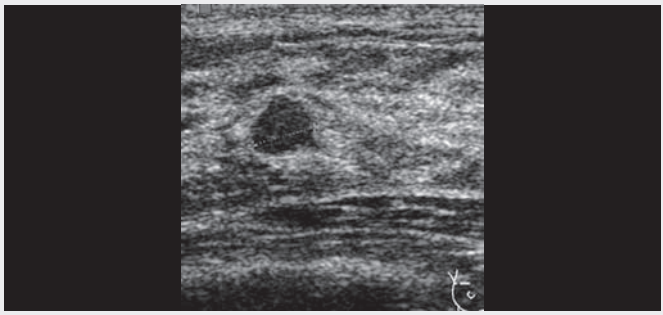

Fig. 4.36. Echo-poor mass with echo-rich spots representing microcalcifications within the lesion

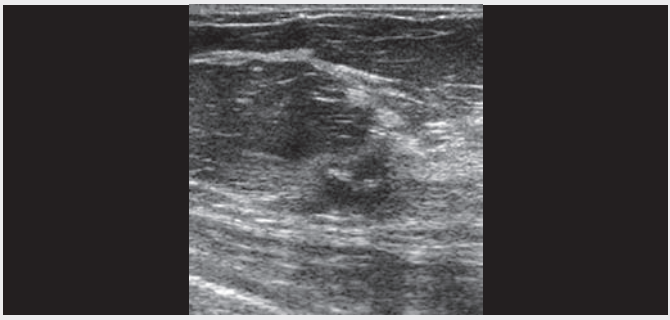

Shadowing is another distinctive feature of invasive ductal carcinoma, reported in 30–40% of cases, which correlates well with the amount of fibrous tissue within the breast cancer. Spiculated masses or diffuse cancers often alter the architecture of the surrounding parenchyma.

High-resolution transducers can reveal further ultrasound features, besides the presence of a nodular lesion, such as thickening, retraction or interruption of the skin. Subcutaneous tissue can also become thicker, and the fat tissue loses its regular structure. The Cooper ligaments and Duret crests become thicker, change their orientation and become more echoic, sometimes with posterior signal attenuation (Fig. 4.37).

Fig. 4.37. Echo-poor solid lesion with thickening of skin and subcutaneous tissue and echo-rich fatty tissues, due to tumour infiltration

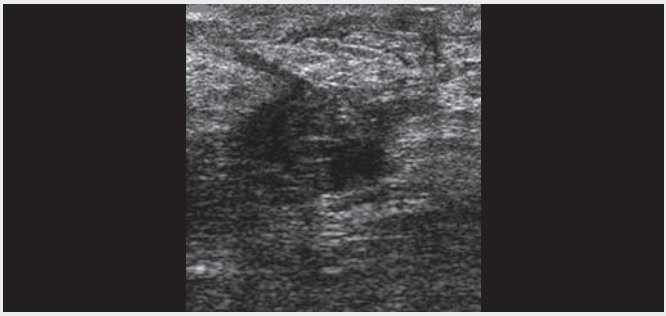

Even peri-lesional ducts may appear abnormal and become stretched and sometimes moderately enlarged. Colour Doppler often shows an increase in the glandular and peri-lesional vascular supply (Fig. 4.38).

Fig. 4.38. Uncircumscribed, echo-poor, solid mass with posterior shadowing and echogenic halo, showing peripheral and central vascular signals

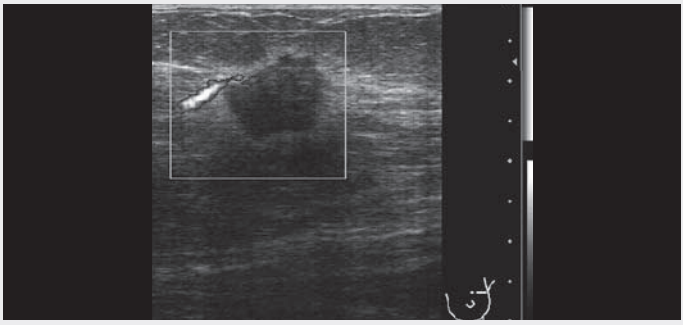

Another kind of breast tumour is **Paget disease** of the nipple, which appears as a scabby lesion of the nipple but is in fact an underlying cancer of the inner glandular tissue, frequently an intraductal carcinoma.

Invasive lobular carcinoma

This neoplasm accounts for 7–10% of all breast cancers. Lobular carcinoma is considered a riddle by even the most expert examiners. Frequently, it looks like an echo-poor lesion with ill-defined margins and minimal or no acoustic shadowing (Fig. 4.39), but sometimes it is difficult to detect even a nodular lesion within the parenchyma.

Fig. 4.39. Large, echo-poor, solid lesion with indistinct margins and three peripheral vascular supplies

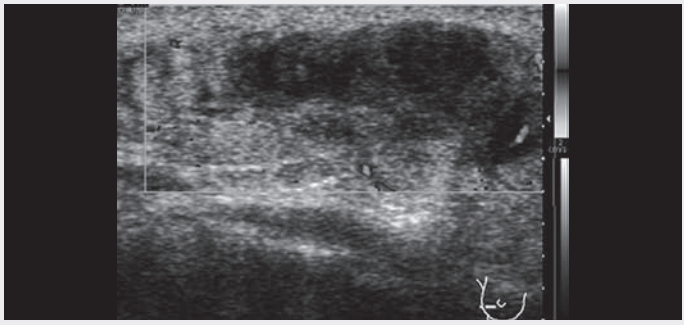

Carcinomas with a good prognosis

Mucinous carcinoma

Mucinous carcinomas account for almost 1–2% of all breast cancers. They are difficult to differentiate from benign masses as they are round or oval and have a homogeneously echo-poor pattern (Fig. 4.40).

Fig. 4.40. (a) Round, echo-poor, solid mass, measuring 9 mm, with circumscribed margins and no posterior acoustic shadowing. (b) A large central vessel is seen on power Doppler

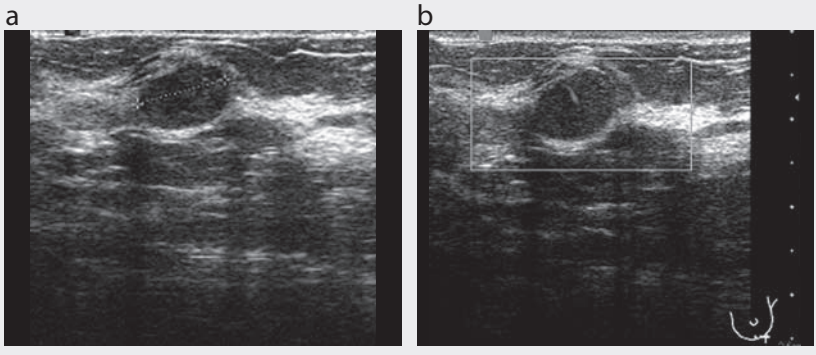

Medullar carcinoma

It is difficult to distinguish between medullar and mucinous carcinomas because both are well differentiated, have a good prognosis and on ultrasound are round with an echo-poor structure and microlobulated margins (Fig. 4.41).

Fig. 4.41. (a) Small (4-mm), echo-poor, solid mass with microlobulated margins. (b) Colour Doppler shows a marked peripheral vascular supply

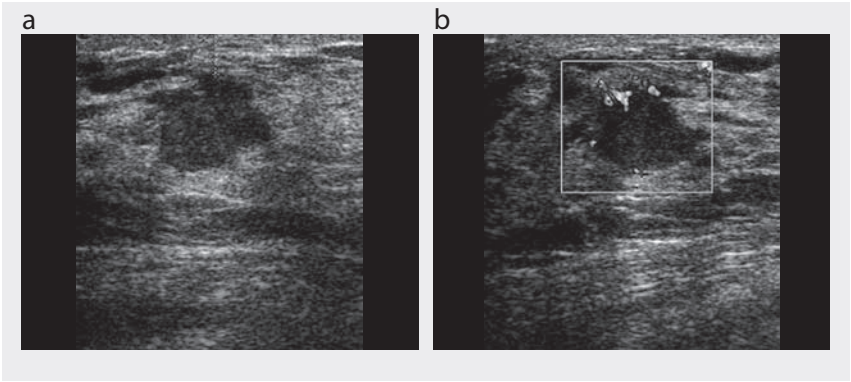

Papillary invasive carcinoma

These are circumscribed masses with lobulated margins and large calcifications, which are found inside or, less frequently, peripherally. They are frequently located beneath the nipple. As for medullar and mucinous carcinomas, malignancy should be suspected from signs such as poorly defined and incompletely circumscribed margins.

Inflammatory breast cancer

Inflammatory breast cancer accounts for 2% of all breast cancers, occurring most frequently during the 4th to 5th decade of a women's life. Clinically, it resembles mastitis, but it has a more rapid evolution, and rapid metastatic diffusion causes early death. The inflammatory state is sustained by neoplastic emboli within mammary and dermal lymphatic vessels.

On ultrasound, the skin and the derma appear thick and echo-rich. Sonography can detect echo-free tubular structures, which are congested lymphatic vessels, and echo-free lines behind the skin, which are due to interstitial liquid collection. Cooper ligaments are thickened and distorted. There may be marked, diffuse attenuation of ultrasound waves, which obscures deeper tissues. Some echo-poor nodules can be visualized and can be biopsied (Fig. 4.42).

Fig. 4.42. (a), (b) Axial and mediolateral mammographic views of the right and left breasts (CCD and OBL D: right breast; CCS and OBL S: left breast): diffuse increase in glandular density in the outer lower quadrant of the left breast, with thickening of the skin and fibrous septa. (c), (d) Ultrasound appearance of the lower (c) and inner (d) quadrants of the left breast. (c) Echo-poor nodule with blurred margins, with associated skin infiltration and diffuse attenuation of ultrasound waves that obscures the deeper localized tissues. (d) Skin thickening and subcutaneous fat oedema in the adjacent tissues of the inner lower quadrant

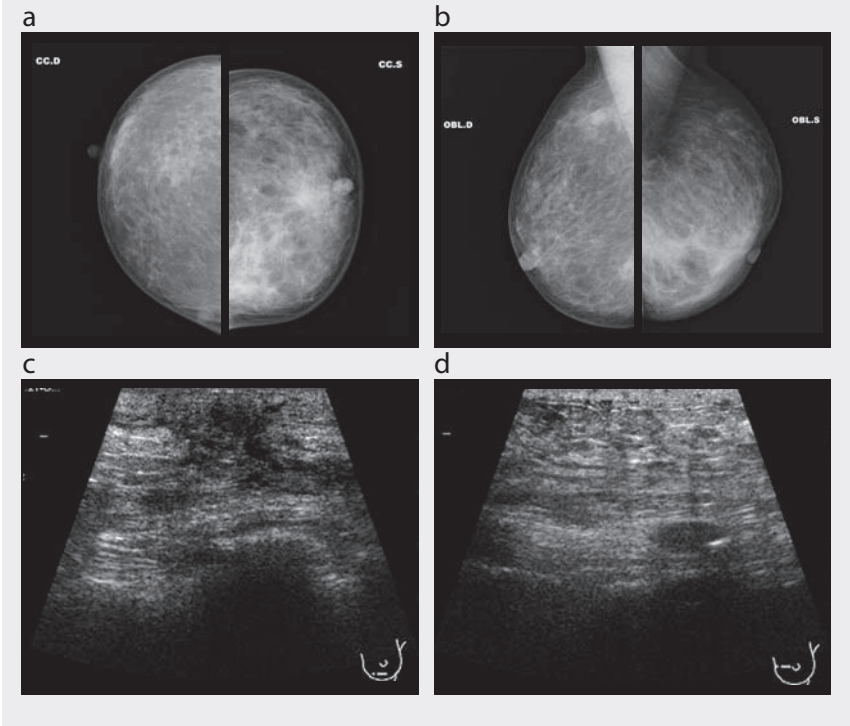

Male breast carcinoma

Male breast cancer (1% of all male neoplastic disease) appears clinically as a retroareolar mass with a fibrous or wooden consistency, sometimes associated with a bloody discharge. These cancers are often invasive ductal carcinomas that do not differ morphologically from female breast cancer, except for a higher incidence of skin infiltration (Fig. 4.43).

Fig. 4.43. Bleeding from the right nipple in a 50-year-old man: echo-poor, solid lesion with irregular morphology, uncircumscribed margins, faint posterior shadowing and a significant vascular supply

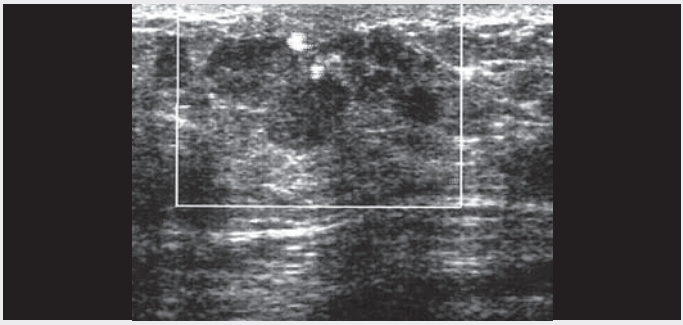

Metastatic carcinoma

Metastasis is very rare. Melanoma is the most frequent source of metastatic breast lesions, and less frequently pulmonary, kidney and liver tumours.

Rare neoplasms

Several rare classes of breast neoplasm show ultrasound features similar to those of commoner breast tumours, with no specific differences among the subgroups. Sarcomas and lymphomas (non-Hodgkin) often show a round or irregular morphology; the only difference is their rapid growth.

Local staging

Clinical or radiological detection of a breast lesion must be followed by correct staging (TNM system) in order to identify the appropriate complete therapy (surgery, radiotherapy, chemotherapy, hormonotherapy). Ultrasound examination is useful for the detection of multifocal, multicentric or bilateral disease and in studying axillary lymph nodes.

Normal nodes are oval and have an echo-poor cortex of variable thickness (generally < 10 mm, depending on the woman's weight) and an echo-rich hilum (fat) in which the vascular branches are located and which are visible on power Doppler.

Metastatic nodes are larger (> 1 cm), become round and show diffuse cortical thickening that displaces the lymph node hilum (Fig. 4.44).

Fig. 4.44. Metastatic axillary lymph node with a round shape, no echo-rich hilum, posterior shadowing and vascular signals only in the peripheral cortex

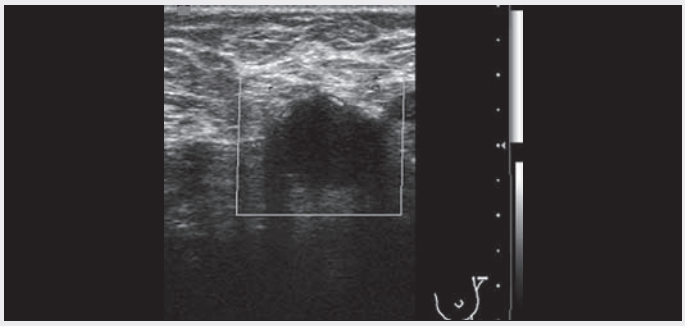

Sometimes, focal cortical thickening can be observed in a lymph node, but this finding does not necessarily indicate metastatic disease. Conversely, lymph node metastases may be very small (micrometastases), and the lymph node may appear normal on sonography. Therefore, all women with breast cancer should undergo biopsy of axillary lymph nodes suspected of being involved or undergo removal of sentinel nodes during surgery.

Chapter 5

Paediatric ultrasound

5

Paediatric ultrasound

Introduction

Ultrasound incorporating new technological improvements is widely used in paediatrics, and high-resolution images are produced because children's bodies have low levels of fat. Nevertheless, it should be remembered that children are not small adults but have their own specificities and specific pathological conditions, especially malformations. If necessary, the examination room should be heated, and infants must be covered. The parents should be present in the room to help keep the infant quiet and calm. The examination should be as short as possible, and the operators should be specially trained. The ultrasound system used must have appropriate high-frequency probes, and accessories such as pillows should be available. A child's history should be well known before the examination is begun. The more the physician (or operator) knows about the child's symptoms, the easier he or she can solve the medical problem and begin treatment.

Ultrasound is the imaging modality of choice for children with abdominal pain, abdominal masses and intra-abdominal anomalies. Several diseases that occur frequently should be excluded by ultrasound examination. Although ultrasound imaging is a powerful technique, it is sometimes insufficient, and other modalities, such as plain X-rays, CT scan, MRI and nuclear medicine, if available, are required to confirm a diagnosis. For example, cystography is needed to evaluate vesico-ureteral reflux, and evaluation of tumour extension requires CT or MRI. Use of ultrasound imaging, however, will save time and reduce costs and can avoid exposure to radiation with no reduction in diagnostic accuracy. Misuse of ultrasound must be avoided, as it discredits the technique and the operator and wastes time and money.

Liver and biliary tract

Indications

Ultrasound is the preferred initial imaging modality for evaluating the liver and biliary tract in children. Typical indications are hepatomegaly, jaundice, anomalous hepatic assessment, ascites, suspected liver abscess or liver mass, abdominal trauma, right upper abdominal pain and screening for endemic echinococcosis. Ultrasound gives information on the size and structure of the liver and demonstrates both

localized lesions (tumour, cyst and abscess) and diffuse diseases. It can also be useful for histological and therapeutic purposes, as it can be used to guide fine-needle biopsies, punctures and drainage of abscesses.

Preparation

Fasting is not necessary before an examination of the hepatic parenchyma; however, 2–6 h of fasting, depending on the age of the child, is necessary for a study of the gall bladder, the intrahepatic and extrahepatic bile ducts and the hilus of the liver.

Examination technique

The child should lie in the supine position initially and later on the left or right side. No premedication is needed (an important advantage of ultrasound). Coupling agent is applied liberally, first over the right upper abdomen, then over the rest of the abdomen as the examination proceeds.

Scanning should be carried out in the longitudinal, transverse and oblique planes, systematically, including scans through the intercostal and subcostal routes. Convex probes should be used, ranging from 3.5 to 7 MHz, and linear probes of at least 7–15 MHz for neonates. The frequency should always be as high as possible.

Doppler ultrasound is useful for locating vessels and for ensuring the permeability of the vascular structures. It is helpful for assessing the presence and direction of blood flow in the hepatic artery, hepatic veins and portal veins. Normal vascular flow patterns can be readily seen in children of all ages.

Normal findings

The normal hepatic parenchymal echogenicity is uniform, with clear, delineated vessels. Its sonographic appearance is similar to that of the renal medulla during the first 6 months of life, but the echogenicity becomes similar to that of the cortex later (Fig. 5.1). Its surface is smooth, and the inferior edge is wedge-shaped. The vertical diameter in the right middle clavicular line is 5 cm at birth, then increases gradually to reach 10 cm at 5 years and 14 cm at puberty (Fig. 5.2). The tip of the liver should not extend below the inferior pole of the right kidney.

Fig. 5.1. Normal echo texture and echogenicity of the liver in a 10-month-old boy. Longitudinal scan showing similar echogenicity in the liver (L) and the renal cortex of the right kidney (RK)

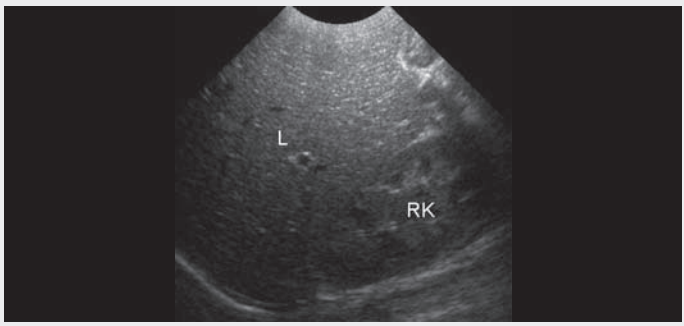

Fig. 5.2. Liver measurement in the midclavicular line. Longitudinal scan shows the length, from the inferior tip of the liver to the liver dome at the diaphragm; the surface of the liver is smooth and the inferior edge is wedge-shaped. L, liver; RK right kidney

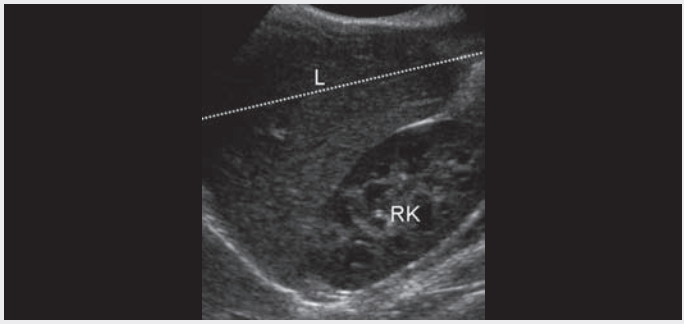

The intrahepatic bile ducts are not seen in infants. The cystic duct is difficult to identify, and the common hepatic duct cannot be distinguished from the common bile duct. The size of the common bile duct increases linearly with age; its diameter should not exceed 1 mm in neonates, 2 mm in infants up to 1 year of age, 4 mm in children 1–10 years of age and 6 mm in adolescents (Fig. 5.3).

The normal gall bladder is seen as a cystic structure with an echo-free content. In neonates and infants under 2 years of age, the gall bladder is < 3 cm long and < 1 cm wide; in children aged 2–16 years, the length is < 8 cm and the width < 3.5 cm. The wall of the gall bladder is thin and well defined, with measurements similar to those in adults (usually < 3 mm) (Fig. 5.4).

Fig. 5.3. Normal common bile duct in a 7-month-old boy. Longitudinal scan shows the common bile duct, 1.1 mm in diameter (arrows), in front of the portal vein

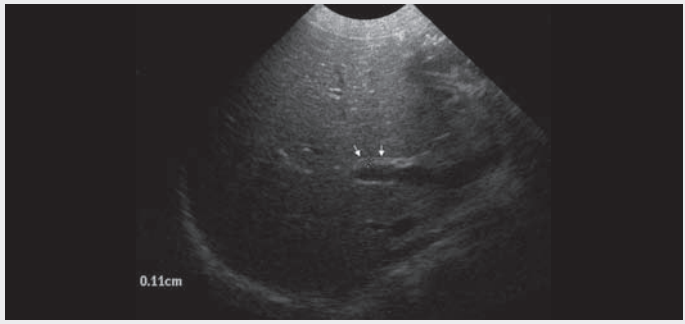

Fig. 5.4. Normal gall bladder. Transverse (a) and longitudinal (b) scans in a 6-year-old boy show the gall bladder (G) as a cystic structure with echo-free contents, measuring 5.4 cm in length and 1.9 cm in width, with a wall thickness of about 2 mm

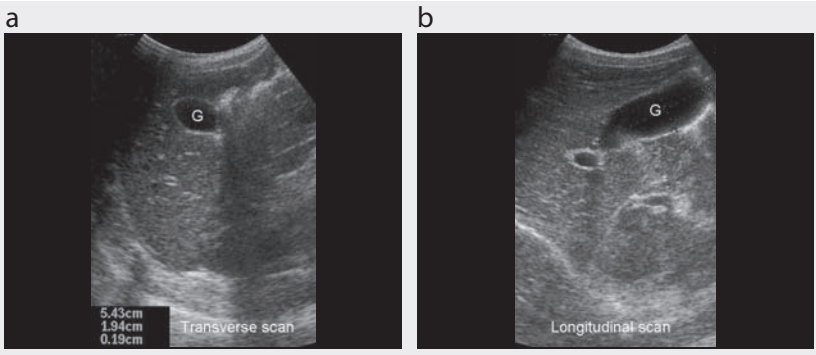

The intrahepatic vessels and ducts are well delineated, especially the portal vein branches and the hepatic veins (Fig. 5.5). The branches of the portal vein show strong echoes from the wall. The portal vein diameter is 4 mm in a neonate and 8–10 mm in children (Fig. 5.6).

Fig. 5.5. Normal intrahepatic vessels, oblique scans in a 5-year-old boy. (a) Portal vein branches (arrows). (b) Right hepatic vein (RHV), middle hepatic vein (MHV) and left hepatic vein (LHV). IVC, inferior vena cava

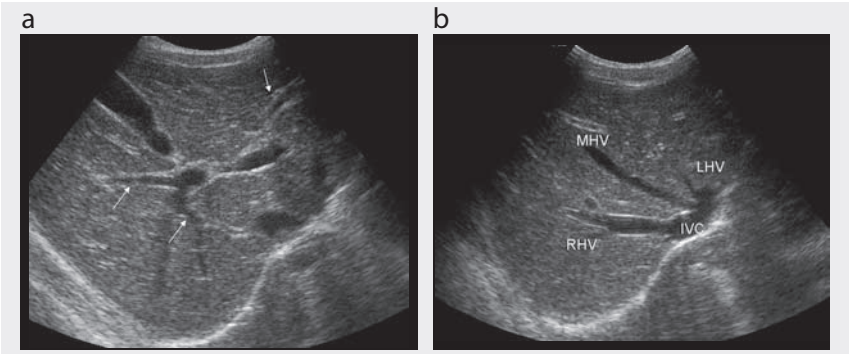

Fig. 5.6. Normal portal vein diameter. Longitudinal scan in a 7-month-old boy shows a portal vein with a diameter of 4.5 mm, the bile duct in front of the vein and the right branch of the hepatic artery in cross-section between these tubular structures

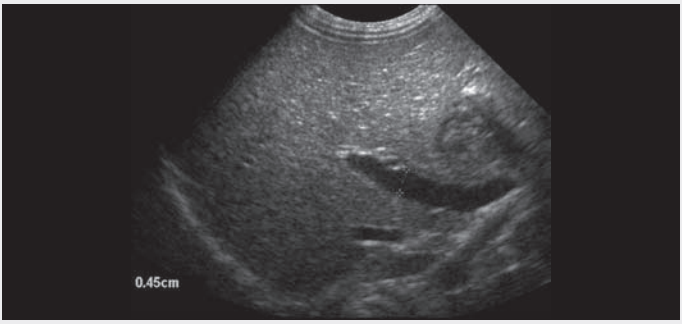

Pathological findings

Hepatic tumours

Hepatic tumours are rare in children, with an estimated frequency of 3% of all paediatric tumours. Malignant tumours are by far the most frequent, accounting for two thirds. Ultrasound is important in the diagnosis and monitoring of tumours; most cases can be diagnosed by combining ultrasound with clinical and biological data.

Primary malignant hepatic tumours

Ninety per cent of malignant hepatic tumours in children are of epithelial origin and consist of hepatoblastomas and hepatocellular carcinomas. The most specific radiological sign of malignancy is amputation or thrombosis of a portal vein branch

or hepatic vein. The absence of this sign does not, however, eliminate a diagnosis of malignancy, especially in the case of tumours located in the periphery of the liver.

Hepatoblastoma is by far the commonest malignant hepatic neoplasm in children under the age of 3 years, with a median age of 1 year. The tumour is more common in males than in females and can be seen in neonates. The tumour most often presents as a painless mass. It generally occurs in a healthy liver and is usually associated with Beckwith-Wiedemann syndrome, biliary atresia or familial polyposis coli. Serum α-fetoprotein levels are markedly elevated in 90% of cases.

The sonographic appearance of hepatoblastoma is variable: it may be echo-poor, isoechoic or echo-rich in comparison with the normal liver tissue and a pseudocapsule may be present. The tumour is usually unifocal and in the right lobe of the liver. It may be multicentric or diffuse throughout the liver. Hepatoblastomas are typically heterogeneous, containing calcifications and necrotic areas (Fig. 5.7). They tend to invade vascular structures, especially the portal vein. Doppler imaging usually shows increased hepatic arterial flow. Metastatic disease occurs in 10–20% of cases, most commonly in the chest.

Fig. 5.7. Hepatoblastoma in a 2-year-old boy. (a) Transverse scan shows a large heterogeneous mass occupying the right lobe of the liver. (b) Contrast-enhanced CT during the hepatic arterial phase showing the tumour with heterogeneous enhancement and calcifications (arrows)

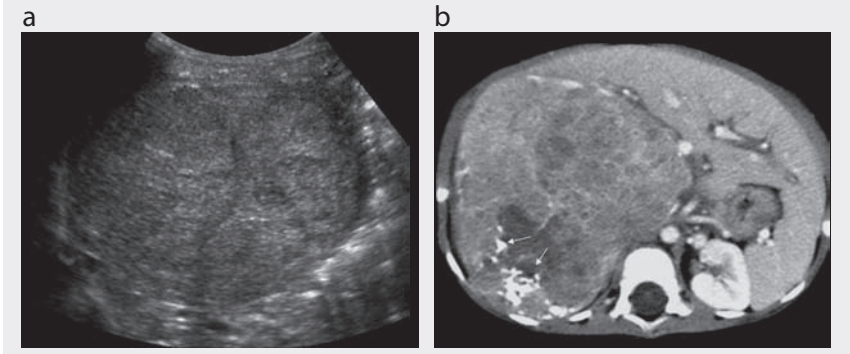

Hepatocellular carcinoma is the second commonest paediatric malignant liver tumour after hepatoblastoma, generally occurring in children over 3 years of age. Preexisting liver disease, such as familial cholestatic cirrhosis, hepatitis B virus infection, tyrosinaemia and type I glycogen storage disease, is present in about one half of cases. Serum α-fetoprotein levels are elevated in up to 50% of cases. The tumour is often extensively invasive or multifocal at the time of diagnosis. The ultrasound findings are similar to those of hepatoblastoma.

Biopsy is necessary to differentiate hepatoblastoma from hepatocellular carcinoma and tumours with low serum α-fetoprotein.

Undifferentiated embryonal sarcoma is a rare malignant tumour, which primarily affects children between 6 and 10 years of age; α-fetoprotein levels are normal. The usual presenting features are an abdominal mass and pain. On ultrasound, the tumour commonly appears as a predominantly cystic mass with multiple septations of varying thickness (Fig. 5.8). Punctate calcification may be seen in these tumours.

Fig. 5.8. Undifferentiated hepatic embryonal sarcoma in a 7-year-old girl. Transverse scan shows a predominantly cystic mass containing fluid-filled locules and thin intermixed septa; RK, right kidney

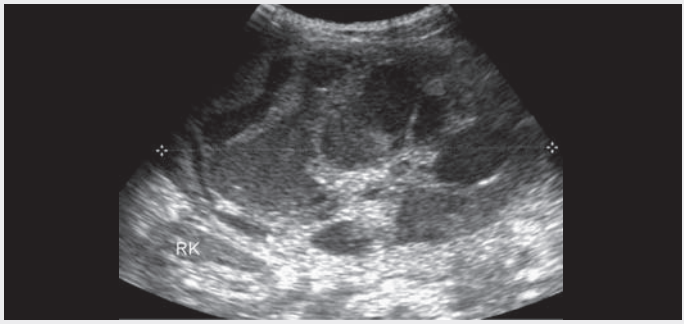

Embryonal rhabdomyosarcoma of the biliary tree is a rare malignant tumour that occurs in children aged 2–5 years. The child presents with jaundice in most cases. Ultrasound shows bile-duct dilatation, which is often proximal to a usually inhomogeneous echogenic mass, which may be quite echo-rich (Fig. 5.9).

Fig. 5.9. Hepatobiliary embryonal rhabdomyosarcoma in a 22-month-old boy. (a) Oblique ultrasound scan reveals a multicystic septated mass occupying the hepatic hilum (arrows). (b) Coronal T1-weighted enhancement magnetic resonance image shows extension of the tumour along the extrahepatic bile duct (arrows); the portal vein is slightly compressed

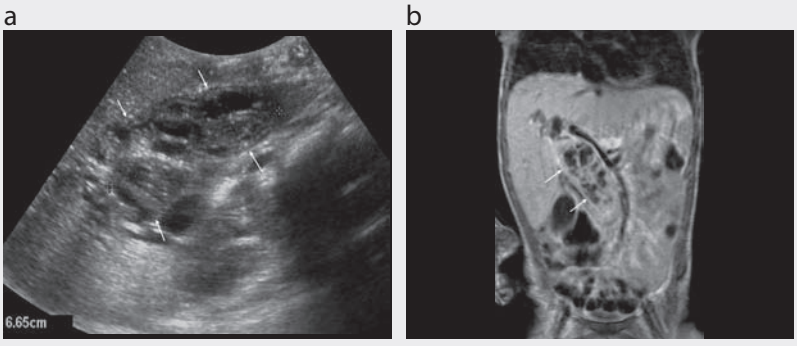

Hepatic metastases

The malignant tumours of children that most frequently metastasize to the liver are Wilms tumours, neuroblastomas and lymphomas. Neuroblastomas may affect the liver in stage IV or IV-S disease. Hepatic metastases appear on ultrasound as hepatomegaly with multiple well-delineated echo-poor or echo-rich lesions (Fig. 5.10).

Fig. 5.10. Stage IV-S neuroblastoma in a 5-month-old boy. (a) Oblique ultrasound scan shows hepatomegaly and diffuse heterogenicity of the liver parenchyma with multiple echo-rich metastases. (b) Axial contrast-enhanced CT shows a primary right adrenal mass (arrows) and heterogeneous hepatic parenchymal enhancement due to liver metastases

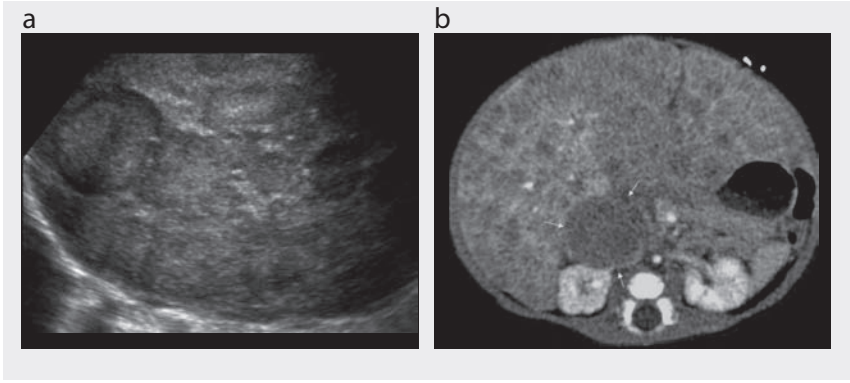

Benign hepatic tumours

Benign hepatic tumours are rare in children. The most frequent are haemangioendothelioma, haemangioma, cystic mesenchymal hamartoma, focal nodular hyperplasia and adenoma.

Haemangioendothelioma is a benign vascular tumour that occurs in children under 6 months of age. Its natural history is similar to that of cutaneous haemangioma, with a rapid proliferation phase lasting 12–18 months, followed by a slower involution phase, lasting 5–8 years. Haemangioendotheliomas can be solitary or multifocal. They are found either because of hepatomegaly or fortuitously, sometimes at antenatal ultrasound. Associated cutaneous haemangiomas have been reported in 9–87% of cases and are frequently seen with multifocal hepatic lesions. Ultrasound shows heterogeneous lesions, typically with echo-poor regions and calcifications (Fig. 5.11). The tumour margins may be well circumscribed. Colour Doppler shows dilatation of the hepatic artery and hepatic veins. The progression is often simple, with calcification and regression of the lesion within an average of 1 year. The prognosis of the diffuse multinodular form is poor. The sonographic aspect is that of a metastatic liver with multiple echo-poor nodules or a rosette associated with obvious signs of hypervascularization, as seen by Doppler. In extensive forms, before

regression of the lesion, life-threatening complications can occur, such as massive haemoperitoneum due to spontaneous tumour rupture, anaemia, thrombocytopenic coagulopathy, refractory congestive heart failure and obstructive jaundice.

Fig. 5.11. Haemangioendothelioma in a newborn boy. (a) Oblique scan shows a heterogeneous mass replacing most of the liver and containing calcifications (arrows). (b) Doppler ultrasound shows prominent high-flow vascular structures

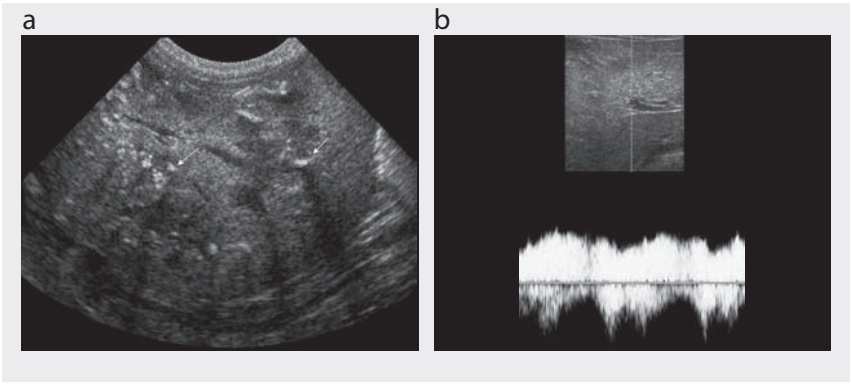

Haemangioma or cavernous haemangioma is rare in children. It is usually asymptomatic and is detected as an incidental finding on sonography. The classical common appearance on ultrasound is a well-defined, echo-rich lesion with acoustic enhancement. The echogenicity may vary due to internal fibrosis, thrombosis, necrosis and occasionally calcification. Compression tends to reduce the hyperechogenicity.

Cystic mesenchymal hamartoma is considered to be a developmental anomaly originating in the connective tissue along the portal tracts, rather than a true neoplasm. It usually affects children under 2years of age and is slightly more common in boys than girls. The child may present with an abdominal mass and normal α-fetoprotein levels. Mesenchymal hamartomas may be detected as echo-poor lesions on antenatal ultrasound. Postnatal ultrasound shows a predominantly cystic lesion with echogenic septa (Fig. 5.12). The cystic locules are echo-free or echo-poor. Occasionally, solid material is identified with the appearance of a complex mass. The prognosis after surgery is generally good.

Focal nodular hyperplasia can be seen in children of any age, with a female prevalence. It consists of normal hepatocytes, bile ducts and Kupffer cells. The etiology is thought to be a localized hepatocyte response to an underlying congenital vascular malformation. The lesion is usually asymptomatic. Ultrasound shows a well-demarcated mass that is either echo-rich or isoechoic with the liver parenchyma. A central stellate scar is seen in approximately 20% of cases; demonstration of arterial flow in the central scar is highly suggestive of the diagnosis (Fig. 5.13).

Fig. 5.12. Cystic mesenchymal hamartoma in a 17-month-old boy. (a) Transverse ultrasound scan reveals a large hepatic mass containing multiple echo-free cystic areas surrounded by thin septa. (b) Axial and (c) coronal reformatted contrast-enhanced CT scans show a predominantly cystic mass composed of multiple cystic spaces (C) of varying size and enhanced solid areas within the mass ((c), arrows); L, liver

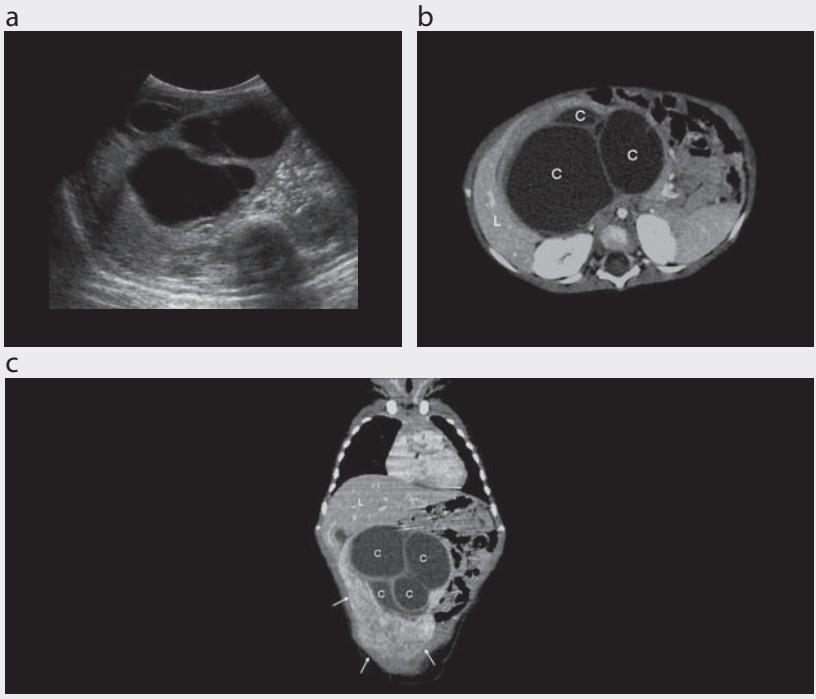

Fig. 5.13. Focal nodular hyperplasia in a 3-year-old girl. Axial sonogram shows a sharply marginated echo-rich mass within the right lobe (arrows), with a central echo-poor area due to fibrosis

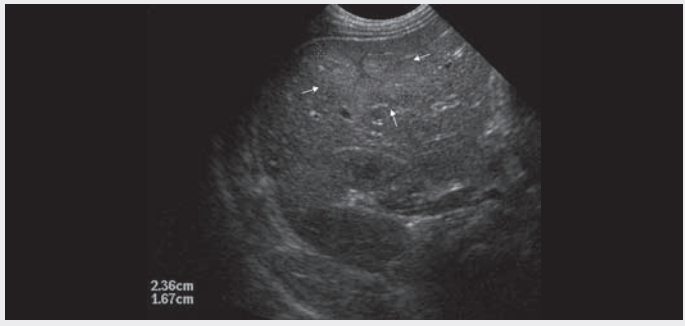

Adenoma is very rare in children, occurring under specific conditions, such as hormone treatment, type I glycogen storage disease, Fanconi anaemia and galactosaemia. These children may be asymptomatic or may present with hepatomegaly or abdominal pain. The appearance on ultrasound is nonspecific, as the lesion may be echo-poor, isoechoic or echo-rich to normal liver. Most are heterogeneous because of the presence of haemorrhage and necrosis. Colour and pulse Doppler show central venous flow and peripheral venous and arterial flow, in contrast to focal nodal hyperplasia, in which central arterial flow at the site of the central scar is more typical.

Non-neoplastic diseases

Abscess

The clinical findings and the imaging appearance of liver abscesses are variable and nonspecific. Patients present with fever, abdominal pain, hepatomegaly, abnormal liver function tests and leukocytosis. Ultrasound can provide early diagnosis. The ultrasound features vary with the evolution of the lesion. Initially, an abscess may appear to be solid and echo-rich relative to the normal hepatic parenchyma but eventually develops into an echo-poor or echo-free area with posterior acoustic enhancement. Later, abscesses are usually spherical or ovoid, and the wall is irregular or thick but may be well defined. They can be unilocular or multilocular. The ultrasound pattern can vary from purely echo-free to highly echogenic. Internal septations, fluid and debris may be present.

Pyogenic liver abscesses are rare in children and occur predominantly in the first 5 years of life (Fig. 5.14). Bacteria can invade the liver by a number of routes. The common causative agent is *Staphylococcus aureus* in infants and children and *Escherichia coli* in neonates.

Fig. 5.14. Pyogenic hepatic abscess in a 2-year-old boy. Longitudinal scan through the right lobe of the liver shows a unilocular, highly echogenic abscess (A) with a fluid–debris level (arrow)

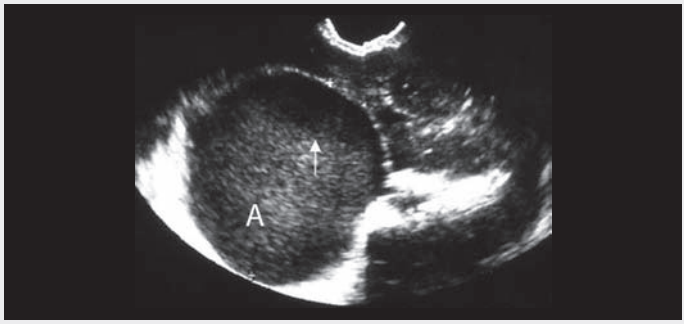

Fungal microabscesses are found almost exclusively in immunocompromised children. The common causative agents are *Candida albicans* and *Aspergillus* species.

Amoebic liver abscesses are commonest in children < 3 years of age. They are caused by the parasite *Entamoeba histolytica*, which is endemic in tropical and subtropical climates.

Antibiotic therapy with percutaneous drainage of macroscopic abscesses under ultrasonographic control is now the treatment of choice for most liver abscesses.

Hepatic trauma

The liver is one of the most frequently injured abdominal organs in childhood. The right hepatic lobe is injured more often than the left and the posterior segment of the right lobe more often than the anterior segment. Hepatic injuries include subcapsular and parenchymal haematomas, contusions, lacerations and rupture (Fig. 5.15). On ultrasound, subcapsular haematomas often show a lenticular-shaped fluid collection (Fig. 5.16). Intrahepatic haematomas are frequently initially echo-rich and ill-defined within the hepatic parenchyma but become echo-free and diminish in size with time and progressive liquefaction. Hepatic lacerations result in linear or branching parenchymal defects that may be superficial or deep (Fig. 5.17). Hepatic fractures are deep parenchymal lacerations. Haemoperitoneum often accompanies hepatic injuries.

Late complications of hepatic trauma are biloma and pseudoaneurysm. Bilomas appear as well-defined fluid collections in the liver or peritoneal cavity (Fig. 5.18). Pseudoaneurysms are round lesions that show flow on Doppler.

Fig. 5.15. Hepatic contusions. Oblique scan in a 7-year-old boy with abdominal trauma shows a heterogeneous, echo-rich area in the right hepatic lobe (arrows)

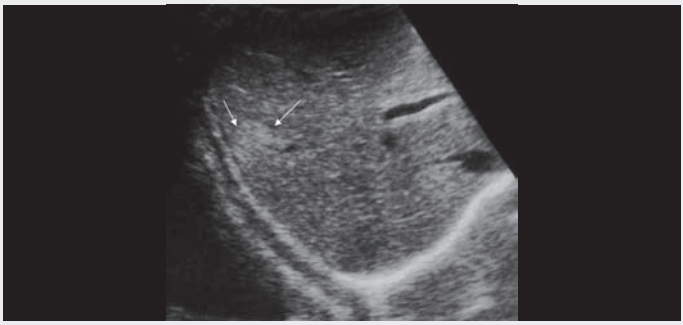

Fig. 5.16. Hepatic subcapsular haematoma in a newborn boy; oblique scans. (a) A huge echo-rich subcapsular haematoma (H), sharply delineated from the hepatic parenchyma. (b) One month later, decreased echogenicity

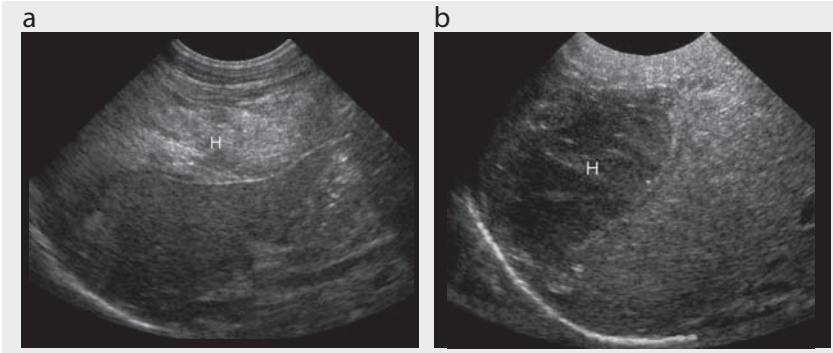

Fig. 5.17. Hepatic laceration in a 4-year-old boy with abdominal trauma. Axial scan shows a superficial linear parenchymal defect (arrows)

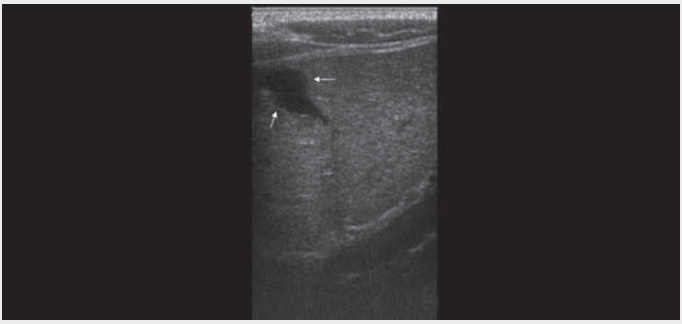

Fig. 5.18. Hepatic biloma in a 6-year-old girl with abdominal trauma. Oblique scan performed 12 days later shows a large intrahepatic contusion (C) within the right lobe, with a more central, well-defined fluid collection representing biloma (arrows)

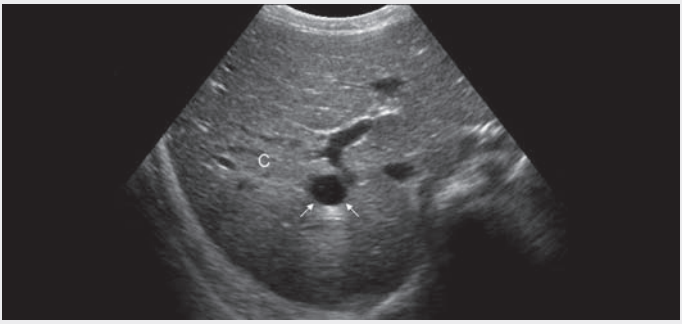

Hydatid cyst

Hydatid disease is due to the development of larvae of canine *Echinococcus granulosus* in humans. Human infestation is accidental, due to ingestion of parasite eggs. In children, a hepatic localization is the most frequent after the lung. The clinical manifestations of abdominal hydatidosis are variable. Ultrasound is the initial modality of choice for positive and topographic diagnosis of hydatid cyst in the liver and may be the only preoperative morphological examination. The sensitivity of ultrasound for diagnosis is 95–100%. Several classifications of ultrasound findings have been proposed; the most commonly used worldwide is Gharbi's classification, described in 1981:

Type I: pure fluid collection (Fig. 5.19)
Type II: fluid collection with a split wall (Fig. 5.20)
Type III: fluid collection with septa or multicystic appearance (Fig. 5.21)
Type IV: cyst with heterogeneous echo patterns (Fig. 5.22)
Type V: reflecting thick walls or a densely calcified lesion (Fig. 5.23).

Type I appears to be the most frequent in children. Sometimes, the cyst ruptures or becomes infected. In the liver, the most frequent complication is cystic rupture into the biliary ducts, through the diaphragm or into the peritoneum. In these cases, ultrasound may show a dilated biliary tract with fragments of membranes in the gall bladder or the common biliary duct, Budd-Chiari syndrome with compression of the hepatic vein by a hydatid cyst, multiple peritoneal cysts, ascites and, in some cases, diaphragmatic breach with a communicating supradiaphragmatic space (Fig. 5.24).

Fig. 5.19. Liver hydatid cyst type I. Axial scan shows a large, pure fluid collection, rounded, with well-defined borders, in the left hepatic lobe. C, cyst

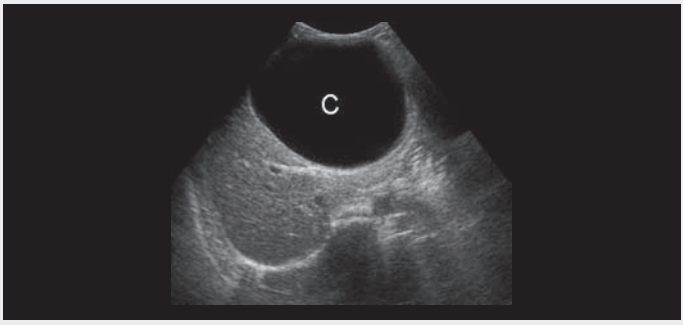

Fig. 5.20. Liver hydatid cyst type II. Oblique scan shows a fluid collection containing detached membranes typical of hydatid disease (arrows); a unilocular echo-poor cyst (C) is seen anteriorly

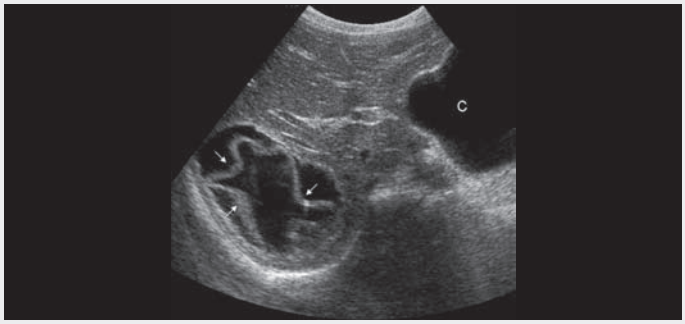

Fig. 5.21. Liver hydatid cyst type III. Oblique scan shows a fluid collection with multiple secondary vesicles (arrows)

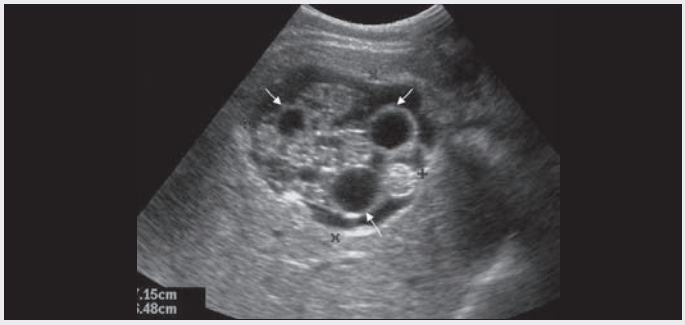

Fig. 5.22. Liver hydatid cyst type IV. Oblique scan shows a cyst with heterogeneous echo patterns in the right hepatic lobe (arrows); serological cultures revealed *Echinococcus granulosus* infection

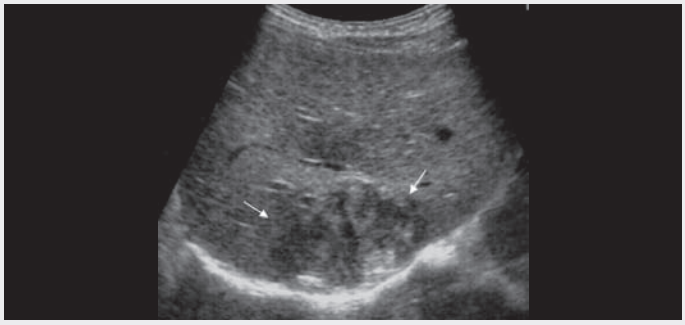

Fig. 5.23. Liver hydatid cyst type V. Oblique scan shows a densely calcified lesion in the right hepatic lobe with acoustic shadowing (arrow)

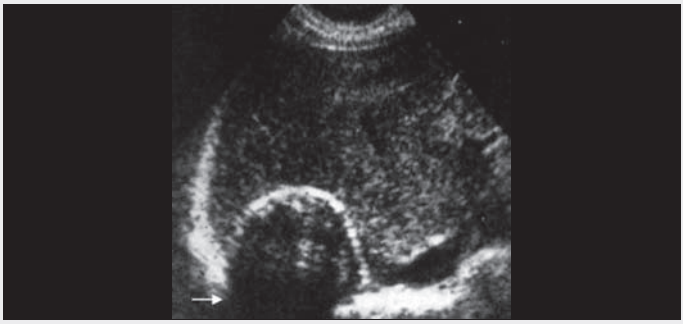

Fig. 5.24. Hydatid cyst that has ruptured into the biliary duct in a 14-year-old girl. Oblique scan shows a hydatid cyst (C) in the right hepatic lobe with a dilated biliary duct (arrows)

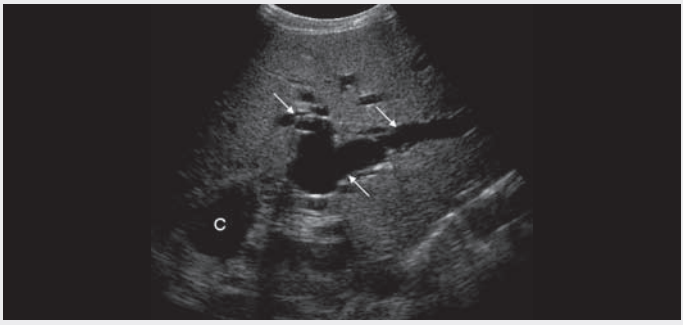

Biliary cyst

Biliary cysts are relatively rare in children. They may be multiple or solitary. Multiple cysts usually occur in association with inherited syndromes, such as autosomal dominant polycystic disease, Turner syndrome and tuberous sclerosis. Biliary cysts are usually detected incidentally on imaging. On ultrasound, they usually appear as echo-free, unilocular, round or oval masses with no visible wall (Fig. 5.25).

Fig. 5.25. Biliary cyst in a newborn girl. Oblique ultrasonogram reveals a well-delineated, echo-free mass with no visible wall

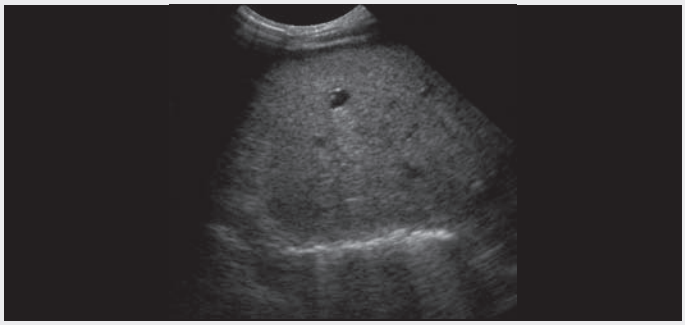

Steatosis

Steatosis, or fatty hepatic infiltration, is rare in children. Fat deposition occurs commonly in metabolic disorders, such as glycogen storage disease, fructose intolerance, tyrosinaemia, Wilson disease and Reye syndrome. It can be focal or diffuse. Regions of fatty liver appear brighter than the spleen and are echo-rich on sonography. Nodular fatty infiltration shows no mass effect, is sharply delineated, crossed by hepatic vessels and close to a hepatic vein, and it has a morphological appearance that allows differentiation from other lesions (Fig. 5.26). It may be located in subcapsular areas, the posterior part of segment IV, the anterior part of segment I, areas surrounding the gall bladder and in front of the hepatic hilum. The ultrasound findings are the same as in adults.

Fig. 5.26. Nodular fatty infiltration in an 8-year-old girl with cystic fibrosis. (a) Oblique scan shows a focal echo-rich area (arrows) in the right hepatic lobe of the liver (L). (b) Axial contrast-enhancement CT scan confirms the focal fatty infiltration in the liver (arrow) and shows diffuse small calcifications within the pancreas (P)

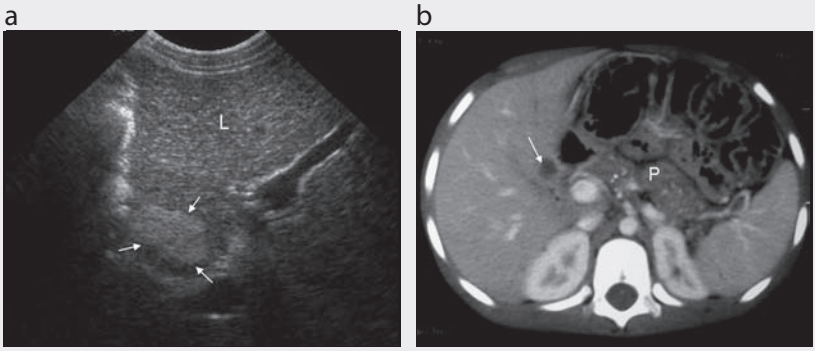

Hepatitis

Hepatitis is common in children and is not diagnosed by imaging. It is usually of viral origin and may be due to hepatitis A, B, C, D or E viruses. Noninfectious causes of hepatitis include drugs, toxins, autoimmune diseases and sclerosing cholangitis.

Hepatomegaly is the commonest manifestation of acute hepatitis, although the liver is often sonographically normal. In severe disease, ultrasound shows a heterogeneous parenchyma with increased echogenicity. Sonography may also show thickening of the gall bladder wall, lymphadenopathy and ascites. The ultrasound findings should be correlated with clinical information and laboratory results.

Chronic hepatitis may be sequelae of acute hepatitis, with eventual progression to cirrhosis. A liver biopsy may be necessary to confirm the diagnosis.

Biliary atresia

Biliary atresia consists of an absent or severely deficient extrahepatic biliary tree, which affects 1 in 10 000 neonates. Its etiology is unknown; possible causes include viral infection, ischaemic injury, abnormal bile–acid metabolism, pancreatic–biliary maljunction, genetic effects and development anomaly (Fig. 5.27).

Biliary atresia is often confused with neonatal hepatitis syndrome, a disease that develops secondarily to conditions such as infection (cytomegalovirus, herpes simplex virus, toxoplasmosis, protozoa and syphilis), metabolic defects (α1-antitrypsin deficiency, galactosaemia, glycogen storage disease, tyrosinosis) and Alagille syndrome.

Biliary atresia and neonatal hepatitis syndrome are the common causes of conjugated hyperbilirubinaemia, as two overlapping conditions, usually present at 3–4 weeks of life in infants with jaundice. In both conditions, hepatic function tests show elevated serum levels of transaminases and bilirubin. It is important to distinguish the two, as neonatal hepatitis is managed medically, whereas biliary atresia requires early surgical intervention to prevent biliary cirrhosis.

Fig. 5.27. Anatomical types of biliary atresia. Type I (a), common bile-duct atresia; type II (b), common hepatic duct atresia with a small gall bladder; type III (c), right and left hepatic duct atresia

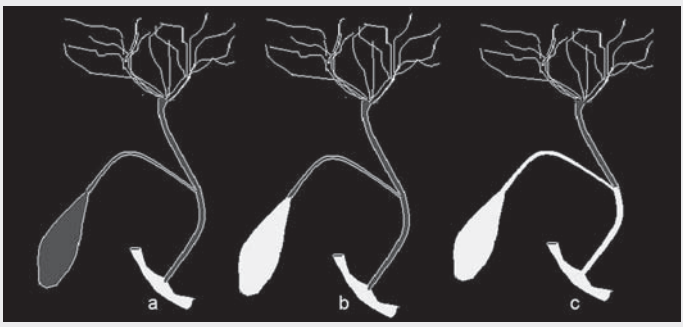

On sonography, both biliary atresia and neonatal hepatitis syndrome can show normal or increased echogenicity of the liver parenchyma. The liver size is usually normal, and ductal dilatation is absent in both conditions. In biliary atresia, a marked increase in periportal echoes may be seen, which may represent early periportal fibrosis. A triangular or tubular echogenic density adjacent to the portal vein bifurcation has also been described in children with biliary atresia and has been called the triangular cord sign, considered to represent the fibrous remnant of biliary atresia. This sign is relatively specific for extrahepatic biliary atresia (Fig. 5.28).

Fig. 5.28. Biliary atresia in a 41-day-old girl with jaundice. Longitudinal sonogram shows an echogenic cord (long and short arrows) anterior to the portal vein (PV) and the hepatic artery (HA), indicating fibrosis along the course of the common hepatic duct; there is also a small gall bladder

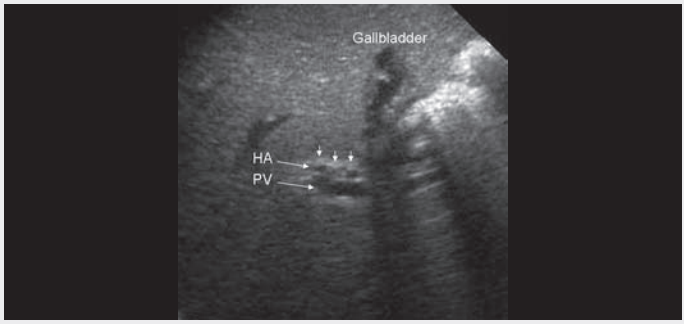

In neonate hepatitis syndrome, the gall bladder may be large, normal or small. In biliary atresia, the gall bladder is usually small or absent and not visualized (Fig. 5.29).

Fig. 5.29. Small gall bladder in biliary atresia (arrow) in a newborn boy. Oblique scan

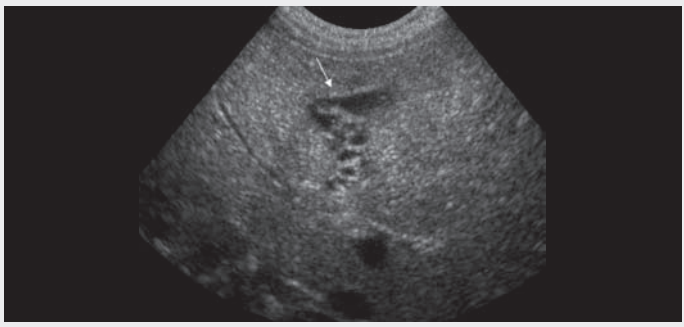

A change in gall bladder size after a milk feeding suggests that the common hepatic and common bile duct are patent; this is seen only in neonatal hepatitis.

In 10–20% of children with biliary atresia, other anomalies are found, such as choledochal cyst, polysplenia, preduodenal portal vein, azygous continuation of the inferior vena cava, diaphragmatic hernia, situs inversus or hydronephrosis. The abdomen should be examined for signs of end-stage liver disease, including ascites, hepatofugal flow in the portal and splenic veins and collateral venous channels.

Alagille syndrome (also known as arteriohepatic dysplasia) is characterized by a paucity of interlobular bile ducts. It is usually an autosomal dominant trait and is associated with cholestatic jaundice, pulmonary artery stenosis, butterfly vertebrae and hemivertebrae, and abnormal facies (deep-set eyes, pointed chin, frontal bossing, bulbous tip of the nose). The ultrasound findings are similar to those in biliary atresia. In these children, histological analysis reveals a paucity and hypoplasia of the interlobar ducts. Hepatobiliary scintigraphy and MRI cholangiopancreatography can also provide useful information for evaluating the patency of intra- and extrahepatic biliary ducts.

When neonatal hepatitis and biliary atresia cannot be differentiated by imaging, percutaneous liver biopsy may be necessary, especially when scintigraphy is not available or when small-bowel activity cannot be demonstrated on hepatobiliary scintigraphy. Cholangiography is indicated when the imaging and pathological findings suggest a diagnosis of biliary atresia. It may be performed percutaneously, endoscopically or intraoperatively via the gall bladder. When extrahepatic biliary atresia is confirmed intraoperatively, a Kasai portoenterostomy is performed, which may be effective in infants under 3 months. Poor results are seen in cases of cirrhosis. Liver transplantation may be the final option.

Changes in the Doppler-assessed portal venous velocity have been described in children with biliary atresia, and a correlation between decreased velocity and poor postoperative prognosis has been reported. Patients with reduced portal venous velocity, elevated hepatic arterial resistance or a flattened hepatic vein needed transplantation, while children with normal velocity do well with portoenterostomy alone.

Choledochal cyst

Choledochal cysts are malformations of the extrahepatic and intrahepatic bile ducts. Their origin is unknown, but they may be the result of an anomalous junction of the pancreatic and distal common bile duct, resulting in reflux of pancreatic enzymes into the biliary tree, which causes chemical cholangitis and eventually dilatation of both the common bile duct and the entire biliary tree.

The child may be asymptomatic or have pain, an abdominal mass and cholestatic jaundice. Sonography shows a well-defined cystic mass in the region of the porta hepatis that is in continuity with the hepatic bile duct and separate from the gall bladder. The cyst may measure 2–35 cm. The pancreas and pancreatic duct should be examined for evidence of pancreatitis or ductal dilatation. Antenatal ultrasound may show a choledochal cyst as early as 15–20 weeks' gestational age. Biliary scintigraphy and MRI cholangiography can be used to confirm that the dilated cystic structure communicates with the biliary tree. Five types of choledochal cysts with several subtypes have been described by Todani et al. (Fig. 5.30).

Fig. 5.30. Four anatomical types of choledochal cysts (Alonso-Lej classification). Type I, fusiform dilatation of the common bile duct; type II, true diverticulum arising from the common bile duct; type III, choledochocoele; type IV, multiple intra- and extrahepatic cysts

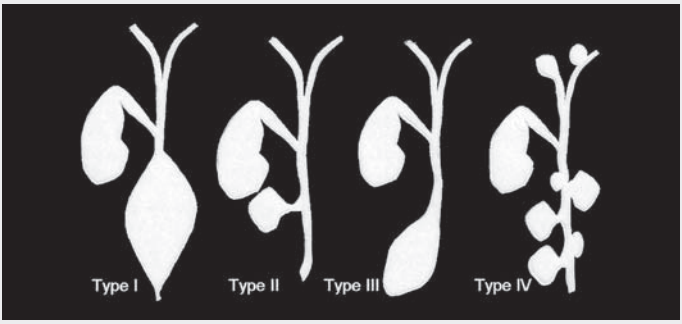

Fig. 5.31. Choledochal cyst type I. (a) Oblique scan and (b) axial scan show diffuse fusiform dilatation of the common bile duct (arrows). (c) MRI cholangiogram shows a lobular choledochal cyst (CC) in the porta hepatis with cystic dilatation of the left (L) and right (R) hepatic ducts; the gall bladder (GB) is separate

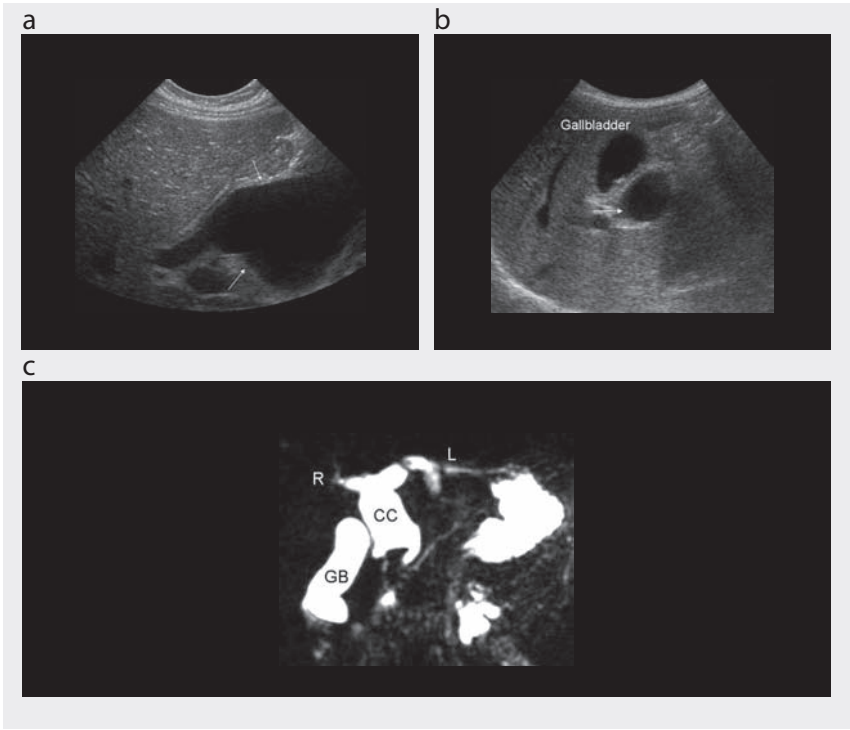

Type I cysts, which are characterized by segmental or diffuse fusiform dilatation of the common bile duct, are the commonest, accounting for 75–95% of cases (Fig. 5.31). The Todani type II choledochal cyst consists of a true diverticulum arising from the common bile duct and is found in 2% of cases. Todani type III is a choledochocoele that involves only dilatation of the intraduodenal portion of the common bile duct and is found in 1–5% of cases. Todani type IV accounts for about 10% of cases and is divided into two subtypes: type IVA is the second commonest form and consists of multiple intra- and extrahepatic cysts; type IVB involves multiple extrahepatic cysts and is rare. Type V, or Caroli disease, consists of single or multiple intrahepatic biliary cysts; it is rarely seen in neonates or young infants. Imaging shows multiple, branching, tubular structures, corresponding to dilated biliary radicals (Fig. 5.32). The portal radicals may be partially or completely surrounded by dilated ducts, and there may be dilatation of the common bile duct. Caroli disease is usually associated with hepatic fibrosis, portal hypertension or polycystic kidney disease.

The differential diagnosis of choledochal cyst includes hepatic cyst, enteric duplication cyst, pancreatic pseudocyst, hepatic artery aneurysm and spontaneous perforation of the common bile duct. Use of colour Doppler to identify vessels in

cases of aneurysm is helpful, as it is helpful to identify the digestive layers in cases of digestive duplication cysts. The commonest complications of choledochal cyst are cholelithiasis, choledocholithiasis, pancreatitis, abscess, malignancy and cirrhosis.

Fig. 5.32. Caroli disease in a 3-year-old boy. Oblique sonogram shows multiple intrahepatic cyst structures, with a branching pattern similar to that of the bile duct (arrow)

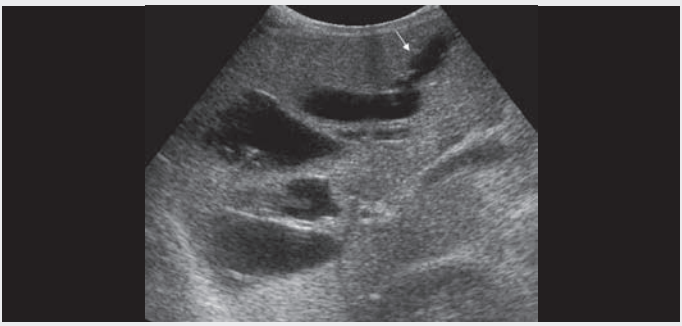

Inspissated bile syndrome

Inspissated bile syndrome, or bile plug, consists of extrahepatic obstruction of the bile ducts by biliary sludge in full-term infants. Ultrasound shows dilated bile ducts containing moderately or highly echogenic material without acoustic shadowing. Sludge may be seen within the gall bladder (Fig. 5.33). The causes include total parenteral nutrition, Hirschsprung disease, intestinal atresia, rhesus incompatibility, haemorrhage and cystic fibrosis.

Fig. 5.33. Inspissated bile syndrome in a 2-month-old boy. Oblique sonogram shows dilated common bile ducts containing echogenic material without acoustic shadowing (arrows); there is also sludge within the gall bladder (GB)

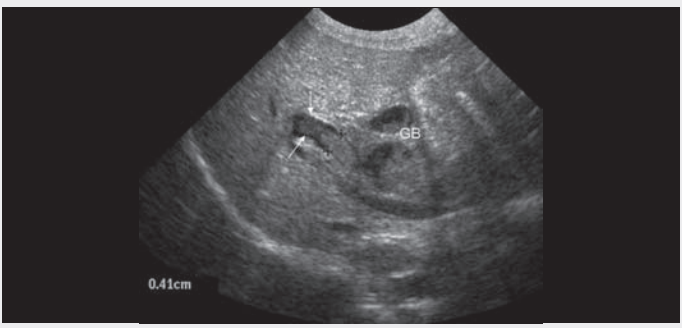

Cirrhosis

Cirrhosis is rare in neonates but may occur in older children. It can cause jaundice. This condition, consisting of chronic destruction of the hepatic parenchyma with replacement by fibrosis and nodular regeneration, may be caused by chronic hepatitis, congenital hepatic fibrosis, biliary atresia, cystic fibrosis, metabolic disease (Wilson disease, glycogen storage disease, tyrosinaemia, galactosaemia, α-antitrypsin deficiency), Budd-Chiari syndrome or total parenteral nutrition.

On ultrasound, a dystrophic liver appears, with an atrophic right hepatic lobe and medial segment of the left lobe, and compensatory hypertrophy of the lateral segments of the left and caudate lobes. The hepatic echo pattern is often heterogeneous, with multiple regenerating nodules. Other signs of cirrhosis, including ascites and portal hypertension, are often seen. Colour Doppler is useful to determine the permeability and the direction of portal flow, to look for porto-systemic shunts and the aspect of the hepatic veins, and to visualize flow in the splenic and mesenteric veins, the hepatic artery and the inferior vena cava.

Cholelithiasis and choledocholithiasis

Gall stones in infancy are generically asymptomatic; their incidence is approximately 1.5%. Common causes of cholelithiasis in infants and children include furosemide therapy, malabsorption, total parenteral nutrition, Crohn disease, cystic fibrosis, bowel resection and haemolytic anaemia. Calculus formation can also be idiopathic. The sonographic appearance of a gall stone is an echo-rich intraluminal structure that causes distal acoustic shadowing and which moves with changes in the child's position (Fig. 5.34).

Cholecystitis is an inflammation of the mucosa of the gall bladder wall due to bacterial infection. Acute cholecystitis is uncommon in infants and children. It may be either calculous or acalculous; 50% of paediatric cases are caused by stones obstructing the cystic duct. Imaging findings in acute cholecystitis include gall bladder distension, intraluminal sludge, wall thickening > 3 mm, pericholecystic fluid and inflammatory changes in the pericholecystic fat (Fig. 5.35).

Fig. 5.34. Infantile gall stone secondary to sickle-cell disease in a 3-year-old boy. Oblique sonograms through the gall bladder demonstrate multiple small gall stones (arrows), with distal acoustic shadowing (arrowheads)

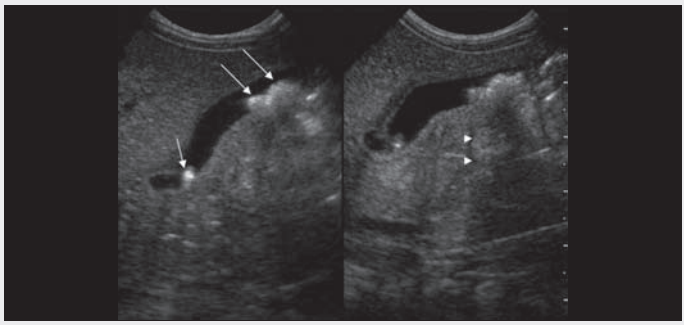

Fig. 5.35. Acute calculous cholecystitis in a 5-year-old girl. (a) Oblique and (b) transverse scans show thickening (two-headed arrow) of the gall bladder wall, which appears echo-poor, and small shadowing calculi in the gall bladder (arrowhead)

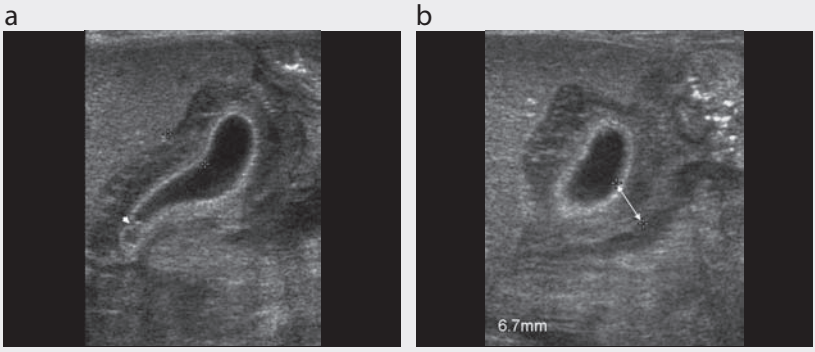

Complications of acute cholecystitis include gangrene, emphysema of the gall bladder wall and perforation. The presence of a Murphy sign (localized subhepatic pain during ultrasound exploration) can assist diagnosis. Irregularities in the thickened gall bladder wall may suggest gangrenous changes, bubble gas signs indicate emphysema and pericholecystic fluid suggests perforation.

Hydrops, or gall bladder distension, is characterized by massive dilatation of the gall bladder in the absence of inflammation. It may be asymptomatic or manifested as a right mass with abdominal pain (Fig. 5.36). The common causes include Kawasaki disease (mucocutaneous lymph node syndrome), scarlet fever, sepsis, leptospirosis, ascariasis, typhoid fever, total parenteral nutrition and familial Mediterranean fever.

Fig. 5.36. Hydrops of the gall bladder in a 2-year-old girl. Longitudinal scan shows a markedly dilated gall bladder and normal wall thickness; the echoes inside the gall bladder represent sludge

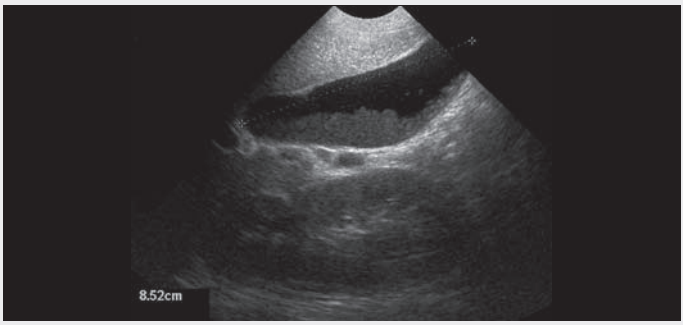

Spleen

Indications

Ultrasound is the preferred imaging modality for initial evaluation of the spleen in children with splenomegaly (haematological, infectious or rheumatic disease), palpable abdominal mass, ascites, suspected spleen abscess, abdominal trauma, suspected endemic echinococcosis or liver disease.

Preparation

No particular preparation is needed.

Examination technique

No premedication is needed. The child lies in the supine position initially and later on the left or right side. Coupling agent is applied liberally, first over the left upper abdomen and then over the rest of the abdomen as the examination proceeds. Scanning should be performed in the longitudinal, transverse and oblique planes, including scans through the intercostal and subcostal regions. The examination should be carried out with high-frequency convex or linear probes ranging from 3.5 to 7 MHz. Ultrasound Doppler is useful for locating vessels and for ensuring the permeability of the vascular structures.

Normal findings

The normal spleen has a homogeneous echo texture, similar to that of the liver (Fig. 5.37). The splenic hilar vessels are usually obvious, but intrasplenic vessels are not. The size of the spleen depends on the age of the child: in neonates, the normal length is 4 cm, which increases linearly with age by about 0.5 cm per year (Fig. 5.38). The upper limit of normal spleen length is 6 cm at 3 months, 7 cm at 12 months, 8 cm at 2 years, 9 cm at 4 years and 10 cm at 8 years. In adolescents, the upper limit for length is 12 cm for girls and 13 cm for boys; the upper limit is 7 cm for width and 3 cm for thickness. In general, the tip of the spleen should not extend below the inferior pole of the left kidney.

Fig. 5.37. Normal echo texture and echogenicity of the spleen (S) in a 5-year-old boy. Longitudinal scan shows a homogeneous echo texture; splenic hilar vessels are well visualized (arrow)

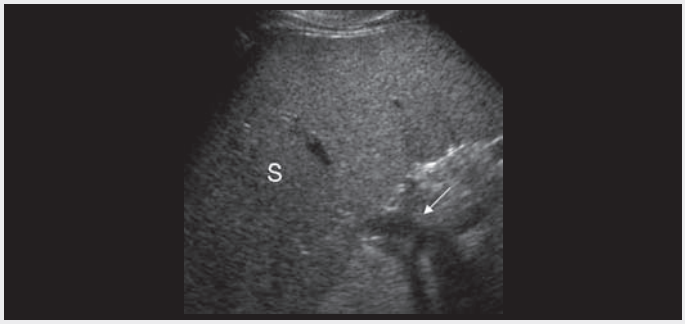

Fig. 5.38. Spleen size in a 2-month-old girl. Longitudinal scan shows a spleen measuring 4.26 cm between the lower and upper pole

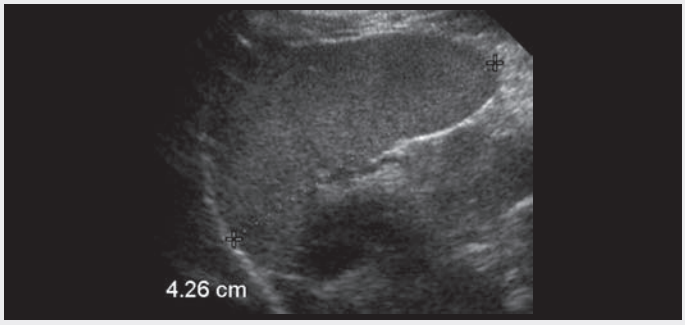

Pathological findings

Anomalies of form, number and position

Splenic lobulation

Splenic lobulation is simple persistent fetal lobulation with no particular pathological symptoms. It is frequent in children and appears sonographically as a medial or anterior notch within the splenic parenchyma (Fig. 5.39).

Fig. 5.39. Splenic lobulation in a 5-month-old girl. Longitudinal scan shows lobulation (arrows) of the spleen (S)

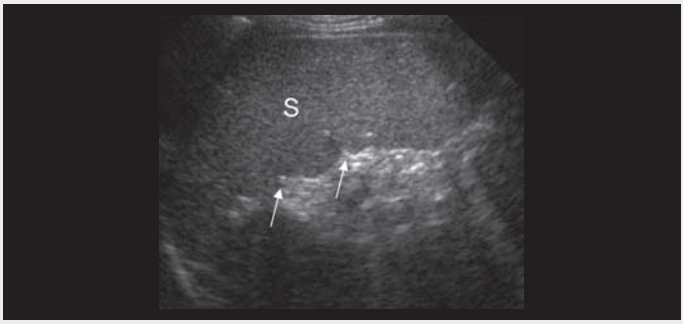

Accessory spleen

Single or multiple accessory spleens are common anatomical variants, found in 10–30% of people at autopsy. They are inborn disorders, resulting from defective fusion of splenic mesenchymatous aggregates. A single accessory spleen is usually smooth and presents as a round or oval formation < 4 cm in diameter. Its echogenicity

Fig. 5.40. Accessory spleen in a 3-year -year boy. Longitudinal scan shows a small nodule (arrows) of tissue adjacent to the splenic hilum and the left kidney (LK), with echogenicity similar to that of the adjacent splenic (S) parenchyma

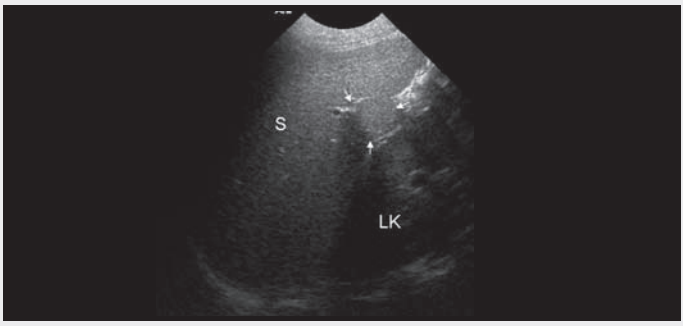

is similar to that of the normal spleen (Fig. 5.40). Accessory spleens are usually located in the splenic hilum and along the splenic vessels, but can be found remotely, even in the thorax. Accessory spleens may develop after splenectomy.

Wandering spleen

Wandering spleen is a disorder characterized by laxity of the suspensory splenic ligaments, which allows the spleen to lie in an ectopic location. In the event of vascular pedicle laxity, the spleen may be mobile in the abdominal cavity. These spleens, also known as portable lamps, are vulnerable to ischaemia and splenic infarction due to torsion of the pedicle. The imaging findings are an absence of splenic tissue in the upper left quadrant and a mass elsewhere in the abdomen with a shape and echo texture similar to those of normal spleen. Ultrasound allows a diagnosis of ectopic spleen, and Doppler consolidates a diagnosis of ischaemia or infarction by visualizing either torsion of the pedicle or defective vascularization of the splenic parenchyma.

Polysplenia and asplenia

Polysplenia and asplenia are rare and are often associated with visceral heterotaxy, cardiac and pulmonary abnormalities, interruption of the inferior vena cava and azygous continuation and a preduodenal portal vein or bile duct atresia (Fig. 5.41). Polysplenia is characterized by multiple splenic nodules in the left or right upper quadrants (Fig. 5.42). Asplenia is characterized by an absence of splenic tissue. Polysplenia is sometimes completely isolated and is detected fortuitously, in contrast to asplenia, which is generally found in the polymalformation syndrome. Asplenia must be differentiated from splenic atrophy post-infarction in sickle-cell anaemia.

Fig. 5.41. Polysplenia with interruption of the inferior vena cava in a 5-year-old boy. (a) Ultrasonography shows two spleens (S) in the upper right quadrant, associated with situs inversus. (b) Axial contrast-enhancement CT scan shows azygous continuation (arrow) of the inferior vena cava

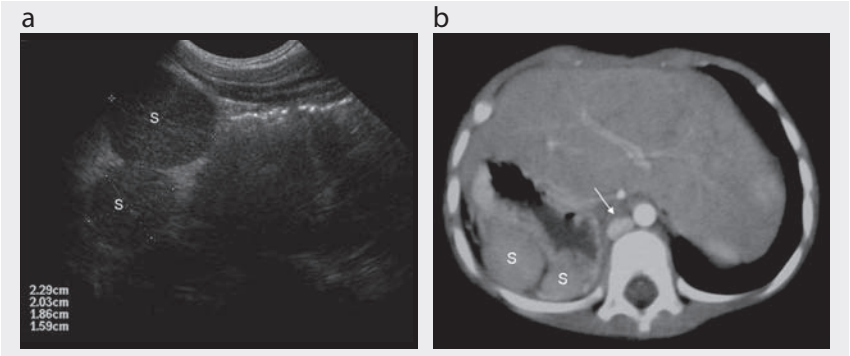

Fig. 5.42. Polysplenia in a 7-month-old girl. Multiple small spleens (S) are seen in the upper left quadrant; just above the diaphragm, a small quantity of pleural effusion (PE) is seen, with an atelectatic lower lobe of the left lung (LL)

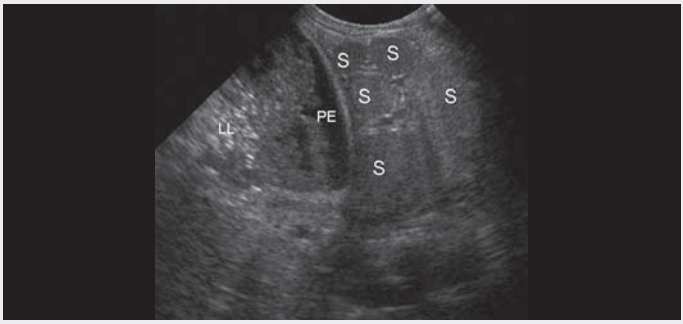

Anomalies of size

Splenic atrophy

Splenic atrophy may be seen in sickle-cell anaemia after splenic infarction (Fig. 5.43), coeliac disease and in Fanconi anaemia.

Fig. 5.43. A 15-year-old boy with splenic atrophy and infarction secondary to sickle-cell disease. Oblique sonogram shows splenic atrophy with increased echogenicity of the spleen parenchyma (arrow) and multiple echo-poor nodular lesions (N)

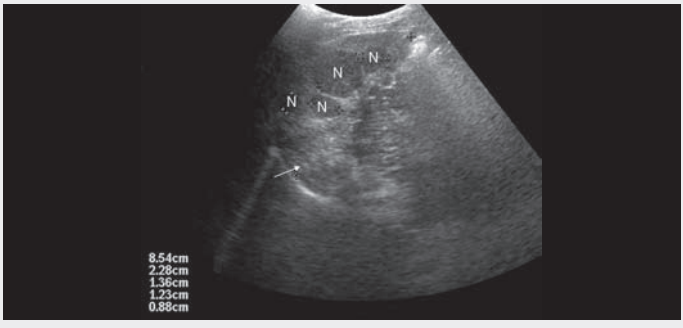

Splenomegaly

Splenomegaly in children is usually the result of infectious or parasitic processes but can be found in many paediatric conditions, either as part of the general condition (portal hypertension, haemolytic anaemia, lymphoma, leukaemia, overload disease) or in isolation as a sign of another condition, such as Gaucher disease. The ultrasound findings are usually nonspecific (Fig. 5.44).

Fig. 5.44. Splenomegaly in a 2-year-old girl with thalassaemia. Longitudinal scan shows a large, homogeneous spleen (S) compressing the left kidney (LK)

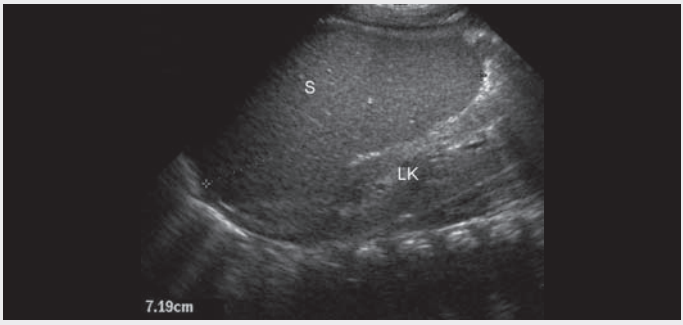

Portal hypertension

Portal hypertension usually results from increased resistance to hepatopetal portal venous flow. The clinical signs include splenomegaly, ascites, prominent abdominal vein, haematemesis and hepatic encephalopathy. The ultrasound findings in portal hypertension include a large portal vein, decreased or reversed portal venous flow, increased calibre of the hepatic artery, portosystemic shunts, splenomegaly, a thick lesser omentum, ascites and signs of cirrhosis. Colour Doppler detects the flow, localizes the obstacle in the portal or hepatic vein and indicates whether another imaging modality, follow-up or shunting treatment is needed.

Parasitic and viral infections

Parasitic and viral infections, such as Epstein-Bar virus infection and cat-scratch disease, are major causes of splenomegaly in children. In areas in which *Plasmodium falciparum* is endemic, so-called tropical idiopathic splenomegaly is common in young people. This clinical entity is defined by splenomegaly with or without hepatomegaly, elevated immunoglobulin M and coagulopathy of unclear secondary etiology. Splenomegaly is also common in fungal infections and in protozoan diseases such as malaria and leishmaniasis.

Haemoglobinopathy and haematological malignancies

Haemoglobinopathy and malignancies such as leukaemia and lymphoma may be associated with splenomegaly (Fig. 5.45).

Fig. 5.45. Splenomegaly in an 11-year-old boy with Hodgkin lymphoma. Longitudinal scan shows splenomegaly with multiple echo-poor lesions

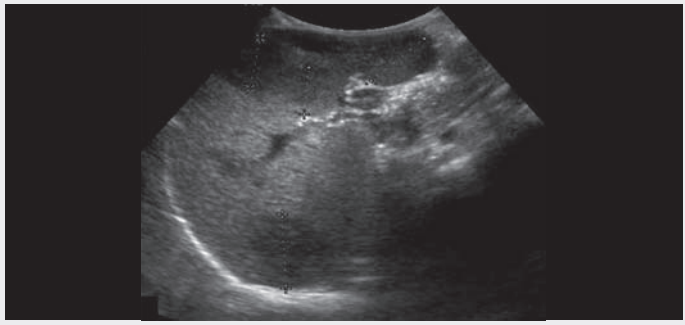

Focal lesions

Bacterial and fungal sepsis

Bacterial and fungal sepsis can be the cause of single or multiple nodular intrasplenic lesions. Patients usually present with fever and upper left quadrant pain, and splenomegaly is found on physical examination. Imaging shows splenomegaly with multiple small abscesses that are echo-poor on sonography and clearly demarcated. Calcifications may be seen after treatment (Fig. 5.46).

Fig. 5.46. Splenic microabscesses secondary to *Mycobacterium tuberculosis* infection in a 4-year-old girl. Oblique scans. (a) Echo-rich lesions (caliper), well demarcated, in the splenic parenchyma (S), surrounded by an echo-poor halo. (b) 8 months later, multiple calcifications (arrows) in the spleen (S)

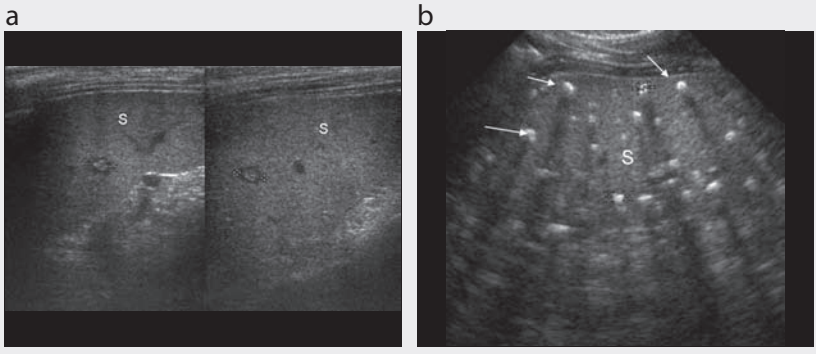

Epidermoid cyst

Epidermoid cysts are congenital lesions, which are often rich in cholesterol crystals. They are generally isolated, unilocular and rarely calcified. The imaging findings are nonspecific. On sonography, they usually appear as unilocular, smooth-walled, echo-free lesions (Fig. 5.47). Septations and wall calcification are infrequent. The internal echogenicity is probably due to cholesterol crystals or lipid droplets. Epidermoid splenic cysts can be complicated by intracystic haemorrhage or splenic rupture in the case of large cysts.

Fig. 5.47. Epidermoid splenic cyst in an 8-year-old girl. Longitudinal scan reveals a round, sharply marginated cyst (C) with internal echoes; S, spleen

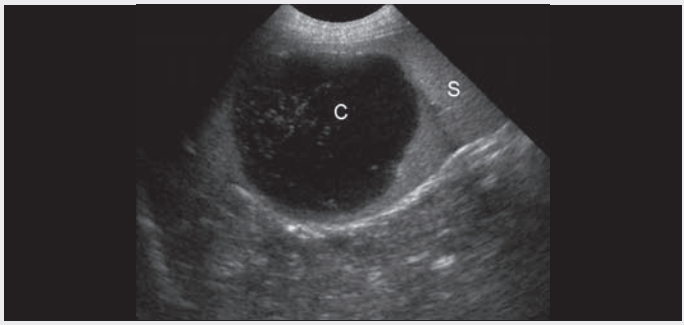

Splenic angioma

Splenic angioma is a congenital malformation which is rarely encountered in childhood. Angiomas are composed of vascular channels lined with a single endothelial layer and filled with red blood cells. They may be isolated or part of a syndrome, such as Klippel-Trenaunay-Weber and Beckwith syndromes. Immature angiomas are characterized by a proliferative phase, a phase of stabilization, then spontaneous regression with calcifications.

The imaging findings of splenic angioma are similar to those of the liver. The ultrasound appearance is an echo-rich, homogeneous lesion with well-defined margins (Fig. 5.48). Calcification may occur. Colour Doppler shows a prevalence of veins with broad, low-flow vascular lakes or a prevalence of capillaries.

Fig. 5.48. Splenic angioma in a 6-year-old girl. (a) Axial noncontrast CT image shows a large low-density mass within the spleen. (b) Arterial phase contrast-enhanced CT shows a bright enhancement of the lesion (arrows)

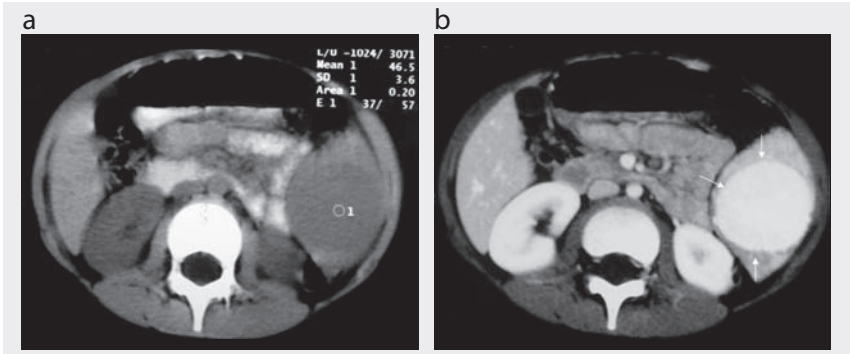

Hydatid cyst of the spleen

Splenic hydatid disease is rare but not exceptional. It has been reported to account for up to 4% of cases of abdominal hydatid disease. The ultrasound aspect is similar to that of hydatid cyst of the liver (Fig. 5.49).

Fig. 5.49. Splenic hydatid cyst in a 9-year-old boy. Transverse scan shows fluid collection with multiple secondary vesicles (arrows) within the splenic parenchyma (S), which compresses the left kidney (LK)

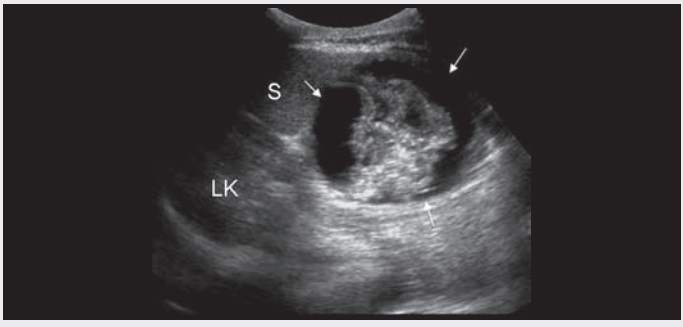

Splenic lymphangioma

Lymphangiomas are congenital malformations of the lymphatic and venous systems that result in a mass of dilated lymphatic channels with aberrant or obstructed outflow. They are considered to be benign vascular tumours and can occur elsewhere; the splenic location is rare. Progression is slow, with inflammatory and infectious episodes.

The lesion may be cystic, solid or mixed. Typically, ultrasound shows multiple well-defined echo-free or echo-poor lesions throughout the spleen. Colour and pulse Doppler may give an objective vascular pattern within the fine loculations, which confirms the diagnosis of haemolymphangioma. In cases of haemorrhagic or infectious complications, fine echoes and thick loculations can be seen. The extension study is best performed with CT or MRI.

Trauma

Splenic lesions are the most frequent traumatic abdominal lesions in children. The imaging characteristics of splenic trauma are similar to those seen in the liver. They are classified as parenchymal haematoma, subcapsular haematoma (Fig. 5.50), contusion (Fig. 5.51), laceration or fracture (Fig. 5.52).

Fig. 5.50. Splenic injury after trauma in a 12-year-old boy. Longitudinal scan shows a heterogeneous, echo-poor parenchymal haematoma (PH) with a large elliptical subcapsular haematoma (SH), causing a mass effect on the adjacent spleen parenchyma

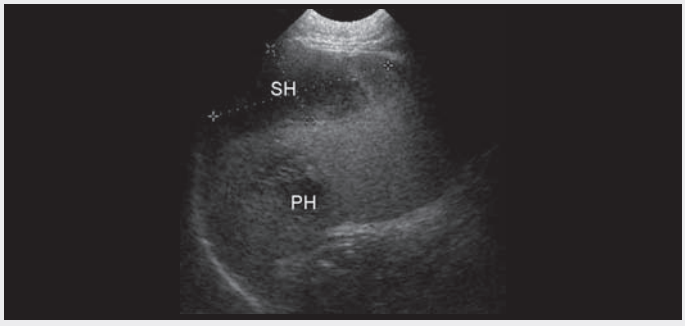

Fig 5.51. Splenic contusion in an 8-year-old boy. Longitudinal sonogram shows an echo-poor parenchymal region in the lower pole of the spleen (S); calipers indicate longitudinal diameter of the spleen

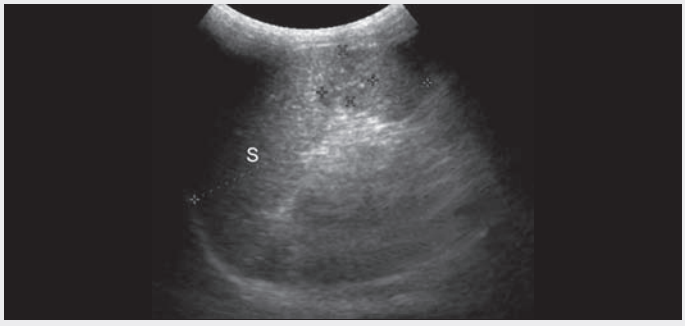

Fig. 5.52. Splenic laceration. Longitudinal scan shows a branching laceration within the splenic parenchyma (arrows). S, spleen

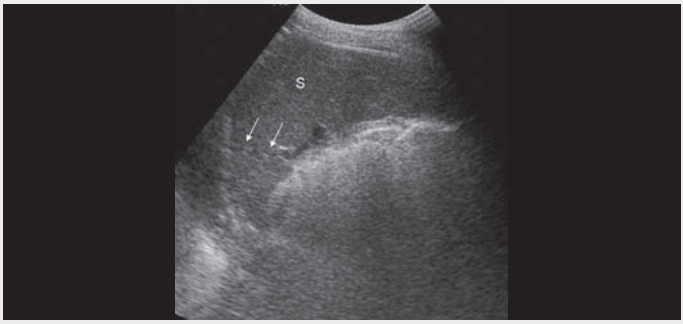

Hepatosplenomegaly

Haematological diseases

Leukaemia, Hodgkin disease and lymphomatous infiltration are frequently the cause of massive hepatosplenomegaly. The usual associated signs are nodular formations, echo-poor lesions in the spleen or liver, lymph node enlargement, kidney infiltration, pleural effusion, ascites and other abdominal masses.

Metabolic diseases

The diseases that result in hepatosplenic infiltration are mainly glycogenosis and dyslipidaemia; storage diseases may also have this result.

Pancreas

Indications

Ultrasound allows study of the echoic structure of the pancreatic parenchyma, detection of focal lesions and characterization of its consistency and limits. Typical indications are: jaundice, an upper abdominal mass, abdominal pain, recurrent chronic pancreatitis, polycystic kidneys and abdominal trauma.

Preparation

Infants should take nothing by mouth for 3 h before the examination. If they require fluid to prevent dehydration, only water should be given.

Examination technique

No premedication is needed. The child lies in a supine position initially and subsequently on the left or right side. Scanning should be in the longitudinal, transverse and oblique planes, including scans through the intercostal and subcostal regions. The ultrasound examination is carried out with high-frequency convex probes ranging from 3.5 to 7 MHz and linear probes of at least 7–15 MHz for neonates.

Ultrasound Doppler makes it possible to localize vessels and assess the permeability of vascular structures.

Normal findings

The normal pancreas in children is homogeneous and nearly isoechogenic with the liver (Fig. 5.53); however, in neonates, especially when premature, the pancreas can be echo-rich to the liver. Fatty replacement is not a normal finding in children. The dimensions of the pancreas vary directly with age. The pancreatic head and tail are usually similar in size and larger than the neck and body (Fig. 5.54). The upper anteroposterior dimension of the body is 1.5 cm, and the normal anteroposterior dimensions of the head and tail range from 1 to 2.5 cm. The main pancreatic duct may be seen as a single- or double-track echogenic line (Fig. 5.55). Its normal diameter should be no more than 1–2 mm.

Fig. 5.53. Normal echo texture of the pancreas in a 3-month-old boy. Transverse sonogram; homogeneous pancreatic parenchyma (arrows) with echogenicity similar to that of the adjacent liver parenchyma (L). IVC, inferior vena cava; SV, splenic vein; Ao, aorta

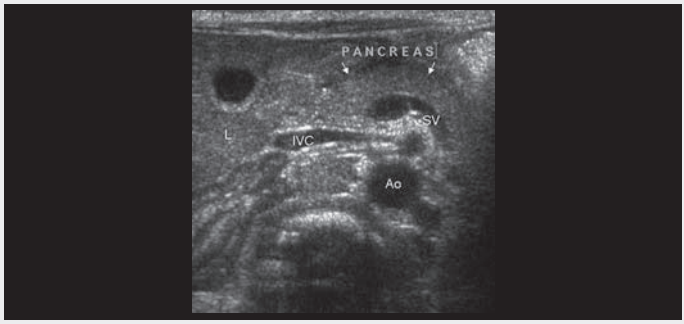

Fig. 5.54. Anatomical compartments of the pancreas. Transverse scan through the anterior pararenal space showing the head (H), neck (N), body (B) and tail (T) of the pancreas

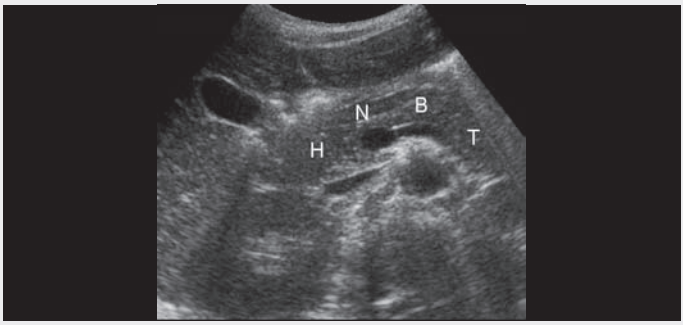

Fig. 5.55. Normal pancreatic duct in a 6-year-old boy. Transverse scan shows the pancreatic bile duct as a double echogenic line (arrow)

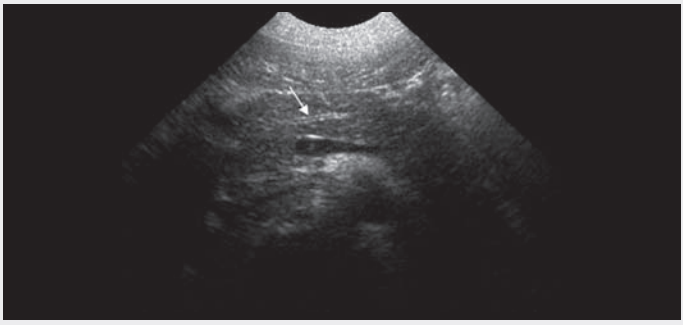

Pathological findings

Congenital and developmental anomalies

The pancreas develops from dorsal and ventral primordia, which usually fuse in utero. The ventral bud gives rise to the pancreatic head and the uncinate process, and the dorsal bud forms the remainder of the pancreatic head, as well as the body and tail. After fusion, the ventral duct joins the distal portion of the dorsal pancreatic duct to form the Wirsung duct. The proximal portion of the dorsal duct may regress or persist as an accessory duct, the Santorini duct. The Wirsung duct drains into the major papilla of Vater, while the Santorini duct empties into the accessory duodenal papilla, proximal to the ampulla of Vater.

Pancreas divisum

Pancreas divisum is the commonest and clinically most important major anatomical variant. It results from failure of the dorsal and ventral pancreatic ducts to fuse. The child may be asymptomatic or present with pancreatitis. It usually cannot be diagnosed with ultrasound but is suggested by CT, MRI or endoscopic retrograde cholangiography.

Pancreas anular

Although uncommon, pancreas anular is the second commonest congenital anomaly of the pancreas. It is characterized by two separate ventral moieties encircling the second part of the duodenum and results in a variable degree of duodenal obstruction. Most cases are diagnosed in infancy at the time of surgery for duodenal atresia or stenosis. The diagnosis is best made with CT and MRI, which show a thick circumferential band of pancreatic tissue encircling the duodenum. Many other associated abnormalities have been described: the commonest are intestinal malrotation, tracheo-oesophageal fistula, cardiac abnormalities, anal atresia and trisomy 21.

Congenital short pancreas

In congenital short pancreas, only the pancreatic head develops. The diagnosis can be made by sonography, CT and MRI and is based on identification of a pancreatic head and the absence of pancreatic tissue in the expected locations of the neck, body and tail. Polysplenia may be an associated finding.

Cystic fibrosis

Cystic fibrosis is a recessively inherited disease, with an estimated prevalence of 1 per 2000. The major pathological finding is obstruction of the ducts and ductules by mucoid secretion, which eventually leads to glandular atrophy, fibrosis and fatty replacement. Ultrasound shows a normal-size pancreas that is echo-rich to the liver.

Other causes of congenital pancreatic lipomatosis are Shwachman-Diamond syndrome, characterized by exocrine pancreas insufficiency, neutropenia, metaphyseal dysostosis and dwarfism.

Acute pancreatitis

Acute pancreatitis is uncommon in childhood. The commonest etiology is trauma, usually in motor vehicle accidents; other causes include non-accidental injury, post-surgical trauma, systemic disease, congenital anatomical abnormalities, metabolic diseases and drug toxicity. The systemic diseases include Reye syndrome, lupus, haemolytic uraemic syndrome, sepsis, shock and viral infections. Mumps virus has been specifically implicated as a causal agent.

A diagnosis of acute pancreatitis is usually based on combined clinical and biochemical findings. Ultrasound is the imaging procedure of choice for initial evaluation of possible pancreatitis. It shows focal or diffuse enlargement of the gland, with dilatation of the pancreatic duct and decreased echogenicity of the gland (Fig. 5.56). Severe acute pancreatitis often shows diffuse pancreatic enlargement, heterogeneous attenuation and inflammatory changes in the contiguous peripancreatic fat. The late complications of pancreatitis include pseudocyst fluid collection, abscess, vascular complications and extrapancreatic collection. Pseudocyst fluid collection and abscess occur more than 4 weeks after the onset of acute pancreatitis. On ultrasound, a pseudocyst is an encapsulated, echo-free or echo-rich collection with variable transmission (Fig. 5.57). A pancreatic abscess is a collection of pus, usually in close proximity to the pancreas. Pseudoaneurysm is a complex mass with enhanced transmission and turbulent arterial flow on duplex or colour flow Doppler imaging. CT is considered the procedure of choice for demonstrating the complications of pancreatitis, such as parenchymal necrosis, abscesses, haemorrhage and extrapancreatic collection.

Fig. 5.56. Acute pancreatitis in a 7-year-old girl. Transverse scan shows a diffuse, enlarged pancreas (P)

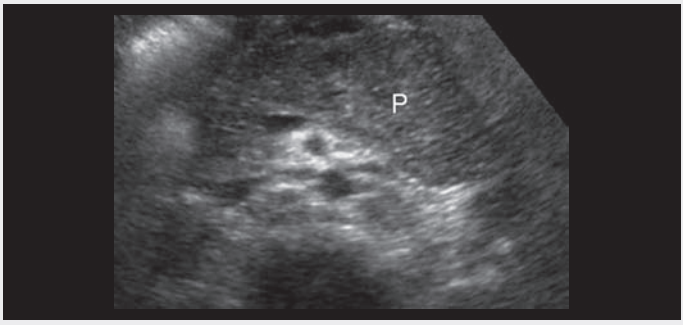

Fig. 5.57. Pancreatic pseudocyst in a 7-year-old girl due to accidental trauma on the handlebars of a bicycle. (a) Longitudinal scan shows well-defined pseudocyst (between calipers) anterior to the pancreatic body (P). (b), (c) Post-contrast CT images show the pseudocyst in the pancreas body and tail (arrows). L, liver; S, spleen

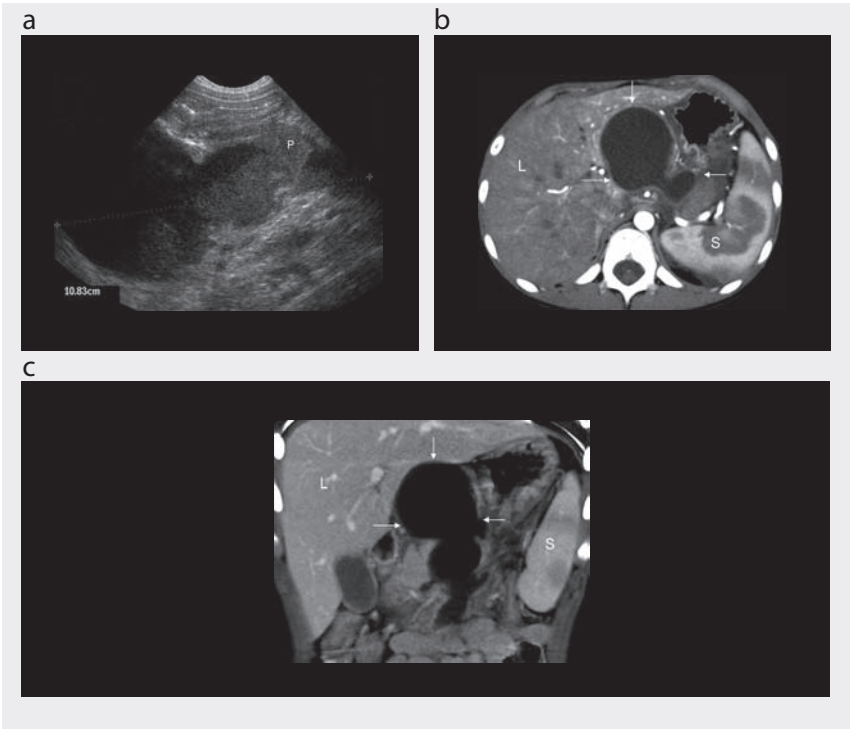

Chronic pancreatitis

Chronic pancreatitis is a continuing inflammatory process of the pancreas characterized by irreversible morphological changes, typically causing pain and permanent loss of exocrine and endocrine function. It is most commonly due to hereditary pancreatitis. Acute pancreatitis rarely becomes chronic in children. On ultrasound, the pancreas appears echogenic, with calcification and ductal dilatation (Fig. 5.58).

Fig. 5.58. Chronic pancreatitis in an 8-year-old boy. (a) Axial ultrasound scan through the anterior pararenal space shows pancreatic duct dilatation (arrow) and slightly echo-rich parenchyma; st, stomach. (b) Corresponding axial contrast-enhanced CT scan reveals the atrophic pancreatic parenchyma and the duct dilatation (arrow)

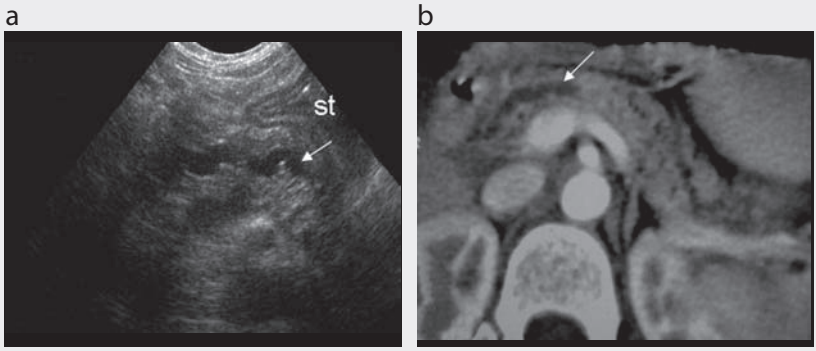

Trauma

Traumatic pancreatic injuries account for fewer than 5% of abdominal injuries. Most are due to motor vehicle accidents, bicycle handlebars or child abuse, and they are the commonest cause of acute pancreatitis in children. Early diagnosis is important, as a delay of more than 24 h is associated with increased morbidity. Ultrasound may show interruption of the pancreas, peripancreatic fluid collections and altered echogenicity (Fig. 5.59, Fig. 5.60).

Fig. 5.59. Pancreatic laceration in a 7-year-old girl after abdominal trauma. Transverse scan shows a heterogeneous pattern and enlargement of the pancreas neck, body and tail, with a branching laceration (arrow)

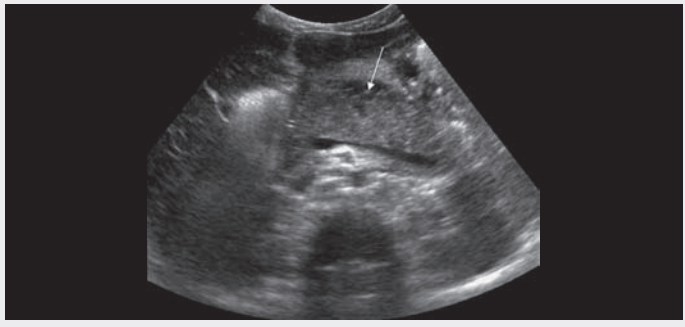

Fig. 5.60. Pancreatic fracture in a 12-year-old boy after trauma. (a) Axial contrast-enhanced CT image shows disruption of the pancreatic parenchyma between the body and tail at the site of transaction (arrows), with fluid in the peripancreatic space (arrowhead). (b) Transverse scan performed 2 weeks after injury shows formation of a pseudocyst (calipers)

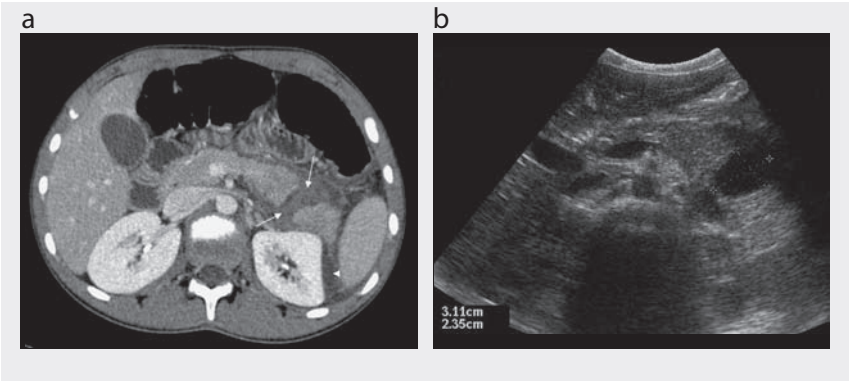

Pancreatic tumours

Pancreatic tumours, both benign and malignant, are extremely rare in children. They are classically divided into three groups: exocrine, endocrine and cystic.

Exocrine tumours

The exocrine tissues of the pancreas give rise to benign and malignant tumours that are hormonally inactive. Pancreatoblastoma is the commonest exocrine tumour; it arises from the pancreatic acinar cells, usually in the head or tail of the gland. It is a low-grade malignancy with a favourable outcome. It occurs most commonly in children aged 1–8 years. On ultrasound, a pancreatoblastoma is a well-defined, large mass, typically with a mixture of cystic and solid components.

Endocrine tumours

Islet-cell tumours are usually functioning and benign. They include insulinoma, gastrinoma, VIPoma (a tumour that produces vasoactive intestinal peptide), glucagonoma and somatostatinoma. Insulinoma is the commonest: children present with hypoglycaemia, and the symptoms are relieved by intravenous glucose. Insulinomas are typically small, round or oval masses. On ultrasound, they may be echo-rich, homogeneous masses, and the tumour margin may be well circumscribed.

Cystic tumours

The commonest cystic mass is a papillary epithelial tumour, which occurs primarily in adolescent girls and young women. The tumour is typically large and usually arises in the pancreatic tail. On sonography, it is a well-demarcated mass with variable solid and cystic components, reflecting the presence of haemorrhage and cystic degeneration (Fig. 5.61).

Fig. 5.61. Cystic pancreatic tumour in a 15-year-old girl. Transverse scan shows a large, predominantly cystic mass in the pancreatic tail, with a well-defined wall (arrows). P, pancreas

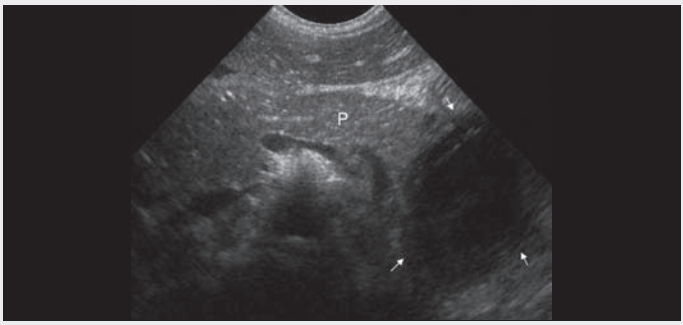

Multiple pancreatic cystic tumours may be seen in von Hippel-Lindau disease, an autosomal dominant polycystic disease, and in cystic fibrosis.

Digestive tract

Indications

The main indications for exploration of the digestive tract are:

- acute and chronic, generalized or localized pain, including suspected intussusception, indeterminate appendicitis, ascites and peritonitis;
- abdominal masses;
- vomiting, including suspected hypertrophic pyloric stenosis or the controversial gastro-oesophageal reflux in the recurrent bronchitis etiology;
- blunt abdominal trauma;
- congenital abdominal abnormalities.

Preparation

No specific preparation is needed in urgent and acute cases. In general, fasting 2 h before the examination is helpful. A full bladder is useful for checking the pelvis. Mothers should be present to breastfeed or to give infants food, water or milk.

Examination technique

Infants should be in the supine position initially and later on the left or right side. Older children should, if possible, take a deep breath and hold it while a specific area is being scanned.

The operator should start with the appropriate probe, which should be of the highest frequency, and then decrease the frequency if there is insufficient penetration. A frequency of 5–10 MHz is suitable for most children, and the correct gain should be set to obtain the best image. The operator should place the transducer centrally at the top of the abdomen and gradually move it clockwise. Gradually compressing the abdomen and gently pushing the bowel gas away allow better visualization if the abdomen is gassy.

The observations should include bowel-wall thickness, bowel motility, bowel contents, free fluid or collections in the abdomen and any mass or cyst related to the bowel. Doppler techniques, if available, are helpful, particularly in cases of suspected appendicitis, masses, intussusception and bowel inflammatory diseases. It is essential to check all the intra-abdominal organs.

Normal findings

Ultrasound usually demonstrates five layers of the wall of the digestive tract between the cervical oesophagus and the rectum: the echo-rich lumen interface, the echo-poor mucosa, the echo-rich submucosa, the echo-poor muscle layer and the echo-rich interface with the surrounding tissue (Fig. 5.62).

Most of the lower part of the cervical oesophagus can be seen behind the left lobe of the thyroid gland (Fig. 5.63; see also Fig. 5.174). The abdominal oesophagus and the cardia are seen behind the left liver lobe (Fig. 5.64).

Fig. 5.62. Normal echo texture of the wall of the digestive tract. Longitudinal scan shows the five layers

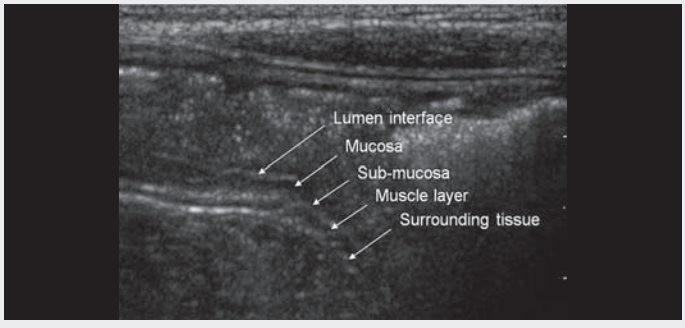

Fig. 5.63. Anatomy of normal cervical oesophagus in a 5-year-old boy. (a) Transverse and (b) longitudinal scans of the cervical oesophagus (arrow) behind the left lobe of the thyroid gland (Th)

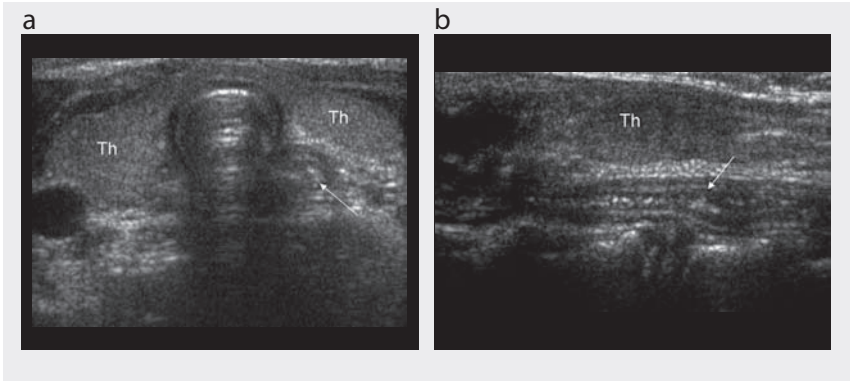

Fig. 5.64. Anatomy of normal abdominal oesophagus in a 15-month-old boy. Longitudinal scan shows the abdominal oesophagus, 2.73 cm in length; the stomach (st) is easily identified under the liver (L).

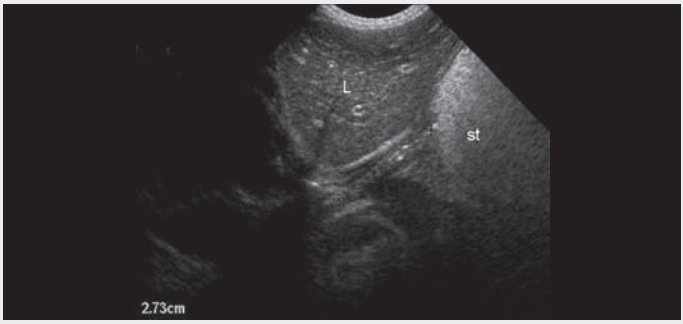

When the stomach is empty, it is easily identified below the left diaphragm as a star-shaped body. After a meal, pylorus (Fig. 5.65) and the rectum are observed behind the bladder (Fig. 5.66). The thickness of the normal digestive tract is ≤ 3 mm.

Fig. 5.65. Normal stomach anatomy in a 3-year-old girl. Longitudinal scan through the stomach shows the normal aspect of the fundus (F), antrum (A) and pylorus (Py)

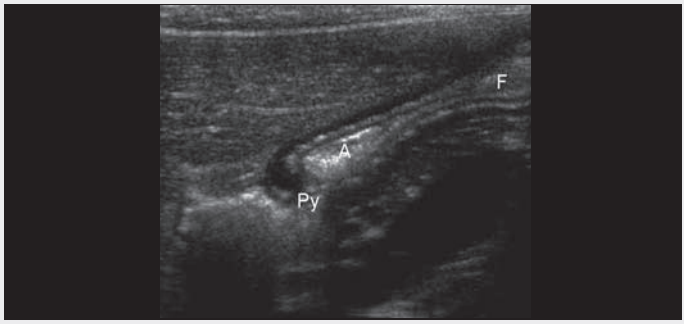

Fig. 5.66. Normal rectal anatomy in 6-month-old boy. (a) Transverse and (b) longitudinal scans show the rectum (R) posterior to the bladder (B)

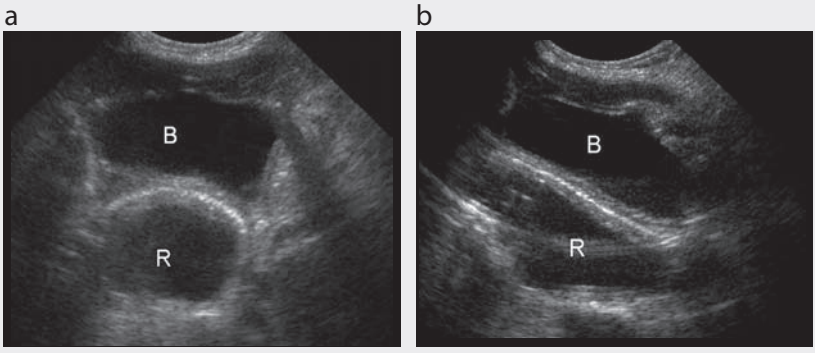

Pathological findings

Acute and chronic generalized or localized pain

Intussusception

Intussusception occurs most commonly between the ages of 6 months and 2 years. A proximal segment of the bowel (the intussusceptum) telescopes into a more distal segment (the intussuscipiens). Its incidence is seasonal. About 90% of intussusceptions are ileocolic and are thought to be due, in this age group, to enlarged lymphoid follicles (mesenteric adenitis) in the terminal ileum. Ultrasound is useful in the diagnosis of intussusception. The commonest site is the region of the ascending and transverse colon underneath the liver, but an intussusception can occur anywhere along the colon and, if severe, can protrude from the rectum.

Typical alternating echo-poor and echo-rich bands of mucosa and muscle layer can be seen, described as the target appearance in cross-section and as pseudokidney

in the longitudinal section (Fig. 5.67). Doppler shows hypervascularity. Poor vascularity suggests possible infarct of the bowel. The presence of free fluid trapped between the colon and the intussusceptum or in the Douglas pouch is associated with a significantly lower rate of success of reduction, with ischaemia of the bowel or peritonitis. Reduction of the intussusception in these situations is absolutely contraindicated.

Intussusception can be reduced with gas under ultrasound. The latter plays an important role in the follow-up of intussusception reduction by gas, water or barium enema and may allow detection of relapse of the intussusception or other complications.

Fig. 5.67. Intussusception in a 10-month-old boy with abdominal pain. (a) Supine radiograph shows a soft-tissue mass to the left of the midline (arrows). (b) Transverse sonogram shows a central intussuscipiens (CI) adjacent to echo-rich intussuscepted mesenteric fat (F); the outer surrounding intussusceptum (SI) is thickened and echo-poor due to oedema and haemorrhage of layers of the bowel wall

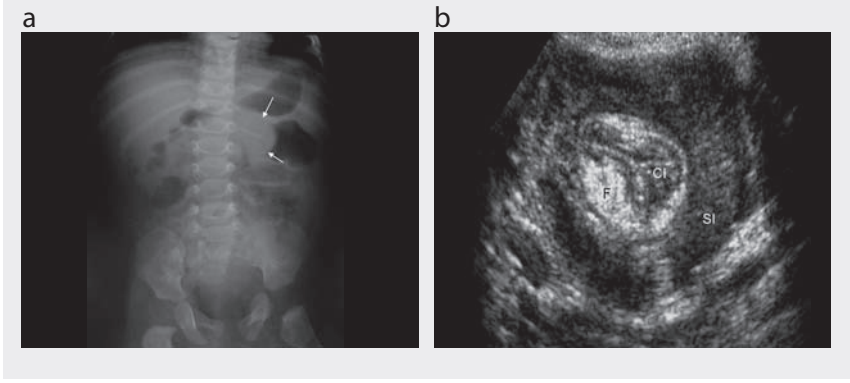

Appendicitis

Appendicitis is one of the commonest paediatric emergencies, occurring at any age but primarily in late childhood. In acute appendicitis, a child will typically present clinically with initial pain in the umbilical region or the right iliac fossa, with exquisite tenderness and fever. The ultrasound findings are similar to those in adults. It is generally easier to visualize the appendix in children than in adults because the transducer has a high frequency and the distance to the appendix is short.

The normal appendix, which is generally clearly seen, should be < 6 mm in diameter (Fig. 5.68). A diagnosis of appendicitis requires identification of an abnormally inflamed appendix, which is noncompressible, round and with a diameter > 6 mm; the surrounding mesentery and omentum are highly echogenic (Fig. 5.69). Fecaliths are identified in 20–30% of cases (Fig. 5.70). Increased vascularity may be seen with Doppler imaging (Fig. 5.71). If the appendix is perforated, a pelvic mass may be seen, with liquid in the Douglas pouch. Sometimes, ileus may be present, or there may be enlarged lymph nodes or a peri-appendiceal abscess and pus collection (Fig. 5.72).

Fig. 5.68. Normal appendix in a 4-year-old boy. Longitudinal sonogram through the right lower quadrant shows a normal-sized appendix (arrows), measuring < 6 mm in diameter. Note the central echogenic stripe representing the mucosa and submucosa and the peripheral echo-poor wall

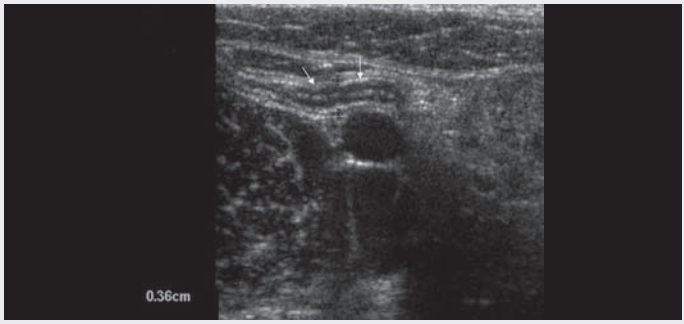

Fig. 5.69. Acute appendicitis in a 6-year-old girl. Longitudinal scan through the right lower quadrant shows a fluid-filled appendix (A) between calipers

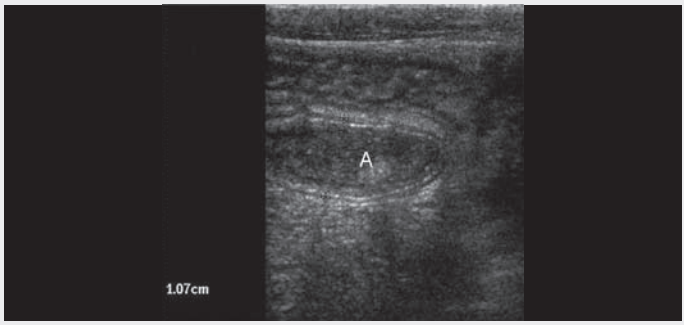

Fig. 5.70. Acute appendicitis in a 5-year-old boy. Longitudinal scan shows a fecalith (arrow) within an enlarged appendix (A) between calipers

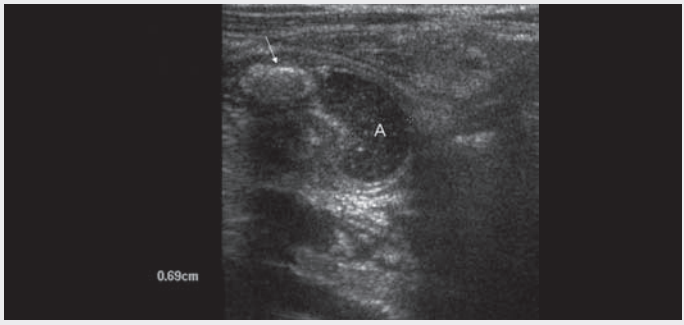

Fig. 5.71. Acute appendicitis in an 8-year-old girl. Longitudinal colour flow Doppler image shows a dilated appendix with peripheral hyperaemia

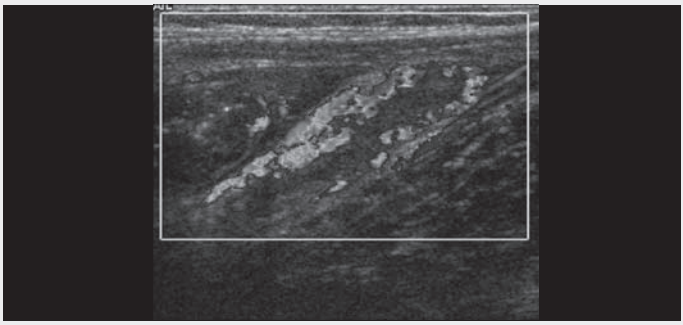

Fig. 5.72. Peri-appendiceal abscess in a 4-year-old girl. Transverse scan through the right lower quadrant shows a localized fluid collection representing a peri-appendiceal abscess (arrows). Note the echogenic fecalith (F) on the right side and the surrounding inflammation

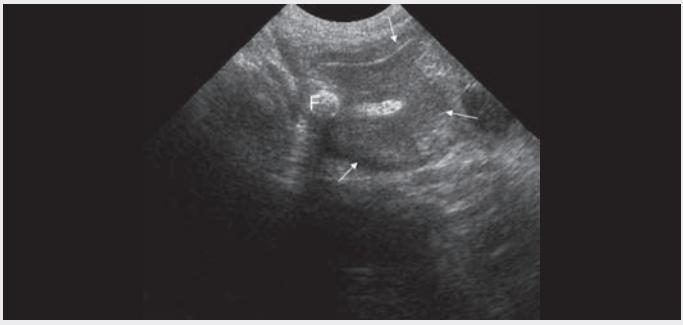

Mesenteric lymphadenitis

Mesenteric lymphadenitis is the main differential diagnosis of appendicitis. It is a viral mesenteric lymph node infection with nearly the same clinical presentation as appendicitis but with a normal white count. Ultrasound shows multiple nodal enlargement (more than one in the right iliac fossa), > 1 cm in size, with a normal appendix and normal appearance of the bowel wall (Fig. 5.73).

Fig. 5.73. Mesenteric lymphadenitis in a 5-year-old boy. Longitudinal scan shows multiple enlarged mesenteric lymph nodes between calipers

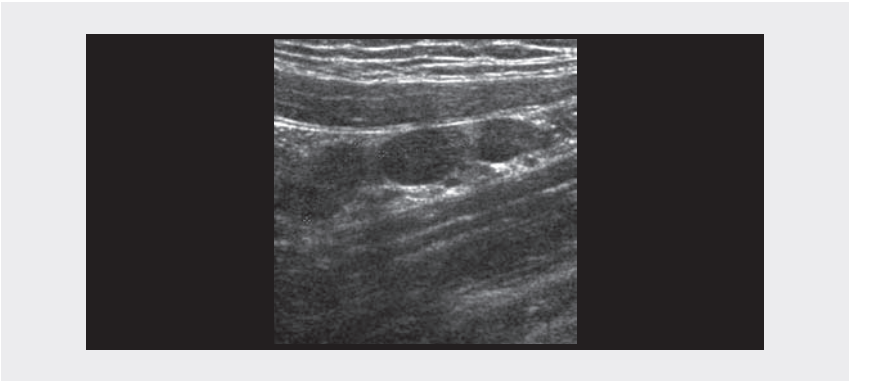

Abdominal masses

Ultrasound is useful for exploring abdominal masses in order to define the consistency, the organ affected and potential complications.

Cystic abdominal masses

A cystic mass in the abdomen is a common finding. The main types of cyst in the digestive tract, except for ascites, are parasitic masses, mesenteric or omental cysts and duplication cysts.

Parasitic masses are mainly hydatid cysts in children > 2 years in endemic areas. The most frequent abdominal location is the liver, but the spleen, kidneys and peritoneum may be affected. The ultrasound findings depend on the age of the cyst and whether it is complicated, corresponding to its developmental stage. In the Gharbi classification, the cyst appears as an echo-free space with a well-defined border (type I), as a fluid collection with a floating membrane (type II), as a septated fluid collection (type III), as a heterogeneous body (type IV) or as a calcified formation (type V). The complications of the cyst seen by ultrasound include compression of the neighbouring organs and rupture.

Lymphangiomas, the most common of **mesenteric** or **omental cysts**, are congenital malformations of the lymphatic vessels in the mesentery, with no communication with the intestine. They are generally large and homogeneous but often multiloculated and with a thin wall, which is sometimes partially solid (Fig. 5.74). Doppler imaging may show septal vascularization. These masses may be intimately associated with the intra-abdominal organs (bowel wall, liver, kidneys, pelvis), and ascites may be present.

Digestive tract duplication, also known as **duplication cyst**, is a spherical or tubular structure lined with gastrointestinal epithelium, which contains smooth muscle in its wall. It is due to incomplete canalization of the bowel. The cyst may

Fig. 5.74. Mesenteric cyst in a 3-year-old girl. (a) Transverse ultrasound scan shows a large cystic (C) lesion with thin internal septations (arrows). (b) Axial contrast-enhanced CT demonstrates a well-circumscribed cystic mass with smooth, thin walls and faint, thin septations (arrows)

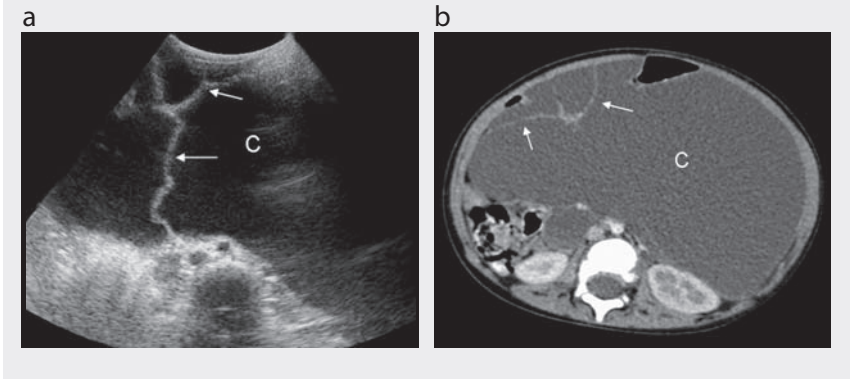

occur anywhere in the gastrointestinal tract, from the oesophagus to the rectum, but is usually found in the distal ileum, oesophagus, duodenum or stomach. Duplication cysts are of variable size and are sometimes palpable. They may communicate with the lumen of the bowel. Ultrasound examination shows certain identifying features, such as an echogenic mucosa and an echo-poor muscular layer. Most cysts are clear and echo-free, but internal echoes may be seen if there has been bleeding or if they communicate with the digestive tract lumen (Fig. 5.75). Tc-99 pertechnetate scintigraphy can confirm the presence of ectopic gastric mucosa.

Fig. 5.75. Duodenal cyst duplication in an 8-year-old boy with abdominal pain. (a) Longitudinal and (b) transverse scans of the right abdomen show a cystic mass (C) under the liver (L), with floating and layering internal debris (arrowheads); the wall is thickened, with alternating echo-rich and echo-poor layers (arrow)

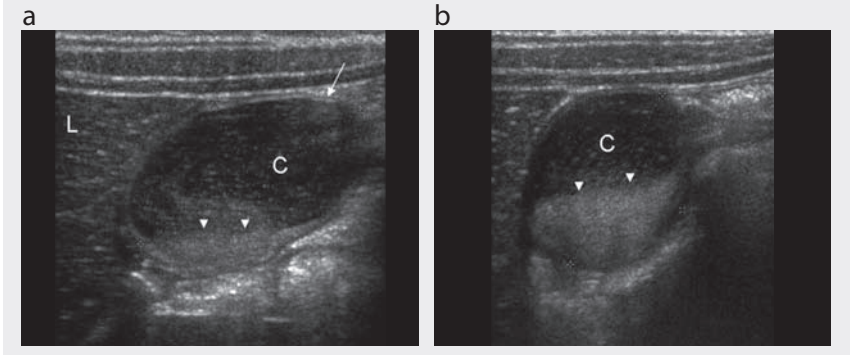

Non-cystic abdominal digestive masses

The main cause is enlarged lymph nodes (Fig. 5.76). Mesenteric lymphadenopathy is a common finding in the abdomens of children, with lymph nodes measuring < 5–6 mm in diameter. Enlarged mesenteric, para-aortic or para-iliac lymph nodes in the abdomen, often multiple or conglomerated into huge masses, suggest lymphoma or tuberculosis (Fig. 5.77). The lymphoma may infiltrate the bowel wall, the mesentery and omentum (Fig. 5.78; Fig. 5.79).

Fig. 5.76. Lymph nodes in a 3-year-old girl with abdominal pain. Transverse scan through the right lower quadrant shows multiple mesenteric lymph nodes (arrows), the largest of which is 1 cm in diameter

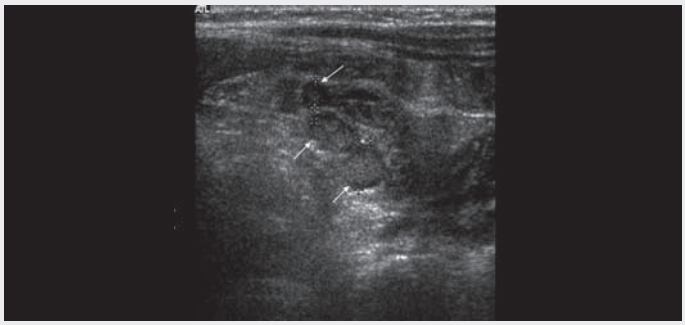

Fig. 5.77. Peritoneal tuberculosis in a 6-year-old girl. (a) Longitudinal and (b) axial scans show diffuse, enlarged, echo-poor mesenteric lymph nodes with calcifications (arrows)

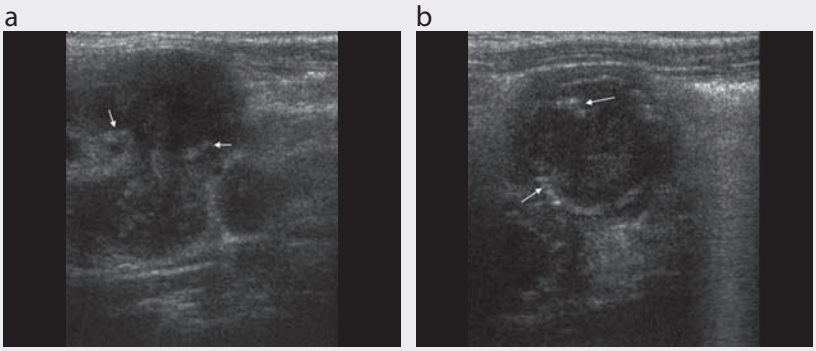

Fig. 5.78. Non-Hodgkin lymphoma in a 7-year-old boy with abdominal pain. Longitudinal scan of the right abdomen shows a large, echo-poor mass (M) with some adjacent ascitic fluid

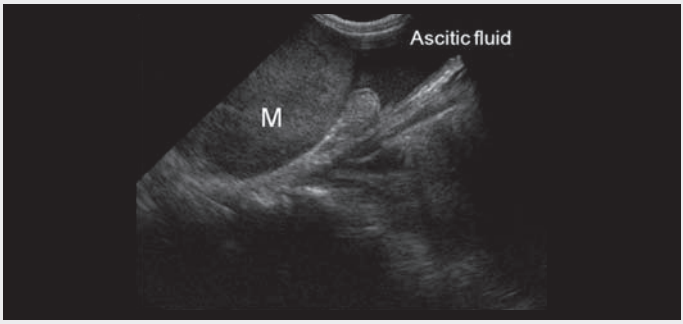

Fig. 5.79. Burkitt lymphoma in a 4-year-old girl. Axial scan through the right lower quadrant of the abdomen shows thickened bowel wall (BW) between calipers, pseudokidney aspect, with an echogenic centre

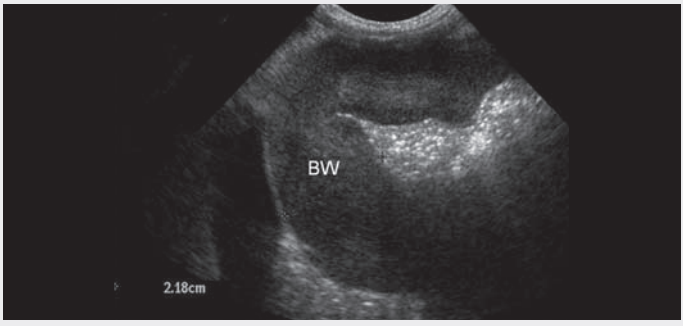

Vomiting

Ultrasound examination must be the first imaging procedure used for vomiting infants. The cause depends on the age of the infant and the clinical and biological findings. Vomiting is frequent in children, and imaging should be limited to infants with a potential organic cause, confirmed by a well-trained physician. Ultrasound must exclude surgical causes of vomiting, such as hypertrophic pyloric stenosis, hiatus hernia, gastro-oesophageal reflux, mechanical bowel obstruction, appendicitis and intussusception.

Hypertrophic pyloric stenosis

Pyloric stenosis is an evolving condition of pyloric muscle hypertrophy, which narrows and elongates the antropyloric canal. The condition can be familial. Typically, it occurs in male newborns between 3 and 6 weeks of age with nonbilous vomiting. Ultrasound is the modality of choice for confirming the diagnosis.

Infants present with projectile vomiting and sometimes a palpable epigastric mass, known as an olive. Marked gastric peristalsis can be seen in infants with a thin abdominal wall. Ultrasound shows a full stomach, which can be totally atonic when an early diagnosis has not been made. In other situations, a hyperperistaltic stomach and a dilated antrum are often seen. Pyloric hypertrophy appears as echopoor thickening of the pyloric muscle and elongation of the canal.

Normally, the pyloric muscle is < 2 mm thick, the canal is < 12 mm long and the pyloric diameter is < 6 mm. In hypertrophic pyloric stenosis (Fig. 5.80), the pyloric muscle is > 3 mm thick and the canal length is > 15 mm. The clinical findings are important for a positive diagnosis, before sending an infant to surgery. If there is any doubt, an upper gastrointestinal barium series will confirm the dilated stomach and the typical narrowing of the antrum.

Fig. 5.80. Hypertrophic pyloric stenosis in a 2-month-old boy. (a) Longitudinal scan shows thickened muscle and elongated pyloric channel over 2 cm (arrows). Note also the redundant mucosa (arrowhead) protruding into the stomach (st). (b) Transverse scan shows the target sign; muscle layer thickness, 4 mm (arrow)

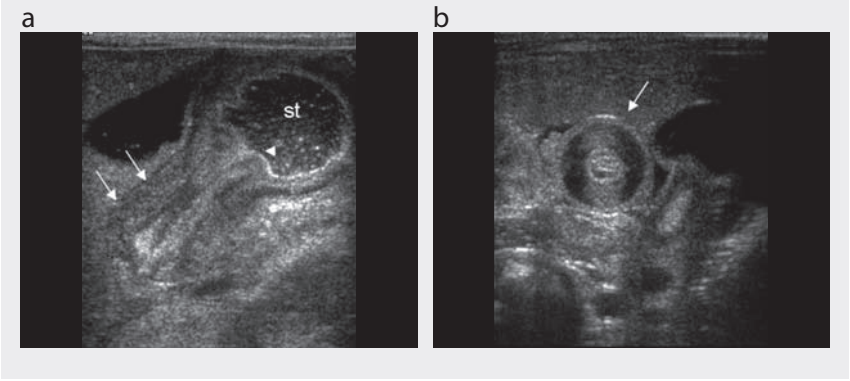

Gastro-oesophageal reflux

Gastro-oesophageal reflux is a retrograde flow of milk and solids from the stomach up the oesophagus. This condition is frequent in infants and is well demonstrated by ultrasound. When an infant has been given a liquid feed before the examination and is placed in the supine position, the gastro-oesophageal junction lies just to the left of the aorta, in the region of the xiphisternum, and can be seen by scanning longitudinally over the upper abdominal aorta. If a gastro-oesophageal reflux is present, air and gastric contents can be seen rising up to the oesophagus (Fig. 5.81). The presence of a hiatus hernia is well demonstrated by ultrasound. Gastro-oesophageal reflux may result in failure to thrive, and aspiration can cause cyanotic spells and chronic lung disease.

Use of ultrasound for identifying gastro-oesophageal reflux is controversial. The accepted procedure is a pH test, in which a probe is placed in the lower oesophagus and acidity in the oesophagus is monitored over 24 h. A conventional barium meal is probably still the most widely used examination, and it has the added advantage of demonstrating the anatomy of the lumen of the oesophagus, the stomach and the bowel.

Fig. 5.81. Gastro-oesophageal reflux in a 3-month-old girl. Longitudinal scan shows bubbling fluid (arrows) in the abdominal oesophagus lying under the heart (H), posterior to the liver (L) and above the stomach (st)

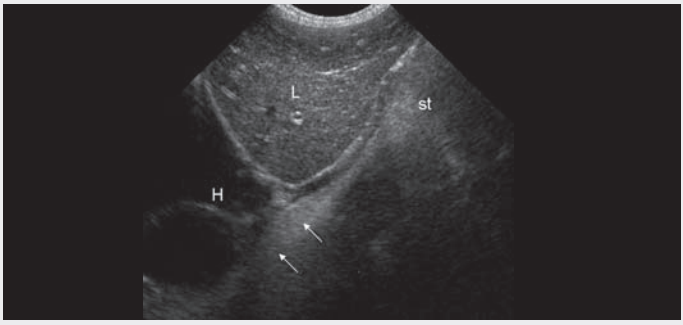

Blunt abdominal trauma

Abdominal trauma is frequent in countries where children often play or walk on the street. An important finding is fluid in the peritoneal cavity (haemoperitoneum). Ultrasound is used to observe all the intra-abdominal organs (liver, spleen, kidneys, bladder, pancreas, bowel and mesentery) that may be affected by the trauma. CT, when available, is useful in complicated cases. Trauma to the bowel may result in intramural haematoma (Fig. 5.82), intra- or retroperitoneal perforation or transaction (Fig. 5.83). Free air in the abdomen indicates traumatic rupture of the digestive-tract wall somewhere between the stomach and the rectum. A bowel haematoma can occur anywhere in the tract wall, but most are found in the duodenum.

Fig. 5.82. Duodenal haematoma in a 10-year-old boy after abdominal trauma. (a) Transverse ultrasound scan shows a smooth echoic mass (H) projecting into and completely obstructing the duodenal lumen, with pancreatic duct dilatation (arrow). (b) Axial contrast-enhanced CT image shows an extending duodenal haematoma (H). (c) Corresponding coronal reformatted CT scan

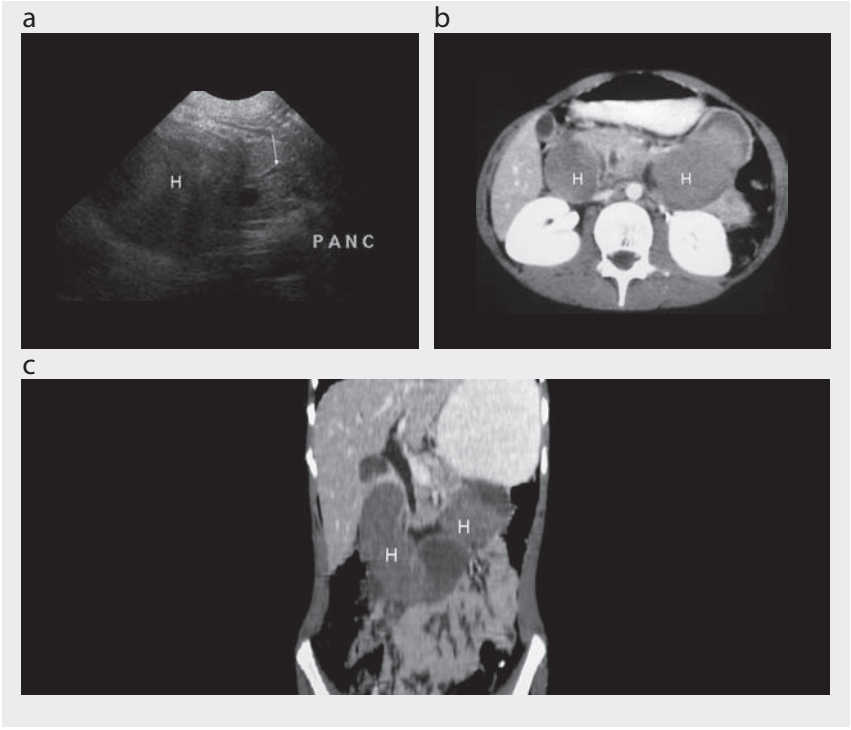

Fig. 5.83. Digestive tract perforation in a 6-year-old boy after abdominal trauma. Longitudinal scan shows subtle bubbles of free air (arrow) in the abdominal cavity, indicating perforation

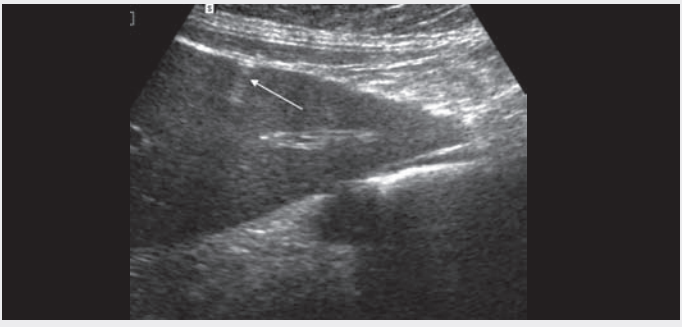

Inflammatory disorders

Crohn disease, or regional enteritis, is the most frequent inflammatory bowel disease in children. The terminal ileum and the proximal colon are involved in the majority of cases. The children affected are usually over 10 years of age at the time of diagnosis. The common clinical findings are abdominal pain and diarrhoea, weight loss, growth failure and perianal fistulae. On sonography, the inflamed bowel appears as a compressible or partially compressible tubular structure on longitudinal views, with a bull's-eye appearance on transverse views (Fig. 5.84). Complications of Crohn disease include abscesses, sinus tracts and fistulae.

Fig. 5.84. Crohn disease in a 13-year-old boy. Longitudinal scan shows thickened ileum (arrow) and increased mesenteric fat (arrowheads)

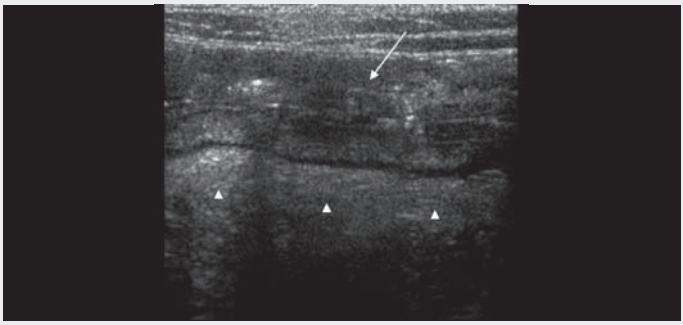

Ulcerative colitis occurs most often in children over 10 years of age. Bloody diarrhoea and abdominal pain are frequent features. The disease characteristically starts in the rectum and extends proximally in a continuous pattern for a variable distance. Ultrasound shows colonic wall thickening, usually by 6–10 mm (Fig. 5.85). Abscess formation and fistulae are unusual.

Fig. 5.85. Ulcerative colitis in an 11-year-old girl with bloody diarrhoea and abdominal pain. (a) Longitudinal and (b) transverse scans show uniform thickening of the left colon with thickening of pericolonic fat (F) and some adjacent ascitic fluid (asterisk)

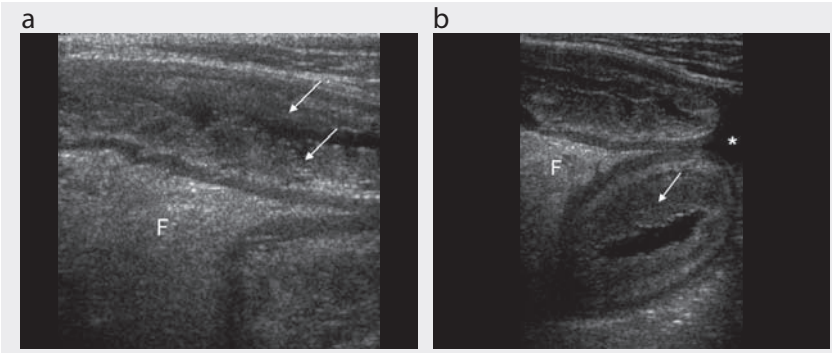

Non-inflammatory disorders

Henoch-Schönlein purpura is the commonest non-inflammatory digestive tract disease in children. It is a nonthrombocytopenic vasculitis that affects the bowel, skin, joints and kidneys. Abdominal pain and rash are the common presenting signs. Abdominal pain is due to bowel haemorrhage or intussusception. The ultrasound findings include high-attenuation intramural bleeding, thickened bowel wall and thickened valvulae conniventes (Fig. 5.86). The bowel lumen may be narrowed or completely obstructed by the haematoma or by intussusception.

Fig. 5.86. Henoch-Schönlein purpura in a 4-year-old girl with abdominal pain. Longitudinal scan shows wall thickening in the distal jejunum associated with small, echo-rich intramural bleeding (arrows)

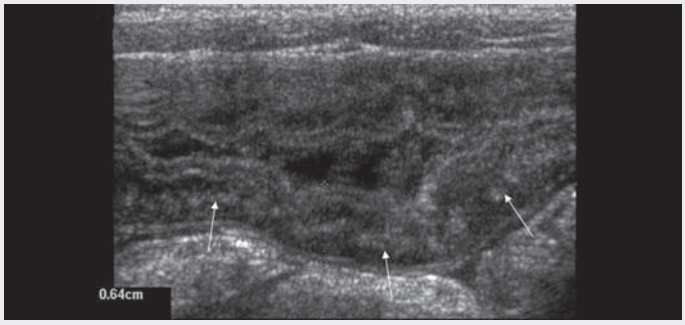

Ischaemic bowel disease

Ischaemic bowel disease is represented in children essentially by necrotizing enterocolitis and haemolytic uraemic syndrome. **Necrotizing enterocolitis** is considered to be the result of hypoxia and superimposed infection in neonates. It is associated with respiratory distress syndrome, birth asphyxia, low Apgar scores and shock. Necrotizing enterocolitis begins in the mucosa and submucosa and may extend through all the layers of the bowel wall; the distal ileum and right colon are usually involved. Sonography can be used to confirm the diagnosis. The early findings are nonspecific and include bowel distension; a later finding is intramural gas (pneumatosis intestinalis), which appears as highly echogenic intramural echoes with acoustic shadowing (Fig. 5.87). Portal venous gas is seen as mobile echoes within the portal vein (Fig. 5.88).

Fig. 5.87. Necrotizing enterocolitis with pneumatosis in a 2-month-old girl presenting with abdominal distension, vomiting and blood in the stools. (a) Longitudinal and (b) transverse scans show pneumatosis intestinalis with intramural gas (arrows), associated with mild bowel-wall thickening and small-bowel dilatation

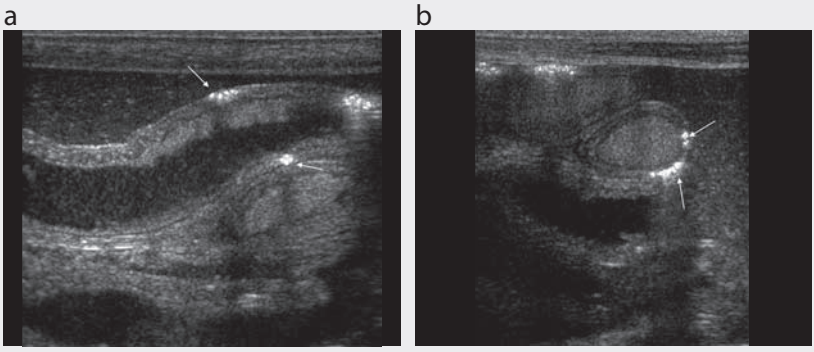

Fig. 5.88. Necrotizing enterocolitis in a 1-month-old girl. Transverse scan through the liver (L) shows multiple, mobile echogenic areas, representing gas (arrows) in the portal veins

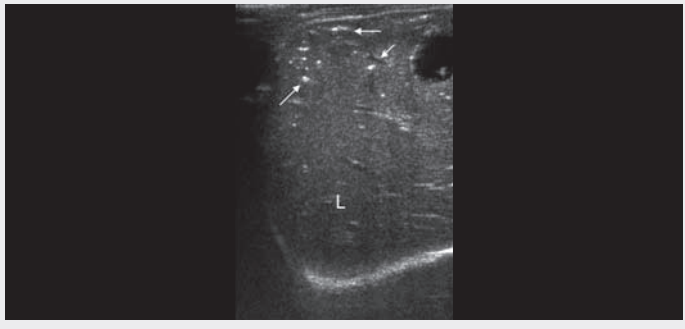

Haemolytic uraemic syndrome is a disorder characterized by a prodrome of bloody diarrhoea followed by acute renal failure, haemolytic anaemia and thrombocytopenia. The cause is thought to be an antigen–antibody reaction to the bacterial toxin *Escherichia coli* serotype O. The sonographic findings include a markedly thickened colonic wall, which is avascular in the prodromal stage.

Urinary tract and retroperitoneum

Indications

Ultrasound is useful for inspecting the urinary tract and the retroperitoneum in children, to confirm any antenatally diagnosed abnormality and to treat children with various congenital and acquired disorders. The main indications for exploration of the urinary tract and the retroperitoneum are urinary-tract infections, confirmation of urinary-tract anomalies detected antenatally, retroperitoneal masses and screening for intra-abdominal congenital abnormalities in some clinical situations.

Preparation

No specific preparation is needed in urgent and acute cases or for studying the retroperitoneum. Examination of the bladder and pelvis is best done in a well-hydrated child with a full bladder, when possible.

Examination technique

The infant should be supine on the left or right side. The bladder and pelvis should be examined first, before the infant micturates. Older children should, if possible, take a deep breath and hold it while a specific area is being scanned. As for all ultrasound examinations, the entire abdomen should be checked, including the kidneys and the retroperitoneum. The bladder and kidneys must be explored before and after micturition; however, an overfull bladder can cause mild fullness of the collecting system.

Colour Doppler, if available, should be used as an adjunct in assessing the renal pelvis and hilar vessels, for a quick overview of kidney blood flow or to demonstrate the vascularity of renal or adrenal masses. The report should state the size of the kidneys and pelvis, the thickness and regularity of the bladder wall and the approximate volume after micturition.

Normal findings

The normal ultrasound appearance of the kidneys in neonates is different from that of adults. It typically shows higher cortical echogenicity and stasis nephropathy resulting from deposition in the tubules of a glucoprotein known as Tamm-Horsfall

protein. The precipitated proteins increase the echogenicity of the medullary pyramids and then disappear spontaneously within the 1st week of postnatal life (Fig. 5.89).

Fig. 5.89. Precipitation of Tamm-Horsfall protein in kidney of a newborn boy. (a) Longitudinal and (b) transverse scans show greater echogenicity in the renal cortex than in the liver (L) and echo-rich areas in the renal pyramids (arrows)

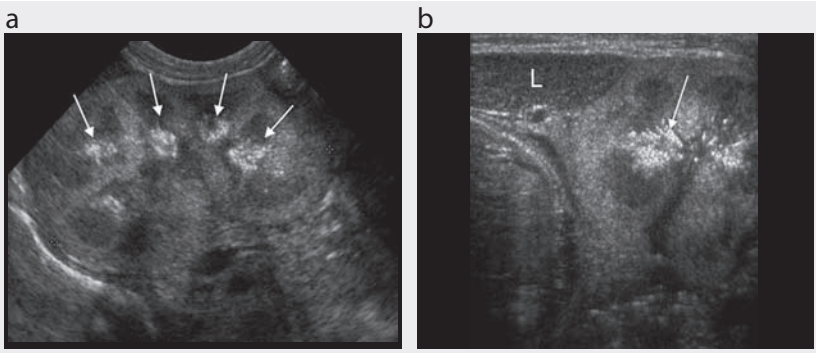

The normal parenchyma is isoechogenic or echo-rich to the liver and spleen up to 6 months of age. The medullary pyramids are prominent, echo-poor, triangular structures with a large base on the renal cortex, regularly arranged around the central collecting system. It is important to demonstrate this normal aspect in neonates and to differentiate between abnormal calyceal dilatation and cysts. The central sinus echoes in a neonate are less evident than in older children or adults because of the paucity of fat in this area (Fig. 5.90).

Fig. 5.90. Normal renal anatomy in a newborn boy. Longitudinal scan shows similar echogenicity of the renal cortex and liver (L), with prominent pyramids (P). The central renal sinus (arrows) is barely discernible

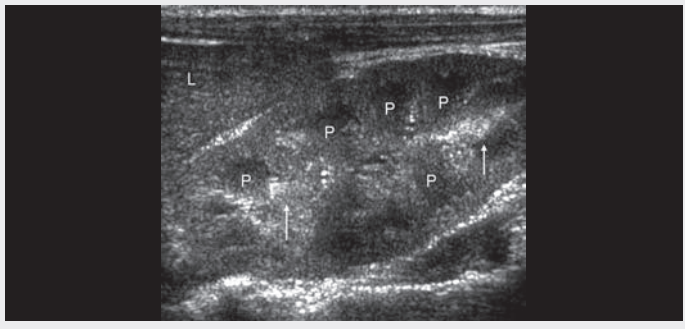

By the end of the 1st year of life, the renal cortex is usually more echo-poor than the adjacent liver or spleen, and the medullary pyramids are even less echogenic. The renal sinus appears as a central echogenic area with an appearance similar to that in adults (Fig. 5.91). Occasionally, fetal renal lobulation persists into postnatal life up to 6 months of age. This should not be confused with renal scarring, which is associated with parenchymal thinning (Fig. 5.92).

The size of the kidney depends on the age of the child: the normal renal length is 4.5 cm at birth, 6 cm at 1 year, 8 cm at 5 years and 10 cm at 10 years (Fig. 5.93).

Fig. 5.91. Normal renal anatomy in an older boy. Longitudinal scan shows that the renal cortex is less echogenic than the liver (L), the renal pyramids are less prominent and the central renal sinus (arrow) is moderately echogenic

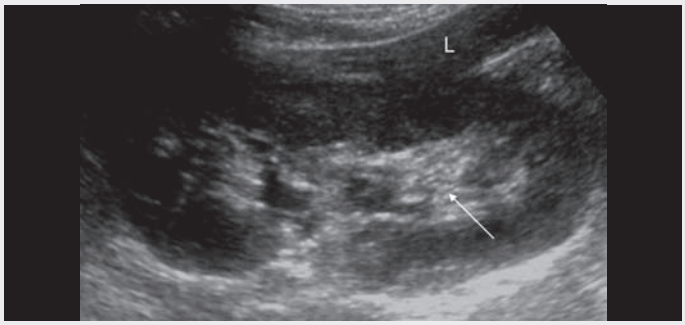

Fig. 5.92. Anatomical variant, fetal lobulation. Longitudinal scans show lobulated renal margin (arrows) and fetal lobulation between the renal calyces, unlike cortical scars, which lie directly over the calyces

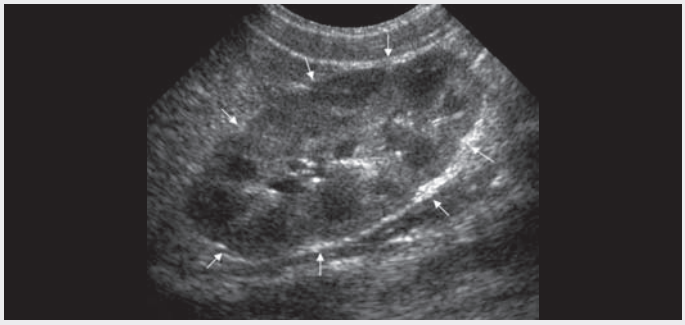

Fig. 5.93. Normal renal length in a 4-month-old girl. Longitudinal scan shows kidney 4.6 cm in length. L, liver, RK, right kidney

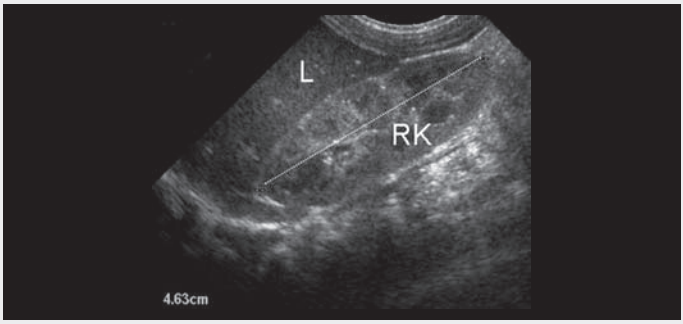

The anteroposterior renal pelvis shows some variation in size, but 10 mm is accepted as the largest diameter in a normal child, if the calyces are not seen (Fig. 5.94). The ureters are normally not seen on ultrasound. The thickness of the normal bladder wall is around 1 mm if the bladder is full and 2–3 mm when it is empty (Fig. 5.95). The bladder capacity depends on age but is never less than 30 ml. The volume after micturition varies from 0 to 15 ml.

The urethra is not seen by ultrasound in normal infants. The resistive index of the renal artery varies with age: in neonates, it is as high as 0.85; it decreases during the postnatal period, and is ≤ 0.7 by the middle of the first decade of life.

Fig. 5.94. Normal anteroposterior renal pelvis. Transverse scan shows anteroposterior renal pelvis (Pe) of the kidney (K), 7 mm in diameter

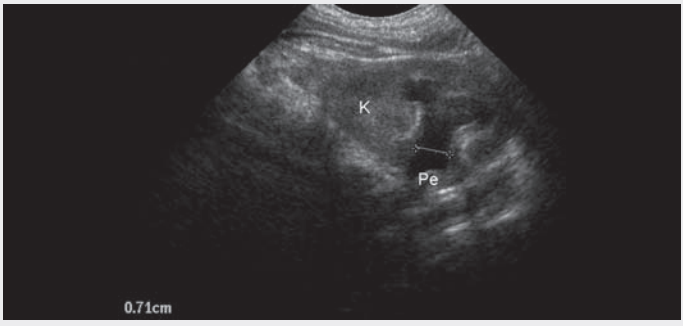

Fig. 5.95. Normal bladder anatomy in a 2-year-old boy. (a), (b) Transverse scans show the bladder (B) as a cystic structure with echo-free contents and a wall thickness (between calipers) of about 1 mm

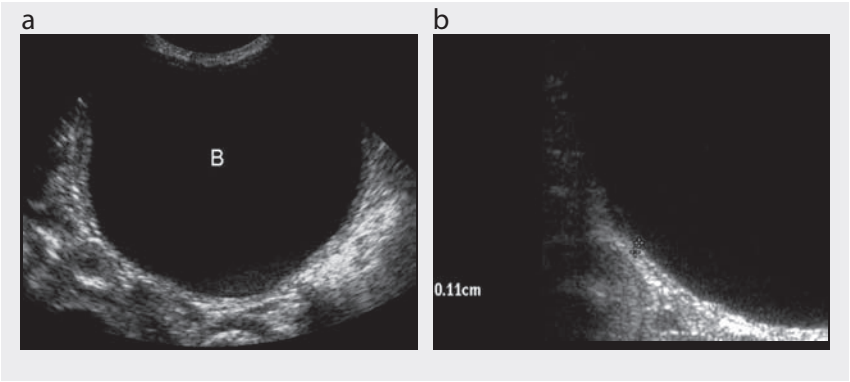

Pathological findings

Anomalies of the upper urinary tract

Congenital anomalies

Congenital anomalies are relatively common. They must be monitored carefully and are readily detected by ultrasound.

Bilateral renal agenesis is rare and incompatible with life. In **unilateral renal agenesis**, one kidney is absent, with compensatory hypertrophy of the contralateral kidney and adjacent organ displacement. Associated genital malformations are common, including absence of the seminal vesicles, seminal vesicle cysts, undescended testes, uterine duplication and vaginal imperforation with haematocolpos.

In **ectopic kidneys**, one or both kidneys are in an abnormal position when they fail to progress along their normal migratory path. In simple ectopia, the kidney and ureter are on the expected sides of the spine, most commonly in the pelvis. Rarely, they are found in the chest. In crossed ectopia, both kidneys are located on the same side of the spine. The ectopic kidney is usually smaller than the normal kidney, is malrotated and frequently has a dysmorphic configuration, such as a pancake kidney, disc or lump shape.

Horseshoe kidneys are characterized by fusion of the lower poles of the kidneys, which appears as a prevertebral mass. The ultrasound findings include anteriorly located renal pelves, a medial orientation of the lower poles of the kidneys and an isthmus of tissue crossing the midline anterior to the great vessels (Fig. 5.96).

In **crossed-fused ectopia**, one kidney may be displaced, cross the middle line and fuse inferiorly with the normally positioned kidney.

Duplex kidney is the commonest renal anomaly. It may be partial or complete. Renal duplication is easy to diagnose by sonography when partially dilated renal calyces occur and if ureterocoele is associated in the bladder. The duplex kidney is larger than the normal single system and has two separate renal sinus echo complexes.

Fig. 5.96. Horseshoe kidneys in a 10-year-old girl. (a) Transverse scan shows isthmus of tissue (arrow) anterior to the aorta (Ao) connecting the lower poles of the kidneys (RK, right kidney; LK, left kidney). (b) Coronal three-dimensional reconstruction of routine CT confirms a diagnosis of horseshoe kidneys

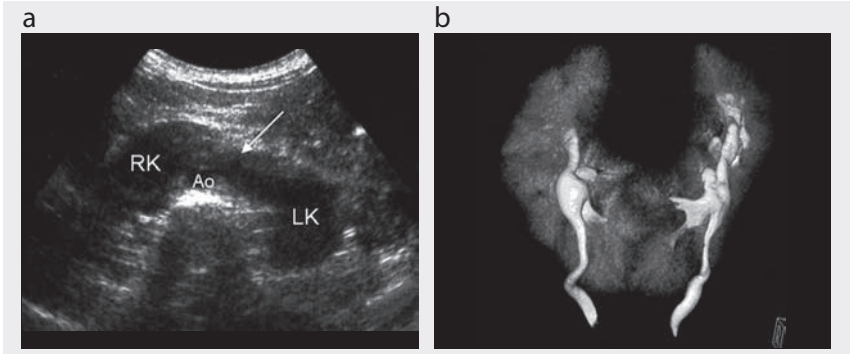

A **small kidney** may be congenital, with normal parenchymal echogenicity, or it may be associated with renal artery stenosis or dysplasia. Acquired small kidney is often a late complication of vesico-ureteral reflux.

Simple renal cysts are rare in children, with an incidence less than 1%. Simple cysts arise in the renal cortex, do not communicate with the collecting system and are more often solitary than multiple. They are usually asymptomatic and detected during examinations for other indications. Calyceal diverticula which communicate with the collecting system through a narrow orifice should be distinguished from simple cysts (Fig. 5.97).

Fig. 5.97. Calyceal diverticula in a 12-year-old boy. (a) Longitudinal scan through the right kidney (RK) shows a round cyst with a smooth, well-defined wall (C). (b) Axial late-phase contrast-enhanced CT scan shows communication with the collecting system and some filling with contrast-enhanced urine (arrow)

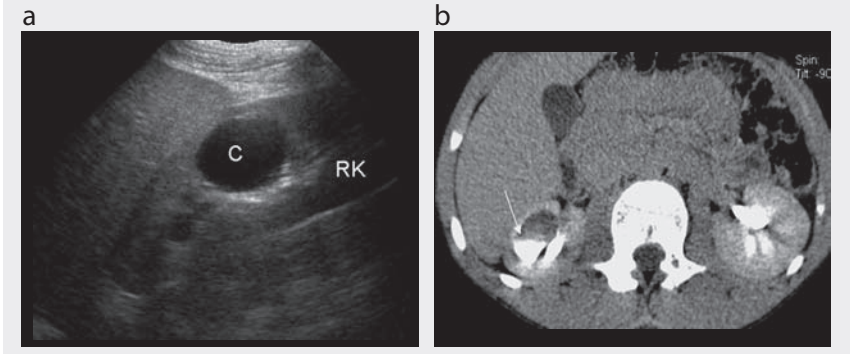

Multicystic dysplastic kidney is a nonhereditary developmental anomaly characterized by the presence of multiple noncommunicating cysts separated by tissue-containing primitive dysplastic elements in one kidney. It is often diagnosed during the antenatal period (Fig. 5.98). Ultrasound shows multiple cysts of varying size with a random distribution, absence of communication between the cysts, no discernible renal pelvis or sinus and absent or dysplastic renal parenchyma (Fig. 5.99). The other kidney may be normal, hydronephrotic or dysplastic.

Fig. 5.98. Multicystic dysplastic kidney in a fetus at 26 weeks' gestation. Longitudinal scan shows enlarged multicystic kidney (K). D, diaphragm; L, lung

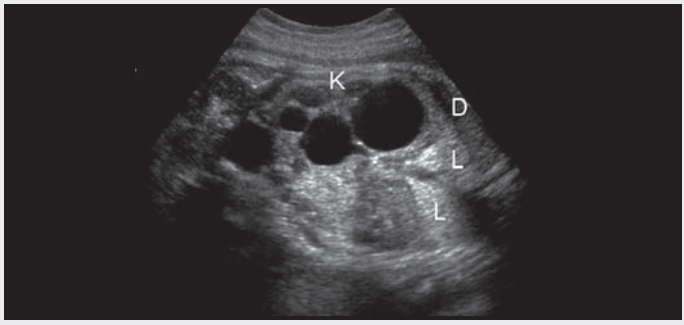

Fig. 5.99. Multicystic dysplastic kidney in a 3-month-old boy. Longitudinal scan shows multiple oval and round cysts (C) of varying sizes in the left renal fossa, with no central renal pelvis or normal renal parenchyma

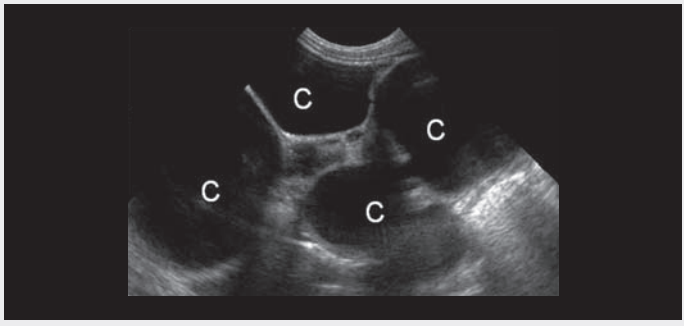

A dysplastic kidney can be unilateral or bilateral. On ultrasound, the kidney appears small and echogenic with small peripheral cortical cysts.

Polycystic kidneys occur as two conditions. In autosomal recessive polycystic kidney, or infantile polycystic kidney, the kidneys are both highly echogenic,

heterogeneous and large (Fig. 5.100). Macrocysts are uncommon but may be seen. An antenatal diagnosis can be made. Depending on age, hepatic fibrosis appears, with increasing echogenicity, particularly in the periportal region, and cystic dilatation of the biliary tree (Caroli syndrome). In older children, portal hypertension may appear, with an enlarged spleen, ascites and digestive varices.

Fig. 5.100. Polycystic kidney in a newborn boy. (a) Longitudinal scan through the kidney shows an enlarged, echogenic kidney (K) and loss of corticomedullary differentiation, with tiny cysts (arrows). (b) Oblique scan through the liver (L) shows multiple small cysts (arrowheads)

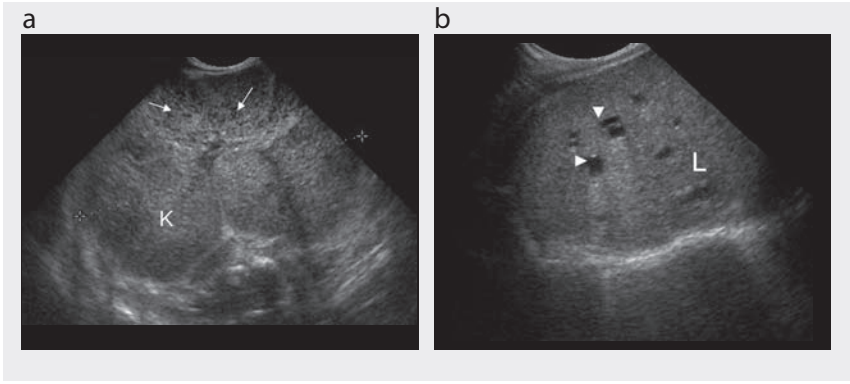

Autosomal dominant renal disease, or adult polycystic kidney, usually manifests after the third decade, but cysts may be found in the kidney during childhood. Both kidneys are affected but unequally, varying from a kidney with a few isolated cysts to one filled with cysts. The more cysts there are in the kidneys, the larger it is, with a lobulated outline. The complications may include haemorrhage, infection and rupture, which can usually be diagnosed by ultrasound.

Renal pelvic dilatation, or pelvi-ureteric junction syndrome, is unilateral and rarely bilateral. The ultrasound findings depend on the degree of hydronephrosis due to the obstruction (Fig. 5.101). The ureters are not seen. A diagnosis is often made during antenatal life (Fig. 5.102).

Megaureter is an enlarged ureter, which may reflux in vesico-ureteral junction. It may be unilateral or bilateral. The ureter is dilated, sometimes to > 10 mm, and elongated. Ultrasound examination shows the dilated ureter and is useful for evaluating the degree and severity of hydronephrosis, to identify ureterocoele into the bladder and to confirm that the bladder wall is normal. Vesico-ureteric reflux must be sought (Fig. 5.103).

A grading system can be used to evaluate the evolution of hydronephrosis: grade 0, no hydronephrosis; 1, only the renal pelvis visualized; 2, some calyces visible, in addition to the renal pelvis; 3, all calyces seen; and 4, all calyces seen, with parenchymal thinning. A simpler solution is to measure the thickness of the renal parenchyma. All these anomalies must be monitored. They are sometimes related to particular syndromes, such as the VACTERL association, consisting of vertebral anomalies, anal atresia, cardiovascular anomalies, tracheo-oesophageal fistula, oesophageal atresia, renal anomalies and limb defects.

Fig. 5.101. Ureteropelvic junction obstruction in a 15-day-old boy. (a) Longitudinal and (b) transverse scans show dilatation of the calyces (C) and renal pelvis (Pe), with a thin rim of parenchyma (arrows) surrounding the collecting system

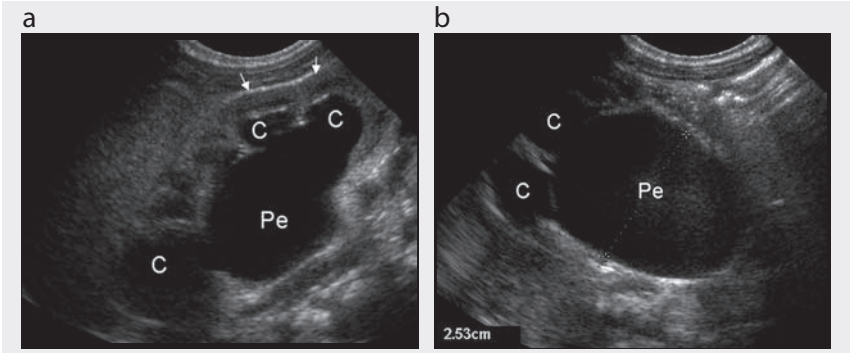

Fig. 5.102. Ureteropelvic junction obstruction in a fetus at 23 weeks' gestation. (a) Longitudinal and (b) transverse scans show marked dilatation of the left renal pelvis (Pe)

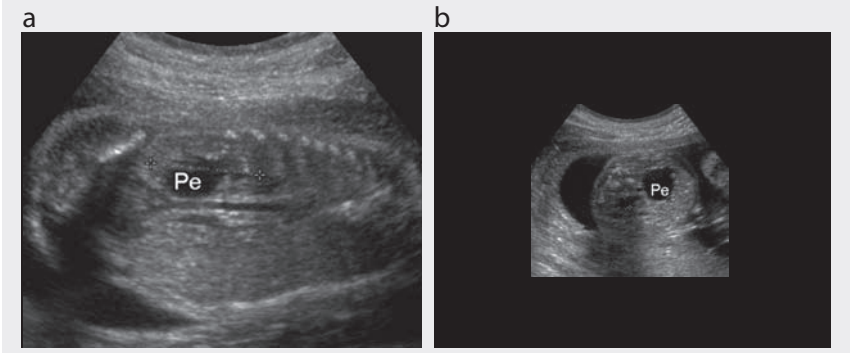

Fig. 5.103. Hydronephrosis due to vesico-ureteral reflux. Longitudinal scans show (a) hydronephrosis (C, calyces; Pe, renal pelvis) and (b) elongation and distension of the upper ureter (U) with echo-free fluid

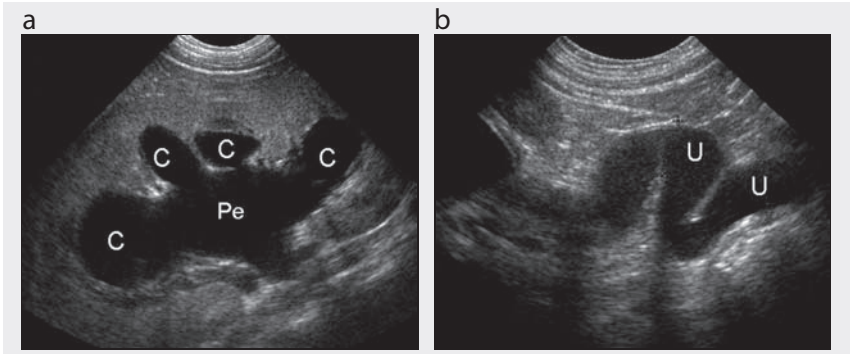

Renal calculi and nephrocalcinosis

Renal stones are common in people in many developing countries, even in childhood, because of a hotter climate. They are often idiopathic. The commonest type of stone consists of calcium oxalate; less commonly they are made of calcium phosphate, cystine or struvite (ammonium magnesium phosphate).

Ultrasound can be used to detect and monitor the stones, to determine the causes and to evaluate dilatation of the renal cavities (Fig. 5.104). The stones cause intensive echoes and, if > 3 mm, a posterior shadow. Ureteral stones may be missed on ultrasound if they are not prevesical. Simple abdominal radiography is usually sufficient.

Fig. 5.104. Urolithiasis in a 6-year-old boy. Transverse scan through the left kidney (LK) shows a renal pelvis stone (S), a highly reflective structure with acoustic shadowing (arrowheads)

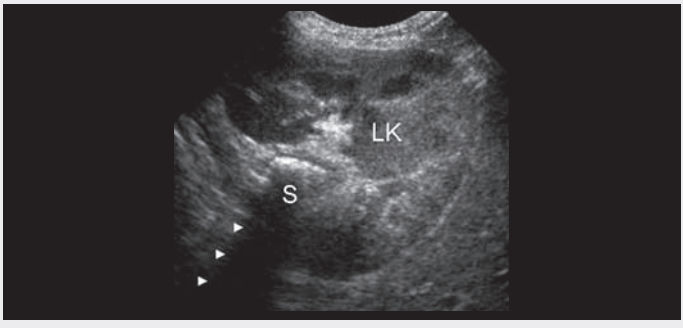

In nephrocalcinosis, ultrasound shows increased echogenicity of the pyramids. Ultrasound is much more sensitive in the early stage of calcium deposition in the kidneys than simple abdominal radiography. Initially, there is a small increase in echogenicity and ringing of the pyramids, which, in severely affected children, eventually fill the medullae and then cast acoustic shadows (Fig. 5.105). Nephrocalcinosis is always bilateral and symmetrical.

Fig. 5.105. Nephrocalcinosis in a 5-year-old boy. Longitudinal scan of the right kidney (RK) shows echo-rich renal pyramids (arrows) with some posterior acoustic shadowing

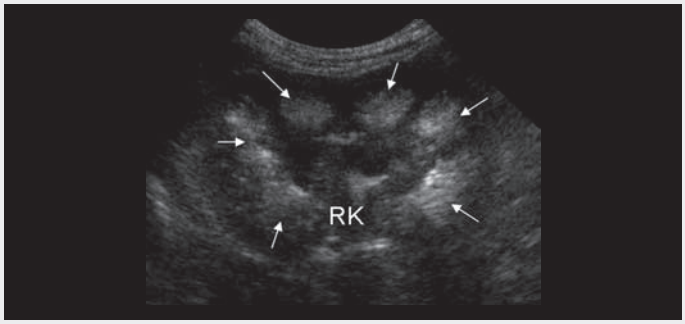

Renal tumours

Wilms tumour (nephroblastoma) is the commonest solid renal tumour in childhood. It occurs in children aged about 3–5 years. The ultrasound appearance depends on the stage and size at presentation. Typically, it is a well-defined, solid renal mass, with a small sliver of remaining normal kidney (Fig. 5.106).

Atypically, the tumour is echo-poor (cystic aspect) or shows some calcification (coarse and linear, as opposed to neuroblastoma).

The tumour may invade the renal vein, causing tumour thrombosis (Fig. 5.107). The contralateral kidney must be carefully examined for bilateral nephroblastomatosis (Fig. 5.108).

Liver metastasis, ascites and lymphadenopathy are rare. The staging of Wilms tumour requires a complementary imaging modality, such as CT.

Other renal tumours include benign mesoblastic nephroma in the neonatal period; malignant rhabdoid tumour, a variant of nephroblastoma, which occurs within the 1st year; lymphoma (Fig. 5.109); multilocular cystic nephroma (Fig. 5.110) and rhabdomyosarcoma. Ultrasound is suitable for detecting these tumours but generally not for differentiating them.

Fig. 5.106. Wilms tumour in a 5-year-old boy. (a) Oblique scan through the left kidney shows a large, heterogeneous mass (M) with areas of increased and decreased echogenicity. (b) Axial contrast-enhanced CT demonstrates a large round hypoattenuating mass (M), distorting and displacing the normal parenchyma (arrow) of the left kidney

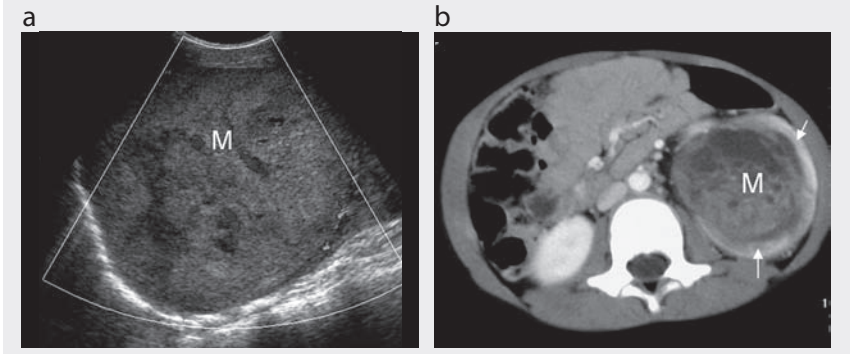

Fig. 5.107. Wilms bilateral tumour in a 2-year-old boy. (a) Oblique scan shows a large mass (M) arising from the left kidney (LK). (b), (c) Oblique scans show extension into the inferior vena cava (IVC) and right atrium (RA) (arrows)

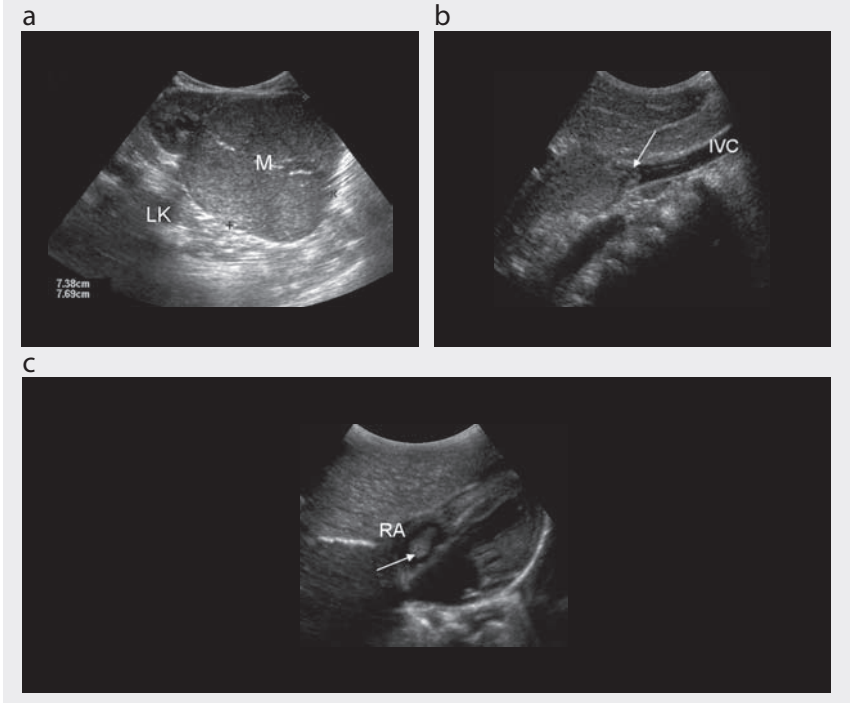

Fig. 5.108. Bilateral Wilms tumour with focal nephroblastomatosis in a 3-year-old girl. (a) Longitudinal scan through the left kidney (LK) and (b) longitudinal scan through the right kidney (RK) show bilateral masses (M). (c) Contrast-enhanced CT shows bilateral masses (M) and a small hypoattenuating well-circumscribed subcapsular mass in the right kidney, representing nephrogenic rests (arrows)

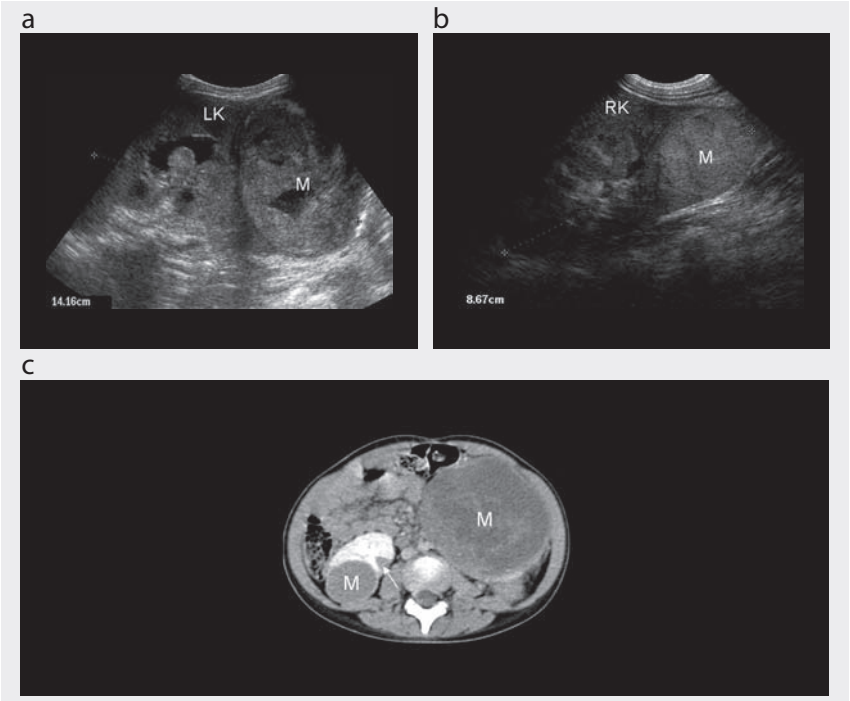

Fig. 5.109. Renal lymphoma in a 2-year-old girl. Oblique scan shows an enlarged, echogenic kidney with loss of corticomedullary differentiation

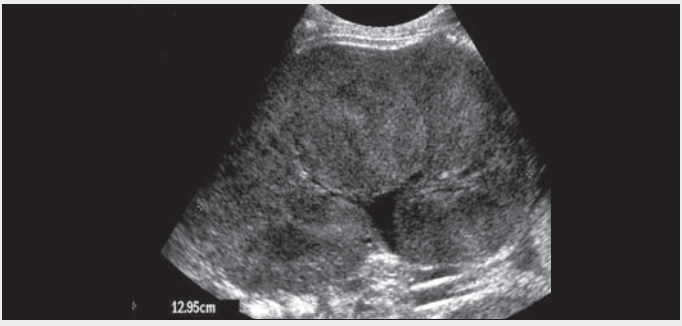

Fig. 5.110. Multilocular cystic nephroma in a 10-year-old girl. (a) Longitudinal scan through the left kidney (LK) shows a complex mass (arrows) containing echo-free locules separated by echogenic septa. (b) Axial contrast-enhanced CT showing the complex mass with multiple cystic areas (C), surrounded by enhancing septations (arrow)

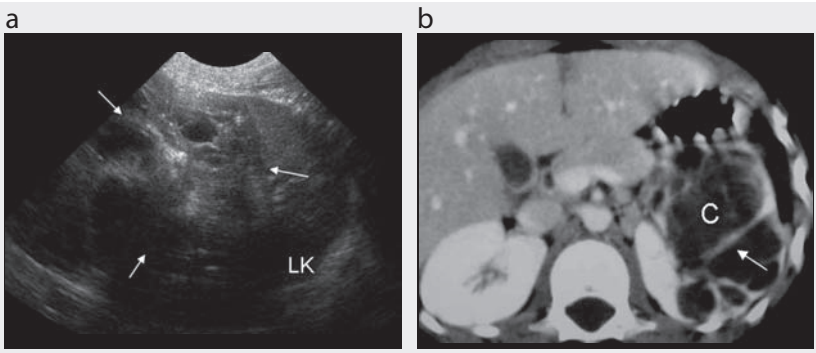

Infectious and parasitic diseases

Acute bacterial pyelonephritis results from an ascending infection and is associated with vesico-ureteral reflux. The common causative agent is *E. coli*. Patients present with fever, abdominal pain, irritability and vomiting. Abnormal findings are usually found on ultrasound in severe infection and include generalized or focal renal enlargement, abnormal parenchymal echogenicity, poor definition of the corticomedullary junction and thickening of the wall of the renal pelvis or ureter (Fig. 5.111).

Fig. 5.111. Acute pyelonephritis in a 1-year-old boy. Longitudinal scan shows a focal enlarged area of increased echogenicity (arrows) in the upper pole of the left kidney

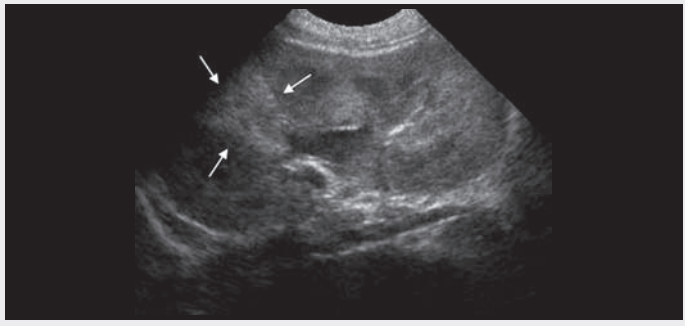

Fig. 5.112. Renal abscesses complicated by pyonephrosis in a 3-month-old boy. (a)–(c) Longitudinal scans of the right kidney show a dilated system containing debris (D) associated with multiple, small echo-poor lesions (arrows) and a large abscess (A) with an irregular thickened wall and internal echoes

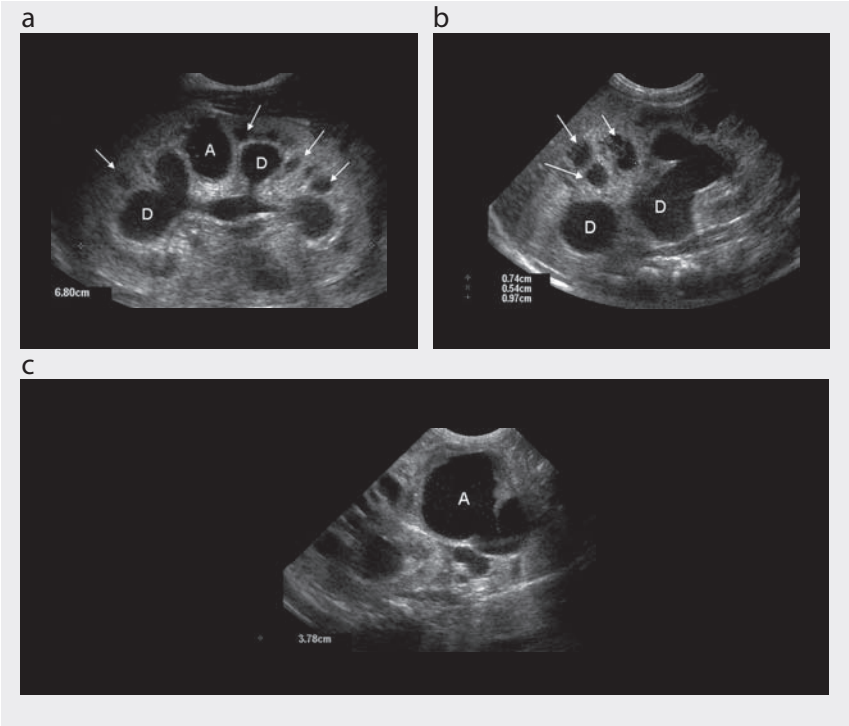

Renal abscesses are relatively uncommon complications of inadequately treated acute pyelonephritis. There are no specific ultrasound findings in childhood. Ultrasound shows a well-defined, echo-poor mass with thick walls, internal septations and fluid–debris levels (Fig. 5.112).

Chronic pyelonephritis usually results from recurrent episodes of vesicoureteral reflux. Ultrasound shows a small kidney with focal parenchymal scarring overlying a blunted calyx (Fig. 5.113).

Hydatid disease of the urinary tract is rare, representing less than 2% of all hydatid locations, and occurs in children over 3 years of age. The ultrasound findings in the kidney depend on the location and the stage of development of the parasite. The most frequent aspect in the kidney is multivesicular, type III in the Gharbi classification. Cystic lesions with urinary-tract dilatation are clearly seen by ultrasound (Fig. 5.114).

Schistosomiasis, due to *Schistosoma haematobium* species, affects the urinary tract of older children, with alterations to the kidneys, ureters and bladder. Ultrasound shows hydronephrosis, a pseudomass or a pseudopolyp and calcifications in the bladder wall.

Fig. 5.113. Chronic pyelonephritis in an 8-year-old girl with recurrent urinary-tract infection. Longitudinal scan shows a small echogenic right kidney (RK) with loss of corticomedullary differentiation and decreased renal parenchyma (arrow). L, liver

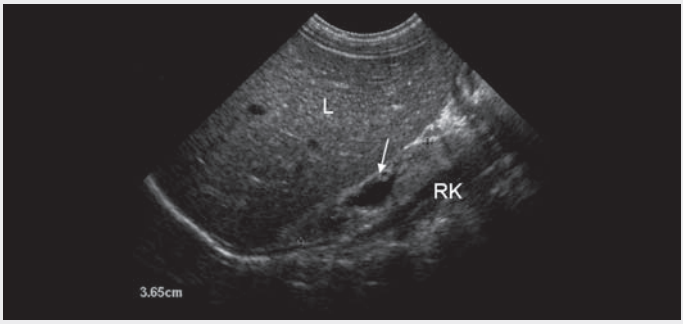

Fig. 5.114. Renal hydatid cyst in a 10-year-old boy. (a) Longitudinal scan shows a multivesicular cyst (C) in the midpole of the left kidney (LK). (b) Axial contrast-enhanced CT shows a low-density cystic mass with no enhancement

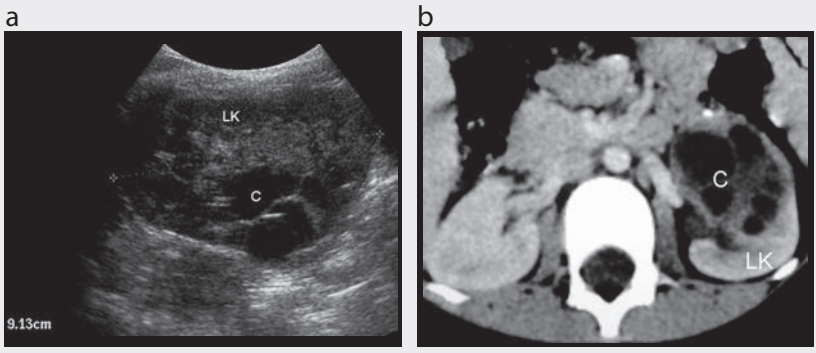

Vascular diseases

Haemolytic uraemic syndrome is characterized by the classic triad of microangiopathic haemolytic anaemia, thrombocytopenia and renal failure. It is caused by an antigen–antibody reaction to bacterial toxins and affects children under 5 years of age who present with a prodromal phase of bloody diarrhoea followed by onset of renal failure. Typical sonographic findings include increased cortical echogenicity and echo-poor pyramids (Fig. 5.115).

Renal vein thrombosis occurs predominantly in newborns. It is usually a complication of severe dehydration and associated haemoconcentration secondary to blood loss, diarrhoea or sepsis. In older children, it may be the result of trauma,

neoplastic invasion of the renal vein, dehydration or nephrotic syndrome. The ultrasound findings include renal enlargement, increased parenchymal echogenicity and loss of normal corticomedullary differentiation (Fig. 5.116). An echogenic thrombus may be identified in the renal vein or inferior vena cava. Colour Doppler imaging shows no flow in the main renal vein and a narrow systolic arterial peak with reversed diastolic flow in the renal artery.

Renal arterial infarction in children is usually a global event and a complication of traumatic dissection. Acute segmental infarction is less common and may result from vasculitis or an embolus from an indwelling arterial line or cardiovascular vegetation. The clinical features and imaging findings are similar to those in adults.

Fig. 5.115. Haemolytic uraemic syndrome in a 3-year-old boy. Longitudinal US Doppler scan through the left kidney (LK) shows echo-rich cortex and echo-poor renal pyramids

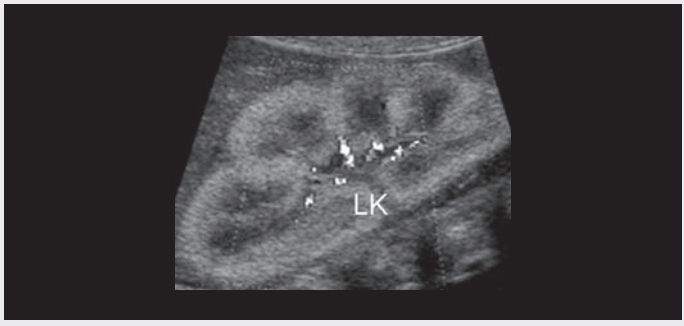

Fig. 5.116. Renal vein thrombosis in a 3-month-old girl with dehydration. Longitudinal scan shows an enlarged right kidney (RK) with loss of normal corticomedullary differentiation

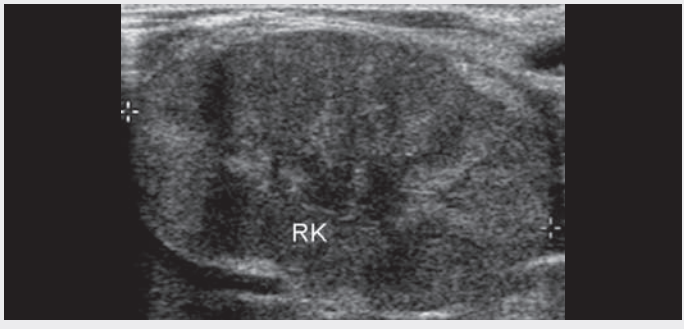

Anomalies of the lower urinary tract

The distal ureter may show **primary megaureter**, defined as ureteral dilatation above a short aperistaltic juxtavesical segment of ureter that has a normal insertion into the trigone. Ultrasound shows the retrovesical ureter pelvic portion, which is rarely visible in normal children (Fig. 5.117).

Fig. 5.117. Right megaureter in a 9-month-old boy. Longitudinal scan through the lower pelvis shows a markedly dilated distal right ureter (U), tapering before entering the bladder (B). Note localized thickening of the bladder wall, corresponding to cystitis (arrow)

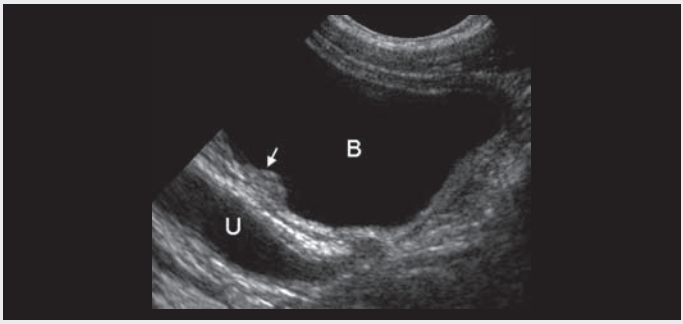

Ectopic ureter refers to abnormal insertion of the ureter into the bladder. This is rarely seen by ultrasound.

Ureterocoele is a cystic dilatation of the intravesical segment of the ureter. It may be small or fill the entire bladder and may even prolapse out of the urethra. Ultrasound shows the ureterocoele as a cyst with a thin membrane and associated anomalies, such as dilated ureter, duplex kidney and obstructive bladder anomalies (Fig. 5.118).

Ultrasound is not the best imaging modality for detecting and staging **vesico-ureteral reflux**. The bladder may show **urachal abnormalities**, involving incomplete obliteration of the urachal lumen, which connects the anterior bladder wall to the umbilicus during fetal development and normally closes during the 5th month of gestation. Four main forms can be distinguished: patent urachus, urachal sinus, urachal diverticulum and urachal cyst. The form detected most frequently is a midline cyst located between the bladder dome and the umbilicus (Fig. 5.119).

Bladder duplication is a rare anomaly, easily diagnosed by ultrasound, which shows two bladders lying side by side.

Congenital diverticulum of bladder is the most frequent bladder abnormality. It is often unilateral and rarely bilateral. Ultrasound shows the size and position of the congenital diverticula and modifications after micturition.

Fig. 5.118. Bilateral ureterocoeles in a 3-month-old boy with urinary infection. Transverse scan through the bladder (B) shows two large ureterocoeles (U)

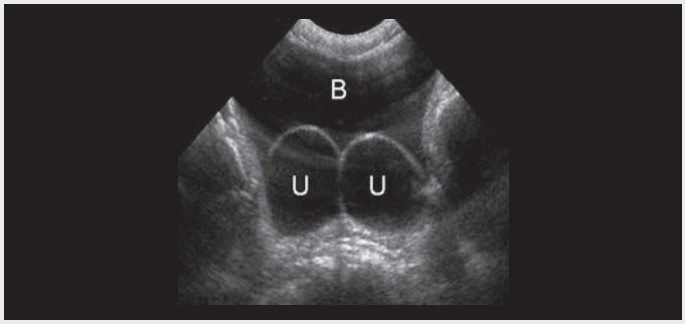

Fig. 5.119. Urachal cyst in a 2-year-old girl. Longitudinal scan shows an urachal cyst (UC) as a well-circumscribed cystic mass located anterior to the midline between the umbilicus and the dome of the bladder (B)

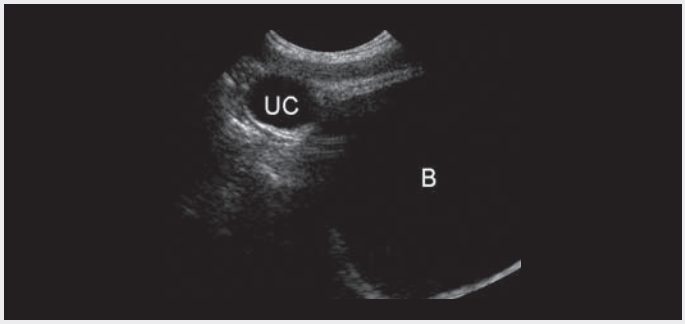

In cases of **Prune belly syndrome**, ultrasound shows the associated abnormalities, which include renal dysplasia, a large bladder and undescended testes.

In **cloacal abnormalities**, the vagina, uterus, bladder, kidneys, lower spinal cord and hips must be evaluated.

Urethral abnormalities include posterior urethral valves, which are the commonest cause of urethral obstruction in newborn boys. Bladder distension and dilated posterior urethra and the upper urinary tract are clearly seen by ultrasound, even antenatally (Fig. 5.120).

Other urethral abnormalities, including anterior urethral valve and urethral duplication, cannot be seen by ultrasound, which shows only the consequence of urethral obstruction, which is mainly dilatation of the urinary tract.

Stones in the bladder and in the male urethra are frequent in hot, poor areas, at any age of childhood. Ultrasound shows the stones, their number, size and position

Fig. 5.120. Posterior urethral valves in a newborn boy. Transversal and longitudinal scans show a dilated urethra (UR) and bladder (B) wall thickening

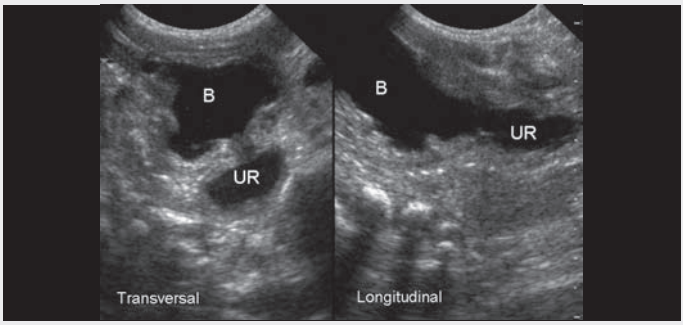

Fig. 5.121. Bladder calculi in a 5-year-old girl. Longitudinal and transversal scans show a stone (S) within the bladder (B)

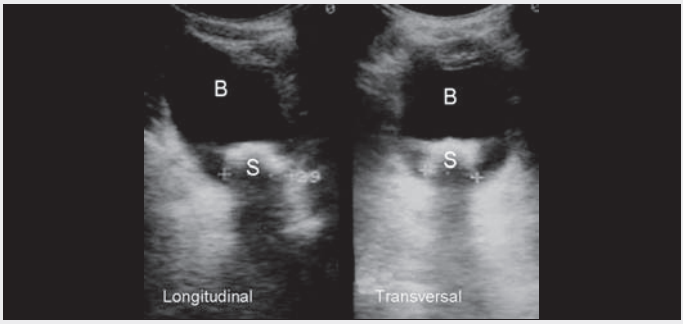

and their consequences: thickening of the bladder wall and dilatation of the bladder and renal cavities (Fig. 5.121).

In **neurogenic bladder**, ultrasound shows the bladder capacity, thickening of the wall, the post-micturition volume and any associated anomalies, such as stones and hydronephrosis.

Most **neoplasms of the urinary bladder** in children are malignant. Rhabdomyosarcomas are the commonest. Ultrasound shows a pedunculated soft-tissue mass projecting into the bladder lumen, referred to as a botryoid appearance or as focal or diffuse wall thickening (Fig. 5.122).

Fig. 5.122. Bladder rhabdomyosarcoma in a 4-year-old boy. transverse and longitudinal scans show an irregular soft-tissue mass (M) within the bladder lumen (B)

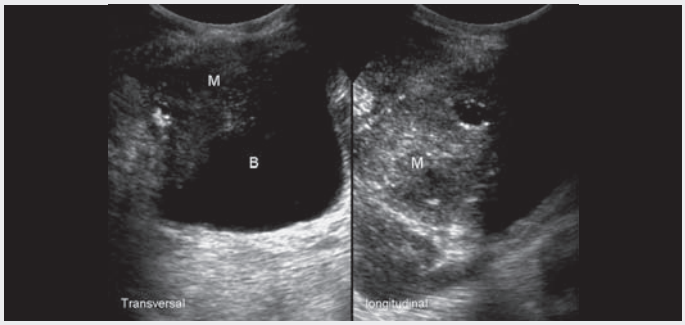

Adrenal glands

The adrenal glands are located on the upper part of kidneys. They have an inverted Y or V shape and are usually seen on the right side through the acoustic window of the liver. The sonographic appearance of normal adrenal glands varies with age. In neonates, they are relatively large and prominent, with an echo-poor cortex and an echo-rich medulla (Fig. 5.123). The adult appearance is acquired at 1–3 years of age, when the adrenals are seen as thin, linear, echo-poor structures.

Fig. 5.123. Normal adrenal gland in a newborn girl. Transverse scan shows the inverted V configuration of the adrenal gland (arrowheads) lying between the liver (L) and the right kidney (RK); echo-rich medulla and echo-poor cortex

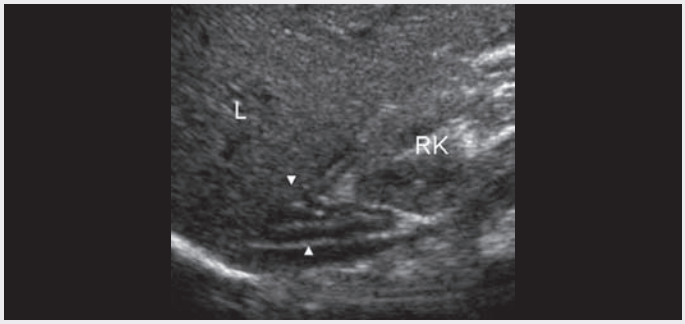

Congenital hyperplasia is the commonest cause of ambiguous genitalia in female infants. The role of ultrasound is to demonstrate the presence of a vagina, uterus and ovaries.

Adrenal haemorrhage is a frequent cause of an abdominal mass in a neonate and sometimes during antenatal life. It is usually secondary to birth trauma or perinatal anoxia. The ultrasound findings depend on the stage of evolution of the haemorrhage. In a fresh haemorrhage, the gland is enlarged and echogenic; 1–2 weeks later, the central area becomes increasingly echo-poor, with some internal echoes, indicating the liquefaction stage (Fig. 5.124). A rim of calcification may appear in the last stage, which is seen clearly by simple radiography. Ultrasound is used to investigate the contralateral gland and the permeability of the renal vein and the inferior vena cava. Bilateral adrenal haemorrhage and renal vein thrombosis can occur.

Fig. 5.124. Adrenal haemorrhage in a newborn boy. Longitudinal scan shows a heterogeneous right adrenal gland with an echo-poor central area and peripheral calcifications. The gland retains its triangular shape. L, liver

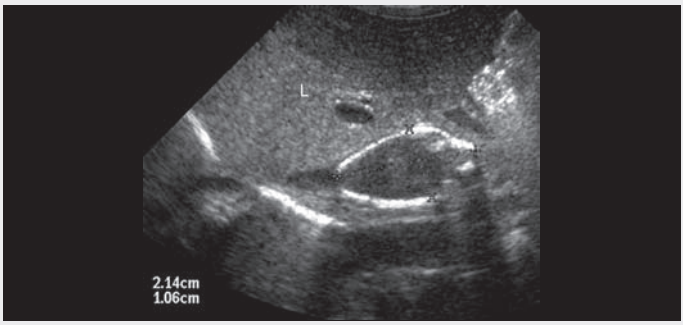

Adrenal abscesses are rare, and ultrasound cannot differentiate them from haemorrhage. The clinical findings are important.

Adrenal cystic lesions are rare and nonspecific.

Neuroblastoma is the commonest solid tumour of childhood. The tumour may arise anywhere along the sympathetic chain, but the most frequent sites are the adrenal gland, retroperitoneum and posterior mediastinum. Neuroblastoma usually occurs in children < 5 years of age. The commonest clinical presentation is an abdominal mass, and about 90% of children have increased serum or urinary levels of catecholamines or their metabolites, particularly vanillylmandelic acid and homovanillic acid.

On ultrasound examination, neuroblastoma appears as a suprarenal or paraspinal solid mass (Fig. 5.125, Fig. 5.126). It may be homogeneous or heterogeneous, with small punctate echogenic areas, and it may contain echo-poor areas as a result of haemorrhage, necrosis or cystic degeneration. The tumour margins may be smooth or irregular. Peripheral or central vascularity can be observed on colour Doppler. Small calcifications may be seen, and these help to differentiate this

Fig. 5.125. Adrenal neuroblastoma in a 5-month-old girl. Longitudinal scan through the liver (L) and the right kidney (RK) shows a large heterogeneous suprarenal mass (M) with smooth margins

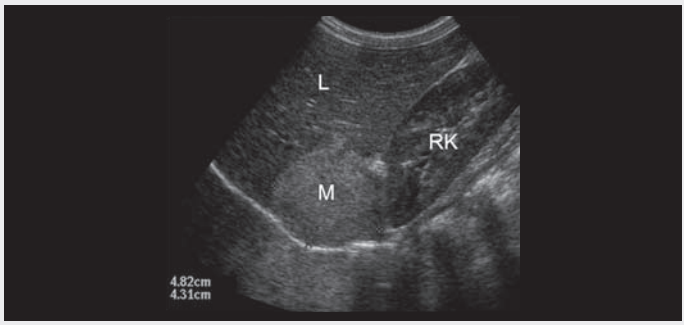

Fig. 5.126. Medial neuroblastoma in a 2-year-old boy. Transverse scan shows a heterogeneous mass (M) surrounding and compressing the abdominal aorta (Ao). The mass contains scattered echo-rich areas representing calcifications, and its margins are irregular; IVC, inferior vena cava

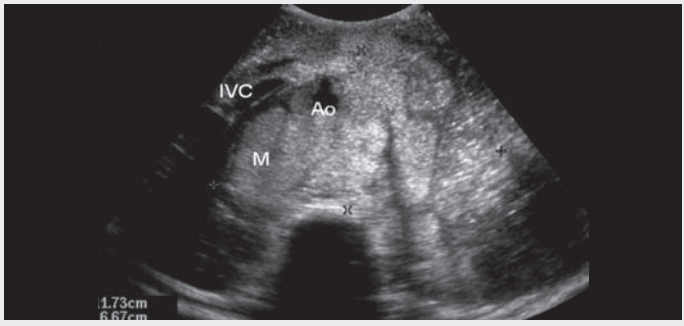

tumour from renal masses (Fig. 5.127). The kidney is displaced but rarely invaded. Ultrasound examination with Doppler is essential for evaluating liver metastasis and infiltration, displacement and encasement of the aorta, inferior vena cava and renal and mesenteric vessels. Pepper syndrome, which is a disseminated neuroblastoma to the liver, skin and bone marrow of infants < 1 year, can be diagnosed by ultrasound (see Fig. 5.10).

Other childhood adrenal tumours are ganglioneuroblastoma, adrenocortical tumours and phaeochromocytomas. These are less common than neuroblastoma. Sonography shows nonspecific, solid, well-defined masses in all cases.

Fig. 5.127. Neuroblastoma in an 18-month-old boy. Axial scan shows a large, heterogeneous suprarenal mass with small calcifications (arrows)

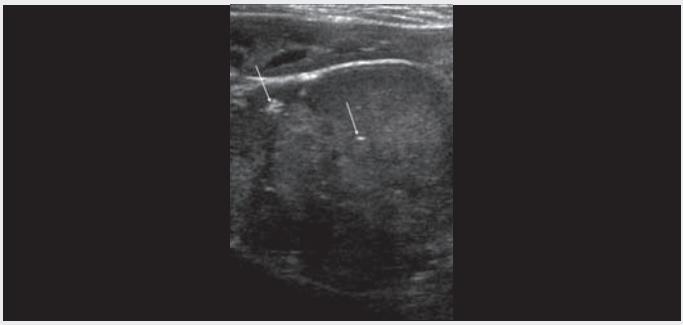

Special conditions

Confirmation of urinary-tract anomalies detected antenatally

This situation is frequent. The role of ultrasound, conducted 2–3 days after birth, is to confirm an antenatal diagnosis, to identify any anomalies and to provide baseline measurements for long-term follow-up, if needed. If the condition requires urgent investigation and treatment, the infant should be referred immediately to the appropriate department.

Imaging protocol for urinary-tract infections

Ultrasound is the investigation of choice for any child with a urinary-tract infection; all children should be thoroughly assessed and investigated after their first proven urinary-tract infection. The protocol for imaging depends on the age of the child and the availability of equipment; it can include, besides the ultrasound, a simple radiography, a urethrocystogram, isotope studies, CT and MRI.

The features of the urinary tract that should be established by ultrasound are:

- the size of the kidneys, any renal scarring, the regularity of the outlines and echogenicity;
- localized or diffuse dilatation of the collecting system and renal thickness;
- the diameter of the ureters in the lumbar and pelvic portions;
- bladder parameters, such as capacity, thickening of the wall, contents, contour and post-micturition volume.

Abdominal trauma

Renal trauma is frequent in children. Ultrasound is the main modality for diagnosis and follow-up in cases of renal trauma, parenchymal laceration and fracture (Fig. 5.128), subcapsular haematoma (Fig. 5.129), shattered kidney or avulsion from the vascular and pelvic pedicle. It also reveals intrarenal or perirenal haematoma, secondary dilatation of the renal cavities, urinary leakage and perinephric collection of urine (Fig. 5.130) and rupture of the bladder wall.

Fig. 5.128. Renal fracture in a 5-year-old girl with abdominal trauma. (a) Longitudinal scan shows a linear area of low attenuation in the mid-pole of the right kidney (RK) that extends into the collecting system (arrows). (b) Axial contrast-enhanced CT reveals the right renal fracture, nonperfused parenchyma in the anterior part of the right kidney, a large parenchymal haematoma (H) and surrounding perirenal haematoma (arrows)

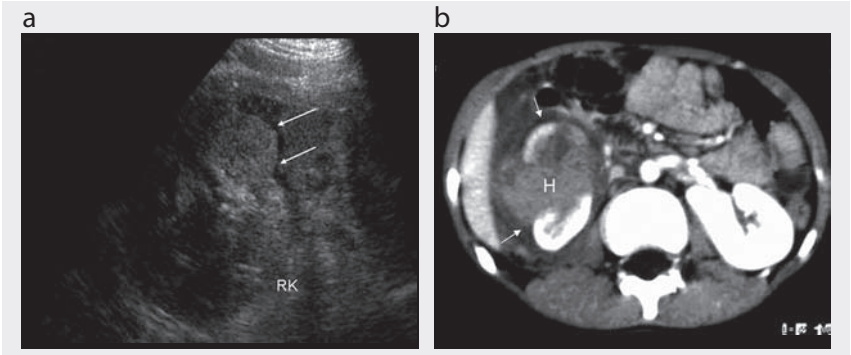

Fig. 5.129. Renal subcapsular haematoma in a 7-year-old boy after trauma. Longitudinal scan through the right kidney (RK) shows an echo-rich subcapsular haematoma (arrows)

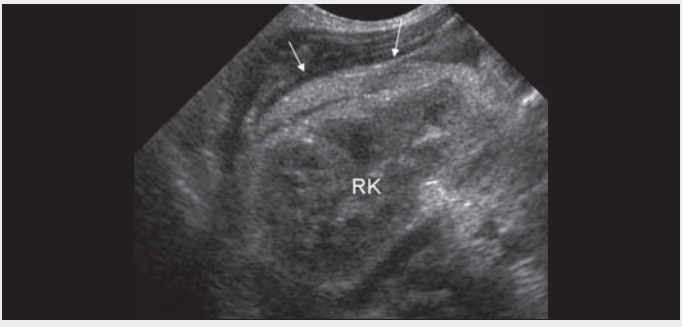

Fig. 5.130. Perirenal collection of urine in a 4-year-old boy after trauma. (a) Longitudinal and (b) transverse scans in the right kidney (RK) show a large perirenal fluid collection (arrows)

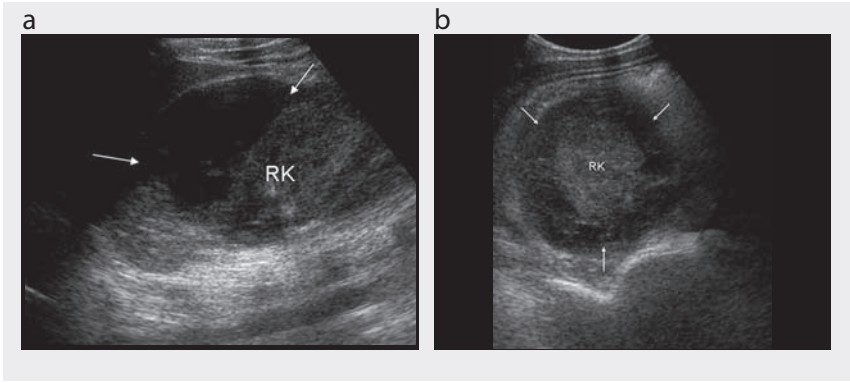

Hypertension

Symptomatic hypertension in children is usually secondary and of renal origin. Ultrasound is used to establish the size and echogenicity of the kidneys, parenchymal thinning and scars, any dilatation of the collecting system and any anomalies of the aorta and renal arteries, such as aneurysm, changes in the calibre of the aorta and renal arterial stenosis. Intra-abdominal tumours should be sought; in particular, both adrenal glands should be examined for a phaeochromocytoma, which can be located anywhere in the abdomen or pelvis.

Screening for congenital renal abnormalities

Ultrasound is the most efficient tool for identifying congenital intra-abdominal anomalies associated with various syndromes.

Enuresis

Enuresis is common clinically, and no exploration is generally needed. In children over 5–6 years, ultrasound may be used to verify the entire urinary tract, including bladder-wall thickening and the post-micturition bladder volume.

Pelvis

Indications

Ultrasound remains the imaging modality of choice for initial evaluation of most abnormalities of the paediatric female pelvis. The main indications are:

- precocious puberty;
- disorders of puberty;

- pelvic pain;
- pelvic mass;
- ambiguous genitalia;
- abnormal vaginal bleeding;
- suspected vaginal foreign body;
- vaginal mass.

Preparation

A full bladder is required for ultrasound examination of the pelvis. The child should drink fluid 1 h before the examination; in urgent situations, the bladder can be filled with sterile normal saline through a urethral catheter.

Examination technique

The examination is usually carried out with the child in a supine position. A coupling agent is used to ensure good acoustic contact between the probe and the skin. Longitudinal scans are conducted, first in the midline between the umbilicus and the pubic symphysis and then more laterally, on the left and right sides. A transverse scan is then performed. If necessary, the child is turned to the oblique position for identification of the ovaries.

The examination should be carried out with the highest-frequency probes, usually 3.5, 5.0 or 7.5 MHz. Doppler may be used if available. In older children, the endorectal route may be useful.

Normal findings

Uterus

The size and appearance of the uterus vary with age and pubertal status. The neonatal uterus is relatively prominent due to the effects of maternal and placental hormones. The cervix is larger than the fundus (fundus-to-cervix ratio, 1:2), the uterus is about 3.5 cm long, with a maximum thickness of about 1.4 cm; the endometrial lining is often echogenic (Fig. 5.131). Some fluid may be seen within the endometrial cavity.

At 2–3 months, the uterus decreases in size, acquiring a tubular shape; the size of the cervix is equal to that of the corpus (Fig. 5.132). In prepuberty, until about 8–9 years of age, the uterus remains small with a tubular configuration (Fig. 5.133). A high-frequency probe can show the central line in some cases. The uterus is 2.5–4 cm long, with a thickness no greater than 10 mm. Some fluid can be seen within the vaginal cavity (Fig. 5.134).

At puberty, the corpus is larger than the cervix, resulting in the adult pear-shaped uterus, measuring 5–8 cm long, 3 cm wide and 1.5 cm thick (Fig. 5.135). The central endometrial stripe is identifiable; its dimensions vary with the phases of the menstrual cycle, with a thickness of 2–3 mm in the early menstrual phase, 8 mm in the proliferative phase and approximately 15 mm in the secretory phase.

Fig. 5.131. Normal neonatal uterus. Longitudinal scan shows a prominent cervix and a thin, echo-rich endometrial stripe (arrowheads)

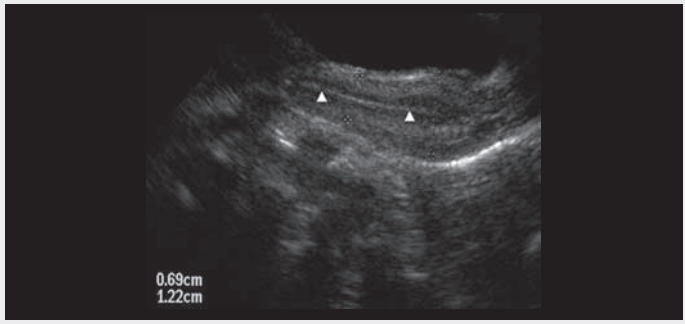

Fig. 5.132. Normal uterus in a 1-year-old girl. Longitudinal scan shows the tubular shape (calipers). B, bladder

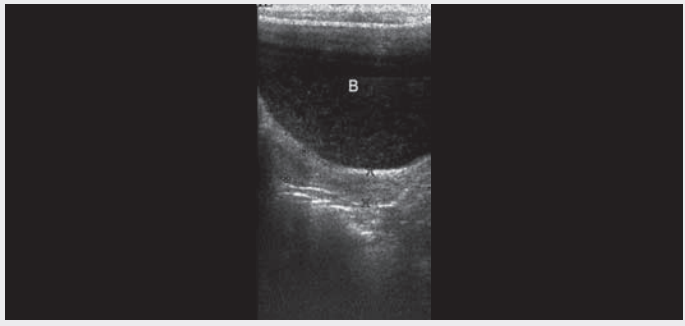

Fig. 5.133. Normal prepubertal uterus in a 7-year-old girl. Longitudinal scan shows a small, tubular uterus with no differentiation between the fundus and the cervix and no recognizable endometrial stripe

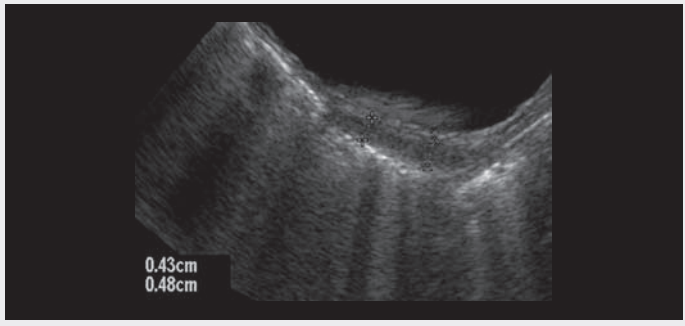

Fig. 5.134. Normal prepubertal uterus in a 7-year-old girl. Longitudinal scan shows some fluid in the vaginal cavity (arrow). B, bladder

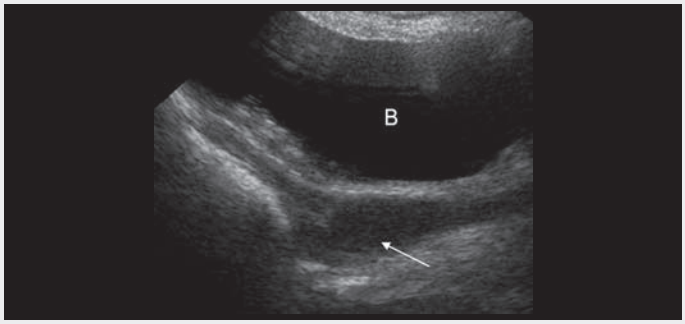

Fig. 5.135. Normal pubertal uterus in a 14-year-old girl. Longitudinal scan shows a pear-shaped uterus with a fundus that is larger than the cervix and an identifiable central endometrial stripe (arrowheads)

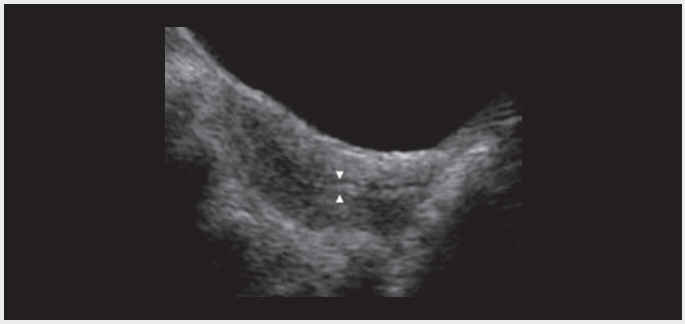

Ovaries

The ovaries, like the uterus, change in size and morphology with age and pubertal status. The ovarian size is usually based on assessment of the ovarian volume, from V = length × width × depth × 0.5. In the neonatal period, the ovarian volume is relatively large (about 3.6 cm^3), with the presence of large follicles (Fig. 5.136). After the neonatal period, the ovarian volume decreases with the decrease in maternal hormone levels. In infancy and early childhood, the ovaries are quiescent and 1–1.2 cm^3 in volume. Microcystic follicles are routinely seen in this period, most measuring 5–10 mm in diameter (Fig. 5.137).

At puberty, the ovarian volume is 1.3–2.3 cm^3, and cystic follicles are more frequent (Fig. 5.138). From around 8 years of age, with the onset of puberty, the size of the ovary increases by at least four times. At puberty, the average volume is 3–5 cm^3, and the length is > 3 cm (Fig. 5.139).

Fig. 5.136. Normal neonatal ovary. Longitudinal scan shows a large ovarian volume with multiple large follicles (arrows)

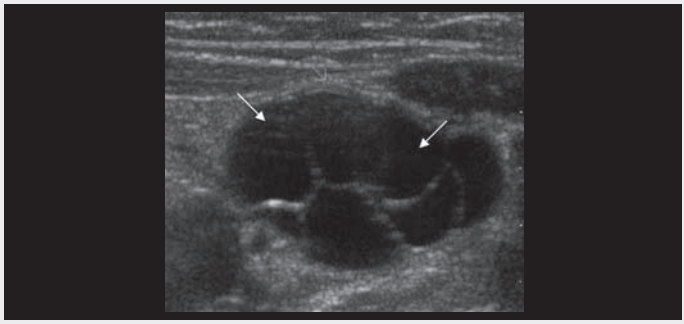

Fig. 5.137. Normal ovary in a 2-year-old girl. Longitudinal scan of the right ovary shows an ovary with a volume of about 1 cm^3 and microcystic follicles (arrows)

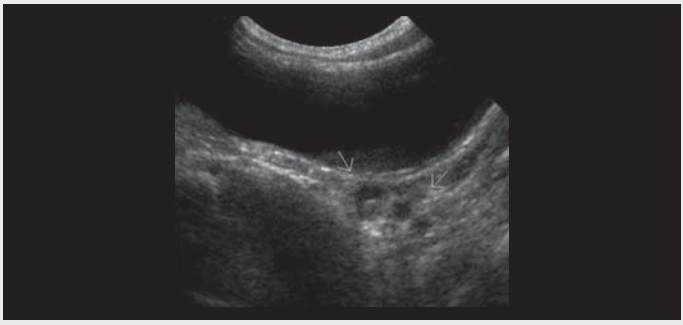

Fig. 5.138. Normal prepubertal ovary in a 7-year-old girl. Longitudinal scan shows multiple small follicles (arrows) < 9 mm in diameter and an ovarian volume of 2 cm^3

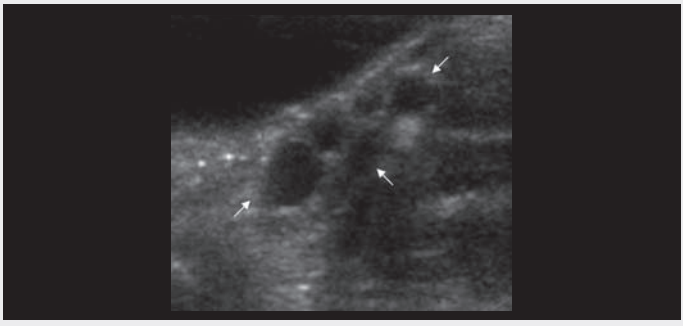

Fig. 5.139. Normal pubertal ovary in a 14-year-old girl. Longitudinal scan of the right ovary shows a large ovary with multiple stimulated (arrow) and unstimulated (arrowheads) follicles

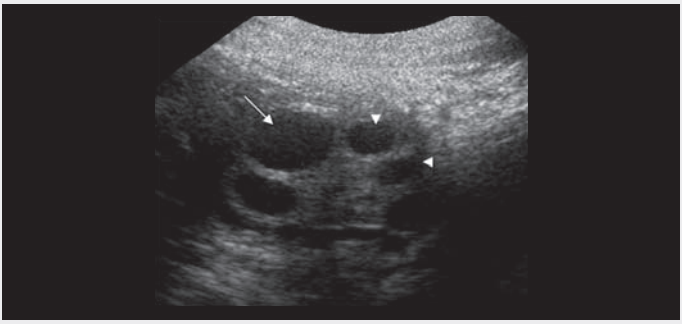

Pathological findings

Ovarian masses

Ultrasound is the initial imaging modality used in the diagnosis of suspected ovarian masses in children or adolescents.

Ovarian cysts

Functional ovarian cysts are the commonest cause of ovarian masses and have a bimodal age distribution, in neonates and adolescent girls. Functional ovarian cysts are often asymptomatic and are discovered incidentally on pelvic ultrasound performed for other reasons. On sonography, the classical cyst is echo-free, with a sharp back wall and excellent through-transmission (Fig. 5.140). The cyst can become large but usually no more than 3 cm. Most functional ovarian cysts are treated

Fig. 5.140. Functional ovarian cyst in an 11-year-old girl. Longitudinal scan shows a large echo-free cyst (c) with an imperceptible wall arising from the right ovary; B, bladder, U, uterus

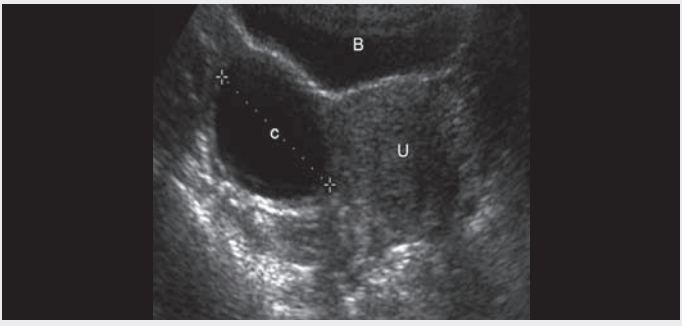

conservatively and resolve spontaneously. Rarely, there are complications, such as ovarian torsion, haemorrhagic cyst or ruptured cyst. In neonates, large cysts can extend into the abdomen. Cysts in adolescent girls are usually confined to the pelvis.

Haemorrhagic ovarian cysts are complications of functional ovarian cysts. The typical clinical presentation is sudden, severe, transient pelvic pain lasting 1–3 h. Ultrasound shows a complex adnexal cystic mass containing septations, low-level echoes, a fluid–debris level or clotted blood (Fig. 5.141). A thick wall and fluid in the Douglas space may also be seen.

Fig. 5.141. Haemorrhagic ovarian cyst. (a) Longitudinal scan of the right adnexal region of a 10-year-old girl shows a large echo-rich cystic mass (C), indicating internal haemorrhage (B, bladder; U, uterus). (b) Longitudinal scan of the left ovary of a 12-year-old girl showing a large complex cyst (C) with internal echoes and septations (arrows). A follow-up scan 1 month later revealed spontaneous resolution

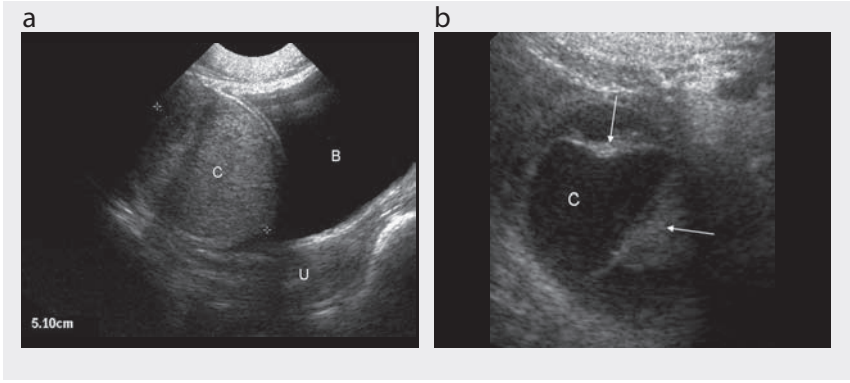

Polycystic ovary disease, also known as the Stein-Leventhal syndrome, is characterized clinically by amenorrhoea, obesity and hirsutism. The endocrine profile of affected children reveals decreased levels of follicle-stimulating hormone and increased levels of luteinizing hormone. The sonographic findings include bilateral enlargement of the ovaries, which contain multiple small follicles, usually 0.5–0.8 cm in diameter (Fig. 5.142). The mean ovarian volume on ultrasound is 12–14 cm^3.

Paraovarian cysts are of paramesonephric or mesothelial origin and arise in the broad ligament or Fallopian tubes. Their classical ultrasound appearance is a fluid-filled mass with thin walls. Paraovarian cysts are indistinguishable from other ovarian cysts, unless a normal ipsilateral ovary is seen separate from the cyst.

Fig. 5.142. Polycystic ovaries in a 14-year-old girl with obesity, amenorrhoea and hirsutism. Longitudinal scan of the right ovary (RO) shows an enlarged ovary with echogenic central stroma and multiple peripheral small follicles (arrows)

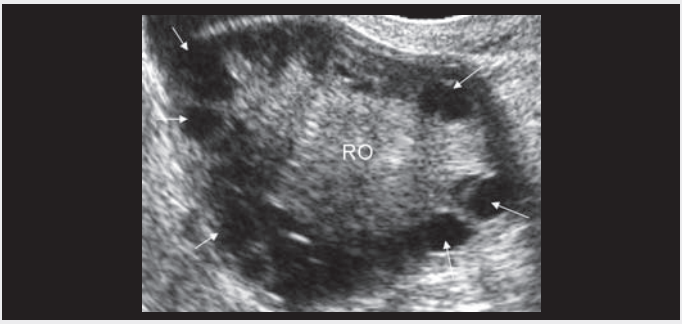

Benign ovarian neoplasms

Mature ovarian teratoma, also known as dermoid cyst, is the commonest ovarian neoplasm in children. Clinically, girls present with a painless pelvic or abdominal mass. The sonographic appearance of teratomas is variable because of their varied contents. The classical ultrasound appearance is a predominantly cystic mass with a mural nodule containing varying amounts of fat and calcification. Septations, internal debris and a fat fluid level may be seen (Fig. 5.143).

Serous and mucous ovarian cystadenomas are much less common than mature ovarian teratoma (Fig. 5.144). They appear as well-defined, thin-walled cystic masses with internal septa of varying thickness and irregularity. Calcification may be seen in the septations or the wall of the tumour.

Fig. 5.143. Benign ovarian teratoma in a 4-year-old girl. (a) Longitudinal scan of the right adnexal shows a large, predominantly cystic mass (C) with peripheral mural nodules (arrows) containing fat (F). (b) Axial and (c) coronal reformed contrast-enhanced CT scans show a well-defined cystic pelvic mass (C) containing calcification (arrow) and a layer of fat (arrowhead); B, bladder. (d) Intraoperative photograph demonstrates the large cystic mass (C)

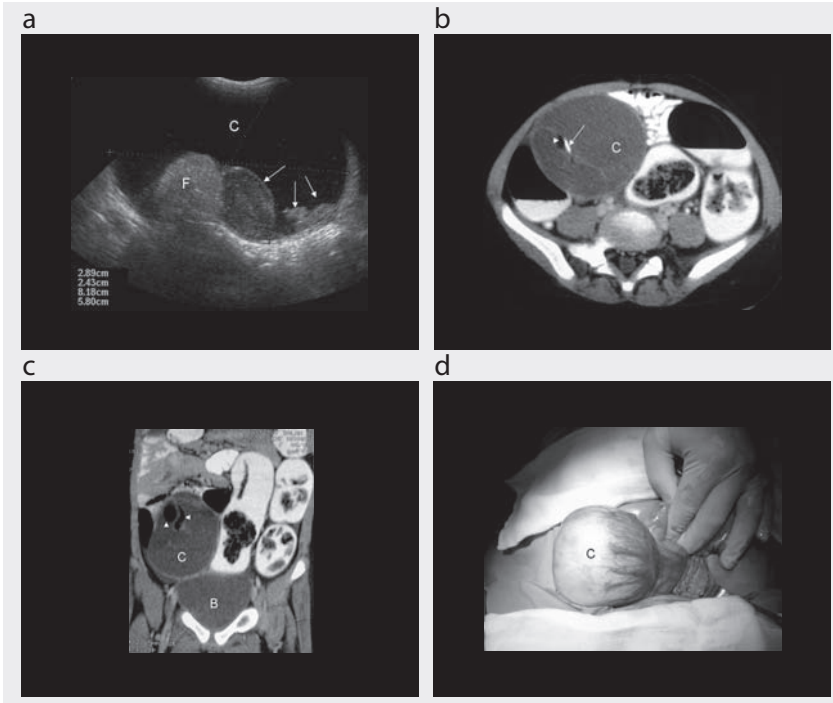

Fig. 5.144. Serous ovarian cystadenoma in a 5-year-old girl with abdominal mass. (a) Transverse and (b) longitudinal scans show a large cystic mass (C) extending from the pelvis into the abdomen

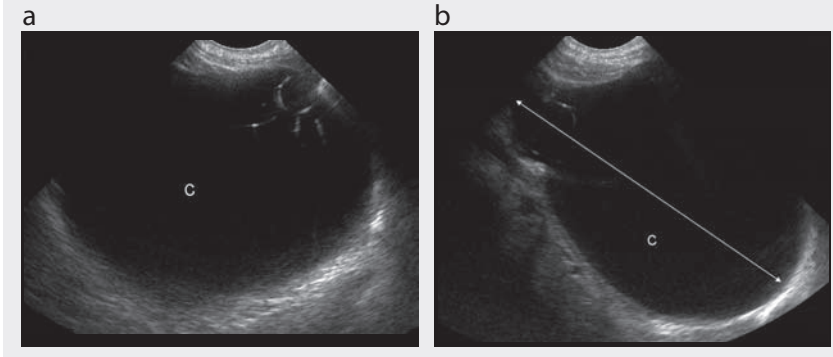

Malignant ovarian neoplasms

Malignant ovarian neoplasms account for only 2–3% of all childhood cancers. On ultrasound, the size and echogenicity of the mass are different from those of other malignancies, such as ascites, lymph nodes and hepatic metastases. The various distinct histological types include germ-cell tumours (dysgerminoma, immature or malignant teratomas, endodermal sinus tumour, embryonal carcinoma and choriocarcinoma), stromal tumours and epithelial carcinomas.

Uterine masses

Uterine masses are uncommon in childhood. The predominant masses found in neonates and infants are due to congenital vaginal or vaginal–uterine obstruction. The term used to describe a vaginal obstruction depends on the fluid content: hydrocolpos refers to dilatation of the vagina by serous fluid, hydrometrocolpos to distension of both the uterus and the vagina by serous fluid, haematocolpos to distension of the vagina by blood, haematometra to distension of the uterus by blood and haematometrocolpos to distension of both the uterus and the vagina by blood.

In neonates, vaginal obstruction is usually caused by vaginal or cervical atresia, high-grade stenosis, a transverse septum or an imperforate membrane. In adolescent girls, vaginal obstruction is most often the result of a simple imperforate membrane, septum or hymen.

Sonography usually suffices for diagnosis, and the imaging findings are similar for newborns and menarchal adolescents. The distended vagina appears as a tubular, fluid-filled, midline mass between the bladder and the rectum (Fig. 5.145). The uterine cavity may be dilated. The echogenicity of the contents may be increased if they are haemorrhagic.

Fig. 5.145. Haematocolpos in an 11-year-old girl with cyclic pain. (a) Longitudinal scan shows a dilated vagina (V) with echo-rich fluid, representing blood but a normal uterus (U). (b) Transverse scan showing the distended vagina medial and posterior to the bladder (B)

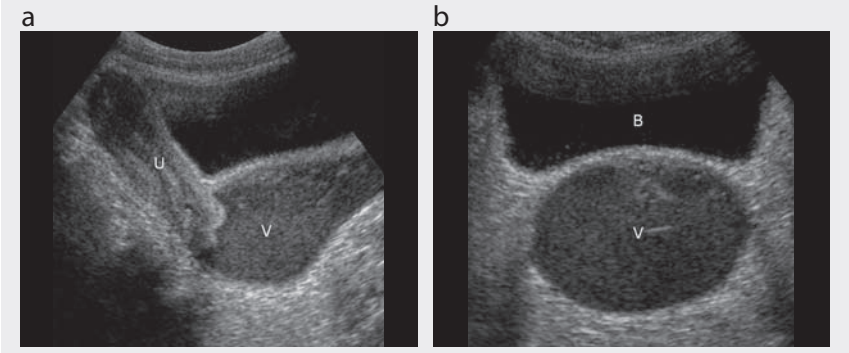

Prepuberal bleeding

A **vaginal foreign body** can be demonstrated on ultrasound as an echogenic image with acoustic shadowing, which is characteristic but not always present.

Vaginal rhabdomyosarcomas are commonly botryoid and are found almost exclusively in young girls. On ultrasound, a vaginal rhabdomyosarcoma appears as a large, solid, heterogeneous or echo-poor mass posterior to the bladder.

Disorders of puberty

Precocious puberty is defined as complete sexual development (including menarche) before 8 years of age. Precocious puberty may be central or peripheral.

Central precocious puberty is idiopathic or due to a cerebral tumour or another cause of intracranial hypertension (e.g. post-meningitis hydrocephalus); it is gonadotrophin-dependent. Ultrasound shows augmentation of uterine and ovarian volumes (Fig. 5.146).

Fig. 5.146. True isosexual precocity in a 5-year-old girl. (a) Longitudinal scan shows a pear-shaped pubertal uterus with a thin echo-rich endometrial stripe (arrowheads). (b) Longitudinal scans of the right and left ovary shows multiple follicles (arrows). B, bladder

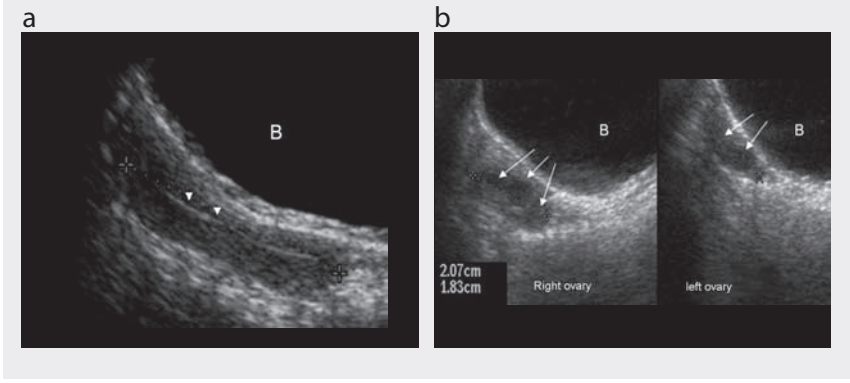

Peripheral precocious puberty, or precocious pseudopuberty, is gonadotrophin-independent. Autonomous ovarian follicular cysts are the most frequent cause, being more common than oestrogen-secreting neoplasms, such as granulosa-cell tumours and gonadoblastomas. In autonomous ovarian follicular cysts, bone age is often normal, and there is no response to stimulation with luteinizing hormone. Ultrasound shows a stimulated uterus and a unilateral follicular ovary.

Primary amenorrhea is defined as no menarche by 16 years of age, no thelarche or adrenarche by 14 years of age, or no menarche more than 3 years after adrenarche and thelarche. The absence of secondary sexual development at clinical examination and Müllerian structures on ultrasound are the basis for selecting laboratory tests. Common causes include gonadal dysgenesis (Turner syndrome with XO karyotype, nonvisualized mosaic or abnormal ovaries; 33% of cases) (Fig. 5.147), Müllerian (uterovaginal) anomalies (Müllerian agenesis, duplication defects with or without obstruction, canalization defects with or without obstruction; 20%), hypothalamic-pituitary causes (15%), constitutional delay (often familial; 10%) and other causes (e.g. systemic, psychiatric; 22%).

Fig. 5.147. Turner syndrome in a 13-year-old girl. Longitudinal scan of the pelvis shows a prepubertal uterus (arrows) with a tubular shape, no recognizable endometrial stripe and no visible ovaries. B, bladder

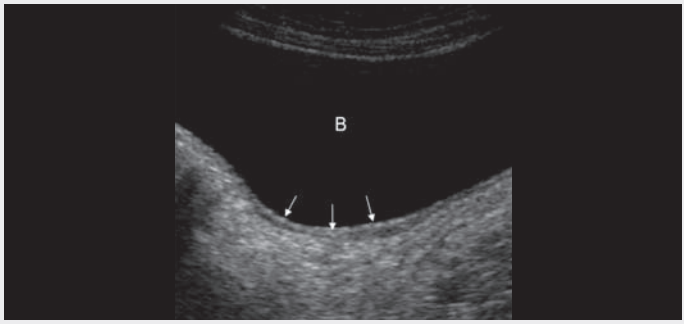

Müllerian agenesis or hypoplasia, often termed Mayer-Rokitansky-Küster-Hauser syndrome, is the result of absent or arrested development of both Müllerian ducts. Müllerian agenesis is the commonest cause of primary infertility after gonadal dysgenesis. The ultrasound findings include vaginal atresia, absent or rudimentary uterus (unicornuate or bicornuate) and normal ovaries. The karyotype is normal (46 XX). Renal or skeletal anomalies may be associated. A functioning endometrium may be present within the rudimentary uterus, resulting in unilateral haematometria.

Adolescents with obstructive uterovaginal anomalies present amenorrhoea and cyclic abdominal pain. Ultrasound is useful for differentiating the frequent haemato(metro)colpos, which is due to an imperforate hymen or a transverse vaginal septum, from the rare haematometra, which is due to cervical dysgenesis (Fig. 5.148). Cyclic abdominal pain with normal menses and haematocolpos may occur due to an obstructed hemivagina with a double uterus, which is almost always associated with ipsilateral renal agenesis.

Fig. 5.148. Haematocolpos with uterus duplex in a 12-year-old girl with an abdominal mass. (a) Longitudinal and (b) transverse scans show a markedly distended vagina (V) posterior to the bladder (B) and filled with blood. (c) Axial scan through the uterus shows the presence of two uteri (U)

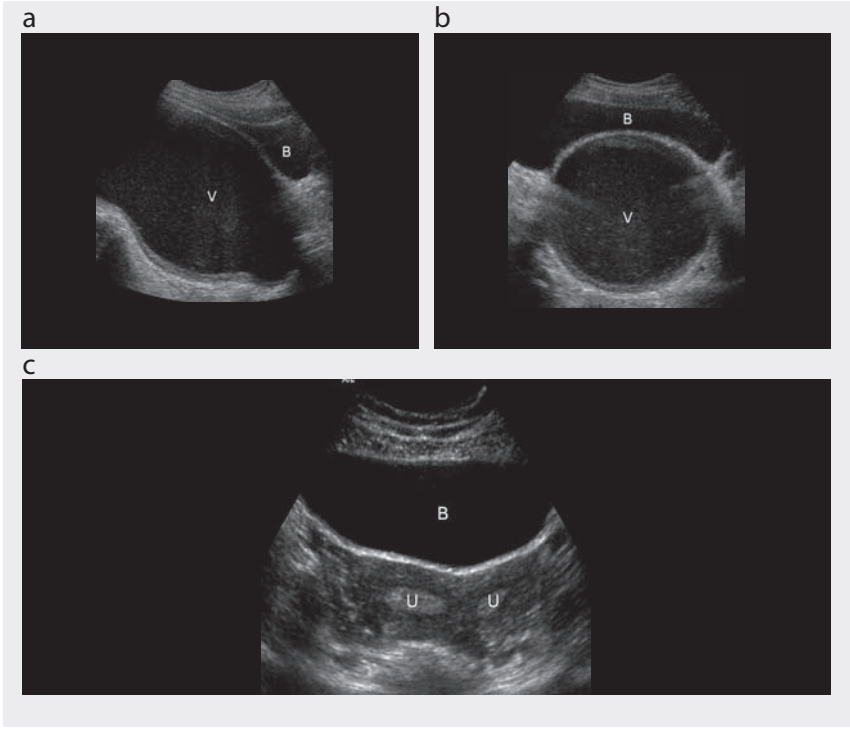

Adnexal torsion

In children, torsion of the normal ovary is rare. It is due to excessive mobility of the ovary and may occur when the Fallopian tubes are long and the ovaries are mobile or when there is a predisposing lesion, such as an ovarian cyst or mass (Fig. 5.149). The classical presentation is acute onset of lower abdominal pain, often associated with nausea or vomiting and leukocytosis. Some children have a history of recurrent pain, reflecting intermittent torsion and detorsion. On ultrasound, the involved ovary appears as an enlarged, echo-poor mass with multiple small peripheral follicles and good sound transmission (Fig. 5.150). Doppler ultrasound commonly shows lack of flow in the adnexum, although arterial flow is occasionally seen. The prognosis is poor when surgery is delayed.

Fig. 5.149. Adnexal torsion secondary to a functional ovarian cyst in an 8-year-old girl with acute pelvic pain. (a) Longitudinal and (b) transverse scans show a large ovarian cyst (C) superior to the bladder (B), arising from the left ovary (LO) and containing a smaller cyst (arrowheads). Radiating echogenic lines surrounding the cyst (arrows) represent the adnexal torsion

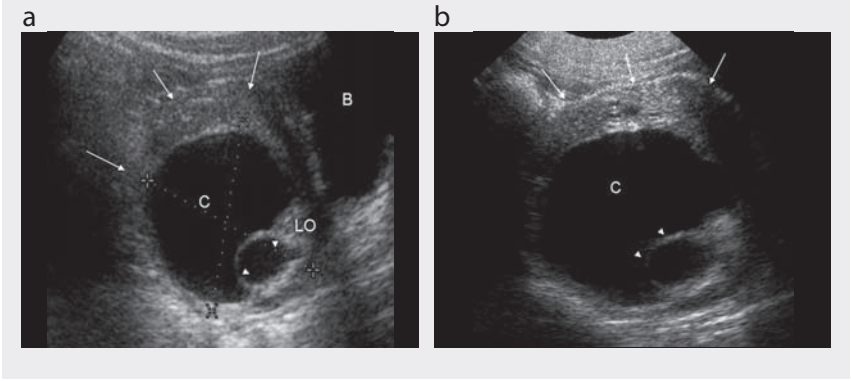

Fig. 5.150. Torsion of normal ovary in a 9-year-old girl. Transverse scans show an enlarged right ovary (RO) with a few peripheral dilated follicles (arrows) and no internal flow on the colour Doppler sonogram

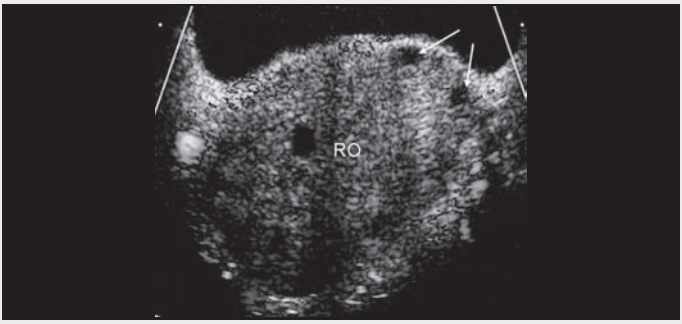

Pelvic inflammatory disease

Pelvic inflammatory disease in sexually active girls is usually due to *Neisseria gonorrhoeae* or *Chlamydia trachomatis*. Less commonly, it is a result of direct extension from an adjacent infection, such as appendicitis, inflammatory bowel disease or post-operative abscess (Fig. 5.151). The clinical features include pelvic pain, fever and adnexal tenderness. The diagnosis is usually established clinically, and imaging is commonly used to identify complications, pyosalpinx or tubo-ovarian abscess, and in assessing response to treatment. The classical sonographic appearance of pyosalpinx is a tubular, fluid-filled adnexal mass containing low-level echoes representing purulent debris. A tubo-ovarian abscess appears as a thick-walled echo-poor mass,

Fig. 5.151. Pelvic inflammatory disease in a 4-year-old girl secondary to extension in the Douglas space of a periappendiceal abscess. (a) Transverse scan of the right lower quadrant shows an enlarged appendix (A) and a loculated heterogeneous fluid collection (arrows). (b), (c) Transverse scans of the pelvis show extension of the collection into the Douglas space. R, rectum; B, bladder

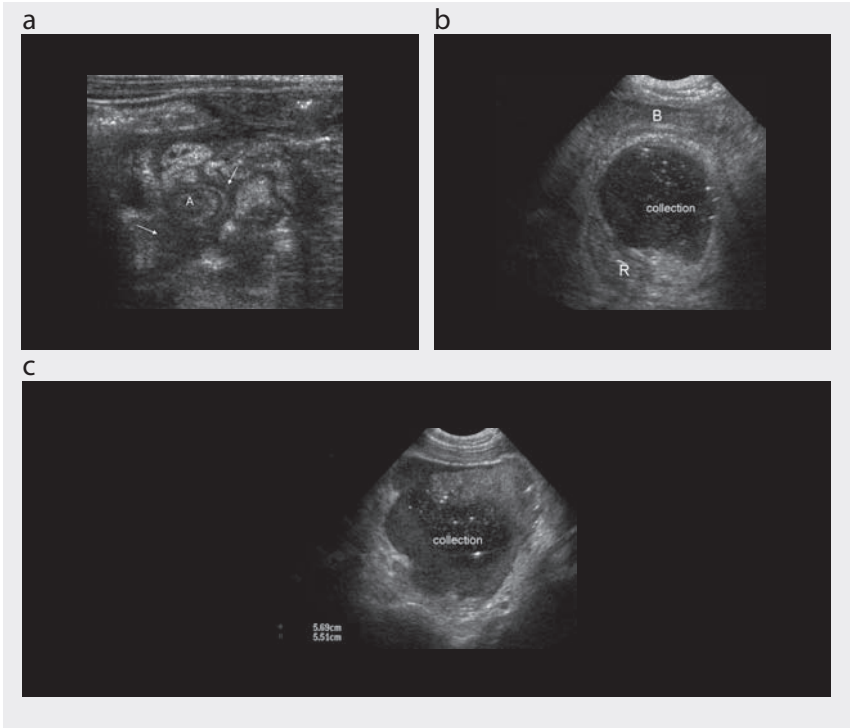

usually containing internal debris, septations or a fluid–debris level. Other sonographic findings include uterine enlargement with poorly defined margins and pelvic lymphadenopathy. Doppler ultrasound usually shows increased colour signals in the uterus, adnexa and pelvic soft tissues.

Intersex states

Intersex states are characterized by ambiguous external genitalia and gonads. The clinical findings include cryptorchidism, labial fusion, clitoromegaly, epispadias and hypospadias (Fig. 5.152). Ultrasound is useful for demonstrating the presence or absence of the uterus in neonates with ambiguous genitalia, which is important for determining the cause of hermaphrodism and for assigning sex.

Most cases of ambiguous genitalia consist of female pseudohermaphrodism due to congenital adrenal hyperplasia. In these cases, ultrasound shows a normal uterus and ovaries (Fig. 5.153). Increased size of the adrenal glands has been reported in neonates and infants with congenital adrenal hyperplasia. Genitography shows urethrovaginal confluence and opacification of the uterine cavity.

Fig. 5.152. Intersex state in a 2-year-old child. Labial fusion associated with clitoromegaly and hypospadias

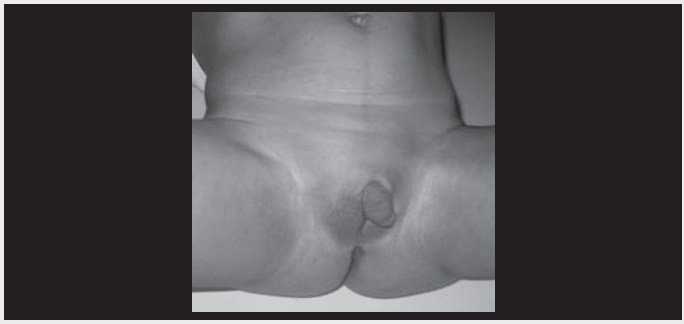

Fig. 5.153. Female pseudohermaphrodism in a 1-month-old infant. (a), (b) Longitudinal scans show a normal uterus (U) and ovaries (O). (c) Lateral genitogram with opacification of the bladder (B), the urethrovaginal confluence (V) and the uterine cavity (U)

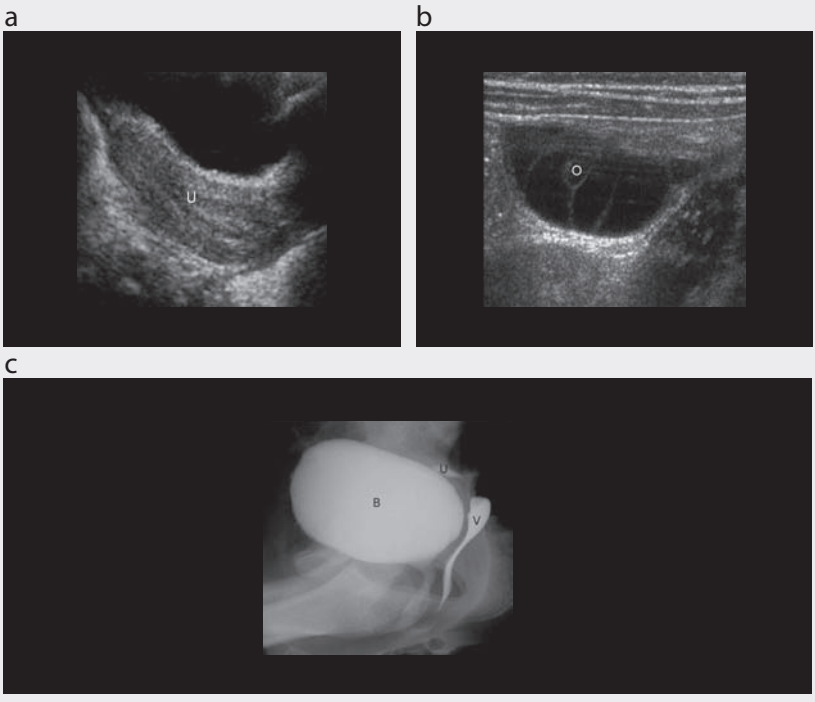

The other intersex states are male pseudohermaphrodism, true hermaphrodism and mixed gonadal dysgenesis. Male pseudohermaphrodites have normal testes, although they may be undescended (Fig. 5.154). True hermaphrodites have

Fig. 5.154. Male pseudohermaphrodism in a 9-month-old infant. (a) Transverse scan of the inguinal region shows an undescended bilateral testis and no uterine cavity. (b) Lateral genitogram shows opacification only of the bladder (B) and urethra

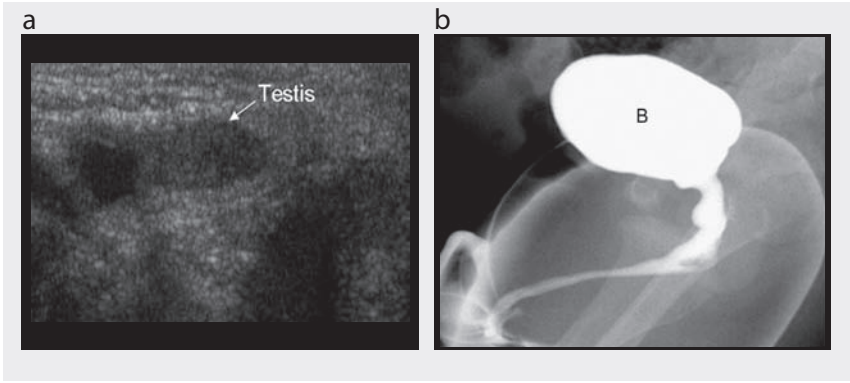

Fig. 5.155. Gonadal dysgenesis in a newborn. (a) Ambiguous external genitalia. (b) Transverse scan shows a bicornuate (arrows) uterus (U) behind the bladder (B). (c) Transverse scan of the pelvis shows a testis (T) above the bladder (B). (d) Lateral genitogram shows opacification of the bladder (B), vaginal cavity (V) and uterus (U)

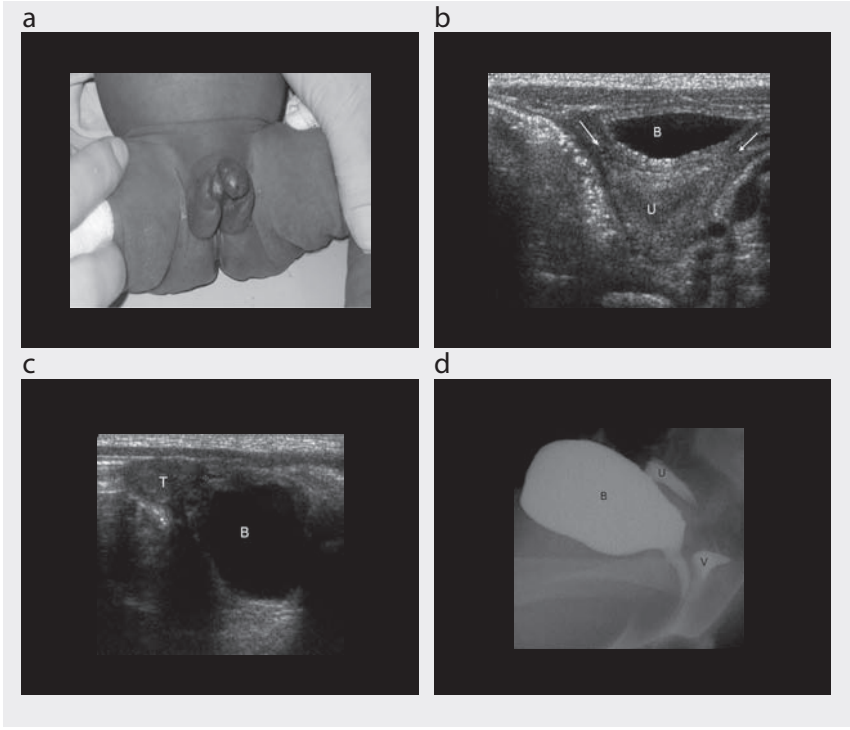

an ovary on one side and a contralateral testis or an ovo-testis. The sonographic appearance of the ovo-testis is that of a heterogeneous ovoid mass containing small cysts.

Children with mixed gonadal dysgenesis have a testis on one side and a streak gonad containing ovarian stroma without ovocytes on the other side. A uterus, which may be bicornuate, is sometimes present (Fig. 5.155).

Other pelvic masses

Ectopic pregnancy is rare in adolescents, but girls in this age group have the highest reported rate of complications. Ultrasound with quantitative assessment of β-human chorionic gonadotropin is the essential diagnostic test.

A palpable mass in the labial or inguinal region of infants with ambiguous genitalia may be due to **ovarian herniation**. Ultrasound shows an ovoid mass, often containing cystic follicles (Fig. 5.156).

Ovary involvement is a late manifestation of **lymphoma**; it is more common in non-Hodgkin lymphoma than in Hodgkin disease. On ultrasound, ovarian infiltration is typically echo-poor and associated with diffuse bilateral enlargement of the ovaries (Fig. 5.157).

Primary pelvic hydatid cyst can be seen in endemic areas but is rare. The ultrasound findings are variable and depend on the age of the cyst (Fig. 5.158).

Fig. 5.156. Ovarian herniation in a 3-month-old girl. Longitudinal scan of the left inguinal region shows a small, irreducible inguinal hernia containing the left ovary and bowel loop

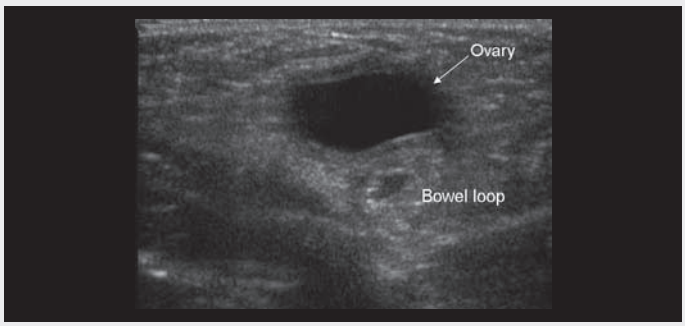

Fig. 5.157. Ovarian infiltration in a 6-year-old girl with Burkitt lymphoma. Longitudinal scan shows an enlarged, echo-poor ovary (O)

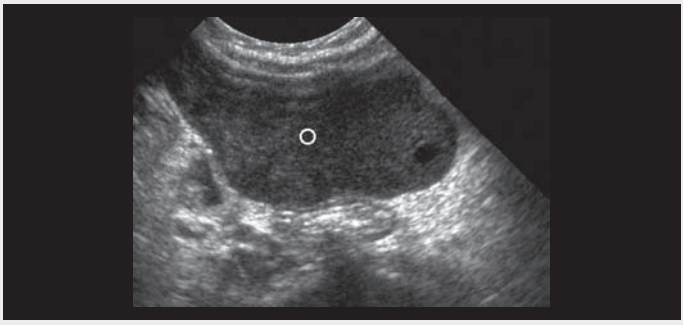

Fig. 5.158. Primary pelvic hydatid cyst in a 9-year-old girl with an abdominal mass. (a) Longitudinal scan shows a large cystic mass (C) extending from the pelvis to the abdomen. (b) Sagittal T2 and (c) sagittal T1-weighted images reveal a pelvic cystic mass (C) located between the uterus and the rectum (R). V, vaginal cavity

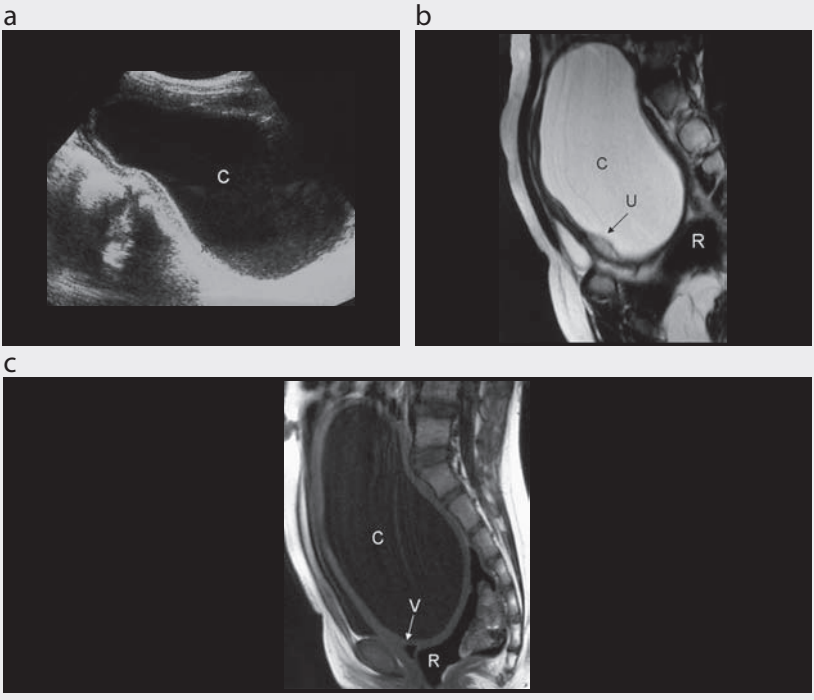

Scrotum

Indications

Ultrasound is useful in most cases of scrotal disease in children. The main indications are in screening for congenital anomalies, cases of acute scrotum, scrotal tumours, trauma and varicocoele and systemic diseases involving the scrotum.

Preparation

No specific preparation is needed in urgent and acute situations.

Examination technique

The child is examined in the supine position, with the scrotum supported by a towel placed on the anterior face of the thighs. High-frequency 7- to 10-MHz transducers are used. A large amount of warm gel is applied to minimize pressure on the scrotal skin, and longitudinal and transverse scans are performed. Examination of the spermatic cord is important, particularly in cases of acute scrotum, varicocoele and suspected testicular torsion. Doppler is performed with optimized parameters; colour, power and pulsed Doppler are used to investigate extratesticular vascularization and testicular perfusion. The assessment of flow with positional and respiratory movements is limited in small children.

Normal findings

The scrotum is divided by the medial raphe or septum, and each half contains a testis, the epididymis and the scrotal portion of the spermatic cord. The normal testis is ovoid, has uniform low-to-medium echogenicity and is surrounded by an echogenic line, which corresponds to the tunica albuginea (Fig. 5.159). Testicular echogenicity increases with age, from echo-poor in neonates, becoming more echogenic between the ages of 8 years and puberty. In adolescents, the testicular mediastinum is seen as a thin echoic line crossing the testis along the superior–inferior axis (Fig. 5.160). The epididymis is visualized on longitudinal views, in three parts: a triangular head with the same echogenicity as the testis (Fig. 5.161), a narrow body located behind the testis and the tail at the inferior pole. Colour Doppler shows the capsular arteries and the intratesticular vessels (Fig. 5.162). Centripetal arteries are identifiable in 65–85% of prepubertal testes and in all postpubertal testes.

The five testicular appendages are the remnants of the mesonephric and paramesonephric ducts. Three can be seen on ultrasound, particularly in cases of hydrocoele. The appendix testis, also known as the hydatid of Morgagni, is usually seen as an oval structure between the testis and epididymis and is isoechoic to the testis. The appendages of the epididymis and the epididymal tail are rarely seen.

Fig. 5.159. Normal testis in a 2-year-old boy. Longitudinal scan shows the testis (T), which is ovoid, moderately echogenic and homogeneous. The tunica albuginea (arrows) is seen as a peripheral echogenic line

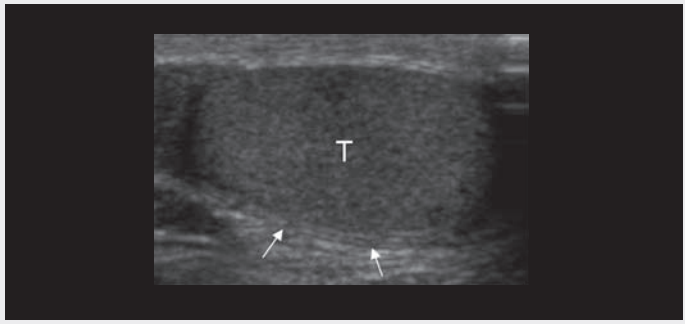

Fig. 5.160. Normal testicular mediastinum in a 2-year-old boy. Longitudinal scan shows the mediastinum (arrows) as an echogenic band running across the testis (T)

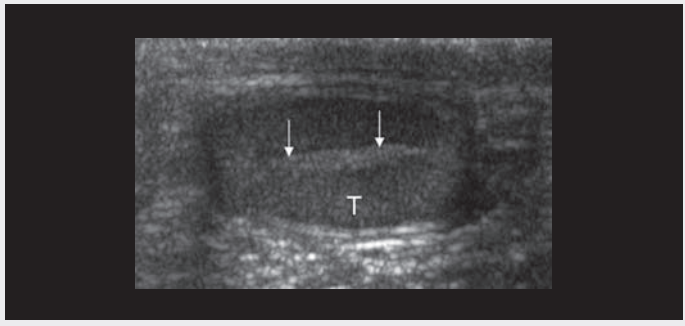

Fig. 5.161. Normal epididymal head in a 2-year-old boy. Longitudinal scan shows the head of the epididymis (E) lying above the testis (T), with similar echogenicity

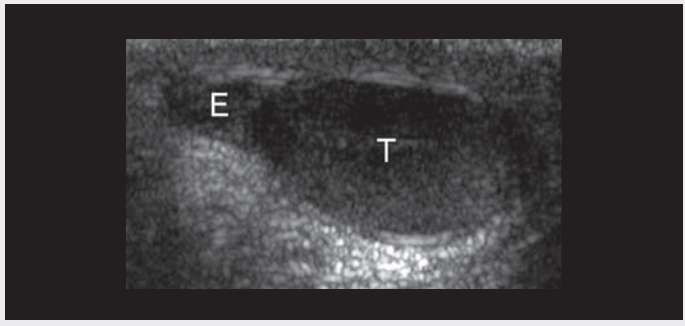

Fig. 5.162. Normal intratesticular vascular anatomy in a 1-year-old boy: colour Doppler shows capsular artery (arrows) and multiple centripetal rami

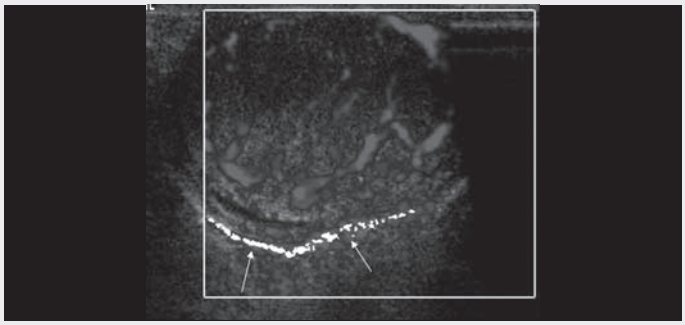

The spermatic cord appears as a smooth linear structure limited by an echo-rich band on longitudinal scans and as an ovoid structure on transversal scans. It contains the testicular, deferential and cremasteric arteries and the pampiniform veins (Fig. 5.163). Vascular visualization and the spectral waveform depend on the sensitivity of the probe, optimization of parameters, the experience of the operator and the age of the boy.

The height, length and width of the left and right testes are measured on longitudinal and transversal scans. The testicular volume is derived from the formula $V = L \times W \times H \times 0.52$, where V = volume, L = length, W = width and H = height. It is 1–2 cm^3 before the age of 12 years and reaches 4 cm^3 in pubertal boys. The scrotal wall is 3–6 mm thick.

The normal inguinal canal is obliterated at birth and can be seen on ultrasound only in cases of abnormal peritoneovaginal communication.

Fig. 5.163. Spermatic cord in a 1-year-old boy. Longitudinal scan shows the spermatic cord (arrowheads) containing the testicular, deferential and cremasteric arteries and the pampiniform veins

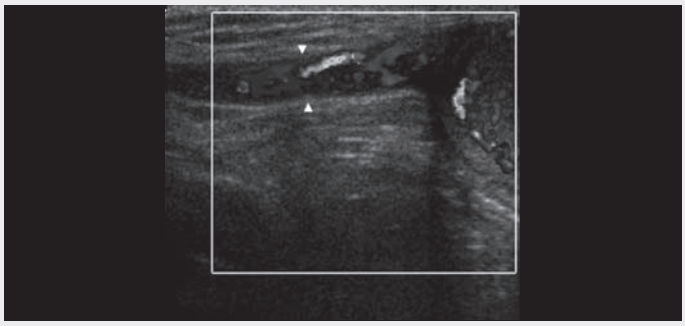

Pathological findings

Anomalies of descent of the testes

The cryptorchid testis can be located at any point along the descent route, but 80–90% of undescended testes are in the inguinal canal. Cryptorchidism is more frequent in premature infants (30% of premature newborns and 5% at full term). Descent of the testis may be completed during the 1st year in 10% of boys. Ultrasound is the initial procedure used to demonstrate a testis in the inguinal canal. The cryptorchid testis is usually small and echo-poor to the normally located testis (Fig. 5.164). When the testis is located in the abdominal cavity, it cannot be seen, and laparoscopy may be required because of possible degeneration. Cryptorchidism is bilateral in 10–30% of boys, and associated urological abnormalities are found in 20%. The main complications of undescended testis are malignant degeneration and infertility. After surgical repair, the undescended testis usually remains smaller and echo-poor compared with the normal testis.

Fig. 5.164. Cryptorchidism of the left testis in a 3-year-old boy. Longitudinal scan shows an incompletely descended testis (T) in the left inguinal canal. The testis is small and less echogenic than the normally located testis

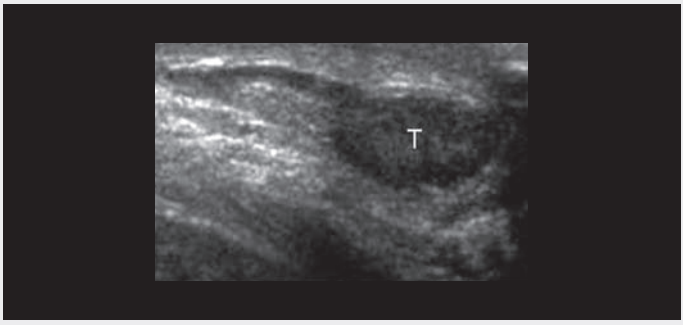

Inguinal scrotal hernia

Intestinal loops and omentum may be found in the scrotal cavity in cases of delayed obliteration of the inguinal canal. In cases of acute scrotum, however, the clinical findings may be inconclusive. Ultrasound examination is effective when it shows gas bubbles in the scrotum. Colour Doppler is useful for assessing the viability of the intestinal loops. The contralateral side is examined to eliminate bilateral inguinal hernia. Peritoneography is rarely indicated.

Hydrocoele

Hydrocoele is the commonest cause of indolent scrotal swelling in children. It consists of an abnormal fluid collection of > 2 ml between the visceral and parietal layers of the tunica vaginalis and or along the spermatic cord. Hydrocoele is a congenital anomaly in neonates and infants, but an inflammatory fluid collection may be acquired in adolescence and in cases of torsion trauma or tumour. An abdomino-scrotal hydrocoele may present as a mass. On ultrasound, congenital hydrocoele appears as an echo-free fluid collection surrounding the anterolateral aspects of the testis and sometimes extending to the inguinal canal (Fig. 5.165). Spermatic cord cysts are a rare form of collection (Fig. 5.166). Most congenital hydrocoeles (80%) resolve spontaneously before the age of 2 years; however, surgery is needed for spermatic cord cysts and abdomino-scrotal hydrocoele.

Fig. 5.165. Bilateral hydrocoele in a 2-month-old boy. (a) Longitudinal and (b) axial scans show a fluid collection (F) surrounding the testis (T) and the epididymis (E)

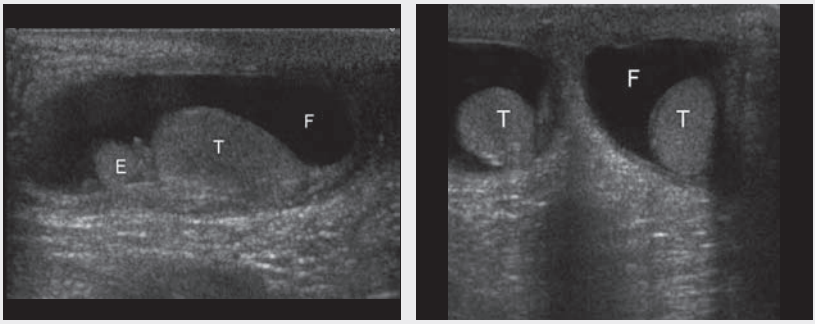

Fig. 5.166. Spermatic cord cyst in a 1-year-old boy. Longitudinal scan shows a cystic lesion (C) in the left spermatic cord with increased sound transmission

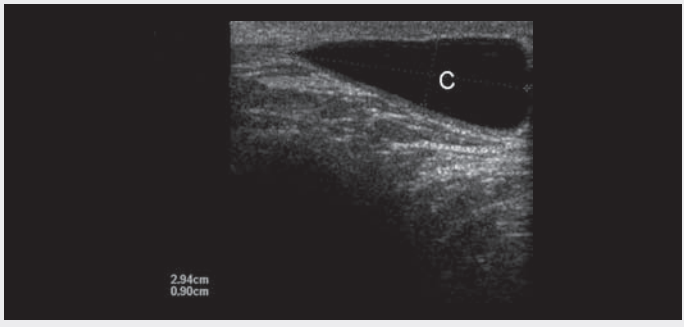

Varicocoele

Varicocoele is frequent in adolescence, seen as dilatation of the veins of the pampiniform plexus of the spermatic cord. On ultrasound, the dilated veins are tortuous, echo-free, tubular structures along the spermatic cord (Fig. 5.167). The reflux is demonstrated clearly by colour Doppler during Valsalva manoeuvre (Fig. 5.168). Treatment should be considered when the growth of the testis is affected. A unilateral left varicocoele should be followed up by abdominal ultrasound examination to search for associated anomalies, such as a renal tumour or left renal vein thrombosis.

Fig. 5.167. Left varicocoele in a 13-year-old boy. Longitudinal scan shows multiple tortuous echo-free structures (arrows) in the supratesticular region (T, testis). Valsalva manoeuvre demonstrates the markedly increased diameter of the peritesticular structures

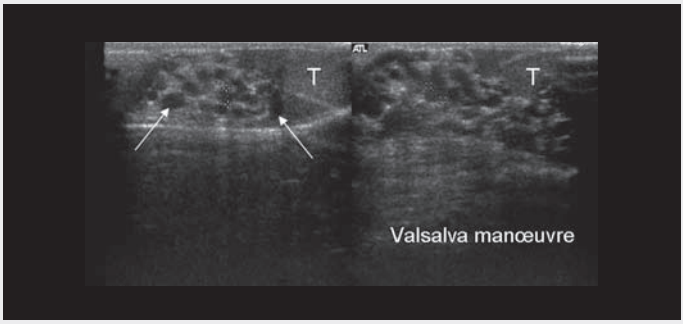

Fig. 5.168. Varicocoele in an 11-year-old boy. Colour Doppler scan during a Valsalva manoeuvre shows increased flow in multiple tubular peritesticular vascular structures. T, testis

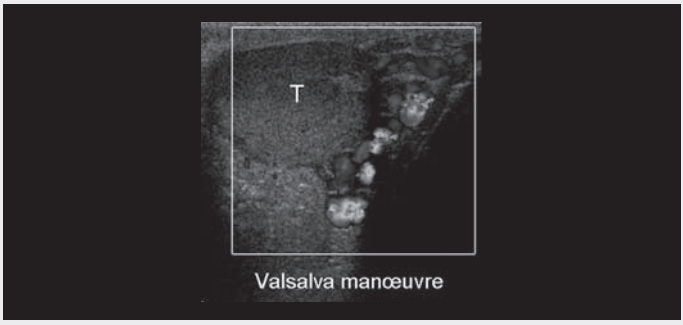

Acute scrotum

Acute scrotum is defined clinically as a suddenly painful scrotum, with redness, swelling and tenderness. Ultrasound with colour Doppler examination can show the typical signs of hydatid torsion, testicular torsion or orchiepidymitis in cases of evidence of infection. An infectious etiology is, however, rare in children. Surgery is often needed for treatment or investigation if the ultrasound examination is inconclusive.

Testicular torsion

Testicular torsion is a common condition, which can lead to ischaemic necrosis of the testis if not urgently reduced. It can occur at any age but is most frequent in neonates and adolescents. The torsion consists of twisting of the spermatic cord, with constriction of venous and arterial flow. On the basis of surgical findings, testicular torsion can be either extravaginal or intravaginal. Extravaginal torsion is seen mainly in neonates and occurs prenatally in most cases (Fig. 5.169). Intravaginal torsion can occur at any age but is commonest in adolescents. Ultrasound examination at an early stage (< 48 h) may show twisting of the vessels on the spermatic cord. The vitality of the testis depends on the degree and duration of ischaemia. When ultrasound is performed at a late stage, testicular infarct is suggested when there is enlargement, a heterogeneous echo pattern and a silent organ. Scrotal skin thickening and hydrocoeles are common associated findings. In chronic torsion, ultrasound shows a small, echo-poor testis with peripheral echogenicity corresponding to calcification in the tunica albuginea (Fig. 5.170).

Fig. 5.169. Extravaginal torsion in a newborn boy. (a) Longitudinal and (b) transverse scans show an enlarged, heterogeneous right testis (T) with echo-poor and echo-rich areas, surrounded by the highly echogenic tunica and a complex hydrocoele (H)

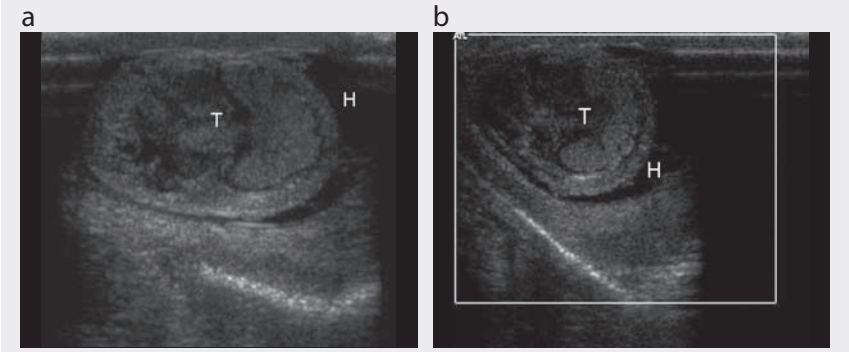

Fig. 5.170. Chronic testicular torsion in a 5-month-old boy. Longitudinal scan of the right testis (T) shows a small, echo-poor testis with an echogenic rim (arrows), indicating tunica calcification

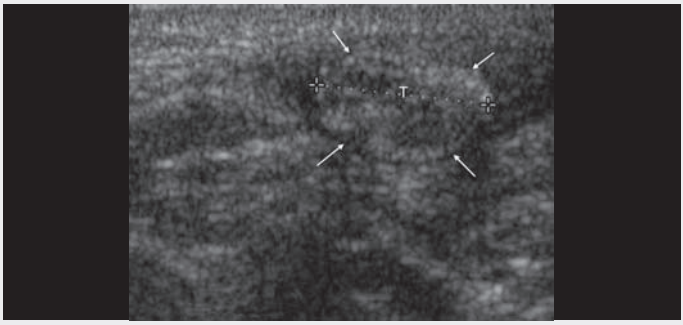

Torsion of the hydatid

Torsion of the hydatid is frequent in adolescents. The twisted appendix can be seen on ultrasound in the upper pole of the testis, associated with inflammatory signs and hyperaemia.

Orchiepididymitis

Orchiepididymitis is the result of retrograde spread of infection. It is a rare cause of acute scrotum in neonates and young children. Urinary-tract infection is frequently associated, affecting the epididymal head in particular. The ultrasound findings include a focally or diffusely enlarged, heterogeneous epididymis with increased blood flow in one or both testes. Adjacent scrotal skin thickening and reactive hydrocoele are also common findings. A differential diagnosis may be made from suspected malignancy, such as lymphoma or leukaemia. Biological and clinical findings are decisive in such cases.

Scrotal masses

Extratesticular masses

Paratesticular rhabdomyosarcoma is the most frequent malignant tumour of the epididymis. Metastases of leukaemia and non-Hodgkin lymphoma may be seen. The other masses of epididymis are epididymal cysts, which are seen as echo-free masses on ultrasound.

Testicular tumours

Testicular tumours are more frequent after puberty. They can be germ-cell or non-germ-cell tumours (Table 5.1; Fig. 5.171). They may appear as acute scrotum in cases of haemorrhage or infarction. Primary lymphoma is rare, but secondary lymphoma

Table 5.1. Classification of childhood testicular tumours

Site	Age	Comments
Germ cell		
Yolk sac tumour	0–5 years	Commonest; fill the entire hemiscrotum
Teratoma	3 months–10 years	Benign before puberty
Teratocarcinoma	Puberty–adult	Similar to the adult form
Seminoma	Puberty–adult	Same as adult form
Gonadoblastoma	5–10 years	Nearly always occur in streak gonads
Non-germ cell		
Sertoli cell	0–1 year	Cause gynaecomastia
Leydig cell	3–6 years	Cause precocious virilization
Adrenal rests	5 years–adult	Occur in children with adrenal hypoplasia
Secondary deposits	Any age	Usually occur in established disease
Lymphoma	Any age	Same as adult pattern

Fig. 5.171. Benign testicular teratoma in a 3-month-old boy. (a), (b) Longitudinal scans of the left scrotum show a large, complex, heterogeneous mass (M) with irregular margins, containing cystic portions (C) and areas of variable echogenicity; colour signal within the mass (arrow)

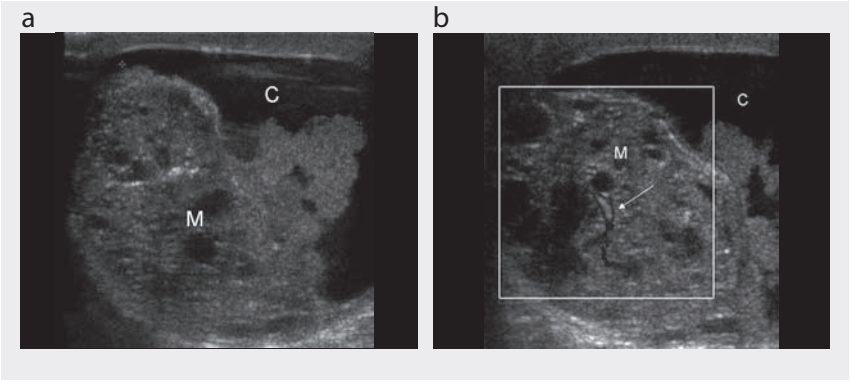

involvement is common. On ultrasound, an enlarged, echo-poor, homogeneous or nodular testis is seen, often with hyperaemia simulating infection. Metastases of retinoblastoma, neuroblastoma or nephroblastoma are rarely located in the testis.

Trauma

Trauma is common in children, often occurring in association with torsion. Ultrasound is useful for demonstrating:

- testicular haematoma, with changing echogenicity over time
- testicular fracture (Fig. 5.172) or rupture
- haematocoele within the layers of the tunica vaginalis.

For follow-up, demonstration of normal blood flow is useful in cases of conservative treatment.

Fig. 5.172. Testicular fracture in a 5-year-old boy after scrotal trauma. Longitudinal scan shows an echo-poor band crossing the right testicular parenchyma (arrows). T, testis

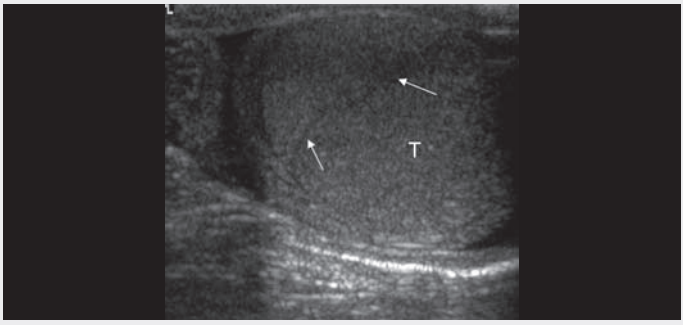

Involvement of the testis in various diseases

The testes may be involved in Henoch-Schönlein purpura, allergic diseases and congenital adrenal hyperplasia. In these diseases, ultrasound findings include scrotal wall thickening, epididymal enlargement, and reactive hydrocoele. Differentiation between them is based on clinical and biological findings.

Fig. 5.173. Testicular microlithiasis in a 6-year-old boy. Longitudinal scan showing multiple, tiny, echo-rich foci in the testis (T)

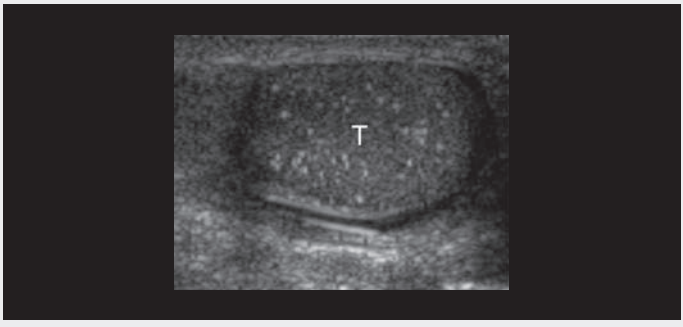

Testicular microlithiasis (Fig. 5.173) is a condition in which calcifications form in the lumen of the seminiferous tubules. It can occur in otherwise normal individuals, but it also has been reported in patients with Down syndrome, Klinefelter syndrome

and cryptorchidism. On sonography, the calcifications are seen as fine, bright, non-shadowing echo-rich foci, which tend to be uniform in size and are distributed in a diffuse pattern or in peripheral clusters. Testicular microlithiasis is considered to be a premalignant condition; thus, it is recommended that patients with microlithiasis have sonographic examinations at least at yearly intervals.

Neck

Indications

Ultrasound is useful for inspecting all the neck organs in children to confirm abnormalities diagnosed antenatally, explore various disorders, perform guided biopsies and treat children. The main indications are:

- congenital anomalies
- palpable cervical masses
- screening and staging cervical lymph nodes
- suspected thyroid disorders
- parathyroid hyperplasia
- salivary gland diseases
- trauma
- suspected tumours (e.g. malignant lymphomas).

Preparation

No specific preparation is needed.

Examination technique

The child lies on his or her back in the supine position with the neck extended over a 5- to 10-cm-thick pillow under the shoulders, depending of the child's age and cooperation. Examination is performed mainly by transverse scans and always with a comparison of the left and right sides. It may be necessary to rotate infants' heads from right to left.

Linear probes should be of as high a frequency as possible (5–12 MHz). Doppler is helpful for demonstrating vascular anomalies and for differentiating thyroid disorders.

Normal findings

The examination should start with identification of all the normal structures in the neck (see Fig. 5.63): the carotid arteries and jugular veins, the thyroid and salivary glands, the cervical muscles, the cervical oesophagus posterior to the trachea and the left lobe of the thyroid, the trachea and lymph nodes (Fig. 5.174).

Fig. 5.174. Normal structure of the neck. Transverse scan through the midportion of the thyroid gland (Th) shows the right and left lobes of the gland in front of the trachea (T). The isthmus is seen anterior to the trachea (arrows). CE, cervical oesophagus (see Fig. 5.63]); CC, common carotid; SCM, sternocleidomastoid muscle

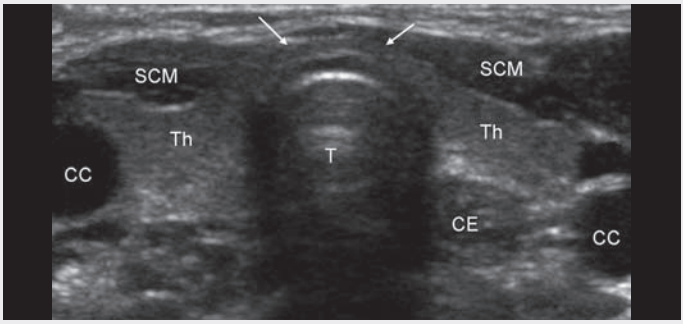

The carotid artery shows typical pulsation, with a round cross-section. The vein has an oval cross-section, with a diameter that depends on the intrathoracic pressure (breathing). The jugular veins increase in size, sometimes hugely, when the infant cries. These vessels are useful for topographical orientation.

The commonest anatomical variation is asymmetrical internal jugular veins, with the right vein larger than the left, presumably due to predominance of right cerebral venous drainage (Fig. 5.175).

Fig. 5.175. Vascular variant in a 3-year-old boy: asymmetry of internal jugular veins. (a) Axial scans through the right internal jugular vein (RIJV) and the left internal jugular vein (LIJV) show that the RIJV is larger than the LIJV. (b) Longitudinal scan confirms the ectasia of the RIJV. Th, thyroid; CC, common carotid

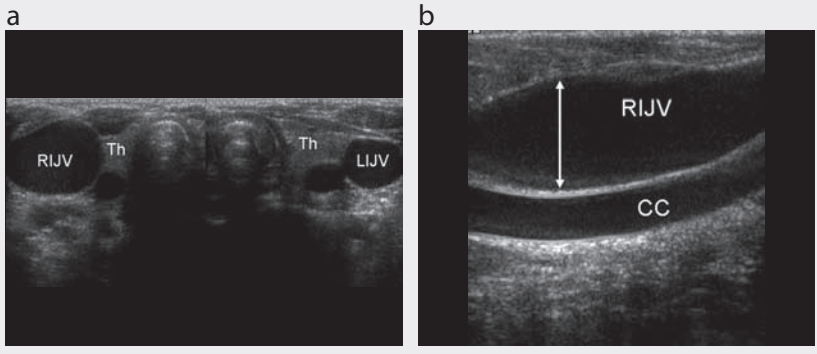

The muscles are echo-poor and are useful for orientation. The normal thyroid gland is echo-rich to the surrounding muscles (Fig. 5.176). In infants and young children, the lateral lobe measures 1–1.5 cm in diameter, 2–3 cm vertically and 0.2–1.2 cm anteroposteriorly. In adolescents, the lateral lobe is 2–4 cm in diameter, 5–8 cm vertically and 1–2.5 cm anteroposteriorly. The right lobe is usually larger than the left. There are usually four parathyroid glands, the paired superior glands having a fairly consistent position near the upper surface of the thyroid lobes. The inferior parathyroid glands are found in close proximity to the lower pole of the thyroid gland and are isoechoic to the thyroid gland. Normal parathyroid glands are difficult to visualize because of their small size. The trachea behind the thyroid gland is marked by strong echoes arising from the air inside; the oesophagus can be seen as a tubular structure behind the left lobe of the thyroid, most clearly in a longitudinal scan. Movement can be seen when the child swallows.

Fig. 5.176. Normal echo texture of the thyroid gland in a 5-year-old girl. Longitudinal scan of the cervical region shows the thyroid gland (Th), which is moderately echo-rich to the surrounding muscle (M)

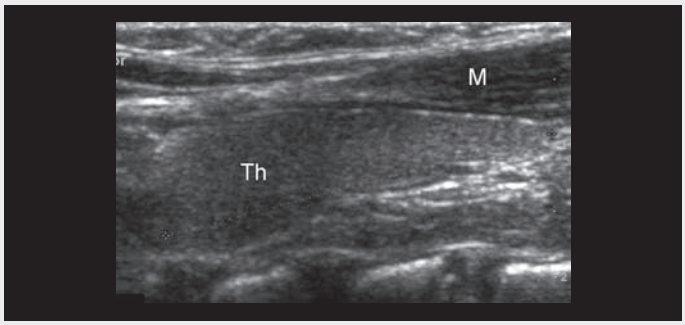

Occasionally, small lymph nodes are seen in children and adolescents. These nodes are considered normal if they are ≤ 10 mm in the longest axis and are oval (ratio of long axis to short axis, > 1.5). Normal lymph nodes are echo-poor with an echogenic linear hilum (the so-called hilus sign), corresponding partially to vascular structures, as demonstrated with a sensitive colour Doppler probe. The vessels normally branch out from the hilus (Fig. 5.177; see also Fig. 4.8 and Fig. 4.9). They can be seen in the submandibular, jugular, submental and posterior cervical chains but not in the supraclavicular region.

Fig. 5.177. Normal appearance of a lymph node in a 7-year-old boy. (a) Longitudinal scan shows a normal lymph node (LN) with an echo-rich hilus (arrowheads). (b) Colour Doppler scan shows normal vessel architecture, with the vessels branching from the hilus in a slightly enlarged lymph node (tonsillitis)

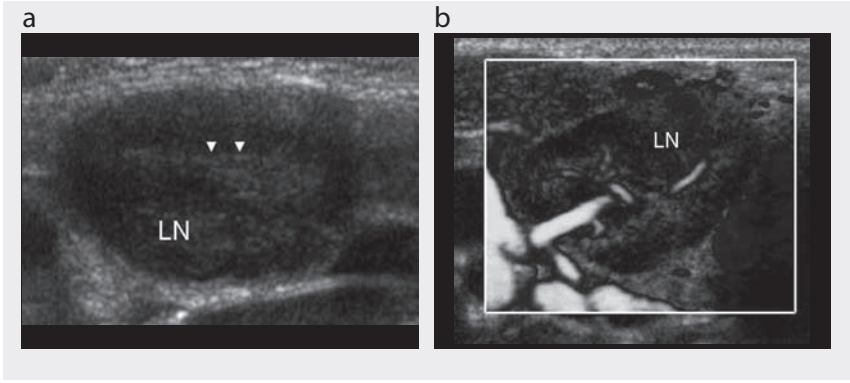

The parotid glands can be demonstrated with a high-frequency transducer placed anterior to the ear lobe and parallel to the base of the mandible. They have the same echo-rich pattern as the normal thyroid and are useful for comparison. The submandibular salivary glands are easily seen below the mandible.

Pathological findings

Congenital cystic malformations

These malformations are the result of abnormal embryogenesis. They are frequent in children and include thyroglossal duct cysts (dermoid cysts and teratomas), branchial cleft cysts, cystic hygromas or lymphangiomas and cervical thymic cysts.

Thyroglossal duct cysts, **dermoid cysts** and **teratomas** can be situated midline or off-midline in the anterior part of the neck. About 65% of thyroglossal duct cysts are located below the level of the hyoid bone. On ultrasound, uncomplicated cysts have well-defined walls and water-clear contents. Sometimes, fine echoes are seen within cystic lesions, caused by haemorrhage, infection or proteinaceous fluid and post-aspiration (Fig. 5.178). The presence of fluid and fat or calcifications within a cystic mass should suggest dermoid cysts or teratomas (see below).

Branchial cleft cysts and **cystic hygromas** may be seen in the lateral neck, whereas cervical thymic cysts can occur anywhere.

Fig. 5.178. Thyroglossal duct cyst in a 5-year-old girl with a midline cervical mass that moved on swallowing. Transverse scan of the infrahyoid neck shows a midline cyst (C), which is not echo-free, just anterior to the thyroid cartilage (arrows) of the larynx

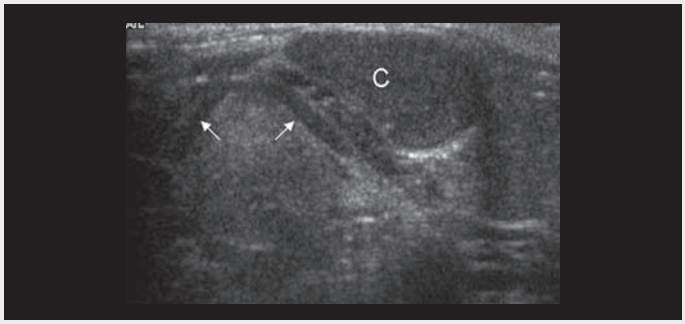

Cervical lymphadenitis

Cervical lymphadenitis is common in children. It is usually caused by viral or bacterial infections. The submandibular and jugular nodes are involved in more than 80% of cases. On ultrasound, they typically appear as discretely enlarged, oval, echo-poor nodes, which may conglomerate (Fig. 5.179). Doppler shows hypervascularity but normal branching from the hilus. The major complication of cervical adenitis is abscess formation.

Tuberculous lymph nodes are common in some areas. Demonstration of enlarged, echo-poor, sometimes rounded lymph nodes with central necrosis (small echo-free areas) and flocculent calcifications (strong echoes) should suggest a diagnosis of tuberculosis (Fig. 5.180).

Fig. 5.179. Cervical adenitis in a 3-year-old boy with fever and a painful cervical mass. (a) Axial scan shows multiple lymph nodes (LN) with heterogeneous echo texture. (b) Colour Doppler scan shows a hypervascular hilum

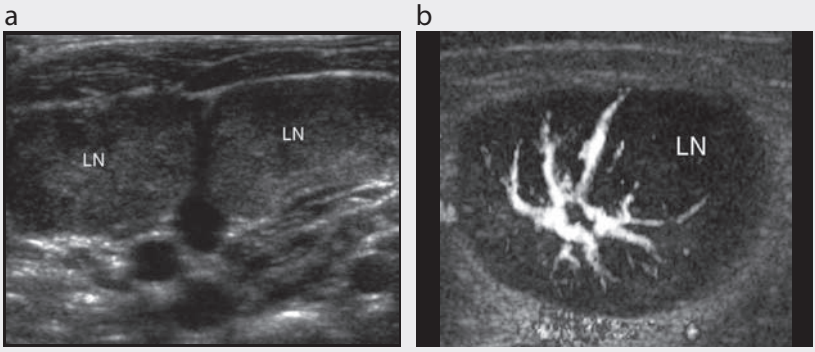

Fig. 5.180. Tuberculous cervical lymph nodes in a 12-year-old girl. (a) Longitudinal and (b) axial scans show an echo-poor lymph node (LN) adjacent to the common carotid (CC) and the internal jugular vein (IJV), with central necrosis (arrows)

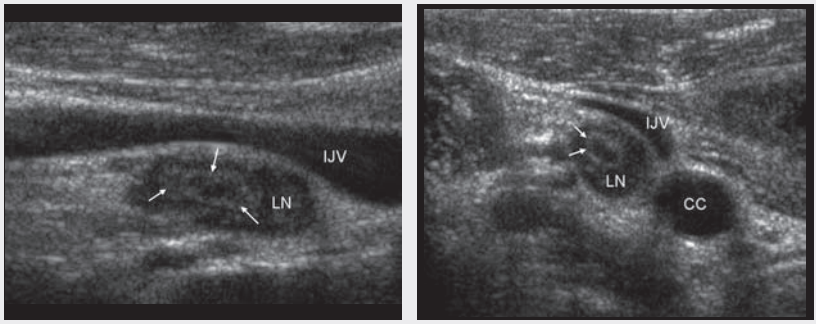

Thyroid diseases

Thyroid problems are not common in children.

Hypothyroidism

Ultrasound is used to establish the absence of the thyroid gland (athyroidism) antenatally or postnatally (Fig. 5.181).

Fig. 5.181. Thyroid agenesis in a newborn girl with hypothyroidism. Transverse scan shows absence of the thyroid gland, with sternocleidomastoid muscles (M) along the anterior border of the trachea (T) and no structure between them. CC, common carotid

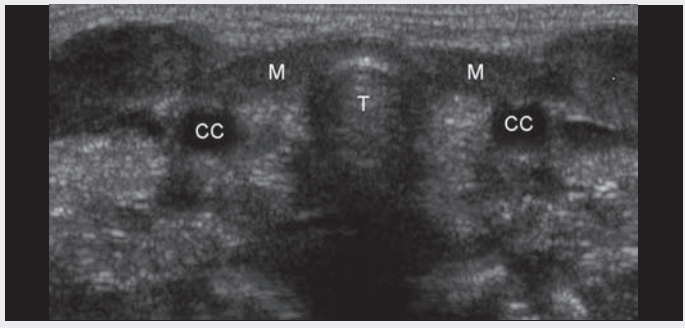

Thyroiditis

Acute purulent thyroiditis is caused mainly by *Streptococcus* or *Staphylococcus* species. Ultrasound shows a slightly enlarged thyroid with a heterogeneous, echo-poor pattern and small echo-free foci (liquefactions). In symptomatic children, the inflammation is often found in the soft tissue around the thyroid, and the thyroid itself is dislocated.

Quervain subacute thyroiditis is rare in children. Ultrasound shows an echo-poor area with blurred limits within the thyroid. Fine-needle puncture may show the pathognomonic giant cells.

Chronic lymphatic thyroiditis (Hashimoto disease) is an autoimmune disorder characterized by infiltration of thyroid tissue by small lymphocytes. It is usually seen in girls reaching puberty (Fig. 5.182). In the early stage, the disorder may cause hyperthyroidism, similar to Graves disease (see below); if there is no spontaneous remission, the disease leads to hypothyroidism. Ultrasound shows a diffusely enlarged heterogeneous gland, hypoechoic relative to the normal thyroid; the presence of hypoechoic micronodules with an echogenic halo is considered to have a relatively high positive value. Initially, the gland may appear slightly enlarged, but it becomes smaller with a pseudolobular appearance as the autoimmune process advances. Doppler shows hypervascularity, especially in the early stage.

Fig. 5.182. Thyroiditis in a 14-year-old girl. Longitudinal scan of the right thyroid lobe (R Th) shows an enlarged, heterogeneous gland with multiple, small, echo-poor foci

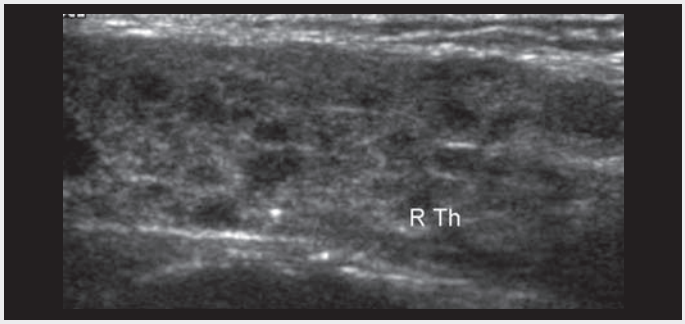

Basedow disease (Graves disease) This autoimmune disease of the thyroid is the commonest cause of hyperthyroidism in childhood, predominantly in girls reaching puberty. Ultrasound shows a symmetrically enlarged gland with a more or less echo-poor, sometimes inhomogeneous pattern. Colour Doppler shows striking hypervascularity, with a peak velocity in the feeding arteries of up to 100 cm/s. Decreased velocity during treatment is a useful indicator for follow-up.

Goitre

'Goitre' is the term used for (nonspecific) enlargement of the thyroid. Thyroid enlargement (diffuse goitre) is found mainly in adolescent girls living in areas with insufficient iodine in the drinking-water. Ultrasound shows an enlarged thyroid with a homogeneous, echo-rich (normal) pattern. An inhomogeneous pattern with echo-rich nodules and degenerative alterations is seen after years without treatment and therefore mainly in adults.

An enlarged thyroid gland in a neonate can cause constriction of the trachea. It can be due to a thyroid disorder in the mother, such as Basedow disease, or hormonal treatment of the thyroid. Ultrasound shows an enlarged gland with a normal echo pattern.

Focal diseases

Follicular adenomas are benign nodules that arise from the thyroid cells and are encapsulated. They grow slowly and are usually endocrine-inactive. Some adenomas, however, are active and cause hyperthyroidism (toxic or hot adenomas). The ultrasound findings are variable, adenomas being round or oval, with a sharp boundary. The echo pattern ranges from echo-poor to echo-rich, like the normal thyroid. Echo-free parts indicate cystic degeneration (Fig. 5.183). A so-called halo, an echo-poor peripheral ring, is often seen, which is caused by a ring of vessels, as demonstrated by colour Doppler. This finding is considered a sign of benignancy. Most endocrine-active adenomas are hypervascular to the surrounding tissue; however, hypervascularity may also be seen in malignant lesions (see below).

Fig. 5.183. Thyroid adenoma in a 15-year-old girl. Longitudinal scan of the right thyroid lobe (R Th) shows a slightly echo-poor solid nodule (N) with a halo

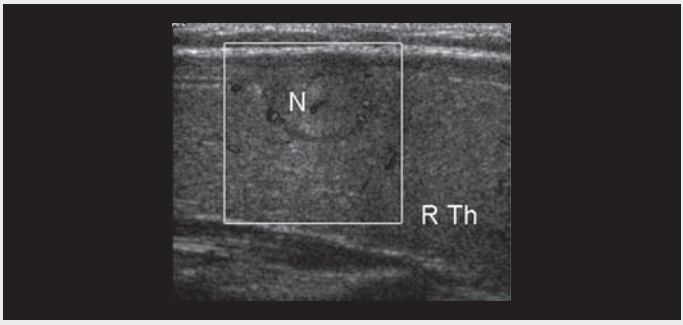

True **cysts** are rare, and most cystic lesions are degenerated solid lesions. Ultrasound shows one or more well-defined, fluid-filled, echo-free lesions within solid nodules. The presence of a cyst in a nodule does not safely exclude malignancy. Echoes within a cystic lesion indicate bleeding, which may be corroborated by pain. Aspiration in these cases reveals a brownish fluid.

Thyroid cancer

Malignant tumours are not uncommon in children, who have 10% of all thyroid cancers. An association has been found with accidental or therapeutic irradiation. Papillary carcinomas, medullary carcinomas and lymphomas are the most frequent types in childhood. Ultrasound shows an echo-poor nodule and, in advanced cases, asymmetric enlargement of the gland. The outline may be irregular, and infiltration of the surrounding tissue or perforation through the capsule of the thyroid may be seen. Microcalcifications are seen as dispersed, intense echoes in the lesion, mainly in papillary carcinomas. Involved cervical lymph nodes show an echo pattern similar to that of the original tumour.

As adenomas and small carcinomas cannot be differentiated on the basis of their ultrasound appearance, any nodule > 10 mm and any nodule that grows rapidly within weeks or months should be biopsied to establish a definite diagnosis.

Parathyroid glands

Normal glands cannot be demonstrated by ultrasound. Hyperplastic glands and adenomas are seen as roundish, oval or triangular nodules, usually situated at the dorsolateral surface of the thyroid and median to the large vessels. They can be echo-poor or heterogeneous. Ectopic tumours are difficult to find with ultrasound.

Salivary gland diseases

The commonest disease of the salivary gland is parotiditis. Ultrasound shows an enlarged gland with a heterogeneous, dispersed pattern. Dilated ducts and stones (intensive echoes) are rarely found in children. Small reactive lymph nodes may be seen around or in the gland. Tumours (e.g. haemangiomas, see below) cause enlargement, with a nonspecific echo pattern.

Trauma

Fibromatosis colli is a benign lesion of the sternocleidomastoid muscle, also called haematoma of the sternocleidomastoid muscle. It is usually seen 1 or several weeks after birth and is related to trauma during delivery. Patients usually present with an anterior neck mass, most commonly on the right side. The lesion frequently regresses within 4–8 months with conservative therapy. Ultrasound shows unilateral, heterogeneous, fusiform enlargement of the sternocleidomastoid muscle (Fig. 5.184).

Fig. 5.184. Fibromatosis colli in a 2-month-old girl with a firm neck mass and torticollis. Longitudinal scan shows fusiform enlargement (arrows) of the sternocleidomastoid muscle (SCM)

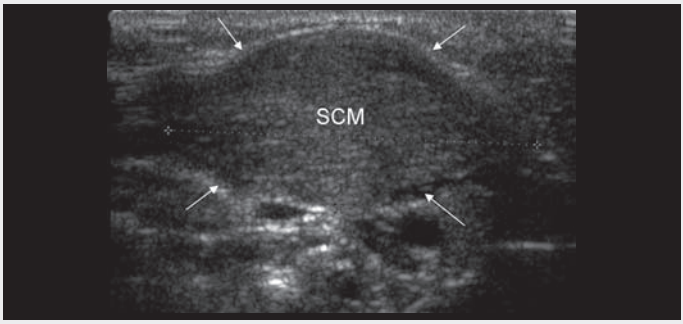

Tumours of the neck

Benign tumours

Haemangioendotheliomas and **haemangiomas** are congenital vascular abnormalities. Most haemangiomas arise in the parotid gland and typically present as soft cutaneous or subcutaneous masses with bluish discolouration. Haemangiomas often undergo a period of initial growth before spontaneous involution. Ultrasound shows a variable echo pattern, which depends on the diameter of the vessels. Within larger cystic structures, sedimented echoes may be seen. Colour Doppler shows hypervascularity. Capillary haemangiomas appear as more echo-rich, heterogeneous masses (Fig. 5.185).

Fig. 5.185. Parotid haemangioma in a 5-month-old girl. (a) Axial scan of the left parotid shows a subtly altered echo texture near a heterogeneous, echo-poor mass (the strong echoes with the acoustic shadow correspond to the mandible, Ma). (b) Pulsed Doppler shows hypervascularity and arterial flow

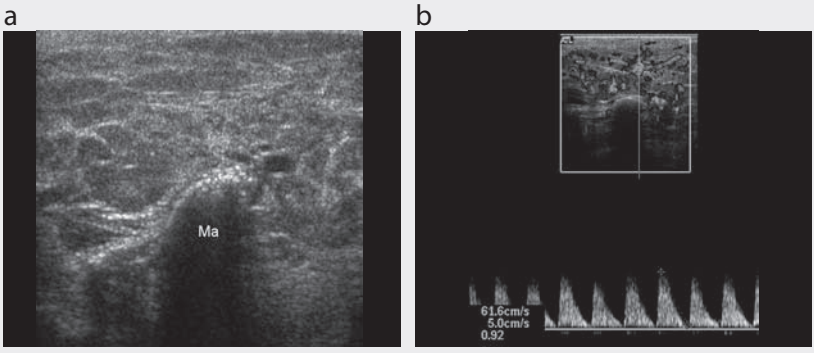

Cystic lymphangiomas (cystic hygromas) appear as cystic, septated masses; haemorrhage may complicate the ultrasound findings (Fig. 5.186).

Typical neck tumours in newborns are **teratomas**, which are situated within or close to a thyroid lobe. They may cause asymmetrical enlargement of the thyroid. The echo pattern is inhomogeneous, with echo-free areas, sometimes similar to those of a lymphangioma.

Fig. 5.186. Cervical cystic lymphangioma in a 7-month-old girl. (a) Clinical photograph shows a soft-tissue mass in the left neck. (b) Axial scan shows a multicystic, fluid-filled mass; the content of the cyst is echogenic, representing blood

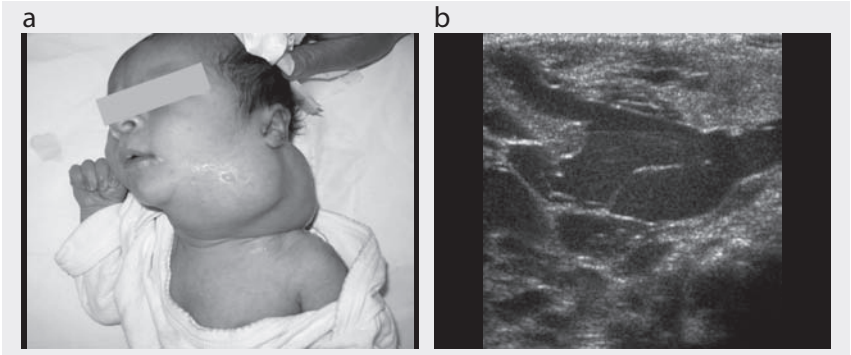

Malignant tumours

Hodgkin disease and **non-Hodgkin lymphoma** are the most frequent malignant cervical tumours in children; rhabdomyosarcoma and neuroblastoma of the neck are also seen. The lymph nodes involved in malignant lymphomas are enlarged, often conglomerated and very echo-poor. Colour Doppler shows hypervascularity but often normal branching of the vessels. Solid tumours have a heterogeneous but predominantly echo-poor pattern. The ultrasound findings are not specific concerning this type of tumour.

Infectious and parasitic diseases

Abscesses are not rare in children, especially in the retropharyngeal region. The inflamed tissue appears oedematous (little sound attenuation) and heterogeneous, with echo-poor or even echo-free areas, indicating abscess formation. The size and shape of cervical abscesses are variable, and they are often limited by the surrounding structures. Dispersed intense echoes within the affected tissue, with a partial acoustic shadow, indicate gas bubbles. The adjacent muscles may be swollen and have a more echo-poor pattern. Thrombosis of the jugular vein is another complication. Ultrasound shows the dilated vessel filled with echoes.

Hydatid cysts can be located anywhere, even in the neck. The most frequent location in the neck is the thyroid gland.

Chest

Indications

Ultrasound exploration of the thoracic cavity is more useful in children than in adults. The main indications are chest wall abnormalities, pleural effusion, peripheral lung lesions, diaphragm abnormalities and mediastinal lesions. Ultrasound is increasingly used in intensive care units to guide interventions and to follow up pleural effusion and chest wall diseases.

Preparation

Before an ultrasound examination, it is important to review the child's chest radiograph to locate the area of interest.

Examination technique

The child lies supine or prone or stands erect, depending on the clinical problem. Having the arm raised above the head increases the rib space distance and facilitates parietal and pleural examination. The posterior chest is best imaged with the child sitting up, while the anterior and lateral chest can be assessed with the child in the lateral supine position. The transdiaphragmatic acoustic window is used, as well as the intercostal spaces and a supraclavicular approach. Views of the upper mediastinum should be obtained in the sagittal and axial planes. Transthoracic chest ultrasound can be performed with high-frequency linear or curved 5- to 10-MHz probes. Colour Doppler is useful for assessing mediastinal vascular and parenchymal abnormalities and for distinguishing the great vessels from a mediastinal mass. The gain and velocity range of colour Doppler should be adapted to the region of interest.

Normal findings

The normal chest wall has cutaneous and subcutaneous layers, muscles and fascia. Below the soft tissue of the chest wall, the ribs appear as curvilinear structures on transverse scans, associated with posterior acoustic shadowing. When the ribs are scanned along the long axis, the anterior cortex should appear as a continuous, smooth, echoic line (Fig. 5.187).

The pleura is easily recognized as an echoic line deep to the ribs. It may not be possible to differentiate the visceral and parietal portions in healthy infants, and echoic air reverberation artefacts at the pleura–lung interface prevent further visualization of the normal parenchyma. The aorta, great vessels and superior vena cava can be seen in the suprasternal view of the mediastinum.

The thymus is commonly prominent in children under 3 years of age. Ultrasound shows a characteristic appearance of echogenic foci or septae within echo-poor parenchyma (Fig. 5.188). The thickness of the thymic lobe decreases with

Fig. 5.187. Normal chest wall in 14-year-old boy. Transverse scan through the lateral chest wall shows ribs (R) as curvilinear structures associated with posterior acoustic shadowing (arrowheads). C, cutaneous and subcutaneous layers; M, muscles and fascia; L, lung; arrows, pleural interface

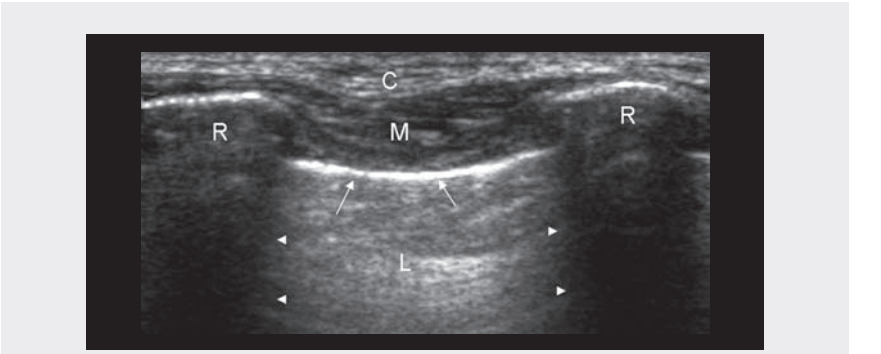

Fig. 5.188. Normal thymus in a newborn girl. Longitudinal scan shows a triangular thymic lobe (T) anterior to the aorta (AO) and posterior to the sternum (S); echo-poor thymic parenchyma with echogenic foci

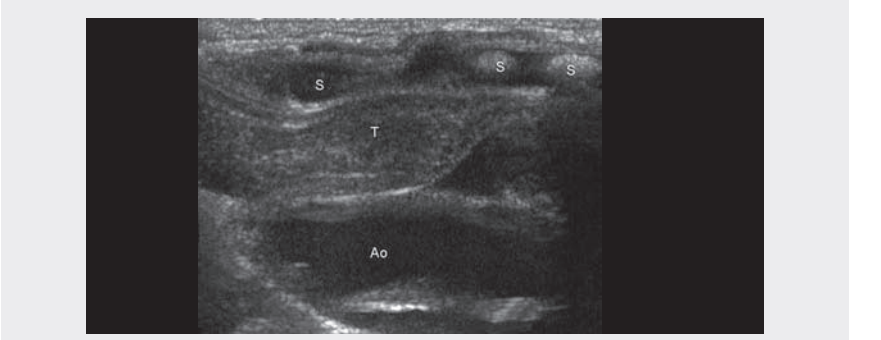

age, from 1.5 ± 0.46 cm for children aged 0–10 years to 1.05 ± 0.36 cm for those aged 10–20 years. The width shows little change with age.

The diaphragm is best examined through the lower intercostal spaces and is seen as a thin echogenic line due to the interface between the diaphragm and the air-containing lung, above the liver and the spleen (Fig. 5.189). Segments that do not border air-containing lung tissue appear echo-poor. The normal downward movement of the diaphragm should be seen on inspiration.

Fig. 5.189. Normal diaphragm in a 10-year-old girl. Oblique scan above the liver (L) shows the diaphragm (arrowheads)

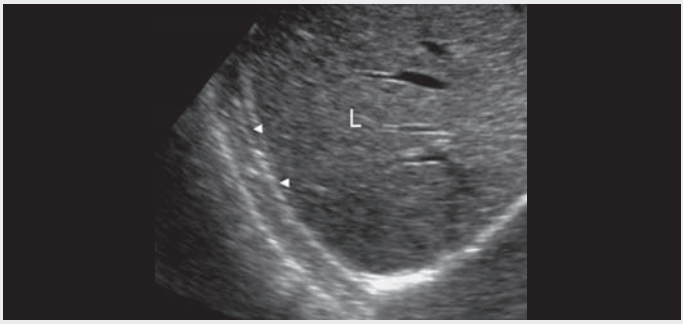

Pathological findings

Soft-tissue abnormalities

Ultrasound is sensitive for detecting anomalies in the chest wall, such as abscesses, haematoma, lipoma, lymphangioma and haemangioma, which are easily diagnosed (Fig. 5.190). Nonspecific aspects, however, may require other imaging modalities, such as conventional X-ray, MRI or CT, especially if an intrathoracic extension of a rib or spinal tumour is suspected.

Fig. 5.190. Thoracic lymphangioma in a 3-year-old boy with a left-side thoracic mass. Longitudinal scan through the left chest wall shows a large cystic mass (C) just anterior to the ribs (R)

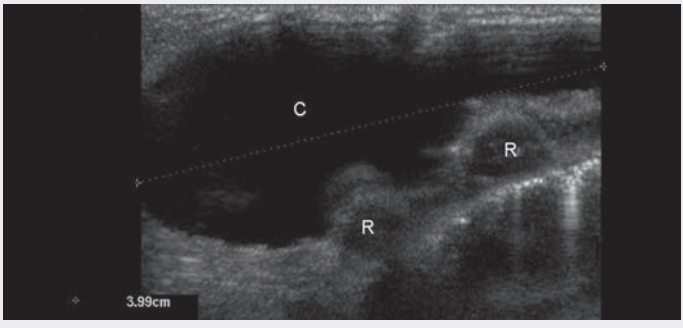

Rib fracture

A fracture after chest trauma appears as an irregularity of the cortex of the rib, associated with a localized haematoma, effusion or soft-tissue swelling. Callus formation can be assessed by ultrasound follow-up.

Pleural effusion

Pleural effusion appears as an echo-free layer between the visceral and parietal portions of the pleura. Ultrasound is indicated to assess the mobility of the liquid and its echogenicity (transudate or purulent) (Fig. 5.191, Fig. 5.192) or to guide puncture in case of septations (Fig. 5.193). It is also useful for differentiating effusion from a parenchymal abnormality (Fig. 5.193), pleural thickening or pleural infiltration and for follow-up.

Fig. 5.191. Echo-free simple pleural effusion in a 7-year-old boy. Longitudinal scan of the left lower lobe shows a large amount of echo-free pleural effusion (PE) with an echogenic area of parenchymal consolidation (arrow)

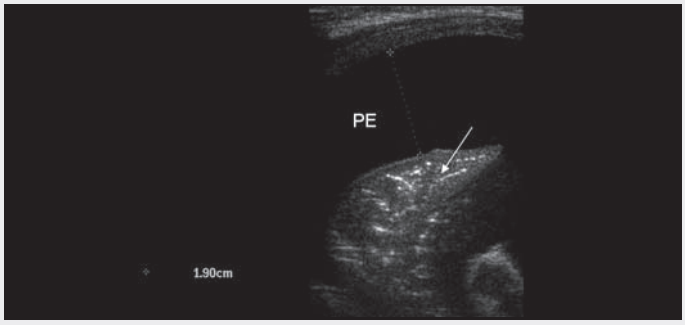

Fig. 5.192. Simple effusion with floating debris in a 5-year-old girl. Longitudinal scan of the left lower lobe shows a large, echo-poor pleural effusion (PE) containing swirling particles (arrows). S, spleen

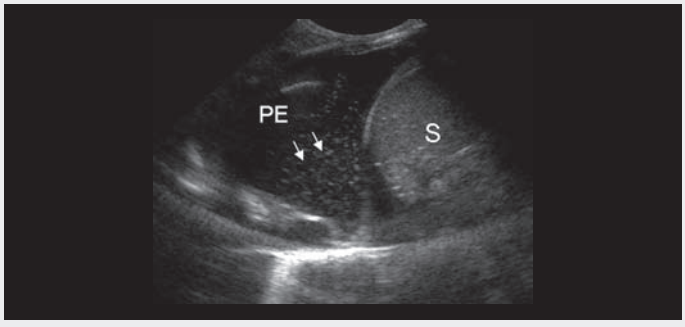

Fig. 5.193. Complicated pleural effusion with multiple loculi in a 10-year-old girl. Intercostal oblique scan shows a multiloculated pleural effusion. The pleural space is filled with profusely thickened septated fluid (arrows)

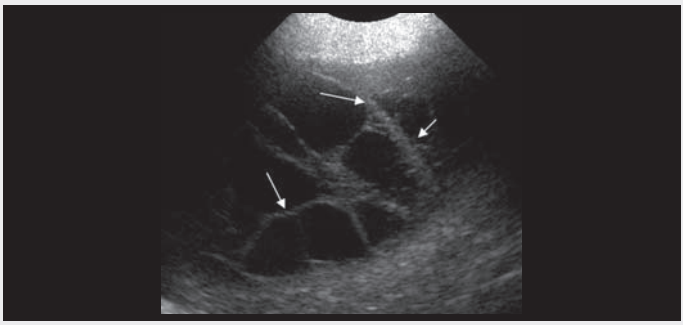

Hydropneumothorax

In some cases, chest radiographs are difficult to read, and a pneumothorax may be missed in a child in the supine position in an intensive care unit. Pneumothorax can be demonstrated from sonographic signs: the absence of lung sliding, the absence of air artefacts and thickening of the pleural line. Hydropneumothorax can be identified with ultrasound as air artefacts within the pleural effusion.

Diseases of the lung parenchyma and mediastinum

Diseases of the lung parenchyma that connect it to the pleural surface by replacing alveolar air with mucus, haemorrhage or inflammatory or purulent liquid create an acoustic window that allows visualization of abnormal parenchyma.

Pneumonia and lung abscesses

Lobar pneumonia, segmental pneumonia affecting the pleura and pleural consolidation are detectable by ultrasound. In the early phase of consolidation, the lung appears diffusely echogenic, resembling the sonographic texture of the liver (Fig. 5.194). A bronchogram is represented by linear echoes; on colour Doppler, the pulmonary artery branches supplying the segment are clearly seen. Fluid bronchograms are identified as echo-free tubular structures, representing fluid-filled airways. Pulmonary consolidation may be observed in haemorrhage, lymphomatous infiltration or contusion. It is important to consider clinical and biological data as well as other imaging modalities. Ultrasound is useful for follow-up during antibiotic treatment of pneumonia.

Abscess formation resulting from complicated pyogenic pneumonia can be identified with ultrasound as an echo-free, hypoechoic or septated mass. Differential diagnosis from hydatid cyst of the lung in endemic areas and in older children

Fig. 5.194. Pulmonary consolidation in a 9-year-old boy. Longitudinal scan of the right lower lobe shows a triangular region of echogenic parenchyma of the lung. The bright echoes (arrows) represent air in the bronchi (sonographic air bronchogram).

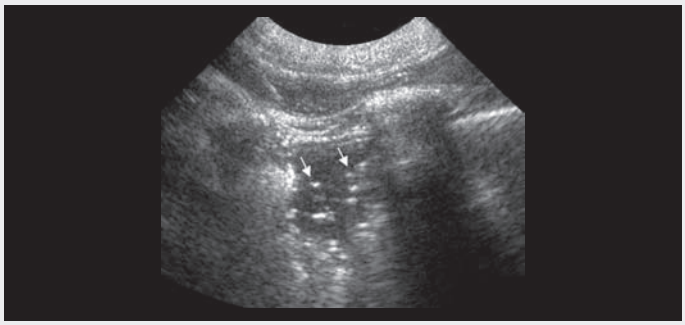

(> 2 years) can be difficult (Fig. 5.195). In these cases, ultrasound and laboratory exploration may be helpful in identifying another location.

Fig. 5.195. Pulmonary hydatid cyst in a 6-year-old boy. Longitudinal scan of the left lung (L) shows a large hydatid cystic mass (HC) with a regular thick wall (arrow)

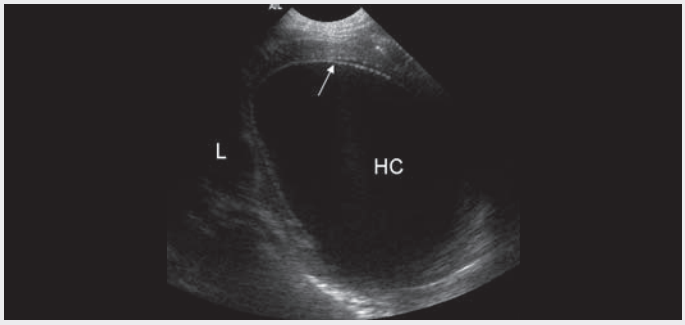

Neoplasms

Pneumoblastomas are solid, heterogeneous, compressive tumours, which can be explored by ultrasound-guided biopsy of the mass. Extension of the tumour is identified by CT or MRI. Metastases of lymphomas or neuroblastomas are rarely explored by ultrasound.

Mediastinal masses or lymph nodes can be detected by ultrasound. Frequently, a normal or hypertrophied thymus must be differentiated from an anterior mediastinal mass, often by ultrasound. Enlarged, irregular lymph nodes raise suspicion of

malignancy. Colour Doppler can be used to guide biopsy of mediastinal masses and lymph nodes in the anterior and upper mediastinum.

Diaphragmatic abnormalities

The diaphragm normally moves down on inspiration and up on expiration. In diaphragmatic paralysis, it either remains high and fixed or may show paradoxical movements, so that it moves upwards during inspiration. Movement of the diaphragm is usually observed by fluoroscopic screening during respiration; however, careful ultrasound examination of both hemidiaphragms can provide information on diaphragmatic movement.

Diaphragmatic and hiatus hernia can be demonstrated by ultrasound, as can discrete masses of variable echogenicity. Joining with intra-abdominal organs, Brownian movement and duplicated digestive wall in hernia of the digestive tract can also be seen.

Neonatal cranial ultrasound

Indications

The main indications for exploration of the neonatal brain are haemorrhage, ischaemia, convulsions, malformation, infection or a tumour.

Preparation

No specific preparation is needed. The infant lies in the supine position; one of the parents should be present to calm the infant if necessary.

Examination technique

Equipment

A high-resolution, real-time, two-dimensional machine with dedicated settings for cranial ultrasound and Doppler and colour flow capability should be available. High-frequency transducers (5–10 MHz) with a small footprint to match the size of the fontanelle should be used. Depending on the manufacturer, two probes may be needed: one 5-MHz probe for full-term infants and examination of the posterior fossa and one 7.5-MHz probe for premature infants and examination of periventricular areas. Ideally, a high-frequency (7- to 10-MHz) linear probe should be available to scan the extracranial fluid space and superior sagittal sinus. A hand-held colour ultrasound device is required in intensive care units.

Technique

Ultrasound scans are made through the anterior fontanelle with sequential coronal and parasagittal projections. The posterior fontanelle is examined for detailed depiction of the periventricular white matter or small amounts of blood in the lateral ventricles. A scan through the mastoid fontanelle provides optimal visualization of the posterior fossa structures. Coronal, sagittal and parasagittal views should be taken, and oblique, surface and axial views may be needed (Fig. 5.196).

Fig. 5.196. Scanning area for evaluation of the brain through the anterior fontanelle (AF). (a) Coronal scans. (b) Sagittal scans

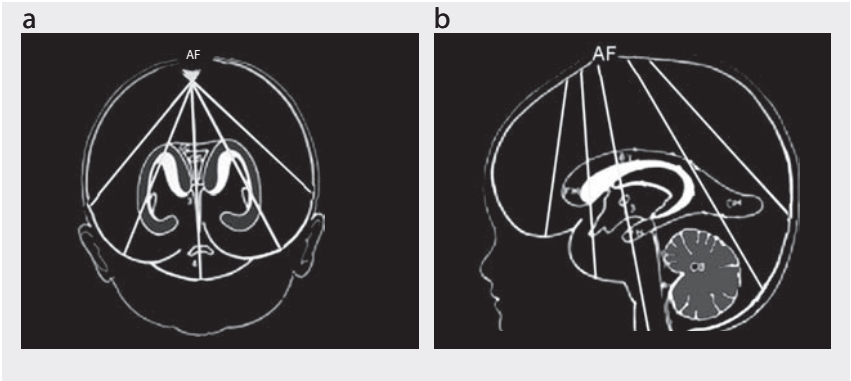

Normal findings

Normal anatomical structures

Normal anatomical structures that should be identified are:

- ventricles and fissures: frontal horn, fourth ventricle, third ventricle, lateral ventricles (choroid plexus and atria), Sylvian fissure and extra-axial space (Fig. 5.197);
- brain parenchyma: corpus callosum, caudate nucleus, basal ganglion, thalamus, all the lobes, cerebellar vermis and cerebellar hemispheres (Fig. 5.198);
- arterial structures (colour Doppler): anterior cerebral arteries, middle cerebral arteries at their origin and in the Sylvian fissure, posterior cerebral arteries, basilar artery and internal carotid arteries in the carotid siphon;
- venous structures (colour Doppler): superior sagittal sinus and its draining veins, inferior sagittal sinus, straight sinus, confluence of sinuses, lateral sinuses, internal cerebral veins, vein of Galen and draining veins of the ventricles.

Fig. 5.197. Normal ventricle anatomy in a 3-month-old boy. (a), (b) Coronal scans and (c) sagittal midline scan through the anterior fontanelle show the normal ventricular system. FH, frontal horn; S, Sylvian fissure; LV, lateral ventricle; CP, choroid plexus; V3, third ventricle; V4, fourth ventricle; CC, corpus callosum; CV, cerebellar vermis

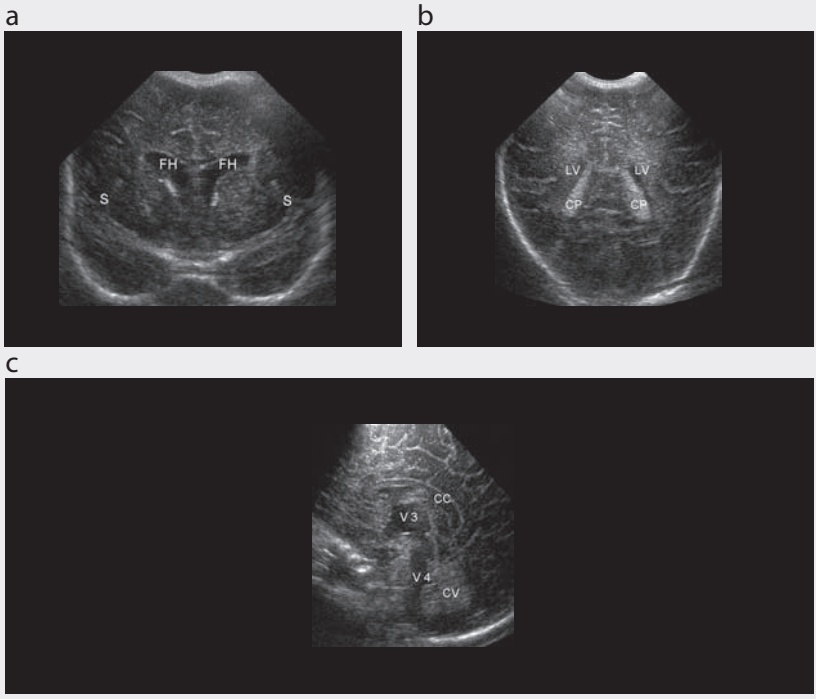

Fig. 5.198. Normal brain anatomy in a newborn boy. Coronal midline scan through the anterior fontanelle, with the thalami (Th), the caudate nucleus (CN) and the basal ganglion (GB) on each side of the ventricular system. FP, frontal parenchyma; TP, temporal parenchyma; S, Sylvian fissure; V3, third ventricle

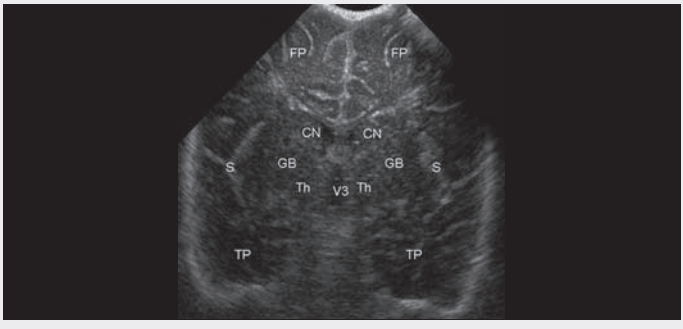

Normal variants

A number of normal variants should be recognized. **Cavum septum pellucidum** is an anterior midline cavity located between the two leaves of the septum pellucidum (Fig. 5.199).

Fig. 5.199. Cavum septum pellucidum in a newborn boy. Coronal scan shows an anterior midline cavity (arrow) located between the frontal horns (FH)

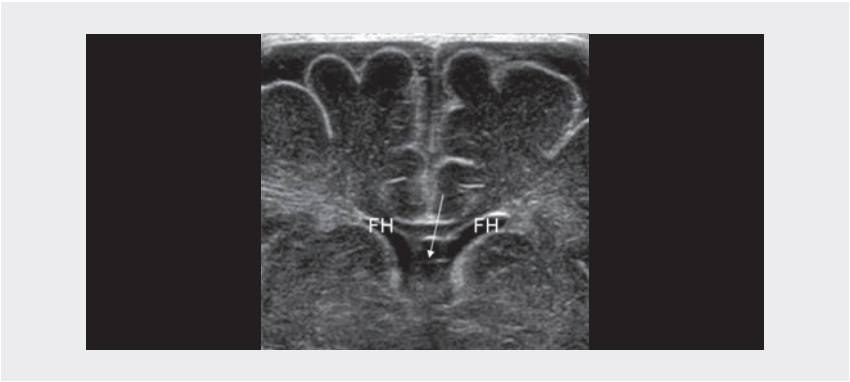

Cavum vergae is a posterior midline fluid–fluid space which usually communicates with the cavum septi pellucidi and is obliterate from posterior to anterior. **Cavum veli interpositi** is an anatomical variation that may appear as a cyst in the pineal region in neonates. **Connatal cysts** are cysts measuring 3–10 mm adjacent to the supralateral margin of the frontal horns, with no sign or symptom of infection, haemorrhage or hypoxia. They are due to approximation of the walls of the frontal horns of the lateral ventricles proximal to their external angles. They are found mainly anterior to the foramen of Monro.

In premature infants, the lateral ventricles may be small or invisible. A **lobular choroid** *plexus* may be seen occasionally and be confused with an adherent clot.

Calcar avis is a paramedian protrusion of the calcarine gyrus into the medial segment of the lateral ventricle at the junction of the trigone with the occipital horn. On parasagittal oblique images, these normal parenchymal structures may simulate intraventricular clots. They can be recognized by their characteristic location, their contiguity with the calcarine gyri and the presence of a central echogenic sulcus that has normal perfusion on colour Doppler.

Periventricular hyperechogenicity is a normal variant when it is smooth and less echo-rich on ultrasound than the choroid plexus. It is due to parenchymal immaturity.

Haemodynamics

The arterial spectrum shows low resistance and strong, continuous diastolic flow with systolic peaks. The amplitude of the diastolic component of the arterial cerebral blood flow is thus directly related to the distal circulatory resistance (Fig. 5.200). The

resistive index ([peak systole–end diastole]/peak systole) does not always correlate with the cerebral blood flow, and blood-flow velocity and venous velocity should be measured.

Fig. 5.200. Normal haemodynamic study of the anterior cerebral artery of a newborn boy. The systolic velocity is 46 cm/s, the diastolic velocity is 10.7 cm/s, and the medium velocity is 23.5 cm/s. The resistive index is 0.77.

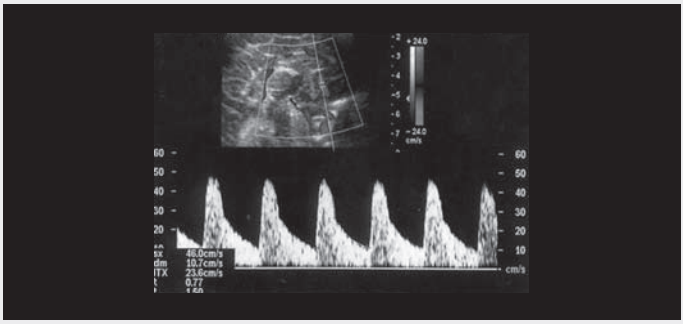

Pathological findings

Premature brain

Cranial ultrasound Doppler is the main screening method for imaging unstable, incubated, ventilated infants in a neonatal intensive care unit. It has good diagnostic sensitivity and some limitations. Use of MRI has been the subject of many prospective studies.

Early perinatal exploration is based on a sonographic examination before the third day of life to examine either an intracranial lesion found on morphological examination or a normal morphological image but an abnormal haemodynamic result.

The morphological examination is pathological. Subependymal **germinal matrix haemorrhage** has an excellent prognosis when it is identified and must therefore be sought at the first evaluation. **Intraventricular haemorrhage** is sometimes associated with precocious dilatation, characterized by echo-rich intraluminal images. If the examination is conducted early or if there is a doubt about the images, the examination should be complemented with a colour Doppler analysis of the aqueduct of Sylvius to show intermittent up- and downstream flow, either spontaneous or after pressure on the fontanelle (or abdomen). This examination is useful in daily practice and is highly reliable, even though it is nonspecific.

Intraventricular haemorrhage associated with an **ischaemic–haemorrhagic periventricular infarct** appears as an echo-rich lesion, which is often globular, sometimes digitiform and generally unilateral. Imaging of periventricular hyperechogenicity should include the intensity. The appearance is massive globularity, sometimes with a speculated periphery and a digitiform aspect extending to the white subcortical

matter, usually containing echo-rich nodules, which are rarely microcystic at this age. The topography is uni- or bilateral and may be limited to the frontal regions or behind the atria or extend to other regions, including the temporal area. Some periventricular hyperechogenicity seen during initial exploration may be transitory.

An echo-rich basal ganglion or thalamus is a rare lesion but can occur in premature infants. Lesions of the basal ganglion seen on initial sonographic examination may be attenuated on follow-up and then reconfirmed.

When analysis of the posterior region of the brain is technically difficult because of a small fontanelle, an overlapping suture or respiratory ventilation that makes access to the anterior fontanelle difficult, or when there is doubt about the normality of the posterior regions of the brain, the examination should be complemented by exploration through the posterior fontanelle, which gives direct access to regions behind the atria and the occipital horns. The temporal regions can also be studied through the temporal bone (mastoid view).

If the morphological examination appears normal but the haemodynamic analysis is pathological, a special pulsed Doppler study should be conducted. The data to be sought include fluctuations of Doppler spectra, usually contemporaneous with haemodynamic instability; low flow, characterized by systolic and average speeds lower than normal; high flow, with high systolic and average speeds; and anomalies of vascular resistance.

Early follow-up

Early follow-up (before 10 days of life) is also based on sonography. This examination is performed to screen for intraventricular haemorrhage in an infant with normal morphology but pathological haemodynamics or secondary clinical complications (respiratory complications, ductus arteriosus or enterocolitis) that could lead to haemorrhage. Ultrasound is also used to screen for ischaemic–haemorrhagic infarct in an infant with intraventricular haemorrhage. Early follow-up is necessary to confirm the existence and persistence of periventricular hyperechogenicity, to screen for heterogeneity in the echogenicity and to confirm the existence of another lesion (e.g. in the basal ganglion).

Follow-up of a haemorrhagic lesion

Ultrasound will show the classical evolution of an intraventricular clot and is used to screen for ventricular dilatation and its morphological evolution (Fig. 5.201). Complementary pulsed Doppler can show an increase in the resistive index due to intracranial hypertension. The sensitivity of the technique can be increased by fontanelle compression for determination of [resistive index after compression – basal resistive index] / basal resistive index, which indicates progression of ventricular dilatation. Doppler analysis is particularly useful when cerebrospinal fluid is to be removed, because it can show the efficacy of the therapy and guide the frequency of punctures.

Fig. 5.201. Convulsion in a preterm 34-week-old infant with hyaline membrane disease. (a) Coronal scan 2 days after birth shows an intraventricular haemorrhage (arrows). (b) Coronal and (c) sagittal scans performed 13 days later show progressive dilatation of the lateral and third ventricles, with arrows indicating a blood clot. (d) Pulsed Doppler shows intracranial hypertension with negative diastolic velocity and a resistive index of 1.29

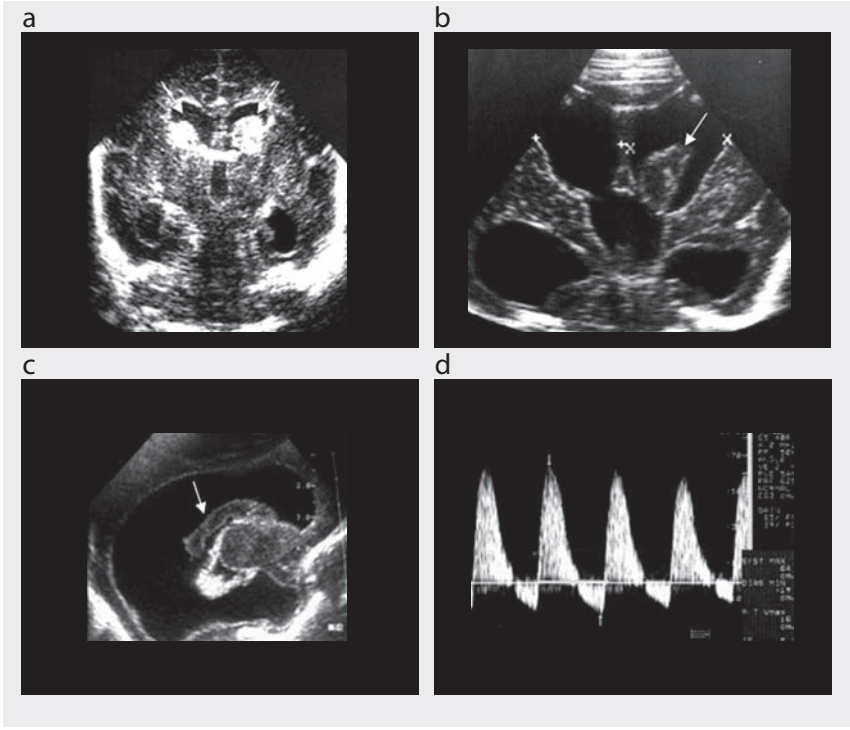

Intermediate follow-up

An intermediate follow-up (between 3 weeks after birth and theoretical term) makes it possible to determine the presence of cysts in the white matter, consisting of rapidly confluent macrocysts, which are rare, or more frequent microcysts. It may be difficult to distinguish real microcysts from normal parenchyma within the echo-rich matter. Use of a high-frequency probe and special acoustic windows (the posterior fontanelle if possible) is useful for diagnosis. Intermediate follow-up can also reveal persistence of prolonged periventricular hyperechogenicity or ventriculomegaly, often manifested only by a rounded aspect of the frontal horns on a coronal scan, or the existence of an undetected white-matter lesion. Ventriculomegaly is stable and can be due to widening of the pericerebral spaces.

Role of MRI

The anomalies found on early MRI are haemorrhage in a ventricle or the germinal matrix; anomalies of the white matter, consisting of cystic images of periventricular leukomalacia, hyperintense T1 punctate lesions, diffuse hypersignal of the white matter and haemorrhagic infarct; and lesions of the basal ganglion, in addition to haemorrhage of the posterior fossa, consisting of cerebellar or extra-axial haemorrhage, which is frequently unilateral.

MRI and ultrasound findings correlate well for severe lesions (85–95% for germinal matrix haemorrhage or intraventricular haemorrhage and 96% for major periventricular hyperechogenicity) but less well for lesions of moderate (55%) or medium (72%) severity. Diffusion-weighted MRI shows the extent of some white matter anomalies more clearly than conventional MRI, and there is a strong correlation with later neurological evolution. Early MRI is considered useful when sonographic imaging shows moderate or doubtful anomalies or when there is discordance with the clinical or electrical presentation of the infant.

Long-term follow-up

Long-term follow-up is necessary because of the correlation between anomalies in neuromotor development and peri- or postnatal lesions of the white matter. It is based on MRI, which can indicate ventriculomegaly, ventricular deformity, late myelinization, hypoplasia of the corpus callosum and diminution of the cerebral volume.

Lesions are staged by either ultrasound or MRI. Cranial ultrasound can be used to differentiate intraventricular haemorrhage, white-matter injury and periventricular leukomalacia, basal ganglia lesions and secondary isolated ventriculomegaly.

Intraventricular haemorrhage (Fig. 5.202) is graded as isolated germinal matrix haemorrhage (grade I), moderate haemorrhage without dilatation of the ventricles (grade II), severe haemorrhage, often with hydrocephalus (grade III), and severe haemorrhage with ischaemic–haemorrhagic infarct (grade IV).

White matter injury with periventricular leukomalacia (Fig. 5.203) is graded into localized periventricular hyperechogenicity (grade I), which can be frontal or parietal, located in the post-trigonal regions or punctiform. Extended hyperechogenicity, limited to the periventricular white matter, unilateral, bilateral or even extending into the subcortical white matter but without cystic lesions is classified grade II. Cystic periventricular leukomalacia (grade III) is characterized by small (< 5 mm) or large (> 5 mm) cystic lesions or limited to the periventricular or subcortical white matter.

Fig. 5.202. Classes of intraventricular haemorrhage. (a) Grade I, germinal matrix haemorrhage (arrows). (b) Grade II, bilateral haemorrhage (arrowheads) of moderate severity. (c) Grade III, haemorrhage with echo-rich clots (arrowhead) occupying the entire dilated ventricle. (d) Grade IV, preterm 30-week-old infant with sepsis and a right intraventricular haemorrhage extending into the periventricular region (empty arrow)

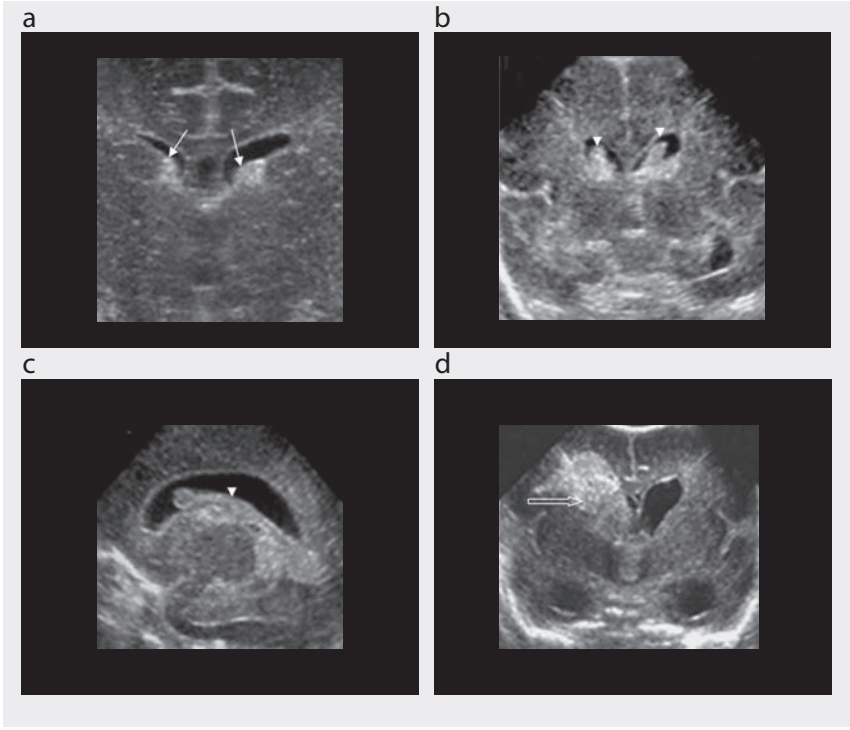

MRI shows haemorrhagic lesions of the germinal matrix, intraventricular haemorrhage with ischaemic–haemorrhagic infarcts; focal lesions of the periventricular white matter, ranging from a few small grade I lesions to numerous extended, cystic grade III lesions; diffuse echo-rich white matter; basal ganglion lesions; and late anomalies, including ventriculomegaly, delayed myelinization and reduced brain volume.

Ultrasound should thus be performed before the 3rd day, before the 10th day, 1 week later and at full term. Screening is more frequent if progressive lesions are detected. Use of early MRI depends on the sonographic results and a possible discordance between the clinical and electrical data. MRI should be performed at 4 months or 1 year for all premature infants.

Fig. 5.203. Periventricular leukomalacia in a preterm infant. (a) Coronal scan shows a periventricular area of increased echogenicity. (b) Longitudinal lateral scan shows periventricular hyperechogenicity with marked bilateral cavitations (arrow). (c) Coronal scan in a 30-week-old preterm infant shows periventricular hyperechogenicity that has evolved into small cysts (arrowheads)

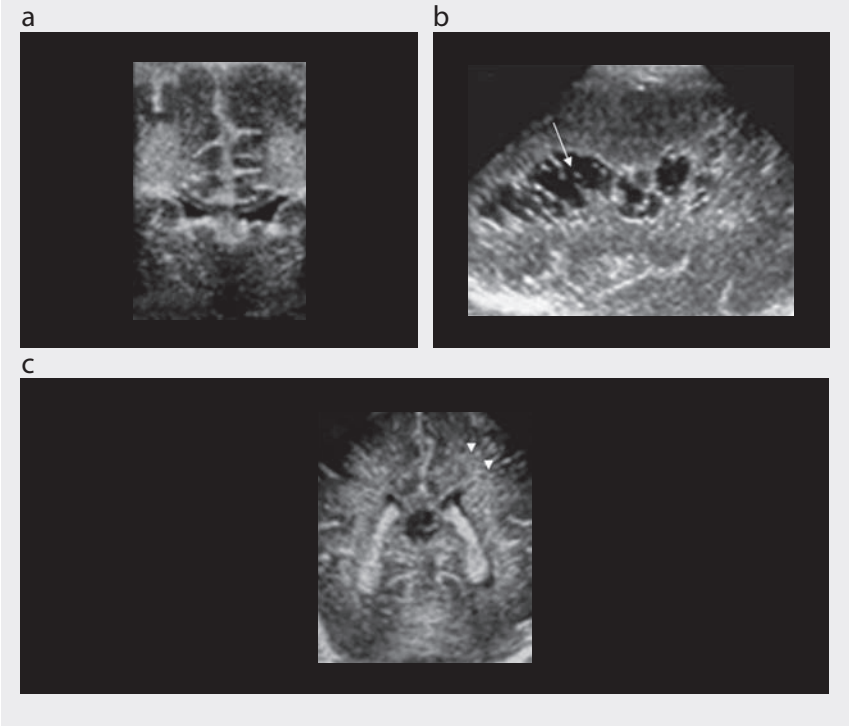

Ischaemic lesions

Antenatal cerebral lesions of vascular origin are frequently detected, particularly those associated with malformations, such as porencephaly, multicystic encephalomalacia, hydrocephalus and disorders of neuronal migration. Reducing the risk for ischaemia is essential for preventing intrauterine asphyxia, maintaining ventilation, perfusion and adapted glycaemia and controlling episodes of seizure. Ultrasound exploration of anoxic–ischaemic lesions should be conducted with high-frequency probes (7.5–10 MHz) and colour Doppler (Fig. 5.204). Colour Doppler is useful for diagnosis, whereas haemodynamics assist in establishing a prognosis.

Fig. 5.204. Cerebral anoxic–ischaemic lesions. (a) Coronal scan shows cortical necrosis. (b) Coronal scan shows bilateral parasagittal ischaemia. (c) Coronal scan shows grey nucleus ischaemia. (d) Sagittal scan shows cerebral trunk ischaemia with diffuse hyperechogenicity of the cerebral trunk. (e) Sagittal scan in a normal newborn shows an echo-poor posterior cerebral trunk

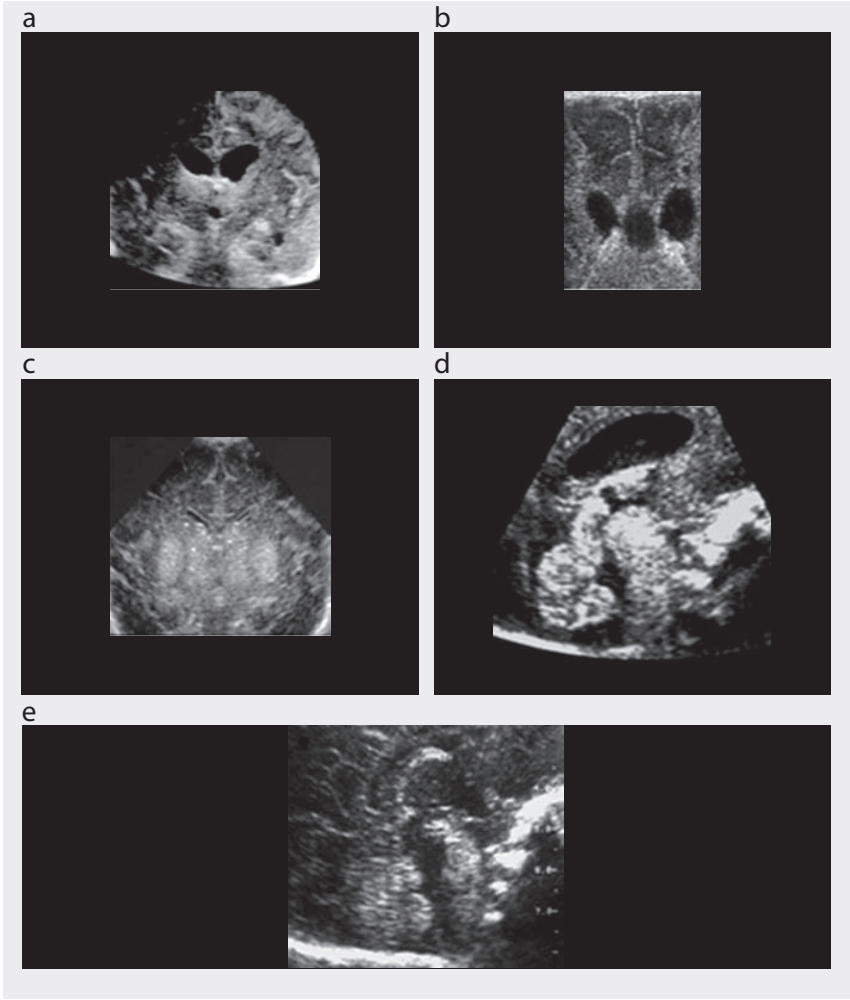

Anoxic–ischaemic encephalopathy

This disorder appears as an ischaemic echo-rich lesion of the white matter, cortex or subcortex, increased cerebral blood flow velocity and decreased vascular resistance due to arteriolar vasoplegia (Fig. 5.205). Decreased resistance with increased diastolic flow is the main sign of immediate danger and guides resuscitation.

Fig. 5.205. Prolonged hypoxia during neonatal surgery for oesophageal atresia. (a) Coronal scan performed 4 days later shows diffuse ischaemia with echogenic white matter (arrowheads). (b) Pulsed Doppler shows decreased blood pressure with a resistive index of 0.47

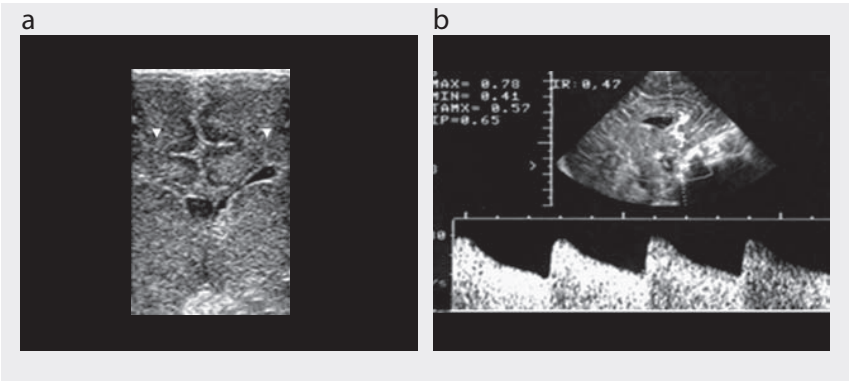

Arterial ischaemic infarct

This condition is difficult to diagnose clinically in newborns. Perinatal asphyxia is the most frequent cause, but other factors include hypoxia, thrombosis (polyglobulia, hyperviscosity, meningitis, meningoencephalitis, poisoning) and emboli due to congenital cardiopathy or placental failure. The increasing frequency of neurological sequelae of cardiac surgery is of concern. The hypothermia and complete circulatory arrest that accompany external circulation favour physiopathological mechanisms such as microemboli, hypoxia and insufficient regional cerebral perfusion.

On ultrasound, ischaemic infarct shows early hyperechogenicity near the origin of the middle cerebral artery or the Sylvian fissure; cystic cavitations occur within 3–4 weeks. Colour Doppler can show an arterial thrombus. Thrombosis of the superior sagittal sinus and the profound venous system is rare, and clinical diagnosis is difficult and nonspecific. It is now rarely due to infection, and severe dehydration is the principal cause. The thrombosis usually results in diffuse oedema of the cerebral parenchyma and rarely in venous ischaemic–haemorrhagic infarct, the location and extent of which determine the prognosis. Thrombosis of the superior sagittal sinus is more frequent than that of the profound venous system. Sonographic and colour Doppler examinations give reliable signs (Fig. 5.206): an echo-rich thrombus in the superior sagittal sinus and total or partial interruption of flow in colour Doppler with no spectral analysis.

Fig. 5.206. Thrombosis of the superior sagittal sinus in a newborn. (a) Coronal scan shows a triangular echo-rich image in the midline, corresponding to the superior sagittal sinus; absence of flow on colour Doppler. (b) Coronal T1-weighted magnetic resonance image confirms the venous thrombosis

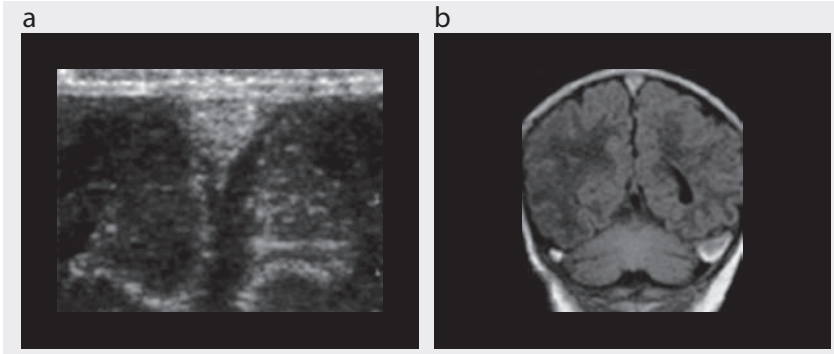

Severe haemodynamic distress

Neonatal and infant respiratory failure lead to multiple vascular anomalies, including rhythm disorders and flow abnormalities, seen as fluctuating and changed Doppler spectra, and the disappearance or reversal of diastolic flow due to increased vascular resistance (Fig. 5.207, Fig. 5.208).

Fig. 5.207. Preterm 26-week-old infant. Duplex colour Doppler shows normal arterial velocity, with a systolic flow of 26.5 cm/s and a diastolic flow of 5 cm/s (median, 12.6 cm/s)

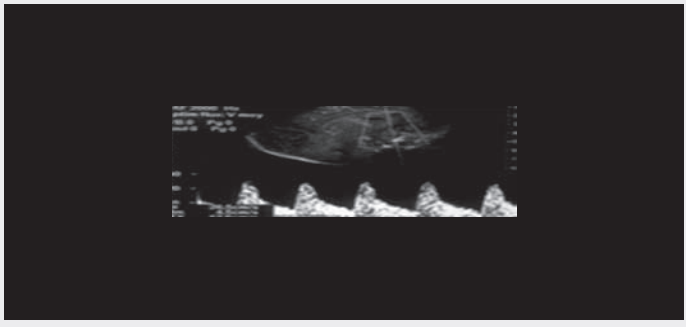

Fig. 5.208. Mature newborn with neurological distress. Duplex colour Doppler shows low arterial velocity, with a systolic flow of 28 cm/s and a diastolic flow of 8 cm/s (median, 16 cm/s)

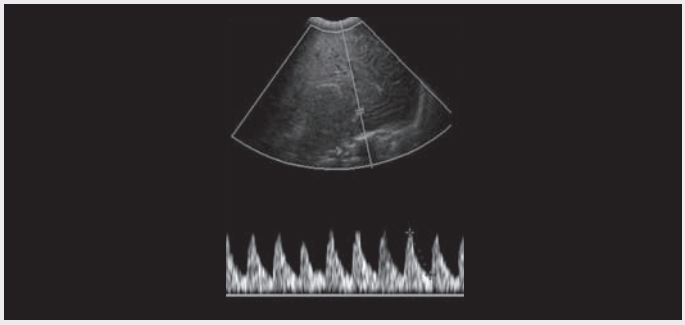

Cerebral malformations

Cerebral malformations are now rare in the neonatal period because they are usually identified during the fetal period by ultrasound and MRI. They include anencephaly, exencephaly, inencephaly, lissencephaly, holoprosencephaly, meningocoele, meningoencephalocoele and myelomeningocoele. While diagnosis of an aneurysm of the Galen vein is simple with colour Doppler, evaluating its prognosis requires a complete haemodynamic assessment of afferent vessels and a fetal MRI to detect any anoxic–ischaemic lesions.

The rare malformations that are diagnosed neonatally include lesions of the corpus callosum, anomalies of the posterior fossa and neuronal migration. Complete or partial agenesis and hypoplasia of the corpus callosum are easily diagnosed with ultrasound (Fig. 5.209). No other investigation is necessary, but the assessment should be complemented by MRI to detect associated malformations and particularly those of the central nervous system. The complexity of the pathology of the posterior fossa usually requires several imaging methods. Although the Dandy-Walker complex can be diagnosed by ultrasound alone, other anomalies, such as hypoplasia or atrophy of the vermis and agenesis of the vermis without cystic pathology, require MRI assessment.

Fig. 5.209. Agenesis of the corpus callosum in a 4-month-old boy. Coronal scan shows absence of corpus callosum, characteristic Viking horn or bull's horn configuration of the frontal horns (FH) and third ventricle displaced upwards (V3)

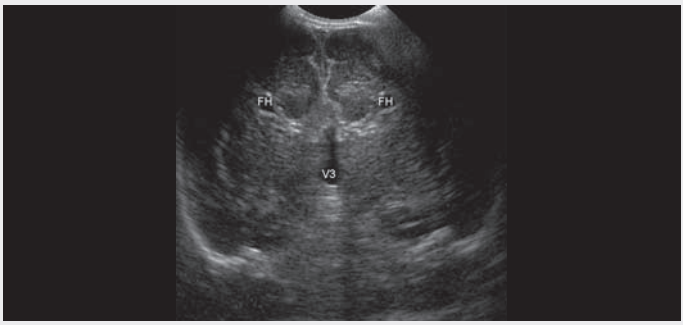

Extra-axial fluid

Ultrasound imaging allows accurate localization of extra-axial fluid (Fig. 5.210). Echo-free fluid penetrates the inter-hemispheric region between the grooves in the subarachnoid space. Colour Doppler shows the absence of subdural arteries and their consistent subarachnoid presence.

Fig. 5.210. Extra-axial fluid, coronal scans. (a) Enlargement of the subarachnoid spaces in a 3-month-old girl. (b) Subdural collection separated from the cerebral surface by the arachnoid

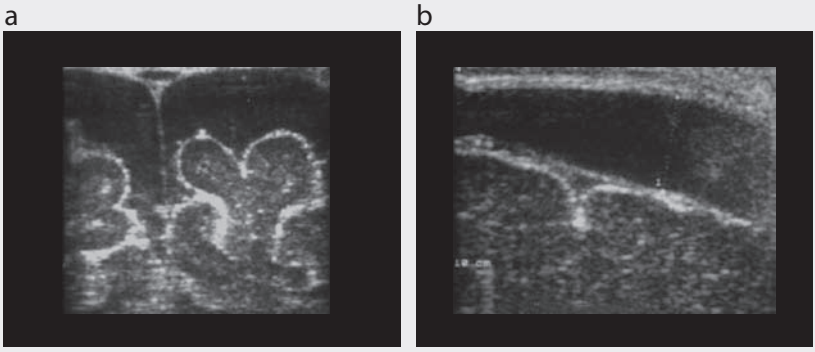

Infections

Ultrasound should be used to locate intraventricular echoes, echo-rich ependymal thickening, ventriculitis, cerebral abscesses, subdural empyema, ischaemic lesions, sinus thrombosis or secondary ventricular dilatation (Fig. 5.211). Cytomegalovirus infection shows progressive subependymal cysts, the candelabra sign of thalamostriate vasculopathy, anomalous neuronal migration and ventricular dilatation (Fig. 5.212).

Fig. 5.211. Cerebral infections. (a) Sagittal scan shows diffuse ventriculitis in *Pneumococcus* meningitis (arrowheads). (b) Coronal scan shows a right frontal abscess (A) in *Proteus* meningitis. (c) Coronal scan shows a large subdural empyema (arrow). (d) Coronal scan shows an ischaemic cortical area (empty arrow)

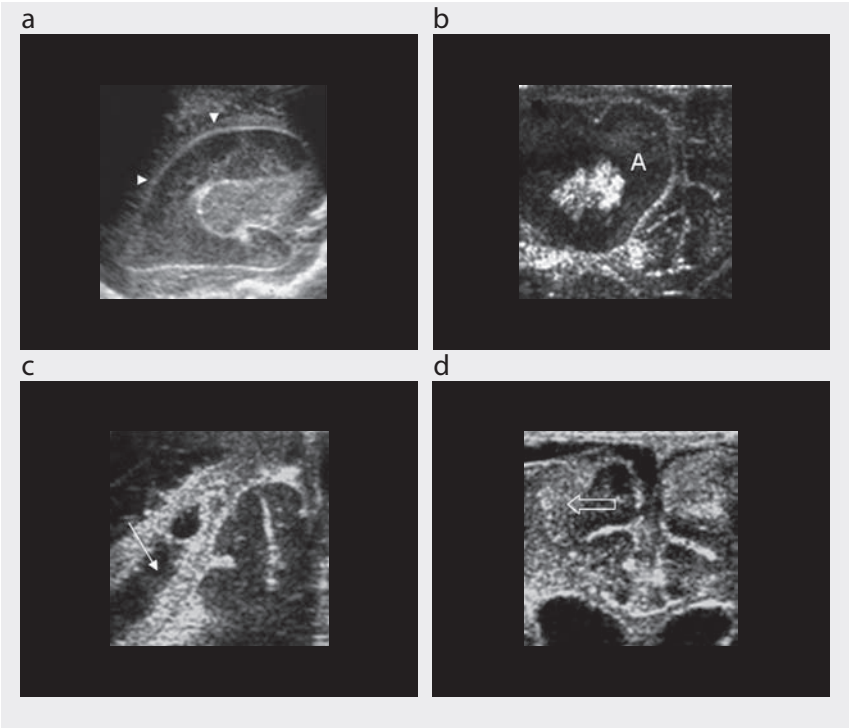

Fig. 5.212. Congenital cytomegalovirus infection in a 3-month-old boy. (a) Coronal scan shows parenchymal calcifications (arrows). (b) Coronal and (c) sagittal scans show subependymal cysts (arrowheads). (d) Sagittal scan shows a candelabra image at the level of the thalamostriate vessels (empty arrow)

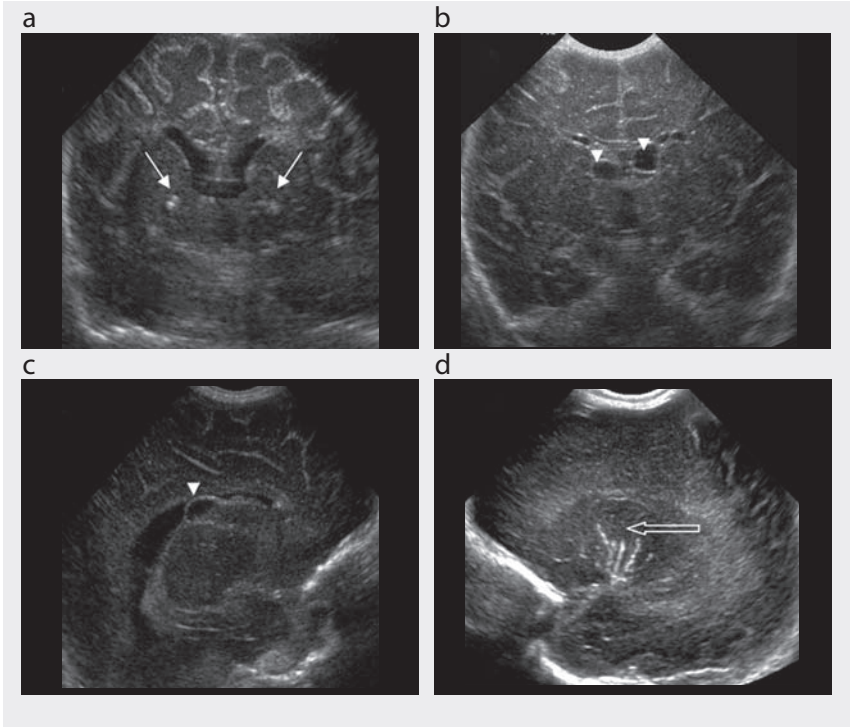

Cerebral tumours

Cerebral tumours are exceptional in neonates and young infants. Although cranial ultrasound can demonstrate tumours, CT and MRI remain the modalities of choice. These tumours are frequently associated with hydrocephalus, especially in posterior fossa tumours; the ventricular dilatations are easily seen by ultrasound.

Diagnosis of a papilloma of the choroid plexus is based on specific ultrasound findings. The tumour has an echo-rich aspect, lobulated contours and an intraventricular location. Hydrocephalus results from several complex mechanisms, including obstruction of the ventricle by the tumour, associated intraventricular haemorrhage, decreased absorption of cerebrospinal fluid and increased ventricular pulsation.

Spine

Indications

The spinal cord is examined by ultrasound in neonates and infants less than 6 months of age with signs of spinal disease. Typical indications are:

- midline skin masses on the back;
- midline cutaneous malformations on the back, such as a dimple or a haemangiomatous or hairy lesion;
- deformities of the spinal column;
- neurological disturbances;
- spinal cord injury due to traumatic birth or meningeal tear;
- syndromes with associated spinal cord compression.

Ultrasound can be used in the antenatal period to predict the anatomical level of spinal dysraphism in most cases. As sonography can show the entire spectrum of intraspinal anatomy and pathological conditions with high resolution, it should be considered the initial imaging modality of choice for investigating the spinal cord in neonates and for deciding whether CT or MRI should be performed.

Preparation

There is no specific preparation.

Examination technique

Infants are usually examined in the prone position, curved over a pillow. For examination of the craniocervical junction, the neck must be flexed. Sagittal and axial planes of the spinal canal and cord can be examined, from the craniocervical junction to the sacrum. In older children, progressive ossification of the posterior elements of the vertebrae obviates useful examination, and paramedian scans may be sufficient.

Movement of the spinal cord and cauda equina can be evaluated with real-time ultrasound in M-mode. The brain is examined systematically through the fontanelle. Examinations should be performed with high-frequency linear transducers (5–12 MHz).

Normal findings

The normal spinal cord appears on ultrasound as an echo-poor tubular structure containing fine, homogeneous internal echoes, surrounded by a nearly echo-free area corresponding to the cerebrospinal fluid. A well-defined echogenic interface highlights the boundaries of the cord, with a change in acoustic impedance between the spinal cord and surrounding cerebrospinal fluid (Fig. 5.213). The diameter of the

Fig. 5.213. Normal spinal cord in a 1-month-old boy. Sagittal scan of the thoracic spinal canal shows the spinal cord (SC) within the subarachnoid space (SA), anterior to the vertebral bodies (VB); the thin white line in the centre of the cord (arrow) corresponds to the central canal

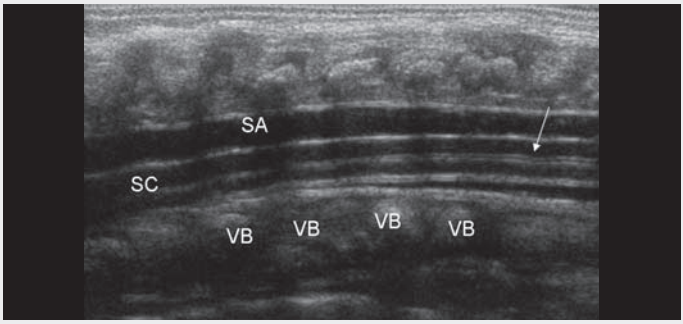

spinal cord varies; it is largest at the cervical and lumbar levels and smallest at the thoracic level. An axial scan of the spinal cord shows an echo-poor, oval or round spinal cord with an echogenic central complex within the echo-free subarachnoid space (Fig. 5.214).

Fig. 5.214. Normal spinal cord in a 4-month-old boy. Axial scan at the level of T12 shows the spinal cord (SC), nerve roots (arrowheads), subarachnoid space (SA), vertebral body (VB), vertebral arch (VA) and muscle (M)

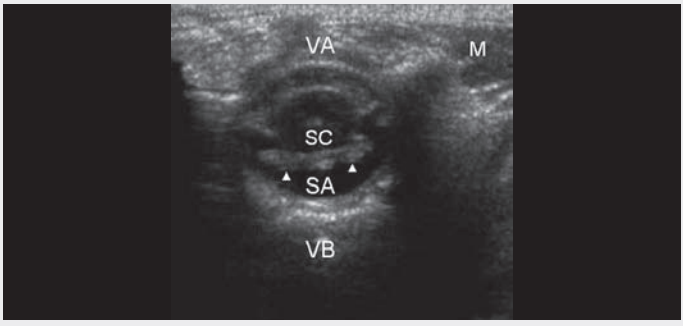

The vertebral bodies of the column are seen as echogenic structures ventral to the spinal cord. The echogenic vertebral arches produce ventral shadows on axial scans. Pulsatile motion of the cord and small vascular structures on the anterior and posterior surfaces of the cord, presumably representing anterior and posterior spinal arteries and veins, are seen routinely with the Doppler technique.

Fig. 5.215. Normal medullaris conus in a 12-day-old boy. Sagittal scan shows the echo-poor cord and the tapered termination of the spinal cord (arrow) at the level of the L1–L2 vertebrae; elements of the cauda equina producing linear reflections directed caudally (arrowheads)

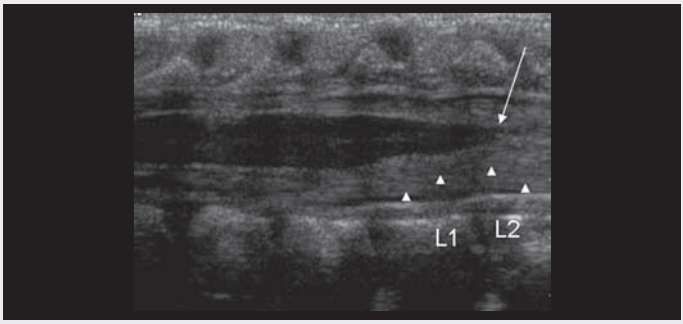

Fig. 5.216. Ventriculus terminalis in a 5-day-old girl. Sagittal scan shows a small ependymal cystic structure (arrows) at the transition from the tip of the conus medullaris (CM) to the origin of the filum terminale. NR, nerve roots

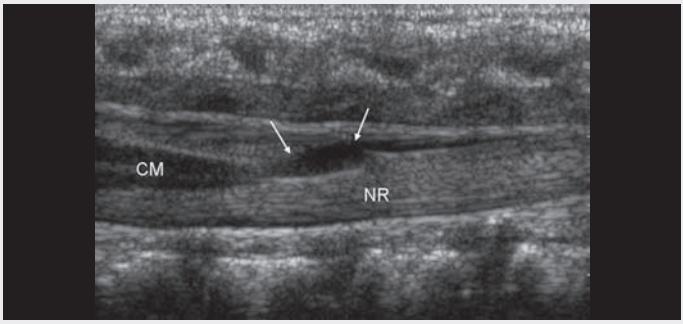

At birth, the spinal cord is relatively straight owing to the straight bony spine. It contains a central canal, which extends from the cervicomedullary junction to the lower end of the spinal cord. Transient dilatation of the central canal can be seen, but it should be no greater than 2 mm in diameter. The conus medullaris should normally end at the level of the L1–L2 vertebrae (Fig. 5.215). It is cone-shaped and may be slightly bulbous, with a low, central cerebrospinal fluid cavity, which is the ventriculus terminalis, a small, ependymal, oval, cystic structure positioned at the transition from the tip of the conus medullaris to the origin of the filum terminale (Fig. 5.216). This structure has a longitudinal diameter of 8 mm and a transverse diameter of 2–4 mm. The ventriculus terminalis develops during embryogenesis as a result of canalization and retrogressive differentiation of the caudal end of the

developing spinal cord and regresses in size during the first weeks after birth. This variant causes no clinical symptoms. The filum terminale is best visualized on the axial view. It should not be greater than 2 mm in diameter; it runs along the posterior wall of the thecal sac (Fig. 5.217).

Fig. 5.217. Normal filum terminale. (a) Sagittal and (b) axial scans show the filum terminale along the posterior wall of the thecal sac, measuring less than 2 mm in diameter. CM, conus medullaris; NR, nerve roots; SA, subarachnoid space

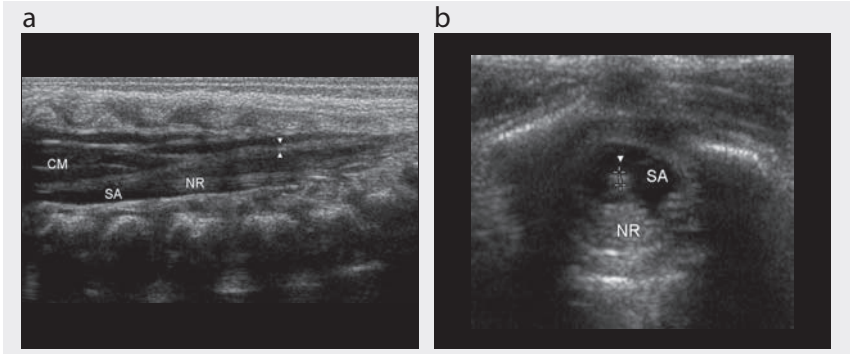

Pathological findings

Congenital malformations

Spinal ultrasound is conducted in children with spinal dysraphism in order to recognize associated malformations, such as myelocoele, myelomeningocoele, meningocoele, Chiari II syndrome, tight filum terminale syndrome, spinal lipoma, dorsal dermal sinus, hydromyelia, syringomyelia, diastematomyelia, arachnoid cyst and caudal regression syndrome. Cranial ultrasound can also show associated malformations of the brain, such as hydrocephalus and hypoplasia or aplasia of the corpus callosum.

Myelocoele or myelomeningocoele occurs in 2 of 1000 live births, with a slight female predominance. It results from localized failure of fusion of neural folds dorsally during embryogenesis. These two conditions are associated with Chiari II malformation and tethered spinal cord syndrome. In Chiari II syndrome, the cerebellar vermis herniates through the foramen magnum into the cervical spinal canal, and the fourth ventricle is narrowed and positioned low.

Ultrasound shows a low-lying spinal cord extending into the cystic back mass; the bone abnormalities are clearly seen on CT. The ultrasound appearance of tethering is a low-lying or blunt-ended conus medullaris below L2–L3, which is due to abnormal fixation of the spinal cord. Ultrasound shows an abnormally thickened filum terminale exceeding 2 mm in diameter at the level of L5–S1, sometimes in combination with a centrally located small cyst or lipoma. Typically, the tethered cord is positioned eccentrically, and failure of pulsatile movement of the spinal cord and nerve roots can be demonstrated with M-mode scanning.

Spinal lipoma is an intraspinal mass of fat and fibrous tissue that occurs in continuity with the adjacent spinal cord. It is the commonest type of occult spinal dysraphism and is classified as lipomyelocoele or lipomyelomeningocoele, fibrolipoma of the filum terminale or intradural lipoma.

In lipomyelocoele, the lipoma lies adjacent to the cleft spinal cord and extends into the central canal of the cord and into the spinal canal, causing tethering of the neural tissue. Dorsally, the lipoma is continuous with the subcutaneous fat and covered by intact skin. Lipomyelocoele is always associated with spina bifida and anomalies of the vertebrae. Spinal ultrasound shows an echogenic intraspinal mass adjacent to the deformed spinal cord. Dorsally, the mass is contiguous, with slightly echo-poor subcutaneous fat. In children with lipomyelomeningocoele, a dilated subarachnoid space can be seen. Associated malformations, such as hydromyelia and syringomyelia, can be detected with spinal ultrasound.

Dorsal dermal sinus, another type of occult dysraphism, is an epithelium-lined tract running from the skin to the spinal cord, cauda equina or arachnoid. Most are located in the lumbosacral region. Scrupulous spinal ultrasound shows the entire length of the tract, from the skin to the spinal space. When the tract is in the subcutaneous fat, it is slightly echo-poor and is sometimes difficult to detect with ultrasound.

Diastematomyelia is characterized by a sagittal cleft in the spinal cord, which is usually divided into two asymmetric hemicords (Fig. 5.218). Each hemicord has a separate arachnoidal and dural sheath if a fibrous, cartilaginous or osseous septum is present. Ultrasound performed in the axial plane typically shows both hemicords in cross-section, each with a central canal and ipsilateral nerve roots. In children with an osseous septum between the hemicords, the spinal cord is rarely seen at the level of the septum because of the shadow it produces. Spinal ultrasound can demonstrate associated malformations such as hydromyelia and syringomyelia (Fig. 5.219) and thickened filum terminale (Fig. 5.220).

Fig. 5.218. Diastematomyelia in a 3-month-old boy. Transverse scan shows two hemicords (arrows) within the spinal canal, separated by a sagittal septum (spur, empty arrow)

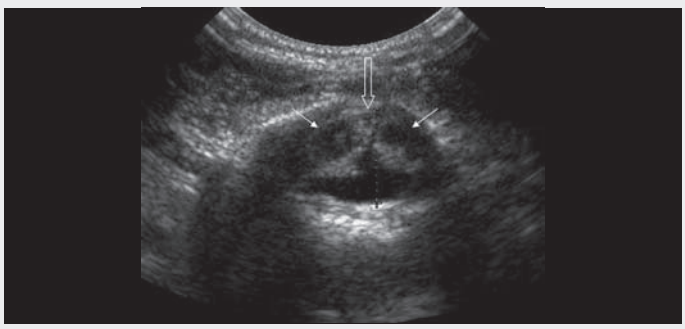

Fig. 5.219. Hydromelia in 1-month-old girl. Longitudinal and transverse scans of the thoracolumbar spinal canal show a dilated central canal (arrows). SC, spinal cord; SA, subarachnoid space

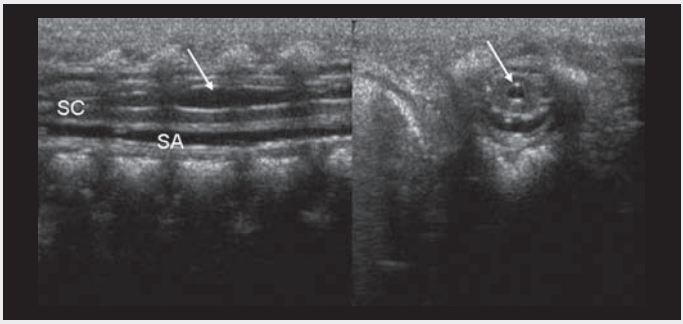

Fig. 5.220. Tight filum terminale syndrome in a 2-month-old boy. Longitudinal scan of the lumbosacral region shows a thickened filum terminale (arrowheads). SA, subarachnoid space

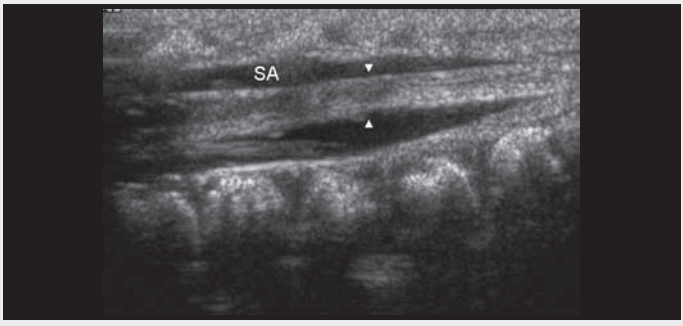

Congenital hydromyelia or syringomyelia may be the result of deregulation of cerebrospinal fluid circulation or a variant of dysraphism malformation. Spinal ultrasound shows dilatation of the central canal of the spinal cord.

Caudal regression syndrome corresponds to a spectrum of anomalies of the caudal end of the trunk, which vary from isolated partial agenesis of the sacrococcygeal spine to more severe deformities such as sirenomelia. Spinal ultrasound shows a blunt, deformed conus medullaris which terminates above the normal level of L1, with major sacrum deformities and other spinal dysraphism. Associated malformations are imperforate anus, genitourinary anomalies and renal dysplasia.

Neoplasms

Spinal tumours are less common in children than in adults and are extremely rare in infants under 6 months of age. Ultrasound can help to detect neoplasms and in deciding whether MRI should be performed. Neoplasms of the spinal cord are clearly seen with MRI.

Infection and trauma

Ultrasound can also be used as the initial imaging method in suspected birth trauma or infection of the spinal cord. It allows detection of epidural or subdural haemorrhage and complete spinal cord transection. Direct signs, such as oedema, venous congestion and haemorrhage, increase the echogenicity of the spinal cord and an epidural fluid collection; indirect signs, such as displacement of the spinal cord due to haemorrhage, are also used. Follow-up examinations reveal resorption of intraspinal blood collections, changes in cord calibre and persistently increased echogenicity due to early glial proliferation in children with myelomalacia.

In all cases, MRI is the imaging procedure of choice.

Musculoskeletal system

Indications

- musculoskeletal pain
- trauma
- suspected child abuse
- obstetrical trauma
- infectious conditions
- soft-tissue lesions
- foreign bodies
- ganglion cyst
- bursitis
- joint effusion
- neonatal hip dysplasia.

Preparation

No special preparation is needed.

Examination technique

The position of the patient depends on the organ or region to be examined and the pathology. Sagittal and axial scans of the region of interest may be performed. Doppler techniques (colour and pulsed) are helpful for demonstrating the vascular

component of a lesion or deep or superficial vein thrombosis. Dynamic compression with probe and colour Doppler imaging can facilitate detection of superficial vascular masses. Bilateral examination and comparison with the healthy side in various scanning planes may avoid a misdiagnosis.

Ultrasound examination of the musculoskeletal system is best performed with high-frequency linear or curved probes (7–15 MHz), when available.

Normal findings

At birth, the cartilaginous epiphysis is clearly seen on ultrasonography. The bone appears as a highly echogenic structure with distal acoustic shadowing, while the cartilage is more echo-poor than the adjacent soft tissue, with sparkling echoes inside it (Fig. 5.221). Ossified elements appear as bright linear or curvilinear structures and can be irregularly shaped (Fig. 5.222).

The sonographic appearance of the tendons and ligaments in children is similar to that in adults. When tendons are examined in the longitudinal plane, they appear as echo-rich structures with well-defined echogenic margins and a fibrillar appearance due to the bundles of tendon fibres. Ligaments appear as echo-rich bands with internal fibrils that join the nonossified echo-poor epiphyses of adjacent bones.

In joints, the capsule has a concave configuration; the distance between the anterior capsule and the bone is normally less than 3 mm.

Fig. 5.221. Normal epiphysis in a 3-month-old boy. Coronal scan of the hip shows the echo-poor cartilaginous epiphysis (E) with scattered internal echoes and the metaphysis (M), appearing as a bright linear structure with distal acoustic shadowing. G, acetabular cartilage

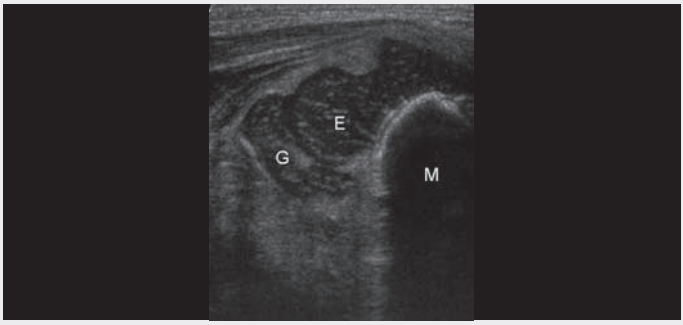

Fig. 5.222. Normal ossification centre in 5-month-old girl. Sagittal scan of the knee shows the ossification centre of the femoral epiphysis (OC) as a bright curvilinear structure within the cartilaginous epiphysis (E). M, metaphysis

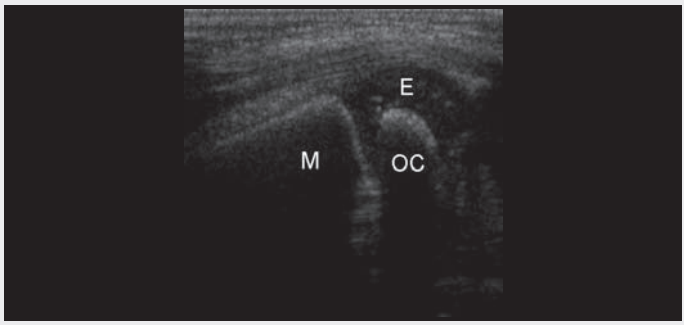

Pathological findings

Bone and joint abnormalities

Neonatal abnormalities

Developmental dysplasia of the hip, formerly called congenital hip dislocation, is a spectrum of abnormalities, ranging from mild acetabular dysplasia and reducible subluxation to irreducible subluxation of the femoral head. It is most common in breech infants and fetuses with oligohydramnios. The diagnosis is suspected clinically when physical examination reveals asymmetric skin folds, limited abduction of the hip or abnormal Barlow or Ortolani manoeuvre. Ultrasound is used systematically for diagnosis in newborns aged 1 month. As femoral head ossification centres appear at 3–6 months, simple radiographic examination is not useful in newborns. Ultrasound allows direct visualization of the cartilaginous components of the hip and makes it possible to determine the position of the femoral head and the depth of the acetabulum and to evaluate dynamic instability (Fig. 5.223, Fig. 5.224). The method for hip ultrasound reported by Graf and Harke includes evaluation of acetabular morphology, the angle of the acetabular roof (alpha angle), coverage of the femoral head and dynamic subluxation during stress manoeuvres. A combination of static (anatomical) and dynamic (physiological stress) examinations is now the standard. Colour Doppler is not generally part of the standard examination but is reported to be helpful in assessing femoral head perfusion, especially in children being treated in a Pavlik harness.

Club foot or **talipes equinovarus** can be studied relatively simply and noninvasively by ultrasound and should be part of routine assessment of neonatal clubfoot. Particularly in neonates, ultrasound complements current radiographic techniques because it demonstrates the anatomical relations of unossified bones, such as in the talonavicular and calcaneocuboid joints. Congenital limitation of dorsiflexion, the anterior position of the talus in the ankle mortise and the addition of the foot are

Fig. 5.223. Normal hip in a 1-month-old boy. Coronal flexion scan shows that the femoral head (H) is seated in the concavity of the acetabulum (A), and approximately half the diameter of the femoral head lies on either side of the ilium (IL). IS, ischium; L, labrum

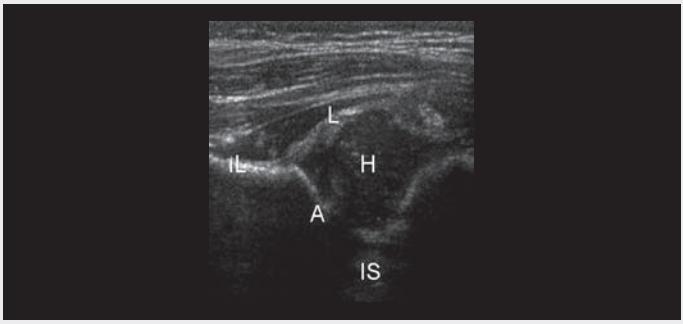

Fig. 5.224. Subluxated hip in a 2-month-old girl. Coronal flexion scan shows that the femoral head (H) is positioned laterally but maintains contact with the bony acetabulum (A) and the labrum (L). IL, ilium; IS, ischium

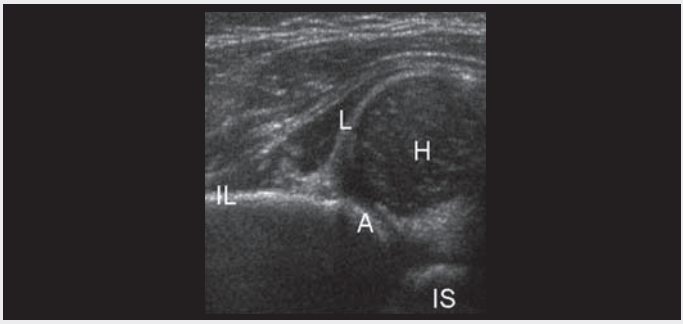

easily measured on sonograms. Furthermore, changes in the range of movement resulting from conservative treatment and surgical correction can be quantified. The hip should also be examined systematically, to identify associated hip dysplasia.

Limping child

Irritable hip is a clinical syndrome that most commonly affects children between the ages of 3 and 8 years. It is most often due to transient synovitis, a self-limiting condition for which no cause has been found. Ultrasound of the hip is recommended to detect echo-free effusions and to exclude other hip anomalies.

In synovial diseases, ultrasound is the method of choice for detecting joint effusions and for differentiating joint fluid from synovial thickening. Colour Doppler can show the extent of the vascular supply of the synovium, providing a qualitative representation of the degree of synovial inflammation. It is particularly effective for mapping the number and distribution of joints involved and has proved to be better than plain film and clinical examination for grading the involvement of joints.

Legg-Calve-Perthes disease is an idiopathic, avascular necrosis of the capital femoral epiphysis. The clinical findings include hip or knee pain, limp and limitation of internal rotation. Boys are affected more often than girls. The usual age at onset is 4–8 years. The four identifiable radiographic stages of the disease are ischaemia, revascularization, reossification and healing. Plain radiographic examination is the imaging procedure of choice for diagnosis, and ultrasound is used for staging and confirmation of diagnosis. The capital femoral epiphysis can be normal or show joint effusion.

Slipped femoral capital epiphysis is a disorder of adolescence caused by repetitive stress of weight-bearing. It is the commonest chronic Salter-Harris type 1 injury. The characteristic radiographic findings are medial, posterior and inferior positioning of the femoral head with respect to the femoral shaft. Ultrasound is used to identify children for whom improvement of the epiphyseal position by treatment is possible and safe. A new classification into acute, acute-on-chronic and chronic slipped femoral capital epiphysis has been proposed on the basis of objective sonographic data. Joint effusion represents physial instability or regression, and remodelling is a sign of chronicity. Acute slipped femoral capital epiphysis is characterized by effusion, whereas slip without effusion but with remodelling is designated as chronic, and acute-on-chronic is associated with both effusion and remodelling.

Osgood-Schlatter lesion is tibial osteochondrosis that affects pre-adolescent and early adolescent athletes. It is due to traction apophysitis of the patellar tendon insertion on the tibia tubercle. Its diagnosis is usually clinical, but radiographs and MRI can be used to exclude other causes of knee pain. Ultrasound may show thickening of the patella tendon, which may appear indistinct and partly echogenic. Fragmentation of the tibial tuberosity and echo-rich surrounding soft-tissue oedema may also be present.

Ultrasound is an effective method for detecting **occult fractures** in children. It is sensitive and specific for diagnosing small cortical fractures and, later, for demonstrating periosteal formation at the fracture site.

Fracture-separation of the epiphysis in neonates is difficult to diagnose radiologically because the cartilaginous epiphysis is radiolucent. Ultrasound in conjunction with physical examination is the method of choice in diagnostic evaluation, by providing clear differentiation of the bone, the cartilaginous epiphyses and the joint space, recording the direction and extent of displacement and demonstrating the presence of blood and debris in the joint space (Fig. 5.225). Ultrasound is also suitable for detecting, localizing and characterizing a variety of traumatic disorders of the muscles, tendons and ligaments in children. In the context of the battered child, it is useful for diagnosing and following up associated visceral injuries.

Fig. 5.225. Fracture-separation of the distal humeral epiphysis in a newborn girl. Sagittal scan shows displacement (arrow) of the humeral epiphysis (E). M, metaphysis

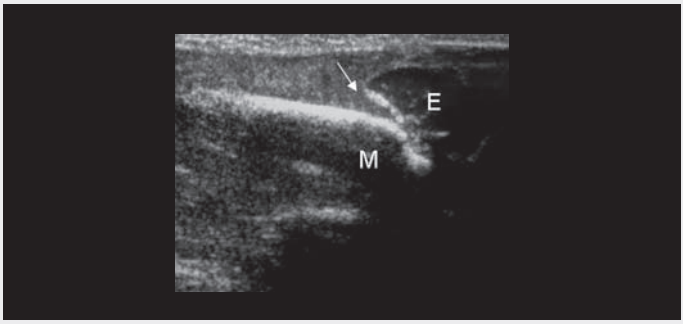

Infections

Osteomyelitis

Bone can be infected by extension from contiguous soft-tissue or joint infection or via the bloodstream from a remote source. Acute haematogenous *osteomyelitis* is frequent in children. Gram-positive cocci are common, but many infectious agents are seen. Haematogenous osteomyelitis usually involves the highly vascularized metaphyses of the fastest growing bones, such as the distal femur, proximal tibia and proximal humerus. The clinical manifestations are pain, fever, swelling and increased inflammatory markers in blood serum. Blood culture is positive in 50% of cases of acute osteomyelitis and is often required to diagnose infection accurately.

At the earliest stage of acute osteomyelitis, all imaging modalities show soft-tissue swelling and hyperaemia adjacent to the affected bone. Ultrasound is accurate in showing these nonspecific abnormalities and must be performed as soon as possible, before antibiotic therapy is established. The diagnosis is confirmed by MRI, if available, and bone scintigraphy with technicium-99m. MRI shows marrow alteration and the extent of disease in bone, soft tissue and adjacent joint at the same time. The most characteristic ultrasonic feature of osteomyelitis is subperiosteal fluid collection contiguous with the bone (Fig. 5.226). When the initial study does not show these features, it must be repeated regularly, at best daily during the 1st week. Ultrasound is the modality of choice for diagnosing subperiosteal and superficial abscesses and for guiding aspiration of these collections. MRI, nuclear medicine and CT are indicated to demonstrate intraosseous sequestering or collection during follow-up, and also for profound localization. Nuclear medicine is useful in multifocal forms. Early diagnosis and treatment of acute osteomyelitis preclude chronicity.

Fig. 5.226. Acute osteomyelitis with subperiosteal abscess in a 6-year-old boy. (a) Longitudinal and (b) axial scans show a spindle-shaped (arrows) subperiosteal fluid collection (C) contiguous with the bone (B)

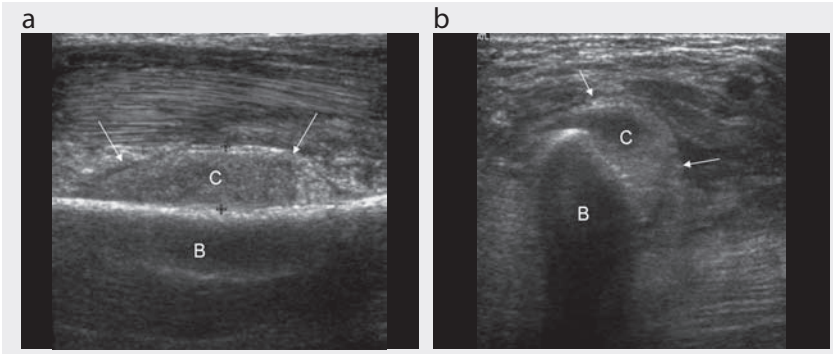

Septic arthritis

Septic arthritis results from haematogenous inoculation of joints in septicaemia or contiguous extension from a focus of osteomyelitis. Group B streptococcus is the commonest causative organism in neonates, while *Staphylococcus aureus* is the commonest in infants. Treatment is urgent because of the high risk for progression toward destructive joints. Radiographs are usually normal in the early stages, and ultrasound is sensitive for confirming joint effusion (Fig. 5.227) and for evaluating periarticular soft tissues. The capsule-to-bone width and echogenicity of the fluid are variable (Fig. 5.228). Fluid aspiration must be conducted with care, regardless of the ultrasound findings. Colour Doppler helps to eliminate venous thrombosis, which is frequently associated.

Fig. 5.227. Septic arthritis in a 4-year-old girl. Sagittal scan of the right hip shows fluid (F) distending the joint capsule, which has a convex margin (arrows)

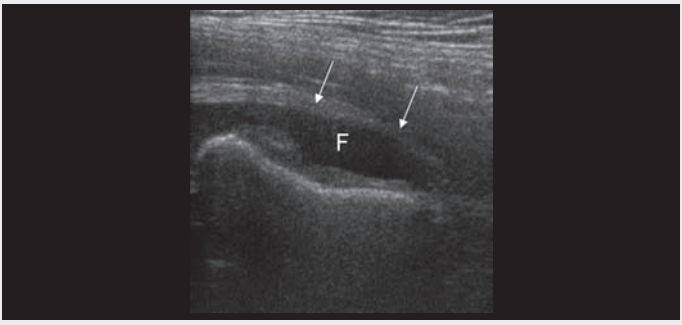

Fig. 5.228. Septic hip dislocation in a newborn girl presenting with fever and lack of movement of the right hip. (a) Frontal radiograph of the pelvis shows hip dislocation (arrow). (b) Coronal scan of the right hip shows septic arthritis with dislocation of the femoral head (H). F, fluid; IL, ilium; A, acetabulum; arrow, labrum

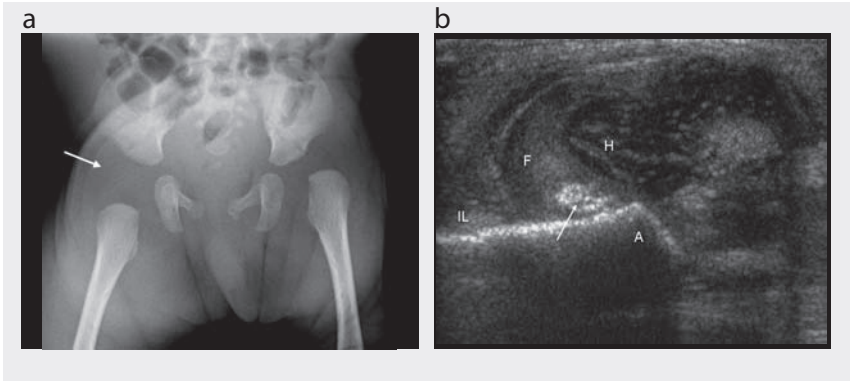

Soft-tissue abnormalities

Vascular lesions

Haemangioma or capillary haemangioma is one of the more common soft-tissue lesions in children. It contains vascular and nonvascular elements, such as fat, fibrous tissue and smooth muscle. Typically, it appears shortly after birth, initially with rapid growth and then usually undergoing spontaneous involution. The lesion can arise within superficial or deep soft tissues. Greyscale ultrasound shows a homogeneous or heterogeneous mass, which is usually predominantly echo-poor. Ultrasound is useful in diagnosis because it can demonstrate a pattern of low internal reflectivity and may also show compressibility of the lesion. The characteristic marked internal blood flow can easily be seen on colour Doppler, which also shows high vessel density.

Vascular malformations include arteriovenous, venous, capillary and lymphatic malformations. They are not often present at birth but become apparent as the child develops. Vascular malformations are usually sporadic but can be associated with genetic disorders, including Maffucci syndrome, Klippel-Trenaunay syndrome and Parker-Weber syndrome.

Arteriovenous malformation is a high-flow vascular lesion characterized by multiple blood vessels with direct arteriovenous connections and shunting. The sonographic findings include enlarged, tortuous vessels, turbulent blood flow with high systolic arterial flow, and reversed flow or pulsatile waveforms in the systemic vein. Colour Doppler imaging, CT and MRI after injection of contrast agents can show direct communication between the vessels involved.

Venous malformation is a slow-flow vascular lesion characterized by abnormal venous space and a normal arterial component. Clinically, it presents as a soft, compressible mass, usually of bluish colour. The sonographic findings include an echo-poor or echo-rich mass with low monophasic flow or no flow at all. The vein often contains phleboliths, characterized by echogenic foci with posterior acoustic

shadowing (Fig. 5.229). Colour Doppler shows the presence of large feeding vessels, and the probe may have to press onto the skin to confirm the vascularity.

Capillary malformation is characterized by a collection of small vascular channels in the dermis. Images are usually normal, although increased thickness of the subcutaneous fat and prominent venous channels may be seen in some children.

Lymphatic malformations, also known as **lymphangiomas** and **cystic hygromas**, are composed of dilated lymphatic channels. They are rarer than haemangiomas. About 75% are found in the neck, and 50–60% are found at birth. Cystic lymphangioma can readily be examined by high-resolution ultrasonography. As expected from their cystic nature, they typically appear as thin-walled, multilocular, predominantly fluid-filled masses.

Fig. 5.229. Venous malformation in a 3-year-old girl. Transverse scan shows an ill-defined, echo-poor mass (M) containing phleboliths (arrows) within the muscles

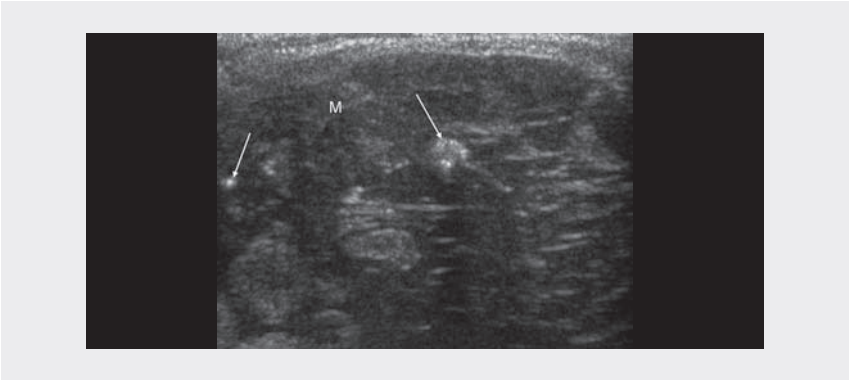

Benign nonvascular lesions

Lymph nodes may be found in a variety of locations in children, especially in the cervical region. On ultrasound, they are well-defined, homogeneous lesions, usually near vascular bundles. They have a characteristic vascular pattern, with extensive vascularity centrally; if they are benign and reactive, they often have a highly echogenic hilum (hilus sign). Benign nodes are small, with a greater longitudinal axis. Malignant lymph nodes are rounded, enlarged, of lower echogenicity and may have identifiable peripheral vascularity on colour Doppler, depending on the primary tumour; the resistivity index of malignant lymph nodes is higher (> 0.80) than that of reactive ones.

Fibromatosis colli (see also section on Neck Trauma, above) is a benign lesion of the sternocleidomastoid muscle, which is postulated to be due to birth trauma or peripartum injury. Infants usually present with an anterior neck mass by 2 weeks of life. The lesion frequently regresses over 4–8 months with conservative therapy. Greyscale ultrasound shows a subtle alteration of the echo structure and muscular enlargement within the sternal or clavicular head of the sternocleidomastoid. An

echo-poor mass, an echo-rich mass and mixed echo texture have all been described in fibromatosis colli.

Fibromatosis is a histologically benign but locally aggressive lesion. It usually occurs after puberty but has been reported in younger children. On ultrasound, the echogenicity and homogeneity of the lesion are nonspecific.

Lipomas are the commonest fat-containing soft-tissue masses in children. They are composed of mature adipose tissue. On sonography, they appear as oval, usually well-defined, homogeneous masses, which in general are echo-rich with no detectable blood flow on colour Doppler.

Lipoblastoma is a rare fatty tumour that occurs almost exclusively in children under 3 years of age. It contains multiple lobules of immature fatty tissue separated by fibrous septa. Sonography often does not allow differentiation between lipoma and lipoblastoma.

Neurofibromas are the commonest neural tumours in children. They arise within peripheral nerve fibres, occurring either sporadically or in association with neurofibromatosis type I. On ultrasound, benign neurofibromas are homogeneous, well-defined, round or oval echo-poor lesions with a characteristic location in the neurovascular bundle.

Dermoid and epidermoid cysts are benign developmental choristomas. The lesions have a smooth contour and variable internal echogenicity on ultrasound. Most appear as oval, well-defined echo-free masses, with calcifications or fatty components.

Soft-tissue **haematoma** is usually caused by a myotendinous injury or a direct blow and tends to resorb after 6–8 weeks. The ultrasound findings depend on the time of imaging after the injury. In the acute phase, a haematoma may appear as a cloud of fine echoes and is sometimes difficult to differentiate from normal or swollen muscle. Later, ultrasound may show a complex ovoid mass with internal echoes and septations, which eventually becomes echo-free. The surrounding subcutaneous soft tissues usually show no inflammatory change.

Popliteal cyst occurs behind the knee and is less common in children than in adults. It is an echo-free lesion with acoustic enhancement behind and between the semimembranosus tendon and the medial head of the gastrocnemius muscle.

A **chronic foreign body** may cause inflammation in the surrounding tissue and present as a soft-tissue mass well after a traumatic event. Children in particular may not remember introduction of the foreign body. Wood splinters are common and are not seen on plain radiographs. Ultrasound may identify chronic or acute foreign bodies in subcutaneous tissues (Fig. 5.230). Most appear as an echo-rich focus associated with acoustic shadowing or reverberating comet-tail artefacts, surrounded by an echo-poor area due to surrounding oedema. If ultrasound is performed after an attempt has been made to remove the foreign body, the examination can be difficult. Ultrasound can be used to guide removal.

Fig. 5.230. Foreign body in a 5-year-old girl. Longitudinal scan shows an echogenic linear structure (arrows) indicating a wood splinter and a surrounding echo-poor area representing oedema

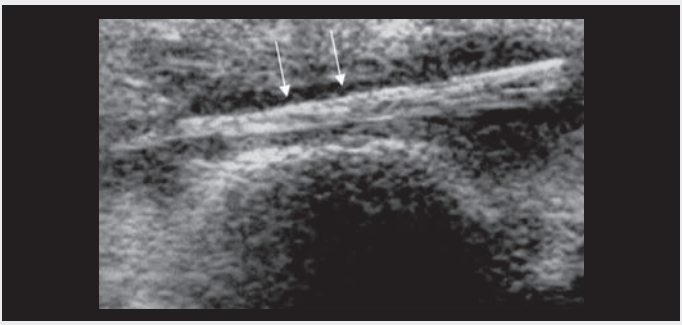

Malignant tumours

Malignant tumours are rare in children; they are generally considered to represent about 1% of all soft-tissue tumours. The commonest lesion is rhabdomyosarcoma, and the next commonest is synovial sarcoma. Rare sarcomas include fibrosarcoma, neurofibrosarcoma, malignant histiocytoma, leiomyosarcoma, alveolar part sarcoma and liposarcoma.

The imaging features of these malignant soft-tissue tumours are nonspecific. They can be homogeneous or heterogeneous and well circumscribed or poorly defined and infiltrative. On sonography, they may be echo-poor, isoechoic or echo-rich to the adjacent soft tissues. The role of ultrasound in the initial diagnosis of a soft-tissue malignancy is to determine whether the lesion is solid and then to define those lesions for which a clear diagnosis can be made by ultrasound alone. Ultrasound is useful for guiding biopsy once staging with MRI has been performed. Core needle or surgical biopsy is often necessary for a definitive diagnosis.

Soft-tissue infections

Cellulitis is an infection of the subcutaneous soft tissues. *Staphylococcus aureus* and *Streptococcus pyogenes* are the commonest organisms involved. The clinical findings are erythema, cutaneous oedema and tenderness. Ultrasound shows increased echogenicity of the subcutaneous fat, often with fluid in the fascial layers (Fig. 5.231). A differential diagnosis can be made from osteomyelitis and deep venous thrombosis. Skeletal scintigraphy and MRI can be used to distinguish between cellulites and osteomyelitis.

Abscesses are suppurative fluid collections circumscribed by a wall. Ultrasound shows an echo-poor or echo-free fluid collection with internal mobile echoes, septations and a hyperaemic wall. Colour Doppler demonstrates

Fig. 5.231. Cellulitis in a 6-year-old girl. (a) Longitudinal scan of the left leg shows increased echogenicity of the subcutaneous fat (arrows). (b) Longitudinal scan of the right leg shows normal subcutaneous fat. M, muscle; B, bone

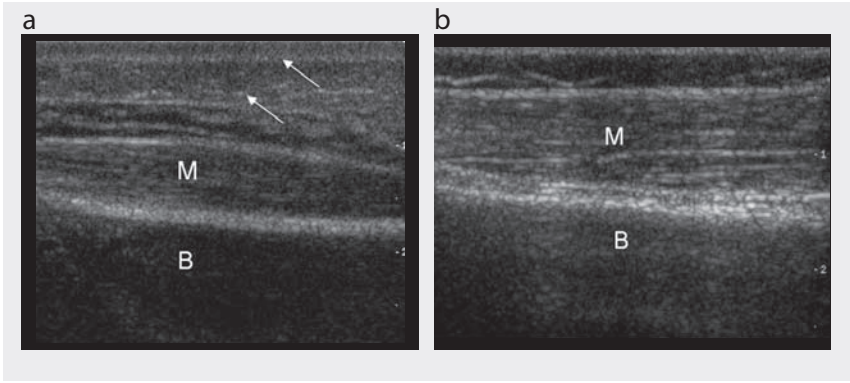

the absence of blood flow in the lesion. Ultrasound may be used to guide aspiration. A haematoma or necrotic tumoral lesion is suspected on the basis of the clinical background.

Soft-tissue inflammatory disorders

Juvenile rheumatoid arthritis is the commonest cause of arthritis in children. The cause is unknown. Ultrasound can show echo-rich tenosynovitis, echo-poor joint fluid, synovial thickening, pannus or a synovial cyst.

Dermatomyositis or juvenile dermatomyositis is an idiopathic inflammatory myopathy with diffuse nonsuppurative inflammation of striated muscle and skin. Ultrasound can show a diffuse echo-rich muscle with subcutaneous calcifications or muscle atrophy.

Special clinical situations

Abdominal pain

Abdominal pain is a frequent symptom in children, and in 80% of cases no diagnosis is made. Minimum exploration should, however, be done to exclude an organic disorder. Before imaging is begun, the medical history of the child should be recorded carefully. Acute or chronic, generalized or localized pain, fever, a palpable mass and the age of the child are the main aspects to be considered.

Ultrasound is a suitable imaging tool in such situations, because it is harmless and versatile. Other modalities, such as chest radiography, are necessary to complement ultrasound in some situations.

Acute abdominal pain

In acute abdominal pain, ultrasound is used to demonstrate or exclude the following mechanical and inflammatory disorders:

- Abdomen: ascites, masses, abscesses, inguinal hernia;
- Liver and bile ducts: focal lesions, dilatation of the bile ducts, cholecystitis;
- Pancreas: pancreatitis;
- Spleen: enlargement, focal lesions;
- Digestive tract: appendicitis, regional lymphadenitis, gastroenteritis, colitis, ileal intussusception, ileal volvulus (bowel malrotation), rheumatoid purpura with intestinal wall haematoma, gastroduodenal ulcer;
- Urinary tract: dilatation of the renal pelvis and ureters;
- Chest: pleural effusion, pneumonia.

Chronic abdominal pain

In chronic pain, in addition to the disorders listed above, the following should be considered:

- Abdomen: tumours, enlarged (mesenteric) lymph nodes, intestinal parasitosis, hydatid cysts, hernias;
- Gall bladder: abnormalities (choledochal cysts), stones;
- Digestive tract: tumours, enlarged mesenteric lymph nodes, foreign bodies (bezoars), bowel malrotation;
- Urinary tract: obstructive syndromes, calculi, pyelonephritis, tumours;
- Genitalia: pelvic or scrotal mass, ovary cysts, haematocolpos, hydrometrocolpos, pregnancy in older girls;
- Outside the abdomen: pneumonia, spinal anomalies, tuberculosis, psoas muscle abscess.

Neonatal intestinal obstruction

Duodenal obstruction

Intrinsic obstruction: atresia, stenosis, diaphragm

The usual diagnostic approach in neonatal digestive pathology has changed in the past few years. Digestive malformations have become more common, and ultrasonic exploration or digestive MRI, if available, allow precise assessment of the malformation and clear etiological orientation. Neonatal bowel obstruction has multiple causes. Duodenal obstructions are easy to recognize and always require radical surgery.

Therapeutic decisions can be made only after a precise differential diagnosis. Once the presence of an obstruction has been established, its cause must be determined. Plain abdominal films are usually essential to localize the obstruction but cannot always identify an intestinal perforation. Ultrasonography is therefore an essential complement to plain abdominal films, leading to increasingly precise

categorical diagnosis of an organic occlusion, continual visualization of the colon and precise localization of the obstruction, indicating use of a contrast enema in low small-bowel obstruction.

There are multiple causes of duodenal obstruction, including obliteration of the duodenal lumen (due to duodenal atresia, stenosis or diaphragm), obstructive complications of malrotation, with obstruction by Ladd bands, and midgut volvulus. Rarely, it is due to obstructive duodenal duplication. The obstructive role of a preduodenal portal vein or an annular pancreas is not clear.

The pathophysiology of duodenal atresia or stenosis is incompletely understood, but absent recanalization of the digestive lumen between the 8th and the 10th week is the most likely explanation. It thus consists of an early disorder of organogenesis, with biliopancreatic regional anomalies and many other malformations, including oesophageal atresia, renal abnormalities, vertebral malformations and congenital heart disease. Duodenal atresia or stenosis is also commonly associated with trisomy 21.

Intrinsic congenital obstruction of the duodenum is relatively rare, occurring in 1/10 000 to 1/40 000 births. It is now frequently diagnosed prenatally, with hydramnios in 50% of cases. It is located exclusively in the second part of the duodenum, and in 80% of cases the obstruction occurs below the ampulla of Vater.

The typical presentation is a flat abdomen and early bilious vomiting. Plain radiography reveals the double-bubble sign, representing air in the stomach and proximal duodenum, contrasting with the absence of gas in the intestine distal to the duodenum (Fig. 5.232). Most clinicians consider this radiological aspect sufficient to make a diagnosis and to refer the newborn to a paediatric surgeon; however, the surgeon should be given a more precise pretherapeutic ultrasonographic assessment, based on both the double liquid bubble and an annular pancreas. Early ultrasound can also distinguish a diaphragm from atresia (Fig. 5.233). The absence of malrotation must be verified by studying the position of the mesenteric vessels by ultrasound (Fig. 5.234). Ultrasonographic study of the colon and rectum is essential: if the atresia

Fig. 5.232. Duodenal atresia in a newborn boy. Supine radiograph shows gas in the stomach (S) and a markedly dilated duodenal bulb (D), producing the double-bulb sign

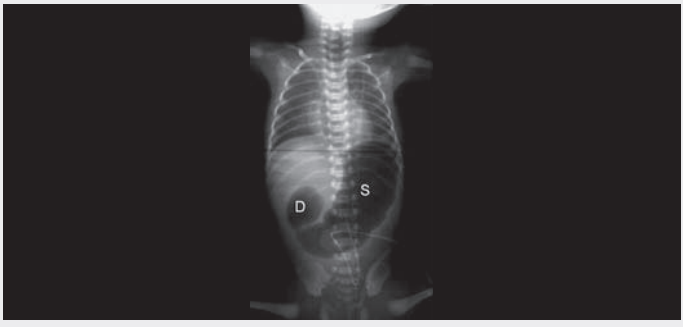

Fig. 5.233. Duodenal diaphragm in a newborn girl. Transverse scans (a), (b) show a thin convex, curvilinear structure extending across the lumen of the second portion of the duodenum (arrow) after a normal supine radiograph

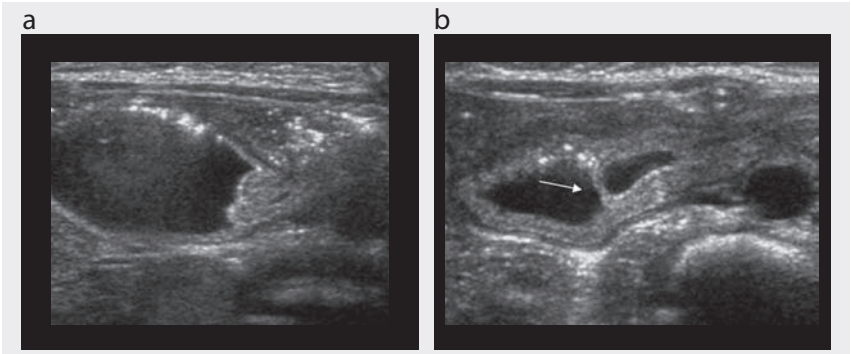

Fig. 5.234. Normal mesenteric vessels in a newborn boy. Transverse scan shows the superior mesenteric vein (SMV) anterior to and to the right of the artery (SMA). Ao, abdominal aorta

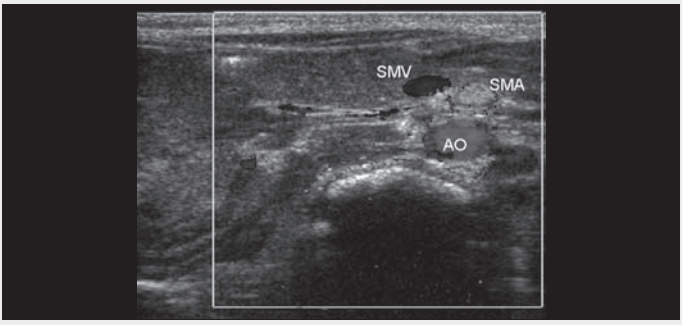

is single, the colon diameter is normal (Fig. 5.235); if there are multiple atresias, there is a microcolon. Associated malformations of the heart, kidneys and bile ducts should also be sought by ultrasound.

If the duodenal dilatation is severe with no gas distal to the obstruction, atresia or a tight diaphragm should be suspected; however, complete obstruction due to malrotation cannot be ruled out. When there is less duodenal dilatation and especially when gas is seen distal to the duodenal obstruction, a precise diagnosis cannot be made, as it could be due to duodenal atresia with biliary duct bifidity, a diaphragm, malrotation with duodenal compression by a Ladd band or malrotation with midgut volvulus, which is the most important differential diagnosis.

Fig. 5.235. Normal rectum in single atresia in a newborn boy. Longitudinal scan shows a rectum (R) of normal diameter. B, bladder

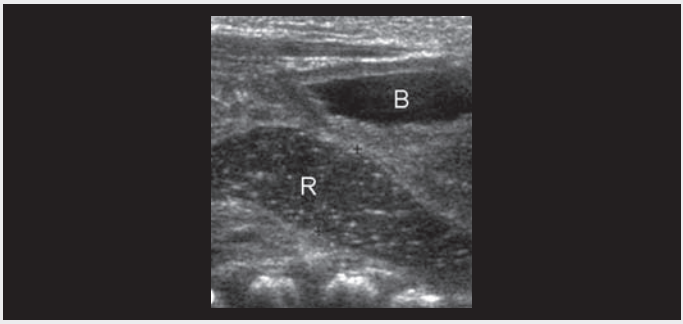

Obstructive complications of malrotation

Malrotation in neonates, which is seldom asymptomatic, usually presents as obstructive complications, such as Ladd band obstruction or malrotation with midgut volvulus, which requires urgent surgical intervention because of the risk for digestive ischaemia.

Rotation anomalies are not a distinct entity but a continuum of malformations, reflecting an embryological attack at any time during development of the primitive intestinal gut. Interruption of intestinal rotation at 90° (nonrotation) does not incur a major risk for volvulus because the mesentery root is long enough; however, if rotation stops at 180°, the jejunum follows the duodenum and occupies the right lower quadrant, and there is no duodenojejunal flexure. The ileocaecal junction joins the subhepatic area abnormally through peritoneal duodenocolic bands, and Ladd bands pre-cross the duodenum, frequently causing greater or lesser extrinsic compression. The first jejunal loop and the last ileal loop are close to each other, and the mesenteric root is extremely short, resulting in a high risk for volvulus. The presence of green vomiting in a newborn must therefore be considered a sign of malrotation with midgut volvulus, pending proof of a different cause.

The typical plain abdominal radiological image is of incomplete duodenal obstruction, with little distal digestive gas. When the obstruction is complete, the volvulus cannot be distinguished from duodenal atresia, and the plain radiograph may appear normal, which is dangerous if it halts the investigation. Therefore, an upper gastrointestinal series should always be conducted to show the abnormal position of the duodenojejunal flexure and the torsion whirl. Even so, if obstruction is complete and the whirl tight, the volvulus will not be seen. Axial imagery and ultrasound show the position of the mesenteric vessels. Ultrasound detection of inversion of the mesenteric vessels in malrotation must sometimes be confirmed in an upper-gastrointestinal series, while volvulus can be diagnosed by ultrasound

alone. In this urgent context, ultrasonographic diagnosis should be used to confirm the malrotation (Fig. 5.236) and localize the volvulus mass (Fig. 5.237), and the torsion should be visualized by colour Doppler.

The mesenteric whirl is seen as a prevertebral mass 15–20 mm in diameter located in front of the aortic axis, with clear ultrasonic characteristics: the superior mesenteric artery is surrounded by the whirl built up by the superior mesenteric vein, which is usually turgescent, and by the mesentery and the digestive loops. Colour Doppler shows the clockwise direction of the whirl and sometimes the number of whorls.

Fig. 5.236. Digestive malrotation in a newborn girl. Transverse scan shows inverted positioning of the mesenteric vessels (arrows), with the superior mesenteric artery (SMA) lying to the right of the superior mesenteric vein (SMV). Ao, abdominal aorta

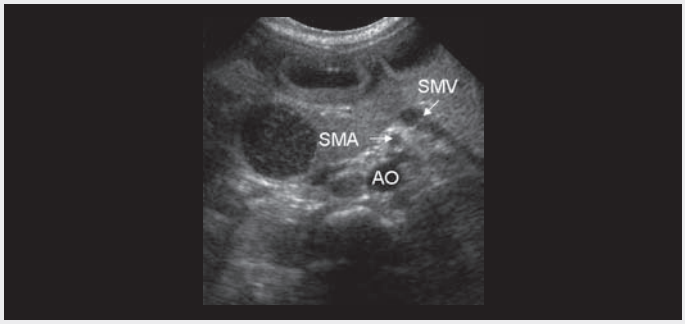

Fig. 5.237. Malrotation with midgut volvulus in a newborn boy with bilious vomiting. Transverse scan (colour Doppler) shows a prevertebral mass 19 mm in diameter in front of the aortic axis; swirl pattern of the superior mesenteric vein (SMV) as it twists around the superior mesenteric artery (SMA)

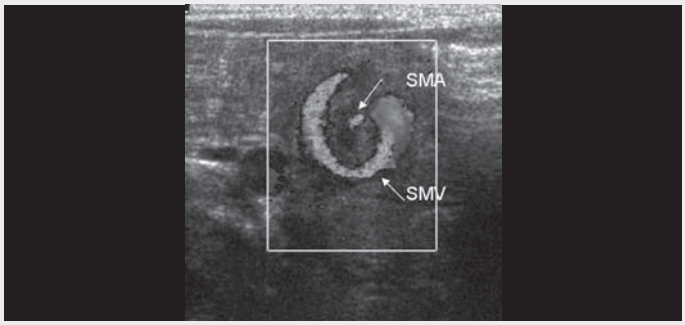

Fig. 5.238. Malrotation with midgut volvulus in a newborn girl. Transverse scans shows (a) no flow in the prevertebral mass and (b) cross-sections of fluid-filled small bowel loops with a thin wall

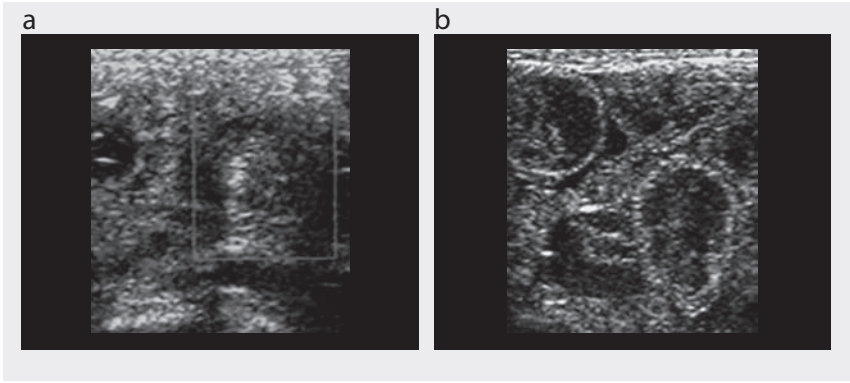

This diagnosis must always be accompanied by an ultrasonic evaluation of the prognosis, particularly if there are clinical signs of digestive ischaemia, such as shock, bloody diarrhoea or abdominal distension. The evaluation should include a search for thickening or thinning of the digestive wall, motionless loops, peritoneal fluid, haemodynamic anomaly of the superior mesenteric artery and absence of flow in colour Doppler in the whorl of torsion (Fig. 5.238).

Small-bowel obstruction

Postnatal small-bowel obstruction can usually be confirmed on the basis of clinical and radiological assessments. The cause is more difficult to determine and is the true diagnostic challenge of a paediatric radiologist. The mechanism of these obstructive lesions varies, from jejunoileal atresia to multiple atresias; an abnormal meconium consistency, as in meconium ileus in cystic fibrosis; or abnormal small-bowel peristalsis, as in megacystis-microcolon-intestinal hypoperistalsis syndrome. To identify the mechanism, the imaging method must show intestinal peristalsis, allow measurement of the loops on both sides of the site of obstruction and specify the intraluminal contents of the proximal and distal loops.

A plain abdominal film shows proximal bowel distension, while contrast enema shows the consequences of a digestive obstruction on the distal bowel and its contents. Ultrasound shows digestive motility, proximal loop dilatation, and distal digestive collapse and provides details of the fluid or meconial content on both sides of the obstructive site. As the gas content of the digestive bowel is sometimes dangerous, an ultrasound should be conducted immediately after birth.

Small-bowel atresia

Small-bowel atresia and stenosis account for 40% of organic obstructions. Atresia is responsible for 95% of neonatal obstructive syndrome, and screening by ultrasound and MRI is frequently performed at the fetal stage. Small-bowel atresia is the result of a mechanical ischaemic accident occurring after week 12 of gestation in the region of the superior mesenteric artery. Ischaemic necrosis of variable severity leads to resorption of the digestive segment in aseptic media and fibrous scarring or disappearance. This can be due to a primary vascular accident near the superior mesenteric artery or secondary to a volvulus, an internal hernia, intussusception or parietal narrowing (laparoschisis).

The clinical findings of jejunoileal atresia are characteristic and appear within the first hours of life. Bilious emesis is constant and the more proximal the obstacle, the earlier and more abundant is the vomiting; the more distal the object, the greater the abdominal distension. Usually there is an inability to pass meconium.

The diagnosis is based on a combination of plain abdominal films and ultrasonography. The radiological examination shows bowel loops dilated with air and fluid, especially when the atresia is located low in the bowel. There is no distal bowel gas, the colon is not seen, and there is no gas in the rectum. Radiological evaluation of a neonatal obstructive syndrome can be difficult. With a distal obstruction, it is not always easy to differentiate the small from the large bowel, and the obstructive site is difficult to evaluate because of the liquid content distal to it. As fetal screening indicates imaging immediately after birth, the diagnostic efficacy of plain abdominal films is reduced. Radiological data should therefore be complemented by neonatal ultrasound for diagnosis of small-bowel obstruction (Fig. 5.239). On sonography, fluid dilatation is seen up to the obstruction, and the loops of the thin-walled small bowel show increased hyperperistalsis. The transition zone is clearly seen, from the presence of collapsed, gasless distal loops of the small bowel if the obstructive site is in the jejunum or the middle small bowel or a microcolon if the atresia is located in the distal small bowel. Peritoneal effusion is seen frequently.

Fig. 5.239. Ileal atresia in a newborn girl. Transverse scans shows (a) fluid-filled, dilated, hyperperistaltic segments of the small bowel and (b) a small microcolon (arrow)

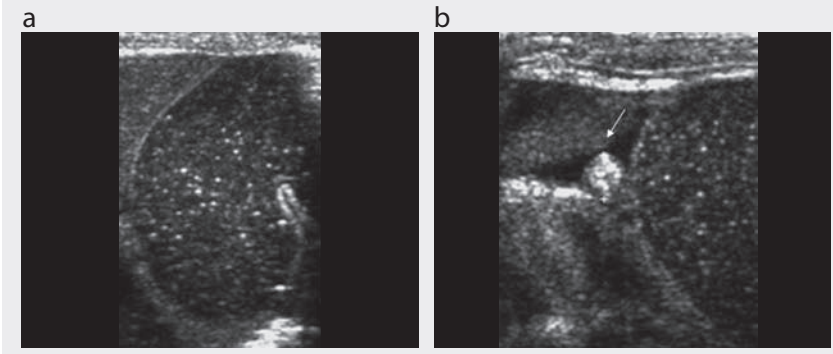

Meconium ileus

Meconium ileus is an obstruction in the final ileum due to an intraluminal obstacle made up of meconium of anomalous consistency. This condition occurs in 10–20% of newborns with cystic fibrosis, which is an anomaly of secretion of the exocrine glands. Thus, the composition of the meconium is abnormal, with low water content and high albumin content, and it adheres to the mucosa of the digestive tract. Pellets of desiccated meconium are found in the distal ileum below a collection of viscous meconium in dilated loops. The meconium ileus results in abdominal distension, bilious vomiting and failure to pass meconium.

The suggestive radiological findings are no air–fluid level, asymmetrical dilatation of the bowel loops and a granular pattern in the right iliac fossa, but they are seldom present. Generally, meconium ileus appears as a nonspecific low obstruction and is difficult to differentiate from low small-bowel atresia on clinical and radiological grounds. This differential diagnosis is, however, essential because uncomplicated meconium ileus can be treated effectively by hyperosmolar contrast enema.

Contrast enema generally allows a differential diagnosis. In distal small-bowel atresia, the microcolon opacifies quickly and there is a frank backward flow into the distal small-bowel loops. In meconium ileus, the colon fills slowly and with difficulty to reveal the meconium pellets impacted in the distal ileum (Fig. 5.240). Contrast enema is not always diagnostic, as there may be no opacification of the distal small-bowel loops due to perforation during filling.

Fig. 5.240. Meconium ileus in a newborn boy. Contrast enema demonstrates a microcolon, with a dilated distal ileum containing multiple pellets of meconium (arrows)

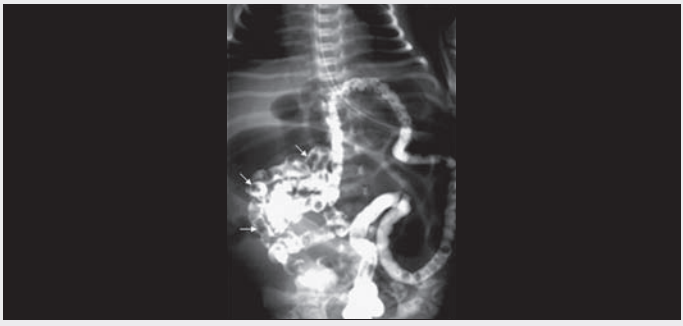

Ultrasound is useful in the diagnosis of meconium ileus (Fig. 5.241). In order to confirm an organic obstruction, dilatation of all the small-bowel loops and marked microcolon must be demonstrated. The appearance of the bowel loop content is diagnostic: dilated loops with an echogenic content (contrasting with the echo-free, fluid-filled loops in small-bowel atresia), a pseudo-thickened layer secondary to concentric layers of

Fig. 5.241. Meconium ileus in a newborn boy. (a), (b) Transverse scans show a dilated distal ileum with echogenic content and pseudo-thickened layers with ultrasound granular pattern of bowel gas trapped in the echogenic meconium (arrow)

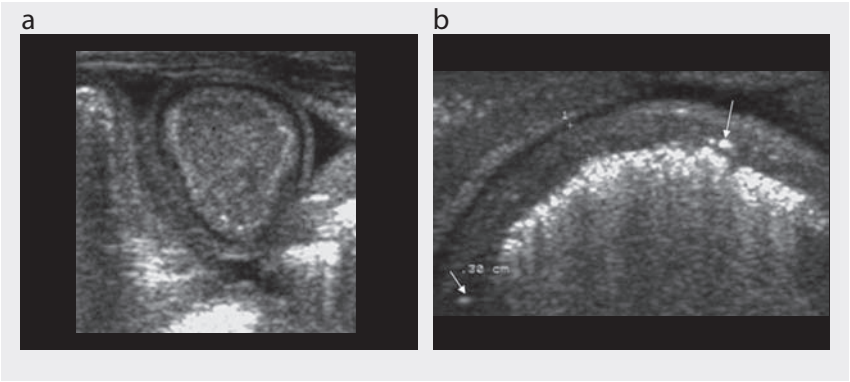

inspissated meconium in contact with the mucosa, an echographic granular pattern of bowel gas trapped in the echogenic meconium and echogenic pellets within the distal ileum.

Megacystis-microcolon-intestinal hypoperistalsis syndrome

This syndrome consists of intestinal obstruction associated with nonobstructive megacystis, probably of myopathic origin. At the digestive level, there is a short small bowel, a microcolon, no or ineffective peristalsis and, frequently, malrotation. The prognosis is poor without effective treatment, and death occurs before 6 months.

The physiopathology of this syndrome is poorly understood. The hypoperistalsis is attributed to various factors, such as ganglionic immaturity of the intestinal tract, axonal dystrophy, a degenerative disease of the smooth muscles or destruction of the smooth muscle and the neurogenic environment with fibrosis of the digestive wall.

Clinically, the newborn presents with severe abdominal distension secondary to megacystis and failure to pass meconium. On ultrasound, the infant has a large bladder, often with pelvic ureter and calyx dilatation. The digestive anomalies that confirm the diagnosis are moderate dilatation of nonperistaltic loops, major microcolon and malrotation (Fig. 5.242).

Fig. 5.242. Megacystis-microcolon-intestinal hypoperistalsis syndrome. Antenatal diagnosis at 32 weeks by MRI with ultrasound confirmation. (a) Mild small-bowel loop dilatation, no peristalsis. (b) Major microcolon (arrow) and malrotation. (c) Superior mesenteric vein (arrowhead) on the left of the superior mesenteric artery (empty arrow). (d) Megacystis and dilatation of the renal cavities. B, bladder; MC, microcolon; LK, left kidney

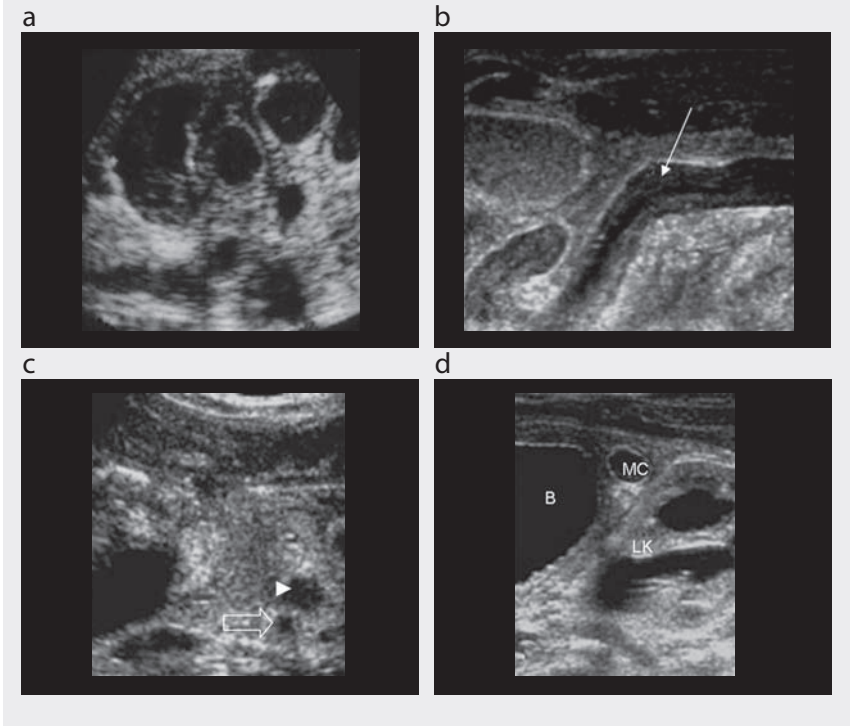

Complications of bowel obstructions

Meconium peritonitis is a frequent complication of meconium ileus (30%) and small-bowel atresia (45%). It results from antenatal digestive perforation, generally above an obstacle (atresia or volvulus). It evolves towards sterile plastic organization of the fluid and the appearance of peritoneal calcifications. The diagnosis is made antenatally by ultrasound from the presence of peritoneal and sometimes scrotal calcifications of irregular form.

Meconium peritonitis can present as a meconium (pseudo)cyst. The meconium bursts into the peritoneal cavity and initiates an intense fibroblastic reaction. The meconium is then gradually circumscribed by fibrous adherences in contact with the gathered loops. A capsule is formed by fibrous granulation, which is then calcified and encircles the fluid. A diagnosis can be made during fetal ultrasonography and confirmed by fetal MRI, which shows a cyst with a hypersignal (meconium), a microcolon and proximal small-bowel dilatation. Meconium cysts are sometimes found postnatally as an obstructive syndrome or abdominal mass. Plain abdominal film and ultrasound are necessary and sufficient to show cysts, peripheral calcifications, a microcolon and dilated small-bowel loops (Fig. 5.243, Fig.5.244). Cystic fibrosis should be suspected.

Fig. 5.243. Meconium pseudocyst in a newborn boy. Supine radiograph shows a large meconium pseudocyst with calcified walls (arrows)

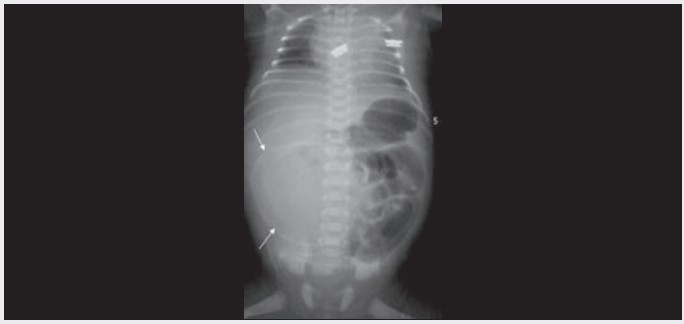

Fig. 5.244. Meconium pseudocyst in a newborn boy. Axial scans of the left quadrant show a large cystic mass (C) with calcified rim (arrow) containing internal debris, a dilated small bowel (SB) and a microcolon (MC)

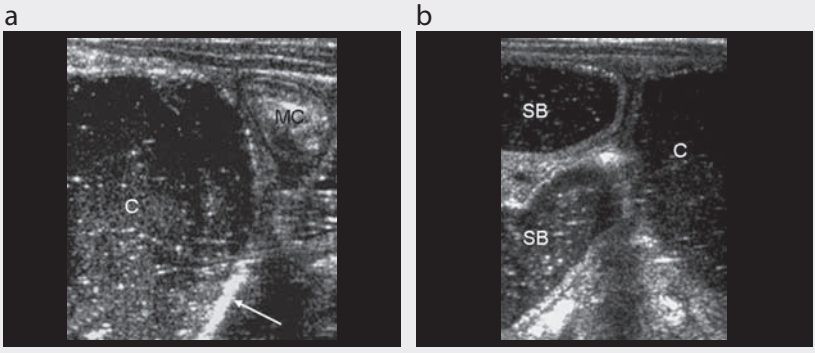

Chapter 6

Musculoskeletal system

6

Musculoskeletal system
Tendons

Use of ultrasound for studying diseases of the musculoskeletal system is increasing because of improvements in the equipment, which permit visualization of small structures that were previously inaccessible. This chapter focuses on the main diseases involving myotendinous and ligamental structures of the upper and lower members.

Tendons are composed of collagen (30%), proteoglycans (68%) and elastin (2%). Collagen fibres, 85% of which consist of type I collagen, form the primary fascicles. These give rise to secondary fascicles, which are separated by a fine, loose net of connective tissue known as the endotendon, which brings together the small nerve endings, lymphatic vessels, venules and arterioles. The endotendon is connected to the tissue surrounding the tendon, known as the epitenon. Vascularization occurs through the musculo-tendinous junction, the periphery of the tendon and the enthesis (junction with the bone). The tendon is hypervascularized during its formation but is less vascularized when mature. This basic architecture is common to all tendons.

The external covering of tendons can be vascular or avascular. Vascular tendons are covered by a single layer of synovia and loose areolar tissue, known as the paratenon, which contains the vessels that perfuse the tendons. The paratenon, together with the epitenon, gives rise to the peritendon. Avascular tendons are surrounded by a synovial sheath composed of visceral and parietal leaflets connected by a mesotendon, through which vascular structures penetrate via the vincula. These tendons receive nutrients by diffusion of synovial fluid and through the vincula. Most of the tendons of the musculoskeletal system are vascular. Only the long head tendon of the brachial biceps and the flexor and extensor tendons located in the wrists, ankles, hands and feet are avascular.

Tendons are highly resistant, and healthy tendons do not rupture. In normal tendons, lesions occur either at sites of biomechanical differences between tissues (the myotendinous junction or adjacent to bone) or in hypovascularized regions, which are considered critical, such as the third distal of the calcaneus tendon and close to the insertions of the supraspinal and brachial biceps tendons. Mechanical and vascular factors are implicated in tendinopathies, which are expressed histopathologically by the presence of tendinosis, corresponding to mucoid degeneration of the tendon, often accompanied by neovascularization, necrosis and dystrophic calcifications.

Repetitive stress on a tendon causes two types of degenerative alteration. In eccentric contraction, tendinous fibres are stretched to 5–8% more than their length, and small ruptures start to appear inside the tendon. With increased temperature, relaxation transforms 5–10% of the generated energy into heat, raising the temperature inside the tendon up to 45 °C.

Ultrasound findings

Normal tendon and tendinopathy

The normal tendon tends to present a fibrillar, echo-rich aspect on ultrasound (Fig. 6.1). The factors that determine the echotexture include insertion of muscle fibres inside the tendon, the tendinous architecture, entheses, the type of equipment and the examiner's experience.

Fig. 6.1. Fibrillar, homogeneous, echo-rich aspect of the tendon of the long head of the brachial biceps (arrow): longitudinal scan

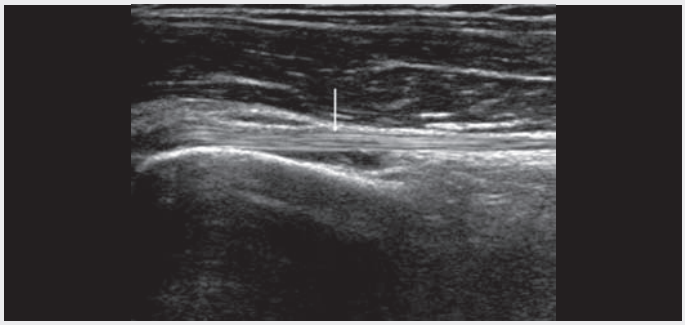

The insertion of muscle fibres inside the tendon can be illustrated by the rotator cuff of the shoulder (Fig. 6.2).

In certain musculotendinous units, more than one muscle venter contributes to the structure of the tendon. The supraspinal tendon (supraspinatus) is composed of five layers, one represented by entwinement of its fibres with those of the infraspinatus tendon (Fig. 6.3).

At the entheses, the tendon changes its histology at the point of insertion into the bone and presents fibrocartilage, which is echo-poor on ultrasound (Fig. 6.4).

Fig. 6.2. (a), (b) Supraspinal muscle fascicles represented by echo-poor bands (arrows) attached inside the tendon, simulating a fracture

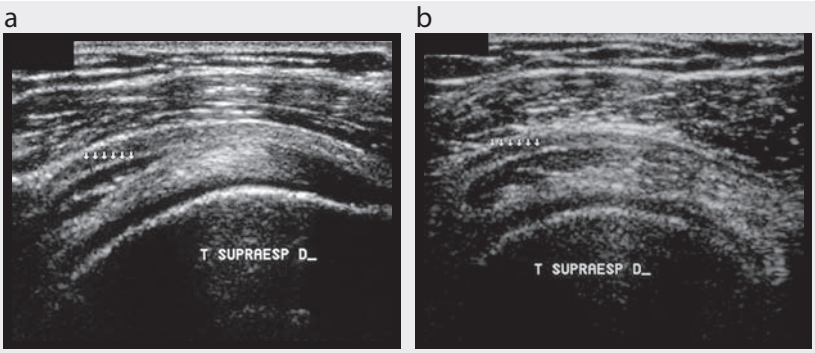

Fig. 6.3. Normal heterogenicity of the supraspinal tendon due to different spatial orientation of the layers of the tendon, generating a three-band aspect (stars)

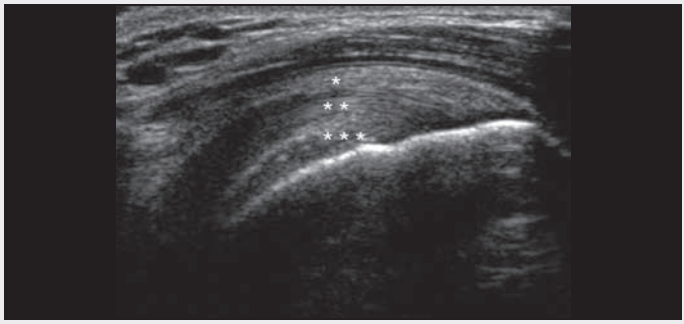

Fig. 6.4. Fibrocartilaginous insertion of supraspinal tendon with an echo-poor aspect (calipers) adjacent to the osseous cortex

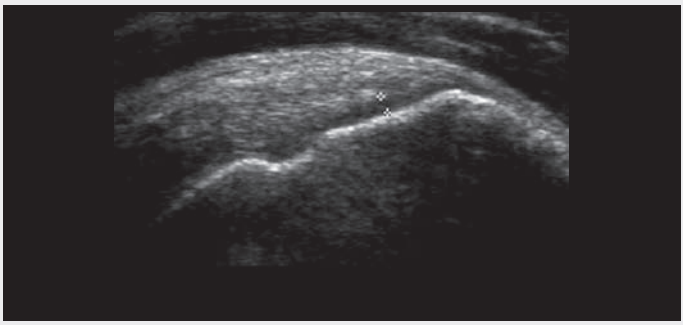

Equipment with transverse ultrasound beams significantly reduces the anisotropy generated by oblique arrival of the beam on the tendon surface, which forms echo-poor areas in the interior.

Alterations in tendinopathies start with a reduction in the echogenicity of the tendon (Fig. 6.5), sometimes accompanied by an increase in tendon thickness, secondary to the entry of water molecules into the triple-helix structure of the collagen between hydrogen bridges, which break up during tendinous degeneration. In chronic cases, calcifications can be seen as small, echo-rich foci, which is the main differential diagnoses from fibrosis and small partial ruptures.

During tendon degeneration, the process may remain stable or evolve to rupture, which can be partial or involve the entire thickness (transfixing).

Fig. 6.5. Tendinopathy of the forearm extensors, seen as a poorly defined, echo-poor area (arrow) inside the tendon

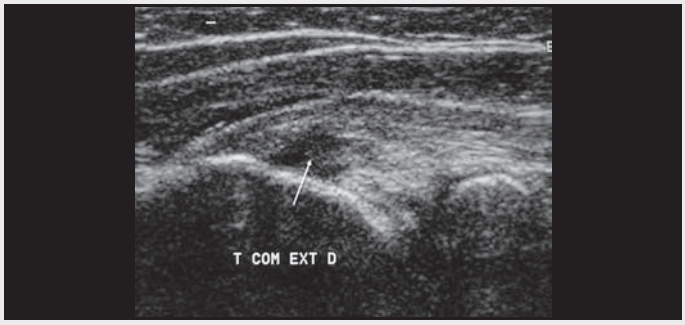

Upper limbs

Shoulder

About 60% of alterations of the shoulder are due to lesions of the rotator cuff, which is the deepest muscle group of the shoulder joint, forming a single functional unit involving the humerus head, which contributes to the stability of the glenohumeral joint and the movements of the upper member. It is composed of the supraspinatus (arm abductor), subscapularis (internal rotator), infraspinatus and teres minor (external rotators) muscles. The tendons join 15 mm proximal to the insertions at the larger and smaller tubercles of the humerus and cannot be separated by dissection. The thickness of the tendons varies from 5 mm to 12 mm. The difference from the contralateral side considered to be normal is 2 mm, and variations above this limit should be considered pathological. The function of the synovial bursae in the periscapular area is to reduce the attrition between soft tissue and bone structures. The largest is the subacromial-subdeltoid bursa, located below the acromion and the deltoid muscle venter, starting at the coracoid process and finishing some 3 cm from the larger tubercle of the humerus.

Fig. 6.6. Extra-articular section of the tendon of the long head of the brachial biceps (TCLB). (a), (c) Examination technique. Transversal (b) and longitudinal (d) scans. tme, smallest humerus tubercle; tma, largest humerus tubercle; lig trans, transverse ligament

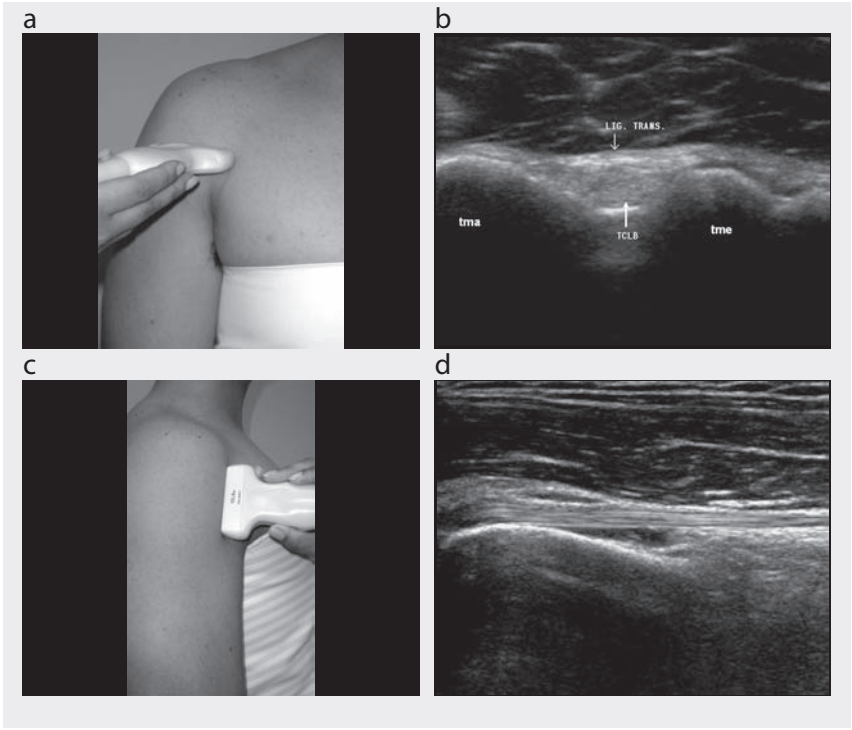

The patient must cooperate during an ultrasound examination of the tendons of the rotator cuff, as external and internal rotation manoeuvres are necessary (Fig. 6.6, Fig. 6.7, Fig. 6.8, Fig. 6.9, Fig. 6.10). Both the infraspinatus and the teres minor tendon can be evaluated either by placing the hand on the contralateral shoulder or adopting the same position as for examination of the supraspinal tendon. The pathological processes involving the rotator cuff usually affect the supraspinatus tendon, due to normal degeneration of the tendons, trauma, inflammatory arthritis or tendinosis due to excessive traction or impact syndrome.

Impact syndrome is the commonest cause of pain in the shoulder. It is defined as a group of signs and symptoms characterized by pain and progressive disabling caused by mechanical attrition of the elements of the coracoacromial arch with the structures of the subacromial soft tissues. Abduction (between 70° and 130°) associated with external rotation or anterior elevation with internal rotation of the arm are the commonest movements that cause secondary pain after subacromial impact.

Fig. 6.7. Subscapular tendon (arrow). (a), (c) Examination technique, with external rotation of the arm for better exposure of the tendon. Transversal (b) and longitudinal (d) scans. TS, subscapular tendon; PC, coracoid process; SB, bicipital sulcus; arrow, tendon of the long head of the brachial biceps; tme, smallest humerus tubercle

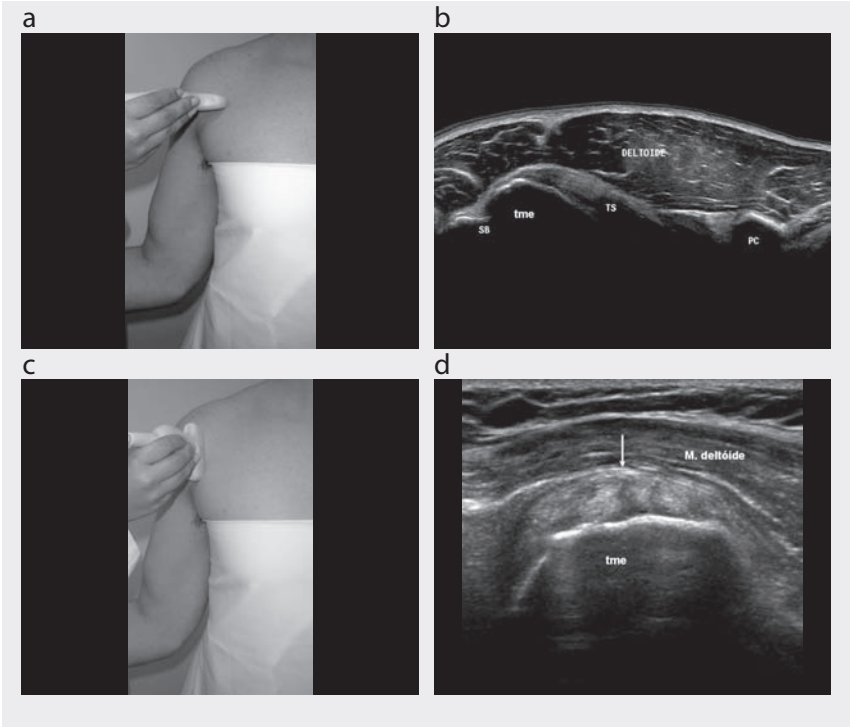

Fig. 6.8. Supraspinal tendon. (a), (c) Examination technique, with internal rotation of the arm, extension and adduction for better exposure of the tendon. Longitudinal (b) and transversal (d) scans. TS, supraspinal tendon; PC, coracoid process; bolsa, bursa subacromial sac-subdeltoid; GPS, peribursal fat; TI, infraspinal tendon; ACR, acromion; cabeca umeral, humeral head

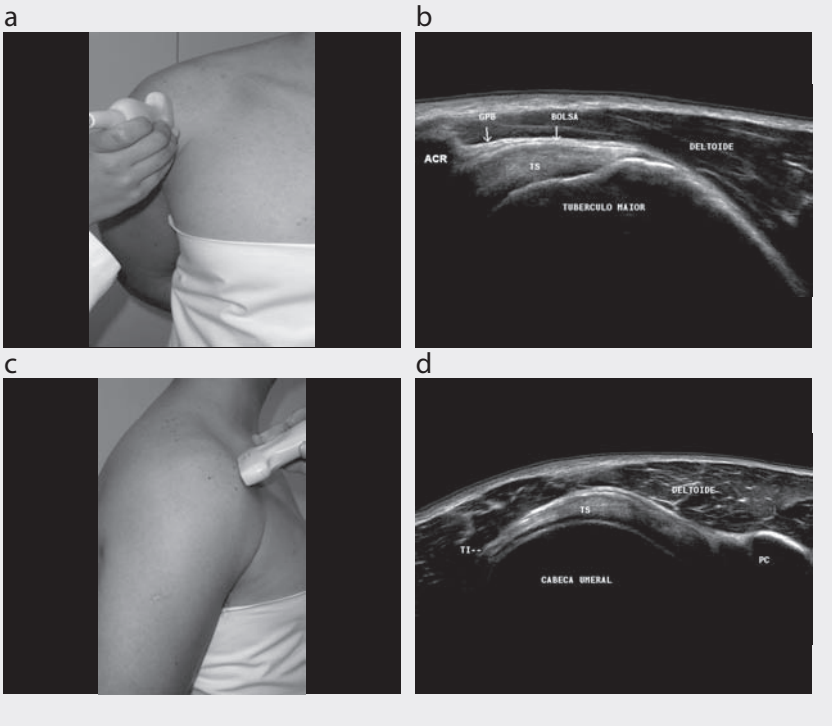

Fig. 6.9. Infraspinatus tendon (arrow). (a), (b) Examination technique. (c) Ultrasonographic examination. IF, infraspinatus muscle; glen, glenoid; t infraesp, infraspinatus tendon

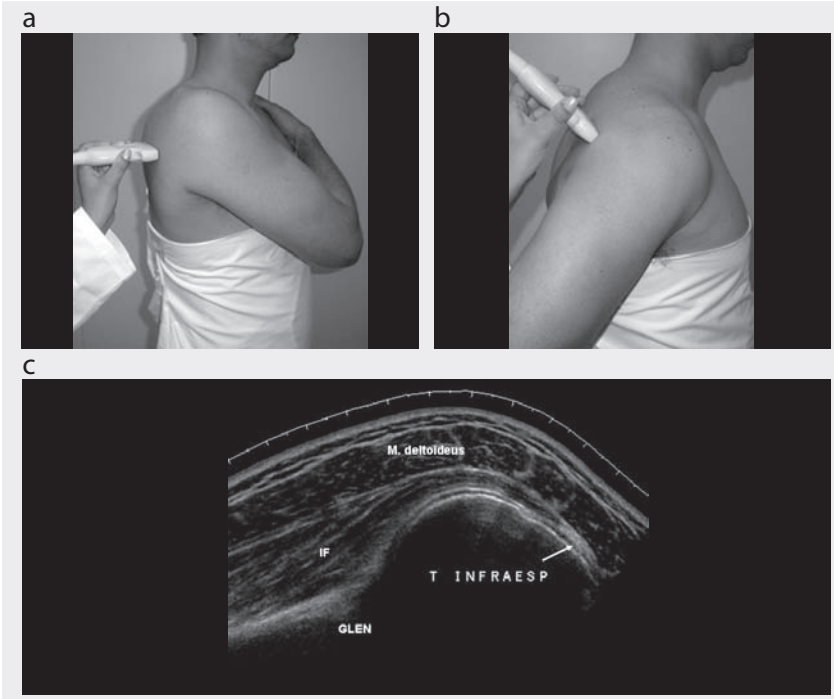

Fig. 6.10. Tendon (arrow) of the teres minor muscle (REM). Ultrasonography, showing more abrupt sharpening and less echogenicity than the infraspinatus tendon due to the presence of muscle fascicles among the tendon fibres

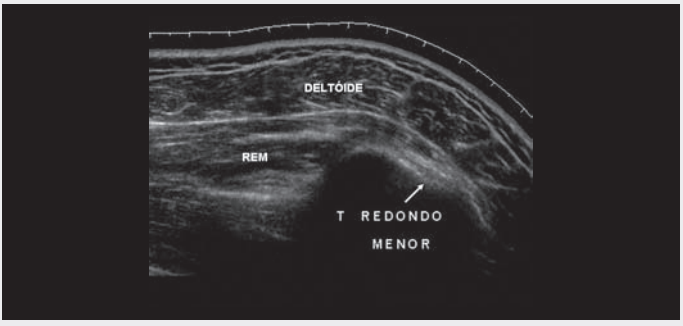

Partial ruptures

Partial ruptures may have two distinct ultrasonographic patterns (Fig. 6.11). Echo-poor or echo-free lesions due to discontinuity of the fibres initially present linearly with delaminating of the tendon, especially if the trauma mechanism is secondary to eccentric contraction of the rotator cuff tendons. More commonly, a mixed lesion is seen, with an echo-rich centre surrounded by an echo-poor halo indicating perilesional fluid. The echo-rich centre is due to retracted tendon fibres or to a new acoustic interface generated by the rupture. Although these patterns predominate, they are not the only ones.

Some lesions are characterized by linear, echo-rich images along the tendon fibres. The continuity of this echo-poor image can be identified with high-frequency transducers (Fig. 6.12).

Fig. 6.11. Commonest ultrasonographic aspects of partial lesions of the rotator cuff. (a) Echo-free lesion (arrows) delaminating the tendon. (b) Mixed-type fracture, with echo-rich and echo-free areas inside (arrow)

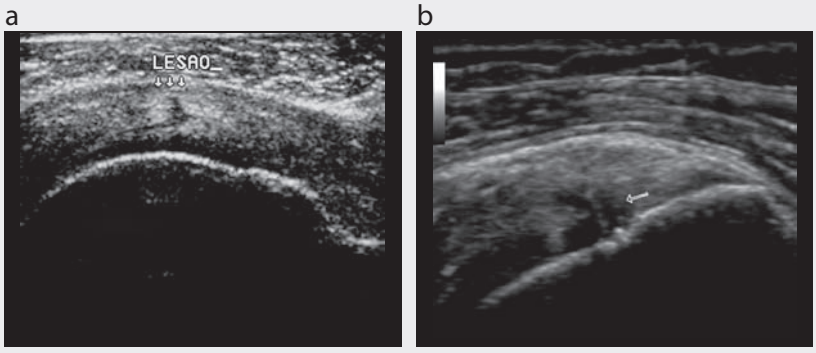

Fig. 6.12. Unusual partial rupture. Ultrasonograph showing that the echo-poor linear image is continuous with the echo-rich area (arrows)

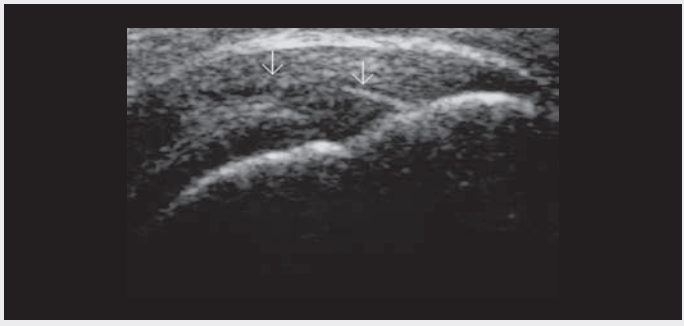

Complete rupture

Complete, transfixing ruptures of the entire thickness of the tendon are diagnosed from direct and indirect signs.

The **direct (primary) signs** can be divided into two large groups: alteration of the tendinous outline, including the absence and focal tapering of the tendon, and alterations of the echo texture, comprising heterogeneous echogenicity and an echo-free intratendinous focus or split.

When the tendon is not visible, the deltoid muscle touches the head of the humerus (bald humeral head sign), and a small echogenic strip can be seen between the two structures, indicating either thickening of the synovial bursa or repairing tissue (fibrosis) on the tendon. In the absence of the supraspinatus tendon, the deltoid muscle can act without an antagonist, resulting in subluxation of the humeral head with reduction of the subacromial space (Fig. 6.13).

Fig. 6.13. Bald humeral head sign. Unidentified supraspinal tendon (arrow) with reduction of the subacromial space. ACR, acromion

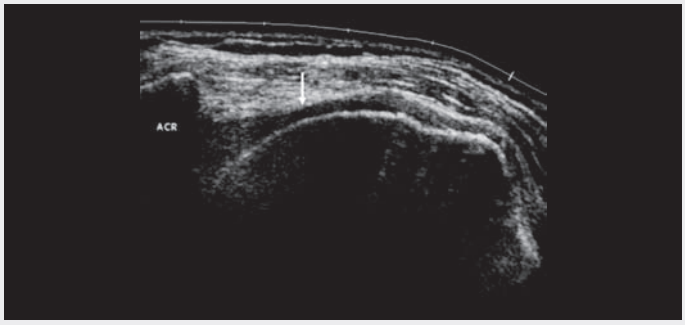

In the absence or focal tapering of the tendon, the usual convexity of the tendon is altered. In more severe ruptures, herniations of the synovial bursa and of the deltoid muscle itself represent the defect (Fig. 6.14). In less severe ruptures, tapering may be seen, with rectification of the bursal surface, and it is difficult to determine whether it is a complete rupture (transfixing) or a partial lesion. In these situations, it is useful to check the percentage of tapering, which corresponds to the depth of the concavity formed by the outline of the subacromial-subdeltoid bursa: if it is greater than 50%, it is a complete lesion; if it is less than 50%, it is a partial lesion.

Discontinuity of the fibres without alteration of the tendon outline indicates a connection between the glenohumeral joint and the subacromial-subdeltoid bursa.

Heterogeneous tendon echogenicity is the source of most faulty diagnoses, as an increase may represent a small partial or complete rupture, calcification or fibrosis (Fig. 6.15). Sometimes, the echogenicity can be increased by associated findings, such as a posterior acoustic shadow in a calcification or the linear form of the larger

Fig. 6.14. Absence of focus on the anterior portion of the supraspinal tendon (T) in both longitudinal (a) and transverse (b) views, accompanied by thickening of the subacromial-subdeltoid bursa (arrow). TSE, remnant of supraspinal tendon; TMA, largest humerus tubercle; TLCB, long head of brachial biceps tendon; ART AC, acromion-clavicle joint

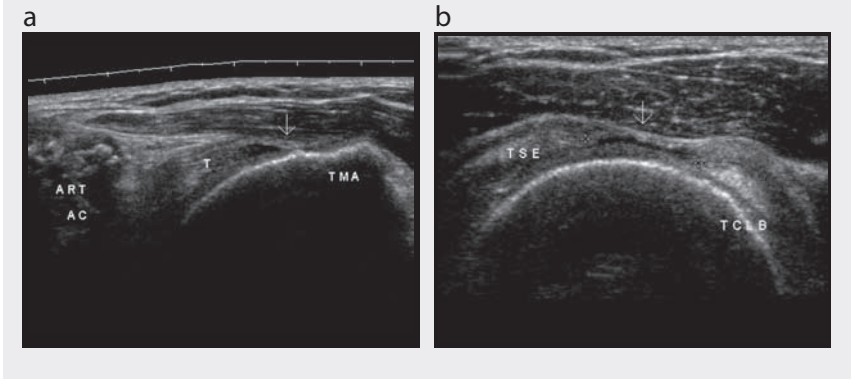

Fig. 6.15. Change in tendon echogenicity, with a small, linear, echo-rich, intratendinous image (arrow) with no posterior acoustic shadow and an unspecified aspect

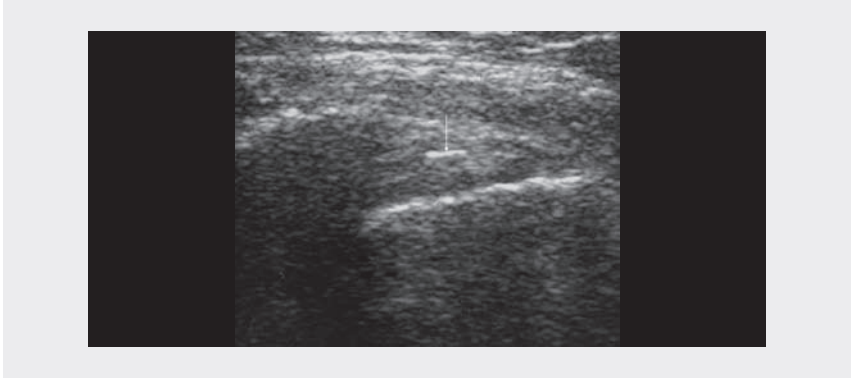

tubercle of the humerus in ruptures. Calcifications sometimes have a slightly echo-rich aspect, with no acoustic shadow, surrounded by an artefactual linear, echo-poor image, simulating rupture in transition with the tendon. In such cases, a simple radiographic examination will confirm the presence of calcification.

In acute lesions, echogenic blood may fill the area of the rupture, impeding any change to the tendon and thus a diagnosis. As the echo texture of the tendon is heterogeneous, the transducer should be compressed on the tendon. In ruptures associated with tendinopathy, the usual convexity of the tendon may be lost (Fig. 6.16). Another manoeuvre that can be used to remove doubt is returning the arm to the neutral position, causing relaxation of the subacromial-subdeltoid bursa and mobilization of the fluid inside the lesion.

Fig. 6.16. Supraspinal tendon in longitudinal scan, before (a) and after (b) compression. (a) Heterogeneous tendon with a normal outline. (b) Rectification and tapering of the tendon close to its insertion (arrow), showing the presence of rupture

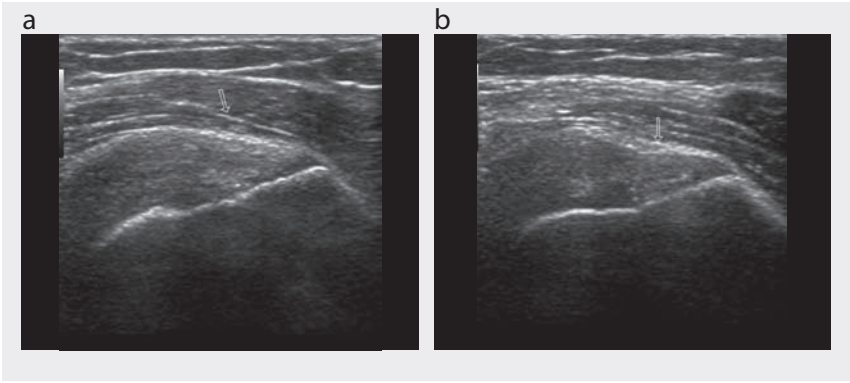

Fig. 6.17. Irregular outline of the largest tubercle of the humerus (arrow), associated with complete rupture (transfixing) of the supraspinatus tendon (rotura, arrow)

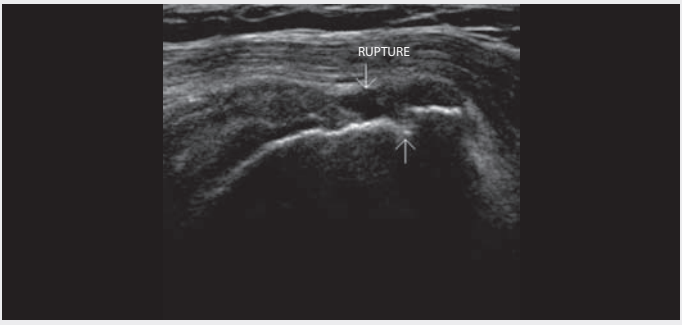

The **indirect (secondary) signs** include an irregular contour of the largest tubercle of the humerus. Most partial or complete ruptures of the tendon situated up to 1 cm from the insertion present some alteration on the bony surface of the largest tubercle. About 70% of partial lesions are accompanied by irregularity of the cortical bones, from small defects to bone fragments and exostosis. It may be caused by a posterosuperior impact or be secondary to traction of fixed tendinous fibres on the surface of the largest tubercle (Fig. 6.17).

Liquid is present in the acromion-clavicular joint (Geyser sign) only when the subacromial-subdeltoid bursa is connected to the acromion-clavicular joint. A periarticular cyst is formed, secondary to the passage of the glenohumeral to the acromion-clavicular joint through rupture of the rotator cuff.

Liquid in the glenohumeral joint is identified either from distension of synovial recesses of the joint or from the amount of fluid accumulated in the synovial sheath

of the long head tendon of the brachial biceps. In general, the synovial recesses are posterior, easy to access and located anterior to the tendinous muscle of the infraspinatus. Liquid accumulation occurs when the distance between the glenoid posterior labrum and the infraspinatus tendon is > 2 mm. The synovial recesses may also be axillary, located below the inferior margin of the tendinous muscle of the teres minor (Fig. 6.18). External rotation during dynamic testing increases the sensitivity of the examination. They may also be approached through the axillary cavum; in this case, the diagnostic criteria are that the distance between the bone surface and the joint capsule must be > 3.5 mm and the difference between the two sides must be > 1 mm.

Liquid in the subacromial-subdeltoid bursa is suspected when the bursa presents a thickness > 1.5–2 mm. Although this phenomenon may also be seen in asymptomatic people, ultrasonographic detection of fluid in the bursa and the glenohumeral joint is highly specific for predicting rupture of the rotator cuff (Fig. 6.19).

Fig. 6.18. (a), (b) Glenohumeral articular haemorrhage (stars) below the inferior margin of the teres minor muscle (MRM) and anterior to the tendinous muscle transition of the infraspinatus (MIF). glen, glenoid

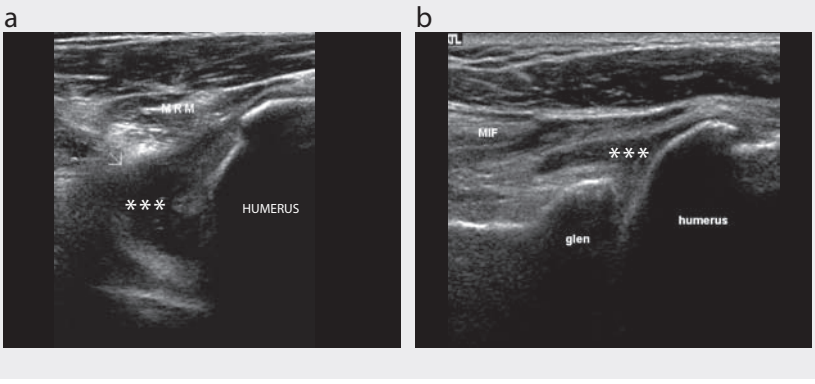

Fig. 6.19. Partial lesion of the supraspinatus tendon (arrow), containing fluid and distending the subacromial-subdeltoid bursa (stars)

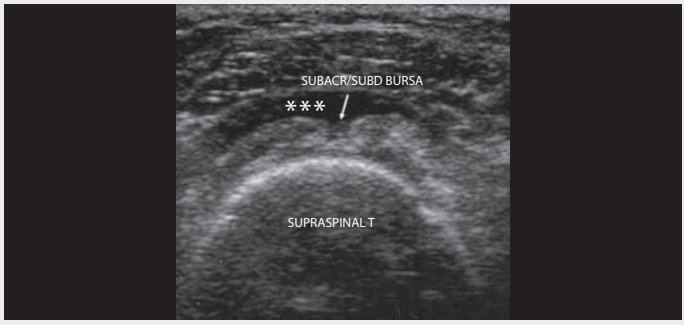

The cartilage interface sign, also called the naked tuberosity sign, corresponds to linear hyperechogenicity below the lesion, representing the external outline of the hyaline cartilage that covers the humerus head. It is generated by posterior acoustic reinforcement due to the echoic rupture (Fig. 6.20).

Appropriate treatment should be based on an understanding of the type and dimensions of the tendinous rupture, the appearance of the glenohumeral joint on simple X-ray, the degree of muscle atrophy of the rotator cuff and the case history.

Fig. 6.20. Cartilage interface sign (arrow). (a) Longitudinal and (b) transverse scans of the supraspinal tendon (T), with two other signs: focal absence of the tendon (star) and irregular outline of larger tubercle of the humerus (umero); parietal thickening of the subacromial-subdeltoid bursa (bolsa SASD)

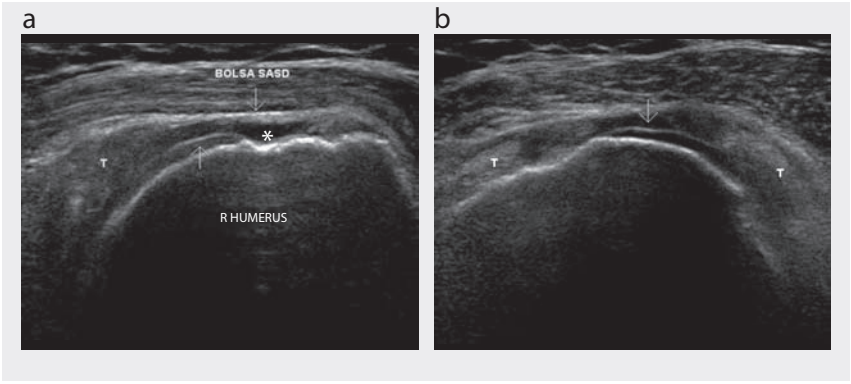

Elbow

The musculotendinous structures of the elbow are made up of four groups of muscles: posterior, anterior, lateral and medial.

The largest posterior muscle is the brachial triceps, formed by three heads that merge to form a single tendon inserted into the upper margin of the olecranon and the antebrachial fascia (Fig. 6.21). Conjunction of small enthesophytes is common, but rupture is rare. In the periolecranon area, three synovial bursae can be identified, one subcutaneous, one intratendinous and one between the elbow joint capsule and the brachial triceps tendon.

Fig. 6.21. Brachial triceps tendon (t). (a) Examination technique and (b) longitudinal scan. f, olecranon fossa

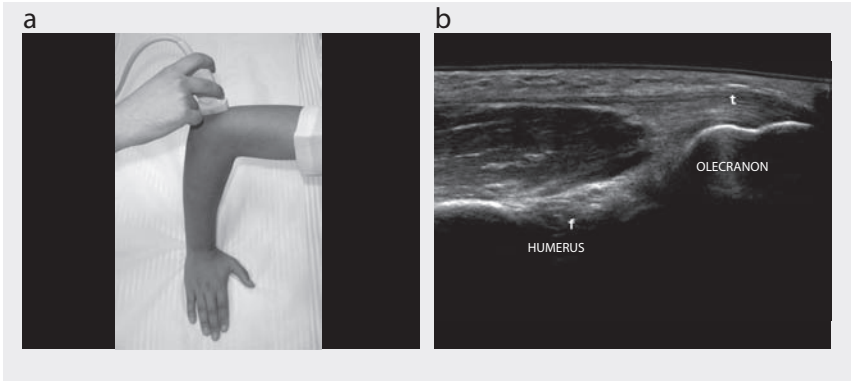

The anterior group comprises the brachial and brachial biceps muscles. The two heads of the biceps join to form a tendon 6–7 cm long covered by a paratenon, with insertion into the posterior face of the radius tuberosity (Fig. 6.22). A hypovascularized area is seen close to the insertion, and the presence of tendinopathy is common. Two synovial bursae are found in the area: the bicipitoradial, between the radius and the brachial biceps tendon, close to its insertion, and the interosseous, between the ulna and the brachial biceps tendon.

The lateral group comprises the common extensor tendon, originating in the lateral epicondyle of the humerus, formed by the carpi radialis brevis extensor, finger extensors, digiti minimi extensor and carpi ulnaris extensor tendons (Fig. 6.23). This group also includes the brachioradial and supinator muscles and tendons.

The medial group is composed of the pronator teres muscle and the common flexor tendon, formed by the musculotendinous units of the palmaris longus, digitorum superficialis flexor, carpi radialis flexor and carpi ulnaris flexor, fixed in the medial epicondyle (Fig. 6.24).

Lateral and medial epicondylitis are overuse syndromes characterized by pain and increased sensitivity of the epicondyles, generally related to tendinopathy. The common tendon of the forearm extensors is involved in 80% of cases, initially affecting the deep portion, corresponding to the carpi radialis brevis extensor (Fig. 6.5). In medial epicondylitis, ulnar neuropathy is associated in 60% of cases.

Fig. 6.22. Brachial biceps tendon (t, arrow). (a) Examination technique; transverse scan in the axial plane, from the forearm proximal to insertion in the radius tuberosity. (b) Tendon positioned along the brachial artery, a, gradually going deeper (c), posterior to the bifurcation of the brachial artery, a. (d) Ulnar artery beside the tendon. Longitudinal scan. (e) Examination technique. (f) Ultrasound scan. L, lateral area; M, medial area; tuber. radio, tuberosity

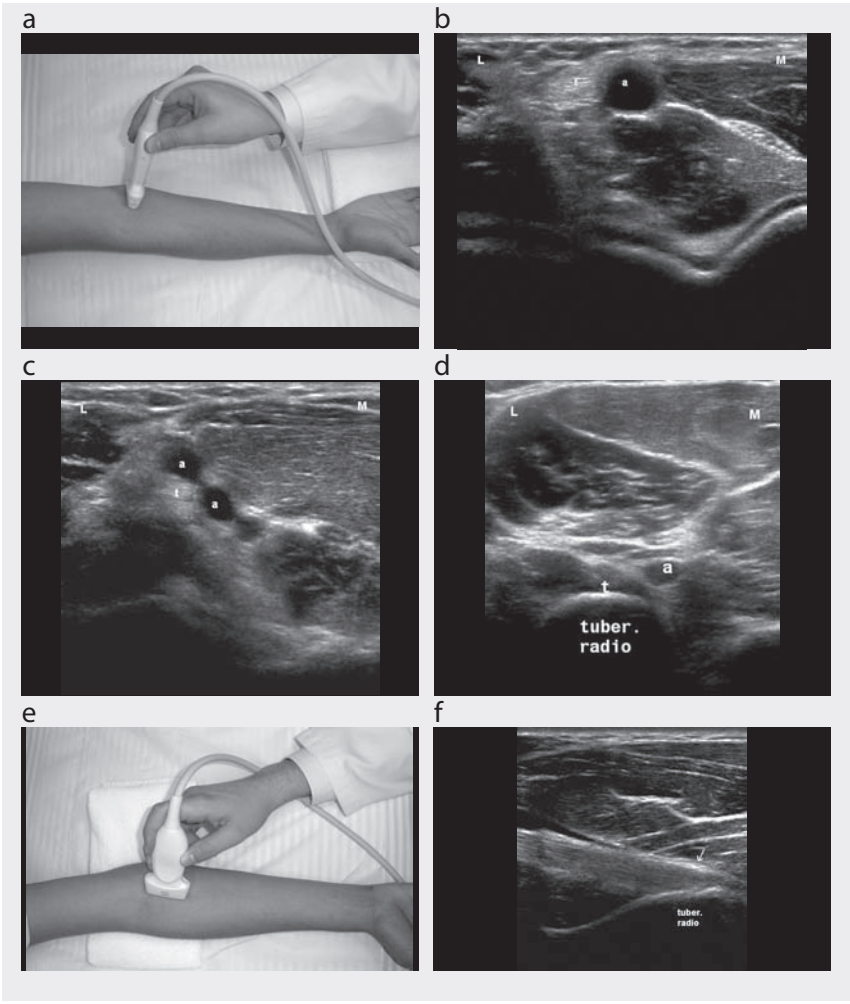

Fig. 6.23. Common tendon of the forearm extensors. (a) Examination technique. (b) Ultrasound scan; common tendon of the forearm extensors (arrow). br, brachioradial muscle; el, lateral epicondyle; cr, radius head

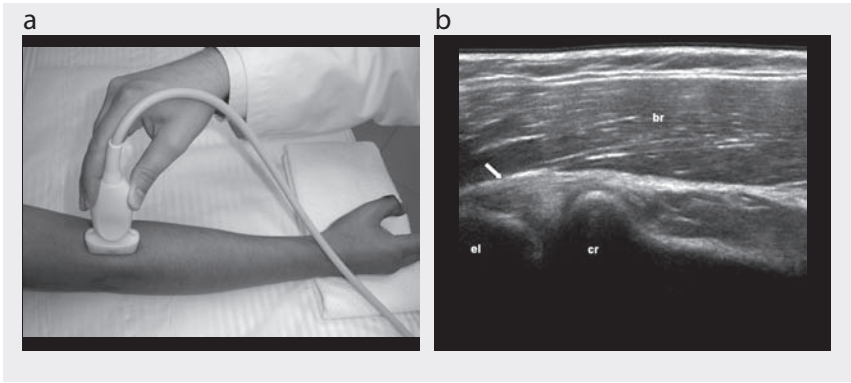

Fig. 6.24. Common tendon of the forearm flexors. (a) Examination technique and (b) ultrasound scan. epic. medial, medial epicondyle. t, common tendon of forearm extensors

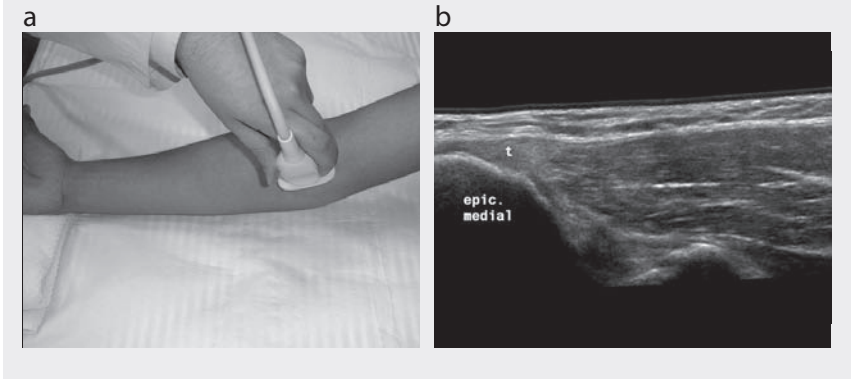

Wrist

The tendon groups of the wrist are flexors and extensors. The flexor tendons are located on the palmar face and comprise the digitorum flexor, carpi radialis flexor, carpi ulnaris flexor and pollicis longus flexor. The digitorum flexor tendons and the pollicis longus tendons pass through an osteofibrous tunnel—the carpal tunnel—bordered by the flexor retinaculum (anterior) and the carpus bones (posterior, lateral, medial). The other structures found inside the carpus, forming a kind of compartment, are fat, the median nerve and two synovial bursae: the radial, surrounding the long flexor tendon of the pollex, and the ulnar, involving the superficial and deep digital flexor tendons (Fig. 6.25).

Fig. 6.25. Carpal tunnel (arrow). (a) Section plane at the proximal carpal tunnel with ultrasound beam. (b) Structures found inside the carpal tunnel. (c) Ultrasound scan. Dotted line, retinaculum of flexors; ESC, scaphoid; TFRC, carpal radial flexor tendon; CG, Guyon channel; *, median nerve; t, finger flexor tendon; PIS, pisiform; t, trapeze; n, ulnar nerve; a, artery

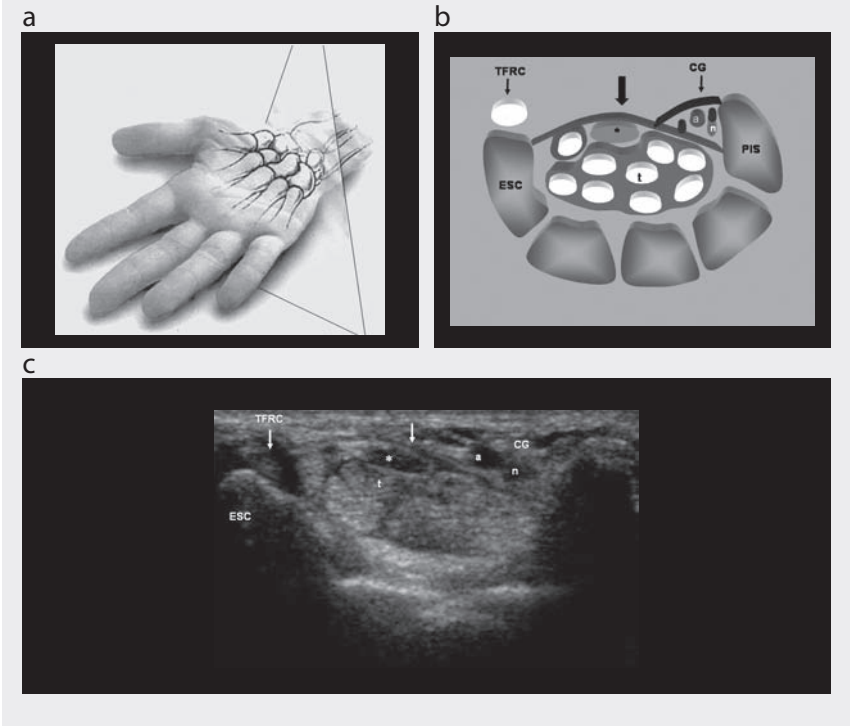

The six synovial compartments of the extensors on the dorsal region of the wrist have individual synovial sheaths and are maintained in position by the retinaculum (dorsal carpal ligament; Fig. 6.26). The sheaths of the second, third and fourth compartments are connected; the presence of a small amount of fluid within them is normal, especially in the sheaths around the tendons of the second compartment.

The first compartment contains the abductor pollicis longus tendon and the pollicis brevis extensor in a single synovial sheath, situated on the lateral fascia of the wrist in contact with the radius stylohyoid process. It is the extensor compartment most frequently involved in stenosing tenosynovitis (De Quervain tenosynovitis; Fig. 6.27). This condition can be secondary to inflammatory arthritis, to acute or repetitive microtraumas due to gripping movements or to ulnar deviation of the wrist. It is more frequent in women and is bilateral in up to 30% of cases. Clinical examination reveals pain during palpation of the radial border of the wrist, and it may be difficult to differentiate from thumb carpometacarpal joint arthritis in the initial stages.

Fig. 6.26. Synovial compartments of the extensors of the wrist. (a) Examination technique. (b) Transverse view of the wrist at the level of the distal radio and ulna. (c) Ultrasound image. Sonography: star, tuber of Lister; 1, long abductor tendons and short extensor of the thumb; 2, radial extensor tendons of the carpus; 3, long extensor tendon of the thumb; 4, extensor tendons of the fingers; 5, extensor tendon of the fifth finger; 6, ulnar extensor tendon of the carpus

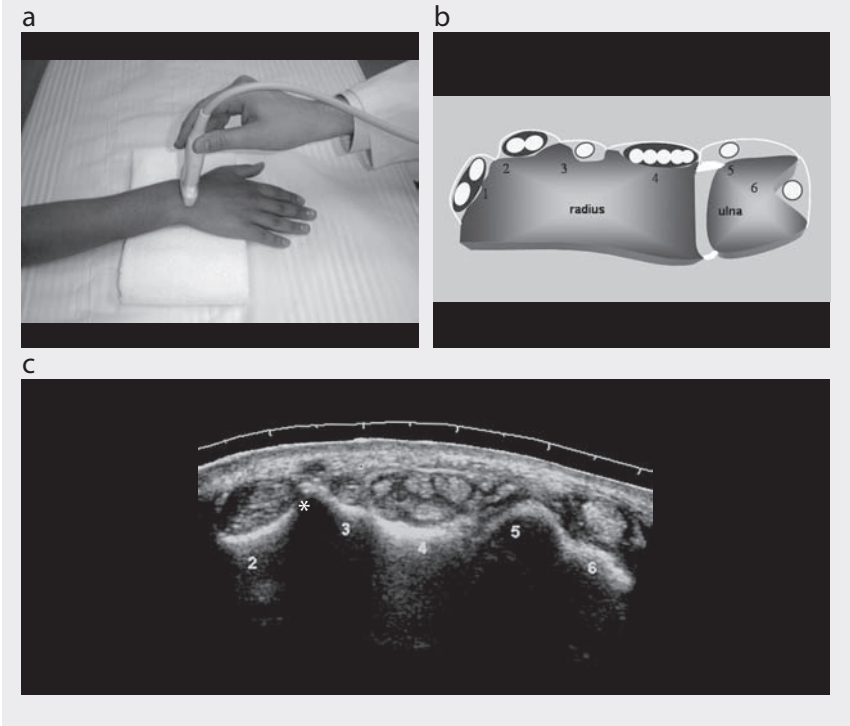

The second compartment contains the short and long radial extensor tendons of the carpus in the anatomical snuffbox. The long radial extensor tendon is situated at the base of the second metacarpal and the short tendon in the dorsal area of the third metacarpal.

The third compartment corresponds to the long extensor tendon of the pollex, medial to the tubercle of the radius (Lister tubercle). It borders the anatomical snuffbox medially, passing over the radial extensor tendons (posterior) and inserts into the dorsal region of the distal phalange at the base of the thumb.

The fourth compartment is composed of the common tendons of the digital extensors and the indicis extensor. The common extensor tendon is inserted in the medial and distal phalanges of the second to the fifth fingers. The end of the indicis extensor is located at the proximal phalange of the second finger.

Fig. 6.27. De Quervain tenosynovitis. (a) B-scan showing thickening of the synovial compartment (arrow) and the retinaculum (echo-poor halo, stars) of the extensors. (b), (c) Colour Doppler showing increased flow in the retinaculum, sometimes the only alteration seen

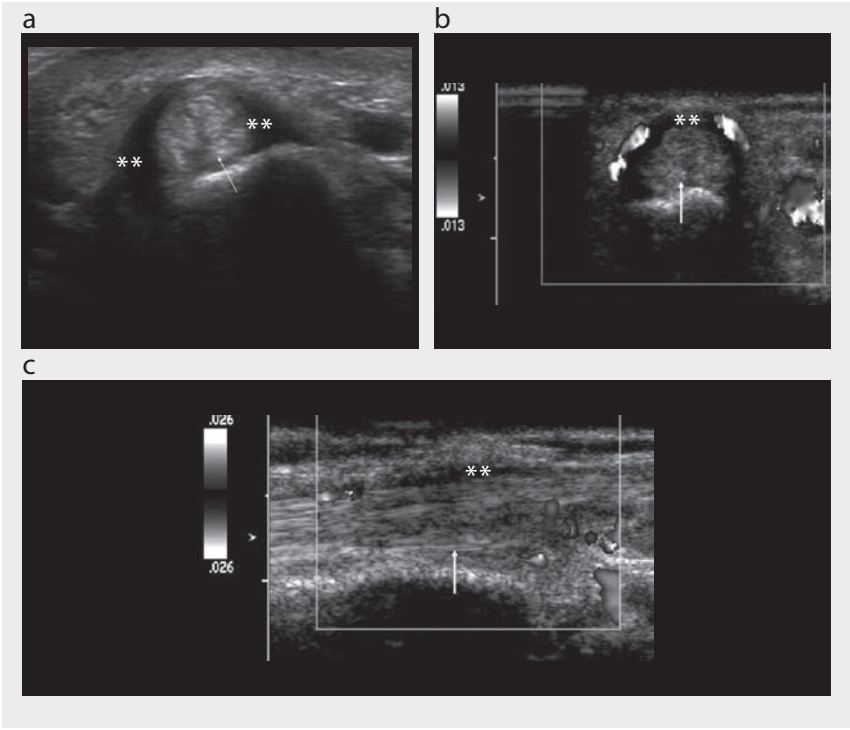

The fifth compartment contains the extensor tendon of the fifth finger, seen posterior to the radioulnar joint, with insertion in the medial and distal phalanges of the fifth finger.

The sixth compartment corresponds to the carpi ulnaris extensor tendon, situated adjacent to the styloid process of the ulna and attached to the base of the fifth metacarpal. This is the second most common location of tenosynovitis, due to repetitive catching of an object. This wrist tendon is the most vulnerable to subluxation or luxation (Fig. 6.28).

Fig. 6.28. (a) Subluxation of the ulnar extensor tendon of the carpus, with deformation of the ulna head. (b) Topical tendon (arrow)

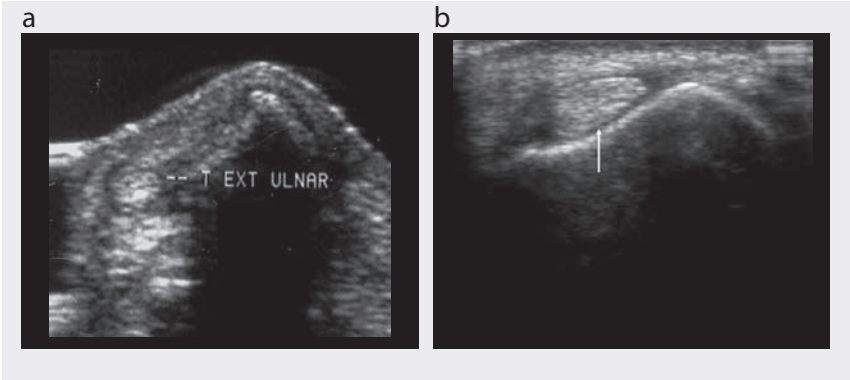

Fingers

The tendinous anatomy of the fingers is different in the palmar and dorsal regions. A central tendon is inserted in the base of the medium phalanx on its dorsal face. Two tendinous bands meet near the base of the distal phalanx, medially and laterally to this tendon, forming the terminal tendon. Narrow strips of collagen, known as sagittal bands, link these structures to provide stability and allow harmonious extension. Because of this complex anatomy, the term 'digital extensor apparatus' is used rather than 'extensor tendon of the finger' (Fig. 6.29).

The flexor tendons are located in the palmar region of the hand and fingers. The superficial flexor tendon at the level of the proximal phalanx is anterior to the flexor digitorum profundus. In its distal course, it divides into two bands, with insertion in the medial phalanx posterior to the flexor digitorum profundus, which runs to the base of the distal phalanx (Fig. 6.30). In contrast to the extensor apparatus, the flexor tendons have a synovial sheath all along the phalanges.

In cases of tenosynovitis, there may be some parietal thickening, fluid or increased flow in the synovial sheath on colour Doppler (Fig. 6.31).

Fig. 6.29. (a–e) Digital extensor apparatus. TT, terminal tendon; tlub, lumbrical muscle tendon; bs, sagittal band; mtc, metacarpal bone; 1, tendon and interosseous muscle; 2, central tendon; 3, divisions of the central tendon; 4, collateral ligaments; 5, intermetacarpal transverse ligament

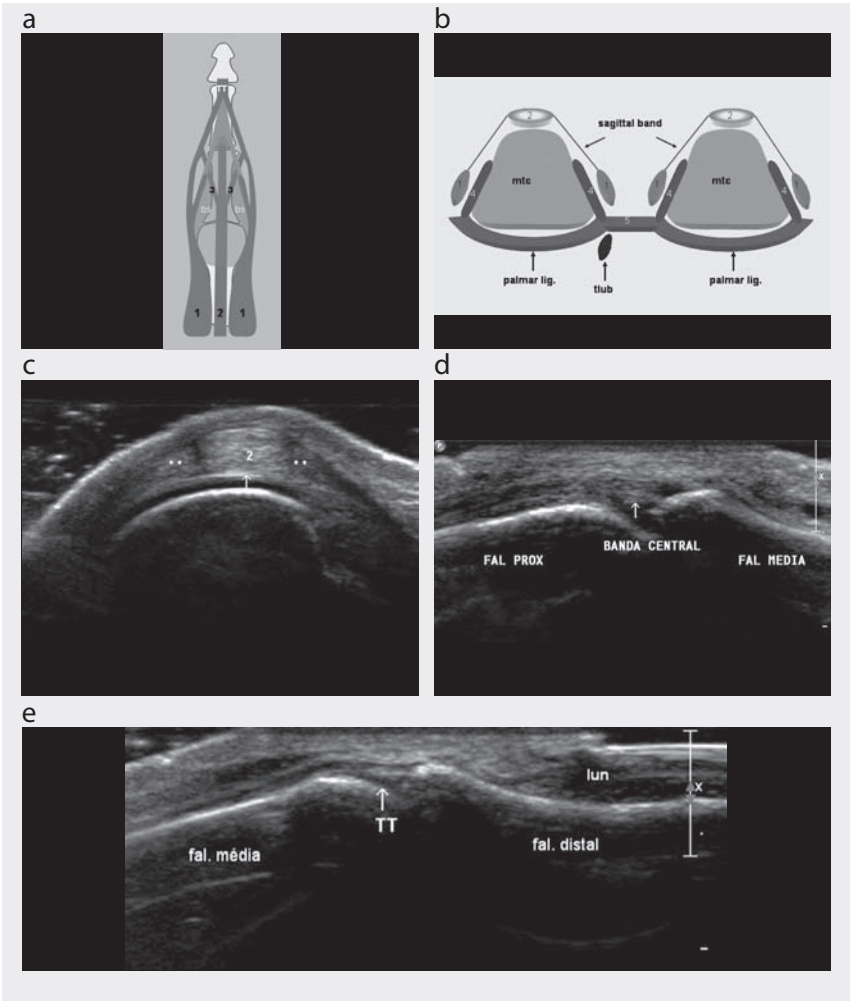

Fig. 6.30. Flexor tendons. (a) Surgical view. (b)–(e) Sections at which transverse scans of the flexor tendons were made. (f) Longitudinal scan of the flexor tendons of the proximal, medial and distal phalanges. FS and continuous arrows, superficial flexor tendon; FP and stars, deep flexor tendon; dotted arrow, flexor tendons

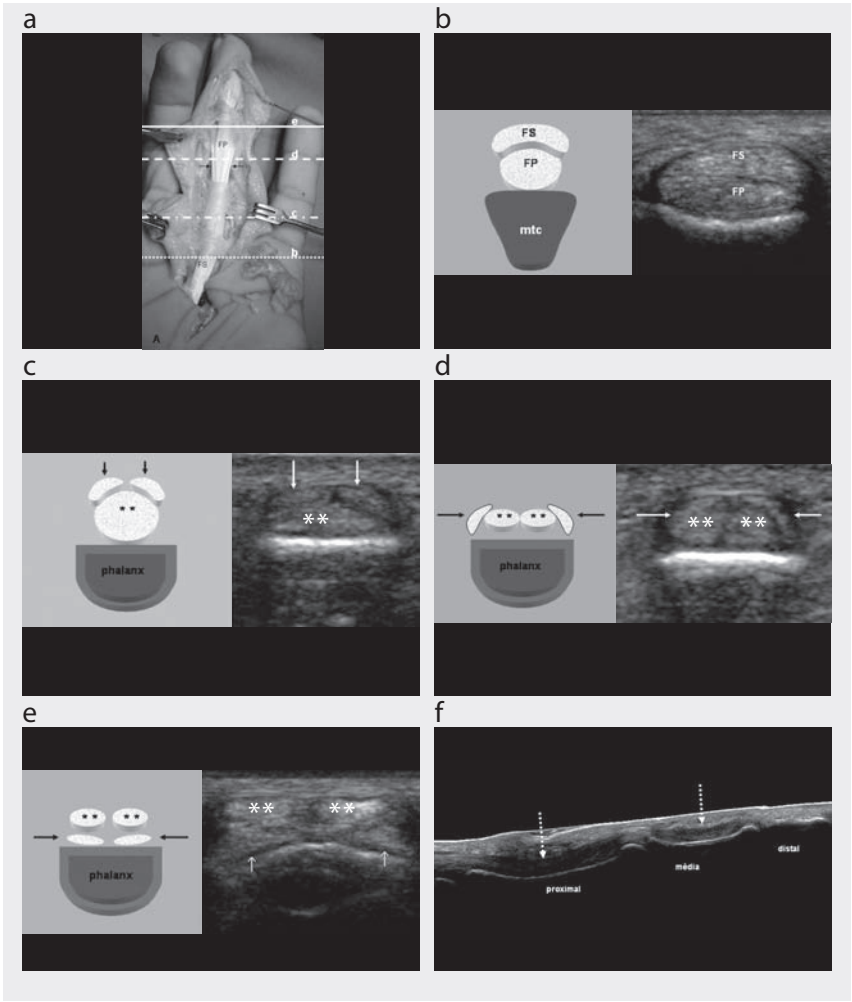

Fig. 6.31. Tenosynovitis of the flexors of the second finger. (a), (b) Longitudinal and (c) transverse scans of the tendon flexors, indicating thickening of the synovial sheath (arrow in (a)) with a large flow increase on colour Doppler (b), (c)

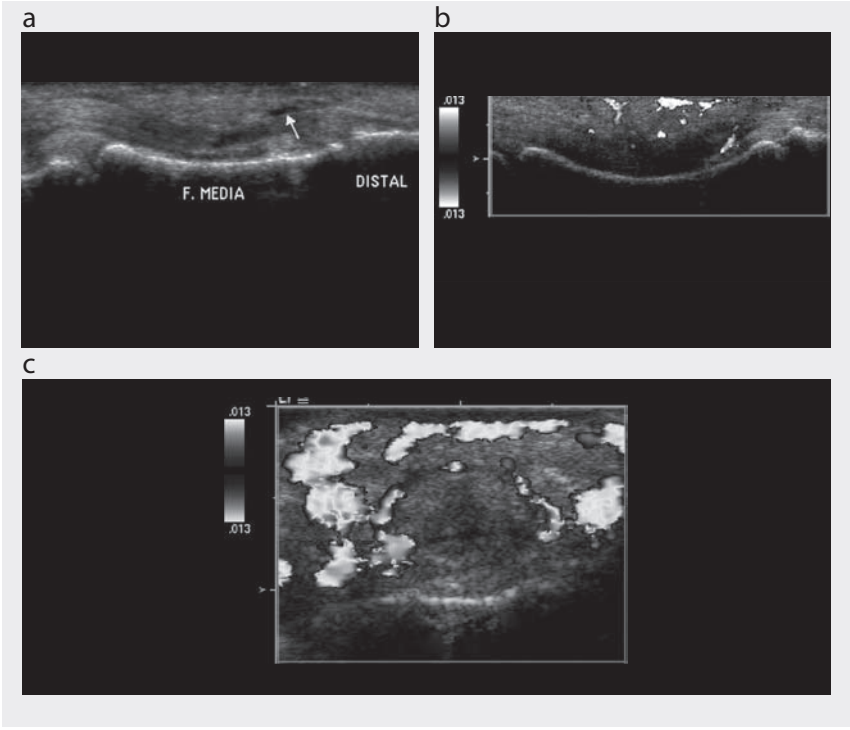

Lower limbs

Hip

The hip, like the shoulder, has a cuff made up of the musculotendinous units of the glutei minimus and medius, which are responsible for the internal rotation and abduction movements of the joint. The tendon of the gluteus minimus is situated in the anterior plane of the largest femoral trochanter, and the gluteus medius is in the lateral and posterosuperior planes, with intertwined fibres. There is a hypovascularized area, similar to that of the supraspinatus and infraspinatus tendons (Fig. 6.32).

Adjacent to the tendons, three synovial bursae are seen: the trochanteric bursa, the bursa of the subgluteus minimus and the bursa of the subgluteus medius. A bursa of the subgluteus maximus has been proposed.

A painful greater trochanter is a common condition. One of the main causes is tendinopathy of the glutei and trochanteric bursitis (Fig. 6.33, Fig. 6.34). These are not always readily diagnosed with ultrasound due to the oblique path of the tendons and patient characteristics, such as obesity.

Fig. 6.32. Tendons of the gluteus minima and media. (a) Insertions of the two tendons. (b) Examination technique. Longitudinal scans of the (c) gluteus minima tendon (arrow) and (d) the gluteus media tendon (arrow), with forms and echogenicity similar to that of the rotator cuff tendons of the shoulder. mi, insertion of gluteus minima tendon; me, insertion of gluteus media tendon

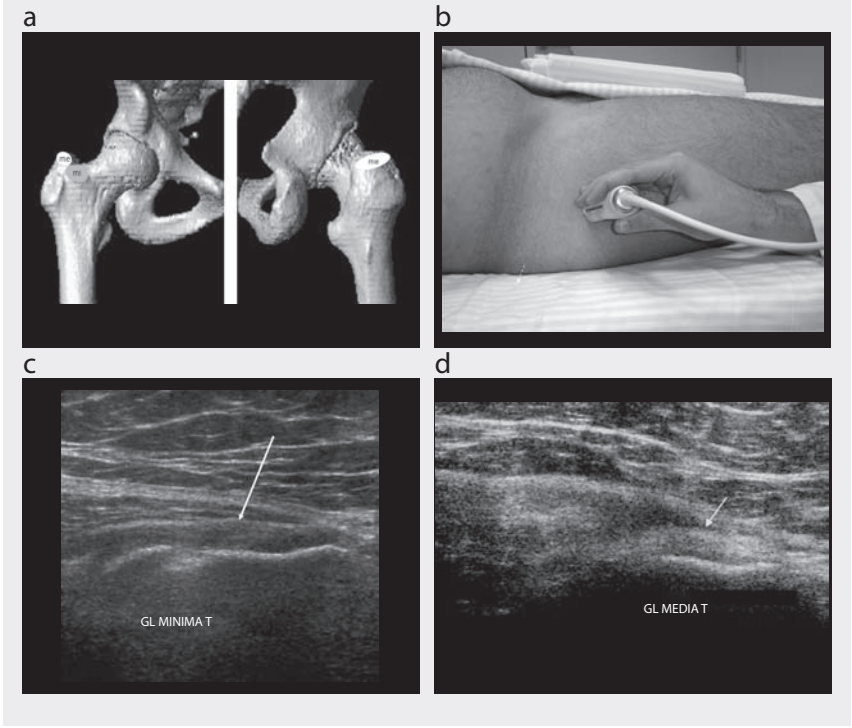

Fig. 6.33. Tendinopathy of the glutei enhanced by thickening and hypoechogenicity (arrow). (a) Transverse and (b) longitudinal scans

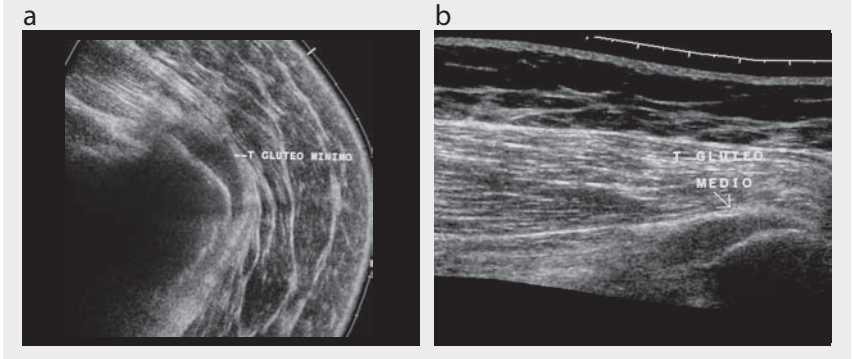

Fig. 6.34. Bursitis involving the synovial bursa of the medium subgluteus, containing a moderate amount of fluid (star)

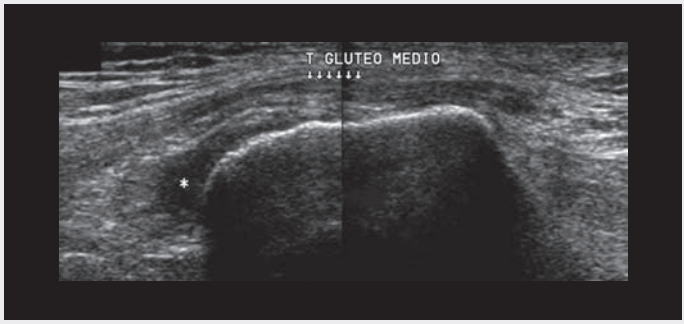

Ultrasound examination is useful in cases of hips with a snapping, characterized by pain associated with an audible or tangible snap during movement of the hip. The cause may be intra- or extra-articular. The extra-articular factors are friction of the fascia lata against the largest femoral trochanter (Fig. 6.35) or of the tendon of the iliopsoas against the iliopectineal eminence.

Fig. 6.35. Snapping hip. Transverse scan of the largest femoral trochanter (troc), indicating thickening of the fascia lata (arrow) situated lateral to the hip on internal rotation (rot int); on external rotation (rot ext), the fascia lata is in anterior position (arrow), producing a snap

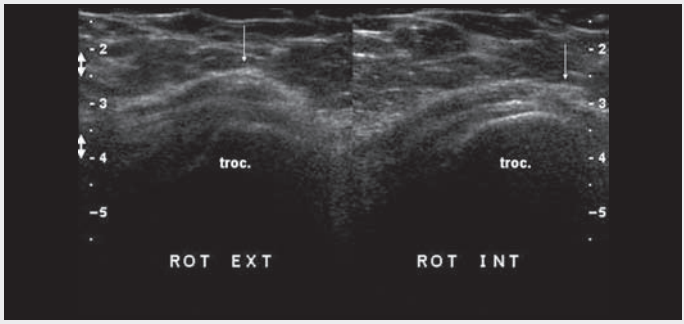

Knee

The patellar tendon in the periarticular area of the knee is that most frequently injured. It is situated between the subcutaneous tissue and the pretibial bursa (deep infrapatellar bursa), posterior to the inferior half of the tendon. The acoustic shadow of the cortical bone is used to identify its insertion into the patella and into the tuberosity of the tibia. Posterior to the tendon is a pad of fat known as the infrapatellar or Hoffa pad, which is joined to the articular synovia. The normal tendon is formed of parallel, homogeneous fibres, visualized as alternate echo-poor and echo-rich bands (Fig. 6.36). The average tendon is 4 mm thick and 21 mm wide. Sedentary people have thinner, ribbon-shaped tendons. Its function is to transmit the strength of the femoral quadriceps muscle to the tuberosity of the tibia.

Fig. 6.36. Patellar tendon. (a) Examination technique. (b) Ultrasound, indicating the patellar tendon and the Hoffa pad (GH), which is echo-poor with linear echo-rich images

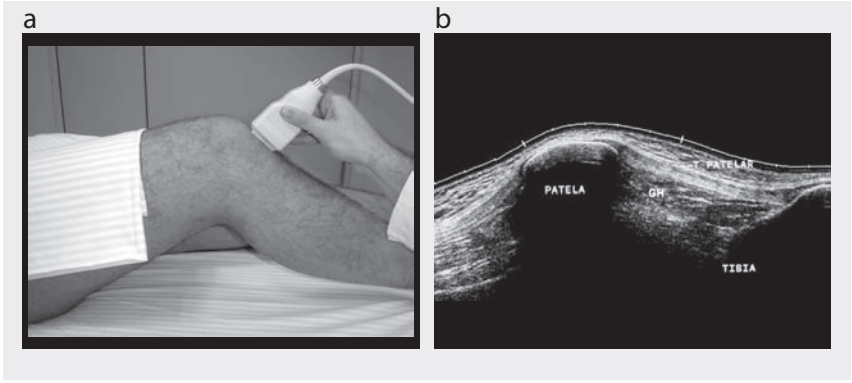

The term 'jumper's knee' is used to describe a painful patellar tendon. The condition is common among athletes and young adults who practise sport regularly, secondary to excessive effort, especially in sports that require extension of the knee, such as running, basketball and football. Usually, the dominant side is affected. From the histopathological point of view, jumper's knee is characterized by the presence of tendinosis, usually beginning at the proximal insertion of the tendon into the apex of the patella.

Ultrasound may show not only echographic alterations of the tendon (Fig. 6.37), but also oedema of the infrapatellar pad and, in severe cases, thickening and irregularity of the tendinous envelope.

An important differential diagnosis of jumper's knee is Osgood-Schlatter disease, which consists of osteochondrosis or osteochondritis of the anterior tuberosity of the tibia. It is common in adolescent boys who practise sport frequently. Microtraumas due to functional activity of the tendon appear to be responsible for the lesion. Clinically, the complaint involves pain and local oedema. Simple X-ray is not sufficient in these cases, because it does not show the earliest alterations, which

are thickening and reduction of the echogenicity of the distal portion of the tendon, accompanied by oedema of the soft tissues around the anterior tuberosity of the tibia, sometimes associated with bone fragmentation (Fig. 6.38).

Fig. 6.37. Patellar tendon. Longitudinal scan, showing (a) proximal tendinopathy (arrow) and (b), (c) rupture

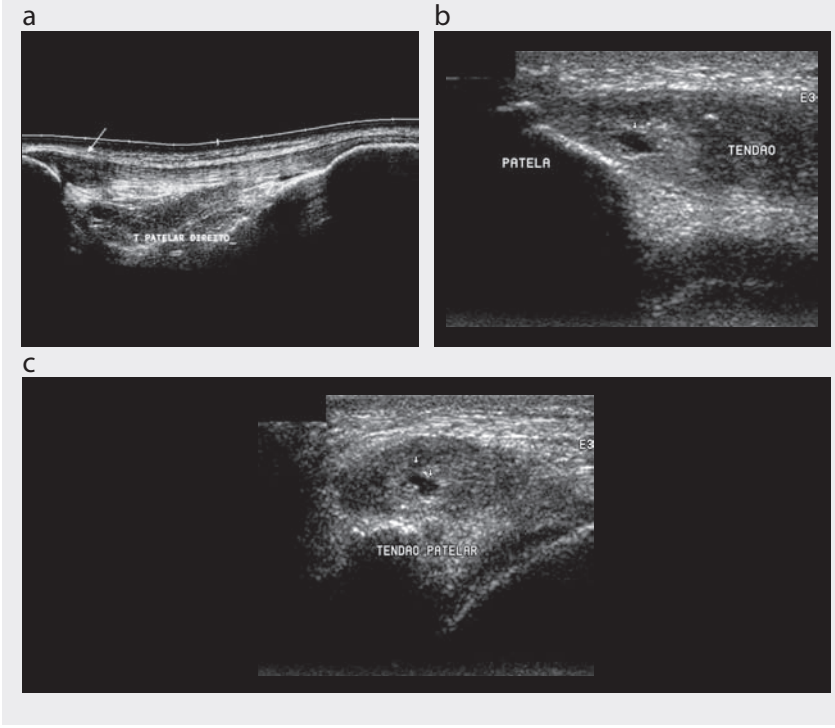

Fig. 6.38. (a) Osgood-Schlatter disease, with thickening of the insertion of the patellar tendon into the tibia, undefined, irregular contours (stars) and a small fragmented bone in the apophysis (arrow). (b) Normal contralateral side

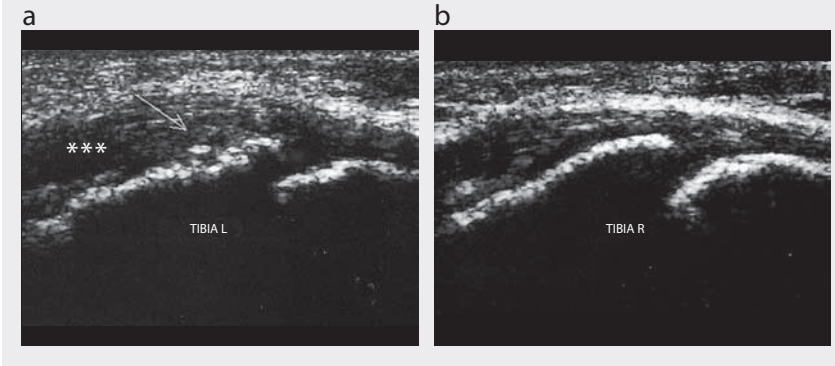

The suprapatellar, prepatellar and pes anserinus tendon bursae are the main synovial bursae in the region. The suprapatellar bursa is used in research on joint effusion, which is in the joint cavity in about 90% of cases. Inflammatory processes are common in the synovial bursae situated anterior to the patella (Fig. 6.39) and adjacent to the pes anserinus tendons.

Fig. 6.39. Prepatellar bursitis. (a) Fluid (stars) and parietal thickening of the synovia. (b) Colour Doppler showing increased flow (arrows)

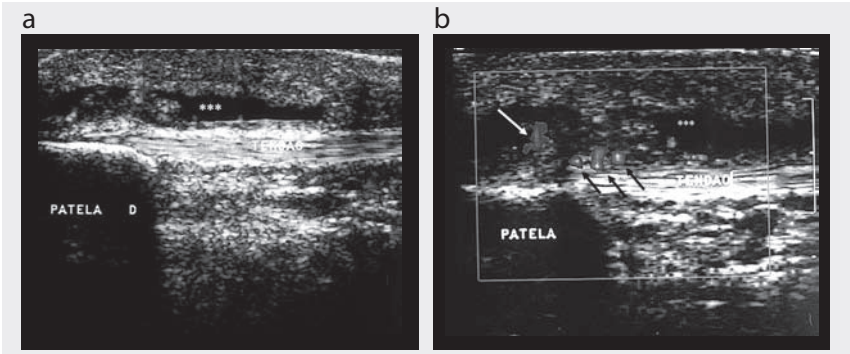

Ankle

About 20% of lesions in runners involve the calcaneal (Achilles) tendon. This tendon is formed by the junction of the tendons of the gastrocnemius and soleus muscles in the middle third of the leg, with insertion into the superior tuberosity of the calcaneus bone. The tendon is about 15 cm long and 3.5–6.9 mm thick, and is larger in men and in tall and elderly people. The tendinous envelope is a paratenon. A retrotibial fat pad (Kager fat pad) is found anterior to the tendon, which may be affected in inflammatory processes. Between the Kager fat pad, the superior tuberosity of the calcaneus bone and the calcaneus tendon, there is a synovial bursa (retrocalcaneal), measuring less than 2 mm in the anteroposterior position; its function is to protect the distal portion of the calcaneus tendon from constant friction against the calcaneus bone. Posterior to the calcaneus tendon is another, acquired synovial bursa, which is superficial (subcutaneous) and may be seen when distended with fluid.

On ultrasound examination, the calcaneus tendon has a crescent appearance in the transversal plane, with its anterior concave and posterior convex faces distally rectified. Longitudinally, it presents a fibrillar echogenic pattern, although it may be echo-poor closer to its insertion (Fig. 6.40).

Alterations to the tendon can be either acute or chronic or be associated with a background disease, such as diabetes mellitus, collagenosis, rheumatoid arthritis, gout or familial hypercholesterolaemia. Tendinous xanthoma is a diagnostic criterion of heterozygous familial hypercholesterolaemia, the calcaneus tendon being the most frequently affected. Ultrasound is useful for demonstrating the xanthomatous deposition, which

occurs as fusiform thickening of the tendon associated with echo-poor foci (Fig. 6.41). As the ultrasonographic signs usually precede clinical manifestation of the disease, ultrasound is the recommended method for diagnosing and monitoring this condition.

Fig. 6.40. Calcaneus tendon. (a) Examination technique. Ultrasound examination in the (b) longitudinal and (c) transverse planes

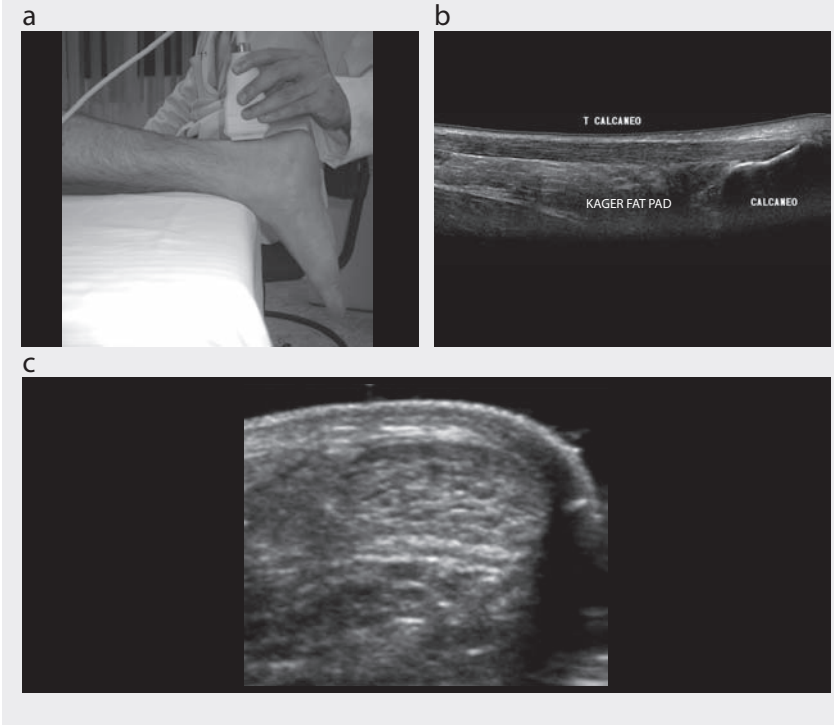

Fig. 6.41. Xanthoma of the calcaneus tendon: thickening associated with heterogeneous echo texture of the tendon due to xanthomatous deposition. (a) Transverse and (b) longitudinal scans

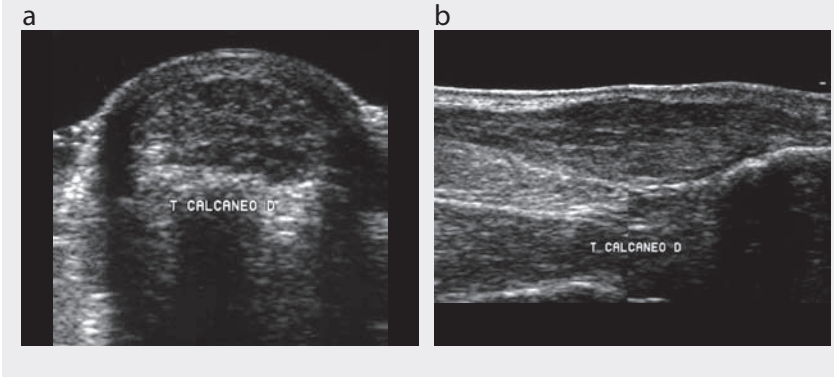

Other common conditions responsible for pain in the region are peritendinitis, paratendinitis and tendinopathies. The pathological processes involving the calcaneus tendon are usually situated in a hypovascularized region 2–6 cm proximal to insertion of the tendon into the calcaneus bone. In tendinopathies, the tendon is thickened, with altered echogenicity, which, in the subtlest cases, is seen as loss of the anterior concavity of the tendon in transversal (oblique) images (Fig. 6.42).

Fig. 6.42. Calcaneus tendinopathy, with thickening and alteration of the echogenicity ((a), stars) and contour ((b), arrows) of the tendon

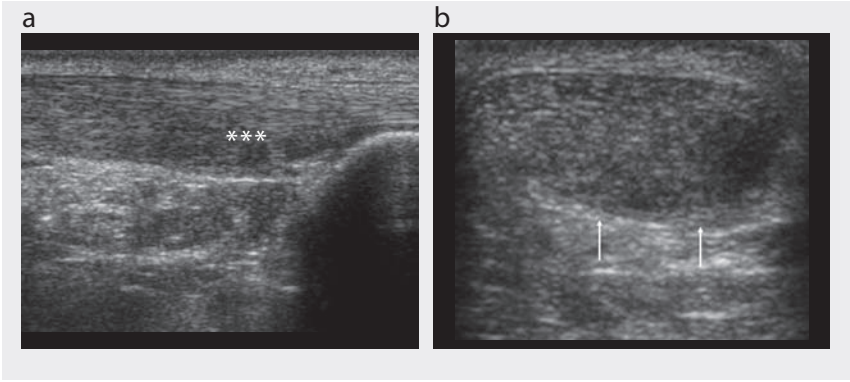

In Haglund deformity, the calcaneus tendon is altered close to its insertion, with hypertrophy of the posterosuperior tuberosity of the calcaneus, affecting the retrocalcaneal bursa and the calcaneus tendon. Consequently, there is retrocalcaneal bursitis and tendinopathy (Fig. 6.43). Insertion tendinopathy may also be due to chronic overload (overuse) in athletes, seen as regions of calcification or intratendinous ossification associated with insertional osteophytes.

Paratendinitis is an inflammation of the paratenon. The echographic outline is blurred, corresponding to thickening (Fig. 6.44), which may extend to the adjacent soft tissue (peritendinitis). Although described separately, these two processes may represent spectra of the same disease.

Unsatisfactory evolution of the pathological process leads to rupture. When partial ruptures affect the anterior surface of the tendon, their diagnosis is facilitated by the inward invagination of the Kager fat pad (Fig. 6.45). Intrasubstance ruptures, especially small ones, can, however, be confused with severe tendinosis, which is difficult to differentiate by imaging. The presence of peritendinitis may suggest partial rupture, as these conditions coexist in up to 68% of cases.

Local oedema and limitation of plantar flexion in complete tendon ruptures may lead to an erroneous clinical diagnosis in up to 25% of acute cases. Ultrasound diagnosis of a complete rupture may be difficult, especially when the paratenon is intact. In diagnostic doubt, it is advisable to conduct plantar and dorsal flexion manoeuvres,

Fig. 6.43. Haglund deformity. Tuberosity of the calcaneus ((a), arrow; (b), (c), stars) associated with tendinopathy of the calcaneus tendon, resulting in retrocalcaneal bursitis and subcutaneous bursitis ((d), stars; (e), arrow) on colour Doppler (longitudinal and transverse planes) and MRI (f)

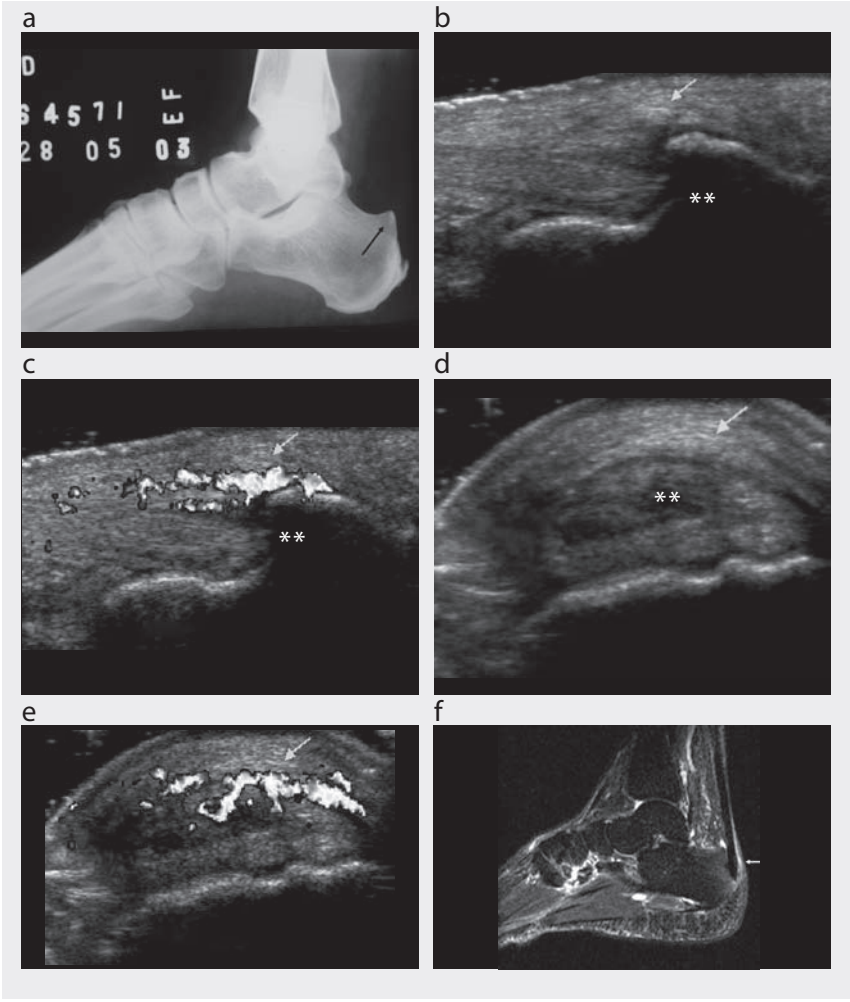

Fig. 6.44. Calcaneus paratendinitis. Thickening and hypoechogenicity of the posterior paratenon (arrow) in the longitudinal (a) and transverse (b) planes

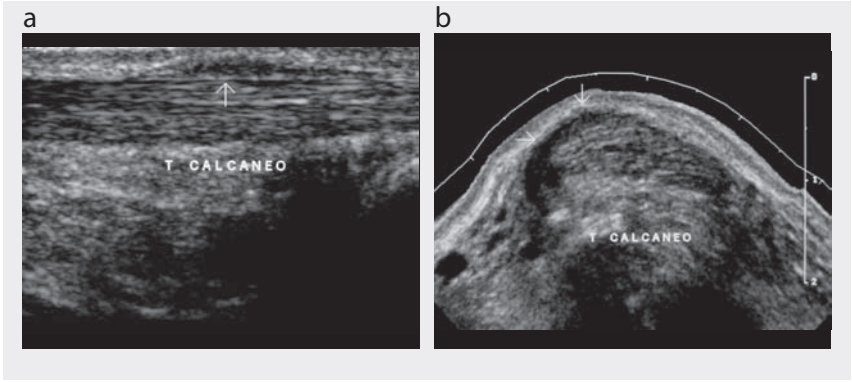

Fig. 6.45. Partial lesion with inward invagination of the Kager fat pad (arrows). (a) Ultrasound. (b) MRI

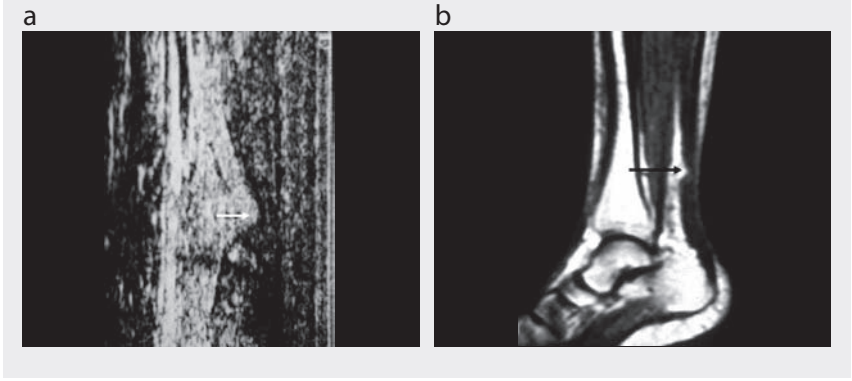

which not only confirm a clinical hypothesis but contribute to therapeutic choices by verifying the proximity of the tendinous stumps (Fig. 6.46).

Another useful sign of complete lesions is the presence of posterior acoustic shadow on the retracted tendinous stumps (Fig. 6.47), secondary to the oblique acoustic bundle on their surfaces, which have an irregular outline. Use of hyperflow in colour Doppler in chronic cases is controversial. In some descriptions, neovascularization is correlated with failed scarring; others correlate it with pain symptoms that are not related to the prognosis.

Fig. 6.46. Complete rupture of the calcaneus tendon ((b), arrows), characterized by dorsal flexion of the foot; haematoma (stars) in the unaffected paratenon ((a), (b), dotted arrow)

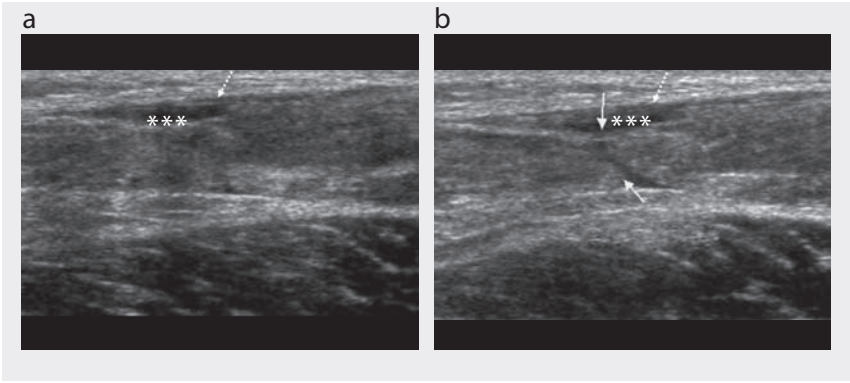

Fig. 6.47. Anisotropy characterized by acoustic shadow in the topography of the tendinous stumps (arrows). Stars, tendinous rupture

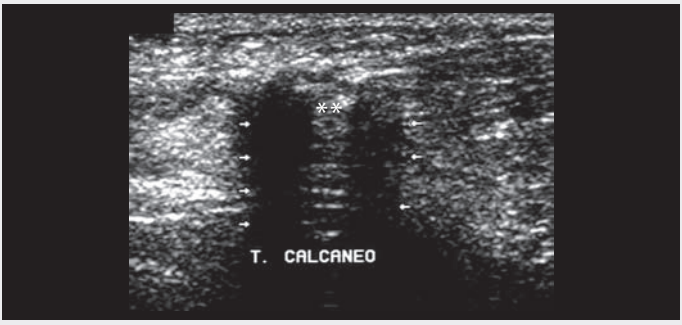

Finger pulley systems

The flexor system of the second to fifth fingers is composed of five annular and three cruciform pulleys, corresponding to thickening of the synovial sheath of the flexor tendons. The odd annular pulleys are situated on the metacarpophalangeal (A1), proximal interphalangeal (A3) and distal interphalangeal (A5) joints, which are bound in the capsuloligamentous structures. The even pulleys are situated and inserted in the phalanges: A2 in the proximal two thirds of the proximal phalange and A4 in the middle portion of the middle phalange. The cruciform pulleys are interposed between the annular pulleys (Fig. 6.48).

The thumb is slightly different, with an annular pulley for each of the metacarpophalangeal (A1) and interphalangeal (A2) joints and one of variable position (Av) on the

Fig. 6.48. Pulleys of the flexors of the fingers (a) and the thumb (b). TF, flexor tendons; A, annular pulleys; C, cruciform pulleys; ob, oblique pulley

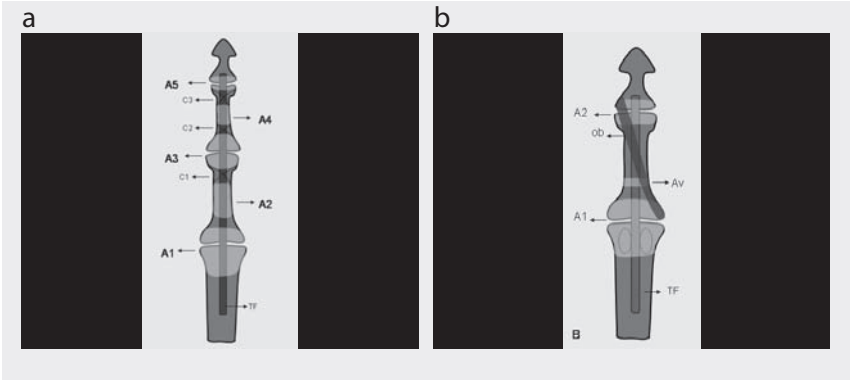

proximal half of the proximal phalange. There is also an oblique pulley extending from the ulnar aspect of the proximal phalange to the radial aspect of the distal phalange (Fig. 6.48).

The main function of the pulleys is to maintain the flexor tendons in contact with the cortical bones of the phalanges and the metacarpophalangeal joints and interphalanges, transforming the movement of the flexor tendons during flexion of the fingers into rotation and torque at the level of the interphalangeal and metacarpophalangeal joints. The most important pulleys in terms of functionality are the annular ones, especially A2 and A4 for the second and fifth fingers and A2 for the thumb. The cruciform pulleys have a secondary role, allowing approach of the annular pulleys during flexion of the fingers while maintaining the effectiveness of the movement.

Lesions of the pulleys appear after vigorous flexion of the proximal interphalangeal joints at an angle wider than 90°, with extension of the distal metacarpophalangeal and interphalangeal joints, resulting in heavy mechanical overload on the A2 and A3 pulleys.

It is important to identify the type of lesion in order to guide treatment. In partial ruptures, the treatment is conservative; complete ruptures can be treated either conservatively or by surgery, depending on the patient's age and level of activity and on the number of pulleys involved. Lack of treatment of this type of lesion can lead to osteoarthritis and contractures in flexion of the proximal interphalangeal joints. In acute trauma, with oedema and local pain, known as tenosynovitis, displacements of the proximal interphalangeal joints and ruptures of the pulleys are not easily differentiated by physical examination, and diagnosis is based on imaging methods.

The cruciform pulleys cannot be visualized by ultrasonography. All the annular pulleys can be identified with high-resolution linear transducers with a frequency of 17 MHz. At a frequency of 12 MHz, only the A2 and A4 pulleys can be identified (Fig. 6.49), as the dimensions of the pulley are directly proportional to the size of the hand.

Fig. 6.49. Ultrasonography of the A2 annular pulley with a 17-MHz high-resolution transducer in the (a) longitudinal and (b) transverse planes. T, tendon

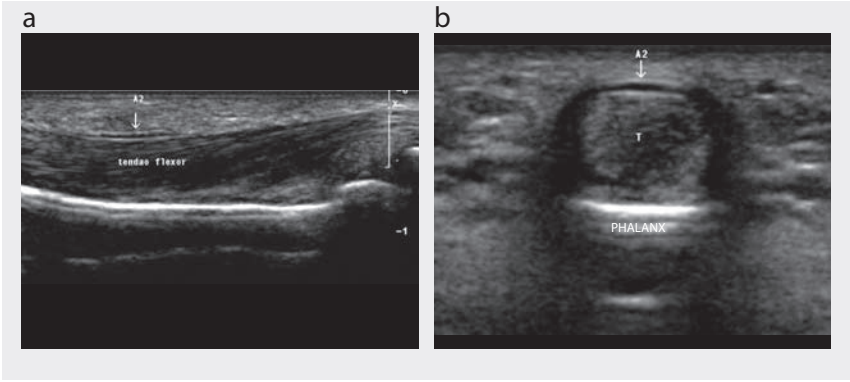

Diagnosis of lesions of the pulleys is based on the presence of two indirect signs. The first is peritendinous fluid, and the second is an increase in the distance between the phalangeal cortical bone and the posterior surface of the flexor tendons. The normal distance is 1 mm; in complete ruptures and ruptures of more than one pulley, the space between the phalange and the flexor tendons is as shown in Table 6.1. Measurements are made as shown in Fig. 6.50.

Table 6.1. Indirect signs of pulley lesions

Pulley	Place of measurement	Partial lesion	Complete lesion
A2	15–20 mm distal to the base of the proximal phalange	1.0 mm < D < 3.0 mm	D > 3.0 mm
A4	Middle portion of the middle phalange	1.0 mm < D < 2.5 mm	D > 2.5 mm

D, distance between phalangeal cortical bone and posterior surface of flexor tendons

The A2 pulley is that most commonly ruptured (Fig. 6.51). When the distance is greater than 5.0 mm, the A3 pulley is also involved. The pulleys, especially the A1 pulley, can become thicker (Fig. 6.52), and the finger resembles a trigger because the flexor tendons move with difficulty in the osteofibrous tunnel.

Fig. 6.50. (a), (b) Points for measuring the distance of the cortical bone in relation to the flexor tendons (dotted lines) for diagnosis of A2 and A4 annular pulley lesions

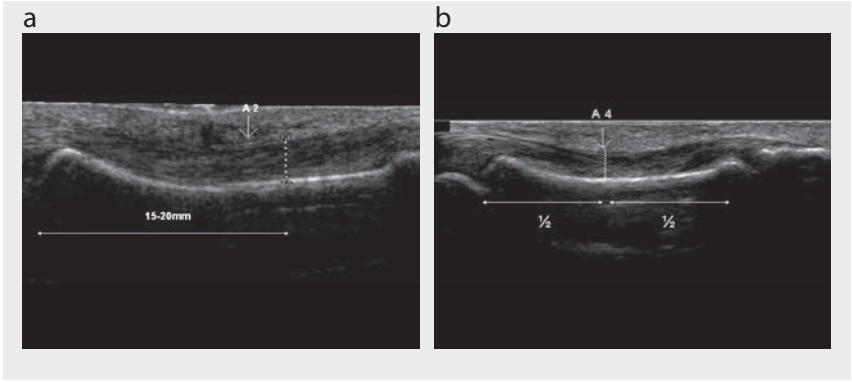

Fig. 6.51. Lesion of the A2 annular pulley. (a) Increased distance of the proximal phalangeal cortical bone in relation to the flexor tendons (arrow), which increases (0.4 cm) when the finger is flexed (b), (c)

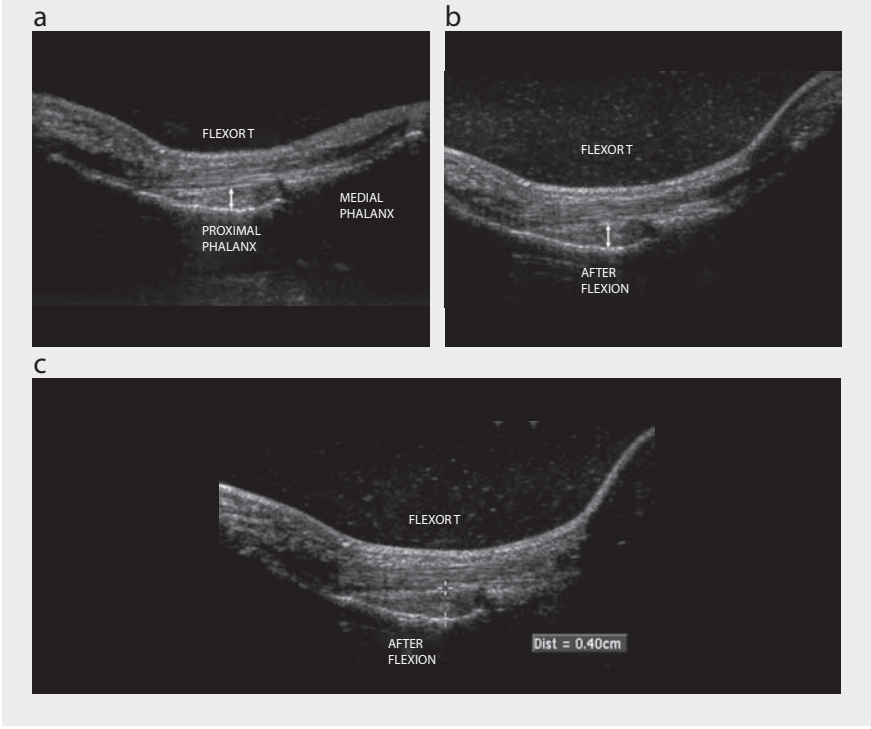

Fig. 6.52. Finger in trigger position: thickening of the A1 annular pulley ((a), calipers, arrow) and the thumb flexor tendons (T), seen (b) as an echo-poor halo in the tendons to the right

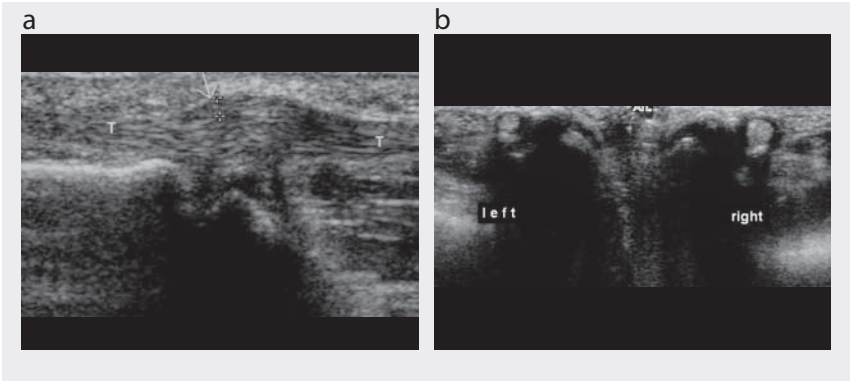

Ligaments

Structural features

Ligaments are made up of thick connective tissue, consisting mostly of type I collagen. The collagen fibres form bundles or fascicles, which are wavy and have a less regular, more heterogeneous histological aspect than tendons on ultrasonography. The presence of synovia or adipose tissue in the fascicles contributes to the heterogeneity of some ligaments, such as the deltoid (Fig. 6.53) and anterior cruciate ligaments.

Ultrasound is used mainly to study extra-articular ligaments in the diagnosis of acute ruptures and to monitor treatment or chronic lesions that result in instability of the joint.

Fig. 6.53. Heterogeneous echo texture (stars) of the deep portion of the deltoid ligament (posterior tibiotalar ligament) containing adipose tissue. LTTP, posterior tibiotalar ligament; TTP, posterior tibial tendon

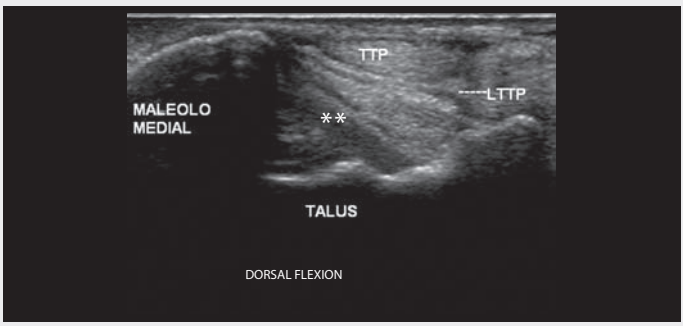

Lateral ligament complex of the ankle

The commonest lesions associated with sport are of the lateral ligament complex of the ankle (16–21%). These become chronic in more than 40% of cases if not appropriately treated. The lateral ligament complex of the ankle is made up of three ligaments: the calcaneofibular and the anterior and posterior talofibular.

The **anterior talofibular ligament** reinforces the articular capsule, presenting either horizontally or with a discreetly inferior inclination (0–20º) from the anterior border of the lateral malleolus to the lateral face of the talus body. A section parallel to the fibres shows a rectilinear trajectory and a uniform thickness of 2–3 mm, with a homogeneous or discreetly heterogeneous echo-rich texture. A transversal scan shows that the ligament is flat, with a concave–convex aspect composed of an upper, larger band and a lower one (Fig. 6.54). The upper band joins the fibular origin of the anterior tibiofibular ligament, while the lower one joins the fibular origin of the calcaneofibular ligament. In the neutral position, the fibres are relaxed and parallel to the long axis of the talus. Plantar flexion and inversion of the foot cause some stretching, generating tension in the fibres.

Fig. 6.54. Anterior talofibular ligament. (a) Examination technique. Ultrasound scan indicating the two sides of the ligament in the (b) transverse plane and its flat aspect in the (c) longitudinal plane3. FTA, anterior talofibular

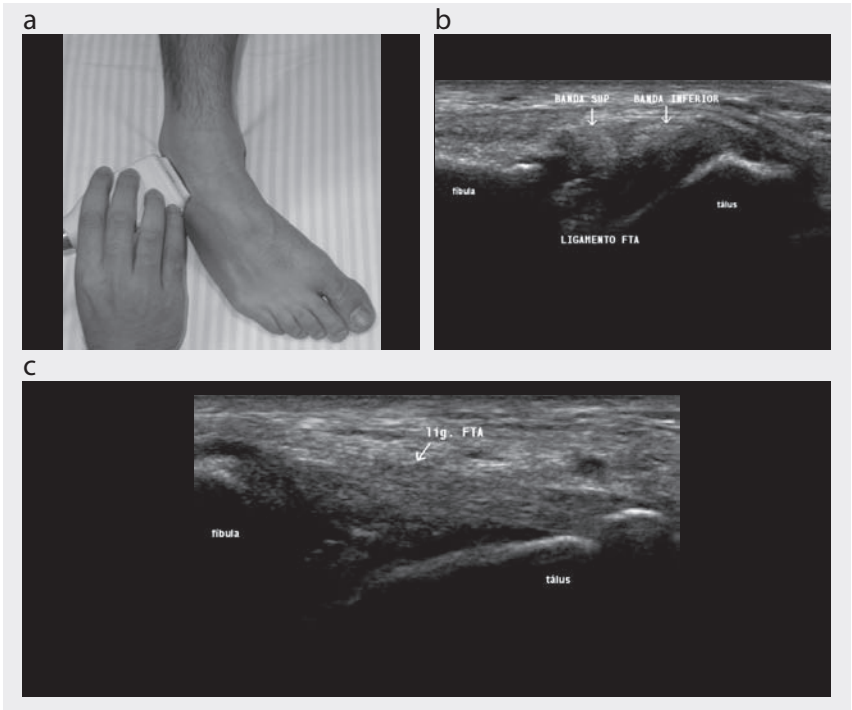

The **calcaneofibular ligament** has a string-like aspect and runs in a coronal posteroinferior oblique plan, forming an angle of approximately 45º in relation to the fibular diaphysis, joining the lower aspect (but not the extremity) of the anterior margin of the lateral malleolus at a small tubercle situated on the lateral border of the calcaneus (Fig. 6.55).

Fig. 6.55. Calcaneofibular ligament. (a) Examination technique. Ultrasound scans in the (b) transverse and (c) longitudinal planes, showing the string-shaped ligament in close contact with the fibular tendons (T). Star, calcaneofibular ligament

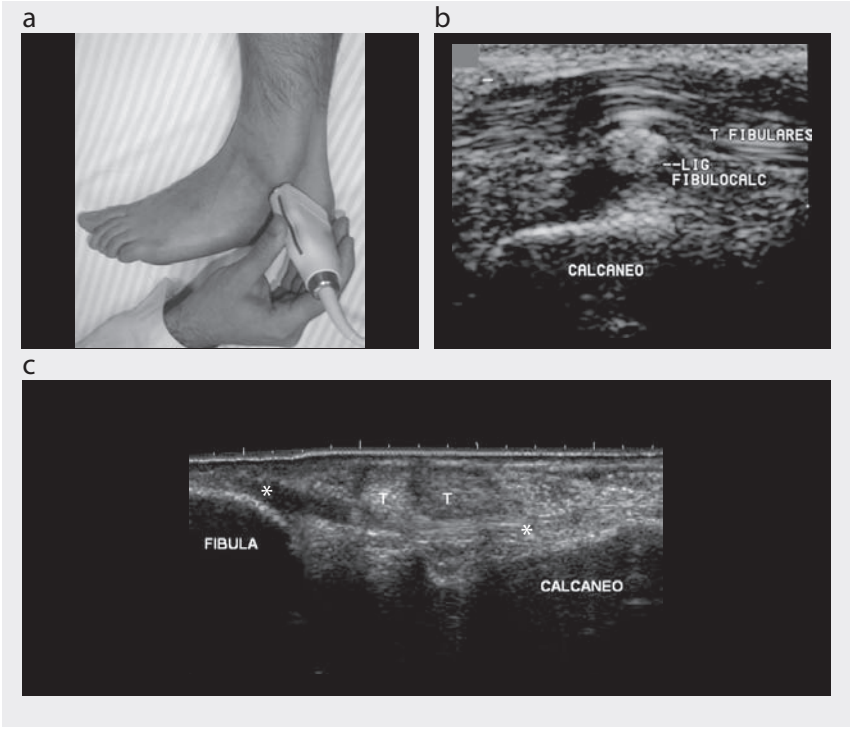

The **posterior talofibular ligament** is difficult to examine by ultrasound. It looks like a bundle, with interposed bands of adipose tissue, and inserts into the internal concave margin of the distal malleolar fossa of the fibula and the lateral tubercle of the posterior process of the talus. The ligaments of the lateral complex are the most frequently injured in ankle sprains, usually due to plantar flexion and supination with inversion of the foot. If the force of the inversion is progressive, the lesions will occur in sequence, from the weakest to the most resistant ligament: the anterior talofibular (in 70% of cases); the calcaneofibular (20–25%), usually accompanied by a lesion of the anterior talofibular, making the hindfoot unstable; ligaments of the sinus tarsus; and the posterior talofibular ligament, which is injured only in ankle luxation.

A diagnosis is frequently made solely by clinical evaluation; however, the accuracy of diagnosis of an acute lesion is reduced in 50% of cases by pain and local oedema, and imaging methods are recommended. MRI has been reported to be more accurate than ultrasound for the diagnosis of ligament lesions; however, the studies were conducted before the advent of high-resolution transducers, and there has been no recent comparison of the performance of ultrasound and MRI with current ultrasound equipment.

Ligament lesions can be classified according to the time since the trauma (acute and chronic lesions) and the extent or severity of the rupture (partial or complete). Ultrasound diagnosis is based on direct and indirect signs. The nonspecific, indirect signs in calcaneofibular ruptures are oedema or subcutaneous bruises on the lateral face of the ankle; articular effusion in the anterolateral talofibular recess; lesions of the anterior talofibular ligament; and fluid in the synovial sheath of the fibular tendons.

The direct signs are intrinsic alterations in the form, thickness and echogenicity of the ligament. Some are typical of partial lesions and others of complete lesions; some lesions present both situations, differing only in severity. In partial lesions, thickening and hypoechogenicity are seen. In lesions that are partial or complete, depending on how severely the ligament is affected, tapering, discontinuity and elongation with waving (looseness) of the contours are observed. Complete lesions, such as an absent ligament, complete discontinuity (Fig. 6.56) and amputation of the ligament with frayed stumps, are poorly defined or resemble a nodule (pseudotumour).

These signs are due either to intense oedema and haemorrhage (in partial or complete acute lesions) or to repairing tissue (in subacute or subchronic lesions). About 50% of ruptures of the anterior talofibular ligament are accompanied by fracture or avulsion of a talus bone fragment, and about 45% involve the middle third of the ligament. In the coronal plane, an echo-poor focus can be seen adjacent to the apex of the lateral malleolus.

Fig. 6.56. Complete rupture (acute) of the anterior talofibular ligament (arrow) associated with fluid–debris (stars), with the remaining ligament stump adjacent to the fibula (dotted arrow)

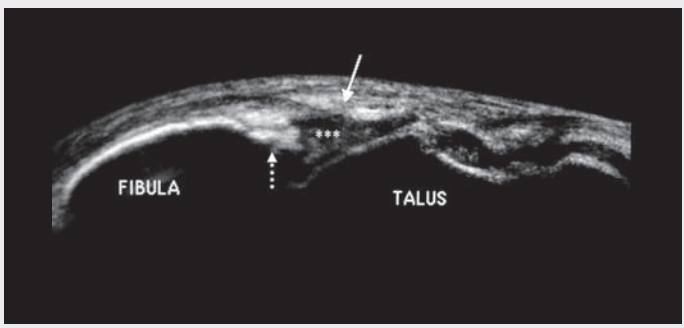

Oedema of the soft tissue disappears during healing, which begins 7 days after a trauma. The ligament is always thickened; the first evidence of repair of a ligament, with visualization of echoes filling the discontinuities, appears about 5 weeks after a trauma. An echo-rich focus can be seen inside the scarred ligament, corresponding to calcifications, and bone irregularities are found adjacent to the insertions into the fibula and the talus as a consequence of bone avulsion.

If the scarring process does not take place appropriately, the lesion becomes chronic and may lead to instability, resulting in ligament inadequacy. Chronic lesions are characterized by lack of or significant tapering or stretching of the ligament and may be accompanied by small amounts of intra-articular fluid. In dynamic studies (drawing manoeuvre) of instability, the ligament is elongated (Fig. 6.57).

Fig. 6.57. Chronic lesion of the anterior talofibular ligament (FTA). (a) Drawing manoeuvre; ultrasonographic examination (b) before and (c) after the manoeuvre shows an elongated ligament and increased articular space, which is filled with fluid (stars)

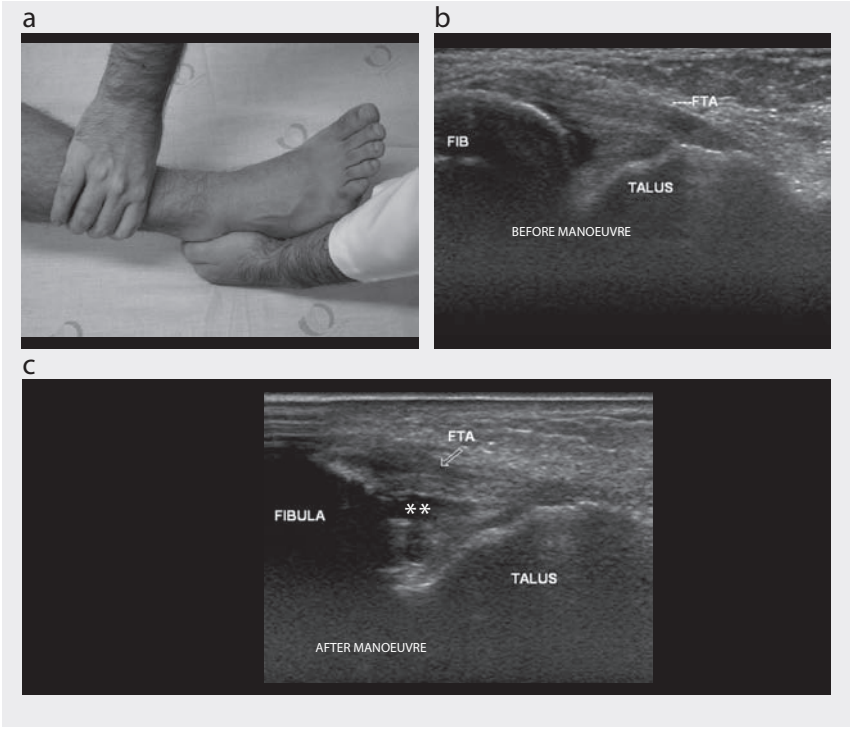

Muscle

Muscle is the largest individual mass of corporal tissue, corresponding to 40–45% of a person's weight. It is classified as elastic or nonelastic. Elastic muscle tissue is made up of muscle fibres joined into fascicles, which form the muscle. Nonelastic structures are made up of muscle surrounded by sheaths formed by connective tissues and muscle fasciae. The endomysium is an extensive network of capillaries and nerves involving all muscle fibres. Muscle fibres are bound into fascicles by perimysium, a fibroadipose septum made up of vessels, nerves and conjunctive and fat tissue. The epimysium, composed of dense conjunctive tissue, separates muscle venters and different muscles, such as the semimembranosus and the femoral biceps in the posterior thigh. The fascia is situated externally to the epimysium and contains a whole muscle.

Muscles may contain slow-twitch (type I) fibres rich in oxygen or fast-twitch (type II) fibres, with anaerobic metabolism. The proportion of each type of fibre inside the muscle venter is determined genetically, by type of physical training and by the location, form and function of the muscle. Posture muscles have linearly arranged fascicles, a prevalence of type I fibres and many mitochondria, allowing sustained low-energy contraction. The muscles in the superficial areas of the extremities, usually passing over more than one joint, have fibres with a pennate distribution and contain predominantly type II fibres. Muscles with these characteristics give more vigorous contractions and have a propensity to rupture.

Muscle contractions can be divided into isotonic and isometric. In isometric contractions, the length of the muscle fibre remains constant with changes in the applied load on the muscle. In isotonic contractions, the length of the muscle fibre changes, either shortening (concentric contraction) or lengthening (eccentric contraction). Usually, agonist muscles involved in a certain movement undergo concentric contraction due to the stability of the closest joint, which is determined by the eccentric contraction of the antagonist muscle, which is also responsible for slowing down the movement. This occurs, for instance, during a kick, when the stability of the knee joint is maintained by contraction of the ischiotibials, so that the femoral quadriceps can execute the movement.

Muscle ruptures

Muscle ruptures are secondary to direct or indirect trauma. Direct traumas, or contusions, involve compression of the muscle against a bone structure, so that the lesion is due to crushing. Indirect traumas are due to stretching of muscle fibres and can be generated by passive hyperextension of the fascicles, although they usually occur during eccentric contraction of the muscle.

Thus, both morphological and functional factors increase the risk for muscle lesion, the main ones being passing over more than one joint, eccentric contraction, predominance of type II fibres (quick contraction) and a superficial location at the extremities, mainly in the lower limbs. The site of the lesion depends on age and physical condition and is due to biomechanical particularities that determine weaker

areas. In the immature skeleton, lesions are usually found at the interface between tendon and bone, with a greater probability of fracture due to avulsion. In athletes and other young adults, lesions usually occur in the musculotendinous area, while in elderly people ruptures usually affect the tendon, resulting in tendinosis. When the lesion is of muscular origin, pain is restricted to the affected region, beginning immediately after the trauma. Sometimes, subcutaneous bruises can be seen 12–24 h after a trauma. If the alteration occurs in a tendon, the symptoms are diffuse and irradiated.

The approach described below is indispensable for correct interpretation of ultrasound findings. The elastic elements appear as elongated, echo-poor structures surrounded by nonelastic elements, which are echo-rich. In nonelastic structures, the endomysium is not seen on ultrasound, thereby preventing visualization of each muscle fibre. The perimysium is observed in a longitudinal section as multiple, parallel, linear, echo-rich images, separating the fascicles. Their orientation varies with the architecture of the muscle under study. In transverse section, the perimysium is seen as multiple points or irregular lines of varied lengths. The epimysium is seen as parallel, echo-rich lines external to the widest axis of the muscle and indistinguishable from the fascia (Fig. 6.58).

Fig. 6.58. Normal architecture of muscle venter. (a) Transverse and (b) longitudinal scans. Stars, muscle fascicles; arrow, perimysium; dashed arrow, epimysium and fascia

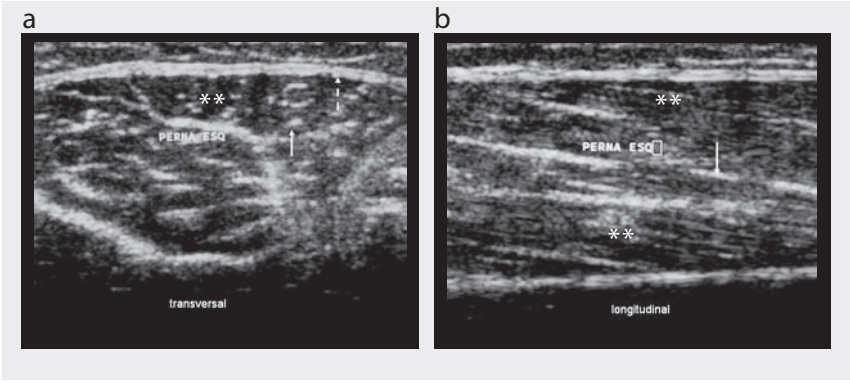

In post-trauma evaluation, ultrasound can be used for diagnosis, to identify the muscle involved, to grade the rupture or to monitor the healing process and possible complications, thus helping to predict the length of rest. A system for grading muscle lesions by ultrasound is illustrated in Table 6.2. Its clinical usefulness and inter- and intra-observer differences are, however, not yet established. In practice, the most important information for the orthopaedist is whether there is significant rupture of the muscle fibres or bruises.

In stretching and in bruises with no significant rupture of the muscle fibres, the only finding is a poorly defined echo-rich area, sometimes associated with a discreet increase in the volume of the muscle venter (Fig. 6.59). In these situations, the case

Table 6.2. Ultrasound grading of muscle lesions

Grade	Description	Ultrasound findings
0	Stretching	Normal
1	Stretching associated with lesion involving < 5% of muscle fibres	Small, striated, echo-poor images 3–7 cm long and 2–10 mm in diameter
2	Partial rupture	Discontinuity of fibroadipose septa and of muscle fascicles, associated with haematoma
3	Complete rupture	Retraction of muscle venter with formation of a pseudo-mass, accompanied by haematoma. The epimysium may be torn.

Fig. 6.59. Poorly defined, echo-rich zone (arrow) in the long adductor of the anterior right thigh, compatible with oedema secondary to stretching (grade I lesion)

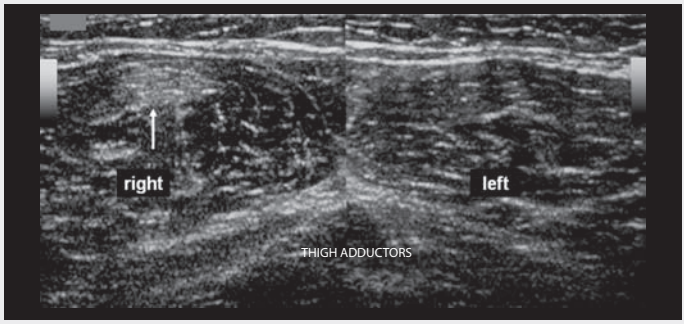

history is important, as other conditions, such as denervation, myositis, late-onset muscle pain, compartmental syndrome, rhabdomyolysis and post-exercise condition, may present the same aspect.

The diagnosis must be made as soon as possible, because fluid (blood) may appear or accumulate after days or a few weeks. The earlier treatment is started, the less likely haematoma formation will be. Because the echogenicity may change in the post-exercise period, ultrasound evaluation should be conducted 2–48 h after the trauma. Examinations should be conducted during movement, at rest and during isometric contraction to help identify fibre discontinuity. Serial ultrasound examinations are used to monitor the evolution of grade II and III lesions (Fig. 6.60, Fig. 6.61), which are likely to have sequelae, especially if there is a large haematoma. Muscles have a high potential for regeneration, with cells originating in the endomysium; however, the process is slow, beginning 48 h after an acute event but taking from 3 weeks to 4 months to be completed. On ultrasound, regeneration is seen as slightly echo-rich tissue (Fig. 6.62) surrounding a haematoma, which is slowly reabsorbed. Fibroadipose septa gradually appear inside the tissue, taking the place of the rupture, so that the normal architecture of the muscle is restored.

Fig. 6.60. (a), (b) Partial muscle rupture (grade II lesion, arrow), associated with a small bruise

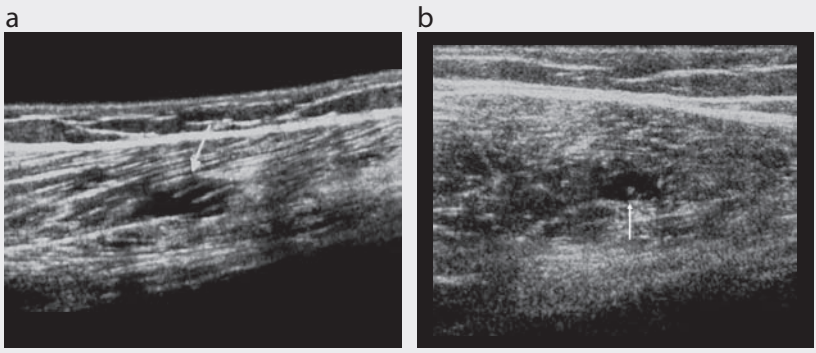

Fig. 6.61. Complete rupture (grade III lesion, arrow) in the musculotendinous transition of the long adductor of the thigh, filled with heterogeneous material (bruise). Dotted arrow, remaining tendon

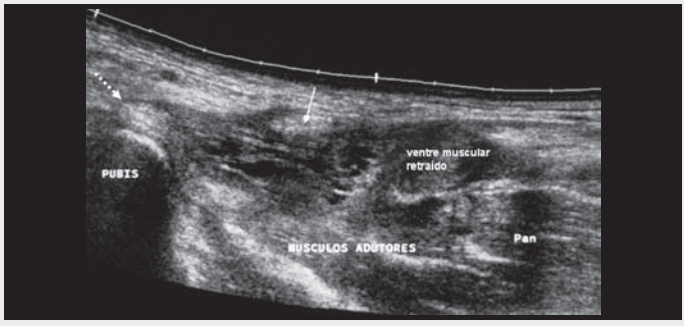

Fig. 6.62. Repairing tissue, characterized by discreetly echo-rich material (arrow), on the periphery of the subfascial partial lesion

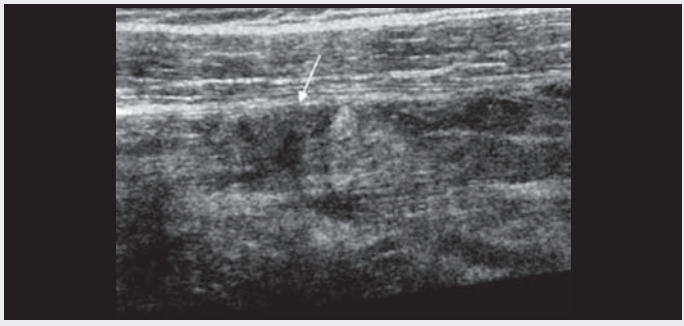

Rupture complications

Acute

After severe ruptures or in patients with coagulation anomalies, **haemorrhages** may lead to compartmental syndrome.

Rhabdomyolysis may occur after serious trauma caused by crush, infection, hypoxia or drugs (e.g. cocaine) and secondary to metabolic alterations. It requires surgery. It is seen as an irregular, echo-poor area within the muscle, its volume being increased in areas of multiple necrosis.

A haematoma is rarely infected to such an extent that **abscesses** are formed that require surgical drainage.

Chronic

Most small lesions and intermuscular haematomas evolve without sequelae. Intramuscular lesions, larger lesions and recurrent lesions may lead to the appearance of fibrosis, cysts, myositis ossificans or hernia.

Fibrosis: In large ruptures, repair of the muscle involves two processes: regeneration of muscle fibres and formation of fibrosis. When the latter predominates, an irregular, focal, echo-rich or radiated area can be seen on ultrasound (Fig. 6.63), frequently adhering to the epimysium and sometimes resulting in focal retraction of the fascia. It remains unchanged during muscle contraction manoeuvres. The presence of fibrous scarring predisposes the muscle to recurrent ruptures.

Fig. 6.63. Ultrasonography of the femoral rectum muscle. (a) Longitudinal, (b) transverse plane. Fibrosis, characterized by an echo-rich zone (arrow) with partially clear edges, located inside the femoral rectum muscle venter and entering the vastus intermedius through a discontinuity of the muscle fascia (dotted arrow)

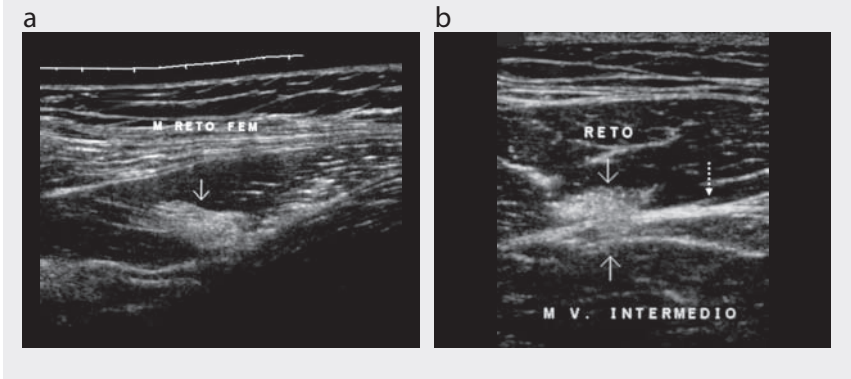

Muscle cyst is a rare complication and is due to incomplete resorption of a haematoma (Fig. 6.64). It also favours new muscle rupture.

Myositis ossificans is usually the result of a lesion caused by direct trauma, with formation of an intramuscular haematoma, or by repeated microtraumas, mainly

Fig. 6.64. Intramuscular cyst (cisto) in the lateral vastus, secondary to previous rupture

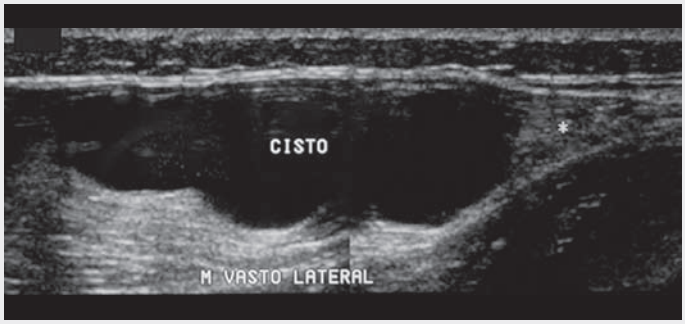

Fig. 6.65. Ossifying myositis. (a) X-ray and (b) ultrasound, showing lamellar calcification parallel to the femoral diaphysis cortex (arrow)

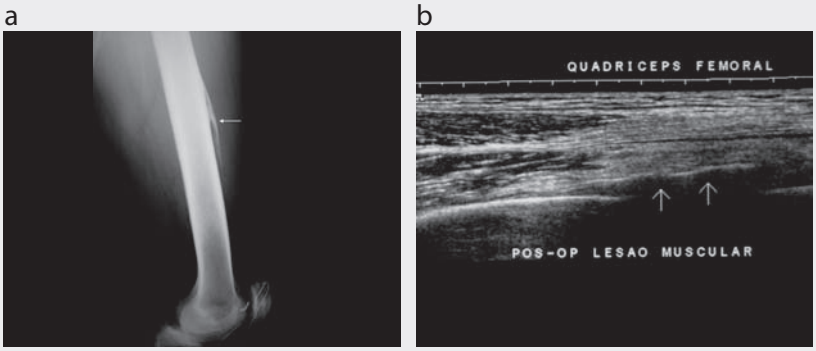

in athletes. The calcifications, which are initially lamellar, evolve to real heterotopic ossification, seen as linear, echo-rich images parallel to the adjacent cortical bone. Myositis ossificans is frequently situated inside the femoral quadriceps, particularly in the femoral rectum (Fig. 6.65).

Muscular hernia is a condition in which muscle tissue protrudes through a discontinuity or weakness of congenital or acquired fascia. The commonest causes are chronic compartmental syndrome, trauma and postoperative alterations. On ultrasound, the hernia is seen as a clearly defined nodular image in a mushroom form, its echogenicity depending on the stage of evolution. Initially, due to its proximity to fibroadipose septa, the nodule is echo-rich; afterwards, it becomes echo-poor (Fig. 6.66) due to the presence of oedema. A dynamic examination is essential, as the hernia may be fixed or intermittent, the latter being apparent only on isometric contraction of the muscle. Diagnostic sensitivity is also increased by conducting the

Fig. 6.66. Muscle hernia. (a), (b) Ultrasound and (c), (d) colour Doppler, showing an echo-rich nodular form (arrow) entering an existing defect in the fascia of the anterior leg, accompanied by a perforating vessel

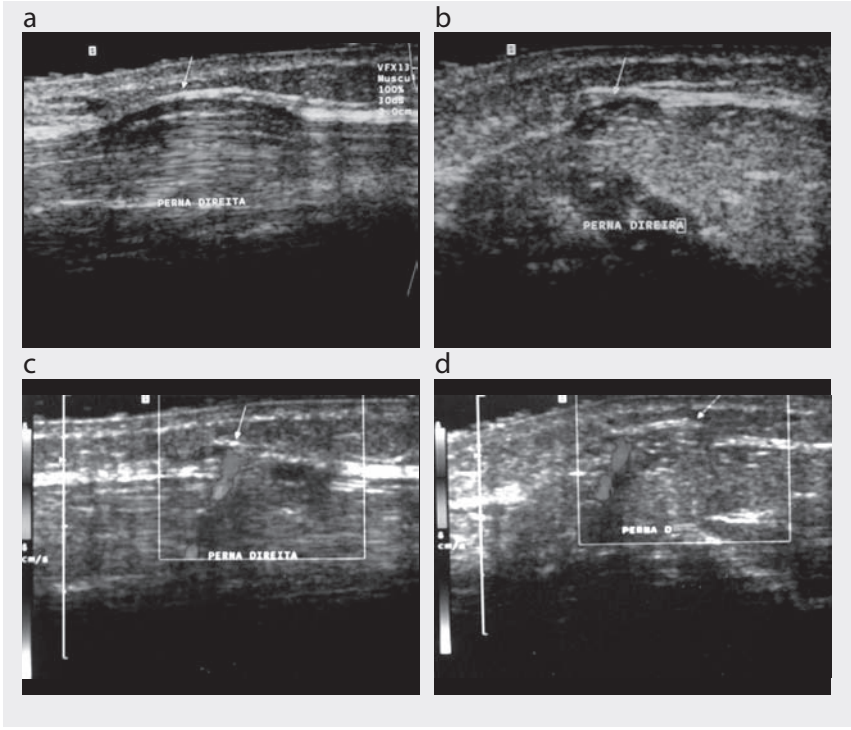

examination after exercise: a muscle hernia is more obvious during exercise, with increased local blood flow and the consequent increase in muscle volume (10–15%).

Other disorders

Baker cyst

Baker cyst, initially described by Adams in 1840 and by W. Morant Baker in 1877, is the commonest synovial cyst in the human body. The synovial bursa of the gastrocnemius and semimembranosus connects with the knee joint in 50% of normal adults, and degeneration and reduced elasticity of the joint capsule in older people might explain the high prevalence of articular problems. Baker cyst arises from lesions of the synovia or any intra-articular process that leads to fluid formation, resulting in distension of the gastrocnemius and semimembranosus bursa. This condition, which is extremely common in people with rheumatoid arthritis, is characterized by a cystic body with echo-free contents, located medially in the popliteal fossa,

between the tendon of the semimembranosus muscle and the medial head of the gastrocnemius. The bursa of these two muscles has four horns—two anterior (medial and lateral) and two posterior (medial and lateral)—which may be filled with fluid, either separately or together (Fig. 6.67, Fig. 6.68). Thus, although a Baker cyst is situated in the medial area of the popliteal fossa, it can vary slightly in location and form, sometimes with extension into the muscle planes and even into the vastus medialis, and gastrocnemius muscles.

Fig. 6.67. Bursa of the gastrocnemius and semimembranosus muscles, with the two anterior (a) and the two posterior (b) horns. CLG, lateral head of the gastrocnemius; CMG, medial head of the gastrocnemius; tsmm, semimembranosus muscle tendon

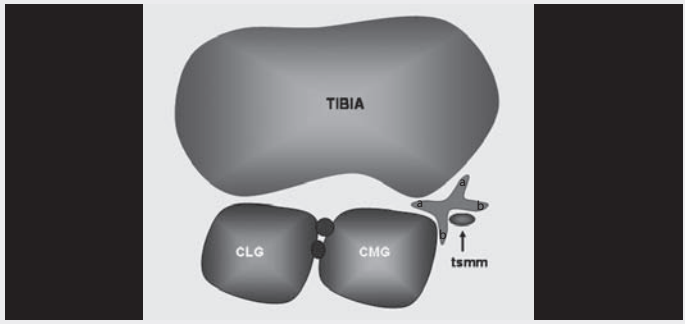

Fig. 6.68. Baker cyst, showing communication with the articular cavity (arrows); CMG, medial head of the gastrocnemius muscle

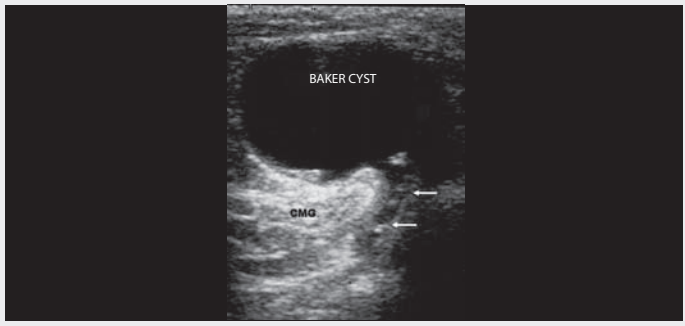

Parietal thickening, free bodies, septations and internal echoes are observed in cases of haemorrhage, infection or arthropathy caused by crystal deposits, sometimes with formation of a fluid–fluid level. The cysts may sometimes rupture, with acute pain, simulating deep-vein thrombosis. This can readily be diagnosed with ultrasound as loss of definition of the cyst wall, with fluid diffusing through the muscle and subcutaneous planes, associated with oedema of soft tissue (Fig. 6.69).

Fig. 6.69. Rupture of Baker cyst: heterogeneous content and septae due to undefined inferior wall, with perifascial free fluid (arrow)

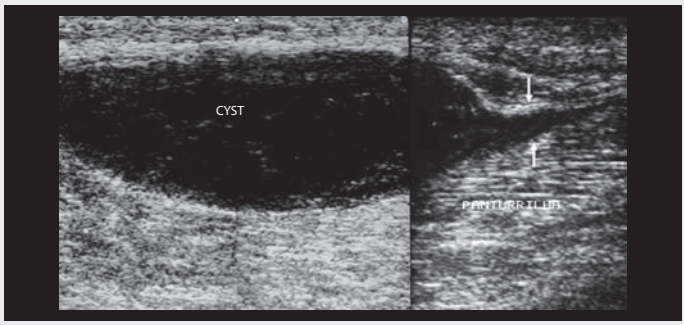

Morton neuroma

Morton neuroma is a thickening of the interdigital nerve, usually in the third intercapitometatarsal space. Its cause is uncertain but is probably related to repetitive trauma or ischaemia resulting in neural imprisonment. It is prevalent in women aged 40–60 years and can be symptomatic or asymptomatic. When it is symptomatic, it leads to pain and paraesthesia, which worsens with walking. It is unilateral in 73–90% of cases.

On ultrasound examination, Morton neuroma is seen as an echo-poor nodule between the metatarsal heads, plantar to the transverse metatarsal ligament. Its diagnosis is confirmed when there is continuity with the interdigital nerve (Fig. 6.70), as other conditions, such as neurofibroma, schwannoma, angiolipoma or angioleiomyoma, may have a similar ultrasonographic aspect. Neuromas can be accompanied by intermetatarsal bursitis, which can also occur separately, characterized by increased fluid (> 3 mm), compressibility in dynamic manoeuvres and a location superficial to the deep transverse metatarsal ligament.

Fig. 6.70. Morton neuroma. (a) Examination technique. (b) An echo-rich nodule (N) seen in the longitudinal and (c) transverse planes, situated in the plantar area of the third space between the third and fourth metatarsal heads, with thickening of the interdigital nerve (arrow)

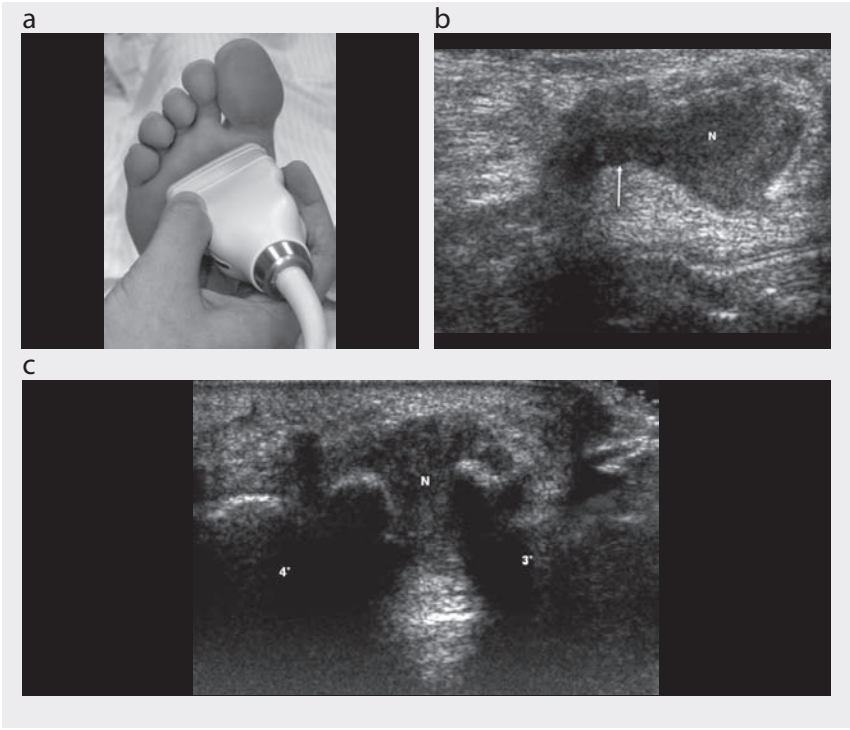

Plantar fasciitis

Plantar fascia, or aponeurosis, originates in the posteromedial tuberosity of the calcaneus and has medial, central and lateral sections. The central section is the strongest and thickest (2–4 mm), with five bands in the middle part of the metatarsals. Inflammation or degeneration of the central section of the plantar fascia (fasciitis) is the commonest cause of pain in the plantar area of the calcaneus, corresponding to 7–9% of all lesions in runners. Other conditions can result in the same symptoms, including stress fractures of the calcaneus, tarsal tunnel syndrome, seronegative arthropathies and neuritises. Microruptures in the fascia are due to repetitive traction microtraumas, which lead to inflammation and angiofibroblastic proliferation, as observed in tendinosis. The predisposing factors include systemic diseases (rheumatoid arthritis, gout and spondyloarthropathy), splayfoot, concave foot and ill-fitting shoes.

Fig. 6.71. Plantar fascia. (a) Examination technique. (b) Ultrasound scan showing a striped, echo-rich image, starting in the inferior tuberosity of the calcaneus (calipers)

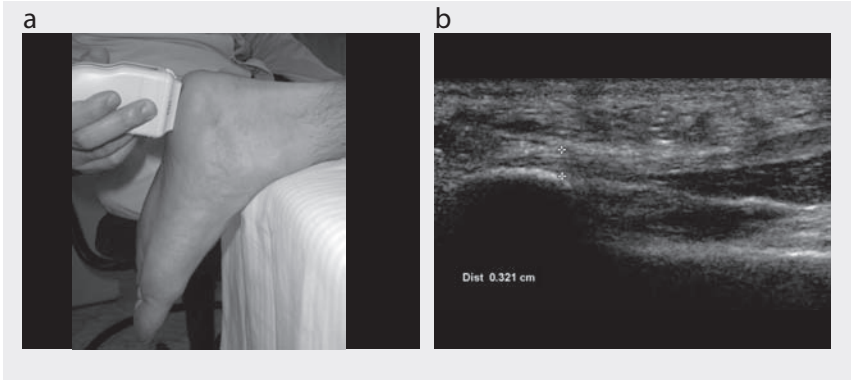

Fig. 6.72. Plantar fasciitis. Thickening and hyperechogenicity of the plantar fascia at its insertion into the calcaneus (calipers)

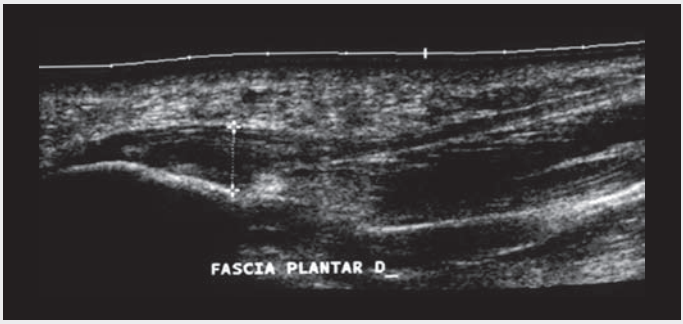

On ultrasound, the normal fascia presents a fibrillar aspect (Fig. 6.71), except in patients with discreet hypoechogenicity near the calcaneus due to an anisotropic effect. In fasciitis, there is some thickening (> 5 mm) and reduced echogenicity of the fascia, usually close to its insertion into the calcaneus, and some calcification (Fig. 6.72). Bilaterality is not uncommon. Ultrasound can, however, lead to false-negative results.

The commonest findings with MRI in suspected plantar **fasciitis**, in decreasing order of frequency, were perifascial oedema, oedema of the calcaneus medullary bone, signal alteration inside the fascia and thickening of the plantar fascia. Thus, if the **fasciitis** is slight, it is not seen by ultrasound; nor can bone oedema be seen by this technique.

Superficial fibromatosis

Superficial fibromatosis is due to proliferation of benign fibrous tissue, with aggressive biological behaviour. Palmar (Dupuytren contracture), plantar (Ledderhose disease) and penile (Peyronie disease) fibromatoses are part of a spectrum of the same disease, although they may occur separately.

In Ledderhose disease, there is some thickening, with a nodular aspect and reduced echogenicity, beginning in the area of the plantar cavum (Fig. 6.73). Isolated nodules must be differentiated from granulomas and from rheumatoid nodules.

Fig. 6.73. Plantar fibromatosis. Echo-rich nodules (N) with well-defined outlines inside the plantar fascia (arrows) in (a) transverse and (b) longitudinal planes

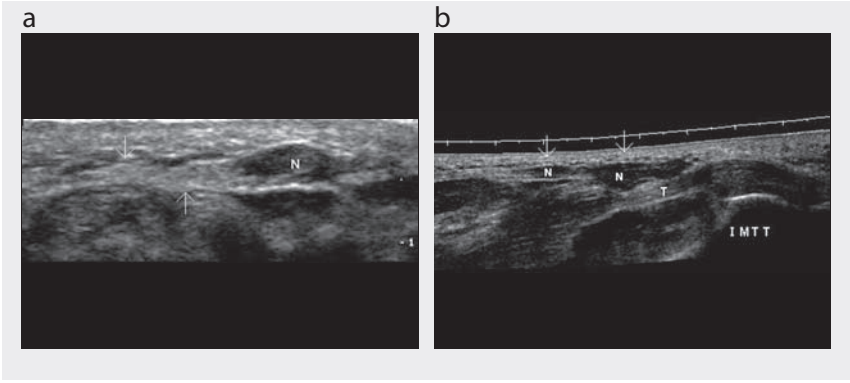

The ultrasound aspect of Dupuytren contracture is similar to that of palmar fibromatosis, extending from the third to the fifth finger. It is prevalent in middle-aged or elderly men, alcoholics and patients with epilepsy who have taken phenobarbital for long periods. Patients report repeated microtrauma in the area. The nodules tend to converge over time, forming fibrous strings, with consequent retraction or palmar aponeurosis.

Compressive neuropathies: Carpal tunnel syndrome

Compression of the middle nerve inside the carpal tunnel is the most frequent peripheral compressive neuropathy and that most easily treated. The syndrome is characterized by paraesthesia or pain on the palmar face, from the first to the radial half of the fourth finger, associated with weakness and atrophy of the thenar musculature in the most advanced cases.

More than half a century elapsed between Paget's description of its symptoms in 1854 and full understanding of the syndrome. The diversity of clinical aspects of compression of the middle nerve led to a certain confusion in characterization of this syndrome, which partly explains this relatively long period.

Usually, when peripheral nerves pass over a joint, they also pass over osteofibrous tunnels, with a risk for neural displacement during movement. As the tunnels are relatively inelastic, however, they are vulnerable to compressive neuropathy. The physiopathology of carpal tunnel syndrome has been the subject of much speculation. Nerve compression can be due to anatomical, intrinsic or mechanical factors.

The anatomical factors are related to conditions that determine a decrease in the dimensions of the carpal tunnel (acromegalia, wrist bone alterations and alterations of the distal radius) or an increase in the content of an osteofibrous tunnel (tumours, anomalous muscle venters, synovitis or haematomas). The intrinsic factors include neuropathy secondary to diabetes mellitus, alcoholism, amyloidosis, infections, gout or tenosynovitis and situations that alter the water balance, such as pregnancy, use of oral contraceptives, hypothyroidism or long periods of haemodialysis. The mechanical factors vary from repeated flexion and extension movements to excess weight on the extended carpal tunnel in patients who use a cane or a crutch.

The process starts with modification of the microcirculation, with a decrease in epineural capillary flow. As the pressure increases, epineural, endoneural and arteriolar capillary flow is reduced. This leads to endoneural oedema, associated with increased capillary permeability, resulting in macrophage migration. These inflammatory cells produce cytokines, which cause proliferation of the fibrous tissue, involving the neural sheath and the axon itself, culminating in axonal degeneration and demyelination.

If the causal factor is small and of short duration, the alterations are reversible; however, if the compression persists and becomes more intense, irreversible lesions can form, creating a vicious circle and resulting in persistent symptoms or symptoms generated by submaximum effort. The first symptoms are paraesthesia and hyperaesthesia, as the middle nerve is made up mainly (94%) of sensitive fibres. As the disease develops, motor fibres become involved, leading to weakness and atrophy of the thenar musculature.

Ultrasound criteria for diagnosis of carpal tunnel syndrome are a reduction in the echogenicity of the middle nerve due to oedema, accompanied by tapering in the distal carpal tunnel and an increase in its upstream area (Fig. 6.74).

These authors not only described qualitative alterations to the median nerve but also established quantitative criteria for the diagnosis of carpal tunnel syndrome. Hardening of the median nerve in the proximal carpal tunnel, at the level of either the distal radius or the pisiform bone, was evaluated by measuring the area of the nerve in transverse section. Tapering of the median nerve in the distal carpal tunnel in the hamate bone is measured in transverse section as the ratio between the largest and smallest axes of the median nerve (tapering ratio). Thin tapering corresponds to a ratio > 3. Cambering (incurvation, arching) of the retinaculum of the flexors is evaluated as the distance between the top of the flexor retinaculum and an imaginary line drawn between the trapeze and the hamate. Values > 4 mm are considered abnormal. The most useful criterion for a diagnosis of compressive neuropathy is an

Fig. 6.74. Thickened, echo-rich median nerves, with a reduced number of neural fascicles to the right, replaced by echo-rich tissue corresponding to adipose tissue and fibrosis

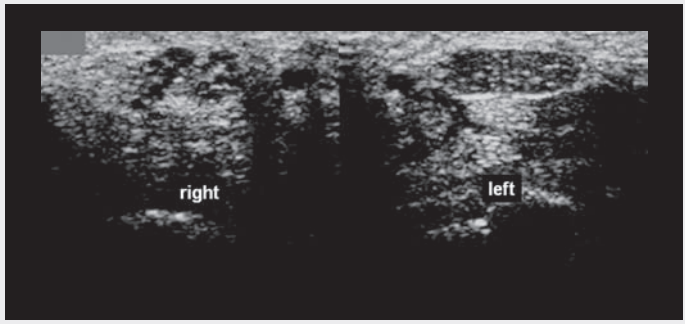

Fig. 6.75. Measurement of the area of the median nerve (0.07 cm^2) using (a) direct and (b) indirect methods. ESC, scaphoid; PIS, pisiform; CG, Guyon channel

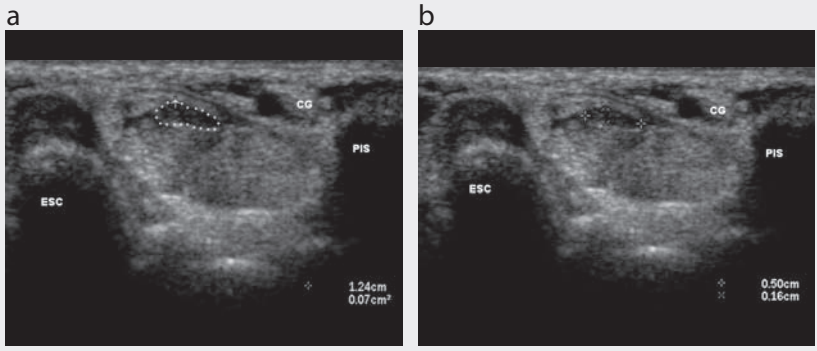

Fig. 6.76. Thickened median nerve (NM) inside a carpal tunnel (a) with a transverse section of 0.16 cm^2 (b).

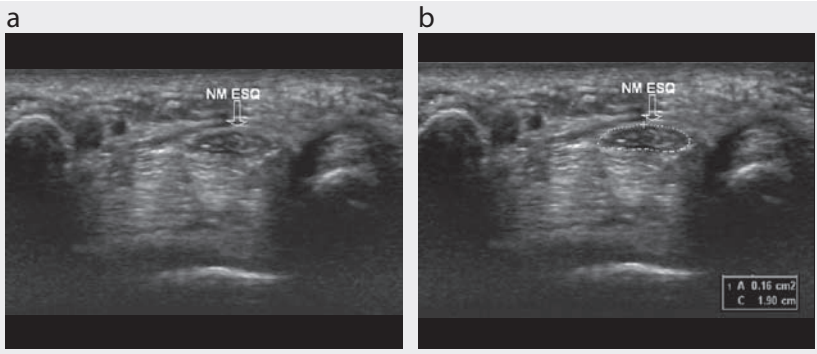

increase in the cross-sectional area of the median nerve. Distal tapering of the nerve and incurvation of the retinaculum of the flexors showed poor reproducibility in subsequent studies.

The cross-sectional area of the median nerve can be measured either indirectly or directly. In the indirect method, the formula for the area of the ellipse $[p(D_1 \times D_2) / 4]$ is used, in which D_1 and D_2 represent the transverse and anteroposterior diameters of the median nerve (Fig. 6.75 a). In the direct method, the area is calculated by ultrasound, from a continuous trace around the nerve (Fig. 6.75 b). Regardless of the method used, the neural sheath must always be excluded from the measure.

The cut-off point of the cross-sectional area for differentiating between normal and thickened nerves has been the subject of controversy in the literature, suggestions varying from 9 to 15 mm^2. This wide variation is due to the use of different equipment, inclusion of people of both sexes in the same study, studies of people of different ages, different severity of disease and imprecise measurement area. Each unit should establish its own value on the basis of the population being studied. For women, we have adopted cross-sectional area cut-off points of 9 mm^2 measured by the indirect and 10 mm^2 measured by the direct method (Fig. 6.76).

Recommended reading

Safety of diagnostic ultrasound

- Abramowicz JS et al. Fetal thermal effects of diagnostic ultrasound. American Institute of Ultrasound in Medicine. *Journal of Ultrasound in Medicine*, 2008,27:541-559. PMID:18359908
- Barnett SB. Safe use of ultrasound contrast agents. *Ultrasound in Medicine & Biology*, 2007,33:171-172. doi:10.1016/j.ultrasmedbio.2006.07.001 PMID:17239523
- *Basic physics of ultrasonographic imaging*. Geneva, World Health Organization, 2005.
- Bioeffects Committee of the American Institute of Ultrasound in MedicineAmerican Institute of Ultrasound in Medicine consensus report on potential bioeffects of diagnostic ultrasound: executive summary. *Journal of Diagnostic Medical Sonography*, 2011,27:3-13. doi:10.1177/8756479310394986
- Bly S, Van den Hof MC. Obstetric ultrasound biological effects and safety, SOGC Clinical Practice Guidelines. *Journal of Obstetrics and Gynaecology Canada*, 2005,27:572-580. PMID:16100635
- Claudon M et al. Guidelines and good clinical practice recommendations for contrast-enhanced ultrasound (CEUS) – update 2008. *Ultraschall in der Medizin (Stuttgart, Germany : 1980)*, 2008,29:28-44. doi:10.1055/s-2007-963785 PMID:18270887
- Duck FA. Hazards, risks and safety of diagnostic ultrasound. *Medical Engineering & Physics*, 2008,30:1338-1348. doi:10.1016/j.medengphy.2008.06.002 PMID:18635388
- Fowlkes JB. American Institute of Ultrasound in Medicine consensus report on potential bioeffects of diagnostic ultrasound: executive summary. *Journal of Ultrasound in Medicine*, 2008,27:503-515. PMID:18359906
- *Guidelines for the safe use of diagnostic ultrasound equipment*. London, British Medical Ultrasound Society, 2009. http://www.bmus.org/policies-guides/BMUS-Safety-Guidelines-2009-revision-FINAL-Nov-2009.pdf
- *Manual of diagnostic ultrasound*. Geneva, World Health Organization, 1995.
- Effects of ultrasound and infrasound relevant to human health. *Progress in Biophysics and Molecular Biology*, 2007,93:1-420.
- Stratmeyer ME et al. Fetal ultrasound: mechanical effects, American Institute of Ultrasound in Medicine. *Journal of Ultrasound in Medicine*, 2008,27:597-605. PMID:18359910
- Whitworth M, Bricker L, Neilson JP et al. Routine compared with selective ultrasound in early pregnancy. *Cochrane Summaries*, 14 April 2010.

Obstetrics

- Acharya G et al. Reference ranges for serial measurements of blood velocity and pulsatility index at the intra-abdominal portion, and fetal and placental ends of the umbilical artery. *Ultrasound in Obstetrics & Gynecology*, 2005,26:162-169. doi:10.1002/uog.1902 PMID:15883983
- American College of Obstetricians and GynecologistsACOG Practice Bulletin No. 101: Ultrasonography in pregnancy. *Obstetrics and Gynecology*, 2009,113:451-461. PMID:19155920
- Arduini D, Rizzo G. Prediction of fetal outcome in small for gestational age fetuses: comparison of Doppler measurements obtained from different fetal vessels. *Journal of Perinatal Medicine*, 1992,20:29-38. doi:10.1515/jpme.1992.20.1.29 PMID:1608021
- Benacerraf B. *Ultrasound of fetal syndromes*. Philadelphia, Churchill Livingstone, 2007
- Benacerraf BR. The history of the second-trimester sonographic markers for detecting fetal Down syndrome, and their current role in obstetric practice. *Prenatal Diagnosis*, 2010,30:644-652. doi:10.1002/pd.2531 PMID:20572106
- Berghella V et al. Cerclage for short cervix on ultrasonography: meta-analysis of trials using individual patient-level data. *Obstetrics and Gynecology*, 2005,106:181-189. doi:10.1097/01.AOG.0000168435.17200.53 PMID:15994635
- Berghella V, Bega G. Ultrasound evaluation of the cervix. In: Callen PW, ed.. *Ultrasonography in obstetrics and gynecology*, 5th ed. Philadelphia, Saunders-Elsevier, 2008: 698–720
- Birnholz JC. An algorithmic approach to accurate ultrasonic fetal weight estimation. *Investigative Radiology*, 1986,21:571-576. doi:10.1097/00004424-198607000-00010 PMID:3525451
- Bricker L, Neilson JP, Dowswell T. Routine ultrasound in late pregnancy (after 24 weeks'gestation). *Cochrane Database of Systematic Reviews*, 2008,4:CD001451- doi:10.1002/14651858.CD001451.pub3
- Callen PW. *Ultrasonography in obstetrics and gynecology*, 5th ed. Philadelphia, Saunders-Elsevier, 2008
- Campbell S, Thoms A. Ultrasound measurement of the fetal head to abdomen circumference ratio in the assessment of growth retardation. *British Journal of Obstetrics and Gynaecology*, 1977,84:165-174. doi:10.1111/j.1471-0528.1977.tb12550.x PMID:843490
- Campbell S, Wilkin D. Ultrasonic measurement of fetal abdomen circumference in the estimation of fetal weight. *British Journal of Obstetrics and Gynaecology*, 1975,82:689-697. doi:10.1111/j.1471-0528.1975.tb00708.x PMID:1101942
- Chamberlain PF et al. Ultrasound evaluation of amniotic fluid volume. I. The relationship of marginal and decreased amniotic fluid volumes to perinatal outcome. *American Journal of Obstetrics and Gynecology*, 1984,150:245-249. PMID:6385713
- Chen M et al. Ultrasound screening for fetal structural abnormalities performed by trained midwives in the second trimester in a low-risk population--an appraisal. *Acta Obstetricia et Gynecologica Scandinavica*, 2009,88:713-719. doi:10.1080/00016340902934688 PMID:19412800
- Dighe M et al. Sonography in first trimester bleeding. *Journal of Clinical Ultrasound*, 2008,36:352-366. doi:10.1002/jcu.20451 PMID:18335508

- Eik-Nes SH. The 18-week fetal examination and detection of anomalies. *Prenatal Diagnosis*, 2010,30:624-630. doi:10.1002/pd.2576 PMID:20572118
- Eik-Nes SH, Grøttum P. Estimation of fetal weight by ultrasound measurement. I. Development of a new formula. *Acta Obstetricia et Gynecologica Scandinavica*, 1982,61:299-305. PMID:7148403
- Eik-Nes SH, Grøttum P, Andersson NJ. Prediction of fetal growth deviation by ultrasonic biometry: I. Methodology. *Acta Obstetricia et Gynecologica Scandinavica*, 1982,61:307-312. doi:10.3109/00016348209156952 PMID:7148404
- Hadlock FP et al. Sonographic estimation of fetal weight. The value of femur length in addition to head and abdomen measurements. *Radiology*, 1984,150:535-540. PMID:6691115
- Hadlock FP et al. Estimation of fetal weight with the use of head, body, and femur measurements--a prospective study. *American Journal of Obstetrics and Gynecology*, 1985,151:333-337. PMID:3881966
- Harman CR, Baschat AA. Arterial and venous Dopplers in IUGR. *Clinical Obstetrics and Gynecology*, 2003,46:931-946. doi:10.1097/00003081-200312000-00025 PMID:14595236
- Hill LM, Breckle R, Gehrking WC, O'Brien PC. Use of femur length in estimation of fetal weight. *American Journal of Obstetrics and Gynecology*, 1985,152:847-852. PMID:3895952
- International Society of Ultrasound in Obstetrics & GynecologyCardiac screening examination of the fetus: guidelines for performing the 'basic' and 'extended basic' cardiac scan. *Ultrasound in Obstetrics & Gynecology: the official journal of the International Society of Ultrasound in Obstetrics and Gynecology*, 2006,27:107-113. PMID:16374757
- International Society of Ultrasound in Obstetrics & Gynecology Education CommitteeSonographic examination of the fetal central nervous system: guidelines for performing the 'basic examination' and the 'fetal neurosonogram'. *Ultrasound in Obstetrics & Gynecology: the official journal of the International Society of Ultrasound in Obstetrics and Gynecology*, 2007,29:109-116. doi:10.1002/uog.3909 PMID:17200992
- Nicolaides KH, Rizzo G, Hecher K. *Placental and fetal Doppler*. Nashville, Parthenon Publishing Ed., 2000
- Nzeh DA, Rimmer S, Moore WMO, Hunt L. Prediction of birthweight by fetal ultrasound biometry. *The British Journal of Radiology*, 1992,65:987-989. doi:10.1259/0007-1285-65-779-987 PMID:1450836
- Ott WJ, Doyle S, Flamm S. Accurate ultrasonic estimation of fetal weight. Effect of head shape, growth patterns, and amniotic fluid volume. *American Journal of Perinatology*, 1986,3:193-197. doi:10.1055/s-2007-999866 PMID:3718640
- *Practice guidelines for the performance of obstetric ultrasound examination*. American Institute for Ultrasound in Medicine (AIUM), 2007. www.aium.org
- Rose BI, McCallum WD. A simplified method for estimating fetal weight using ultrasound measurements. *Obstetrics and Gynecology*, 1987,69:671-675. PMID:3547218
- Rumack CM, Wilson SR, Charboneau JW, Johnson JAM. *Diagnostic ultrasound*. St Louis, Elsevier-Mosby, 2005
- Sabbagha RE, Minogue J, Tamura RK, Hungerford SA. Estimation of birth weight by use of ultrasonographic formulas targeted to large-, appropriate-, and small-for-gestational-age fetuses. *American Journal of Obstetrics and Gynecology*, 1989,160:854-860, discussion 860–862. PMID:2653039

- Salomon LJ et al. International Society of Ultrasound in Obstetrics & Gynecology (ISUOG). Practice guidelines for performance of the routine mid-trimester fetal ultrasound. *Ultrasound in Obstetrics & Gynecology: the official journal of the International Society of Ultrasound in Obstetrics and Gynecology*, 2011,37:116-126. doi:10.1002/uog.8831 PMID:20842655
- Shepard MJ et al. An evaluation of two equations for predicting fetal weight by ultrasound. *American Journal of Obstetrics and Gynecology*, 1982,142:47-54. PMID:7055171
- Vintzileos AM et al. Fetal weight estimation formulas with head, abdominal, femur, and thigh circumference measurements. *American Journal of Obstetrics and Gynecology*, 1987,157:410-414. PMID:3618691
- Warsof SL, Gohari P, Berkowitz RL, Hobbins JC. The estimation of fetal weight by computer-assisted analysis. *American Journal of Obstetrics and Gynecology*, 1977,128:881-892. PMID:888868

Gynaecology

- Callen PW. *Ultrasonography in obstetrics and gynecology*, 5th ed. Philadelphia, Saunders-Elsevier, 2008.
- Fulghesu AM et al. Ultrasound in polycystic ovary syndrome – the measuring of ovarian stroma and relationship with circulating androgens: results of a multicentric study. *Human Reproduction (Oxford, England)*, 2007,22:2501-2508. doi:10.1093/humrep/dem202 PMID:17635847
- Chang HC, Bhatt S, Dogra . VS. Pearls and pitfalls in diagnosis of ovarian torsion. *Radiographics*, 2008,28:1355-1368. doi:10.1148/rg.285075130 PMID:18794312
- Junqueira BLP et al. Müllerian duct anomalies and mimics in children and adolescents: correlative intraoperative assessment with clinical imaging. *Radiographics*, 2009,29:1085-1103. doi:10.1148/rg.294085737 PMID:19605658
- Timmerman D et al. Logistic regression model to distinguish between the benign and malignant adnexal mass before surgery: a multicenter study by the International Ovarian Tumor Analysis Group. *Journal of Clinical Oncology*, 2005,23:8794-8801. doi:10.1200/JCO.2005.01.7632 PMID:16314639
- Rumack CM, Wilson SR, Charboneau JW, Johnson J-AM, eds. *Diagnostic ultrasound*. St Louis, Elsevier Mosby, 2005.
- Savelli L, Cacciatore B. Salpinges. In: *Gynecological and early pregnancy ultrasound* [ISUOG Educational series]. London, International Society of Ultrasound in Obstetrics and Gynecology, 2003.
- Twickler DM, Moschos E. Ultrasound and assessment of ovarian cancer risk. *AJR. American Journal of Roentgenology*, 2010,194:322-329. doi:10.2214/AJR.09.3562 PMID:20093591
- Varras M et al. Tubo-ovarian abscesses: spectrum of sonographic findings with surgical and pathological correlations. *Clinical and Experimental Obstetrics & Gynecology*, 2003,30:117-121. PMID:12854857

Breast

- Athanasiou A et al. How to optimize breast ultrasound. *European Journal of Radiology*, 2009,69:6-13. doi:10.1016/j.ejrad.2008.07.034 PMID:18818037
- Boisserie-Lacroix M et al. Breast ultrasonography: an overview. *Gynecologie, Obstetrique & Fertilite*, 2006,34:1170-1177. doi:10.1016/j.gyobfe.2006.10.015 PMID:17140836

- Chen SC et al. Analysis of sonographic features for the differentiation of benign and malignant breast tumors of different sizes. *Ultrasound in Obstetrics & Gynecology*, 2004,23:188-193. doi:10.1002/uog.930 PMID:14770402
- Coll D. Breast tumor imaging. *Cancer Treatment and Research*, 2008,143:515-546. doi:10.1007/978-0-387-75587-8_20 PMID:18619231
- Costantini M et al. Characterization of solid breast masses: use of the sonographic breast imaging reporting and data system lexicon. *Journal of Ultrasound in Medicine*, 2006,25:649-659. PMID:16632790
- Costantini M et al. L. Solid breast mass characterisation: use of the sonographic BI-RADS classification. *La Radiologia Medica*, 2007,112:877-894. doi:10.1007/s11547-007-0189-6 PMID:17885742
- Gokalp G, Topal U, Kizilkaya E.. Power Doppler sonography: anything to add to BI-RADS US in solid breast masses? *European Journal of Radiology*, 2009,70:77-85. doi:10.1016/j.ejrad.2007.12.007 PMID:18243623
- Heywang-Koebrunner S, Schreer D, Dershaw I. *Diagnostic breast imaging mammography, sonography, magnetic resonance imaging, and interventional procedures,* 2nd edition. Stuttgart, Thieme, 2001.
- Hines N, Slanetz PJ, Eisenberg RL. Cystic masses of the breast. *AJR. American Journal of Roentgenology*, 2010,194:W122-W133. doi:10.2214/AJR.09.3688 PMID:20093563
- Hong AS et al. BI-RADS for sonography: positive and negative predictive values of sonographic features. *AJR. American Journal of Roentgenology*, 2005,184:1260-1265. PMID:15788607
- McCavert M et al. Ultrasound is a useful adjunct to mammography in the assessment of breast tumours in all patients. *International Journal of Clinical Practice*, 2009,63:1589-1594. doi:10.1111/j.1742-1241.2009.02102.x PMID:19686337
- Moon HJ et al. Probably benign breast lesions on ultrasonography: a retrospective review of ultrasonographic features and clinical factors affecting the BI-RADS categorization. *Acta radiologica (Stockholm, Sweden: 1987)*, 2010,51:375-382. doi:10.3109/02841851003662780 PMID:20350247
- Nicholson BT et al. Nipple–areolar complex: normal anatomy and benign and malignant processes. *Radiographics*, 2009,29:509-523. doi:10.1148/rg.292085128 PMID:19325062
- Raza S et al. US of breast masses categorized as BI-RADS 3, 4, and 5: pictorial review of factors influencing clinical management. *Radiographics*, 2010,30:1199-1213. doi:10.1148/rg.305095144 PMID:20833845
- Rinaldi P et al. Cystic breast lesions: sonographic findings and clinical management. *Journal of Ultrasound in Medicine*, 2010,29:1617-1626. PMID:20966473
- Smith GE, Burrows P. Ultrasound diagnosis of fibroadenoma – is biopsy always necessary? *Clinical Radiology*, 2008,63:511-515. doi:10.1016/j.crad.2007.10.015 PMID:18374713
- Stavros AT et al. Solid breast nodules: use of sonography to distinguish between benign and malignant lesions. *Radiology*, 1995,196:123-134. PMID:7784555
- Yang W, Dempsey PJ. Diagnostic breast ultrasound: current status and future directions. In: Sickles EA, ed. Breast imaging. *Radiologic Clinics of North America*, 2007,45:845-861. doi:10.1016/j.rcl.2007.06.009 PMID:17888773

Paediatric ultrasound

- Bianchi S, Martinoli C. *Ultrasound of the Musculoskeletal system*. Berlin, Springer-Verlag, 2007.
- Bruyn R. *Paediatric ultrasound: how, why and when*. Philadelphia, Churchill Livingstone, 2005.
- Chateil J, Brisse H, Dacher J. Ultrasound in pediatric urology. *Journal de Radiologie*, 2001,82:781-800. PMID:11443296
- Devred P, Tréguier C, Ducou-Le-Pointe H. Echography of the hip and other imaging techniques in pediatrics. *Journal de Radiologie*, 2001,82:803-816. PMID:11443297
- Donnelly LF. *Pediatric Imaging: the fundamentals*. Saunders-Elsevier, 2009.
- *Effective choices for diagnostic imaging in clinical practice* [WHO Technical Report Series 795]. Geneva, World Health Organization, 1990: 144.
- Garel L et al. US of the pediatric female pelvis: a clinical perspective. *Radiographics*, 2001,21:1393-1407. PMID:11706212
- Gervais DA et al. Percutaneous imaging-guided abdominal and pelvic abscess drainage in children. *Radiographics*, 2004,24:737-754. doi:10.1148/rg.243035107 PMID:15143225
- Kuhn JP, Slovis TL, Haller JO. *Caffey's Pediatric Diagnostic Imaging*, 10th ed. Philadelphia, Elsevier/Mosby, 2003.
- Levy JA, Noble VE. Bedside ultrasound in pediatric emergency medicine. *Pediatrics*, 2008,121:e1404-1412. doi:10.1542/peds.2007-1816 PMID:18450883
- Lowe LH, Johanek AJ, Moore CW. Sonography of the neonatal spine: part 1, Normal anatomy, imaging pitfalls, and variations that may simulate disorders. *AJR. American Journal of Roentgenology*, 2007,188:733-738. doi:10.2214/AJR.05.2159 PMID:17312061
- Lowe LH, Johanek AJ, Moore CW. Sonography of the neonatal spine: part 2, Spinal disorders. *AJR. American Journal of Roentgenology*, 2007,188:739-744. doi:10.2214/AJR.05.2160 PMID:17312062
- Lucaya J, Strife JL. *Paediatric chest imaging*. Berlin, Springer 2002.
- Petit P, Pracros J. Role of ultrasound in children with emergency gastrointestinal diseases. *Journal de Radiologie*, 2001,82:764-778. PMID:11443295
- *Rational use of diagnostic imaging in paediatrics* [WHO Technical Report Series 757]. Geneva, World Health Organization, 1987
- Rosenberg HK. Sonography of pediatric neck masses. *Ultrasound Quarterly*, 2009,25:111-127. doi:10.1097/RUQ.0b013e3181b6720b PMID:19730051
- Sivit CJ. Imaging children with abdominal trauma. *AJR. American Journal of Roentgenology*, 2009,192:1179-1189. doi:10.2214/AJR.08.2163 PMID:19380540
- Stringer DA, Babyn PS, eds. *Pediatric gastrointestinal imaging and intervention*, 2nd ed. London, BC Decker Inc Hamilton, 2000
- *Training in diagnostic ultrasound: essentials, principles and standards* [WHO Technical Report Series 875]. Geneva, World Health Organization, 1998

Musculoskeletal system

- Al-Shawi A et al. The detection of full thickness rotator cuff tears using ultrasound. *The Journal of Bone and Joint Surgery. British Volume*, 2008,90:889-892. doi:10.1302/0301-620X.90B7.20481 PMID:18591598
- Beggs I. Ultrasound of the shoulder and elbow. *The Orthopedic Clinics of North America*, 2006,37:277-285. doi:10.1016/j.ocl.2006.03.004 PMID:16846761
- Blum A, Carillon Y, Railhac J et al. Instability [Chapter 10]. In: Davies AM, Hodler J. *Imaging of the shoulder: techniques & applications*. Heidelberg, Springler-Verlag, 2005.
- Davies AM, Whitehouse RW, Jenkins JPR. *Imaging of the foot & ankle.* Heidelberg, Springer, 2003:179–199.
- De Maeseneer M et al. Sonography of the normal ankle: a target approach using skeletal reference points. *AJR. American Journal of Roentgenology*, 2009,192:487-495. doi:10.2214/AJR.08.1316 PMID:19155415
- Dong Q, Fessell DP. Achilles tendon ultrasound technique. *AJR. American Journal of Roentgenology*, 2009,193:W173- doi:10.2214/AJR.09.3111 PMID:19696253
- Fessell DP, Jacobson JA. Ultrasound of the hindfoot and midfoot. *Radiologic Clinics of North America*, 2008,46:1027-1043. doi:10.1016/j.rcl.2008.08.006 PMID:19038611
- Finlay K, Friedman L. Ultrasonography of the lower extremity. *The Orthopedic Clinics of North America*, 2006,37:245-275. doi:10.1016/j.ocl.2006.03.002 PMID:16846760
- Ilaslan H, Sundaram M. Advances in musculoskeletal tumor imaging. *The Orthopedic Clinics of North America*, 2006,37:375-391. doi:10.1016/j.ocl.2006.05.003 PMID:16846768
- Jamadar DA et al. Musculoskeletal sonography technique: focused versus comprehensive evaluation. *AJR. American Journal of Roentgenology*, 2008,190:5-9. doi:10.2214/AJR.07.2433 PMID:18094286
- Khoury V et al. Musculoskeletal sonography: a dynamic tool for usual and unusual disorders. *AJR. American Journal of Roentgenology*, 2007,188:W63-73. doi:10.2214/AJR.06.0579 PMID:17179329
- McNally E. *Practical musculoskeletal ultrasonography*. Philadelphia, PA, Churchill Livingstone, 2005.
- Meyers PR et al. Shoulder ultrasound. *AJR. American Journal of Roentgenology*, 2009,193:W174- doi:10.2214/AJR.09.3229 PMID:19542411
- Nazarian LN. The top 10 reasons musculoskeletal sonography is an important complementary or alternative technique to MRI. *AJR. American Journal of Roentgenology*, 2008,190:1621-1626. doi:10.2214/AJR.07.3385 PMID:18492916
- Robinson P. Sonography of common tendon injuries. *AJR. American Journal of Roentgenology*, 2009,193:607-618. doi:10.2214/AJR.09.2808 PMID:19696272
- Zlatkin MB. Shoulder instability [Chapter 7]. In: Zlatkin MB. *MRI of the shoulder*, 2nd ed. Philadelphia, PA, Lippincott Williams & Wilkins, 2003.

Index

Notes

Pages numbers ending in f refer to figures
Pages numbers ending in t refer to tables

[A]

[B]

[C]

[D]

[G]

[H]

[N]

[O]

[S]

[T]

[U]

[W]

[X]

[Y]

[Z]